frontiers | Research Topics

Correlative light and volume electron microscopy: Methods and applications

Edited by
Christopher Guerin, Feng-Xia Alice Liang and Saskia Lippens

Published in
Frontiers in Cell and Developmental Biology
Frontiers in Molecular Biosciences

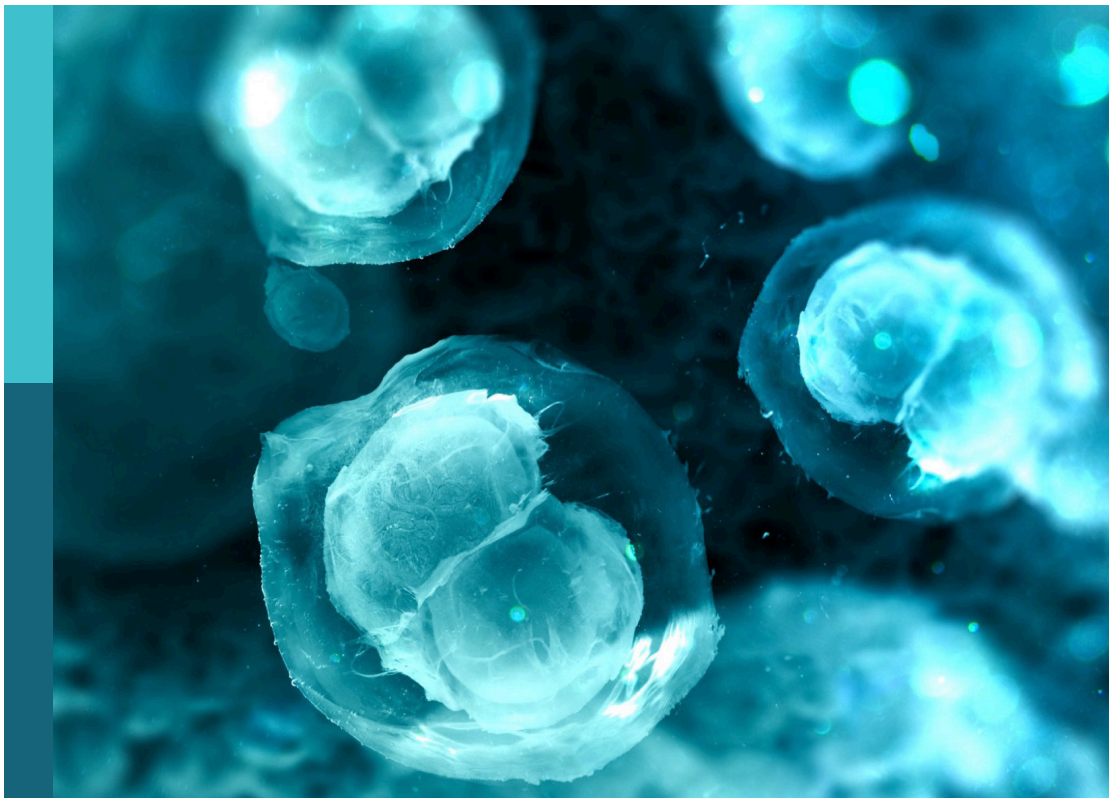

ISSN 1664-8714
ISBN 978-2-83251-605-8
DOI 10.3389/978-2-83251-605-8

About Frontiers

Frontiers is more than just an open access publisher of scholarly articles: it is a pioneering approach to the world of academia, radically improving the way scholarly research is managed. The grand vision of Frontiers is a world where all people have an equal opportunity to seek, share and generate knowledge. Frontiers provides immediate and permanent online open access to all its publications, but this alone is not enough to realize our grand goals.

Frontiers journal series

The Frontiers journal series is a multi-tier and interdisciplinary set of open-access, online journals, promising a paradigm shift from the current review, selection and dissemination processes in academic publishing. All Frontiers journals are driven by researchers for researchers; therefore, they constitute a service to the scholarly community. At the same time, the *Frontiers journal series* operates on a revolutionary invention, the tiered publishing system, initially addressing specific communities of scholars, and gradually climbing up to broader public understanding, thus serving the interests of the lay society, too.

Dedication to quality

Each Frontiers article is a landmark of the highest quality, thanks to genuinely collaborative interactions between authors and review editors, who include some of the world's best academicians. Research must be certified by peers before entering a stream of knowledge that may eventually reach the public - and shape society; therefore, Frontiers only applies the most rigorous and unbiased reviews. Frontiers revolutionizes research publishing by freely delivering the most outstanding research, evaluated with no bias from both the academic and social point of view. By applying the most advanced information technologies, Frontiers is catapulting scholarly publishing into a new generation.

What are Frontiers Research Topics?

Frontiers Research Topics are very popular trademarks of the *Frontiers journals series*: they are collections of at least ten articles, all centered on a particular subject. With their unique mix of varied contributions from Original Research to Review Articles, Frontiers Research Topics unify the most influential researchers, the latest key findings and historical advances in a hot research area.

Find out more on how to host your own Frontiers Research Topic or contribute to one as an author by contacting the Frontiers editorial office: frontiersin.org/about/contact

Correlative light and volume electron microscopy: Methods and applications

Topic editors

Christopher Guerin — Flemish Institute for Biotechnology, Belgium

Feng-Xia Alice Liang — New York University, United States

Saskia Lippens — Flemish Institute for Biotechnology, Belgium

Citation

Guerin, C., Liang, F.-X. A., Lippens, S., eds. (2023). *Correlative light and volume electron microscopy: Methods and applications*. Lausanne: Frontiers Media SA. doi: 10.3389/978-2-83251-605-8

Table of contents

frontiers in Cell and Developmental Biology

ORIGINAL RESEARCH
published: 15 December 2021
doi: 10.3389/fcell.2021.737621

Preservation of Fluorescence Signal and Imaging Optimization for Integrated Light and Electron Microscopy

Pieter Baatsen[1,2], *Sergio Gabarre*[1,2,3], *Katlijn Vints*[1,2], *Rosanne Wouters*[2,4], *Dorien Vandael*[1,2], *Rose Goodchild*[2,5], *Sebastian Munck*[2,3]* *and Natalia V. Gounko*[1,2]*

[1]*VIB-KU Leuven Center for Brain and Disease Research, Electron Microscopy Platform and VIB-Bioimaging Core, Leuven, Belgium,* [2]*KU Leuven Department of Neurosciences, Leuven Brain Institute, Leuven, Belgium,* [3]*VIB-KU Leuven Center for Brain and Disease Research, Light Microscopy Expertise Unit and VIB Bioimaging Core, Leuven, Belgium,* [4]*VIB-KU Leuven Center for Brain and Disease Research, Laboratory for Membrane Trafficking, Leuven, Belgium,* [5]*VIB-KU Leuven Center for Brain and Disease Research, Laboratory for Dystonia Research, Leuven, Belgium*

OPEN ACCESS

Edited by:
Feng-Xia Alice Liang,
NYU Grossman School of Medicine, United States

Reviewed by:
Kirk James Czymmek, Donald Danforth Plant Science Center, United States
Ira Kurtz, University of California, Los Angeles, United States
Richard Webb, The University of Queensland, Australia
Christopher Peddie, Francis Crick Institute, United Kingdom

***Correspondence:**
Sebastian Munck
sebastian.munck@kuleuven.vib.be
Natalia V. Gounko
natalia.gunko@kuleuven.vib.be

Specialty section:
This article was submitted to Cellular Biochemistry, a section of the journal Frontiers in Cell and Developmental Biology

Received: *07 July 2021*
Accepted: *25 November 2021*
Published: *15 December 2021*

Citation:
Baatsen P, Gabarre S, Vints K, Wouters R, Vandael D, Goodchild R, Munck S and Gounko NV (2021) Preservation of Fluorescence Signal and Imaging Optimization for Integrated Light and Electron Microscopy. Front. Cell Dev. Biol. 9:737621. doi: 10.3389/fcell.2021.737621

Life science research often needs to define where molecules are located within the complex environment of a cell or tissue. Genetically encoded fluorescent proteins and or fluorescence affinity-labeling are the go-to methods. Although recent fluorescent microscopy methods can provide localization of fluorescent molecules with relatively high resolution, an ultrastructural context is missing. This is solved by imaging a region of interest with correlative light and electron microscopy (CLEM). We have adopted a protocol that preserves both genetically-encoded and antibody-derived fluorescent signals in resin-embedded cell and tissue samples and provides high-resolution electron microscopy imaging of the same thin section. This method is particularly suitable for dedicated CLEM instruments that combine fluorescence and electron microscopy optics. In addition, we optimized scanning EM imaging parameters for samples of varying thicknesses. These protocols will enable rapid acquisition of CLEM information from samples and can be adapted for three-dimensional EM.

Keywords: in-resin-fluorescence, correlated light and electron microscope, integrated light and electron microscope, electron microscopy, light microscopy

INTRODUCTION

Our ability to define the molecular and cellular mechanisms of life often requires that specific molecules are detected in cell or tissue samples in the context of various subcellular structures. Correlative light and electron microscopy (CLEM) does so by marking target molecules in a sample in such a way that they can be visualized by light microscopy (LM), and their cellular context studied by electron microscopy (EM). CLEM has been practiced in a more rudimentary form for many years, employing enzyme-based (e.g., horseradish peroxidase) markers and specific stains, and using mainly transmission electron microscopy (TEM) of osmicated thin sections. However, CLEM has evolved over the last decade to a more mature methodology with different approaches, specialized equipment and employing both scanning electron microscopy (SEM) and TEM (Müller-Reichert and Verkade, 2012). Currently, the most frequent way of marking molecules of interest is by using fluorescent tags and then correlating fluorescence with ultrastructural EM imaging of the same sample. Of particular interest are approaches that image living cells using fluorescence microscopy (FM) and then correlate

these data with EM images acquired after fixation, high-pressure freezing, and freeze-substitution (Brown et al., 2009). Alternatively, fluorescence in a region of interest can be imaged, outlined by laser branding, and the laser marks re-identified in EM for post-hoc co-registration of the two images (Urwyler et al., 2014; Vints et al., 2021). However, these methods are time-consuming and are often comparatively imprecise. The problem of inaccurate correlation represents a major issue for understanding the relationship between individual molecules and small subcellular structures, for example, intracellular vesicles, organelle contact sites, and small subcellular domains such as the neuronal synapse.

A fundamental issue in achieving high accuracy CLEM is that most FM samples are hundreds of nanometers or micrometers thick, while TEM requires ultrathin sections (50–100 nm). Therefore, the best way to alleviate the Z-integration problem is to simultaneously image the same thin section with both types of microscopy. New specialized CLEM instruments have been developed that combine FM and EM optics in one unit to facilitate this approach (Agronskaia et al., 2008; Peddie et al., 2014). While one type of integrated light and electron microscope (ILEM) combines fluorescence optics with TEM (Agronskaia et al., 2008), the majority are SEMs. One representative ILEM, used here, has a stage with fluorescent optics and an adapter (SECOM-stage, Delmic, Delft, Netherlands, see also Zonnevylle et al., 2013) that couples to a JEOL JSF7200 SEM (Tokyo, Japan).

Successful CLEM with these instruments still requires that samples are prepared and labeled in ways that are compatible with both forms of microscopy. FM is typically done with minimal treatments, so molecules retain their native state and structure, and, as a result, fluorescent proteins retain fluorescence and macromolecules retain antigenicity. In contrast, EM requires multiple treatments that alter macromolecular structures. Firstly, the biological material is primarily composed of chemical elements with low atomic numbers (carbon, oxygen, nitrogen, hydrogen) that poorly scatter electrons and thus provide inherently low EM contrast (Reimer and Kohl, 2008). Consequently, EM imaging is typically performed after biological samples are incubated with compounds containing high-atomic-number elements and that bind to cellular structures like membranes and nucleic acids. Secondly, high-resolution EM requires ultrathin sections of plastic embedded samples. In order to prevent loss of cell-components like proteins, membranes, etc. by extraction during dehydration and infiltration of the plastic, samples are treated to form a crosslinked and stable structure. This requires chemicals like glutaraldehyde and osmium tetroxide, which alter the structure of most macromolecules and strongly quench fluorescence signals in the sample (pre-processing fluorescence; for example, from genetically encoded fluorescent proteins or antibodies labeling). These treatments also impair affinity labeling, like immunolabeling, and thereby reduce post-embedding fluorescent signals (Griffiths, 1993; Watanabe et al., 2011).

Sample fluorescence that remains preserved after embedding is referred to as in-resin fluorescence (IRF). IRF is achievable via high-pressure freezing, freeze-substitution, and the use of acrylic embedding resins such as Unicryl, Lowicryl, or LR White. In particular, Lowicryl resins can be polymerized by UV at sub-zero temperatures, which is beneficial for the preservation of membranes and protein structures (Kukulski et al., 2011; Bharat et al., 2018). With interest in CLEM, their use has been described for cultured cells (Peddie et al., 2014, 2017) and zebrafish embryos (Nixon et al., 2009). It also enabled the correlation of single-molecule localization microscopy and SEM (Johnson et al., 2015). It appears that the presence of water in the substitution medium improves the visualization of membranes (Walther and Ziegler, 2002) and plays a role in the fluorescence of GFP. This latter effect was demonstrated by the re-occurrence of GFP-fluorescence that had faded under high-vacuum upon allowing water to evaporate and enter the high-vacuum chamber of the SEM containing the GFP sample (Brama et al., 2015). This could be compatible with the fact that relaxation of the excited state of GFP is related to a proton transfer chain that includes water (Tsien, 1998). In line with this, reportedly (Peddie et al., 2014), a short freeze-substitution protocol (Mcdonald and Webb, 2011) as opposed to a longer one such as applied to zebrafish embryo's (Nixon et al., 2009), appears necessary for retaining fluorescence in cells. The much smaller cells would become too dehydrated with the longer FS-times necessary to prepare the larger zebrafish embryo's optimally. Nonetheless, this subject still contains unknown factors, and successful results have been obtained with longer FS-times and cells (e.g., Kukulski et al., 2011). Here, with this in mind, we tested different sample preparation conditions to optimize IRF, resulting in a CLEM imaging method where IRF is used to define the identity of specific neurons in ultrastructural images of the mouse brain imaged with ILEM.

We also explore how to best use SEM to derive detailed ultrastructure from thin sections. SEM- and ILEM-imaging of thin sections uses backscattered electrons, as this signal discriminates between atoms with high and low atomic numbers. Therefore, biological samples are typically treated with, amongst others, uranyl acetate to achieve this contrast. There are, however, additional parameters that affect image quality. In the past, other groups have obtained results with SEM-imaging of similar preparations using different accelerating voltages and instruments, while information on other parameters was sparse or lacking (Peddie et al., 2014; Markert et al., 2016; Bouwer et al., 2017). More recently, it was shown that biasing the sample can ameliorate SEM-imaging of sections (Vos et al., 2021). In this study, we show how different imaging parameters affect image quality and propose guidelines on how to optimize basic SEM settings in function of section thickness for high-resolution thin-section imaging.

Finally, all of the above considerations and the findings in this paper are equally well applicable to 3D-CLEM by array tomography, whether performing fluorescent and electron imaging on separate equipment or using an ILEM as also used in this study.

MATERIALS AND METHODS

Animals

All animal experiments were approved by the KU Leuven Ethical Committee (protocol P019/2017) and were performed in accordance with the Animal Welfare Committee guidelines of

the KU Leuven, Belgium. In total, the brains of two 4 C57BL/6 mice and 2 virus-injected C57BL/6 mice at P21 were used. Mice were euthanized with a mixture of ketamine and xylazine as per institutional guidelines.

The lentiviral vectors harboring a green fluorescent protein (GFP) reporter were kindly provided by Dr. J. de Wit (Schroeder and De Wit, 2018). At P0, mouse pups mice were used for neonatal stereotaxic virus injection. Pups were anesthetized by hypothermia and then stabilized on a glass Petri dish filled with ice to sustain anesthesia during the injection. After disinfection of the injection area with 70% EtOH, 20 nl (around 1,010 transducing units/ml; diluted 1:10 in 1x PBS) of high titer lentivirus with a non-targeting shRNA viral control vector (TTCTCCGAACGTGTCACGT) (Wang et al., 2012) was injected with a speed of 4 nl/s directly through the skin and skull using a Nanoject II Auto-Nanoliter Injector (Drummond). Bilateral injections in CA1 hippocampus were made using a depth of 1.1 mm, with two injections per brain hemisphere.

Mice were transcardially perfused with 10 ml of 4% paraformaldehyde (PFA) (#15714, EMS, United States) in 0.1 M phosphate buffer, pH 7.4 (hereafter "PB") for 10 min and then the brains were postfixed overnight in the same solution at 4°C. Next day, after washing twice in PB, 100 μm-thick coronal vibratome sections of virus injection hippocampus and 80 μm-thick sagittal vibratome sections of the cerebellum were made from. The discs of 1.35 mm of ROI were cut from the vibratome sections of the hippocampus and cerebellum with a punch and submerged in 10% of BSA in 0.1 M PB solution as a cryo-filler.

Cell Culture

All culture media and sera are from Life Technologies. HeLa cells expressing GFP in the cytoplasm were routinely grown in Dulbecco's modified Eagle's medium (DMEM/F12) supplemented with 10% fetal calf serum (FCS) and cultured in 10 cm Petri dishes. All cells were maintained in a humidified chamber with 5% CO2 at 37°C.

HeLa PSEN1/PSEN2 knockout (HeLa dKO) cells were generated with CRISPR/Cas9 genome editing as described (Sannerud et al., 2016). Shortly, HeLa cells were double transfected using JetPrime (Polyplus) with the pX330 plasmid containing guide sequences against the genomic sequence target for both PSEN1 (5′- ATGAGCCACGCAGTCCATTC -3′) and PSEN2 (5′-TGTCACTCTGTGCATGATCG-3′). dKO clones were selected by serial dilution. Full knockout was confirmed by genomic sequencing and western blot analysis. For stable GFP expression, lentiviral particles were produced by co-transfection of Hek293 T cells with lentiviral plasmid (pCHMWS-GFP), packaging plasmid (pCMV ΔR8.74) and envelope (pMD2. G) plasmid using JetPRIME (Polyplus). HeLa dKO cells were transduced with these viral particles diluted in normal cell culture medium containing polybrene (8 ng/μl, Sigma). Cells stably expressing GFP were selected with puromycin (3 μg/ml, Sigma) 24 h after transduction.

In order to prevent proteolysis during the variable waiting periods before actual high-pressure freezing, cells were fixed with 4% PFA in 0.1 M PB pH7.4, then washed, scraped and pelleted in the same buffer to a final volume of 1.5 ml. Alternatively, cells were not fixed at first but exposed to 0.05% Trypsin-EDTA (#253000-054, Gibco, United States) to detach from the bottom of the culture plate, washed with 0.1 M PB and pelleted, and then finally fixed. In both cases, after pelleting the cells at 200xg, they were resuspended in 10% BSA (A9647, Sigma-Aldrich) as a cryo-filler, and finally pelleted at 1000xg.

Immunolabeling

The cerebellar sections were washed three times in 0.1 M PB pH7.4 on ice for 10 min and incubated in 0.3% hydrogen peroxide (H1009, Sigma-Aldrich) in the same buffer for 30 min on ice. After three washes with the same buffer again, sections were incubated in 0.5% sodium borohydride (#71320, Sigma-Aldrich) for 30 min at room temperature, followed by three 10 min washes with 0.1 M PB. The sections were incubated in blocking buffer containing 1% BSA, 0.01% glycine (G7126, Sigma-Aldrich), 0.01% lysin (L5501, Sigma-Aldrich), 1% normal donkey serum (D9663, Sigma-Aldrich), 0.05% Triton X-100 (#22146, EMS), 0.1% cold water fish gelatin (#25560, EMS) in 0.1 M PB for 2 h on ice. Samples were stained with primary antibody, mouse anti-Calbindin-D28 K (#AgCB10 abs, Swant, Switzerland), at 1:5,000 dilution in the same blocking buffer, at 4°C overnight. The following day, slices were washed four times in 0.1 M PB on ice and probed with secondary antibody, donkey anti-mouse conjugated to Alexa Fluor 488 (A-21202, Invitrogen) at 1:200 dilution in blocking buffer for 2 h on ice.

High-Pressure Freezing (HPF) and Freeze-Substitution (FS)

For high-pressure freezing, cells or discs (1.35 mm diameter) punched out of hippocampal or cerebellar tissue slices (100 μm thick) were loaded in membrane carriers of a HPF (Leica EMPACT2) and vitrified at 2050 bar. The frozen carriers were stored under liquid nitrogen until further processing.

The frozen samples were freeze-substituted in a Leica AFS2 apparatus using our protocol (see below and **Table 1**) based on the original quick-freeze substitution (QFS) protocol (Mcdonald and Webb, 2011; Peddie et al., 2014), In addition, we constructed a sample holder to hold the samples during the QFS-run, but that fits snugly into the Leica AFS2 apparatus as well, and facilitating the transfer of the carriers from QFS-holder to the flow rings of the AFS (see **Supplementary Figure S2**).

Briefly, the membrane carriers with samples were transferred to cryotubes (72.694.005, Sarstedt, Germany) with 1.5 ml of freeze-substitution (FS) medium, containing 0.1, 0.2, or 0.5% uranyl acetate (#02624-AB, SPI) and 5% dH_2O in acetone (#1002990500, Merck), and placed in a QFS-holder. After loading the QFS-holder at −180°C, the liquid nitrogen was removed from the QFS-box, the box was closed and allowed to reach −80°C. After reaching −80°C temperature, the QFS-holder was tipped on its side, the box closed again and agitated on a rotary shaker at 50 cycles/min. The temperature was monitored, and at −50°C, the QFS was stopped and the QFS-holder transferred swiftly to the waiting pre-cooled to −50°C Leica AFS2 apparatus. Our holder fits precisely in the space left in the AFS2 chamber when solution exchange bottles are left out, but flow rings left in place.

TABLE 1 | IRF protocol with freeze-substitution steps after transfer of samples from QFS-box to Leica AFS2 freeze-substitution apparatus. QFS,quick-freeze substitution.

Reagent	Temp	Time	Repeats
Acetone	–50°C	20 min	2x
Ethanol	–50°C	20 min	1x
20, 40, 60, 80% HM20/ethanol	–50°C	45 min	each step 1x
100% HM20	–50°C	8 h	1x
100% HM20	–50°C	2 h	3x
100% HM20 - UV polymerization	–50°C	48 h	1x
100% HM20 - temperature rise with UV polymerization	–50 - 20 °C	16 h	1x
100% HM20 - UV polymerization	20°C	48 h	1x

After transfer of the carriers to the flow rings filled with acetone pre-cooled to −50°C, the QFS-holder is removed from the chamber and solution exchange bottles, filled with acetone, ethanol (#7103, VWR) and Lowicryl HM20 (#02628-AB, SPI), are inserted in the AFS2 chamber. The first bottle of acetone for washing is already pre-cooled to −50°C during transfer of the carriers and the remaining bottles are cooled to −50°C during the first two washing steps with acetone. The samples are kept in their cryotubes with FS medium at −50°C until the time elapsed from the moment the temperature had reached −80°C (start of agitation) had reached 1.5 h. This is comparable with the protocol by Peddie et al. (Peddie et al., 2014), who try to keep the time elapsed from the insertion of the carriers onto the frozen FS-medium (about −150°C) until the start of washing in acetone at −50°C, the same for every FS run at 3 h. In our case, we chose not to take the melting point of acetone (−95°C) as starting point; taking −80°C as a start of this period is more relevant, as at that temperature, the FS- medium can be considered molten and enveloping the samples entirely. Furthermore, the rate of freeze-substitution at −95°C is about 0 in the presence of 5% water, (as we have used to improve membrane preservation and preserve fluorescence), as elegantly demonstrated by Humbel and Müller (1985) by following substitution rate using tritiated H2O release from the sample in the substitution medium. Even at −80°C it takes days to substitute a test strip infiltrated with methylene blue which release in the substitution medium reflects progression of the substitution process as shown earlier by Zalokar (1966). Thus, we take this period starting at −80°C till first washing step as 1.5 h. The remaining steps follow the protocol as described by Peddie (Peddie et al., 2014), except that here ethanol was used for the last step prior to infiltration by Lowicryl HM20 resin and in the infiltration mixtures (see **Table 1**). Finally, the samples were polymerized at −50°C using UV.

Microtomy and Imaging

For SEM imaging, serial sections of different thicknesses (50–500 nm) were cut on a Leica Ultracut S ultramicrotome. Sections were collected as ribbons of four to five sections on an ITO-coated coverslip [Pluk et al., (2009) resistivity 15–30 Ohm; #06472-AB, SPI], and glow-discharged in a Leica ACE600 coating unit. For TEM, ultrathin 70 nm sections were cut and deposited on 200 mesh support grids (#01801, Ted Pella, United States).

ITO coverslips with sections were mounted to a holder that could be fitted onto the SECOM stage (DELMIC, Delft, Netherlands), which in turn was mounted to a door that would fit the SEM (JSM 7200F LV, JEOL, Japan), comprising our ILEM. This way, the same area of interest could be observed by fluorescence imaging with a Plan Apo VC 100x oil immersion objective lens with a NA of 1.4 (SECOM), followed by electron imaging (SEM). In several tests (**Figures 2–4, Figure 6**), sections were imaged by recording BSE signals in a Zeiss VP Sigma SEM and a Gatan OnPoint BSE-detector. When needed for improving EM imaging, after imaging with ILEM-SEM (**Figure 7C** and **Figure 8A–C**, left), we post-stained the ITO coverslip with 4% uranyl acetate and Reynold's lead citrate (Reynolds, 1963) before imaging again the same ITO coverslip (**Figure 8C**, middle and right).

For observation of ultrastructural details, images were taken with a TEM (JEM1400-LaB6, JEOL, Japan) operated at 80 kV and equipped with an Olympus SIS Quemesa 11 MP camera. Photographs were taken at various magnifications (0.6–20 kx). None of the grids were post-stained.

For verifying fluorescence in resin blocks we used widefield fluorescent imaging (dry, no coverslip) with a Zeiss Axioplan 2 equipped with a Hamamatsu ORCA-SPARK camera and Plan-NeoFluar 63x lens (**Figure 2A**). For fluorescent imaging prior to study in the ILEM, we mounted sections on microscopic slides without coverslips and imaged with a Nikon TiE inverted C2 confocal microscope with a Plan Apo VC 20x dry lens (**Figures 1A–D**, **Figure 2B** right, **Figure 7B**) and Plan Apo 10x dry lens (**Figure 2B** left, **Figure 7A**).

Probe current measurements in the SEM (Zeiss Sigma) were done at some different imaging parameters. To this end, a stub with a Faraday cup (#651-F, Ted Pella, Redding CA, United States) absorbing all impinging electrons and hence allowing to measure the probe current, was placed in the SEM, and imaging parameters were varied in a range typically used for imaging resin sections with biological material. For all SEM imaging in this study, a standard aperture of 30 μm was used.

Monte Carlo Simulation

For simulating interaction volumes of electrons and a carbon sample, we used the program Win XRay, (copyright 2002–2015 McGill University), by Demers, Horny, Gauvin, and Lifshin.

RESULTS AND DISCUSSION

IRF of Cultured Cells

We set out to identify conditions that optimally balance fluorescent signal retention with the preservation and contrasting of cellular structures for EM. As a starting point,

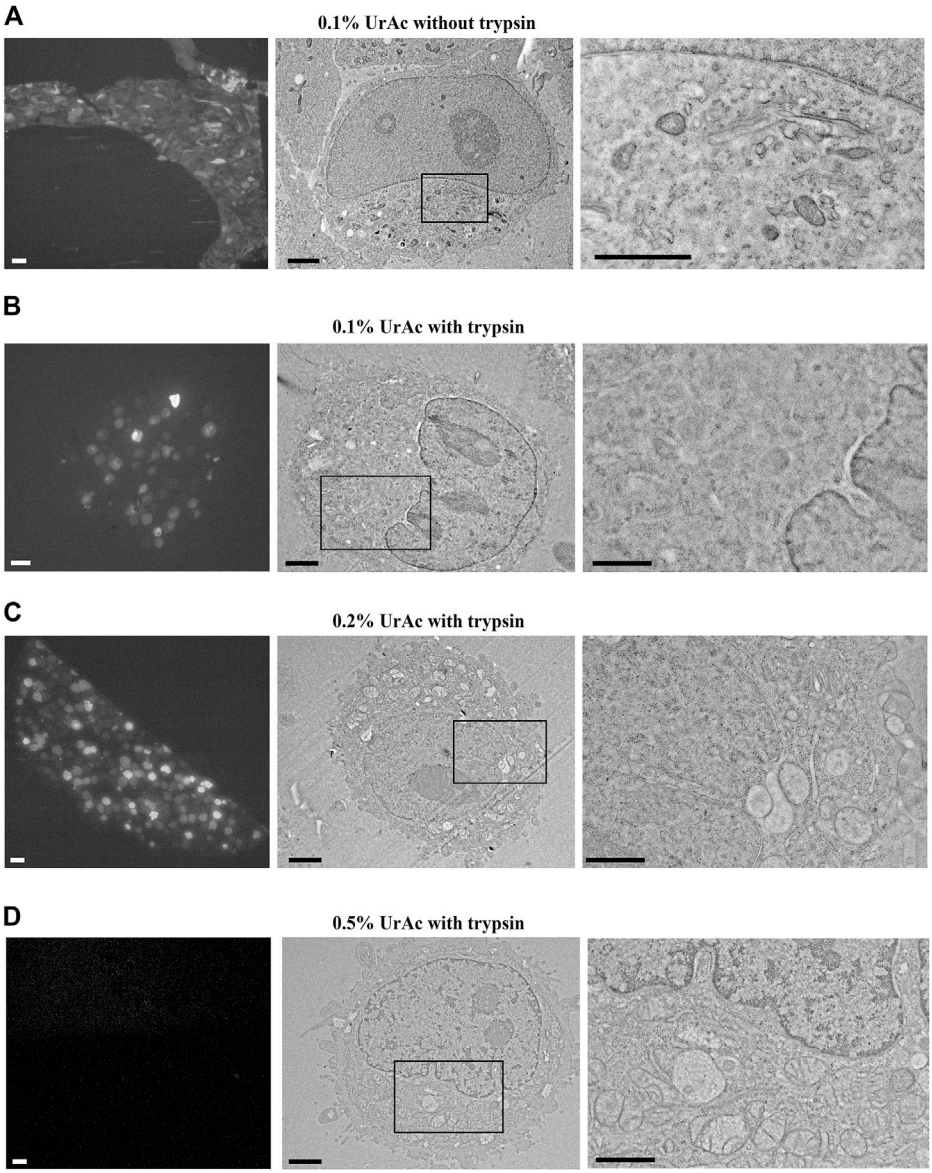

FIGURE 1 | Fluorescence and TEM micrographs of HeLa cells after IRF protocol. **(A)** Cells fixed with 4% PFA and scraped, then processed with 0.1% uranyl acetate; **(B)** Trypsinized cells freeze-substituted with 0.1% uranyl acetate; **(C, D)** Trypsinized cells freeze-substituted and processed with 0.2 and 0.5% uranyl acetate, respectively. Immunofluorescence light microscopy imaging with a Nikon TiE inverted C2 confocal with Plan Apo VC 20x dry lens **(left column)**, TEM at low and high magnification **(resp. middle and right column)**; images in the right column correspond to boxed regions. Note the preservation of fluorescence in conditions **(A–C)** and the best ultrastructure in **(C–D)**. IRF, in-resin fluorescence; PFA, paraformaldehyde; TEM, transmission electron microscopy; UrAc, uranyl acetate. Scale bars: left column = 20 μm; middle = 2 μm; right = 1 μm.

we focused on conditions described by Peddie et al. (Peddie et al., 2014), but varying uranyl acetate percentages in the substitution medium for embedding. Importantly, samples were washed with ethanol immediately prior to the first infiltration step with Lowicryl HM20 acrylic resin (see **Table 1** for details); a procedure previously reported to improve Lowicryl HM20 resin infiltration into biological samples at the end of a freeze-substitution (Monaghan et al., 1998). As pointed out (see Introduction), the presence of water is important for improved ultrastructure and fluorescence of GFP. In our current set-up, water vapor cannot enter the SEM specimen chamber, hence we verified fluorescence outside the specimen chamber.

HeLa cells expressing green fluorescent protein (GFP) were collected by fixation and scraping or by trypsinization. Scraped cells were lightly fixed (4% paraformaldehyde, PFA) to prevent excessive ultrastructural damage that could be expected to be caused by the scraping procedure. It should be noted that fixation with formaldehyde can still cause artifacts like nuclear granulation (Hayatt, 1981) and "false" septate junctions (Nistal et al., 1978). Nonetheless, for practical reasons, we have opted to

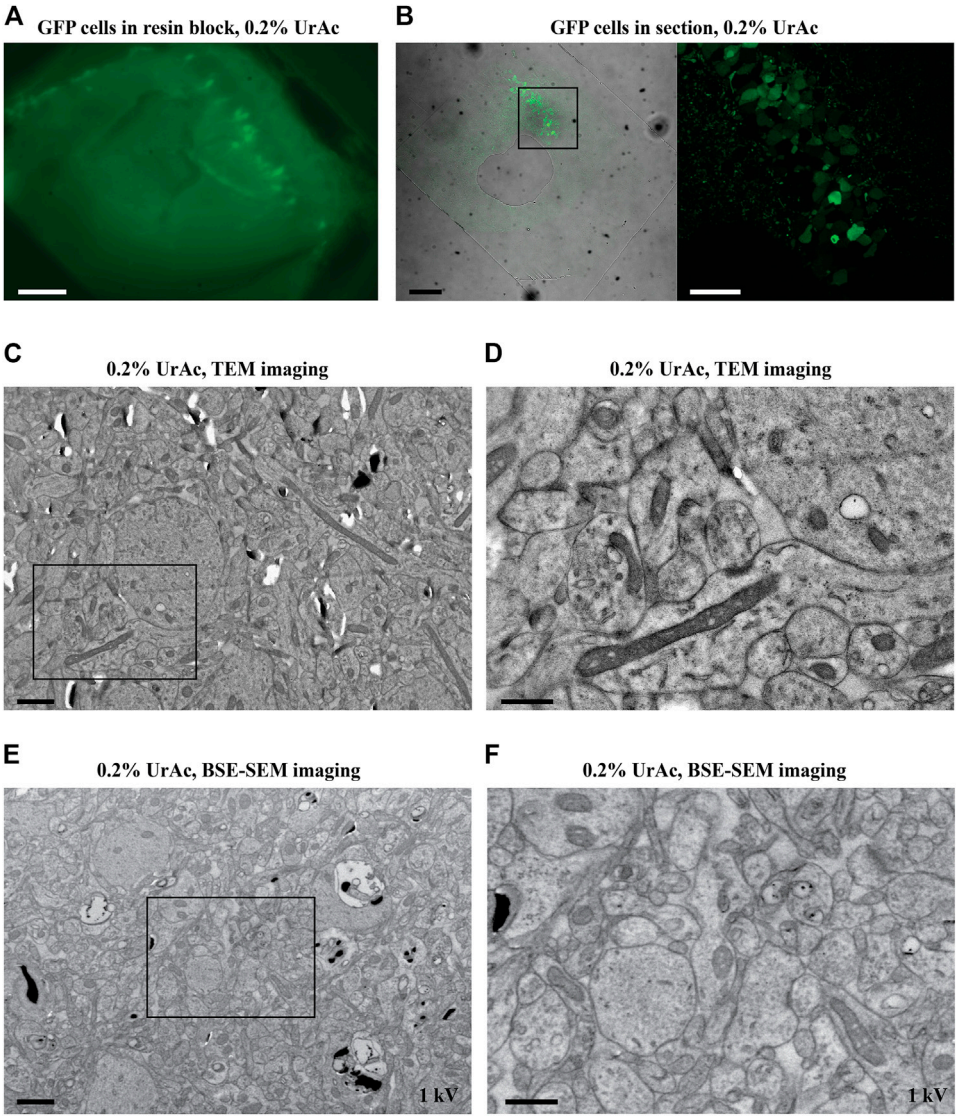

FIGURE 2 | Fluorescence and electron micrographs of mouse hippocampus tissue; IFR protocol freeze-substituted with 0.2% uranyl acetate. The fluorescent signal was preserved in a 100 µm hippocampus slice after IRF protocol as observed in the resin block imaged with widefield Zeiss Axioplan 2 with Plan-NeoFluar 63x lens. **(A)** and after thin sectioning imaged with a Nikon TiE inverted C2 confocal microscope with a Plan Apo VC 20x dry lens **(B, right)** and Plan Apo 10x dry lens **(B, left)**. An enlarged view of the area enclosed in the black square in the left image of **(B)** shows pyramidal cells in CA1 **(B**, **right)**. **(C, D)** TEM imaging of GFP positive CA1 hippocampal cells, showing good ultrastructure. **(D)** A higher magnification image of the area indicated by the black box in **C**. **(E, F)** same sample block as in **(C, D)**, but imaged by SEM using a BSE detector (Gatan OnPoint detector) at 1 kV. The image quality (inverse contrast) is comparable to TEM imaging. WD = 6 mm. Section thickness = 100 nm. Abbreviations: BSE, backscattered electrons detector; GFP, green fluorescent protein; IRF, in-resin fluorescence; SEM, scanning electron microscope; TEM, transmission electron microscopy; UrAc, uranyl acetate; WD, working distance. Scale bars: **A, B** left = 100 µm; **B**, right = 40 µm; **C, E** = 1 µm; **D, F** = 0.5 µm.

use formaldehyde fixed cells to draw a similar baseline for all the samples and relate to our tissue of interest, more specifically brain slices (see below). We tested 0.1, 0.2 or 0.5% uranyl acetate during freeze-substitution. After processing, it appeared that the fixed and scraped cells showed fluorescent signal and ultrastructure in resin sections similar to the trypsinized cells (**Figure 1A** vs **Figure 1B**). However, we found that the resin-embedded sections of HeLa cells retained strong fluorescence when treated with 0.1% or 0.2% uranyl acetate (**Figure 1A–C**, left), whereas the signal was strongly quenched by 0.5% uranyl acetate (**Figure 1D**, left). In terms of TEM, freeze-substitution with 0.1% uranyl acetate resulted in poor ultrastructural preservation, including discontinuous labeling of membranes and the appearance of empty regions of cytoplasm (**Figure 1B**, middle and right).

In contrast, many cellular structures like the Golgi apparatus, endoplasmic reticulum, and mitochondrial cristae were more easily identified in samples freeze-substituted in 0.2% uranyl

acetate (**Figure 1C**, middle and right) or 0.5% uranyl acetate (**Figure 1D**, middle and right). We concluded that 0.2% uranyl acetate provides the best compromise between fluorescence preservation and TEM detection of cellular ultrastructure. However, the tested 0.1% uranyl acetate treatment after fixing cells *in situ* on the tissue culture plates and then scraping (**Figure 1A**), displayed improved ultrastructural preservation and very well delineated small subcellular structures, even despite the sub-optimal uranyl acetate concentration. Early fixation, therefore, provides additional structural preservation and can compensate for lower uranyl acetate concentrations.

Results from earlier experiments by others (Kukulski et al., 2011) demonstrated that very nice ultrastructural preservation is possible with 0.1% uranyl acetate in the freeze-substitution medium. These results can be explained by some differences with the current study, most notably the long substitution time, but perhaps also the use of TEM (having better resolution and other contrast mechanism than SEM) and post-staining of the yeast cells. At the same time, as will be shown below, we have found that it is important to determine the best match between section thickness and accelerating voltage for BSE-SEM study of sections, and could also obtain reasonable results with 0.1% uranyl acetate (see **Figure 4**, 1 kV).

IRF of Brain Samples

We applied the optimized IRF preparation protocol for cells–freeze-substitution in 0.2% uranyl acetate (**Figure 1C**) to lightly fixed (4% PFA) mouse brain tissue where GFP was expressed in hippocampal pyramidal neurons (**Figure 2**). We opted for formaldehyde fixation despite the possibility of occurring artifacts as it prevents anoxia-induced ultrastructural changes that start to occur very early on during the sample preparation process. At the same time, formaldehyde fixation will also allow other standard preparation steps, including pre-embedding staining and other procedures on the brain slices before high-pressure freezing. We again saw well-preserved fluorescence: there was a strong fluorescent signal from the resin-embedded tissue block (**Figure 2A**), as well as the resulting thin sections (**Figure 2B**). Again, the protocol provided good contrast and preservation of ultrastructure in TEM imaging (**Figure 2C**) sufficient to resolve synapses, organelles, and other cellular details (**Figure 2D**). Next, we examined the same samples with our Zeiss Sigma SEM equipped with a backscattered electron detector (BSE; Gatan OnPoint). This SEM allows for relatively rapid navigation and optimization of SEM imaging conditions as compared to the ILEM system. This is because, with the ILEM, stage navigation is controlled by the SECOM stage control software that has no navigation functionalities such as image navigation. The optimization parameters, obtained with the Zeiss SEM and described here, were then used for imaging samples with the ILEM system in this paper. It appeared that this tissue sample also proved to be compatible with good contrast SEM imaging (**Figure 2E** and **Figure 2F**), in fact, comparable to that acquired by TEM (**Figure 2C** and **Figure 2D**). This observation is contrary to our expectations that – as mentioned in the introduction – for larger samples to combine the preservation of fluorescence and ultrastructure would require longer FS-times than for cells (Peddie et al., 2014). After all, tissue would present a "continuum" of membranes functioning as barriers reducing the diffusion rate of uranyl acetate to the core of the tissue. In the case of cells, the surrounding filler (BSA) would not pose such a barrier. We then re-tested the range of uranyl acetate concentrations in the freeze-substitution medium to determine if further improvement was possible. This was not the case, and results were in-line with the HeLa cell data (data not shown): 0.2% uranyl acetate provides better membrane contrast and definition than 0.1% uranyl acetate, while higher concentrations are incompatible with IRF.

Tuning SEM Imaging Conditions

There are several ways that SEM image acquisition settings influence image quality, in terms of signal-to-noise ratio, contrast, resolution, as well as sample charging effects. These are poorly investigated for thin section imaging and are important to define, given that they are central to achieving high-quality CLEM with an ILEM. SEM settings also interact in complex ways. For example, higher probe currents elevate the signal-to-noise ratio, but simultaneously also tend to charge the sample, resulting in drift and bad image quality; higher accelerating voltages increase resolution, but typically again at the expense of charging the sample; reduced working distance (WD) improves image resolution, but alters the collection angle for the backscattered or upper electron detectors. On top of these, sample charging is also related to (low) conductivity of the sample, which will cause local heating and hence the expansion of the sample and plastic deformation.

We first focused on the relationship between accelerating voltage and thin section image quality parameters. This experiment used trypsinized cell samples, freeze-substituted in 0.2% uranyl acetate, that performed well in TEM (**Figure 1C**). We saw gradual improvements in image contrast as we stepped the voltage from 10 to 3 kV (**Figure 3A**). Surprisingly, however, the shift from 3 to 1.5 kV (**Figure 3A**, right vs **Figure 3B–C**) remarkably improved image quality. On further inspection, we determined that improvements involved more than just altered contrast (**Figure 3A**); the transition from 10 to 3 kV (**Figure 3A**) appeared to gradually unveil ultrastructural details, which were then entirely revealed at the 1.5 kV setting (**Figure 3B** and **Figure 3C**). We also imaged a sample prepared with 0.1% uranyl acetate at the optimal 1.5 kV accelerating voltage (**Figures 3D,E**). In this case, we saw low-contrast, poorly defined membranes, alongside some charging (**Figure 3C** vs **Figure 3E**), suggesting that the concentration of high atomic number elements has a role in the background signal.

We reasoned that the as yet unknown masking of ultrastructural details (**Figure 3A**) might relate to charging of the samples. The charging of a sample occurs when not all of the electrons received by the sample can be conducted to ground or scattered by the sample, resulting in a build-up of a negative charge. This in turn repels incoming electrons

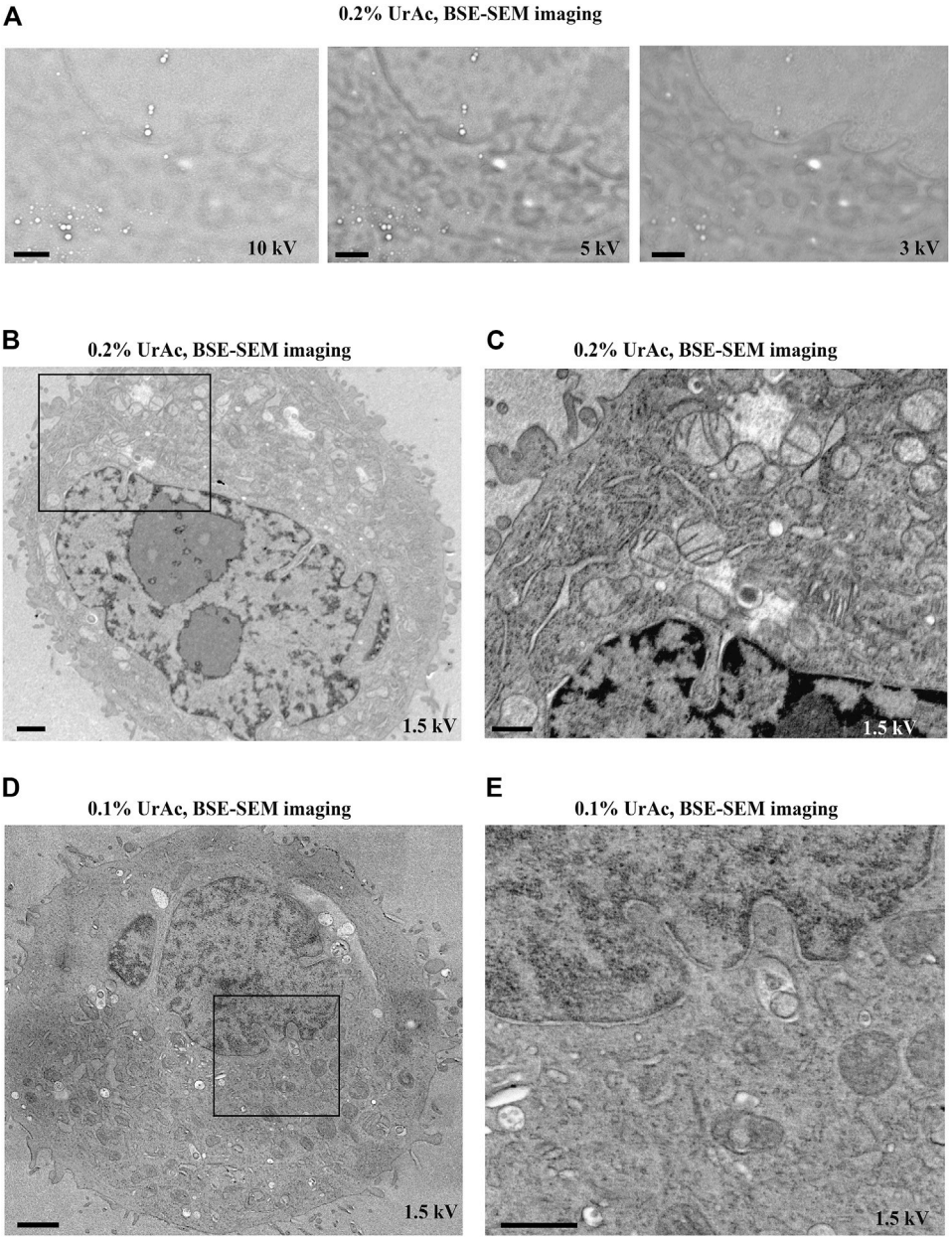

FIGURE 3 | The effect of accelerating voltage and different concentrations of uranyl acetate on image quality (inverse contrast). All images are acquired by SEM and BSE-detector. **(A)** By lowering the accelerating voltage from 10 kV **(A**, **left)** to 5 kV **(A, middle)** to 3 kV **(A**, **right)** imaging of ultrastructural features of trypsinized cells freeze-substituted with 0.2% UrAc gradually improves. **(B, C)** However, the same cells imaged by SEM at 1.5 kV have superior quality, as judged by nuclear details **(B)** and cristae of the mitochondria in an enlarged view of the area **(C)** from the black box in **(B)**. **(D)** Images of representative trypsinized cells freeze-substituted and processed with 0.1% UrAc and imaged with 1.5 kV display a drop in the image quality compared to cells processed with 0.2% UrAc and imaged with same accelerating voltage **(B, C)**. WD **A** left = 6.6 mm, middle = 6.9 mm, right = 7.6 mm; **(B, C)** = 9.7 mm; **(D)** = 9.9 mm. Section thickness = 200 nm. Abbreviations: BSE, backscattered electrons (Gatan OnPoint detector); SEM, scanning electron microscope; UrAc, uranyl acetate; WD, working distance. Scale bars: **(A, B, D)** = 1 μm; **(C, E)** = 0.5 μm.

and saturates the electron detector; images taken of charged samples typically show very bright areas and white streaks. Thus, sample charging relates to the electron dose received per unit area on the one hand and to the conductivity of the sample and quantity of scattered electrons on the other hand. First, we will address electron dose, which is affected by a number of imaging parameters. These include probe current, which, in turn, is affected by the accelerating voltage and can be varied independently to a smaller or larger extent on some instruments, e.g., our Zeiss Sigma and JEOL JSM7200 SEM, respectively. Along the same lines, the dwell time per pixel, and pixel size (in turn, related to magnification), may also affect sample charging. Hence, for a certain probe current, longer dwell-times will result in a higher electron dose, and for a

TABLE 2 | The effect of some imaging parameters on electron dose. Mag, magnification; Pxl, pixel size; Acc V, acceleration voltage; WD, working distance.

Image Name - Mag	WD [mm]	Pxl [nm]	Acc V [kV]	Dwell time [µs]	Probe current [pA]	Electron dose [electrons per nm^2]	Effect
example 1–25 K x	5	8	1	50	180	870	No effect with increasing Acc V
example 2–25 K x	5	8	1,5	50	180	870	
example 3–25 K x	6	8	3	50	175	840	
example 4–25 K x	6	8	5	50	186	900	
example 5–25 K x	5	8	10	50	249	1,200	Little effect with higher Acc V
example 6–25 K x	6	8	5	256	186	4,590	Big effect with higher/lower dwell
example 7–25 K x	6	8	5	8	186	140	time

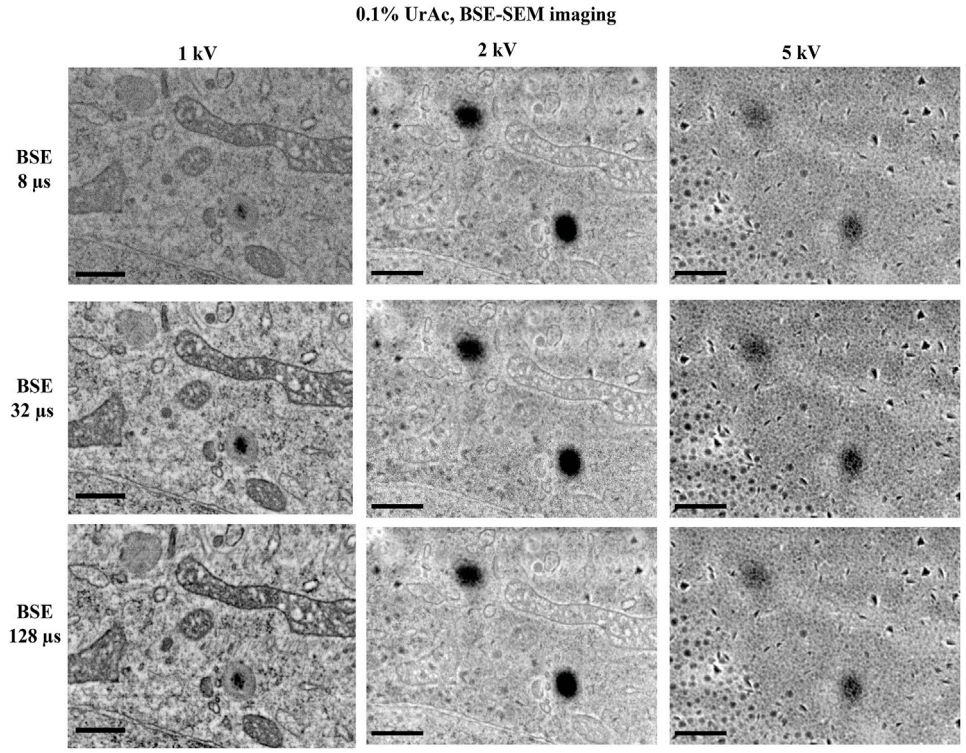

FIGURE 4 | The effect of varying dwell time on image quality. All images are taken from trypsinized cells freeze-substituted and processed with 0.1% uranyl acetate, and imaged by SEM and BSE-detector at an accelerating voltage of 1, 2 and 5 kV. Clearly the image quality was optimal at 1 kV with well resolved mitochondrial details and nuclear envelope. However, at 2 kV the image started to display blob-like structures and at 5 kV no cellular ultrastructure could be discerned; only the blobs were very clear. Reducing the dwell time from 128 µs (third row) per pixel to a mere 8 µs (top row) per pixel has no major effect on the image quality, at none of the tested accelerating voltages. WD 1 kV = 6.1 mm; 2 kV = 4.7 mm; 5 kV = 4.1 mm. Section thickness = 150 nm. Abbreviations: BSE, backscattered electrons (Gatan OnPoint detector); WD, working distance; UrAc, uranyl acetate. Scale bars: 0.5 µm.

certain probe current—dwell time combination, smaller pixel size will increase the electron dose as well.

We first investigated the relation between probe current and accelerating voltage (see Materials and methods), and found very similar electron doses across the range of tested accelerating voltages: 900 electrons per nm^2 with 1–5 kV, and 1,200 electrons per nm^2 at 10 kV (**Table 2**, example 1–5). It should be noted that at higher accelerating voltages (>10 kV), the electron dose increases notably (see **Supplementary Figure S1**). Data in **Table 2** were obtained at WD between 5 and 6 mm, at which we did all our SEM-imaging, but in this range, the probe current hardly changes, as is also apparent from **Supplementary Figure S1**.

The measurements also show how dwell times–expectedly–affect electron dose (**Table 2**, example 6 and 7: a 32-fold decrease in dwell time proportionally affects electron dose). We, therefore, examined whether dwell times caused sample charging and thus accounted for masking of ultrastructural details. However, the high level of masking of ultrastructural details in images acquired at a 5 kV accelerating voltage was similar when these were acquired at a 128 µsec, or an 8 µsec per pixel dwell time (**Figure 4**). Moreover, images acquired at 1 kV accelerating voltage were all of high quality, regardless of dwell

time. Only at 8 µsec per pixel the contrast dropped (because of too low signal). It, therefore, seems that masking of ultrastructural details that appears in SEM thin section imaging is unrelated to sample charging by an increased electron dose.

As far as the other factors potentially responsible for sample charging are concerned, sample conductivity does not change in function of imaging parameters, as the same area was imaged in these experiments. Moreover, higher accelerating voltages may be expected to decrease the probability of sample charging, as will become clear in the next section. This is in contrast with the finding that image quality gets worse with higher accelerating voltage. Hence, increased accelerating voltage within the range used in our experiments, does not affect image quality through charging, neither through increased electron dose nor by the decreased quantity of escaping electrons.

Monte Carlo Simulations for SEM Imaging Conditions

We next hypothesized that image quality—as defined here as "containing well discernable cell-structural information" is determined by an interplay of section thickness and accelerating voltage. This is based on considering that the regions of interest are imaged by backscattered electrons, reflected by the high atomic number metals added to the sample. They originate from deeper regions in the section. Another class of electrons, secondary electrons (SE), originate from a more superficial layer of the section and primarily informs us on the topography of the section. Increasing the acceleration voltage also increases the depth of penetration of the electrons into the section. Hence, it might well be that for a certain section thickness, there will be a maximum acceleration voltage above which the contribution of backscattered electrons will be marginal, as they would originate from regions below the section.

Therefore, we performed mathematical Monte Carlo simulations to predict an "interaction volume" where entering electrons interact with atoms in a sample. Thus, we simulated interaction volumes with samples composed of carbon and respectively 0, 1, 10, and 100% uranium. Interestingly, we find that even up to 10% uranyl acetate, the interaction volume does not differ from simulations with lower percentages of uranyl acetate. On the other hand, samples containing 100% uranyl acetate displayed a markedly smaller interaction volume (see **Supplementary File MC simulations**). He et al. (2018) estimated maximally 3% heavy atoms in the most heavily stained areas of a very strongly contrasted piece of liver tissue. In comparison, our preparation (max. 0.2% uranyl acetate) can hardly be called "heavily stained" and therefore, the interaction volumes for 0–10% can be regarded as representing our samples. **Figure 5** demonstrates how this interaction volume is affected by accelerating voltage. At 10 kV, electrons interact with sample atoms to a depth of about 1 µm, and at 2 kV only of 100 nm. Thus, for thin sections, higher accelerating voltages beam electrons through the sample to the indium-tin-oxide (ITO)-coating of the coverslips used in SEM and/or ILEM system. As seen in **Figure 5B**, imaging a 100 nm section at 10 kV, the entering electrons primarily generate secondary electrons (yellow) in the sample section, and there are a few backscattered electrons-producing interactions (red). At 5 kV, backscattered electrons are also generated in the section, but some of these penetrate through the section and will be dissipated by the ITO-layer.

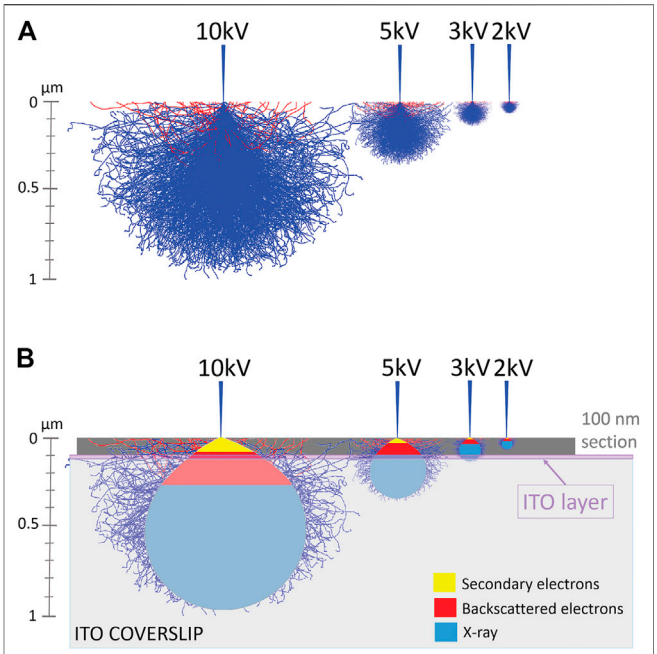

FIGURE 5 | Monte Carlo simulations of the interaction volume of electrons and carbon, demonstrating the relationship between penetration of electrons in a sample and accelerating voltage of the SEM. **(A)** Simulated interaction volumes in carbon sample in function of accelerating voltage of the SEM. **(B)** A schematic indication of the regions of interaction volume that produce secondary electrons (yellow region) and backscattered electrons (red region) is added. Abbreviations: ITO, indium-tin-oxide; SEM scanning electron microscope.

In contrast, at 3 and 2 kV, all backscattered electrons arise from interactions in the thin section, thus producing the highest backscattered-/secondary electron (BSE/SE) ratio and maximal compositional information. At too low accelerating voltages, the interaction volume will not reach the ITO layer and may cause charging (**Figure 5B**, see 2 kV). The simulation can explain why our thin section images had less cellular information if acquired at a 10 kV compared to 3 kV accelerating voltage (**Figure 3A**). Our hypothesis is supported by the observation mentioned above, that masking of ultrastructural details observed in the BSE-image disappeared by lowering the accelerating voltage from 5 to 1.5 kV (100 nm section) (**Figure 3**).

We further experimentally tested the prediction from the model that thinner sections would require lower accelerating voltages (**Figure 6** and **Supplementary Figure S3**). For 300 nm sections, we collected good quality images at 1.5 kV (**Figure 6A**, left), 2 kV, and 3 kV (**Figure 6A**, middle and right). For 200 nm sections, 1.5 kV (**Figure 6B**, left) and 2 kV (**Figure 6B**, middle) generated high contrast images, while quality deteriorated at 3 kV (**Figure 6B**, right). In contrast, all tested accelerating voltages imaged a 50 nm section poorly (**Figure 6C** and **Supplementary Figure S3**). Thus, it appears that the thinner the section, the lower the acceleration voltage at which this "image quality breakdown point" occurs. In fact, 5 kV was also effective, and interfering masking of

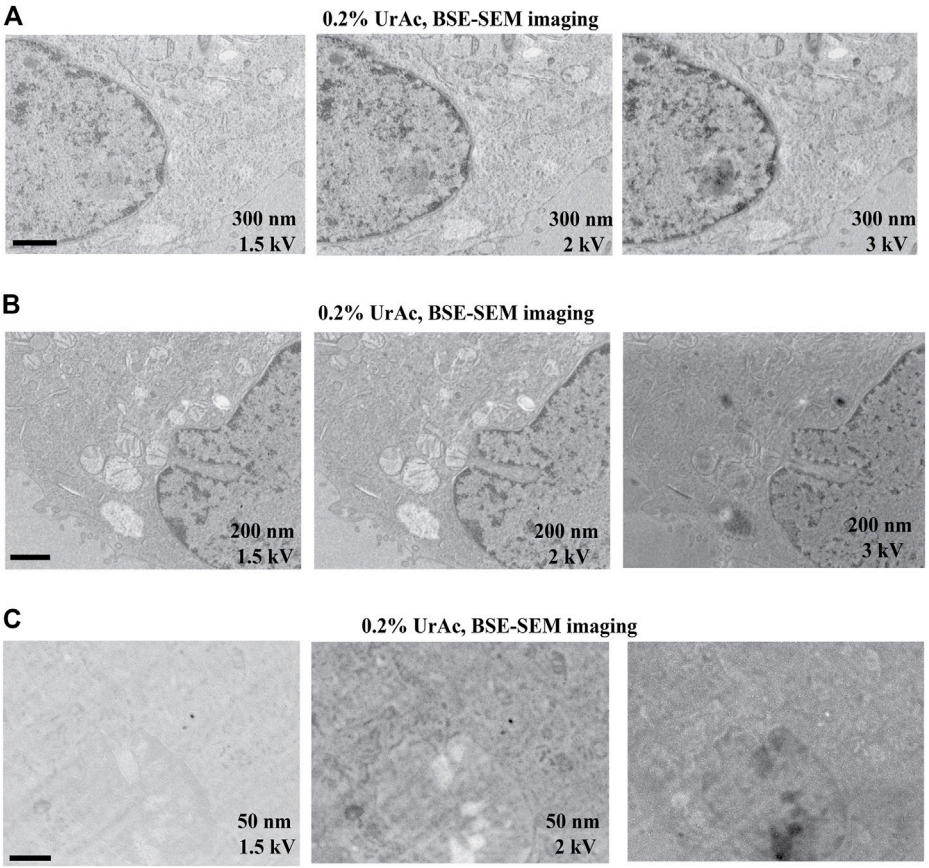

FIGURE 6 | Image quality as function of section thickness (vertical) and accelerating voltage (horizontal). All images represent trypsinized cells freeze-substituted with 0.2% UrAc and sectioned at 300 nm **(A)**, 200 nm **(B)** and 50 nm **(C)**. All images are acquired by SEM and BSE-detector. The thicker the section, the higher the tolerated accelerating voltage is before quality breaks down. WD A 1.5 kV = 5 mm; A 2 kV = 4.6 mm; A 3 kV = 4.3 mm; B 1.5 kV = 5.1 mm; B 2 kV = 4.7 mm; B 3 kV = 4.4 mm; C 1.5 kV = 5.2 mm; C 2 kV = 4.8 mm; C 3 kV = 4.5 mm. Abbreviations: BSE, backscattered electrons (Gatan OnPoint detector); SEM, scanning electron microscope; UrAc, uranyl acetate; WD, working distance. Scale bars: 1 μm.

ultrastructural details only appeared at a 10 kV accelerating voltage (**Supplementary Figure S3**). For example, in 300 nm sections, "image quality breakdown point" occurs at 5 kV, while in 50 nm sections, it occurs at 1.5 kV (see **Table 3** and red demarcating line in **Supplementary Figure S3**). As repeated imaging at different accelerating voltages of the same area will deteriorate the image, the sequence of imaging was reversed without any relevant effects (data not shown). Moreover, in **Supplementary Figure S3** the imaging sequence in each section was 3, 2, 1.5, 1, 5, 10 kV. If masking of ultrastructural details were due to repeated imaging the same region, deterioration would be expected in this order as well. However, in particular in case of the 100 nm section, we see an opposite effect; from 3 to 1.5 kV the image quality improves. Our data imply a relationship between acceleration voltage and section thickness. The exact values of these parameters will depend on the experimental setup used, for instance, different BSE-detectors, different SEM, etc. Also, the type of substrate—silicon wafer, Kapton tape - may affect the outcome; in this respect, it may be relevant that BSE detectors may display some sensitivity to cathodoluminescence, invoked by the interaction of electron beam and ITO. Nonetheless, these observations confirm our prediction and support our hypothesis that image quality (observed in **Figure 3A**) was compromised by an interaction between section thickness and acceleration voltage.

Imaging with ILEM-SEM for simultaneous fluorescence and electron signal detection.

Finally, we further optimized these protocols for imaging with a simultaneous fluorescence and electron signal system (ILEM-SEM) and antibody labeling as a fluorescence source. We collected 80 μm thick sections of fixed mouse brain cerebellum using a vibratome. The cerebellum is a complex brain area that contains many different cell types. We labeled the sections with an antibody against the protein calbindin D28 K and an Alexa Fluor 488 conjugated secondary antibody (Boey et al., 2019). Calbindin is specifically expressed by Purkinje cells in this brain area, and thus this labeling defines cells with this cellular identity. We also confirmed with conventional FM imaging that Alexa Fluor 488 signal was localized to the cytoplasm and dendrites of Purkinje cells present in vibratome sections (**Figure 7A**). We then applied our IRF protocol–the freeze-substitution method with

TABLE 3 | Section thickness vs. Image quality breakdown point. The latter is the accelerating voltage in kilovolt (kV) at which the quality of the image starts to degrade for a certain section thickness in nanometer (nm). Higher accelerating voltages yield worse image quality.

Thickness [nm]	Image quality breakdown point [kV]
50	1.5
100	2
200	3
300	5
500	10

0.2% uranyl acetate and Lowicryl HM20 embedding–to the tissue, followed by mounting ribbons of consecutive 150 nm sections onto ITO coverslips. The thin sections were re-examined in FM to confirm that fluorescent signals had been preserved (**Figure 7B**). We then selected a region that contained three fluorescent Purkinje cells (**Figure 7B**, asterisk) and imaged it at low magnification with our ILEM-SEM (**Figure 7C**, asterisk).

Subsequently, we reselected two cells to evaluate higher magnification imaging using ILEM in FM-mode and then in EM mode (**Figure 8**). We could easily identify the same two fluorescent cells in the next three consecutive sections (**Figure 8A–C**, left). Next, by using ILEM in EM-mode, we observed details of the boxed areas, for example, in **Figure 8A**, representing an area containing the nucleus of the Purkinje cell (white box in **Figure 8A** left FM mode and middle EM mode) and three cross-sectioned dendrites (black box in **Figure 8A** left FM mode and right EM mode). Those images demonstrate that fluorescently marked cellular structures can be identified and studied at the ultrastructural level using an ILEM-SEM system.

Notably, the ultrastructural details were less well-defined than typical for TEM, especially when examining smaller subcellular organelles. In addition, a difference with BSE-SEM images of brain tissue obtained with the Zeiss Sigma with OnPoint detector (**Figures 2C–E**) could be observed. This difference could be due to different factors, including the type of BSE-detector, and the pre-embedding immuno-labelling. Nonetheless, we tested whether further improvement was possible by post-staining with 4% uranyl acetate and Reynold's lead citrate. We imaged the section before post-staining by ILEM-SEM (**Figure 8B** middle and right), where it was possible to delineate the type of the cells and larger organelles like the nucleus and mitochondria, but without fine detail, and smaller organelles were indistinct (**Figure 8B** right). We then re-imaged the next consecutive section after performing a post-staining (**Figure 8C**). There was a striking improvement of contrast and definition: unlabeled non-fluorescent granular cells could be recognized more easily (**Figure 8B**, middle vs. **Figure 8C**, middle), the cristae of mitochondria (**Figure 8B**, middle and right as compared to **Figure 8C**, middle and right) and climbing fiber (synapse asterisk in **Figure 8B**, middle as compared to **Figure 8C**, middle), contacting the fluorescently labeled Purkinje cell, could be clearly discerned. It was also possible to delineate secretory pathway organelles in the Purkinje cell cytoplasm (**Figure 8B**, right vs **Figure 8C**, right). In addition, we could observe by CLEM on some high magnification areas in these cells, that brighter spots in the Soma correspond to lysosome-like organelles (**Supplementary Figure S4**), indicating a higher concentration of calbindin in these organelles as compared to the surrounding cytoplasm. This observation is analogous to what others have found in intestinal endothelial cells (Nemere et al., 1991). With respect to imaging goals with our ILEM-SEM, the intention is to obtain correlated image sets. In a first round, this will be achieved by combining preserved fluorescence images with corresponding lower contrast unstained EM-images. Then, after the image contrast has been improved by post-staining, the navigation parameters determined

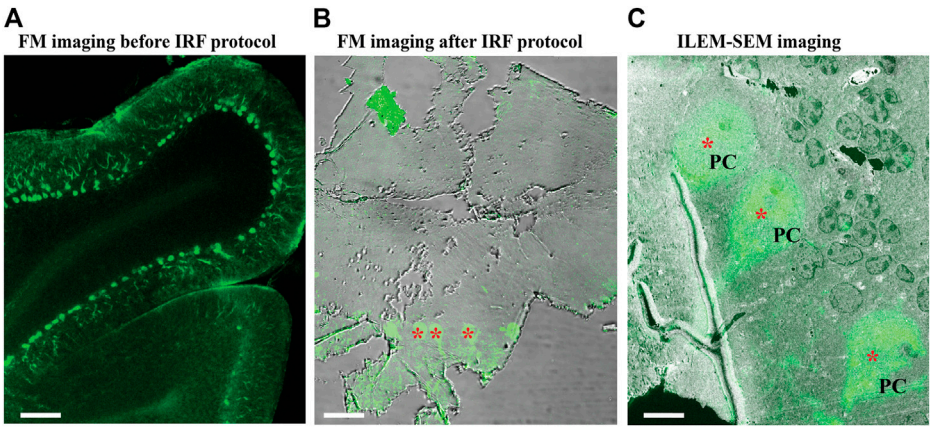

FIGURE 7 | Fluorescence images of immuno-labeled mouse cerebellum imaged with conventional FM and ILEM system (JEOL BSE detector). **(A)** An 80 µm slice of cerebellum labeled with calbindin D28 K primary and Alexa 488-conjugated secondary antibody before embedding with our IRF protocol. Imaged with conventional FM Nikon TiE inverted C2 confocal microscope Plan Apo 10x dry lens, labeled Purkinje cells can be easily recognized (asterisks). **(B)** After embedding with our IRF protocol, 150-nm cerebellar section imaged by conventional FM Nikon TiE inverted C2 confocal microscope Plan Apo 20x dry lens shows that the fluorescent labeling of Purkinje cells (asterisks) was preserved after embedding. **(C)** The same 150 nm section with a layer of Purkinje cells **(**asterisk, in **B)** imaged with fluorescent optics of ILEM-SEM (Plan Apo VC 100x lens) system shows a perfect correlation. Abbreviations: FM, fluorescence microscope; ILEM-SEM, integrated light and electron microscope; IRF, in-resin fluorescence; PC, Purkinje cell. Scale bars: **A** = 100 µm, **B** = 10 µm, **C** = 5 µm.

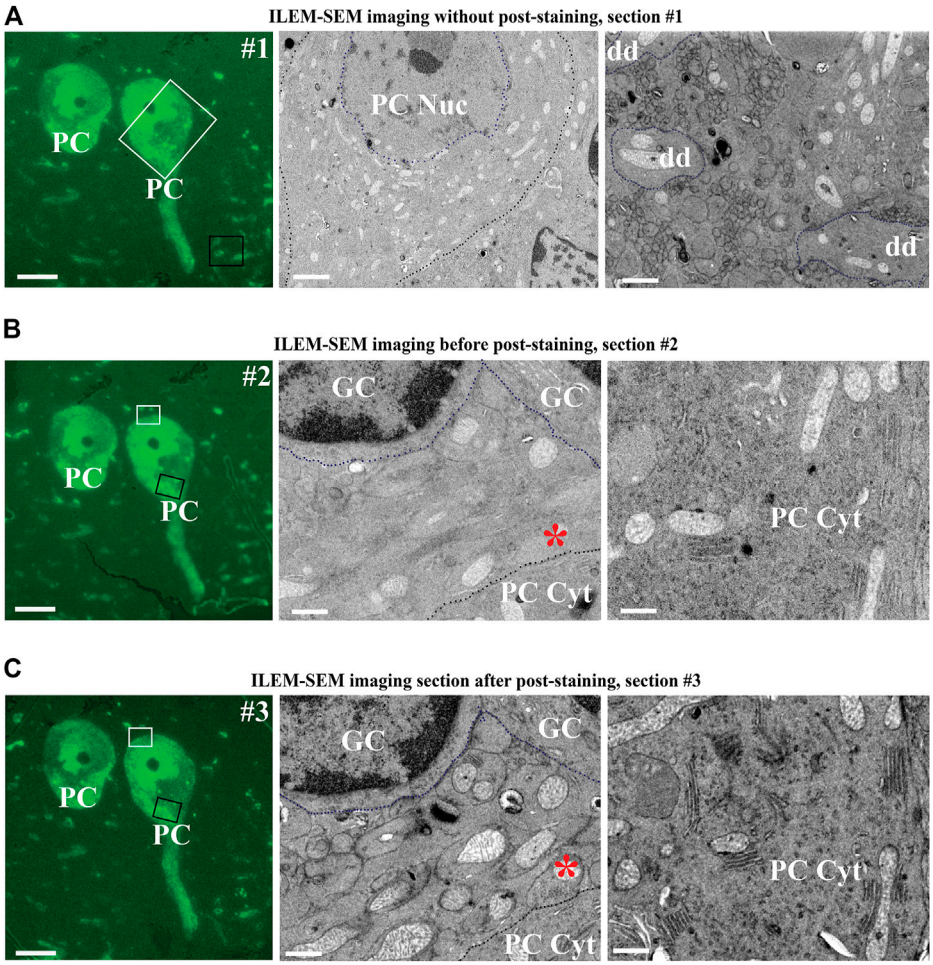

FIGURE 8 | Three consecutive sections of mouse cerebellum immunolabeled for calbindin D28 K and imaged with ILEM-SEM system (JEOL BSE detector). **(A–B, left)** Same two large fluorescent Purkinje cells as in the center of **Figure 7C**, in two immediately adjacent consecutive 150 nm sections without any additional post-staining, imaged at higher magnifications with ILEM-SEM in FM mode with Plan Apo VC 100x lens. **(A–B, middle and right)** ILEM EM mode images indicated by white and black boxes in **A–B,** left. Purkinje cell boundaries **(A–B**, **middle)**, granular cells **(B**, **middle)** and three cross-sectioned dendrites **(A**, **right)** are demarcated by a dotted line for ease of recognition. **(C**, **middle and right)** Higher magnifications ILEM-SEM images from the regions indicated by white and black boxes in **(C,left)**. The images in **C (middle and right)** represent next consecutive section at the same place as in 8 **B (middle and right)**, but after post-staining with uranyl acetate and lead citrate. Post-staining enhanced contrast, so that the mitochondria, membranes, the secretory pathway organelles in PC cytoplasm, and climbing fiber synapse **(**asterisk in **B middle** as compared **C middle)** are now well distinguished. Abbreviations: Cyt, cytoplasm; dd, dendrite; ILEM-SEM, integrated light and electron microscope; IRF, in-resin fluorescence; GC, granular cell; Nuc, nucleus; PC, Purkinje cell. Scale bars: **(A–C),** left = 10 µm; **(A–C)**, middle = 0.6 µm; **(A–C)**, right = 0.8 µm.

and stored by our navigation software (Gabarre et al., 2021) during the first round will be re-used to automatically re-acquire the same but contrast-enhanced set of correlated EM-images. Thus, this two-step ILEM-SEM procedure allows defining cellular identity using antibody labeling and FM, followed by high resolution, fine ultrastructural imaging of subcellular contents and relationships with surrounding cell types.

CONCLUSION

In this study, we describe a procedure to prepare GFP expressing cells or tissue and fluorescent antibody-labeled tissue for CLEM, emphasizing the preservation of fluorescent signals. This procedure involves high-pressure freezing and introducing of a freeze-substitution IRF protocol with embedding in Lowicryl HM20 resin. We found that a concentration of 0.2% uranyl acetate in the freeze-substitution medium is optimal for preserving in-resin fluorescence as well as ultrastructure in cells and can be applied successfully for the same purposes to brain tissue with sufficient contrast. It is of great importance to know how to select optimal imaging conditions for visualizing different types of sample with BSE-imaging in an SEM. Bouwer et al. (Bouwer et al., 2017) proposed applying a negative bias voltage to the sample to decrease the interaction volume for a given acceleration voltage and improve sectioning capabilities in block-face SEM, where the block face is imaged. More recently, Vos et al. (2021) and Lane et al. (2021) extended this approach to BSE-imaging of sections in a SEM. Although very useful, this condition is not available to many SEM-users.

Therefore, in this paper, we focus on BSE-imaging sections without applying such a bias voltage, which is relevant for array tomography (Micheva and Smith, 2007; Oberti et al., 2010; Collman et al., 2015) in the context of optimizing image quality. Our experiments with different parameters defining imaging conditions in the SEM showed that an important factor determining image quality is the relation between section thickness and accelerating voltage. It appears that for a given section thickness, the image quality diminishes when increasing the accelerating voltage above a certain value. The thicker the section, the higher this value. We have shown that charging of the section is not responsible for this diminished image quality. However, these observations can be explained by considering the interaction volume of electrons and matter, where the ratio BSE/SE-signal will diminish at "image quality breakdown point", increasing the proportion of surface information (including defects such as knife marks, surface roughness etc.), masking pertinent biological information. Our observations are very important when considering three-dimensional CLEM experiments, such as array tomography, aimed at constructing a correlated fluorescence and electron three-dimensional reconstruction of a sample. For higher resolution reconstructions, the limiting factor in array tomography is the Z-resolution or the section thickness. Improvement of this resolution requires thinner sections. In our studies, it appeared that 50 nm sections require accelerating voltages not higher than 1 kV.

In conclusion, we have tuned a protocol for the preservation of fluorescent signals present in cells and tissue samples, as well as their ultrastructure, and determined optimal conditions for BSE-imaging with ILEM system. This advancement is important for transitioning from two-to three-dimensional CLEM imaging in an automated fashion with a new generation of ILEM systems.

DATA AVAILABILITY STATEMENT

The raw data supporting the conclusion of this article will be made available by the authors, without undue reservation.

ETHICS STATEMENT

The animal study was reviewed and approved by KU Leuven Ethical Committee (protocol P019/2017).

AUTHOR CONTRIBUTIONS

PB, SM, NG conceived the project and designed the experiments. PB, SG, KV, RW, and DV performed the experiments. PB, SG, KV, RW, DV, RG, and NG analyzed the data. SM and NG contributed reagents, materials, and analysis tools. PB, RG, and NG wrote the paper.

FUNDING

DV is supported by a Methusalem grant from KU Leuven and the Flemish Government awarded to Prof. Bart De Strooper (METH/14/07). SM is supported through FWO I001818N (AKUL/17/044) Single-cell omics in high throughput and at spatial resolution; FWO I001719N, Flanders BioImaging: Towards an integrated, translational and multimodal imaging platform from molecule to man and the ISPAMM (An Image Storage Platform for Analysis Management and Mining (ISPAMM; AKUL/13/39) project. SG is supported by a VIB TechWatch development project (Developing direct super-resolution Correlative Array Tomography (dsCAT)-2017; 2018).

ACKNOWLEDGMENTS

We thank Dr. Joris de Wit for providing us with the lentiviral vectors (VIB-KU Leuven Center for Brain and disease Research, Leuven, Belgium), Dr. W. Annaert (VIB-KU Leuven Center for Brain and disease Research, Leuven, Belgium) for reagents, and all members of the Munck and Gounko laboratories for discussion and comments. Imaging was performed with the help of the Light Microscopy Expertise Unit and the Electron Microscopy Platform of the VIB-KU Leuven Center for Brain and disease Research and the VIB BioImaging Core. DV is supported by a Methusalem grant from KU Leuven and the Flemish Government awarded to Prof. Bart De Strooper (METH/14/07). SM is supported through FWO I001818N, (AKUL/17/044) Single-cell omics in high throughput and at spatial resolution; FWO I001719N, Flanders BioImaging: Towards an integrated, translational and multimodal imaging platform from molecule to man and the ISPAMM (An Image Storage Platform for Analysis Management and Mining (ISPAMM; AKUL/13/39) project. SG is supported by a VIB TechWatch development project (Developing direct super-resolution Correlative Array Tomography (dsCAT)-2017 and 2018).

SUPPLEMENTARY MATERIAL

The Supplementary Material for this article can be found online at: https://www.frontiersin.org/articles/10.3389/fcell.2021.737621/full#supplementary-material

REFERENCES

Agronskaia, A. V., Valentijn, J. A., van Driel, L. F., Schneijdenberg, C. T. W. M., Humbel, B. M., van Bergen en Henegouwen, P. M. P., et al. (2008). Integrated Fluorescence and Transmission Electron Microscopy. *J. Struct. Biol.* 164, 183–189. doi:10.1016/J.JSB.2008.07.003

Bharat, T. A. M., Hoffmann, P. C., and Kukulski, W. (2018). Correlative Microscopy of Vitreous Sections Provides Insights into BAR-Domain Organization *In Situ*. *Structure* 26, 879–886. doi:10.1016/j.str.2018.03.015

Boey, A., Rybakin, V., Kalicharan, D., Vints, K., and Gounko, N. V. (2019). Gold-substituted Silver-Intensified Peroxidase Immunolabeling for FIB-SEM Imaging. *J. Histochem. Cytochem.* 67, 351–360. doi:10.1369/0022155418824335

Bouwer, J. C., Deerinck, T. J., Bushong, E., Astakhov, V., Ramachandra, R., Peltier, S. T., et al. (2016). Deceleration of Probe Beam by Stage Bias Potential Improves Resolution of Serial Block-Face Scanning Electron Microscopic Images. *Adv. Struct. Chem. Imag* 2, 11. doi:10.1186/s40679-016-0025-y

Brama, E., Peddie, C. J., Jones, M. L., Domart, M.-C., Snetkov, X., Way, M., et al. (2015). Standard Fluorescent Proteins as Dual-Modality Probes for Correlative Experiments in an Integrated Light and Electron Microscope. *J. Chem. Biol.* 8, 179–188. doi:10.1007/s12154-015-0143-3

Brown, E., Mantell, J., Carter, D., Tilly, G., and Verkade, P. (2009). Studying Intracellular Transport Using High-Pressure Freezing and Correlative Light Electron Microscopy. *Semin. Cel Dev. Biol.* 20, 910–919. doi:10.1016/j.semcdb.2009.07.006

Collman, F., Buchanan, J., Phend, K. D., Micheva, K. D., Weinberg, R. J., and Smith, S. J. (2015). Mapping Synapses by Conjugate Light-Electron Array Tomography. *J. Neurosci.* 35, 5792–5807. doi:10.1523/JNEUROSCI.4274-14.2015

Gabarre, S., Vernaillen, F., Baatsen, P., Vints, K., Cawthorne, C., Boeynaems, S., et al. (2021). A Workflow for Streamlined Acquisition and Correlation of Serial Regions of Interest in Array Tomography. *BMC Biol.* 19, 152–167. doi:10.1186/s12915-021-01072-7

Griffiths, G. (1993). *Fine Structure Immunocytochemistry*. Heidelberg: Springer-Verlag Berlin Heidelberg, 459.

Hayatt, M. A. (1981). *Fixation for Electron Microscopy*. New York: Academic Press.

Humbel, B., and Müller, M. (1986). "Freeze Substitution and Low Temperature Embedding Scanning Electron Microscopy," Proceedings of the 4th Pfefferkorn conference on Biological specimen preparation in 1985 4 (No. 1), Article 19.

Johnson, E., Seiradake, E., Jones, E. Y., Davis, I., Grünewald, K., and Kaufmann, R. (2015). Correlative In-Resin Super-resolution and Electron Microscopy Using Standard Fluorescent Proteins. *Sci. Rep.* 5, 9583. doi:10.1038/srep09583

Kukulski, W., Schorb, M., Welsch, S., Picco, A., Kaksonen, M., and Briggs, J. A. G. (2011). Correlated Fluorescence and 3D Electron Microscopy with High Sensitivity and Spatial Precision. *J. Cel Biol.* 192, 111–119. doi:10.1083/jcb.201009037

Lane, R., Vos, Y., Wolters, A. H. G., Kessel, L. v., Chen, S. E., Liv, N., et al. (20212021). Optimization of Negative Stage Bias Potential for Faster Imaging in Large-Scale Electron Microscopy. *J. Struct. Biol. X* 5, 100046. doi:10.1016/j.yjsbx.2021.100046

Markert, S. M., Britz, S., Proppert, S., Lang, M., Witvliet, D., Mulcahy, B., et al. (2016). Filling the gap: Adding Super-resolution to Array Tomography for Correlated Ultrastructural and Molecular Identification of Electrical Synapses at theC. Elegansconnectome. *Neurophoton* 3, 041802. doi:10.1117/1.NPh.3.4.041802

Mcdonald, K. L., and Webb, R. I. (2011). Freeze Substitution in 3 hours or Less. *J. Microsc.* 243, 227–233. doi:10.1111/j.1365-2818.2011.03526.x

Micheva, K. D., and Smith, S. J. (2007). Array Tomography: A New Tool for Imaging the Molecular Architecture and Ultrastructure of Neural Circuits. *Neuron* 55, 25–36. doi:10.1016/j.neuron.2007.06.014

Monaghan, P., Perusinghe, N., and Muller, M. (1998). High-pressure Freezing for Immunocytochemistry. *J. Microsc.* 192, 248–258. doi:10.1046/j.1365-2818.1998.00387.x

Müller-Reichert, T., and Verkade, P. (2012). Preface. *Methods Cel Biol*, xvii–xix. doi:10.1016/B978-0-12-416026-2.03001-6

Nemere, I., Leathers, V. L., Thompson, B. S., Luben, R. A., and Norman, A. W. (1991). Redistribution of Calbindin-D28kin Chick Intestine in Response to Calcium Transport*. *Endocrinology* 129 (6), 2972–2984. doi:10.1210/endo-129-6-2972

Nistal, M., Rodríguez-Echandía, E. L., and Paniagua, R. (19781978). Formaldehyde-induced Appearance of Septate Junctions between Digestive Vacuoles. *Tissue and Cell* 10 (4), 735–740. doi:10.1016/0040-8166(78)90059-9

Nixon, S. J., Webb, R. I., Floetenmeyer, M., Schieber, N., Lo, H. P., and Parton, R. G. (2009). A Single Method for Cryofixation and Correlative Light, Electron Microscopy and Tomography of Zebrafish Embryos. *Traffic* 10, 131–136. doi:10.1111/j.1600-0854.2008.00859.x

Oberti, D., Kirschmann, M. A., and Hahnloser, R. H. R. (2010). Correlative Microscopy of Densely Labeled Projection Neurons Using Neural Tracers. *Front. Neuroanat.* 4, 24. doi:10.3389/fnana.2010.00024

Peddie, C. J., Blight, K., Wilson, E., Melia, C., Marrison, J., Carzaniga, R., et al. (2014). Correlative and Integrated Light and Electron Microscopy of In-Resin GFP Fluorescence, Used to Localise Diacylglycerol in Mammalian Cells. *Ultramicroscopy* 143, 3–14. doi:10.1016/j.ultramic.2014.02.001

Peddie, C. J., Domart, M.-C., Snetkov, X., O'Toole, P., Larijani, B., Way, M., et al. (2017). Correlative Super-resolution Fluorescence and Electron Microscopy Using Conventional Fluorescent Proteins In Vacuo. *J. Struct. Biol.* 199, 120–131. doi:10.1016/j.jsb.2017.05.013

Pluk, H., Stokes, D. J., Lich, B., Wieringa, B., and Fransen, J. (20092009). Advantages of Indium-Tin Oxide-Coated Glass Slides in Correlative Scanning Electron Microscopy Applications of Uncoated Cultured Cells. *J. Microsc.* 2333, 353–363. doi:10.1111/j.1365-2818.2009.03140.x

Reimer, L., and Kohl, H. (20082008). *Springer Series in Optical Sciences 36: Transmission Electron Microscopy*. New York: Springer. doi:10.1007/978-0-387-34758-5

Reynolds, E. S. (1963). The Use of lead Citrate at High pH as an Electron-Opaque Stain in Electron Microscopy. *J. Cel Biol.* 17, 208–212. doi:10.1083/jcb.17.1.208

Sannerud, R., Esselens, C., Ejsmont, P., Mattera, R., Rochin, L., Tharkeshwar, A. K., et al. (2016). Restricted Location of PSEN2/γ-Secretase Determines Substrate Specificity and Generates an Intracellular Aβ Pool. *Cell* 166, 193–208. doi:10.1016/J.CELL.2016.05.020

Schroeder, A., and De Wit, J. (2018). Leucine-rich Repeat-Containing Synaptic Adhesion Molecules as Organizers of Synaptic Specificity and Diversity. *Exp. Mol. Med.* 50, 1–9. doi:10.1038/s12276-017-0023-8

Tsien, R. Y. (1998). The Green Fluorescent Protein. *Annu. Rev. Biochem.* 67, 509–544. doi:10.1146/annurev.biochem.67.1.509

Urwyler, O., Izadifar, A., Dascenco, D., Petrovic, M., He, H., Ayaz, D., et al. (2015). Investigating CNS Synaptogenesis at Single-Synapse Resolution by Combining Reverse Genetics with Correlative Light and Electron Microscopy. *Development* 142 (2), 394–405. doi:10.1242/dev.115071

Vints, K., Baatsen, P., and Gounko, N. V. (2021). An Accelerated Procedure for Approaching and Imaging of Optically Branded Region of Interest in Tissue. *Meth Cel Biol* 162, 205–221. doi:10.1016/bs.mcb.2020.08.002

Vos, Y., Lane, R. I., Peddie, C. J., Wolters, A. H. G., and Hoogenboom, J. P. (2021). Retarding Field Integrated Fluorescence and Electron Microscope. *Microsc. Microanal* 27 (1), 109–120. doi:10.1017/S1431927620024745

Walther, P., and Ziegler, A. (2002). Freeze Substitution of High-Pressure Frozen Samples: The Visibility of Biological Membranes Is Improved when the Substitution Medium Contains Water. *J. Microsc.* 208 (1), 3–10. doi:10.1046/j.1365-2818.2002.01064.x

Wang, Q., Yang, L., Alexander, C., and Temple, S. (2012). The Niche Factor Syndecan-1 Regulates the Maintenance and Proliferation of Neural Progenitor Cells during Mammalian Cortical Development. *PLoS One* 7, e42883. doi:10.1371/journal.pone.0042883

Watanabe, S., Punge, A., Hollopeter, G., Willig, K. I., Hobson, R. J., Davis, M. W., et al. (2011). Protein Localization in Electron Micrographs Using Fluorescence Nanoscopy. *Nat. Methods* 8, 80–84. doi:10.1038/nmeth.1537

Zalokar, M. (1966). A Simple Freeze-Substitution Method for Electron Microscopy. *J. Ultrastruct. Res.* 15, 469–479. doi:10.1016/s0022-5320(66)80119-3

Zonnevylle, A. C., Van Tol, R. F. C., Liv, N., Narvaez, A. C., Effting, A. P. J., Kruit, P., et al. (20132013). Integration of a High-NA Light Microscope in a Scanning Electron Microscope. *J. Microsc.* 252 (1), 58–70. doi:10.1111/jmi.12071

Conflict of Interest: The authors declare that the research was conducted in the absence of any commercial or financial relationships that could be construed as a potential conflict of interest.

Publisher's Note: All claims expressed in this article are solely those of the authors and do not necessarily represent those of their affiliated organizations, or those of the publisher, the editors, and the reviewers. Any product that may be evaluated in this article, or claim that may be made by its manufacturer, is not guaranteed or endorsed by the publisher.

frontiers in Molecular Biosciences

ORIGINAL RESEARCH
published: 19 January 2022
doi: 10.3389/fmolb.2021.822232

Integrated Array Tomography for 3D Correlative Light and Electron Microscopy

Ryan Lane[1]*, *Anouk H. G. Wolters*[2], *Ben N. G. Giepmans*[2] and *Jacob P. Hoogenboom*[1]

[1]Imaging Physics, Delft University of Technology, Delft, Netherlands, [2]Department of Biomedical Sciences of Cells and Systems, University Groningen, University Medical Center Groningen, Groningen, Netherlands

Volume electron microscopy (EM) of biological systems has grown exponentially in recent years due to innovative large-scale imaging approaches. As a standalone imaging method, however, large-scale EM typically has two major limitations: slow rates of acquisition and the difficulty to provide targeted biological information. We developed a 3D image acquisition and reconstruction pipeline that overcomes both of these limitations by using a widefield fluorescence microscope integrated inside of a scanning electron microscope. The workflow consists of acquiring large field of view fluorescence microscopy (FM) images, which guide to regions of interest for successive EM (integrated correlative light and electron microscopy). High precision EM-FM overlay is achieved using cathodoluminescent markers. We conduct a proof-of-concept of our integrated workflow on immunolabelled serial sections of tissues. Acquisitions are limited to regions containing biological targets, expediting total acquisition times and reducing the burden of excess data by tens or hundreds of GBs.

Keywords: correlative light and electron microscopy, volume electron microscopy, integrated microscopy, array tomography, serial section electron microscopy, scanning electron microscopy

OPEN ACCESS

Edited by:
Christopher Guerin, Vlaams Instituut voor Biotechnologie, Belgium

Reviewed by:
Kristina D Micheva, Stanford University, United States
Paolo Ronchi, European Molecular Biology Laboratory Heidelberg, Germany

***Correspondence:**
Ryan Lane
r.i.lane@tudelft.nl

Specialty section:
This article was submitted to Structural Biology, a section of the journal Frontiers in Molecular Biosciences

Received: *25 November 2021*
Accepted: *15 December 2021*
Published: *19 January 2022*

Citation:
Lane R, Wolters AHG, Giepmans BNG and Hoogenboom JP (2022) Integrated Array Tomography for 3D Correlative Light and Electron Microscopy. Front. Mol. Biosci. 8:822232. doi: 10.3389/fmolb.2021.822232

INTRODUCTION

A central objective within neuroscience and cell biology is to produce high-resolution (1–10 nm), three-dimensional reconstructions of biological specimen. Volume electron microscopy (EM) is the preferred imaging method in this arena because of its unique ability to resolve features across a wide spectrum of spatial scales (Peddie and Collinson, 2014; Kornfeld and Denk, 2018). While EM provides highly relevant structural information and precise localization of targets, immunogold labeling can only be visualized at high resolution, and in Tokuyasu labeling section areas are typically limited to 0.01 mm^2 for analysis (Liou et al., 1996; Van Rijnsoever et al., 2008). Fluorescence microscopy (FM) provides biologically relevant information by tagging specific biomolecules with fluorescent labels at large scale (Giepmans et al., 2006). Regions of interest (ROI) can in this way be quickly and reliably identified for subsequent high magnification EM imaging. The information from these two imaging modalities are combined in correlative light and electron microscopy (CLEM). ROI retrieval across different microscopes is, however, nontrivial at large scales, particularly when spread across multiple sections (Polishchuk et al., 2000; Bishop et al., 2011; Karreman et al., 2014; Collinson et al., 2017; Booth et al., 2019). Other challenges associated with CLEM include the reliance on fiducial markers and intermediate sample preparation (de Boer et al., 2015; Karreman et al., 2016). One means of combating these challenges is by merging these separate imaging systems into a single, integrated fluorescence and electron microscope (Liv et al., 2013). By detecting fluorescence

expression *in-situ*, it can further be decided in an automated fashion which areas to scan at high magnification and which areas to omit for the sake of higher throughput (Delpiano et al., 2018). For array tomography applications, ROIs can be targeted with increasing magnification through a sequence of feedback loops (Gabarre et al., 2021). Similarly, strategies for rapidly screening sections have been developed for sequential CLEM to limit volume acquisitions to select ROI (Burel et al., 2018; Ronchi et al., 2021).

Despite these potential benefits, an integrated microscope presents new challenges. In conventional array tomography sample preparation, the sample is eluted and restained between imaging methods (Micheva and Smith, 2007). Hence, there is no need to preserve fluorescence labelling, which allows for post-staining to enhance EM contrast (Watson, 1958; Tapia et al., 2012). The traditional way to compensate for diminished contrast is to boost the EM signal by increasing the dwell time per pixel, but this comes at the expense of throughput. An additional complication in integrated CLEM is electron-beam-induced quenching of the fluorescence (Srinivasa Raja et al., 2021). This imposes the constraint that the fluorescence in a given area must be acquired prior to exposure from the electron beam, which prohibits uniformly pre-irradiating the sample with the electron beam to enhance and stabilize contrast (Kuipers et al., 2015). Conversely, in conventional serial-section EM, there are scarce constraints regarding the number of times a particular sample may be scanned, making possible approaches such as that by Hildebrand et al. (Hildebrand et al., 2017).

Our goal is to establish a workflow capable of quickly and efficiently rendering three-dimensional CLEM volumes from serial sections in such a way as to overcome these challenges. Three key initiatives steered the design of our integrated correlative array tomography (iCAT) procedure. First, to prevent damaging or quenching of the fluorescence signal via electron-beam irradiation, each FM field of view must be acquired prior to EM exposure. Second, to compensate for the reduced application of contrast agents, backscattered electron (BSE) collection efficiency is enhanced via a negative stage bias, allowing for higher throughput (Bouwer et al., 2016; Lane et al., 2021). Finally, a high precision EM-FM overlay is facilitated by the use of cathodoluminescent (CL) points, which eliminates the need for artificial fiducial markers (Haring et al., 2017). An alignment method was then developed to reconstruct the correlative image stack. Islets of Langerhans from both rat and zebrafish pancreas tissue were chosen to prototype the imaging and reconstruction workflows. By offering a more holistic visualization of tissue, our integrated approach to 3D CLEM could lead to greater insights in (patho) biology (de Boer et al., 2020).

MATERIALS AND METHODS

Tissue and Sample Preparation

Rat pancreas was prepared as follows: fresh pancreas was cut from an 83 day old rat into small pieces and fixed in 4% paraformaldehyde (PFA; Merck) + 0.1% glutaraldehyde (GA; Polysciences) as described in Ravelli et al. (Ravelli et al., 2013). A complete zebrafish larva (120hpf) was fixed in 2% PFA +2% GA. Both samples were post-fixed in 1% osmium tetroxide and 1.5% potassium ferricyanide in 0.1 M cacodylate buffer, dehydrated through ethanol and embedded in EPON (Serva). 100nm serial sections were cut and placed onto formvar-covered ITO-coated glass coverslips (Optics Balzers). Immunolabeling was performed as described previously (Kuipers et al., 2015). Samples were etched with 1% periodic acid for 10 min, followed by a 30 min blocking step: 1% bovine serum albumin (BSA; Sanquin, Netherlands) in tris-buffered saline (TBS), pH 7.4. Next, anti-insulin was incubated for 2 h (guinea pig; 1:50, Invitrogen, PA1-26938, RRID: AB_794668, for rat pancreas and anti-insulin; 1: 100, Abcam, ab210560, for zebrafish pancreas), followed by washing and subsequent incubation for 1 h with biotinylated secondary antibody (donkey-anti-guinea pig; 1: 400, Jackson Immunoresearch, for rat pancreas and goat-anti-rabbit; 1:400, Dako, for zebrafish pancreas) followed by washing steps. Finally, streptavidin conjugated AF594 (1: 100, Jackson Immunoresearch, for rat pancreas) and streptavidin conjugated TRITC (1:100, Jackson Immunoresearch, for zebrafish pancreas) were added for 1 h followed by washing.

Digital Light Microscopy

The sections, after being placed on the ITO-coated glass slide, are imaged at 30X magnification (~7 μm px^{-1}) using a VHX-6000 digital light microscope (Keyence) operating in reflection mode. To capture every section on the 22 mm × 22 mm ITO-coated glass slide, a 3 × 3 grid of RGB images is acquired and automatically stitched together.

Integrated Microscopy

The integrated microscope is a widefield SECOM fluorescence microscope (Delmic B.V.) retrofitted into the vacuum chamber of a Verios 460 SEM (Thermo Fisher Scientific) (Liv et al., 2013; Zonnevylle et al., 2013). The microscopes share a common optical axis, translation stage, and control software. FM images are obtained with 10s exposures, recorded by a Zyla 4.2 sCMOS camera (Andor—Oxford Instruments). Excitation wavelengths of 405 and 555 nm are used to excite Hoechst and AF594. The SECOM is equipped with a CFI S Plan Fluor ELWD 60XC (0.70 NA) objective (Nikon), which allows for long working distance imaging (1.8–2.6 mm), to prevent electrical breakdown in vacuum, which must be accounted for due to the presence of high electric fields induced by the stage bias (Vos et al., 2021).

SEM imaging is conducted in two rounds: 1) low-magnification (38 nm px^{-1}) scans accompanying each fluorescent acquisition; 2) high-magnification (5 nm px^{-1}) acquisitions on ROI identified by fluorescence expression. Both low and high magnification imaging are performed at 2.5 keV primary beam energy with a −1 kV bias potential applied to the sample stage such that the landing energy is 1.5 keV, which proved optimal for ~100 nm sections. The negative potential bias enhances the backscattered electron

(BSE) signal, which is collected by the insertable concentric backscattered detector (Thermo Fisher Scientific) (Lane et al., 2021).

Alignment and Reconstruction Software

Image data from the integrated microscope is uploaded to a local storage server running an instance of render-ws[1], a collection of open-source web services for rendering transformed image tiles. The tiles and their respective metadata are organized into stacks, configured as MongoDB databases. The alignment routines are arranged in a series of Jupyter notebooks[2], which parse the image metadata for the EM-FM overlay as well as make calls to render-ws via a python wrapper (render-python[3]). EM image stitching and volume alignment are based on the scale-invariant feature transform (SIFT)—an algorithm designed to detect and match local features in corresponding images (Lowe, 1999). SIFT features are stored in render-ws databases where they can be processed by BigFeta[4], a linear least squares solver for scalable 2D and 3D image alignment based on point correspondences. CLEM datasets are ultimately exported to CATMAID (Saalfeld et al., 2009) for google-maps-like visualization. 3D visualizations are done in Fiji (Schindelin et al., 2012) using the Volume Viewer plugin[5].

RESULTS

Section Detection and *In-Situ* Navigation

Simple navigation between serial sections within the integrated microscope is crucial. Following joint EM-FM sample preparation (**Figure 1A**), the sections are imaged by a digital light microscope (DLM) (**Figure 1B**). To facilitate navigation within the integrated microscope (**Figure 1C**), the resulting overview image is used for detecting the boundaries of each section on the ITO-coated glass substrate via a segmentation routine[6] (**Figure 1D**). The overview image (inset 1) is first contrast enhanced and converted to grayscale (inset 2). Intensity-based thresholding is used to create a binary mask image (inset 3), which is then applied to the grayscale image. To retrieve outlines of the section boundaries, the gradient is computed (inset 4). Watershed segmentation is then implemented by flooding the gradient image with a number of markers equal to the number of serial sections in the image (inset 5). The resulting labelled image (inset 6) then serves as input for navigation using a plugin within Odemis[7], the open-source software that controls the microscope (**Figure 1E**).

[1]https://github.com/saalfeldlab/render.
[2]https://github.com/hoogenboom-group/iCAT-workflow.
[3]https://github.com/AllenInstitute/render-python.
[4]https://github.com/AllenInstitute/BigFeta.
[5]https://imagej.net/plugins/volume-viewer.
[6]https://github.com/hoogenboom-group/secdetect.
[7]https://github.com/delmic/odemis.

Targeted Correlative Acquisition of an Individual Region of Interest

To identify ROI in the integrated microscope for subsequent EM acquisition, the correlative imaging scheme is engineered to obtain fluorescence overviews of each section, undamaged by the electron beam. The workflow starts by acquiring a FM and low-magnification EM image tile (**Figure 2A**). The FM tile is acquired prior to the EM tile to preserve the fluorescence signal. An automated registration routine guided by cathodoluminescent (CL) spots is then run to register the image pair (Haring et al., 2017). This sequence of correlative imaging is automatically repeated in a grid-like pattern, encompassing the entire section. FM image tiles are acquired with a 20% overlap such that they can be stitched together to allow for fluorescence-based ROI detection within each section (**Figure 2B**). The field width of the EM tile (~140 µm) is chosen such that it spans the maximum extent possible without entering the overlap region of the neighboring FM image tiles,

$$w_{EM} = w_{FM} - 2\, o_{FM}\, w_{FM}$$

where w_{EM} and w_{FM} are the respective EM and FM fields of view, and o_{FM} is the overlap between adjacent FM tiles. In this way EM-FM registration is performed over as large an area as possible, while avoiding bleaching of the fluorescence. Fluorescence imaging of the entire section prior to EM would fulfil the same objective while circumventing the need for gaps between low-magnification EM image tiles. This would require manually registering the tilesets, however, as the transformation obtained from the CL registration procedure is unique to each image pair.

Fluorescence expression is then used to target areas for additional EM imaging at higher magnification (5 nm px^{-1}) (**Figure 2C**). The ROI is manually navigated to via stage translation, whereby an automated tileset acquisition is initiated (**Figure 2D**). The tiles are spaced with a 10–15% overlap such that they can be stitched during post-processing. The correlative imaging pipeline is then repeated on the remaining serial sections.

2D Stitching and Correlation

Overlaying the fluorescence onto the high-magnification EM requires correlating the datasets across different modalities and spatial scales. Each FM tile is first overlaid onto the corresponding low-magnification EM tile using the metadata generated by the CL registration procedure. A grid of CL spots is recorded with the camera of the fluorescence microscope in the absence of excitation light (**Figure 3A**). The appropriate affine transformation is calculated by localizing each CL spot and matching it with the known position of the electron beam ("cross-modal" registration) (Haring et al., 2017). The stage coordinates are extracted to then correlate and position each image pair in the tileset (**Figure 3A**).

The high-magnification EM tileset is stitched independently of both the FM and low-magnification EM tiles (**Figure 3B**). Stage coordinates are used to first establish a set of potential neighboring tiles. For each tile, SIFT features are extracted and matched between the candidate neighbors. Affine transformation parameters for each tile are then estimated by minimizing the squared distance between corresponding features (Saalfeld et al., 2012; Khairy et al., 2018).

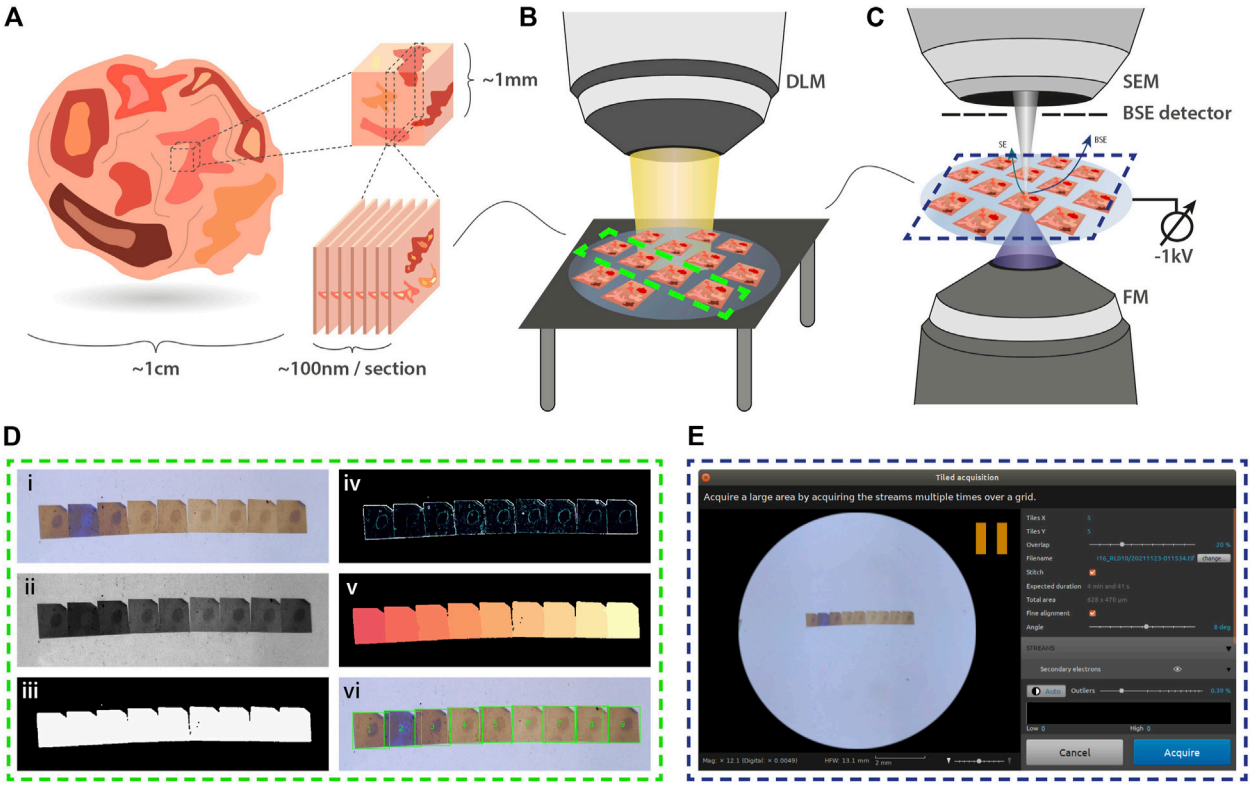

FIGURE 1 | Integrated array tomography. **(A)** Ultrathin sections are prepared for simultaneous FM and EM imaging. **(B)** An overview image of the sections on the ITO-coated glass slide is then acquired by a digital light microscope (DLM). **(C)** Next, the sample is transferred to the integrated microscope for CLEM imaging. SEM imaging is performed using a −1kV bias potential applied to the sample stage to enhance BSE collection from the non-post-stained sections. **(D)** The overview image obtained by the DLM is used for instance segmentation of the serial sections. Descriptions of the image processing steps (i-vi) is provided in the main text. **(E)** The section overview image and bounding box coordinates of each serial section are fed to the microscope software to facilitate navigation.

Next, the low-magnification image tiles are registered to the corresponding area of the stitched high-magnification EM tileset ("cross-spatial" registration, **Figure 3C**). Stage coordinates are used to determine the set of high-magnification tiles that overlap with each low-magnification tile. A composite image of the overlapping tiles is rendered, processed with SIFT, and matched with the features in the low-magnification tile. The affine transformation computed from the feature matching is then propagated to each of the FM tiles such that they are overlaid onto the high-magnification EM tileset. In this way, the low-magnification EM serves as a proxy to correlate the fluorescence to the high-magnification EM. The overlay accuracy is reduced in the areas between low-magnification tiles where the transformation is extrapolated (**Supplementary Figure S1A—F**). This can be corrected for via (manual) landmark registration by e.g. aligning the Hoechst signal to nuclei recognized in the EM using software such as ec-CLEM (Paul-Gilloteaux et al., 2017), which is routinely used for image registration in sequential CLEM experiments (Franke et al., 2019; Tuijtel et al., 2019; Lee et al., 2020). In general, the overlay accuracy cannot be expected to be below the pixel size of the low magnification EM.

Correlative 3D Reconstruction

A robust and scalable solution is required for volume alignment of the high-magnification EM stack, the "backbone" of the multimodal dataset. The stitched sections are downsampled and roughly aligned in z (**Figure 4A**) to facilitate feature mapping between image tiles in adjacent sections. A system of linear equations consisting of SIFT features is then solved to finely align the image stack in 3D (**Figure 4B**) (Khairy et al., 2018). The features extracted during stitching are reused, enabling a faster and more efficient reconstruction of the EM volume.

The 2D correlative alignment procedure (**Figure 3**) is then run on each section, mapping the fluorescence onto the high-magnification EM volume. The nine serial sections of rat pancreas were thereby used to realize a proof-of-concept of the iCAT workflow (**Figure 5A**). An islet of Langerhans was identified from anti-insulin immunofluorescence of AF594 and chosen for subsequent, high-magnification EM imaging (**Figure 5B**). The fluorescence data clearly delineates the endocrine region from the surrounding exocrine tissue, which is characterized by dense endoplasmic reticulum (ER) and the absence of insulin labeling (**Figure 5C**). Although it was chosen as a nuclear marker, Hoechst also binds to the RNA present in the

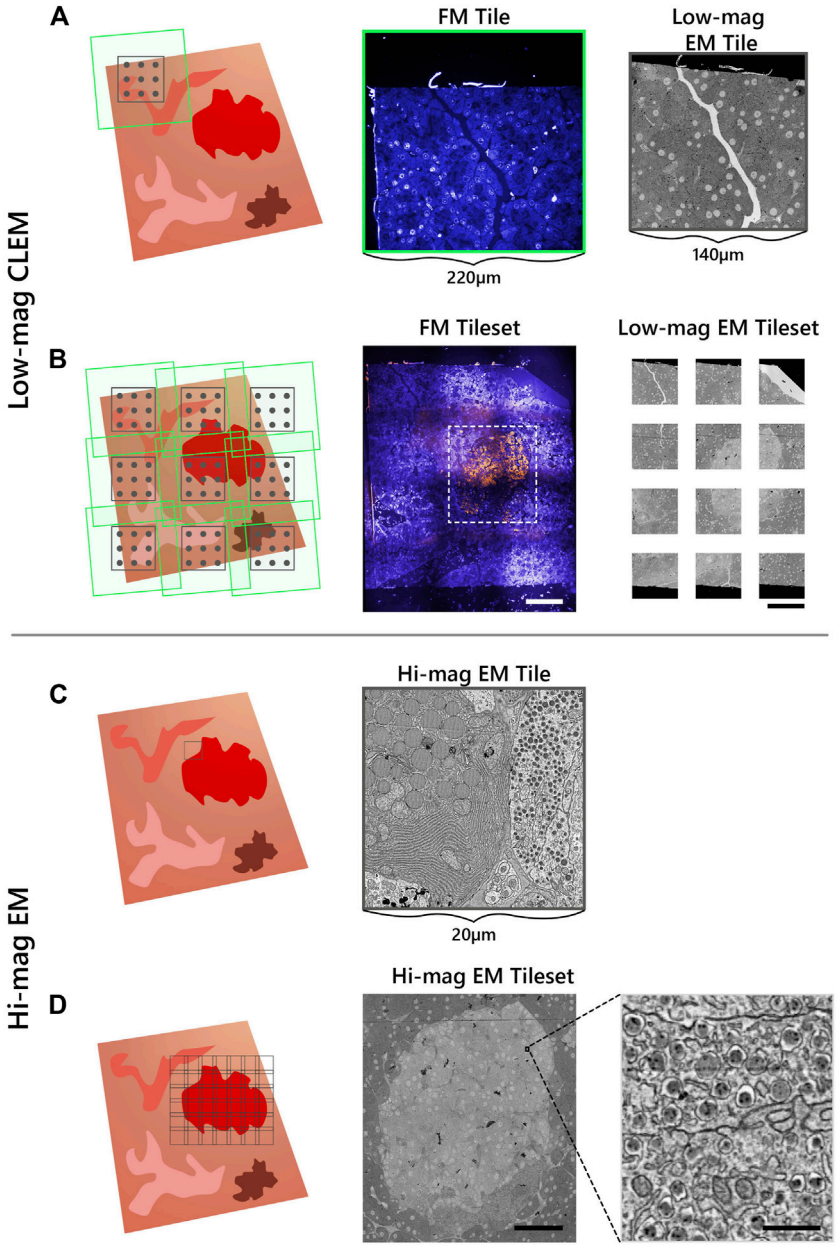

FIGURE 2 | Integrated array tomography provides efficient, high-precision EM-FM imaging without bleaching of the fluorescence. **(A)** Acquisition of correlative FM (green outline) and low-magnification EM (black outline) images, followed by a registration procedure involving CL spots (grey circles) to register the image pair. **(B)** The stage is translated in a grid-like fashion such that there is sufficient overlap between neighboring FM image tiles—leaving a gap between adjacent EM tiles. **(C)** The fluorescence signal is used to identify targets for subsequent EM imaging (black outline). **(D)** The target ROI is captured by an automated tileset of high magnification EM tiles. Scalebars: **(B)** 100µm; **(D)** 50 µm (inset, 0.5 µm).

ER. The endocrine region, in contrast, is characterized by an abundance of insulin-secreting beta cells with distinct nuclei. The high EM-FM registration accuracy afforded by iCAT enables a clear distinction between different types of granules present in the endocrine tissue (**Figure 5D**). Discerning insulin from other hormone granules is nontrivial as all are roughly 100 nm in diameter. Making this differentiation from EM data alone requires expert-level interpretation.

By limiting high-magnification EM to only the islet, the total imaging volume is reduced by a factor ~10 with respect to the full section volume (0.03 mm^2 per islet vs 0.4 mm^2 per section). Similar reductions are realized in the total dataset size (0.1 vs ~1 TB) easing data management requirements. This initial proof of concept was designed around only a limited number of serial sections to more efficiently optimize each procedure in the workflow.

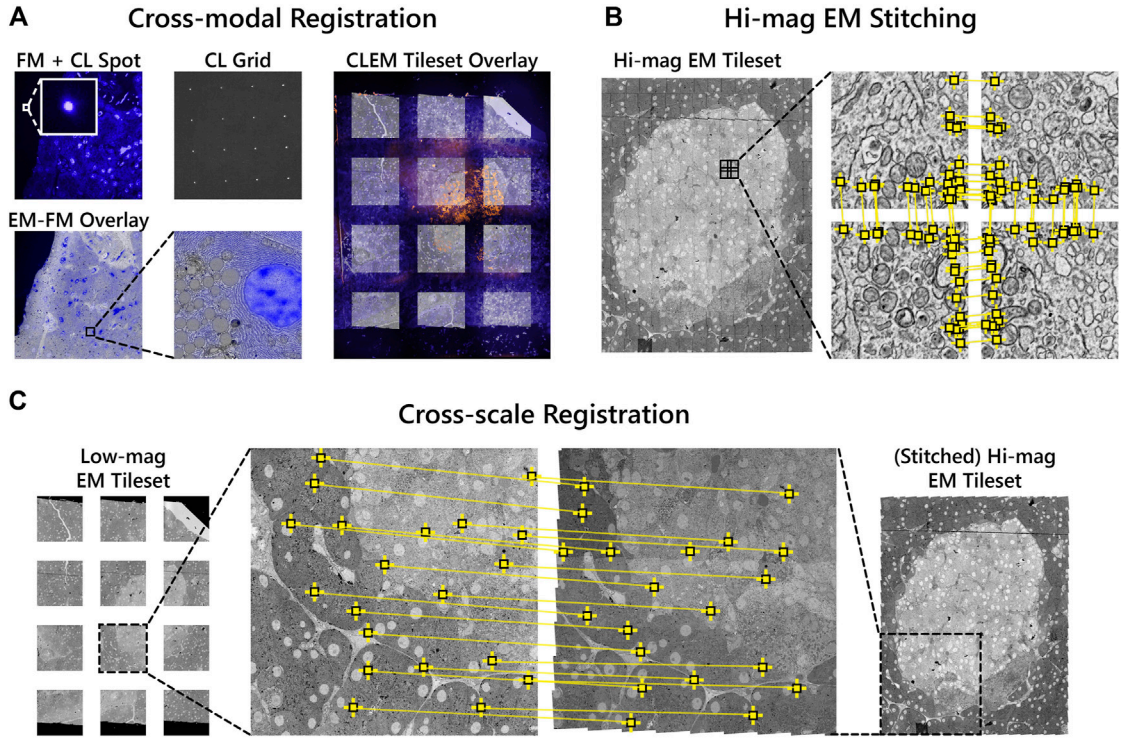

FIGURE 3 | Correlative alignment routine registers tilesets across modalities and scales. **(A)** Automated registration procedure for registering FM and low-magnification EM image pairs using CL spots. FM tiles are then overlaid onto the low-magnification EM tiles of each section. **(B)** SIFT features (yellow squares) are extracted and used to stitch together neighboring high-magnification EM tiles within each section. **(C)** Low-magnification EM images are registered to the corresponding area of the stitched together high-magnification EM tileset. The low-magnification tiles thereby serve as a reference to ultimately overlay the fluorescence onto the high-magnification EM.

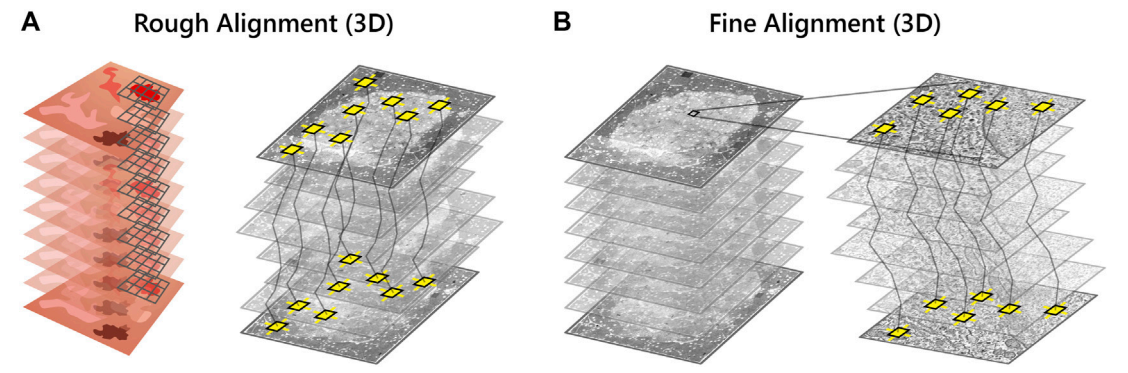

FIGURE 4 | Volume reconstruction of the high-magnification EM stack. **(A)** SIFT features (yellow squares) are used to roughly align the high-magnification EM stack in *z*. A downsampled image of each section is rendered as the full resolution EM tileset is too large (several GB) for feature extraction. **(B)** The EM stack alignment is refined by least squares optimization of the displacement between matched features.

Proof of Concept on Zebrafish Pancreas Tissue

To demonstrate the scalability of the workflow, we applied it to a larger volume of larval zebrafish (**Figure 6**). The Hoechst signal was useful in identifying the exocrine region of the pancreas (**Figure 6B**) as the insulin immunofluorescence from TRITC was weak. TRITC was chosen for its stronger fluorescence in vacuum compared to Alexa dyes (manuscript in preparation); potential causes for the weak immunofluorescence in the zebrafish pancreas are still under investigation. The exocrine region, encompassing an islet of Langerhans, together with the underlying muscle tissue was selected for high magnification EM. The reconstruction of the CLEM volume was cropped to remove the background fluorescence in the swim bladder (**Figure 6C**). Sub-stacks within

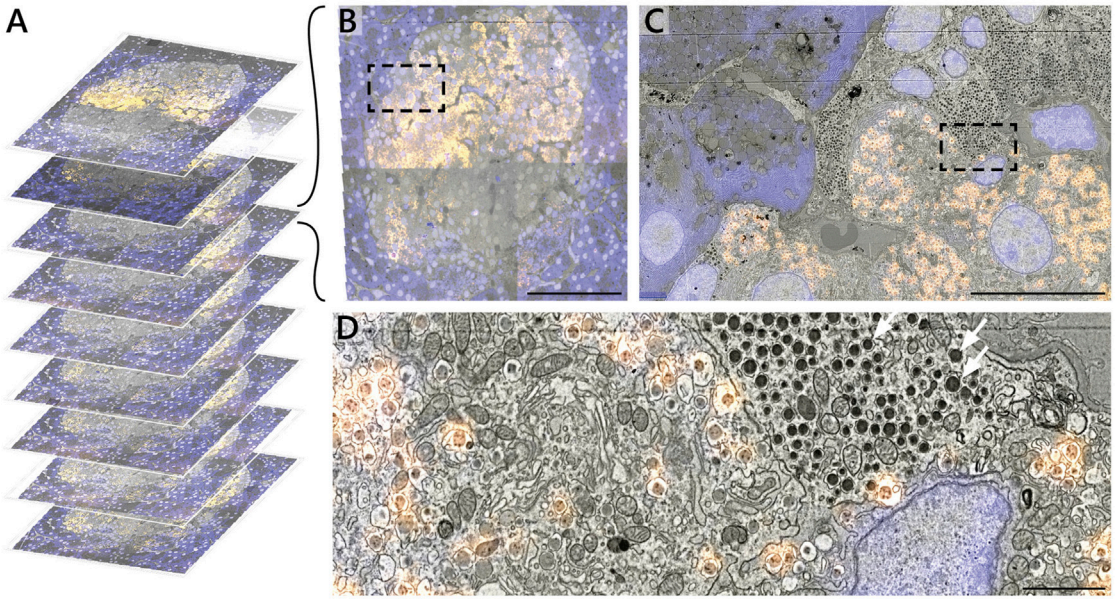

FIGURE 5 | Correlative reconstruction of nine sections of pancreas. **(A)** 2D and 3D alignment routines are combined to yield a CLEM stack of nine serial sections of rat pancreas tissue. **(B–D)** CLEM imaging of the islet of Langerhans at varying spatial resolution. Hoechst (blue) and AF594 (orange) fluorescence signals are superimposed onto the EM ultrastructure. The AF594 signal, in particular, facilitates recognition of insulin granules from e.g. non-fluorescent glucagon granules (white arrows, D). Scale bars: **(B)** 50μm; **(C)** 5μm; **(D)** 1 μm. Raw data at full resolution is available via Nanotomy.

the correlative volume were then extracted for further analysis (**Figures 6D,G**). Note that the ultrastructure is better preserved in most tissues than in the islet (**Figures 6H,I**), a phenomenon previously seen in other species (unpublished results).

We generally observe high EM-FM overlay precision as evidenced by the Hoechst signal confined to the nuclear envelope in the muscle tissue (**Figures 6E,F**). The registration accuracy does, however, exhibit variability in several sections (Movies A.1 and A.2)—more so than is seen in the rat pancreas tissue where it appears limited to the gaps between low-magnification EM tiles. In these instances, the inaccuracy stems from a malfunction in the CL registration procedure itself (**Supplementary Figure S1G—N**). Variations in the EM image intensity, particularly in the islet, can also be observed for a number of sections (**Figure 6H**: *XZ* and *YZ* cross-sections). We attribute these artifacts primarily to ultrastructure preservation as they do not appear to be as prevalent in the muscle tissue. While the SEM imaging parameters and detection settings were held constant throughout the acquisition, day-to-day changes in the environment (e.g. temperature, humidity levels) may have varied.

In total, 66 sections were prepared, of which three ($z = 9, 10, 34$) were discarded due to excess surface debris. The omission of consecutive sections was mitigated by extending the SIFT feature depth search from 2 to 3 such that sections $z = 8$ and $z = 11$ could be registered. Total acquisition times for low-magnification CLEM and high-magnification EM were 7.2 and 71 h respectively, versus 335 h for full section imaging at high-magnification.

DISCUSSION

A new workflow for integrated array tomography for the semi-automated acquisition and reconstruction of volume CLEM data is presented. High-resolution EM is limited to select ROI by targeting areas based on fluorescence expression. This not only expedites acquisition time, but eases the burden on data management requirements. Interpretation of EM data is in turn facilitated by the addition of fluorescent labels. The workflow demonstrated here extends the work of Liv et al. (Liv et al., 2013), which introduced the integrated microscope, and Haring et al. (Haring et al., 2017), which presented the fiducial-free CL registration procedure, to targeted correlative imaging of serial sections. Gabarre et al. (Gabarre et al., 2021) presented an alternative method for integrated array tomography in which light microscopy and EM are combined to localize structures through a series of feedback loops. Our approach differs in several ways. First, fluorescence imaging is done *in-vacuo* as opposed to transmitted light microscopy done at ambient pressure. This allows for more automated EM-FM (or EM-LM) overlay, as the CL registration procedure can only be done in high vacuum (Haring et al., 2017). Additionally, the multi-modal alignment methodology conceived here offers a more scalable solution for generating volumetric CLEM data. Integrated array tomography was inspired in part by the multi-scale approach of Hildebrand et al. (Hildebrand et al., 2017), in which full brain EM imaging of a larval zebrafish was conducted by selecting ROI for subsequent acquisition based on inspection between imaging rounds. In this work, conversely, ROI are

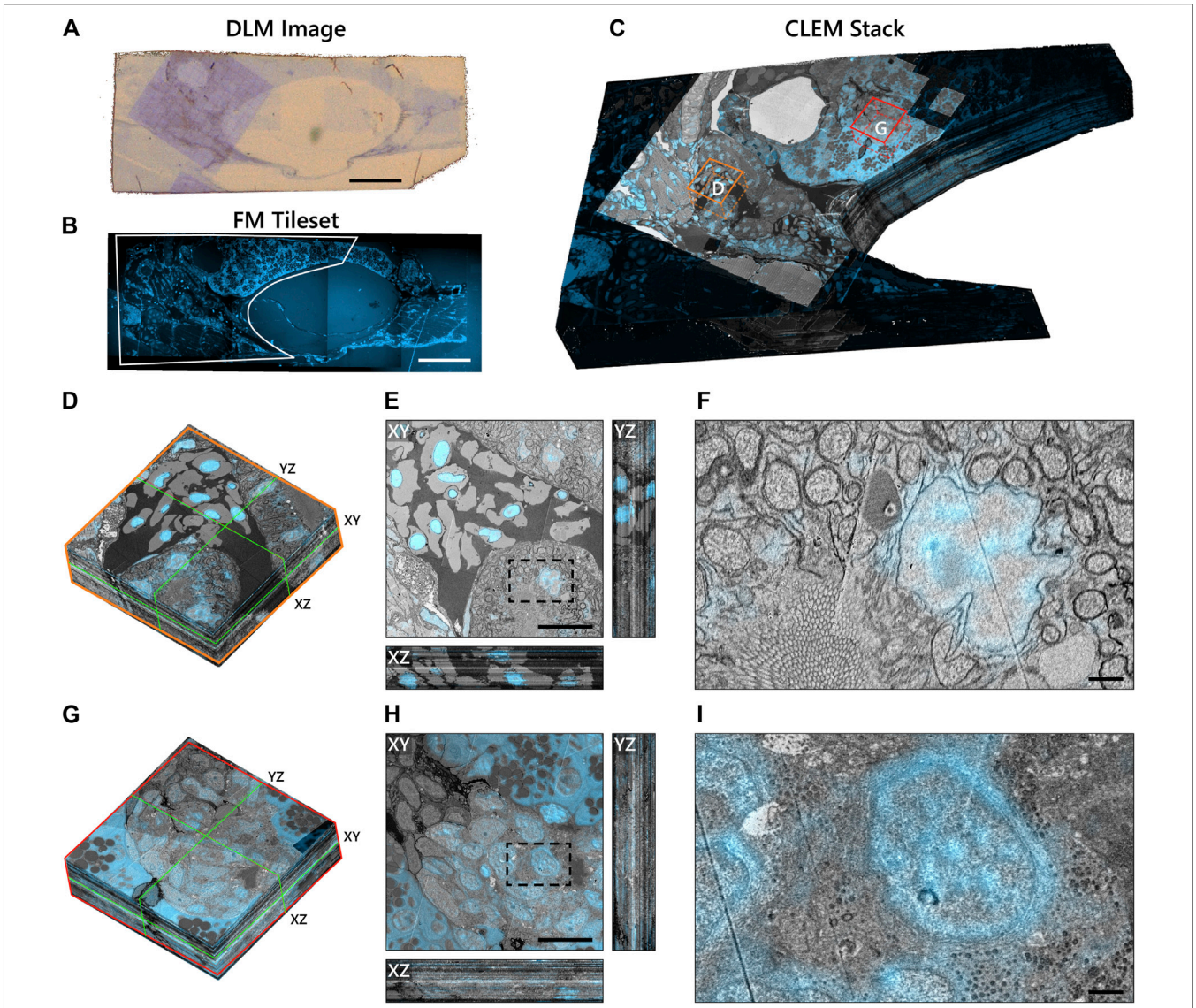

FIGURE 6 | Integrated correlative array tomography applied to 63 serial sections of zebrafish pancreas. **(A)** Contrast-enhanced optical image of an individual serial section obtained by the DLM. The section was re-acquired post-EM imaging, revealing the region of interest irradiated by the electron beam. The biological material can be seen in pale blue in contrast with the bare EPON (brown background). **(B)** Hoechst signal of an individual serial section, outlining (white) the portion of the tissue shown in **(C)**. **(C)** CLEM volume of the zebrafish tissue cropped to the ROI selected for high-magnification EM imaging—plus a portion of the surrounding fluorescence signal. Sub-stacks for inspection are denoted by orange **(D–F)** and red **(G–I)** boxes. **(D)** 3D sub-stack of muscle tissue within the zebrafish pancreas. Green lines indicate orthoslices of the XY, XZ, and YZ planes shown in **(E)**. **(F)** Zoomed-in region of the XY plane showing high-precision FM overlay of Hoechst onto a cell nucleus. **(G–I)** Same as in **(D–F)**, but for an islet of Langerhans. Ill-defined cell and organelle membranes in **(H)** and **(I)** indicate suboptimal preservation of the ultrastructure in this region of the pancreas. Scale bars: **(A,B)** 100μm; **(E,H)** 10μm; **(F,I)** 1 μm. Raw data at full resolution is available via Nanotomy.

identified by *in-situ* fluorescence, bypassing the need for post-processing and alignment between magnification scales.

On-section immunofluorescence and fluorescent staining constitute viable options for FM imaging of resin-embedded sections in high vacuum. Pancreas tissue in particular is well-suited for immunofluorescence due to the prevalence of insulin epitopes. While in both nature and technique development, immunolabeling approaches are always dependent on the capacity for antibodies and epitopes to interact, this is typically inefficient for most antibodies, and particularly so for EPON-embedded sections. We find that approximately 1 in 10 antibodies tested in our lab are applicable for EPON labeling. While acrylic resins (e.g. Lowicryl, LR White) have been shown to be more compatible with immunolabeling, a trade-off must be made between the strength of the fluorescence signal and the quality of the ultrastructure (Watanabe et al., 2011; Paez-Segala et al., 2015). Complications with serial sectioning and ultrastructure preservation (beyond that shown in the zebrafish pancreas) arose when experimenting with Lowicryl; hence EPON was selected as the embedding medium for this study.

Probes typically used for live FM, such as fluorescent proteins, are likewise incompatible with conventional EM sample preparation techniques (de Boer et al., 2015). Although protocols have been developed for retaining fluorescence post-embedding (Kukulski et al., 2011; Watanabe et al., 2011; Peddie et al., 2014; Fu et al., 2020), the same compromises exist between fluorescence retention and ultrastructure preservation. Fluorescent proteins have the additional limitation that the specimen must be genetically modified, rendering them unsuitable for use in native animals and humans. In-resin fluorescence preservation thus remains a challenge—only made more difficult by imposing high vacuum conditions, which may lower fluorescence intensities for biological probes typically optimized for use in aqueous environments (Peddie et al., 2014). We are nevertheless confident that future developments in fluorescent proteins and embedding media will present compelling opportunities to apply integrated array tomography to a variety of biological questions.

We foresee that the multimodal datasets obtained using this method will be instrumental in forthcoming machine learning applications (Eckstein et al., 2020; Liu et al., 2020; Heinrich et al., 2021). Thus far, applications of registered EM-FM datasets appear to be limited to facilitating registration of sequential CLEM data using artificial predictions for the fluorescence signal (Ounkomol et al., 2018; Seifert et al., 2020). Volume EM datasets, particularly in connectomics, are now routinely segmented via deep convolutional neural networks (Buhmann et al., 2021; Heinrich et al., 2021). Acquisition rates and manual annotation of datasets, however, both serve as bottlenecks for reconstructing dense networks of cells and organelles (Kornfeld and Denk, 2018). Given its ability to provide labeled biological information as well as reduce imaging volumes to select regions, integrated array tomography is poised to deliver significant gains in this arena.

Future work will be directed towards further refinement and automation. The CL registration procedure could be made more robust by illuminating the sample with a greater number of CL spots or by increasing the camera integration time. Updates to the alignment software could furthermore allow for the distortion field correction used in Haring et al. (Haring et al., 2017) to achieve sub-5nm overlay precision. Cutting sections manually remains a significant bottleneck for throughput, as it is prone to error and requires expert training (Wanner et al., 2015). We expanded from a single section to nine, to 63, and have now placed more than 100 serial sections onto ITO-coated coverslips. Increasing beyond ~10 μm of biological material, however, is cumbersome without more sophisticated sectioning techniques such as automated tape-collecting ultramicrotome (ATUM) (Hayworth et al., 2014) or magnetic collection (Templier, 2019). These may introduce their respective complications; ATUM, for example, is designed to collect sections on (opaque) Kapton tape. More extensive automation strategies can alternatively be applied to the correlative imaging pipeline. Delpiano et al. (Delpiano et al., 2018) devised a way to automatically detect fluorescent cells using an integrated light and electron microscope. We envision a workflow for fully automated integrated array tomography in which fluorescent ROIs are automatically recognized, navigated to, and acquired, rendering three-dimensional CLEM datasets tailored to answer the specific biological research question.

DATA AVAILABILITY STATEMENT

The datasets presented in this study are available from the Nanotomy repository (http://www.nanotomy.org/OA/Lane2022FiCD/).

ETHICS STATEMENT

The animals used in this study were fed ad libitum with food pellets conducted according to the guidelines for Ethics Committee and Animal Experimentation, University of Groningen.

AUTHOR CONTRIBUTIONS

RL designed and performed the experiments, created the figures, drafted and edited the manuscript. AW prepared the samples for integrated array tomography. BG and JH provided guidance, conceived the study, and edited the manuscript.

FUNDING

This research is financially supported by the Dutch Research Council (NWO) through a Building Blocks of Life grant (737.016.010), NWO Microscopy Valley 12718, Netherlands Electron Microscopy Infrastructure (NEMI), NWO National Roadmap for Large-Scale Research Infrastructure of the Dutch Research Council (NWO 184.034.014), and a ZonMW DTL hotel grant (435005035).

ACKNOWLEDGMENTS

We would like to thank Eric Piel, Philip Winkler, and Andries Effting for technical support and software development related to the SECOM; Isabel Postmes and Daan Gieles for assisting in the development of the image processing routine for section detection; and Elizabeth Carroll for guidance on zebrafish anatomy.

SUPPLEMENTARY MATERIAL

The Supplementary Material for this article can be found online at: https://www.frontiersin.org/articles/10.3389/fmolb.2021.822232/full#supplementary-material

Supplementary Figure S1 | Reduced overlay accuracy due to extrapolation and errors in the CL registration procedure. Overlay (in)accuracy is a combination of the errors in the cross-modal and cross-spatial registration procedures. **(A)** Partial low-magnification CLEM tileset of rat pancreas from which features inside **(B-D)** and outside **(E-F)** a low-magnification EM tile were selected to assess the overlay accuracy (denoted by white squares). **(B)** Cross-modal registration error for a cell nucleus in low-magnification CLEM, measured by calculating the centroid of the nucleus in both modalities and computing the relative displacement. **(C)** Cross-

spatial registration error as measured by the phase correlation between the low and high-magnification EM. **(D)** Sub-100nm overlay accuracy for the cell nucleus in high-magnification CLEM. **(E-F)** Same as in **(B)** and **(D)** for a cell nucleus acquired outside of a low-magnification EM tile. Overlay accuracy is reduced to several hundred nanometers due to the imprecision incurred by extrapolating the cross-modal registration. **(G)** Partial low-magnification CLEM tileset of zebrafish pancreas from a section in which the CL registration procedure achieved the expected precision. **(H-J)** Same as in **(B-D)** but for a nucleus in the zebrafish pancreas. **(K-N)** Same as in **(G-J)** but for the section with the lowest apparent overlay accuracy (1.5μm). The inaccuracy is dominated by an error in the cross-modal registration as the phase correlation **(M)** shows a sub-50nm translation. Possible causes for the error include poor CL spot localization due to noise in the CL signal. Scale bars: **(A)** 50μm; **(B, D, E, F)** 0.5μm; **(G, K)** 50μm; **(H, J, L, N)** 1μm.

REFERENCES

Bishop, D., Nikić, I., Brinkoetter, M., Knecht, S., Potz, S., Kerschensteiner, M., et al. (2011). Near-infrared Branding Efficiently Correlates Light and Electron Microscopy. *Nat. Methods* 8, 568–570. doi:10.1038/nmeth.1622

Booth, D. G., Beckett, A. J., Prior, I. A., and Meijer, D. (2019). SuperCLEM: an Accessible Correlative Light and Electron Microscopy Approach for Investigation of Neurons and Glia *In Vitro*. *Biol. Open* 8 (5), bio042085. doi:10.1242/bio.042085

Bouwer, J. C., Deerinck, T. J., Bushong, E., Astakhov, V., Ramachandra, R., Peltier, S. T., et al. (2016). Deceleration of Probe Beam by Stage Bias Potential Improves Resolution of Serial Block-Face Scanning Electron Microscopic Images. *Adv. Struct. Chem. Imaging* 2 (1), 11–13. doi:10.1186/s40679-016-0025-y

Buhmann, J., Sheridan, A., Malin-Mayor, C., Schlegel, P., Gerhard, S., Kazimiers, T., et al. (2021). Automatic Detection of Synaptic Partners in a Whole-Brain Drosophila Electron Microscopy Data Set. *Nat. Methods* 18, 771–774. doi:10.1038/s41592-021-01183-7

Burel, A., Lavault, M. T., Chevalier, C., Gnaegi, H., Prigent, S., Mucciolo, A., et al. (2018). A Targeted 3D EM and Correlative Microscopy Method Using SEM Array Tomography. *Development* 145 (12), dev160879. doi:10.1242/dev.160879

Collinson, L. M., Carroll, E. C., and Hoogenboom, J. P. (2017). Correlating 3D Light to 3D Electron Microscopy for Systems Biology. *Curr. Opin. Biomed. Eng.* 3, 49–55. doi:10.1016/j.cobme.2017.10.006

de Boer, P., Hoogenboom, J. P., and Giepmans, B. N. G. (2015). Correlated Light and Electron Microscopy: Ultrastructure Lights up!. *Nat. Methods* 12, 503–513. doi:10.1038/nmeth.3400

de Boer, P., Pirozzi, N. M., Wolters, A. H. G., Kuipers, J., Kusmartseva, I., Atkinson, M. A., et al. (2020). Large-scale Electron Microscopy Database for Human Type 1 Diabetes. *Nat. Commun.* 11 (1), 2475–2479. doi:10.1038/s41467-020-16287-5

Delpiano, J., Pizarro, L., Peddie, C. J., Jones, M. L., Griffin, L. D., and Collinson, L. M. (2018). Automated Detection of Fluorescent Cells in In-Resin Fluorescence Sections for Integrated Light and Electron Microscopy. *J. Microsc.* 271 (1), 109–119. doi:10.1111/jmi.12700

Eckstein, N., Buhmann, J., Cook, M., and Funke, J. (2020). "Microtubule Tracking in Electron Microscopy Volumes," in International Conference on Medical Image Computing and Computer-Assisted Intervention, Lima, Peru, October 4–8, 2020 (Springer), 99–108. doi:10.1007/978-3-030-59722-1_10

Franke, C., Repnik, U., Segeletz, S., Brouilly, N., Kalaidzidis, Y., Verbavatz, J. M., et al. (2019). Correlative Single-molecule Localization Microscopy and Electron Tomography Reveals Endosome Nanoscale Domains. *Traffic* 20 (8), 601–617. doi:10.1111/tra.12671

Fu, Z., Peng, D., Zhang, M., Xue, F., Zhang, R., He, W., et al. (2020). mEosEM Withstands Osmium Staining and Epon Embedding for Super-resolution CLEM. *Nat. Methods* 17 (1), 55–58. doi:10.1038/s41592-019-0613-6

Gabarre, S., Vernaillen, F., Baatsen, P., Vints, K., Cawthorne, C., Boeynaems, S., et al. (2021). A Workflow for Streamlined Acquisition and Correlation of Serial Regions of Interest in Array Tomography. *BMC Biol.* 19 (1), 1–15. doi:10.1186/s12915-021-01072-7

Giepmans, B. N., Adams, S. R., Ellisman, M. H., and Tsien, R. Y. (2006). The Fluorescent Toolbox for Assessing Protein Location and Function. *Science* 312 (5771), 217–224. doi:10.1126/science.1124618

Haring, M. T., Liv, N., Zonnevylle, A. C., Narvaez, A. C., Voortman, L. M., Kruit, P., et al. (2017). Automated Sub-5 Nm Image Registration in Integrated Correlative Fluorescence and Electron Microscopy Using Cathodoluminescence Pointers. *Sci. Rep.* 7, 436211–436219. doi:10.1038/srep43621

Hayworth, K. J., Morgan, J. L., Schalek, R., Berger, D. R., Hildebrand, D. G. C., and Lichtman, J. W. (2014). Imaging ATUM Ultrathin Section Libraries with WaferMapper: a Multi-Scale Approach to EM Reconstruction of Neural Circuits. *Front. Neural Circuits* 8, 68. doi:10.3389/fncir.2014.00068

Heinrich, L., Bennett, D., Ackerman, D., Park, W., Bogovic, J., Eckstein, N., et al. (2021). Whole-cell Organelle Segmentation in Volume Electron Microscopy. *Nature* 599, 141–146. doi:10.1038/s41586-021-03977-3

Hildebrand, D. G. C., Cicconet, M., Torres, R. M., Choi, W., Quan, T. M., Moon, J., et al. (2017). Whole-brain Serial-Section Electron Microscopy in Larval Zebrafish. *Nature* 545, 7654345–7654349. doi:10.1038/nature22356

Karreman, M. A., Mercier, L., Schieber, N. L., Shibue, T., Schwab, Y., and Goetz, J. G. (2014). Correlating Intravital Multi-Photon Microscopy to 3D Electron Microscopy of Invading Tumor Cells Using Anatomical Reference Points. *PLoS One* 9, e114448. doi:10.1371/journal.pone.0114448

Karreman, M. A., Hyenne, V., Schwab, Y., and Goetz, J. G. (2016). Intravital Correlative Microscopy: Imaging Life at the Nanoscale. *Trends Cel Biol.* 26 (11), 848–863. doi:10.1016/j.tcb.2016.07.003

Khairy, K., Denisov, G., and Saalfeld, S. (2018). *Joint Deformable Registration of Large EM Image Volumes: A Matrix Solver Approach*. arXiv preprint arXiv: 1804.10019. arXiv.

Kornfeld, J., and Denk, W. (2018). Progress and Remaining Challenges in High-Throughput Volume Electron Microscopy. *Curr. Opin. Neurobiol.* 50, 261–267. doi:10.1016/j.conb.2018.04.030

Kuipers, J., de Boer, P., and Giepmans, B. N. G. (2015). Scanning EM of Non-heavy Metal Stained Biosamples: Large-Field of View, High Contrast and Highly Efficient Immunolabeling. *Exp. Cel Res.* 337 (2), 202–207. doi:10.1016/j.yexcr.2015.07.012

Kukulski, W., Schorb, M., Welsch, S., Picco, A., Kaksonen, M., and Briggs, J. A. G. (2011). Correlated Fluorescence and 3D Electron Microscopy with High Sensitivity and Spatial Precision. *J. Cel Biol.* 192 (1), 111–119. doi:10.1083/jcb.201009037

Lane, R., Vos, Y., Wolters, A. H. G., van Kessel, L., Chen, S. E., Liv, N., et al. (2021). Optimization of Negative Stage Bias Potential for Faster Imaging in Large-Scale Electron Microscopy. *J. Struct. Biol. X* 5, 100046. doi:10.1016/j.yjsbx.2021.100046

Lee, C.-W., Wilfling, F., Ronchi, P., Allegretti, M., Mosalaganti, S., Jentsch, S., et al. (2020). Selective Autophagy Degrades Nuclear Pore Complexes. *Nat. Cel Biol.* 22 (2), 159–166. doi:10.1038/s41556-019-0459-2

Liou, W., Geuze, H. J., and Slot, J. W. (1996). Improving Structural Integrity of Cryosections for Immunogold Labeling. *Histochem. Cel Biol.* 106 (1), 41–58. doi:10.1007/bf02473201

Liu, J., Li, L., Yang, Y., Hong, B., Chen, X., Xie, Q., et al. (2020). Automatic Reconstruction of Mitochondria and Endoplasmic Reticulum in Electron Microscopy Volumes by Deep Learning. *Front. Neurosci.* 14, 599. doi:10.3389/fnins.2020.00599

Liv, N., Zonnevylle, A. C., Narvaez, A. C., Effting, A. P. J., Voorneveld, P. W., Lucas, M. S., et al. (2013). Simultaneous Correlative Scanning Electron and High-NA Fluorescence Microscopy. *PloS One* 8 (2), e55707. doi:10.1371/journal.pone.0055707

Lowe, D. G. (1999). "Object Recognition from Local Scale-Invariant Features," in Proceedings of the Seventh IEEE International Conference on Computer Vision, Kerkyra, Greece, 20-27 September, 1999 (IEEE), 1150–1157. doi:10.1109/iccv.1999.790410

Micheva, K. D., and Smith, S. J. (2007). Array Tomography: a New Tool for Imaging the Molecular Architecture and Ultrastructure of Neural Circuits. *Neuron* 55 (1), 25–36. doi:10.1016/j.neuron.2007.06.014

Ounkomol, C., Seshamani, S., Maleckar, M. M., Collman, F., and Johnson, G. R. (2018). Label-free Prediction of Three-Dimensional Fluorescence Images from Transmitted-Light Microscopy. *Nat. Methods* 15 (11), 917–920. doi:10.1038/s41592-018-0111-2

Paez-Segala, M. G., Sun, M. G., Shtengel, G., Viswanathan, S., Baird, M. A., Macklin, J. J., et al. (2015). Fixation-resistant Photoactivatable Fluorescent Proteins for CLEM. *Nat. Methods* 12 (3), 215–218. doi:10.1038/nmeth.3225

Paul-Gilloteaux, P., Heiligenstein, X., Belle, M., Domart, M.-C., Larijani, B., Collinson, L., et al. (2017). eC-CLEM: Flexible Multidimensional

Registration Software for Correlative Microscopies. *Nat. Methods* 14 (2), 102–103. doi:10.1038/nmeth.4170

Peddie, C. J., and Collinson, L. M. (2014). Exploring the Third Dimension: Volume Electron Microscopy Comes of Age. *Micron* 61, 9–19. doi:10.1016/j.micron.2014.01.009

Peddie, C. J., Blight, K., Wilson, E., Melia, C., Marrison, J., Carzaniga, R., et al. (2014). Correlative and Integrated Light and Electron Microscopy of In-Resin GFP Fluorescence, Used to Localise Diacylglycerol in Mammalian Cells. *Ultramicroscopy* 143, 3–14. doi:10.1016/j.ultramic.2014.02.001

Polishchuk, R. S., Polishchuk, E. V., Marra, P., Alberti, S., Buccione, R., Luini, A., et al. (2000). Correlative Light-Electron Microscopy Reveals the Tubular-Saccular Ultrastructure of Carriers Operating between Golgi Apparatus and Plasma Membrane. *J. Cel Biol.* 148, 45–58. doi:10.1083/jcb.148.1.45

Ravelli, R. B., Kalicharan, R. D., Avramut, M. C., Sjollema, K. A., Pronk, J. W., Dijk, F., et al. (2013). Destruction of Tissue, Cells and Organelles in Type 1 Diabetic Rats Presented at Macromolecular Resolution. *Sci. Rep.* 3 (1), 1804–1806. doi:10.1038/srep01804

Ronchi, P., Mizzon, G., Machado, P., D'Imprima, E., Best, B. T., Cassella, L., et al. (2021). High-Precision Targeting Workflow for Volume Electron Microscopy. *J. Cell Biol.* 220 (9), e202104069.

Saalfeld, S., Cardona, A., Hartenstein, V., and Tomancak, P. (2009). CATMAID: Collaborative Annotation Toolkit for Massive Amounts of Image Data. *Bioinformatics* 25 (15), 1984–1986. doi:10.1093/bioinformatics/btp266

Saalfeld, S., Fetter, R., Cardona, A., and Tomancak, P. (2012). Elastic Volume Reconstruction from Series of Ultra-thin Microscopy Sections. *Nat. Methods* 9 (7), 717–720. doi:10.1038/nmeth.2072

Schindelin, J., Arganda-Carreras, I., Frise, E., Kaynig, V., Longair, M., Pietzsch, T., et al. (2012). Fiji: an Open-Source Platform for Biological-Image Analysis. *Nat. Methods* 9 (7), 676–682. doi:10.1038/nmeth.2019

Seifert, R., Markert, S. M., Britz, S., Perschin, V., Erbacher, C., Stigloher, C., et al. (2020). DeepCLEM: Automated Registration for Correlative Light and Electron Microscopy Using Deep Learning. *F1000Res* 9, 1275. doi:10.12688/f1000research.27158.1

Srinivasa Raja, A., Boer, P., Giepmans, B. N. G., and Hoogenboom, J. P. (2021). Electron-Beam Induced Luminescence and Bleaching in Polymer Resins and Embedded Biomaterial. *Macromol. Biosci.* 21, 2100192. doi:10.1002/mabi.202100192

Tapia, J. C., Kasthuri, N., Hayworth, K. J., Schalek, R., Lichtman, J. W., Smith, S. J., et al. (2012). High-contrast *en bloc* staining of neuronal tissue for field emission scanning electron microscopy. *Nat. Protoc.* 7 (2), 193–206. doi:10.1038/nprot.2011.439

Templier, T. (2019). MagC, Magnetic Collection of Ultrathin Sections for Volumetric Correlative Light and Electron Microscopy. *Elife* 8, e45696. doi:10.7554/eLife.45696

Tuijtel, M. W., Koster, A. J., Jakobs, S., Faas, F. G. A., and Sharp, T. H. (2019). Correlative Cryo Super-resolution Light and Electron Microscopy on Mammalian Cells Using Fluorescent Proteins. *Sci. Rep.* 9 (1), 1369–1411. doi:10.1038/s41598-018-37728-8

Van Rijnsoever, C., Oorschot, V., and Klumperman, J. (2008). Correlative Light-Electron Microscopy (CLEM) Combining Live-Cell Imaging and Immunolabeling of Ultrathin Cryosections. *Nat. Methods* 5, 973–980. doi:10.1038/nmeth.1263

Vos, Y., Lane, R. I., Peddie, C. J., Wolters, A. H. G., and Hoogenboom, J. P. (2021). Retarding Field Integrated Fluorescence and Electron Microscope. *Microsc. Microanal.* 27 (1), 109–120. doi:10.1017/s1431927620024745

Wanner, A. A., Kirschmann, M. A., and Genoud, C. (2015). Challenges of Microtome-Based Serial Block-Face Scanning Electron Microscopy in Neuroscience. *J. Microsc.* 259 (2), 137–142. doi:10.1111/jmi.12244

Watanabe, S., Punge, A., Hollopeter, G., Willig, K. I., Hobson, R. J., Davis, M. W., et al. (2011). Protein Localization in Electron Micrographs Using Fluorescence Nanoscopy. *Nat. Methods* 8 (1), 80–84. doi:10.1038/nmeth.1537

Watson, M. L. (1958). Staining of Tissue Sections for Electron Microscopy with Heavy Metals. *J. Cel Biol.* 4, 475–478. doi:10.1083/jcb.4.4.475

Zonnevylle, A. C., Van Tol, R. F., Liv, N., Narvaez, A. C., Effting, A. P., Kruit, P., et al. (2013). Integration of a High-NA Light Microscope in a Scanning Electron Microscope. *J. Microsc.* 252 (1), 58–70. doi:10.1111/jmi.12071

Conflict of Interest: RL, AHGW, and BNGG declare that the research was conducted in the absence of any commercial or financial relationships that could be construed as a potential conflict of interest. The integrated microscope used in this study is a product of Delmic B.V. of which JPH is a co-founder and shareholder.

Publisher's Note: All claims expressed in this article are solely those of the authors and do not necessarily represent those of their affiliated organizations, or those of the publisher, the editors, and the reviewers. Any product that may be evaluated in this article, or claim that may be made by its manufacturer, is not guaranteed or endorsed by the publisher.

frontiers in Cell and Developmental Biology

ORIGINAL RESEARCH
published: 08 March 2022
doi: 10.3389/fcell.2022.843687

"Orphan" Connexin43 in Plakophilin-2 Deficient Hearts Revealed by Volume Electron Microscopy

Chantal J. M. van Opbergen[1†], Joseph Sall[2†], Chris Petzold[2], Kristen Dancel-Manning[2], Mario Delmar[1†] and Feng-Xia Liang[2*†]*

[1]The Leon H. Charney Division of Cardiology, New York University Grossman School of Medicine, New York, NY, United States, [2]Microscopy Laboratory, Division of Advanced Research Technologies, New York University Grossman School of Medicine, New York, NY, United States

OPEN ACCESS

Edited by:
Paul Verkade,
University of Bristol, United Kingdom

Reviewed by:
Ben N. G. Giepmans,
University Medical Center Groningen, Netherlands
Pedro Machado,
King's College London, United Kingdom
Michaela Wilsch-Bräuninger,
Max Planck Society, Germany

***Correspondence:**
Mario Delmar
Mario.Delmar@nyulangone.org
Feng-Xia Liang
Fengxia.Liang@nyulangone.org

†These authors have contributed equally to this work

Specialty section:
This article was submitted to Cellular Biochemistry, a section of the journal Frontiers in Cell and Developmental Biology

Received: *26 December 2021*
Accepted: *21 February 2022*
Published: *08 March 2022*

Citation:
van Opbergen CJM, Sall J, Petzold C, Dancel-Manning K, Delmar M and Liang F-X (2022) "Orphan" Connexin43 in Plakophilin-2 Deficient Hearts Revealed by Volume Electron Microscopy. Front. Cell Dev. Biol. 10:843687. doi: 10.3389/fcell.2022.843687

Previous studies revealed an abundance of functional Connexin43 (Cx43) hemichannels consequent to loss of plakophilin-2 (PKP2) expression in adult murine hearts. The increased Cx43-mediated membrane permeability is likely responsible for excess entry of calcium into the cells, leading to an arrhythmogenic/cardiomyopathic phenotype. The latter has translational implications to the molecular mechanisms of inheritable arrhythmogenic right ventricular cardiomyopathy (ARVC). Despite functional evidence, visualization of these "orphan" (i.e., non-paired in a gap junction configuration) Cx43 hemichannels remains lacking. Immuno-electron microscopy (IEM) remains an extremely powerful tool to localize, with nanometric resolution, a protein within its native structural landscape. Yet, challenges for IEM are to preserve the antigenicity of the molecular target and to provide access for antibodies to reach their target, while maintaining the cellular/tissue ultrastructure. Fixation is important for maintaining cell structure, but strong fixation and vigorous dehydration (as it is routine for EM) can alter protein structure, thus impairing antigen-antibody binding. Here, we implemented a method to combine pre-embedding immunolabeling (pre-embedding) with serial block-face scanning electron microscopy (SBF-SEM). We utilized a murine model of cardiomyocyte-specific, Tamoxifen (TAM) activated knockout of PKP2. Adult hearts were harvested 14 days post-TAM, at this time hearts present a phenotype of concealed ARVC (i.e., an arrhythmogenic phenotype but no overt structural disease). Thick (200 µm) vibratome slices were immunolabelled for Cx43 and treated with nanogold or FluoroNanogold, coupled with a silver enhancement. Left or right ventricular free walls were dissected and three-dimensional (3D) localization of Cx43 in cardiac muscle was performed using SBF-SEM. Reconstructed images allowed us to visualize the entire length of gap junction plaques, seen as two parallel, closely packed strings of Cx43-immunoreactive beads at the intercalated disc. In contrast, in PKP2-deficient hearts we observed bulging of the intercellular space, and entire areas

Abbreviations: ARVC, arrhythmogenic right ventricular cardiomyopathy; BSA, bovine serum albumin; Ca^{2+}, calcium; Cx43, connexin43; Cx43-Hs, connexin43 hemichannels; dpi, days post tamoxifen injection; EM, electron microscopy; FE-SEM, field emission-scanning electron microscope; IEM, immuno-electron microscopy; LV, left ventricle; PBS, phosphate buffer saline; PFA, paraformaldehyde; PKP2, plakophilin-2; ID, intercalated disc; PKP2cKO, cardiomyocyte-specific, tamoxifen-activated, PKP2 knockout; RV, right ventricle; SBF-SEM, serial block-face scanning electron microscopy; SEM, scanning electron microscopy; TAM, tamoxifen; TEM, transmission electron microscopy; vEM, volume electron microscopy.

where only one of the two strings could be observed, indicating the presence of orphan Cx43. We conclude that pre-embedding and SBF-SEM allowed visualization of cardiac Cx43 plaques in their native environment, providing for the first time a visual complement of functional data indicating the presence of orphan Cx43 hemichannels resulting from loss of desmosomal integrity in the heart.

Keywords: arrhythmogenic right ventricular cardiomyopathy, plakophilin-2, serial block-face scanning electron microscopy, volume electron microscopy, connexin43 hemichannels, nanogold

INTRODUCTION

Plakophilin-2 (PKP2) is an abundant protein of the desmosome, an intercellular adhesion structure (Grossmann et al., 2004). Mutations in PKP2 associate with most cases of gene-positive arrhythmogenic right ventricular cardiomyopathy (ARVC), a pleiotropic disease that can manifest as mainly electrical, structural or both depending on stage progression (Ohno, 2016). As such, while ARVC is best recognized as a cardiomyopathy of right ventricular predominance, catecholaminergic sudden cardiac arrest is common during the subclinical (or "concealed") phase of the disease (Cadrin-Tourigny, 2019; Müssigbrodt et al., 2019). The molecular/cellular mechanisms responsible for these arrhythmias remain unclear and current treatment options are still lacking. Recent studies have demonstrated that in addition to cell-cell adhesion, PKP2 and its intercalated disc (ID) partners translate information initiated at the site of cell-cell contact into intracellular signals that maintain structural and electrical homeostasis (Cerrone et al., 2017; Austin et al., 2019).

To study the role of cardiomyocyte PKP2 expression in cardiac function, we developed a cardiomyocyte-specific, tamoxifen (TAM)-activated, PKP2 knockout murine line [PKP2cKO; (Cerrone et al., 2017)]. Adult PKP2cKO mice present, in a compressed timeline, aspects of the history of human ARVC. Following TAM injection these hearts progress from a normal state, to an arrhythmogenic cardiomyopathy of right ventricular (RV) predominance and eventually biventricular dilated cardiomyopathy and end-stage failure (Cerrone et al., 2017). In Kim et al., PKP2cKO mice were studied 14 days post-TAM, a time point at which hearts present a phenotype of concealed ARVC (i.e., an arrhythmogenic phenotype but no overt structural disease) (Kim et al., 2019). At this stage, ventricular myocytes present increased Connexin43 (Cx43)-mediated membrane permeability. The latter is considered responsible for an excess entry of calcium (Ca^{2+}) into the cells, eventually leading to the arrhythmogenic/cardiomyopathic phenotype.

Gap junction plaque formation is known to depend on proper intercellular adhesion (Beardslee et al., 2000). A recent study from our group showed that PKP2 deficiency can increase cell membrane permeability to ATP, an event prevented by silencing Cx43 expression (Cerrone et al., 2018). In addition, it is known that Cx43 hemichannels (Cx43-Hs) reside in the perimeter of the gap junction plaques (the perinexus) (Rhett et al., 2011) and are capable of flickering with very low probability (Contreras et al., 2003; Verma et al., 2009). We postulate that loss of PKP2 disrupts gap junction plaque integrity, thereby increasing the population of "orphan" Cx43-Hs in the perinexus. The latter would have important translational implications to the molecular mechanisms of inheritable ARVC. Despite functional evidence, visualization of these "orphan" (i.e., non-paired in a gap junction configuration) Cx43-Hs remains lacking.

With the development of confocal microscopy, live cell imaging and super resolution microscopy, the spatiotemporal characteristics of protein landscapes can now be unraveled in high detail. However, fluorescent microscopy has a restricted imaging range within 1 μm of the coverslip, a maximal resolution of ~10–30 nm and is constrained to a small number of photo switchable fluorophores. Therefore, it lacks the ability to detect subcellular protein structures at sub-diffraction limit resolution. In that regard, is super resolution microscopy not the most optimal tool for detailed reconstruction of for example individual gap junction plaques, of which the intercellular space is between 2–4 nm. Immuno-electron microscopy (IEM) is an extremely powerful tool to localize, with nanometric resolution, a protein within its native structural landscape. Yet, challenges for IEM rely in preservation of antigenicity of molecular targets, accessibility for antibodies, while maintaining the cellular/tissue ultrastructure. Colloidal gold particles as post-embedding immunoprobes, combined with immunoglobulins or immunoglobuline-binding proteins (protein A), have been widely used for subcellular localization of specific molecules using EM (Faulk and Taylor, 1971; Roth et al., 1978). Previous studies show that smaller gold particles provide a higher labeling density, but gold particles with a diameter below 4 nm become hard to distinguish on ultrathin biological specimen under transmission EM (TEM). Therefore, gold particles with a diameter ranging from 5 to 15 nm are most convenient for on section immunolabeling (Slot and Geuze, 1981; van Bergen en Henegouwen et al., 1986; Yokota, 1988). Given the fact that colloidal gold particles have limited penetration capabilities into cells or tissues (even when using smaller size gold particles, such as 1–3 nm in diameter) and lack stability during the labeling process, they are not considered an optimal tool for pre-embedding and volumetric imaging (Hainfeld and Furuya, 1992). Attempts to prepare probes combining fluorescent labeling and colloidal gold for correlative microscopy resulted in limited success over the years, in part caused by restricted tissue penetration capabilities and hampered fluorescence intensity of these probes (De Brabander et al., 1985, De Brabander et al., 1986; Powell et al., 1997).

Nanogold particles provide an effective alternative. Nanogold is a neutral molecule with a diameter of 1.4 nm that is stable in a

wide range of pH's and ionic charges (Hainfeld and Furuya, 1992). Previous studies have shown that these 1.4 nm gold–Fab' conjugates can penetrate tissue sections up to 40 μm of thickness, providing a perfect approach for pre-embedding immunolabeling (Sun et al., 1995). Fixation is important to maintain cell structure, but strong fixation and vigorous dehydration (as is routine for EM) can alter protein structure, thus impairing antigen-antibody binding. Since immunolabeling is performed on weakly fixed cells or tissues prior to dehydration, nanogold pre-embedding has a maximum antibody-antigen binding efficiency, comparable to light microscopy labeling. By combining fluorescent probes with covalent bound 1.4 nm clusters of gold atoms, FluoroNanogold allows the visualization of any given antigen using correlative microscopy and/or multimodal microscopy (Cheutin et al., 2007; Giepmans, 2008). Therefore, pre-embedding using nanogold or FluoroNanogold is considered one of the optimal tools for volumetric electron microscopy (volume EM, vEM).

In this study our objective was to visualize and examine, in three-dimensions (3D), the gap junction plaque morphology present in the adult murine heart. We used 200 μm thick sections of adult ventricular free walls of control and PKP2cKO cardiac muscle, pre-embedded with nanogold or FluoroNanogold labeling of Cx43. We measured the characteristics of the intercellular space and of the perinexus using a 3D-vEM approach. Our data show that loss of PKP2 expression led to widening of the intercellular space in the gap junction plaque, and increased abundance of unpaired (orphan) Cx43 channels in the gap junction. We conclude that pre-embedding and serial block-face scanning electron microscopy allowed visualization of cardiac Cx43 plaques in their native environment, providing for the first time a visual complement of functional data indicating the presence of orphan Cx43 hemichannels resulting from loss of desmosomal integrity in the heart.

MATERIALS AND METHODS

Animal Model

We utilized a murine model of cardiomyocyte-specific, Tamoxifen activated knockout of PKP2 (PKP2cKO) previously developed in our laboratory (Cerrone et al., 2017). Mice C57BL/6 were treated in accordance to the Guide for Care and Use of Laboratory Animals published by the US National Institutes of Health. Procedures were approved by the NYU IACUC committee under protocol number 160726-03.

Chemical Fixation, Immunolabeling and Resin Embedding

Control and PKP2cKO mice, 14 days post Tamoxifen injection, were anesthetized by inhalation of 100% CO_2 and then euthanized by cervical dislocation. After euthanasia, hearts were dissected and perfused through a Langendorf column with a fixative solution of 0.1 M phosphate buffer saline (PBS) and 4% Paraformaldehyde (PFA), then subsequently fixed at 4°C overnight in 4% PFA/PBS. Cross sections of the heart were generated using a vibratome (Leica VT1200S, Buffalo Grove, IL) at 200 μm thickness. Sections were stored in a 24-wells plate (Corning Incorporated, Corning, NY) in 4% PFA/PBS, one section per well (**Figure 1A**).

For immunolabeling with Cx43, the vibratome sections were washed with PBS and fixed in freshly made 4% PFA and 0.5% glutaraldehyde/PBS for 1 h. After fixation, all steps were performed on a slow speed shaker. The sections were incubated with 50 mM glycine/PBS for 30 min to eliminate unbound aldehydes. Thereafter they were washed in PBS for 15 min and subsequently permeabilized with 0.05% Triton X-100/PBS for 30 min. After blocking with 3% Bovine Serum Albumin (BSA) in PBS for 1 h, the sections were incubated with anti-Connexin43 (Anti-Connexin43 C-terminus cytosolic, affinity purified rabbit polyclonal, Millipore, Cat. #AB1728, 1:50) in 1% BSA/PBS for 2 h at room temperature, after that they were incubated at 4°C overnight. Sections were washed 6 times for 30 min with 1% BSA/PBS, and incubated with Alexa Fluoro® 546 FluoroNanogold™ Fab' or nanogold Fab' goat anti-rabbit IgG conjugated secondary antibodies (Nanoprobes, Yanphank, NY, 1: 200). Sections were incubated for 2 h at room temperature and then overnight at 4°C. Sections were once more washed with PBS and imaged on an inverted epifluorescence Zeiss AxioObserver microscope with Plan-Neofluar 10x/0.3NA, Plan Apochromat 20x/0.8NA and Plan-Neofluar 40x/0.9NA lenses. For FluoroNanogold labeled tissue sections, fluorescence images were collected with a narrow pass Cy3 filter set, Zeiss part number 43 HE with 550/25 nm exciter, 570 nm dichroic mirror, and 605/70 nm emission filter. After imaging, the sections underwent another fixation step with 2.5% glutaraldehyde/PBS for 2 h, then they were extensively washed with deionized water and 0.02 M sodium citrate buffer (pH 7.0), 3 times for 15 min. Silver enhancement (HQ Silver enhancement kit, Nanoprobes, Yanphank, NY) was performed in the dark for 8 min. Timing of silver enhancement was optimized to maximize the size of gold particles (10–20 nm) without increasing background. Subsequently, sections were washed once with deionized water and imaged with a Zeiss AxiObservor using the brightfield mode. The sections were fixed in 0.5% O_sO_4 in aqueous solution for 15 min and stained with 0.5% uranyl acetate in aqueous solution for 1 h in the dark. Sections were dehydrated in a series of ethanol, exchanged with acetone and embedded in Durcupan ACM Araldite resin (Electron Microscopy Sciences, EMS, PA), using two pieces of ALCARE sheet (Ted Pella Inc.), which were situated and stabilized between two glass slides. The samples were polymerized for 48 h at 60°C.

Serial Block-Face Scanning Electron Microscopy

Using a razor blade, the left and right ventricles were trimmed (**Figure 1C**) and mounted on a standard Gatan 3View aluminum specimen pin (EMS item # 75959-02) using silver conductive epoxy glue (Ted Pella Inc.) to electrically ground the tissue block. The sample was trimmed to a square or rectangular shape and positioned with a Leica ultramicrotome (Leica EM UC6, Buffalo Grove, IL, United States). The sample was then sputter-coated

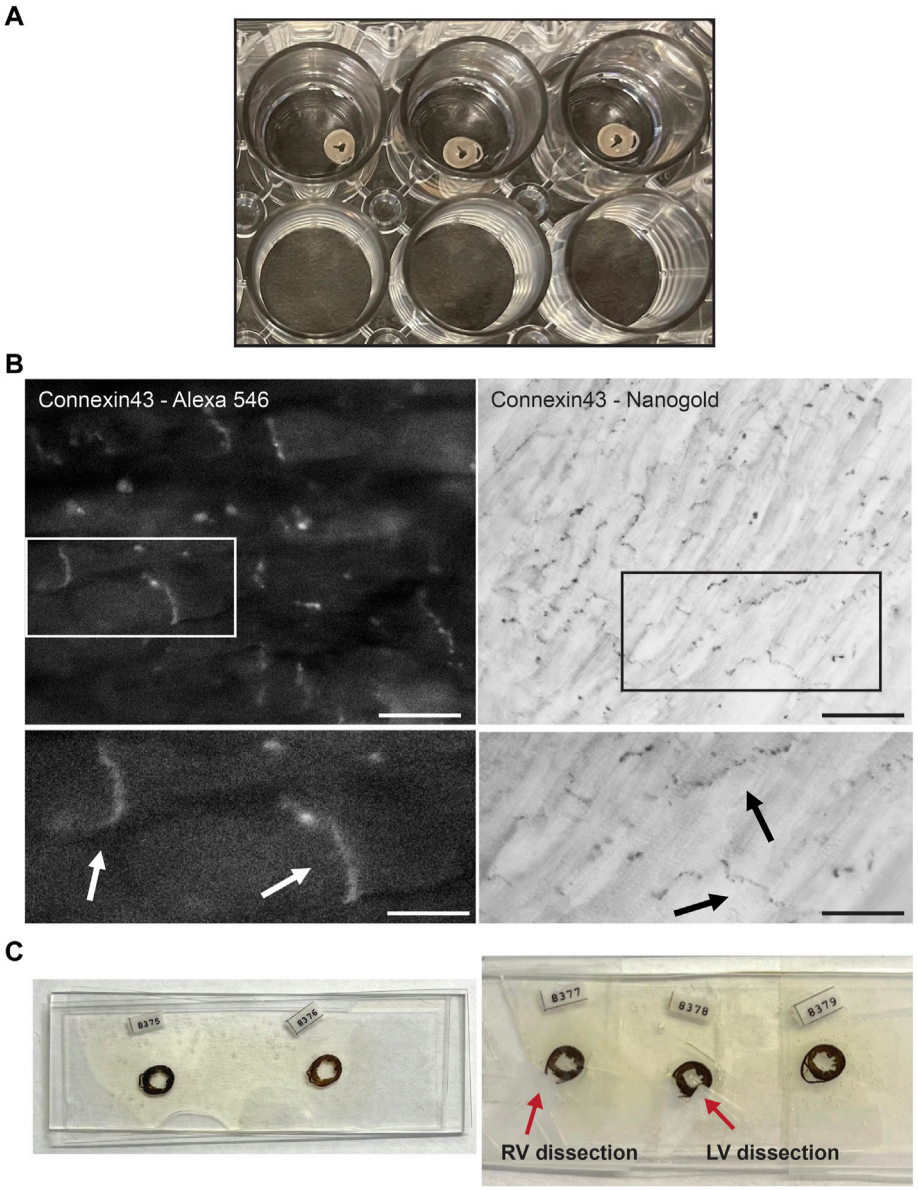

FIGURE 1 | Experimental setup of Connexin43 nanogold labeling in murine cardiac sections. **(A)** Thick cross sections from murine control hearts preserved in 4% paraformaldehyde, stored in a 24 wells plate. Sections are sectioned with a vibratome and of 200 µm thickness. **(B)** FluoroNanogold labeling of adult murine cardiac sections. *Left panel*: FluoroNanogold-546 labeled Connexin43 visualization by light microscopy. Scalebar: 10 µm. Zoom-in at indicated region presented in the panel below, arrowheads depict the intercalated disc (ID). Scalebar: 5 µm. *Right panel*: Nanogold visualization after silver enhancement of Connexin43 by light microscopy. Pictures in both frames are from the same cardiac section. Scalebar: 50 µm. Zoom-in at indicated region presented in the panel below, arrowheads depict the intercalated disc (ID). Scalebar: 10 µm. **(C)** Examples of flat embedded cardiac sections after nanogold labeling. In the left panel the entire cross sections are presented. On the right, two representative examples are shown from dissections of left or right ventricular samples. RV: Right ventricle, LV: Left ventricle.

with a thin layer of 80/20 gold/palladium (Denton Vacuum DESK V sputter coater, NJ, United States). Coating was performed to further reduce any electrical charge during imaging. Serial block face (SBF) imaging was performed using a Gatan OnPoint BSE detector in a Zeiss GEMINI300 VP Field Emission Scanning Electron Microscope (FE-SEM) equipped with a Gatan 3View automatic microtome unit (Gatan, Pleasanton, CA, United States). The system was set to cut sections at 50 nm thickness. Imaging was performed utilizing Focus Charge Compensation nitrogen gas injection set at 40% (2.9E-03 mBar) to reduce imaging artifacts related to sample-charge. Images were collected after each round of sectioning from the block face using the SEM beam at 1.2 keV with a dwell time of 2.0 µs/pixel and a working distance of 7.4 mm. Each frame was 38 × 50 µm with a pixel size of 3.5 nm and slice thickness of 50 nm. Data acquisition occurred in an automated way using the Auto Slice and View G3 software to collect a 1 × 3 montage scan with a 15% (7.5 µm) overlap. A stack of 150 slices was aligned,

stitched, and assembled using the Grid/Collection stitching plugin for ImageJ (Preibisch et al., 2009). A volume of 38 × 105 × 15 μm^3 dimensions was obtained from the tissue block.

Data Processing and Analysis

Data was acquired in an automated way using Gatan Digital Micrograph and analyzed with ORS Dragonfly software (Object Research Systems Inc.). For the experiments, 3 hearts per genotype were used, 3 control and 3 PKP2cKO hearts in total. Each heart was divided in the LV and RV and per ventricle we studied 2–3 regions of interest (ROI). Per ROI, 3–4 gap junction plaques were analyzed. Each gap junction plaque was analyzed throughout the entire structure (3D), meaning from the first plane until the last plane. Per plane (2D), we manually draw the area between Cx43 immunoreactive beads and length of the gap junction plaque, which was calculated by ORS Dragonfly software accordingly. The maximal width was measured in the widest area of the entire gap junction plaque. For 3D segmentation of the inner ID space, we traced the contour of the ID membrane. Hemiplaque length was manually drawn over the gap junction area that did not consist out of a consecutive "double" strand of Cx43 immunoreactive beads and calculated by ORS Dragonfly software.

STATISTICS

Continuous variables are presented as box and whisker plots, reaching from the minimum to maximum value. Categorical variables are presented as percentage or total length. All data sets were tested for normal distribution by the Shapiro-Wilk and Kolmogorov-Smirnov tests, data were considered normally distributed when passing one of these two tests. Normally distributed data were compared using the Student's *t*-test. Non-normally distributed data were compared using the Mann–Whitney Test. Statistical significance was assumed when $p < 0.05$. Statistical tests were performed using GraphPad Prism.

RESULTS

FluoroNanogold Labeling of Connexin43 in Adult Murine Hearts

FluoroNanogold labeling in combination with silver enhancement was tested on thick vibratome (200 µm) sections of control adult murine hearts (**Figure 1A**). FluoroNanogold 546-labeled vibratome sections were imaged with light microscopy and Cx43 fluorescent labeling was clearly detectable in the perinexus (**Figure 1B**, left panel). Negative control stains, in which the primary antibody was omitted, were performed to confirm specificity of Cx43 fluorescent labeling; fluorescent signal appeared completely absent. Subsequently, these sections were processed for silver enhancement. Gold labeled Cx43 was distinctly visible in the gap junction plaques after silver enhancement. (**Figure 1B**, right panel). Pictures in both frames are from the same cardiac section. Further studies, focused on exploring alterations in the gap junction plaque morphology by loss of PKP2 expression, were carried out in left or right ventricular free walls separately (**Figure 1C**) using nanogold as marker.

3D Immuno-EM Reconstruction of Connexin43 Labeling

It is known that loss of *PKP2* expression impairs cell-cell adhesion and loss of cell adhesion destabilizes gap junctions (Bass-Zubek et al., 2008; Sato et al., 2011). In (Kim et al., 2019) we confirmed cell separation at the intercalated disc in hearts of PKP2cKO mice 14 dpi (Kim et al., 2019). In this study, we follow up on these observations and implement a quantitative approach. To characterize the perinexal morphology, we obtained 3D reconstructions of Cx43 in control and PKP2cKO murine hearts by nanogold labeling of ventricular free walls. These corresponding cardiac sections were imaged using SBF-SEM and images were collected with a Gatan 3View system. Reconstructed images allowed us to visualize the entire length of gap junction plaques, seen as two parallel, closely packed strings of Cx43-immunoreactive beads at the intercalated disc (**Figure 2A** upper panel, **Figure 2B** right panel, **Figure 3A**, **Supplementary Video S1**). Separation of these closely aligned Cx43 beads became apparent in the PKP2cKO 14dpi cardiac samples (**Figure 2A** bottom panel, **Figure 3B**, **Supplementary Video S2**), in both in the left and right ventricular free wall. Visualization of these morphological discrepancies was performed by 3D segmentation and conventional image processing (**Figures 2**, **3**).

Visualization of Orphan Connexin43 Hemichannels in PKP2cKO Hearts

In **Figure 2A**, the various frames correspond to different section levels of the same samples, either control, or from a PKP2cKO heart. These pictures emphasize morphological alterations throughout the gap junction plaque structure and highlight the importance of 3D reconstructions for quantitative analyses. Widening of the intercellular space and areas where single Cx43 immunoreactive beads lack opposing beads in close proximity, could be clearly observed in PKP2cKO hearts (**Figure 2A** bottom panel). These observations indicate the presence of orphan Cx43 hemichannels in adult PKP2cKO murine hearts, as suggested in (Kim et al., 2019). To measure the extent of perinexal remodeling, we performed a quantitative analysis on samples from control and PKP2cKO mice; multiple gap junction plaques per heart were included.

Quantification of Perinexal Alterations in PKP2cKO Hearts

Gap junction plaques in 3D were analyzed using ORS Dragonfly software. The inner space within the gap junction plaque was segmented, allowing us to quantify the surface area per plane and throughout the entire structure (**Figure 2B** left panel, **Figure 3**). As gap junction plaques differed largely in depth and length, we

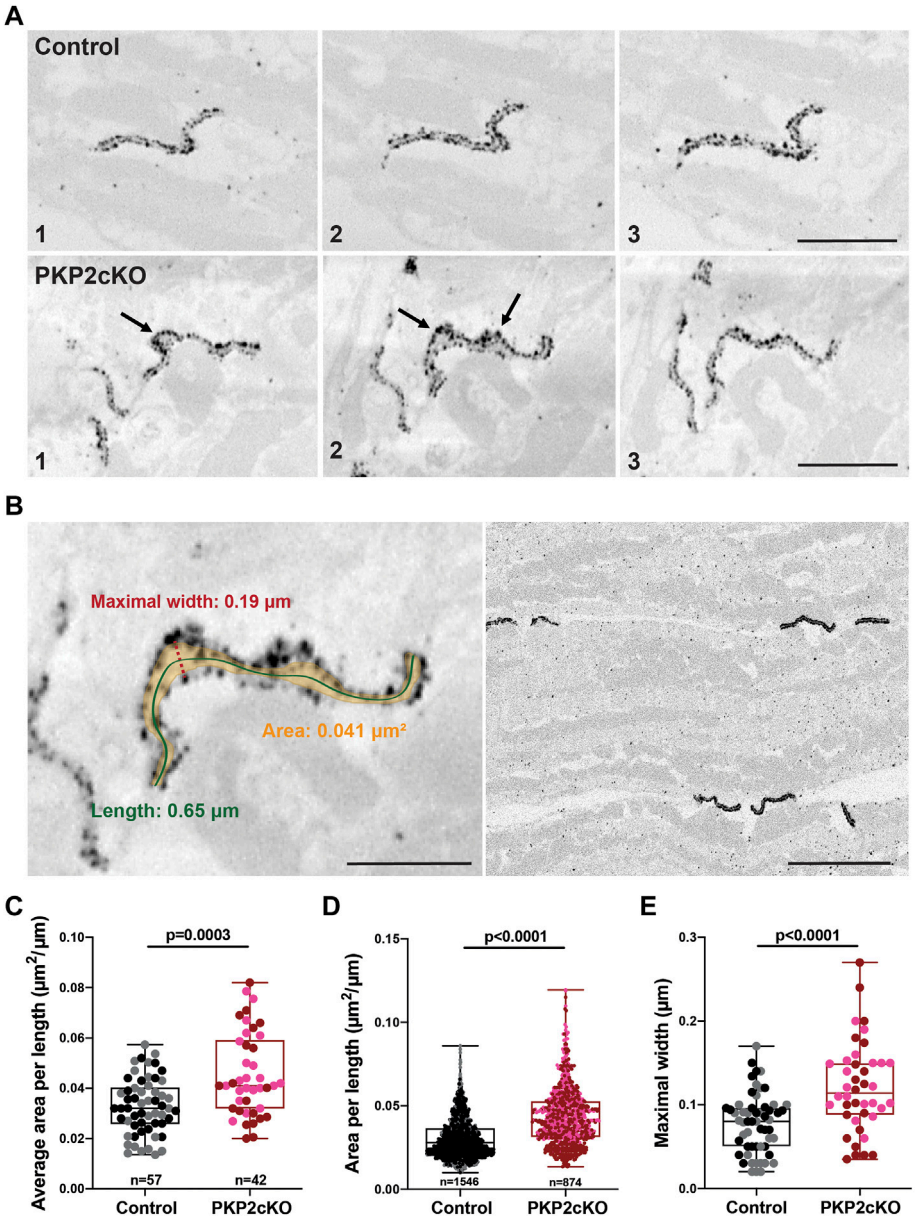

FIGURE 2 | Gap junction plaque separation in adult hearts of Plakophilin-2 conditional knock out mice (PKP2cKO). **(A)** Representative examples of 3D Connexin43 (Cx43) Immuno-Electron Microscopy images of a Control (top panel) and PKP2cKO (bottom panel) heart. The various frames (1–3) correspond to different section levels of the same sample. Arrowheads depict Cx43 hemichannels. Scale bar: 0.5 µm. **(B)** *Left panel*: Example of our method for quantifying parameters shown in **(C–E)**. Scale bar: 0.2 µm. *Right panel*: Low magnification example of multiple gap junction plaques in a Control heart sample. Scale bar: 0.5 µm. **(C,D)** Quantification of 2D surface between intercalated disc (ID) membranes in control and PKP2cKO hearts, corrected for ID length (Area per length), averaged per ID **(C)** and per individual section **(D)**. **(E)** Maximal width between ID membranes, per ID. **(C–E)**: Control; $n = 57$, PKP2cKO; $n = 42$. **(D)**: Control; $n = 1,546$, PKP2cKO; $n = 874$. Data presented as box and whisker (min.–max.) plot. Data points corresponding to left ventricular (LV) and right ventricular (RV) samples represented in separate colors; Control LV; black, Control RV; grey, PKP2cKO LV; red, PKP2cKO RV; pink. Significance in **(C,D)** as per Mann-Whitney test, in **(E)** per Student's *t*-test.

decided to measure in addition the gap junction plaque length and maximal width between the ID membranes (**Figure 2B** left panel). We corrected the surface area of the total gap junction plaque (average area), or individual frame (area), for the gap junction plaque length (average area per length). Very significant differences in the average area per length, area per length of individual frames and maximal width between ID membranes were observed between control and PKP2cKO hearts (**Figures 2C–E**). In **Figures 2C–E**, pooled data of the left ventricle (LV) and RV are presented, in **Figure 4** separate analysis of the LV and RV is shown. When quantifying these parameters in both ventricular walls separately, the differences between control and PKP2cKO hearts appeared to be very significant as well (**Figures 4A,B**).

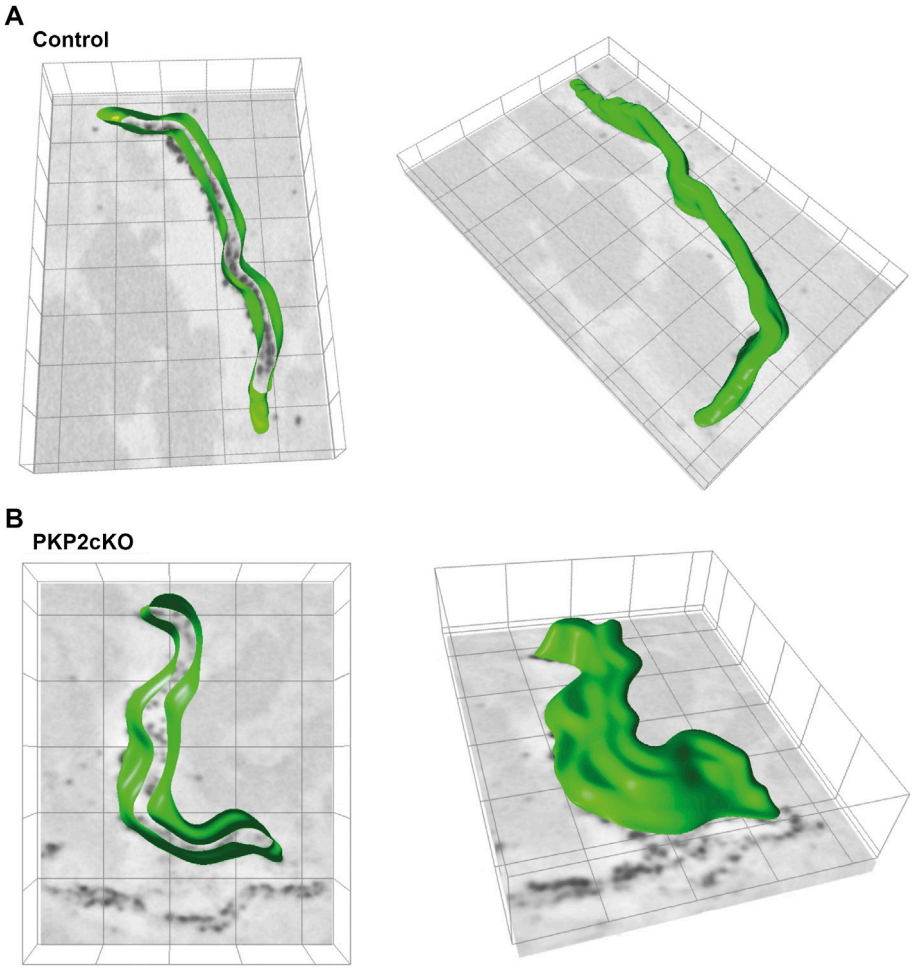

FIGURE 3 | 3D segmentation of the intercalated disc (ID) inner space in adult hearts of control and Plakophilin-2 conditional knock out mice (PKP2cKO). **(A)** *Left panel*: 3D segmentation, middle plane, of the inner space within the gap junction plaque of a control adult murine heart. The green line depicts Connexin43 immunoreactive beads segmented by ORS Dragonfly software. *Right panel*: Top view of the ID inner space 3D segmentation, from the same control sample presented on the left. **(B)** *Left panel*: 3D segmentation, middle plane, of the inner space within the gap junction plaque of a PKP2cKO adult murine heart. The green line depicts Connexin43 immunoreactive beads segmented by ORS Dragonfly software. *Right panel*: Top view of the ID inner space 3D segmentation, from the same PKP2cKO sample presented on the left. Please note widening of the intercellular space and areas where single Connexin43 immunoreactive beads lack opposing beads in close proximity in the PKP2cKO sample.

Detection of Connexin43 Hemiplaques in PKP2cKO Hearts

In addition to bulging of the intercellular space and disconnect of opposing Cx43 channels, in PKP2cKO hearts we also observed gap junction plaques that, for some length, showed only one single strand of Cx43 immunoreactive beads (Cx43 hemiplaques; see **Figure 5A**). We quantified the percentage of gap junction plaques in which Cx43 hemiplaques were observed. As shown in **Figure 5B**, Cx43 hemiplaques were present in both ventricular walls of PKP2cKO hearts, but to a higher extent in the RV (**Figure 5B**). In addition, we quantified the total length of the Cx43 hemiplaque as a function of genotype and for both RV and LV (**Figures 5C,D**). The data show that the total length of Cx43 hemiplaques in the RV was over 3 times longer in PKP2cKO than in control hearts, or in the LV of either control or PKP2cKO hearts. When corrected by the total length of the gap junction plaque, hemiplaques occupied a higher proportion of the areas of Cx43 immunoreactivity in PKP2cKO-derived tissue than in controls, with the RV wall of PKP2cKO hearts showing the highest values.

DISCUSSION

Over the past years, several investigators have studied loss of desmosomal integrity in hearts of ARVC patients by desmosomal protein mutations (Basso, 2006; Gomes et al., 2012; Noorman et al., 2013). Functional data has been largely supported by immunohistochemistry labeling of desmosomal proteins, though the complete structure of the PKP2-deficient ID in three dimensions remains unresolved. As a first step, here we

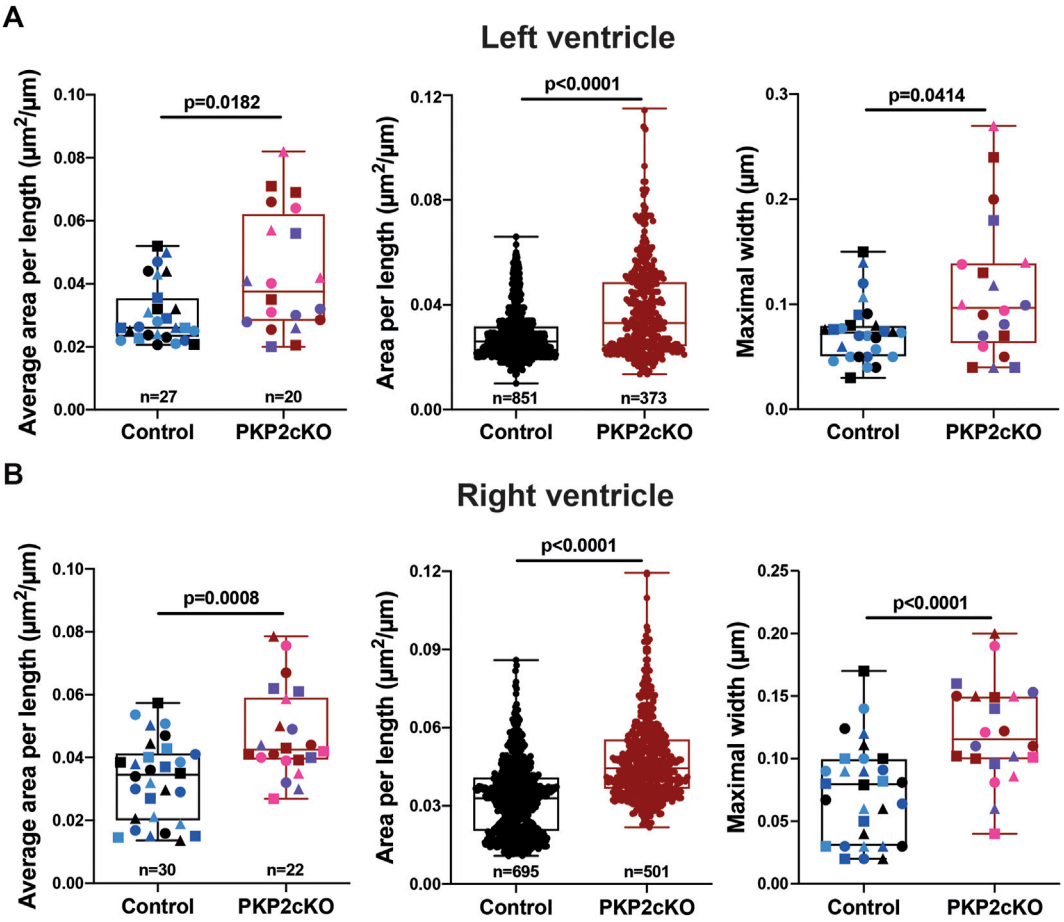

FIGURE 4 | Gap junction plaque separation in left and right ventricular samples of Plakophilin2 conditional knock out hearts (PKP2cKO). **(A)** Quantification of 2D surface between intercalated disc (ID) membranes in left ventricular samples of control and PKP2cKO hearts, corrected for ID length (Area per length), averaged per ID (*left panel*) and per individual section (*middle panel*). *Right panel*: Maximal width between ID membranes, per ID. *Left and right panel*: Control; $n = 27$, PKP2cKO; $n = 20$. Middle panel: Control; $n = 851$, PKP2cKO; $n = 373$. Data presented as box and whisker (min.– max.) plot. Colors depict data points corresponding to different animals. Shapes depict data points corresponding to differenct regions of interest. Significance as per Mann-Whitney test. **(B)** Quantification of 2D surface between intercalated disc (ID) membranes in right ventricular samples of both groups, corrected for ID length (Area per length), averaged per ID (*left panel*) and per individual section (*middle panel*). *Right panel*: Maximal width between ID membranes, per ID. *Left and right panel*: Control; $n = 30$, PKP2cKO; $n = 22$. *Middle panel*: Control; $n = 695$, PKP2cKO; $n = 501$. Data presented as box and whisker (min.–max.) plot. Colors depict data points corresponding to different animals. Shapes depict data points corresponding to different regions of interest. Significance in left and middle panel as per Mann-Whitney test, right panel as per Student's *t*-test.

describe the complete spatial ultrastructure of the gap junction plaques in control, and in PKP2-deficient myocytes prior to the development of a structural disease.

Studies in cell culture systems and in tissue from ARVC-affected patients have previously indicated that loss of expression or mutations in PKP2 can alter the structure and function of gap junctions (Oxford et al., 2007; Saffitz, 2009; Asimaki and Saffitz, 2014). Previous studies showed that PKP2 deficiency in the murine heart increases Cx43-mediated membrane permeability, and that the latter may facilitate ATP efflux (Cerrone et al., 2018) and excessive entry of Ca^{2+} into the cells (Kim et al., 2019). It is also known that Cx43 hemichannels reside in the perimeter of the gap junctions (Rhett et al., 2011) and are capable to flicker with very low probability when undocked (Contreras et al., 2003; Verma et al., 2009). Consistent with those observations, ablation of Cx43 prevented the accumulation of Ca_i^{2+}, and GAP19, a peptide known to block Cx43-Hs without affecting junctional conductance, normalized the intracellular Ca^{2+} homeostasis (Kim et al., 2019). These data support the hypothesis that Cx43-Hs are likely important players in the arrhythmogenic/cardiomyopathic phenotype of these mice. Here, we provide structural data in support of the notion that Cx43 hemichannels are present with a higher abundance in the membrane of PKP2-deficient hearts. We thus postulate that these single strings of Cx43 immunoreactive molecules are the structural counterpart to the excess Cx43 hemichannels detected by functional assays. Of note, previous studies have shown an absence of changes in Cx43 abundance (Cerrone et al., 2017; Kim et al., 2019). Given the timing of our experiments vis a vis the development of a PKP2-dependent cardiac phenotype in these mice, we conclude that the

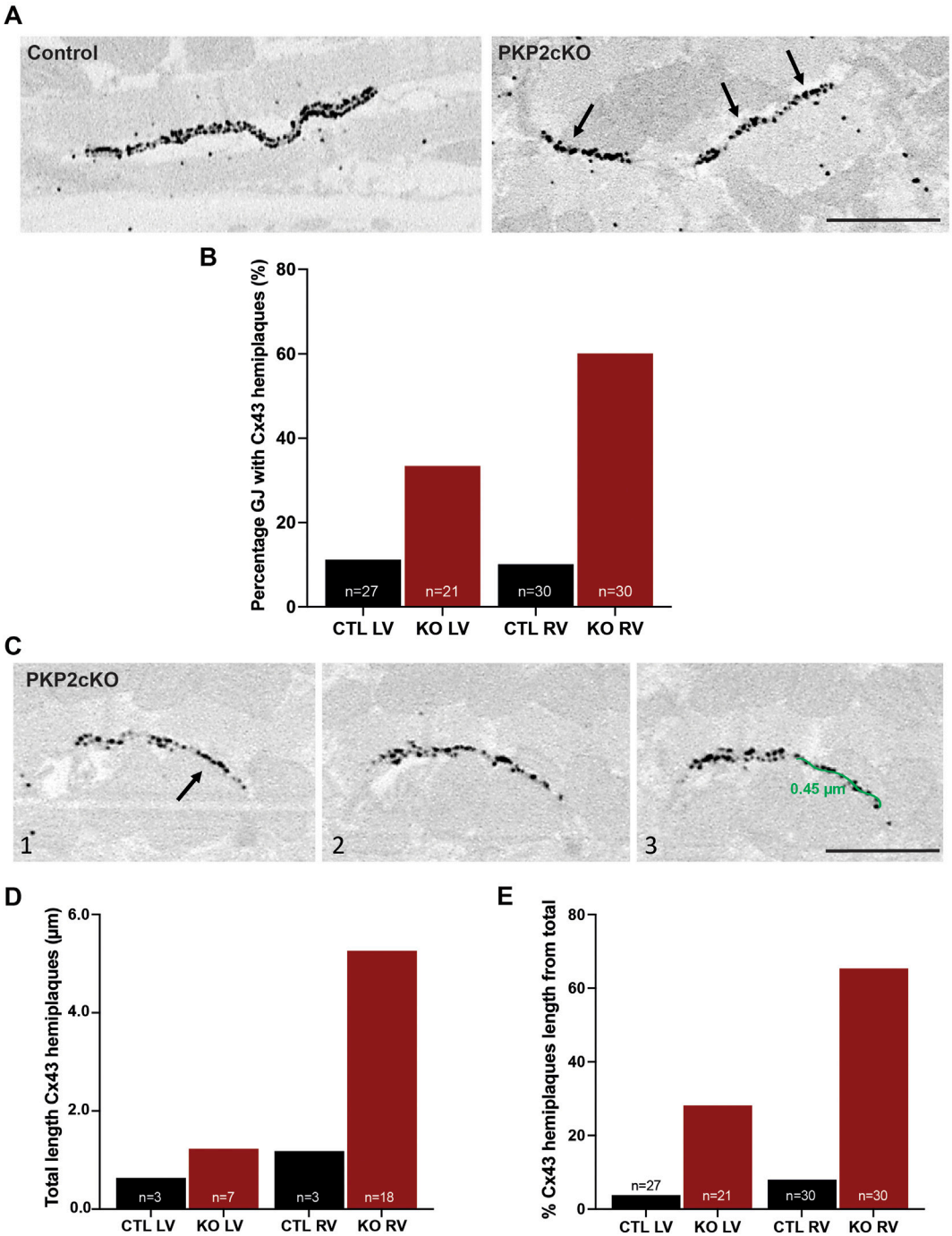

FIGURE 5 | Connexin43 hemiplaques in adult hearts of Plakophilin-2 conditional knock out mice (PKP2cKO). **(A)** Representative examples of gap junction plaques in control and PKP2cKO hearts, emphasizing in the right panel Connexin43 (Cx43) hemiplaques in a PKP2cKO ventricular sample. Arrowheads point out Cx43 hemiplaques. Scale bar: 0.5 µm. **(B)** Quantification of the percentage of gap junction plaques containing Cx43 hemiplaques in control and PKP2cKO hearts, left ventricular (LV) and right ventricular (RV) samples separately. Data presented as percentage of total pool. Control LV; $n = 27$, PKP2cKO LV; $n = 21$, Control RV; $n = 30$, PKP2cKO RV; $n = 30$. **(C)** Representative examples of 3D Cx43 Immuno-Electron Microscopy images of a PKP2cKO heart presenting a Cx43 hemiplaque. The various frames (1–3) correspond to different section levels of the same samples. Arrowheads point out Cx43 hemiplaques. Scale bar: 0.5 µm. **(D)** Quantification of the total length of Connexin43 hemiplaques in control and PKP2cKO hearts, LV and RV samples separately. Data presented as total length of total pool. Control LV; $n = 3$, PKP2cKO LV; $n = 7$, Control RV; $n = 3$, PKP2cKO RV; $n = 18$. **(E)** Quantification length of Connexin43 hemiplaques in control and PKP2cKO hearts, corrected for the total length of the gap junction plaque. LV and RV samples are quantified separately. Data presented as percentage of total length per group. Control LV; $n = 27$, PKP2cKO LV; $n = 21$, Control RV; $n = 30$, PKP2cKO RV; $n = 30$.

nanostructural changes in the ID described here are among the earliest events following loss of PKP2 expression.

We show that the multimodal imaging application offered by nanogold or FluoroNanogold labeling can be applied for vEM in thick cardiac sections. Highlighting it as novel tool for future use in 3D imaging of protein localization in different tissue types. FluoroNanogold is a probe containing two different markers (Takizawa and Robinson, 2000). As such, it opens the possibility of imaging the same sample at both the optical and the EM level (Robinson and Vandré, 1997; Takizawa and Robinson, 2000). The method can be used for multimodal studies, either on different cell types or on the same cell, visualized by correlative microscopy. The very small size of the gold atom clusters allows efficient absorption within fixed tissues prior to embedding (Robinson and Vandré, 1997). Quantum dots are largely used to identify and localize proteins simultaneously with different imaging approaches; however, they can only penetrate up to 4 μm deep into the tissue (Giepmans et al., 2005). Our experiments show that nanogold could easily penetrate in up to 20 μm on both sides of the cardiac vibratome sections. The use of nanogold and FluoroNanogold labeling in adult heart therefore represents a step forward in the development of novel methodologies for visualization of specific protein aggregates in native tissue, at nanometric resolution and in three dimensions.

Making use of FIB-SEM, we previously identified a nanometric separation of the ID membrane in RV samples of PKP2cKO mice (Kim et al., 2019). In hearts of heterozygous PKP2 knock out mice, we implemented high-pressure freezing tissue preservation for tomographic electron microscopy (tomographic EM) purposes (Leo-Macías et al., 2015). Besides clear detection of ID membrane separation, ultrastructural characteristics of the intercellular space could be visualized as well. Tomographic EM, however, did not allow detailed identification of individual gap junction plaques. Labeling Cx43, prior to imaging, is therefore critical to detect orphan hemichannels and asymmetric gap junctions in the ID membrane. In this study, IEM allowed us to examine both parameters (separation of the ID membrane and presence of Cx43-Hs) in parallel, adding an extra visual component to the previously obtained microscopy and functional data reported in Kim et al.

We emphasize that our experimental model (PKP2cKO) neither is intended to "recapitulate" ARVC nor is intended to be a surrogate for studies of human hearts affected with disease. This is in fact true for all animal or cellular models of ARVC that have been published, and an obvious consequence of the limitations inherent to the study of a human disease. The significance of our studies is not in having reproduced conditions that lead to human ARVC, but in having studied a molecule that, when mutated, causes the disease. Whether the structural changes described here occur in human hearts with PKP2 mutations remains undefined. Extrapolation from our data to the specific case of ARVC needs to be done with caution. That said, our model has shown consistency with human informatics data (Montnach et al., 2018) and has been useful in proposing therapeutic approaches to patients with ARVC (e.g., the pilot clinical trial on use of flecainide in ARVC patients; NCT03685149).

In conclusion, the results described in this study support the notion that, at this stage in the progress of the phenotype (i.e., before histologically-detectable disease), we detect a nanometric separation of the gap junction plaque, and the presence of unopposed Cx43-immunoreactive single strings (orphan Cx43-Hs). We propose that these orphan hemichannels are the structural correlate to the functional Cx43-Hs previously detected by (Kim et al., 2019). Our data illustrate the value and the potential of the novel methodology described here for visualization. It also provides further support to the notion that the gain-of-function of Cx43-Hs constitutes an important arrhythmogenic substrate in the setting of PKP2 deficiency. We speculate that block of Cx43-Hs may represent a novel and effective therapeutic strategy to prevent life-threatening arrhythmias in patients with PKP2 deficiency, particularly in the concealed stage of the disease.

DATA AVAILABILITY STATEMENT

The raw data supporting the conclusion of this article will be made available by the authors, without undue reservation.

ETHICS STATEMENT

The animal study was reviewed and approved by the New York University IACUC committee under protocol number 160726-03.

AUTHOR CONTRIBUTIONS

CO, MD, and F-XL conceived the study and drafted the manuscript. JS, CP, and KD-M performed the experiments, imaging, and image processing. CO performed data analysis. CO, JS, CP, KD-M, MD, and F-XL critically revised the manuscript. All authors approved the final version.

FUNDING

Work was supported by NIH grants RO1-HL134328, RO1-HL136179 and RO1-HL145911 (MD), a Transatlantic Network of Excellence from the Leducq Foundation (MD), the Wilton W. Webster Fellowship in Pediatric Electrophysiology from Heart Rhythm Society, and an American Heart Association Postdoctoral Fellowship (CO). Microscopy Laboratory is partially supported by Laura and Isaac Perlmutter Cancer Center Support Grant NIH/NCI P30CA016087. Zeiss Gemini300 SEM with 3View was purchased with NIH S10 OD019974.

SUPPLEMENTARY MATERIAL

The Supplementary Material for this article can be found online at: https://www.frontiersin.org/articles/10.3389/fcell.2022.843687/full#supplementary-material

REFERENCES

Asimaki, A., and Saffitz, J. E. (2014). Remodeling of Cell-Cell Junctions in Arrhythmogenic Cardiomyopathy. *Cel Commun. Adhes.* 21 (1), 13–23. doi:10.3109/15419061.2013.876016

Austin, K. M., Trembley, M. A., Chandler, S. F., Sanders, S. P., Saffitz, J. E., Abrams, D. J., et al. (2019). Molecular Mechanisms of Arrhythmogenic Cardiomyopathy. *Nat. Rev. Cardiol.* 16, 519–537. doi:10.1038/s41569-019-0200-7

Bass-Zubek, A. E., Hobbs, R. P., Amargo, E. V., Garcia, N. J., Hsieh, S. N., Chen, X., et al. (2008). Plakophilin 2: a Critical Scaffold for PKCα that Regulates Intercellular junction Assembly. *J. Cel Biol.* 181 (4), 605–613. doi:10.1083/jcb.200712133

Basso, C., Czarnowska, E., Della Barbera, M., Bauce, B., Beffagna, G., Wlodarska, E. K., et al. (2006). Ultrastructural Evidence of Intercalated Disc Remodelling in Arrhythmogenic Right Ventricular Cardiomyopathy: an Electron Microscopy Investigation on Endomyocardial Biopsies. *Eur. Heart J.* 27 (15), 1847–1854. doi:10.1093/eurheartj/ehl095

Beardslee, M. A., Lerner, D. L., Tadros, P. N., Laing, J. G., Beyer, E. C., Yamada, K. A., et al. (2000). Dephosphorylation and Intracellular Redistribution of Ventricular Connexin43 during Electrical Uncoupling Induced by Ischemia. *Circ. Res.* 87 (8), 656–662. doi:10.1161/01.res.87.8.656

Cadrin-Tourigny, J., Bosman, L. P., Nozza, A., Wang, W., Tadros, R., Bhonsale, A., et al. (2019). A New Prediction Model for Ventricular Arrhythmias in Arrhythmogenic Right Ventricular Cardiomyopathy. *Eur. Heart J.* 40 (23), 1850–1858. doi:10.1093/eurheartj/ehz103

Cerrone, M., Montnach, J., Lin, X., Zhao, Y.-T., Zhang, M., Agullo-Pascual, E., et al. (2017). Plakophilin-2 Is Required for Transcription of Genes that Control Calcium Cycling and Cardiac Rhythm. *Nat. Commun.* 8 (1), 106. doi:10.1038/s41467-017-00127-0

Cerrone, M., van Opbergen, C. J. M., Malkani, K., Irrera, N., Zhang, M., Van Veen, T. A. B., et al. (2018). Blockade of the Adenosine 2A Receptor Mitigates the Cardiomyopathy Induced by Loss of Plakophilin-2 Expression. *Front. Physiol.* 9, 1750. doi:10.3389/fphys.2018.01750

Cheutin, T., Sauvage, C., Tchélidzé, P., O'Donohue, M. F., Kaplan, H., Beorchia, A., et al. (2007). Visualizing Macromolecules with Fluoronanogold: from Photon Microscopy to Electron Tomography. *Methods Cel. Biol.* 79, 559–574. doi:10.1016/S0091-679X(06)79022-7

Contreras, J. E., Saez, J. C., Bukauskas, F. F., and Bennett, M. V. L. (2003). Gating and Regulation of Connexin 43 (Cx43) Hemichannels. *Proc. Natl. Acad. Sci.* 100 (20), 11388–11393. doi:10.1073/pnas.1434298100

De Brabander, M., Geuens, G., Nuydens, R., Moeremans, M., and De Mey, J. (1985). Probing Microtubule-dependent Intracellular Motility with Nanometre Particle Video Ultramicroscopy (Nanovid Ultramicroscopy). *Cytobios* 43 (174S), 273–283.

De Brabander, M., Nuydens, R., Geuens, G., Moeremans, M., and De Mey, J. (1986). The Use of Submicroscopic Gold Particles Combined with Video Contrast Enhancement as a Simple Molecular Probe for the Living Cell. *Cell Motil. Cytoskeleton* 6 (2), 105–113. doi:10.1002/cm.970060207

Faulk, W., and Taylor, M. G. (1971). Communication to the Editors. *Immunochemistry* 8 (11), 1081–1083. doi:10.1016/0019-2791(71)90496-4

Giepmans, B. N. G. (2008). Bridging Fluorescence Microscopy and Electron Microscopy. *Histochem. Cel Biol* 130 (2), 211–217. doi:10.1007/s00418-008-0460-5

Gomes, J., Finlay, M., Ahmed, A. K., Ciaccio, E. J., Asimaki, A., Saffitz, J. E., et al. (2012). Electrophysiological Abnormalities Precede Overt Structural Changes in Arrhythmogenic Right Ventricular Cardiomyopathy Due to Mutations in Desmoplakin-A Combined Murine and Human Study. *Eur. Heart J.* 33 (15), 1942–1953. doi:10.1093/eurheartj/ehr472

Grossmann, K. S., Grund, C., Huelsken, J., Behrend, M., Erdmann, B., Franke, W. W., et al. (2004). Requirement of Plakophilin 2 for Heart Morphogenesis and Cardiac junction Formation. *J. Cel Biol.* 167 (1), 149–160. doi:10.1083/jcb.200402096

Hainfeld, J. F., and Furuya, F. R. (1992). A 1.4-nm Gold Cluster Covalently Attached to Antibodies Improves Immunolabeling. *J. Histochem. Cytochem.* 40 (2), 177–184. doi:10.1177/40.2.1552162

Kim, J.-C., Pérez-Hernández, M., Alvarado, F. J., Maurya, S. R., Montnach, J., Yin, Y., et al. (2019). Disruption of Ca 2+ I Homeostasis and Connexin 43 Hemichannel Function in the Right Ventricle Precedes Overt Arrhythmogenic Cardiomyopathy in Plakophilin-2-Deficient Mice. *Circulation* 140, 1015–1030. doi:10.1161/CIRCULATIONAHA.119.039710

Leo-Macías, A., Liang, F.-X., and Delmar, M. (2015). Ultrastructure of the Intercellular Space in Adult Murine Ventricle Revealed by Quantitative Tomographic Electron Microscopy. *Cardiovasc. Res.* 107 (4), 442–452. doi:10.1093/cvr/cvv182

Montnach, J., Agullo-Pascual, E., Tadros, R., Bezzina, C. R., and Delmar, M. (2018). Bioinformatic Analysis of a Plakophilin-2-dependent Transcription Network: Implications for the Mechanisms of Arrhythmogenic Right Ventricular Cardiomyopathy in Humans and in Boxer Dogs. *EP Europace* 20 (Suppl. l_3), iii125–iii132. doi:10.1093/europace/euy238

Müssigbrodt, A., Knopp, H., Czimbalmos, C., Jahnke, C., Richter, S., Husser, D., et al. (2019). Exercise-related Sudden Cardiac Death of an American Football Player with Arrhythmogenic Right Ventricular Dysplasia/cardiomyopathy and Sarcoidosis. *Clin. Case Rep.* 7 (4), 686–688. doi:10.1002/ccr3.2071

Noorman, M., Hakim, S., Kessler, E., Groeneweg, J. A., Cox, M. G. P. J., Asimaki, A., et al. (2013). Remodeling of the Cardiac Sodium Channel, Connexin43, and Plakoglobin at the Intercalated Disk in Patients with Arrhythmogenic Cardiomyopathy. *Heart Rhythm* 10 (3), 412–419. doi:10.1016/j.hrthm.2012.11.018

Ohno, S. (2016). The Genetic Background of Arrhythmogenic Right Ventricular Cardiomyopathy. *J. Arrhythmia* 32 (5), 398–403. doi:10.1016/j.joa.2016.01.006

Oxford, E. M., Musa, H., Maass, K., Coombs, W., Taffet, S. M., and Delmar, M. (2007). Connexin43 Remodeling Caused by Inhibition of Plakophilin-2 Expression in Cardiac Cells. *Circ. Res.* 101 (7), 703–711. doi:10.1161/CIRCRESAHA.107.154252

Powell, R. D., Halsey, C. M. R., Spector, D. L., Kaurin, S. L., McCann, J., and Hainfeld, J. F. (1997). A Covalent Fluorescent-Gold Immunoprobe: Simultaneous Detection of a Pre-mRNA Splicing Factor by Light and Electron Microscopy. *J. Histochem. Cytochem.* 45 (7), 947–956. doi:10.1177/002215549704500704

Preibisch, S., Saalfeld, S., and Tomancak, P. (2009). Globally Optimal Stitching of Tiled 3D Microscopic Image Acquisitions. *Bioinformatics* 25 (11), 1463–1465. doi:10.1093/bioinformatics/btp184

Rhett, J. M., Jourdan, J., and Gourdie, R. G. (2011). Connexin 43 Connexon to gap junction Transition Is Regulated by Zonula Occludens-1. *MBoC* 22 (9), 1516–1528. doi:10.1091/mbc.E10-06-0548

Robinson, J. M., and Vandré, D. D. (1997). Efficient Immunocytochemical Labeling of Leukocyte Microtubules with FluoroNanogold: an Important Tool for Correlative Microscopy. *J. Histochem. Cytochem.* 45 (5), 631–642. doi:10.1177/002215549704500501

Roth, J., Bendayan, M., and Orci, L. (1978). Ultrastructural Localization of Intracellular Antigens by the Use of Protein A-Gold Complex. *J. Histochem. Cytochem.* 26 (12), 1074–1081. doi:10.1177/26.12.366014

Saffitz, J. E. (2009). Arrhythmogenic Cardiomyopathy and Abnormalities of Cell-To-Cell Coupling. *Heart rhythm* 6 (8 Suppl. l), S62–S65. doi:10.1016/j.hrthm.2009.03.003

Sato, P. Y., Coombs, W., Lin, X., Nekrasova, O., Green, K. J., Isom, L. L., et al. (2011). Interactions between Ankyrin-G, Plakophilin-2, and Connexin43 at the Cardiac Intercalated Disc. *Circ. Res.* 109 (2), 193–201. doi:10.1161/CIRCRESAHA.111.247023

Slot, J. W., and Geuze, H. J. (1981). Sizing of Protein A-Colloidal Gold Probes for Immunoelectron Microscopy. *J. Cel. Biol.* 90 (2), 533–536. doi:10.1083/jcb.90.2.533

Sun, X. J., Tolbert, L. P., and Hildebrand, J. G. (1995). Using Laser Scanning Confocal Microscopy as a Guide for Electron Microscopic Study: a Simple Method for Correlation of Light and Electron Microscopy. *J. Histochem. Cytochem.* 43 (3), 329–335. doi:10.1177/43.3.7868862

Takizawa, T., and Robinson, J. M. (2000). FluoroNanogold Is a Bifunctional Immunoprobe for Correlative Fluorescence and Electron Microscopy. *J. Histochem. Cytochem.* 48 (4), 481–485. doi:10.1177/002215540004800405

van Bergen en Henegouwen, P. M. P., Leunissen, J. L. M., and Leunissen, J. L. (1986). Controlled Growth of Colloidal Gold Particles and Implications for

Labelling Efficiency. *Histochemistry* 85 (1), 81–87. doi:10.1007/BF00508657

Verma, V., Hallett, M. B., Leybaert, L., Martin, P. E., and Howard Evans, W. (2009). Perturbing Plasma Membrane Hemichannels Attenuates Calcium Signalling in Cardiac Cells and HeLa Cells Expressing Connexins. *Eur. J. Cel. Biol.* 88 (2), 79–90. doi:10.1016/j.ejcb.2008.08.005

Yokota, S. (1988). Effect of Particle Size on Labeling Density for Catalase in Protein A-Gold Immunocytochemistry. *J. Histochem. Cytochem.* 36 (1), 107–109. doi:10.1177/36.1.3335766

Conflict of Interest: The authors declare that the research was conducted in the absence of any commercial or financial relationships that could be construed as a potential conflict of interest.

Publisher's Note: All claims expressed in this article are solely those of the authors and do not necessarily represent those of their affiliated organizations, or those of the publisher, the editors and the reviewers. Any product that may be evaluated in this article, or claim that may be made by its manufacturer, is not guaranteed or endorsed by the publisher.

frontiers | Frontiers in Cell and Developmental Biology

TECHNOLOGY AND CODE
published: 01 April 2022
doi: 10.3389/fcell.2022.842342

SuRVoS 2: Accelerating Annotation and Segmentation for Large Volumetric Bioimage Workflows Across Modalities and Scales

Avery Pennington[1], *Oliver N. F. King*[1], *Win Min Tun*[1], *Elaine M. L. Ho*[2], *Imanol Luengo*[1], *Michele C. Darrow*[2] *and Mark Basham*[1,2]*

[1]Diamond Light Source Ltd., Didcot, United Kingdom, [2]The Rosalind Franklin Institute, Didcot, United Kingdom

As sample preparation and imaging techniques have expanded and improved to include a variety of options for larger sized and numbers of samples, the bottleneck in volumetric imaging is now data analysis. Annotation and segmentation are both common, yet difficult, data analysis tasks which are required to bring meaning to the volumetric data. The SuRVoS application has been updated and redesigned to provide access to both manual and machine learning-based segmentation and annotation techniques, including support for crowd sourced data. Combining adjacent, similar voxels (supervoxels) provides a mechanism for speeding up segmentation both in the painting of annotation and by training a segmentation model on a small amount of annotation. The support for layers allows multiple datasets to be viewed and annotated together which, for example, enables the use of correlative data (e.g. crowd-sourced annotations or secondary imaging techniques) to guide segmentation. The ability to work with larger data on high-performance servers with GPUs has been added through a client-server architecture and the Pytorch-based image processing and segmentation server is flexible and extensible, and allows the implementation of deep learning-based segmentation modules. The client side has been built around Napari allowing integration of SuRVoS into an ecosystem for open-source image analysis while the server side has been built with cloud computing and extensibility through plugins in mind. Together these improvements to SuRVoS provide a platform for accelerating the annotation and segmentation of volumetric and correlative imaging data across modalities and scales.

Keywords: segmentation (image processing), annotation, U-net, volume electron microscopy (vEM), X-ray microscopy imaging, open source software, python (programming language), computer vision

OPEN ACCESS

Edited by:
Saskia Lippens,
Vlaams Instituut voor Biotechnologie, Belgium

Reviewed by:
Joris Roels,
Vlaams Instituut voor Biotechnologie, Belgium
Robert Haase,
TU Dresden, Germany

***Correspondence:**
Mark Basham
mark.basham@rfi.ac.uk

Specialty section:
This article was submitted to Cell Growth and Division, a section of the journal Frontiers in Cell and Developmental Biology

Received: *23 December 2021*
Accepted: *22 February 2022*
Published: *01 April 2022*

Citation:
Pennington A, King ONF, Tun WM, Ho EML, Luengo I, Darrow MC and Basham M (2022) SuRVoS 2: Accelerating Annotation and Segmentation for Large Volumetric Bioimage Workflows Across Modalities and Scales. Front. Cell Dev. Biol. 10:842342. doi: 10.3389/fcell.2022.842342

INTRODUCTION

The volume electron microscopy (vEM) and X-ray imaging ecosystems have flourished in recent years, through improvements to previously used techniques and the development of new techniques, all providing functional understandings through structural study (Peddie and Collinson 2014; Yoshiyuki et al., 2018; Xu et al., 2021). It is now common practice to collect 100s of GB of data daily across multiple correlative modalities contributing to the same project. This has shifted the experimental bottleneck to the image processing and analysis pipeline. Often, functional insights can only come from detailed segmentation and annotation of the image data, which currently is

completed manually by an expert researcher. This creates a significant probability of creating "Dark Data," data that is collected, but due to time constraints and complexity, is not fully analyzed, or unintentionally analyzed in a biased way. Of specific concern are "Self Selection" and "Summaries of Data" (Hand, 2020), which are both routinely used to reduce the analytical load on the researcher. Our anecdotal experience supports this and shows that the vast majority of the data that is currently collected goes unanalyzed, or is only partially analyzed, and in many cases the analysis that is performed is qualitative or only takes into consideration a small number of examples or features due to the onerous nature of the task.

There are general computational tools available to ease some of the burden of the segmentation and image analysis process such as IMOD (Kremer et al., 1996), Ilastik (Berg et al., 2017), ImageJ (Abràmoff et al., 2004) and its many plugins, such as Weka (Hall et al., 2009), or commercial software such as Avizo (ThermoFisher.com, 2021). In addition, certain fields such as neuroanatomy have specialized image analysis and segmentation tools such as Knossos (Helmstaedter et al., 2011) that can perform some of these tasks. However, all these tools still often require specialized technical knowledge, substantial experimentation, and often scripting to adapt to complex data, especially data with artefacts or low signal-to-noise ratio. In all cases where machine learning is used, capturing a dataset of expert segmentation or annotations is a necessary first step to explore which methodologies provide the best results. This process works well if the team is composed of both biological and data science experts, however, there is still a significant challenge in providing sufficient amounts of high-quality annotation in a timely fashion.

Recently, several tools that allow non-specialists to use deep learning for image segmentation have been developed. CellProfiler 3.0 combines both a wizard-like interface for applying U-Net models and an extensive suite of tools for shallow machine learning-based segmentation and for analysis of the resulting segmentation (McQuin et al., 2018). CDeep3M is a cloud-based solution for applying deep learning to segmentation but has a command line interface (Haberl et al., 2018). DeepMIB provides a wizard-like interface for running a deep-learning pipeline but doesn't provide any support for developing annotation or analyzing the resulting segmentation (Belevich and Jokitalo, 2021). DeepImageJ, which, in conjunction with ImageJ and Fiji itself, provides a pipeline for prediction of U-Net-based segmentation models as well as many tools for the preparation of training data and the analysis of results (Gomez-de-Mariscal et al., 2021). SuRVoS2 is unique in providing a self-contained GUI tool designed for non-programmers that allows painting of annotations using super-regions, a machine-learning based prediction mechanism for accelerating the annotation process, an integrated system for training and prediction of a U-net model, and tools for analyzing the resulting segmentation.

SuRVoS Workbench (Darrow et al., 2017; Luengo et al., 2017) was originally developed to address this need for an accelerated process of producing initial expert segmentation on which to base subsequent machine learning methods. Annotation in SuRVoS is based around the concept of supervoxels (Lucchi, et al., 2011) which provide a way to select a large number of voxels in 3D with little user effort, yet still respect the boundaries found within the data itself. After using supervoxels to quickly annotate regions within a volume, an iterative shallow machine learning strategy with integrated filters for data augmentation could be applied to predict the label assignments of the volume (**Figure 1**). This involves pre-calculating image features and training a machine learning method such as random forests or SVM (Support Vector Machine) on the provided scribble annotation, and then to predict the segmentation of the whole volume. Because the image features are calculated separately from the machine learning algorithm, this method is considered a "shallow" machine learning approach. A novel hierarchical strategy could restrict annotations and predictions based on parent-child relationships and a "label-splitter" functionality could be used to separate out objects based on their inherent properties for analysis.

Overall, SuRVoS provided a processing pipeline which sped up the segmentation process, in some cases enabling research which wouldn't have been possible if segmentation was completed manually (Strotton et al., 2018). However, with increasing data sizes and rates of collection, SuRVoS became cumbersome due to local memory requirements. We also received multiple requests for usability improvements, especially around installation on various operating systems. And finally, our research and implementation of deep machine learning strategies has advanced. Together, these reasons have motivated the release of SuRVoS2 as both an API backend server and a new client based on the Napari (Napari Contributors, 2021) ecosystem. This edition includes a new client-server architecture, integration of Dask (Rocklin, 2015) for parallelized image processing, and both semi-automatic shallow and deep machine learning pipelines.

METHODS

Segmentation of large 3D volumetric imaging data presents challenges in providing computing resources, project management, and in visualization and interactivity. SuRVoS2 (licensed under Apache 2.0; Basham, 2021) approaches these challenges with the ethos of providing open-source, free-to-use options for accelerated annotation, segmentation and analysis that are data type agnostic.

Client-Server Architecture

Volumetric image segmentation is computationally intensive, but by way of its implementation as a client-server application, SuRVoS2 can be run on high-performance servers (e.g. multi-processor, multi-GPU, or high random access memory (RAM) machines) yet provide an interactive experience for users. The server can be used to run compute-heavy operations, such as segmentation algorithms, while the client is run on a convenient device local to the user, such as a laptop. The client connects to the server and directs the segmentation workflow, and all the intermediate files are stored on a server-accessible file system, with the client downloading only the data needed for interactive segmentation and visualization.

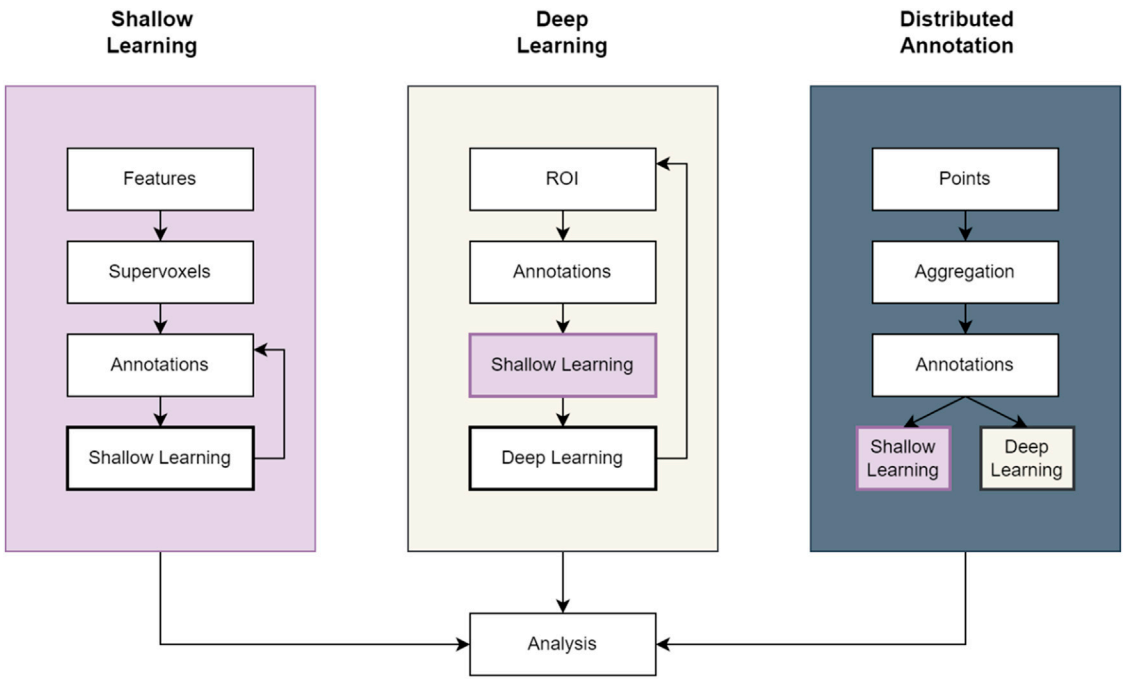

FIGURE 1 | Example workflow pipelines in SuRVoS2. The Shallow Learning pipeline is the same as previously available in SuRVoS using an iterative painting and predicting cycle to produce an output segmentation. The Deep Learning pipeline incorporates the Shallow Learning pipeline to quickly generate expert segmentations on a region of interest (ROI) which can subsequently be used to train a deep learning model for application to the full volume. And finally, the Distributed Annotation pipeline uses geometric data alongside either the Shallow Learning or Deep Learning pipelines to segment objects marked by 3D points.

The client uses a REST (Representational State Transfer) API implemented with the Hug Library (Crosley, 2016) to make requests to the SuRVoS2 server. The REST API uses HTTP (Hypertext Transfer Protocol) to implement a clean interface for functionality such as generating features, segmentation, and analysis. SuRVoS2 can be run headless on a cluster or virtual machine and then the Napari-based client connects over HTTP. This allows the server to run as a service on HPC-based clusters, for example, and could be containerized using Docker (Merkel, 2014) in order to deploy it at large scale in one of the major cloud providers. This enables the core functionality of SuRVoS2 to be run on appropriate computational resources with fast access to the image data resulting in a faster process for the user and enabling the processing of much larger datasets, limited only by server RAM. Additionally, the integration of the REST API and separating the core logic from the user interface allows for future extension of the client side to other devices or browser-based clients, which would further increase access to SuRVoS2 tools and functionality.

Workspace Philosophy

The SuRVoS2 server gathers and manages the information required throughout a complex segmentation project through the use of "Workspaces." A workspace is created from an imaging volume and as the segmentation workflow of choice is used (**Figure 1**), all objects created (features, annotations, supervoxels, segmentation pipelines and analysis outputs; *See* **Table 1**) and the state of the workflow are stored in the workspace file system. The parameters used throughout the workflow can be saved and loaded into a new workspace for application to a naïve dataset. The data objects are generally stored as chunked HDF5 (Hierarchical Data Format 5) files and manipulated using the h5py library (Colette et al., 2017). This chunking mechanism can be globally tuned, allowing the file access performance to be optimized for a given set of hardware.

Napari as a Graphical User Interface (GUI)

Napari is "a fast multi-dimensional image viewer designed for browsing, annotating and analyzing large multi-dimensional images" (Napari Contributors, 2021). It is a well-implemented PyQT-based application framework with a broad user community, which provides an extensible base for building application-specific annotation and segmentation tools. Napari is encouraging the growth of an ecosystem of additional image processing plugins providing features such as animation (Sofroniew, 2021), tracking (Prigent, 2021), and deconvolution (Perdigao, 2021). By utilizing Napari as a common GUI, a user can access a range of tools from multiple authors but following similar conventions for improved ease-of-use and inter-operability.

A key benefit of an interactive GUI for performing image processing operations is the ability to interactively explore an image dataset. Napari provides a broad set of tools for 2D and 3D inspection of the image data, interactive painting of annotations, and visualization of outputs from each stage of a processing pipeline. Additionally, Napari supports overlaying multiple floating point image layers, each with controllable opacity,

TABLE 1 | List of all filters/features, shallow and deep learning, and label splitter/analysis options within SuRVoS2.

Filters and features	Machine learning	Label splitter/Analysis
Produce output images for use in shallow or deep learning pipelines	Uses manual or shallow learning created training annotations to predict classes for other voxels	Inherent characteristics of data or segmented objects used to separate objects into groups
Basic Features:	Shallow Learning:	Mean Intensity
Simple Invert	Random Forest	Standard Deviation of Intensity
Invert Threshold	Extra Random Forest	Variation of Intensity
Threshold	Gradient Boosting	Volume
Rescale	Support Vector Machine (SVM)	Bounding Box Volume
Gamma Correct	Active Contour without Edges (ACWE)	Log Bounding Box Volume
Blob:	Watershed	Position X
Structure Tensor Determinant	Deep Learning:	Position Y
Frangi	2D U-Net	Position Z
Hessian Eigenvalues	3D U-Net [a]	Bounding Box Depth
Denoising:	FPN [a]	Bounding Box Height
Total Variation Denoise	—	Bounding Box Width
Gaussian Blur	—	Oriented Bounding Box Volume
Median	—	Log Oriented Bounding Box Volume
Wavelet	—	Oriented Bounding Box Depth
Edges:	—	Oriented Bounding Box Height
Spatial Gradient 3D	—	Oriented Bounding Box Width
Difference of Gaussians	—	—
Laplacian	—	—
Morphology:	—	—
Dilation	—	—
Erosion	—	—
Closing	—	—
Euclidean Distance Transform	—	—
Skeletonize	—	—
Neighborhood:	—	—
Gaussian Norm	—	—
Gaussian Centre	—	—

[a]*Indicates options where training is currently done using the SuRVoS2 API externally to the graphical user interface (GUI), with the deep learning module for prediction available within the SuRVoS2 GUI.*

which can be helpful when viewing two or more registered images together. In addition, integer-valued annotation layers and geometry layers can be viewed together with floating point image layers allowing many different data types to be displayed concurrently for correlational painting of segmentations and labelling of objects. Using the 3D mode provides options for 3D rendering of data and segmented objects including isosurfaces and attenuated maximum intensity projection.

Napari and the SuRVoS2 plugin can run on Linux, Windows, and Macintosh operating systems (*see* https://github.com/DiamondLightSource/SuRVoS2 for code, installation instructions and documentation). This arrangement of SuRVoS2 as a Napari plugin both extends SuRVoS2 with access to 2D and 3D visualization and annotation tools that Napari offers and likewise, extends Napari by providing a complete system for managing segmentation and image analysis workflows, including an extensive set of filters, supervoxels, and shallow and deep machine learning segmentation options.

Machine Learning Implementations

SuRVoS2 provides both a shallow and a deep machine learning pipeline (**Figure 1**). The shallow learning pipeline is equivalent to the functionality previously available in SuRVoS (Darrow et al., 2017; Luengo et al., 2017) whereby an initial set of training annotations are created and then an image segmentation model consisting of supervoxel-based image features and a random forest or SVM model is trained and evaluated, and then additional annotations or refinements of annotations are produced, and the model retrained and re-evaluated. The deep learning pipeline uses the 2D U-net from FastAI (Howard and Gugger, 2020) as a base and implements this functionality using The Kornia library (Riba et al., 2020) which was built using the Pytorch library (Paszke, et al., 2019), the Torch-IO library, some machine learning functions from scikit-learn (Pedregosa et al., 2011) and some image processing operations in SuRVoS2 also use the Scipy ndimage package (Virtanen et al., 2020) and the scikit-image library (van der Walt et al., 2014). These image processing technologies allow for GPU-accelerated computing to accommodate large datasets. Some additional image processing operations in SuRVoS2 use the Scipy ndimage package (Virtanen et al., 2020). The deep learning pipeline available in SuRVoS2 uses a region of interest (ROI) system whereby smaller, more manageable volumes are segmented either manually or through the shallow learning pipeline and used as training data. By providing one or more segmented ROIs as training data, the deep learning pipeline can transfer this learning to the rest of the volume. A multi-axis 2D U-Net (King, 2021) is

used to predict the output segmentation in different directions, combining the output into a final segmentation. To enable faster processing, Dask is used for parallelized image processing of chunked data. Together these features of SuRVoS2 enable the efficient processing of large datasets.

SuRVoS2 API

Complex segmentation problems usually require custom workflows. A Python API for SuRVoS2 can be accessed from either Jupyter notebooks (Kluyver et al., 2016), Python scripts or any other client capable of performing HTTP requests. A set of Jupyter-specific convenience functions allows for the inspection, creation, and modification of data within a SuRVoS2 workspace and give control of SuRVoS2 segmentation pipelines (*see* https://github.com/DiamondLightSource/SuRVoS2 for a testing notebook with examples). The output of these pipelines can be loaded into a common workspace for visualization and evaluation in the SuRVoS2 GUI. Additionally, SuRVoS2 is extensible by end users through a plugin mechanism composed of two parts: an API and a GUI. The API is implemented as a Python server using the Hug library (Crosley, 2016) to provide the REST API allowing for access to the workspace and all data in it. The GUI is a separate Python file consisting of the PyQT-based (RiverbankComputing.com, 2021) widgets that will be rendered in a tab within the SuRVoS2 user interface. For example, the SuRVoS2 ROI plugin has an API module that stores the ROI on the server and that can create and delete ROIs. Then it has a GUI module that contacts the API, gets the current list of ROIs, displays it, and allows the user to interactively create and delete ROIs.

RESULTS

SuRVoS2 implements multiple new features which accelerate image annotation, segmentation, and analysis. Example case studies have been sourced to highlight these features in the context of vEM and correlative imaging techniques. First, X-ray microCT of human placenta will be used to highlight the deep learning pipeline (Tun et al., 2021); second, cryo soft X-ray tomography (cryoSXT) of *Trypanosoma bruceii* will be used to demonstrate the label splitting and analysis functionalities; third, cryo electron tomography of a virus-infected cell will be used to illustrate the display and manipulation of non-mask based data such as the output from a distributed citizen science-based annotation workflow; fourth, correlative cryoSXT and cryo structured illumination microscopy datasets of a virus-infected cell will be used to demonstrate the ways correlative datasets can be used in the SuRVoS2 pipeline; and finally, an example Jupyter notebook will be used to highlight an advanced implementation of the SuRVoS2 API for clustering, segmentation, and visualization within the GUI.

Deep Learning With the SuRVoS2 Implementation of a 2D U-Net

The two main segmentation methods available in SuRVoS2 can be used together to rapidly generate high quality segmentations for large datasets (Alvarez-Borges et al., 2021; Tun et al., 2021). SuRVoS2 implements a version of the concept of "weak annotation" in which scribble-based annotation is used to train a shallow machine learning model and then the prediction of that model is used as ground truth to train a deep learning U-Net (Lin D. et al., 2016; Khoreva et al., 2017; Li et al., 2018). This approach requires expert evaluation of the output predictions of both the shallow and deep machine learning models and is classified as a semi-automatic method. A subvolume (ROI) of the dataset is first selected, then supervoxels are generated to aid fast annotation of this ROI. This subvolume annotation can be done entirely manually, utilizing the benefits of supervoxels, or partial annotations, in conjunction with extracted image features, can be used to train an ensemble (e.g. a random forest) or an SVM classifier. The trained classifier is then used to predict the missing annotations within the ROI. After this step, the resulting segmented ROI and the corresponding data can then be used as "expert segmentation" data to train a U-Net network. This trained U-Net model is then available to use for predicting segmentation of the entire large dataset (*See* Tun et al., 2021 for validation of this methodology).

U-Net models have advantages over ensemble or SVM methods (Ronneberger et al., 2015; Seo et al., 2020) in terms of generalizing better to new data and in not requiring user-led extraction of image features for training and prediction. The U-Net, by contrast, learns the features to extract from the data during model training. However, deep learning models like the U-Net often require much larger amounts of training data to perform well. Therefore, the practical application of deep learning for segmentation suggests the use of a shallow machine learning pipeline, trained quickly using supervoxels, for the creation of training data that can be used as input to the deep learning pipeline.

To demonstrate the above pipeline, an X-ray micro-tomography dataset (EMPIAR 10562, Tun et al., 2021) collected from a 3 × 3 × 3 mm sample of human placental tissue at Diamond Light Source beamline i13-2 was used (for more details of sample preparation and data collection *see* Tun et al., 2021). The full dataset has dimensions 2520 × 2520 × 2120 pixels and a 256 × 256 × 256 pixel ROI was selected from this dataset using the SuRVoS2 data previewer (**Figure 2A**). A workspace was created from the ROI and the data was denoised using a total variation filter (**Figure 2B**) before supervoxels with an average shape of 10 × 10 × 10 pixels were generated from this denoised volume (**Figure 2C**). A paintbrush tool was used to annotate some regions in the data (**Figure 2D**), separating the background supervoxels (shown in red) and those representing blood vessels (shown in blue). Further feature images were created from the ROI, namely a Gaussian blur, Hessian eigenvalues and normalized Gaussian datasets (not shown). The supervoxel annotations were used, along with the extracted image feature datasets, to train a random forest classifier which was then used to predict the labels for all of the supervoxels in the ROI (**Figure 2E**). At this point, the segmentation of the 256 × 256 × 256 pixel ROI is broadly correct with some minor misclassifications. This ROI segmentation was used to train a 2D U-Net model using an approach which leverages the 3D nature of

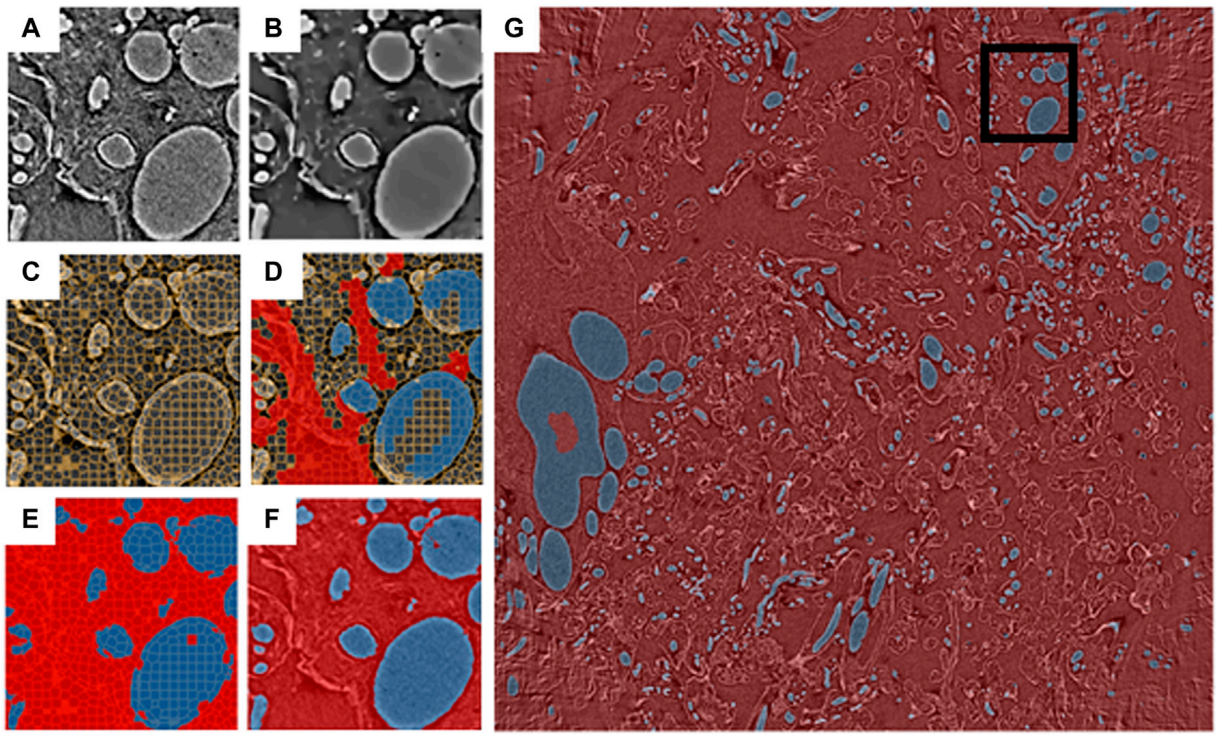

FIGURE 2 | Blood vessels from an X-ray micro-tomography dataset of human placenta segmented using the SuRVoS2 deep learning pipeline. Images **(A–F)** show a central slice of a 256 × 256 × 256 pixel region of interest (ROI), marked in **(G)** with a black box. **(A)** Raw data. **(B)** Data with a total variation denoising filter applied. **(C)** Supervoxels generated from the denoised data. **(D)** Annotations applied to the supervoxels (red: background, blue: blood vessels). **(E)** Supervoxel-based prediction of segmentation labels using a random forest classifier trained on the annotations shown in **(D)**. **(F)** Voxel-based prediction of segmentation labels using a 2D U-Net model trained on the segmentation output from **(E)** and the raw data **(A)**. **(G)** Voxel-based predictions of segmentation labels for a central 100 slices of the full 2520 × 2520 dataset using the 2D U-Net model trained as described in **(F)**.

the data (Alvarez-Borges et al., 2021). To do this, 2D images from the raw data and corresponding segmentation label volumes were sliced in three orthogonal planes to create the stack of training images. This process yielded 768 images of 256 × 256 pixels with the corresponding "ground truths." These are enriched further by augmentations such as flips, contrast adjustments, and geometric distortions. Once trained, the process creates an output by taking the volume to be predicted and again dividing it into three stacks of 2D images, and augmenting this with rotations. This results in each voxel being classified multiple separate times and a voting system is used to select the final outcome of the voxel segmentation. The predicted segmentation of the ROI generated by this U-Net model has improved on the shallow learning segmentation output, addressing many of the misclassifications found there (**Figure 2F**).

Next, a new workspace was created containing a central portion of the full-size dataset (2520 × 2520 × 100 pixels). The U-Net model, trained as described above, was then used to generate segmentations from this larger volume of data (**Figure 2G**). Utilizing the capabilities of the Napari viewer and SuRVoS2 plugin, these segmentations can be rendered in 3D and overlaid with the image data to clearly visualize the now segmented blood vessels (**Figure 3**). Due to the large data size, manual segmentation of this single volume is estimated to have taken approximately 320 h, or around 2 months of person-time. Using the initial, shallow learning implementation of SuRVoS was estimated to have reduced the time spent by half, still taking approximately 1 month of person-time. Using the deep learning pipeline in SuRVoS2, segmentation of this volume was reduced to approximately 1.2 h of person-time to segment the ROI using the shallow learning pipeline and 4 h of computational time on a high performance machine consisting of two Intel® Xeon® Gold 6242R processors each with 20 cores running at 3.1 GHz, and 768 GiB of system memory. The GPU used was an NVIDIA Tesla V100 with 32 GB of available memory.

Data Analysis in SuRVoS2

During segmentation, the class each object is assigned to is often left to the individual researcher based on 2D examination of the objects present in the data, leading to potential subjectivity in the results. The Label Splitter tool was developed as a means to derive classifications directly from the data using the inherent characteristics of each object, such as size, shape, intensity, variation, etc. Category labels and rules to generate classes are still decided by a user, meaning some bias or subjectivity is still present, however it will now be consistently applied, even across multiple normalized datasets.

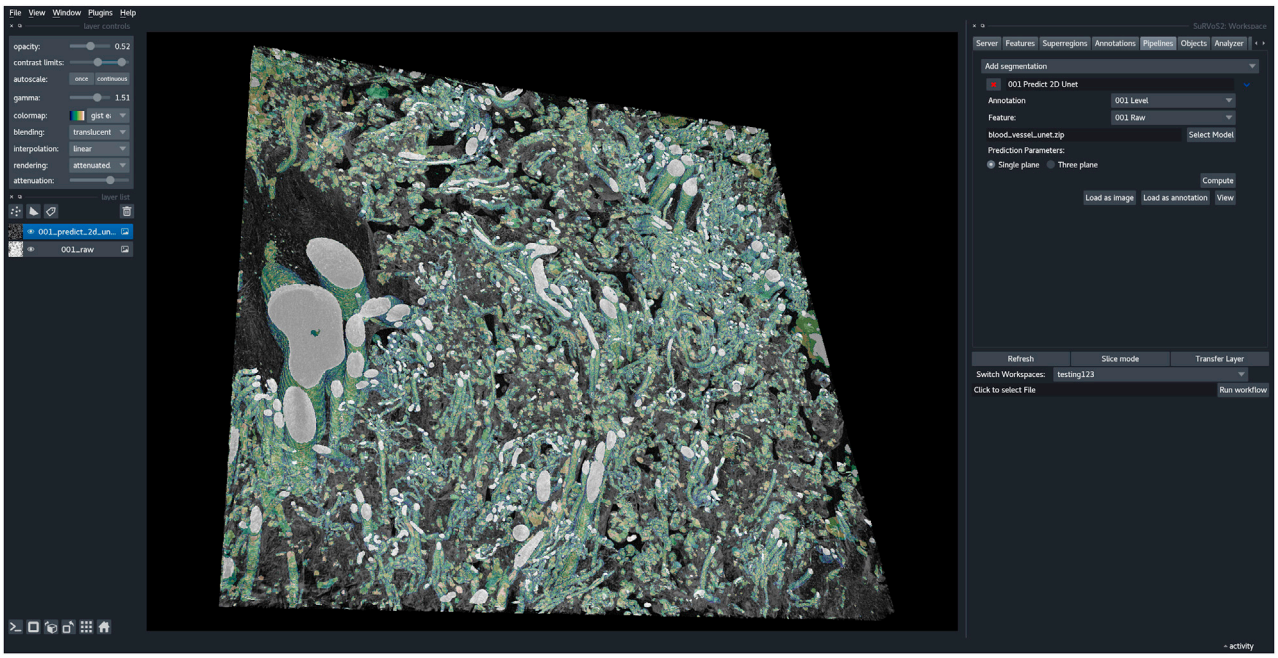

FIGURE 3 | SuRVoS2 plugin integrated into the Napari viewer. The output blood vessel segmentations from the deep learning pipeline in SuRVoS2 visualized using the 3D rendering option and overlaid on the raw data in the Napari viewer.

To demonstrate the functionality of the Label Splitter tool, a cryoSXT dataset of *Trypanosoma bruceii* collected from Diamond Light Source beamline B24 was used (*see* Darrow et al., JoVE, 2018 for more information). Starting from previously segmented objects, the Label Splitter tool displays information about each object that can be used to define rules for separating the objects into classes (**Figure 4** and **Table 1**). These rules can be interactively developed using the table and graph view. The graph is split by a line at the location of the chosen rule value and double clicking on an entry in the table will take the user to the object in the data allowing for clear, specific delineations of classes of object based on the inherent characteristics of the objects.

Rules are applied sequentially to all selected objects creating bespoke classes of objects. After splitting, each new class can be visualized and given a unique label and color (**Figure 5**). The Label Splitter tool can be used on annotation layers regardless of their provenance (manual, shallow learning, deep learning or geometric) and it can also be used iteratively using the output of another Label Splitter instance to create complex and nested hierarchies that can accommodate data with large numbers of different types of objects.

Geometric Data in Segmentation Workflows

SuRVoS2 supports segmentation projects that utilize geometric point data which can be visualized, edited, and used to generate mask-based annotations. Geometric data can be generated in many different ways, for example point-based locations of particles of interest in a 3D volume produced manually or automatically for sub-tomogram averaging (Wagner et al., 2019; Bepler et al., 2020); or through object detection workflows specific to an organelle or other object (Wei et al., 2020), or even points placed on images as part of distributed annotation workflows within a lab or utilizing citizen science platforms (Zooniverse, 2019).

Geometric data is an efficient way to encode knowledge about an image, where a point indicates both an object's class membership and its location. To demonstrate the use of SuRVoS2 with geometric data, point-based data gathered from a crowdsourced workflow focused on finding viruses inside of a cell using cryo electron tomography (cryoET) data collected at Diamond Light Source on eBIC was used (Sutton et al., 2020)

It is possible to either create or import geometric data using Napari. In this case, the data were imported using a simple CSV file format. Points can then be viewed (2D and 3D) and edited/deleted (2D only) while overlaid with the raw image data as reference using the SuRVoS2 plugin (**Figure 6**). Point data can have an encoded class label represented by the point color. The table view lists the coordinates of the 3D point and its class. Double-clicking on the row of a particular point translates the current view to that location, centering the point (**Figure 6**). Together these capabilities provide users the tools needed to evaluate and refine crowdsourced annotations and those generated by automated object detection workflows (Jaeger, 2018).

The Rasterize Points plugin in SuRVoS2 can convert point-based data into segmentation masks by painting ellipsoidal blobs on the 3D point locations. The scale and orientation of the ellipsoids can be set and this operation allows the ellipsoid to be initialized as an Active Contour Without Edges (Chan and

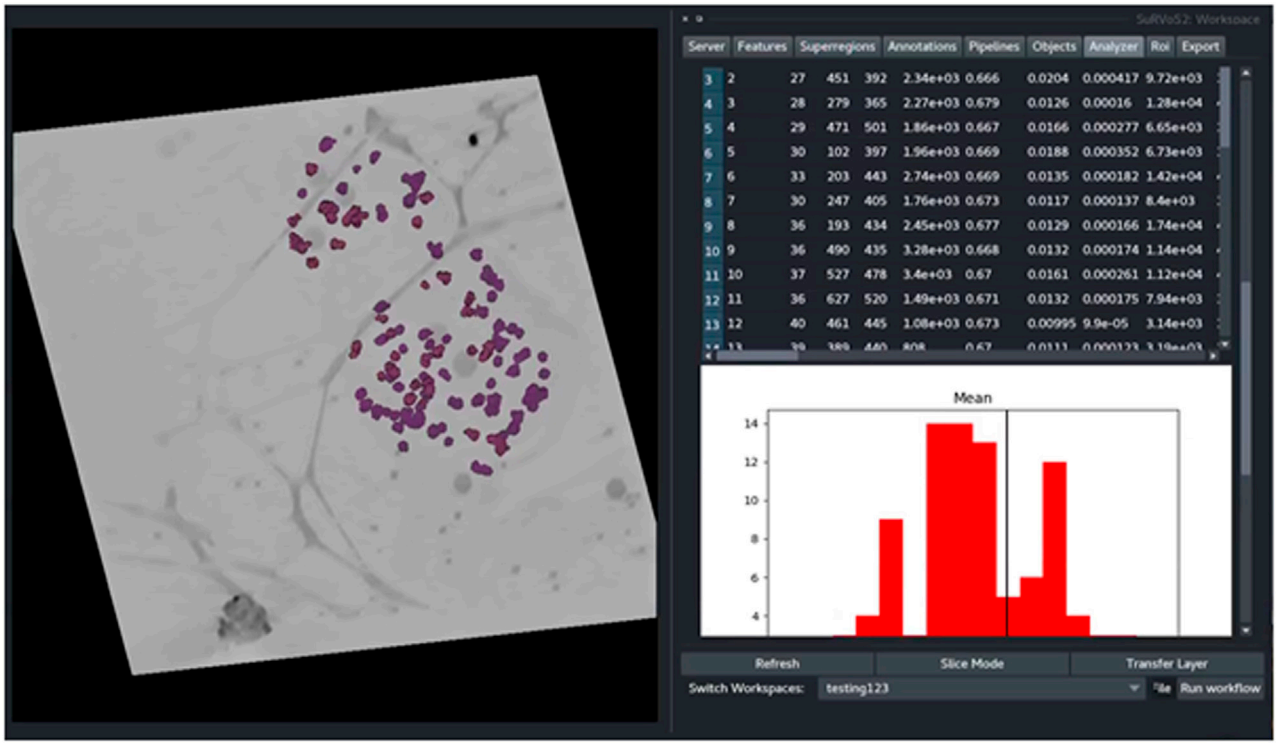

FIGURE 4 | The Label Splitter tool for application of classification rules using inherent characteristics of the segmented objects. Information about each object is displayed on a table and graph. The graph is split by a line at the location of the chosen rule value and double clicking on an entry in the table takes the user to the chosen object in the data.

Vese, 2001) object which can expand or contract, fitting the image data. This or more complex conversion strategies for computationally converting point-based data into segmentations can be designed using the machine learning pipelines within SuRVoS2 (**Figure 1**).

Extended Functionality Using the SuRVoS2 API

SuRVoS2 includes a Python API that can be used from Jupyter Notebooks, allowing the notebook to access, process, and add information into SuRVoS2 workspaces through the SuRVoS2 server (**Figure 7**). Additional functionality implemented through the API includes clustering and visualization of patches sampled from the volume. For example, a set of geometric points is used as sampling locations for uniformly sized patches (e.g. $64 \times 64 \times 64$ pixels) and image features can be computed for each patch using a 2D ResNet model (He, et al., 2015). The features can then be clustered and an embedding made to visualize the features on a 2D plot using Unified Manifold Approximation and Prediction (UMAP; McInnes, et al., 2020) or TSNE (Van der Maaten and Hinton, 2008) (**Figure 7**).

As a second example also starting from geometric data with location and class information, the SuRVoS2 API can be used from any Jupyter client to segment the objects using additional deep learning strategies (such as a 3D U-Net or Feature Pyramid Network (FPN; Lin T et al., 2016) **Figure 7**). The training of the model is performed through the Jupyter notebook, a prediction is made, and the results are visualized as a layer in the SuRVoS2 GUI to allow for inspection of the segmentation. The ability to call standard and additional SuRVoS2 functionality external to the GUI extends the addressable use-cases and provides any researcher with Python programming skills the ability to create bespoke, specialized processing pipelines to address their specific annotation, segmentation, and analysis needs.

Multimodal Correlation of 3D Datasets in SuRVoS2

SuRVoS2 supports the use of correlative, multi-modal imaging data for visualization and annotation. Multiple datasets can be loaded into a workspace and viewed in 2D or 3D as individual layers. The datasets must already be appropriately transformed as this functionality is not currently available in either Napari or SuRVoS2. To demonstrate the use of SuRVoS2 with correlative, multi-modal data, cryoSXT and cryo structured illumination microscopy (cryoSIM) of virus infected cells were aligned externally and displayed within SuRVoS2 (**Figure 8**; EMPIAR 10416 and S-BIAD19 respectively). The opacity of each layer can be controlled allowing for display of both 3D layers simultaneously.

This functionality allows the user to reference one dataset when annotating another dataset, for example using the

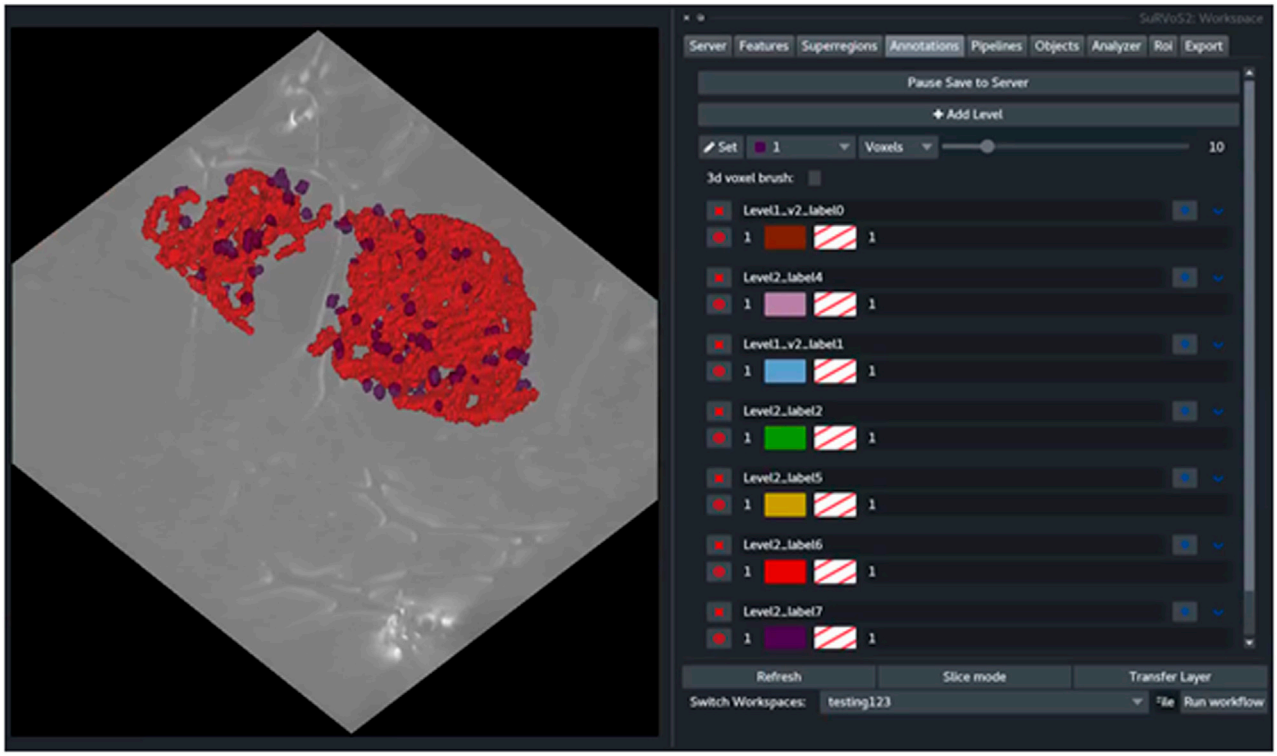

FIGURE 5 | The output of the Label Splitter can be visualized as annotation layers within the SuRVoS2 plugin. Rules are applied sequentially to all selected objects and after splitting, each new class can be visualized and given a unique label and color.

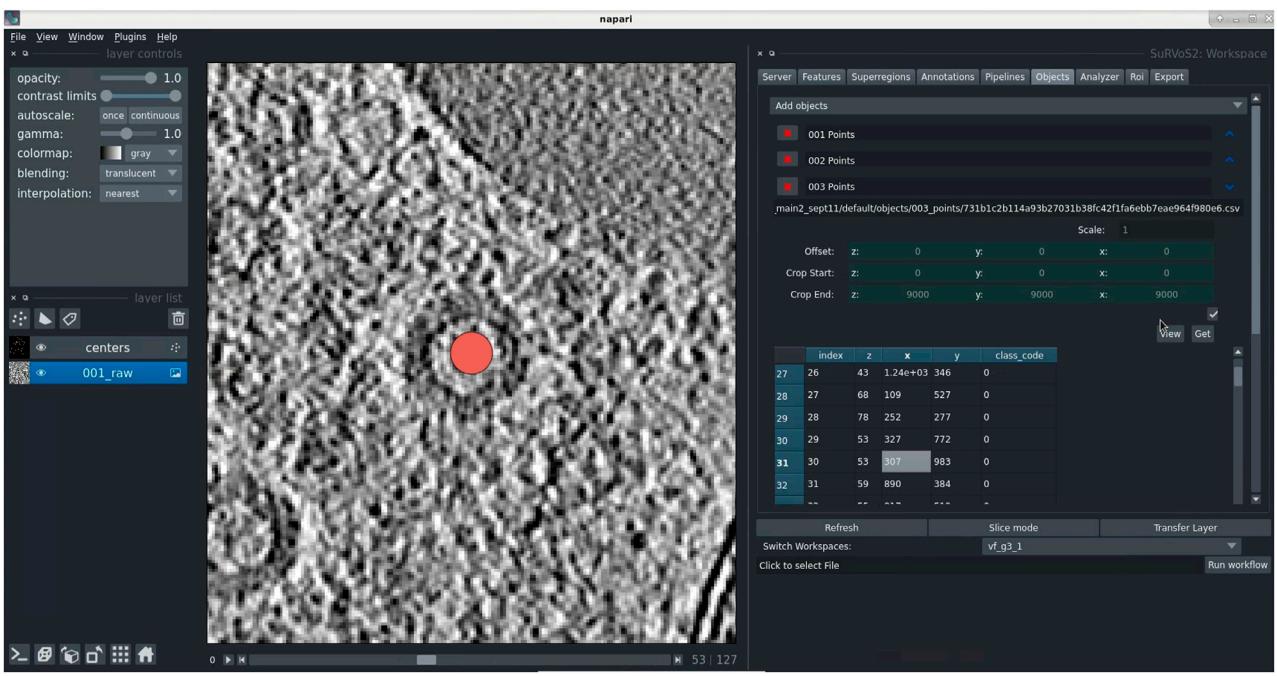

FIGURE 6 | Use of geometric data in SuRVoS2 to analyze crowdsourced annotations. **(A)** Data were imported into the Napari viewer using a simple CSV file format indicating 3D centroid locations and object class. The tools in SuRVoS2 can be used to visualize, edit, and delete geometric data, including a function to take the user directly to an object of interest by double clicking on its entry in the table view.

```
[ ]:
[5]: from survos2.api.regions import supervoxels
[6]: result = survos.run_command('regions', 'create', uri=None, workspace=workspace_name)
[7]: result
[7]: ({'name': '002 Supervoxels', 'kind': 'supervoxels', 'id': '002_supervoxels'},
      False)
[8]: features_src = DataModel.g.dataset_uri("002_gaussian_blur", group="features")
     dst = DataModel.g.dataset_uri(result[0]['id'], group='regions')
[12]:
     arr = view_dataset('002_gaussian_blur', 'features', 10)
```

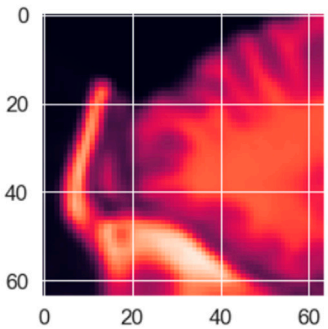


```
[24]: result = supervoxels([features_src],
                           dst,
                          n_segments=100,
                          compactness=0.5,
```

FIGURE 7 | Examples of additional features and use-cases available when using the SuRVoS2 API from within Jupyter notebooks. Example of the SuRVoS2 API being used through a notebook with results which can be visualized using the SuRVoS2 GUI.

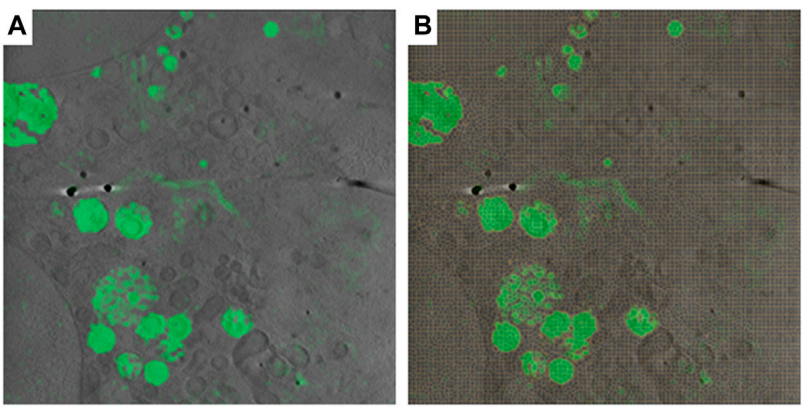

FIGURE 8 | 3D CryoSXT with correlated 3D cryoSIM in SuRVoS2. **(A)** Multimodal imaging can be displayed together as individual layers with control over opacity and color. **(B)** SuRVoS2 specific functionality, such as supervoxels (shown in yellow) can be calculated using one of the datasets for use during segmentation or annotation of the other.

fluorescence to guide segmentation of specific organelles. It is also possible to use other Napari and/or SuRVoS2 functionality to accelerate the annotation or segmentation process. For example, a deconvolution algorithm could be applied (e.g. RedLionfish (Perdigao, 2021) in Napari) to the fluorescence data, followed by calculation of supervoxels and then

segmentation of areas of fluorescence in the non-fluorescence dataset. It is also possible to use the 3D fluorescence dataset as an input feature map during the shallow or deep learning pipelines or as a path to generation of point-based geometric data, although more research is needed to understand best-practices for these applications.

DISCUSSION

Segmentation is a difficult and time-consuming task that absorbs the attention and expertise of domain experts and software engineers alike. The general principles which have led to successful SuRVoS2 segmentations include using step-wise and hierarchical approaches. Rather than attempting to segment all objects in the field of view at once, a more successful strategy may be to segment large regions or distinctive objects from the background as a first step. This can then be followed by additional iterations through the segmentation pipelines, now utilizing the parent-child hierarchy to limit annotation and segmentation calculations to only regions where the objects of interest are to be found. By breaking the problem up into smaller chunks, the semi-automated computational strategies are generally more successful. It is also helpful during the expert annotation stage to be mindful of class imbalances. If an object of interest is only present a small number of times, or only represented by a small number of voxels in the training data, it will be difficult for the deep learning pipeline to accurately detect these objects in the remaining volume. Areas for expert annotation should be chosen carefully to ensure they represent the remaining volume, and secondary areas may be required to emphasize objects which do not occur often.

SuRVoS2 has several key strengths and provides a unique combination of tools that support this iterative process required for producing accurate output segmentations. First, SuRVoS2 encourages interactive visualization and exploration of image volumes and associated geometric data in both 2D and 3D within the user-friendly Napari environment. This is useful when understanding what objects are present in the data and choosing representative ROIs. Second, SuRVoS2 provides several different mechanisms to paint and prepare annotations, including supervoxels for accelerated annotation. And finally, SuRVoS2 provides both a fast mechanism for sparsely training a shallow model to predict annotations as well as a state-of-the-art deep U-Net segmentation model that can learn on densely annotated small ROIs and predict on large volumes.

SuRVoS2 core functionality is available entirely within the GUI for users who wish to interact without programming or scripting. Using the combination of tools available in SuRVoS2 to both annotate data and to train segmentation models, a domain expert can accelerate the process of segmenting their data and further can perform a variety of analyses from the output segmentations, all within the GUI. Additionally, for users familiar with scripting, the SuRVoS2 API and convenience functions allow for accessing and manipulating the entire process of segmentation within a SuRVoS2 workspace from within a Jupyter notebook. Importantly, the SuRVoS2 GUI can be run in parallel with Jupyter notebooks that are accessing the same workspace, providing an interactive analysis or development experience with access to 2D and 3D visualization options. Additionally, application developers can utilize the SuRVoS2 plugin system to extend SuRVoS2 functionality with their own custom plugins. This growing ecosystem within SuRVoS2 and Napari provides an exciting outlook for the future of volumetric image analysis and visualisation.

By separating SuRVoS2 into a client-server architecture, the hardware requirements and installation challenges of the software have been alleviated. The client, installed on a personal or work computer, requires minimal effort to install; and the server installation, which has also been simplified, can be completed by expert technicians on clusters and/or in the cloud to serve a large user base.

Future Development Plans

Now that the client-server architecture has been implemented, the immediate bottleneck associated with processing large datasets within SuRVoS2 has been alleviated, especially when the ROI-based deep learning pipeline is used. However, more efficient use of Dask cluster can be implemented alongside the use of Next Generation File Formats (Moore et al., 2020) to allow further parallelization of image processing operations which will allow SuRVoS2 to scale to even larger datasets.

A second area of development is around use of SuRVoS2 in the cloud. This has been tested with a limited set of virtual machines (Google cloud with Chrome Remote Desktop for client access). This configuration has provided good performance without loss of interactivity. In future, this will be supported through use of a SuRVoS2 server docker container, which could be hosted in the cloud and connected to an external client. This will also enable the possibility of using mobile and browser-based clients for further improvements to accessibility.

Third, SuRVoS2 will benefit from updates and improvements provided by the Napari plugin ecosystem. Napari provides a common user interface paradigm for all Napari plugins to use, easing the burden on researchers to learn bespoke plugins. And the functionality provided by new Napari plugins, especially in the area of segmentation tools, for example Stardist (Schmidt, et al., 2018) and ZELDA (D'Antuono and Pisignano, 2021) can be incorporated within a SuRVoS2 workflow.

A final area of research and development within the SuRVoS2 team is around the need for quantitative quality metrics embedded within the annotation and segmentation process. Segmentation of volumetric biomedical data using machine learning strategies often requires multiple iterative passes of annotation, segmentation, and quantitative evaluation to achieve high-quality results. It is often difficult or impossible to determine how much annotation is required and how detailed the annotation must be to achieve a particular segmentation result. Evaluation of the segmentation output is often manual and subjective and often completed in 2D, highlighting the need for quantitative metrics embedded within the segmentation pipeline to enable the evaluation of the segmentation output. In the future, we plan to explore active learning and collaborative learning techniques (Konyushkova et al., 2015; Luengo et al., 2016; Yang et al., 2017), which will aid the user in selecting regions for annotation to reduce model uncertainty. This deep learning aided segmentation strategy has the potential to further reduce the amount of manually annotated data through smarter selection of ROIs.

CONCLUSION

SuRVoS2 offers a unique set of tools that combine image processing and segmentation with the management of geometric information and the tools available in the Napari viewer. Its redesigned client-server architecture and newly implemented deep learning segmentation pipeline addresses the need to process ever larger datasets. The advanced features provided by the SuRVoS2 API allow users comfortable with scripting to interact through a Jupyter notebook while still accessing the interactive viewing tools. This ecosystem is designed for extensibility through plugin systems both within Napari and SuRVoS2. Together, these features allow for easy exploration of volumetric biomedical and correlative multi-modal data in both 2D and 3D followed by accelerated segmentation pipelines and analysis tools, accelerating data processing and analysis across modalities and scales.

DATA AVAILABILITY STATEMENT

Publicly available datasets were analyzed in this study. This data can be found here: EMPIAR 10562: https://www.ebi.ac.uk/empiar/EMPIAR-10562/ EMPIAR 10416: https://www.ebi.ac.uk/empiar/EMPIAR-10416/ S-BIAD19 (bioimage archive): https://www.ebi.ac.uk/biostudies/BioImages/studies/S-BIAD19?query=S-BIAD19 SuRVoS2 GitHub: https://github.com/DiamondLightSource/SuRVoS2.

AUTHOR CONTRIBUTIONS

MB, MD, and IL conceived of the SuRVoS Workbench software. IL and AP introduced the client-server architecture. AP integrated SuRVoS Workbench into the Napari plugin ecosystem and developed the PyTorch based image processing. OK and AP developed the deep learning pipeline and addressed feature and bug requests from beta-users. WT and MD made feature requests. WT was the main internal tester and trainer. EH Assisted in testing SuRVoS and created the training videos. AP, MD, and OK wrote the paper, all authors reviewed prior to submission.

FUNDING

This work was funded by Wellcome Trust grants 212980/Z/18/Z (AP, WT, MD, and MB) and 220526/Z/20/Z (EH, MD, and MB).

ACKNOWLEDGMENTS

We gratefully acknowledge the Stuart lab at the University of Oxford for providing unpublished test data. We acknowledge EMBL-EBI and the data repositories they facilitate, and those researchers who deposit data, which enables us to re-use previously published data to test new software and algorithms. We are also grateful to the following early adopters and testers of SuRVoS2: Matthew C. Spink, Andrew J. Bodey, Luis Perdigao, and Jennifer Pearson-Farr. This publication uses data generated *via* the Zooniverse.org platform, development of which is funded by generous support, including a Global Impact Award from Google, and by a grant from the Alfred P. Sloan Foundation.

SUPPLEMENTARY MATERIAL

The Supplementary Material for this article can be found online at: https://www.frontiersin.org/articles/10.3389/fcell.2022.842342/full#supplementary-material

REFERENCES

Abràmoff, M. D., Magalhães, P. J., and Ram, S. J. (2004). Image Processing with ImageJ. *Biophotonics Int.* 11 (7), 36–42.

Alvarez-Borges, F. J., King, O. N. F., Madhusudhan, B. N., Connolley, T., Basham, M., and Ahmed, S. I. (2021). U-Net Segmentation Methods for Variable-Contrast XCT Images of Methane-Bearing Sand. *Earth and Space Science Open Archive*. doi:10.1002/essoar.10506807.1

Basham (2021). GitHub - DiamondLightSource/SuRVoS2: Next Generation of SuRVoS. [online] Available at: https://github.com/DiamondLightSource/SuRVoS2 (Accessed December 13, 2021).

Belevich, I., and Jokitalo, E. (2021). DeepMIB: User-Friendly and Open-Source Software for Training of Deep Learning Network for Biological Image Segmentation. *Plos Comput. Biol.* 17 (3), e1008374. doi:10.1371/journal.pcbi.1008374

Bepler, T., Kelley, K., Noble, A. J., and Berger, B. (2020). Topaz-Denoise: General Deep Denoising Models for cryoEM and cryoET. *Nat. Commun.* 11 (1), 5208. doi:10.1038/s41467-020-18952-1

Berg, S., Kutra, D., Kroeger, T., Straehle, C. N., Kausler, B. X., Haubold, C., Schiegg, M., Ales, J., Beier, T., Rudy, M., Eren, K., Cervantes, J. I., Xu, B., Beuttenmueller, F., Wolny, A., Zhang, C., Koethe, U., Hamprecht, F. A., and Kreshuk, A. (2019). Ilastik: Interactive Machine Learning for (Bio)image Analysis. *Nat. Methods* 16 (12), 1226–1232. doi:10.1038/s41592-019-0582-9

Chan, T. F., and Vese, L. A. (2001). Active Contours without Edges. *IEEE Trans. Image Process.* 10 (2), 266–277. doi:10.1109/83.902291

Crosley, T. (2016). Hug: Embrace the APIs of the Future. [online] Hug. Available at: https://www.hug.rest (Accessed December 13, 2021).

D'Antuono, R., and Pisignano, G. (2022). ZELDA: A 3D Image Segmentation and Parent-Child Relation Plugin for Microscopy Image Analysis in Napari. *Front. Comput. Sci.*. doi:10.3389/fcomp.2021.796117

Darrow, M. C., Luengo, I., Basham, M., Spink, M. C., Irvine, S., French, A. P., et al. (2017). Volume Segmentation and Analysis of Biological Materials Using SuRVoS (Super-region Volume Segmentation) Workbench. *J. Vis. Exp.* 126, e56162. doi:10.3791/56162

Gibson, E., Li, W., Sudre, C., Fidon, L., Shakir, D. I., Wang, G., et al. (2018). NiftyNet: a Deep-Learning Platform for Medical Imaging. *Computer Methods Programs Biomed.* 158, 113–122. doi:10.1016/j.cmpb.2018.01.025

Gómez-de-Mariscal, E., García-López-de-Haro, C., Ouyang, W., Donati, L., Lundberg, E., Unser, M., et al. (2021). DeepImageJ: A User-Friendly Environment to Run Deep Learning Models in ImageJ. *Nat. Methods* 18, 1192–1195.

Haberl, M. G., Churas, C., Tindall, L., Boassa, D., Phan, S., Bushong, E. A., et al. (2018). CDeep3M-Plug-and-Play Cloud-Based Deep Learning for Image Segmentation. *Nat. Methods* 15 (9), 677–680. doi:10.1038/s41592-018-0106-z

Hall, M., Frank, E., Holmes, G., Pfahringer, B., Reutemann, P., and Witten, I. H. (2009). The WEKA Data Mining Software. *SIGKDD Explor. Newsl.* 11 (1), 10–18. doi:10.1145/1656274.1656278

Hand, D. J. (2020). *"Dark Data: Why what You Don't Know Matters" Princeton*. Princeton, NJ: University Press.

He, K., Zhang, X., Ren, S., and Sun, J. (2016). Deep Residual Learning. Image Recognition. *2016 IEEE Conference on Computer Vision and Pattern Recognition (CVPR)*, 770–778.

Helmstaedter, M., Briggman, K. L., and Denk, W. (2011). High-accuracy Neurite Reconstruction for High-Throughput Neuroanatomy. *Nat. Neurosci.* 14 (8), 1081–1088. doi:10.1038/nn.2868

Howard, J., and Gugger, S. (2020). Fastai: a Layered API for Deep Learning. *Information* 11 (2), 108. doi:10.3390/info11020108

Jaeger, P. F., Kohl, S. S. A., Bickelhaupt, S., Isensee, F., Kuder, T. A., Schlemmer, H. P., et al. (2018). "Retina U-Net: Embarrassingly Simple Exploitation of Segmentation Supervision for Medical Object Detection," In Proceedings Machine Learning for Health NeurIPS Workshop, (PMLR), 171–183.

Khoreva, A., Benenson, R., Jan, H., Hein, M., and Bernt, S. (2017). "Simple Does it: Weakly Supervised Instance and Semantic Segmentation," in Proceedings of the IEEE conference on computer vision and pattern recognition, 876–885. doi:10.1109/cvpr.2017.181

King, O. (2021). DiamondLightSource/gas-hydrate-segmentation-unets: Code for Segmentation of 3-dimensional X-ray Computed Tomography (XCT) Images of Methane Bearing Sand Using 2d and 3d U-Net Models. (n.d.). RetrievedAvailable at: https://github.com/DiamondLightSource/gas-hydrate-segmentation-unets December 13, 2021).

Kluyver, T., Ragan-Kelley, B., Perez, F., Granger, B., Bussonnier, M., Frederic, J., et al. (2016). "Jupyter Notebooks-A Publishing Format for Reproducible Computational Workflows," in *Positioning and Power in Academic Publishing: Players, Agents and Agendas*. Editors F. Loizides and B. Scmidt (Amsterdam, Netherlands: IOS Press), 87–90.

Konyushkova, K., Sznitman, R., and Pascal, F. (2015). "Introducing Geometry in Active Learning for Image Segmentation," in Proceedings of the IEEE International Conference on Computer Vision, 2974–2982.

Kremer, J. R., Mastronarde, D. N., and McIntosh, J. R. (1996). Computer Visualization of Three-Dimensional Image Data Using IMOD. *J. Struct. Biol.* 116 (1), 71–76. doi:10.1109/iccv.2015.340

Li, Q., Arnab, A., and Torr, P. (2018). "Weakly-and Semi-supervised Panoptic Segmentation," in Proceedings of the European conference on computer vision (ECCV), 102–118. doi:10.1007/978-3-030-01267-0_7

Lin, D., Dai, J., Jia, J., He, K., and Sun, J. (2016). "Scribblesup: Scribble-Supervised Convolutional Networks for Semantic Segmentation," in Proceedings of the IEEE conference on computer vision and pattern recognition, 3159–3167. doi:10.1109/cvpr.2016.344

Lin, T., Dollár, P., Girshick, R., He, K., Hariharan, B., and Belongie, S. (2016). Feature Pyramid Networks for Object Detection. Available at: https://arxiv.org/abs/1612.03144v2.

Lucchi, A., Smith, K., Achanta, R., Knott, G., and Fua, P. (2011). Supervoxel-based Segmentation of Mitochondria in Em Image Stacks with Learned Shape Features. *IEEE Trans. Med. Imaging* 31 (2), 474–486. doi:10.1109/TMI.2011.2171705

Luengo, I., Basham, M., and French, A. P. (2016). "Selective Labeling: Identifying Representative Sub-volumes for Interactive Segmentation," in International Workshop on Patch-based Techniques in Medical Imaging (Cham: Springer), 17–24. doi:10.1007/978-3-319-47118-1_3

Luengo, I., Darrow, M. C., Spink, M. C., Sun, Y., Dai, W., He, C. Y., et al. (2017). SuRVoS: Super-region Volume Segmentation Workbench. *J. Struct. Biol.* 198 (1), 43–53. doi:10.1016/j.jsb.2017.02.007

McInnes, L., Healy, J., Saul, N., and Groβberger, L. (2018). UMAP: Uniform Manifold Approximation and Projection. *J. Open Source Software* 3, 861.

McQuin, C., Goodman, A., Chernyshev, V., Kamentsky, L., Cimini, B. A., Karhohs, K. W., et al. (2018). CellProfiler 3.0: Next-Generation Image Processing for Biology. *Plos Biol.* 16 (7), e2005970. doi:10.1371/journal.pbio.2005970

Merkel, D. (2014). Docker: Lightweight Linux Containers for Consistent Development and Deployment. *Linux J.* 239, 2.

Moore, J. (2020). Next-generation File Format (NGFF) Specifications for Storing Bioimaging Data in the Cloud. Open Microscopy Environment Consortium. This edition of the specification is Available at: The latest edition is Available at: https://ngff.openmicroscopy.org/0.1/https://ngff.openmicroscopy.org/latest/.

Napari Contributors (2021). GitHub - Napari/napari: Napari: a Fast, Interactive, Multi-Dimensional Image Viewer for python. [online] GitHub. Available at: https://github.com/napari/napari (Accessed December 13, 2021).

Paszke, A., Gross, S., Massa, F., Lerer, A., Bradbury, J., Chanan, G., et al. (2019). Pytorch: An Imperative Style, High-Performance Deep Learning Library. *Adv. Neural Inf. Process. Syst.* 32, 8026–8037.

Peddie, C. J., and Collinson, L. M. (2014). Exploring the Third Dimension: Volume Electron Microscopy Comes of Age. *Micron* 61, 9–19. doi:10.1016/j.micron.2014.01.009

Pedregosa, F., Varoquaux, G., Gramfort, A., Michel, V., Thirion, B., Grisel, O., et al. (2011). Scikit-learn: Machine Learning in Python. *J. Mach. Learn. Res.*, 12, 2825–2830.

Perdigao, L. (2021). GitHub - rosalindfranklininstitute/RedLionfish. [online] Available at: https://github.com/rosalindfranklininstitute/RedLionfish/ (Accessed December 13, 2021).

Pérez-García, F., Sparks, R., and Ourselin, S. (2021). TorchIO: a Python Library for Efficient Loading, Preprocessing, Augmentation and Patch-Based Sampling of Medical Images in Deep Learning. *Comput. Methods Prog. Biomed.* 208, 106236. doi:10.1016/j.cmpb.2021.106236

Prigent, S. (2021). Napari Hub | Plugins | Napari-Stracking by Sylvain Prigent. [online] Napari-hub.org. Available at: https://www.napari-hub.org/plugins/napari-stracking (Accessed December 13, 2021).

Riba, E., Mishkin, D., Ponsa, D., Rublee, E., and Bradski, G. (2020). Kornia: An Open Source Differentiable Computer Vision Library for PyTorch, Winter Conference on Applications of Computer Vision. *IEEE Computer Society*, 3663–3672.

Riverbankcomputing.com (2021). Riverbank Computing | Introduction. [online] Available at: https://riverbankcomputing.com/software/pyqt/ (Accessed December 13, 2021).

Rocklin, M. (2015). "Dask: Parallel Computation with Blocked Algorithms and Task Scheduling," in Proceedings of the 14th python in science conference, 136.130

Ronneberger, O., Fischer, P., and Brox, T. (2015). "U-net: Convolutional Networks for Biomedical Image Segmentation," in International Conference on Medical image computing and computer-assisted intervention (Cham: Springer), 234–241. doi:10.1007/978-3-319-24574-4_28

Schmidt, U., Weigert, M., Broaddus, C., and Myers, G. (2018). "Cell Detection with star-convex Polygons," in International Conference on Medical Image Computing and Computer-Assisted Intervention (Cham: Springer), 265–273. doi:10.1007/978-3-030-00934-2_30

Seo, H., Badiei Khuzani, M., Vasudevan, V., Huang, C., Ren, H., Xiao, R., et al. (2020). Machine Learning Techniques for Biomedical Image Segmentation: An Overview of Technical Aspects and Introduction to State-Of-Art Applications. *Med. Phys.* 47 (5), e148–e167. doi:10.1002/mp.13649

Sofroniew, N. (2021). Napari Hub | Plugins | Napari-Animation by Nicholas Sofroniew, Alister Burt, Guillaume Witz, Faris Abouakil, Talley Lambert. [online] Napari-hub.org. Available at: https://www.napari-hub.org/plugins/napari-animation (Accessed December 13, 2021).

Strotton, M. C., Bodey, A. J., Wanelik, K., Darrow, M. C., Medina, E., Hobbs, C., et al. (2018). Optimising Complementary Soft Tissue Synchrotron X-ray Microtomography for Reversibly-Stained central Nervous System Samples. *Sci. Rep.* 8 (1), 12017–12018. doi:10.1038/s41598-018-30520-8

Sutton, G., Sun, D., Fu, X., Kotecha, A., Hecksel, C. W., Clare, D. K., et al. (2020). Assembly Intermediates of Orthoreovirus Captured in the Cell. *Nat. Commun.* 11 (11), 44451–44457. doi:10.1038/s41467-020-18243-9

Thermofisher.com (2021). Avizo Software for Materials Research | Thermo Fisher Scientific - UK. [online] Available at: https://www.thermofisher.com/uk/en/home/electron-microscopy/products/software-em-3d-vis/avizo-software.html (Accessed December 13, 2021).

Tun, W. M., Poologasundarampillai, G., Bischof, H., Nye, G., King, O. N. F., Basham, M., et al. (2021). A Massively Multi-Scale Approach to Characterizing Tissue Architecture by Synchrotron Micro-CT Applied to the Human Placenta. *J. R. Soc. Interf.* 18 (179), 20210140. doi:10.1098/RSIF.2021.0140

Van der Maaten, L., and Hinton, G. (2008). Visualizing Data Using T-SNE. *J. machine Learn. Res.* 9 (11).

van der Walt, S., Schönberger, J. L., Nunez-Iglesias, J., Boulogne, F., Warner, J. D., Yager, N., et al. (2014). Scikit-image: Image Processing in Python. *PeerJ* 2, e453. doi:10.7717/peerj.453

Virtanen, P., Gommers, R., Oliphant, T. E., Haberland, M., Reddy, T., Cournapeau, D., et al. (2020). SciPy 1.0: Fundamental Algorithms for Scientific Computing in Python. *Nat. Methods* 17 (3), 261–272. doi:10.1038/s41592-019-0686-2

Wagner, T., Merino, F., Stabrin, M., Moriya, T., Antoni, C., Apelbaum, A., et al. (2019). SPHIRE-crYOLO Is a Fast and Accurate Fully Automated Particle Picker for Cryo-EM. *Commun. Biol.* 2 (1), 218. doi:10.1038/s42003-019-0437-z

Wei, D., Lin, Z., Franco-Barranco, D., Wendt, N., Liu, X., Yin, W., et al. (2020). MitoEM Dataset: Large-Scale 3D Mitochondria Instance Segmentation from EM Images. *Int. Conf. Med. Image Comput. Computer-Assisted Intervention* 12265, 66–76. doi:10.1007/978-3-030-59722-1_7

Xu, C. S., Pang, S., Shtengel, G., Müller, A., Ritter, A. T., Hoffman, H. K., et al. (2021). An Open-Access Volume Electron Microscopy Atlas of Whole Cells and Tissues. *Nature* 599, 147–151. doi:10.1038/s41586-021-03992-4

Yang, L., Zhang, Y., Chen, J., Zhang, S., Chen, D. Z., and Chen (2017). "Suggestive Annotation: A Deep Active Learning Framework for Biomedical Image Segmentation," in *International conference on medical image computing and computer-assisted intervention*. Editors M. Descoteaux, L. Maier-Hein, A. Franz, P. Jannin, D. L. Collins, and S. Duchesne (Cham: Springer), 399–407. doi:10.1007/978-3-319-66179-7_46

Yoshiyuki, K., Jaerin, S., and Yasuo, K. (2018). Large Volume Electron Microscopy and Neural Microcircuit Analysis. *Front. Neural Circuits* 12. doi:10.3389/fncir.2018.00098

Zooniverse (2016). Available at: https://www.zooniverse.org/ (Accessed October 27, 2019).

Conflict of Interest: Authors AP, OK, WT, IL, and MB were employed by the company Diamond Light Source Ltd. EH was employed by the Rosalind Franklin Institute.

The remaining authors declare that the research was conducted in the absence of any commercial or financial relationships that could be construed as a potential conflict of interest.

Publisher's Note: All claims expressed in this article are solely those of the authors and do not necessarily represent those of their affiliated organizations, or those of the publisher, the editors and the reviewers. Any product that may be evaluated in this article, or claim that may be made by its manufacturer, is not guaranteed or endorsed by the publisher.

frontiers | Frontiers in Cell and Developmental Biology

ORIGINAL RESEARCH
published: 05 April 2022
doi: 10.3389/fcell.2022.849469

Public Volume Electron Microscopy Data: An Essential Resource to Study the Brain Microvasculature

Stephanie K. Bonney[1†], *Vanessa Coelho-Santos*[1†], *Sheng-Fu Huang*[2,3†], *Marc Takeno*[4], *Joergen Kornfeld*[5], *Annika Keller*[2,3]* *and Andy Y. Shih*[1,6,7]*

[1]Center for Developmental Biology and Regenerative Medicine, Seattle Children's Research Institute, Seattle, WA, United States, [2]Department of Neurosurgery, Clinical Neuroscience Center, University Hospital Zürich, University of Zürich, Zürich, Switzerland, [3]Neuroscience Center Zürich, University of Zürich and ETH Zürich, Zürich, Switzerland, [4]Allen Institute for Brain Science, Seattle, WA, United States, [5]Max Planck Institute of Neurobiology, Planegg, Germany, [6]Department of Pediatrics, University of Washington, Seattle, WA, United States, [7]Department of Bioengineering, University of Washington, Seattle, WA, United States

OPEN ACCESS

Edited by:
Christopher Guerin,
Vlaams Instituut voor Biotechnologie,
Belgium

Reviewed by:
Craig Edward Brown,
University of Victoria, Canada
Baptiste Lacoste,
Ottawa Hospital Research Institute
(OHRI), Canada

***Correspondence:**
Annika Keller
Annika.keller@usz.ch
Andy Y. Shih
Andy.Shih@Seattlechildrens.org

[†]These authors share first authorship

Specialty section:
This article was submitted to
Cellular Biochemistry,
a section of the journal
Frontiers in Cell and Developmental
Biology

Received: 06 January 2022
Accepted: 21 February 2022
Published: 05 April 2022

Citation:
Bonney SK, Coelho-Santos V,
Huang S-F, Takeno M, Kornfeld J,
Keller A and Shih AY (2022) Public
Volume Electron Microscopy Data: An
Essential Resource to Study the
Brain Microvasculature.
Front. Cell Dev. Biol. 10:849469.
doi: 10.3389/fcell.2022.849469

Electron microscopy is the primary approach to study ultrastructural features of the cerebrovasculature. However, 2D snapshots of a vascular bed capture only a small fraction of its complexity. Recent efforts to synaptically map neuronal circuitry using volume electron microscopy have also sampled the brain microvasculature in 3D. Here, we perform a meta-analysis of 7 data sets spanning different species and brain regions, including two data sets from the MICrONS consortium that have made efforts to segment vasculature in addition to all parenchymal cell types in mouse visual cortex. Exploration of these data have revealed rich information for detailed investigation of the cerebrovasculature. Neurovascular unit cell types (including, but not limited to, endothelial cells, mural cells, perivascular fibroblasts, microglia, and astrocytes) could be discerned across broad microvascular zones. Image contrast was sufficient to identify subcellular details, including endothelial junctions, caveolae, peg-and-socket interactions, mitochondria, Golgi cisternae, microvilli and other cellular protrusions of potential significance to vascular signaling. Additionally, non-cellular structures including the basement membrane and perivascular spaces were visible and could be traced between arterio-venous zones along the vascular wall. These explorations revealed structural features that may be important for vascular functions, such as blood-brain barrier integrity, blood flow control, brain clearance, and bioenergetics. They also identified limitations where accuracy and consistency of segmentation could be further honed by future efforts. The purpose of this article is to introduce these valuable community resources within the framework of cerebrovascular research. We do so by providing an assessment of their vascular contents, identifying features of significance for further study, and discussing next step ideas for refining vascular segmentation and analysis.

Keywords: cerebrovascular, pericytes, endothelium, blood-brain barrier, astrocyte endfeet, perivascular fibroblasts, microglia, peg-socket interaction

INTRODUCTION

Electron microscopy is an essential tool in cerebrovascular research. It is the primary means to visualize and quantify subcellular structures central to blood-brain barrier function, blood flow regulation and neurovascular communication. These functions rely, for example, on endothelial tight and adherens junctions, caveolar vesicles, organelles (e.g., mitochondria), and the vascular basement membrane, which are all structures on the order of tens to hundreds of nanometers. Two-dimensional (2D) transmission electron microscopy (TEM) is most often used to resolve these ultrastructures, providing cross sectional high-resolution views of the vascular wall. However, vascular cells and their subcellular compartments have sophisticated 3D morphologies inadequately captured in 2D images. For example, mural cells (smooth muscle cells and pericytes) exhibit diverse cellular morphologies and cellular interactions with the endothelium in different regions of the microvasculature (Grant et al., 2017; Ornelas et al., 2021). "Peg-and-socket" contacts between pericytes and endothelial cells, sites where the direct communication between these cells takes place, can only be visualized using electron microscopy. These contacts are likely important for cerebrovascular function since loss of pericyte-endothelial interactions are associated with increased blood-brain barrier permeability (Armulik et al., 2010; Daneman et al., 2010), brain entry of circulating leukocytes (Török et al., 2021), and impaired cerebral blood flow (Kisler et al., 2017; Nikolakopoulou et al., 2019; Hartmann et al., 2021a).

A second limitation of non-automated 2D-EM is that only fields of view in the micrometer range can be imaged, a scale on which microvasculature is sparse. Further, there are distinct functional zones of the microvasculature, including arterioles, capillaries, venules or transitional regions between them, that are difficult to locate and image in 2D. The cellular composition of the vascular wall, i.e., the neurovascular unit, differs between the vascular zones. Arterioles are composed of endothelial cells, smooth muscle cells, perivascular fibroblasts and macrophages, and astrocytic endfeet. In contrast, capillaries are composed of endothelial cells, pericytes encased in the basement membrane and astrocytic end feet. The subcellular structures and organelles of these cell types and the composition of the basement membrane between the cells also differ between microvascular regions. Therefore, to understand the vasculature, data must be collected at an ultrastructural level on a scale of hundreds of micrometers to millimeters.

Recent advances in 3D-EM of brain tissue have overcome these considerable technical challenges (Kornfeld and Denk, 2018; Yin et al., 2020), and several high-content 3D-EM data sets from various species have been generated (e.g., finch, mouse, human). The primary drive behind these efforts has been to map synaptic connectivity between neurons. Initial data sets, such as the *C. elegans* data captured in the 1980s (White et al., 1986), were of smaller size due to challenges in imaging, segmentation and data processing. However, recent collaborative efforts through the Machine Intelligence from Cortical networks (MICrONS) consortium (Dorkenwald et al., 2019; Consortium Microns et al., 2021; Schneider-Mizell et al., 2021) and independent laboratories (Lee et al., 2016; Dorkenwald et al., 2017; Bloss et al., 2018; Shapson-Coe et al., 2021) have generated enormous data sets encompassing up to a cubic millimeter of tissue volume. These publicly available 3D-EM data sets hold immense information on the fine-structure of cerebral microvasculature across different zones of the vascular network, allowing deep exploration of cellular composition, morphology and subcellular interaction between neurovascular cell types. Despite being available in online browsers, these data have yet to be mined and interpreted for insight on cerebrovascular biology. The purpose of this article is to assess large-scale 3D-EM data sets gathered from the brain, and to show vignettes of data on the vasculature held within them.

METHODS

All data sets were explored through the access links provided in **Table 1**. These resources have used Neuroglancer, an open-source browser-based viewer for visualization of large-scale 3D data. An introduction on how to use Neuroglancer can be found at: https://www.microns-explorer.org/visualization. Full details on Neuroglancer can be found at: https://github.com/google/neuroglancer#readme.

In the figure legends, we provide the x, y, z coordinates for the regions of interest shown in each data set, which can be copied and pasted into the x, y, z, query boxes on the top left of Neuroglancer. For **Figures 1** and **3**, web addresses are provided in the figure legend to view annotated MICrONS Layer 2/3 data. However, viewers must first register and agree to terms of service, which can be prompted through the following link: https://neuromancer-seung-import.appspot.com/?json_url=https://globalv1.dafapis.com/nglstate/api/v1/5665719098277888.

The data sets examined here are not exhaustive of those available for public viewing. The reader is directed to the following websites for additional volume EM resources: https://neurodata.io/project/ocp/. https://webknossos.org/publications.

RESULTS

Table 1 provides an overview of the publicly available 3D-EM data sets examined in this study. We first focus on two data sets from the cerebral cortex of adult mice, generated by the MICrONS consortium, which can be accessed through www.microns-explorer.org.

MICrONS Layer 2/3

An initial study examined a region of adult mouse visual cortex spanning a volume of 250 × 140 × 90 µm in cortical layers 2/3 (Schneider-Mizell et al., 2021). All parenchymal cell types were segmented in this data set (neurons, astrocytes, microglia) and the vascular wall was segmented as a combined element of both mural cells and endothelial cells. The vascular network includes a portion of a single cortical ascending venule and surrounding capillaries. Occasionally, neurons or astrocytes are captured

TABLE 1 | Attributes and vascular contents in public 3D-EM data sets from brain tissue.

Source	Species	Brain region(s)	Volume	Vascular content	Access
MICrONS consortium Layer 2/3 https://doi.org/10.1101/2019.12.29.890319 https://doi.org/10.7554/eLife.73783	Mouse (P36 CamKIIa-Cre::B6;CBA-Tg(Camk2a-tTA)1Mmay/j::Ai93)	Primary visual cortex (Layer 1, 2/3)	Size: 250 × 140 × 90 µm volume Resolution: 3.58 × 3.58 × 40 nm per voxel	Portion of ascending venule and surrounding capillary network	https://www.microns-explorer.org/phase1
Lee et al https://www.nature.com/articles/nature17192	Mouse (9 months, male, C57BL/6)	Primary visual cortex (Layer 1, 2/3)	Size 450 × 450 × 150 µm volume Resolution: 4 × 4 × 40 nm per voxel	Portion of penetrating arteriole and surrounding capillary network	https://neurodata.io/data/lee16/
MICrONS consortium Cortical MM^3 https://www.biorxiv.org/content/10.1101/2021.07.28.454025v2.full	Mouse (P87, SLC17a7-Cre::Ai162)	Primary visual cortex and higher visual areas (All cortical layers and white matter)	Size: 1.4 × .87 × 0.84 mm volume Resolution: 4 × 4 × 40 nm per voxel	Numerous penetrating arterioles and ascending venules and extensive microvascular network	www.microns-explorer.org
Bloss et al https://www.nature.com/articles/s41593-018-0084-6	Mouse (12 weeks, male, C57BL/6)	Hippocampus	Size: 350 × 200 × 17 µm Resolution: 3.8 × 3.8 × 50 nm per voxel	Portions of a venule and surrounding capillary network	https://neurodata.io/data/bloss2018/
Dorkenwald et al j0126 https://www.nature.com/articles/nmeth.4206#Sec2 Schubert et al., in preparation	Zebra finch (>90 days post hatch, male)	Basal ganglia (Area X)	Size: 97.9 × 95.6 × 115 µm volume Resolution: 9 × 9 × 20 nm per voxel	Portion of venule and surrounding capillary network	https://syconn.esc.mpcdf.mpg.de (not yet public)
Schubert et al., in preparation j0251	Zebra finch (>90 days post hatch, male)	Basal ganglia (Area X)	Size: 256 × 256 × 384 µm volume Resolution: 10 × 10 × 25 nm per voxel	Portions of arterioles, venules and numerous capillaries	https://syconn.esc.mpcdf.mpg.de (not yet public)
Shapson-Coe et al https://www.biorxiv.org/content/10.1101/2021.05.29.446289v1	Human (45 year old, female)	Cerebral cortex, temporal lobe	Size: Irregular pentagon shape with ~3 mm at longest width, ~2 mm at longest height, and ~0.15 mm in thickness Resolution 4 × 4 × 33 nm per voxel	Thin tissue slice with small portions of parenchymal vessels and capillary network	https://h01-release.storage.googleapis.com/gallery.html

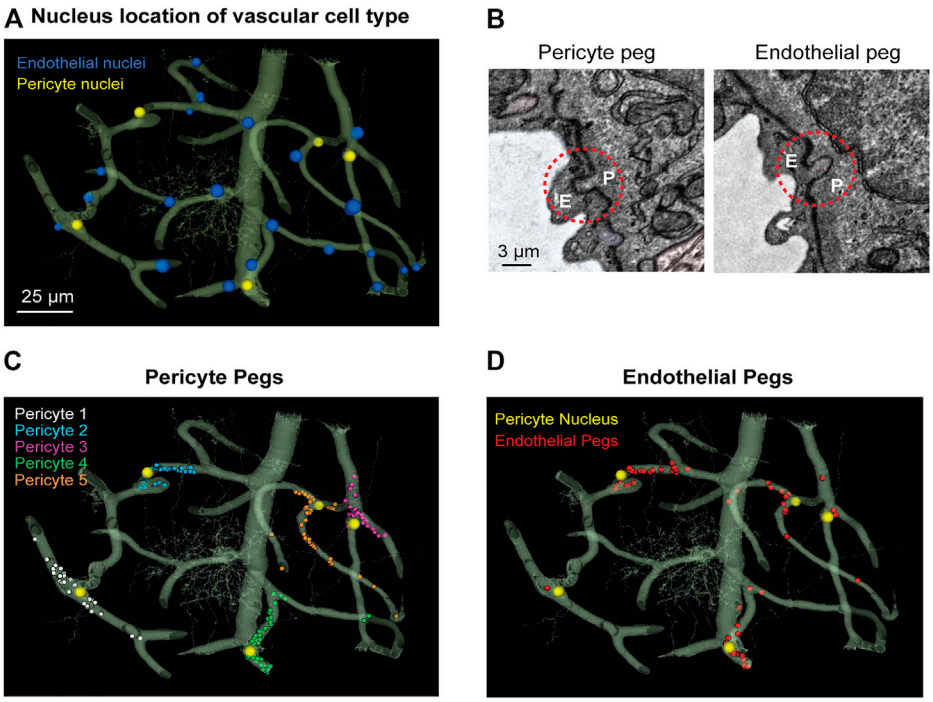

FIGURE 1 | MICrONS Layer 2/3 pericyte-endothelial interactions. **(A)** The location of all endothelial and pericyte nuclei identified within the MICrONS Layer 2/3 data set. **(B)** Examples of pericyte pegs extending into the endothelium (left), and conversely, endothelial pegs extending into the pericyte (right). **(C)** The location of pericyte pegs mapped onto the 3D microvascular network reveals that pegs are enriched at sites of pericyte somata. The pericyte somata are labeled with yellow spheres, and the individual pegs are labeled with smaller colored spheres, color-coded per pericyte. **(D)** The location of endothelial pegs are also enriched around pericyte somata. Images adapted from (Ornelas et al., 2021). Link to annotations (See methods to register and agree to terms of service): https://neuromancer-seung-import.appspot.com/?json_url=https://globalv1.daf-apis.com/nglstate/api/v1/5073246747623424.

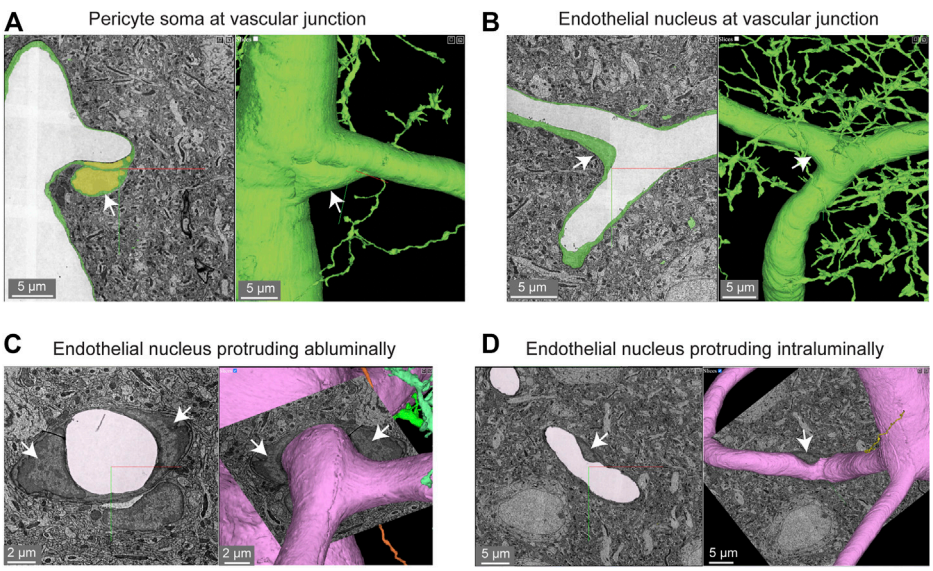

FIGURE 2 | Pericyte and endothelial cell somata can be positioned at vascular junctions. **(A)** Pericyte soma (white arrow) positioned at the junction between the capillary and ascending venule in the MICrONS Layer 2/3 data set. Left panel shows selected vascular wall segmentation in 2D, and the right panel shows 3D rendering of the vascular wall. MICrONS Layer 2/3 x, y, z coordinates at: 82286, 68574, 1719. **(B)** Endothelial nucleus (white arrow) at a capillary junction. Coordinates at: 68291, 61335, 1788. **(C)** Example of two endothelial nuclei that protrude abluminally without affecting the shape of the lumen. Coordinates at: 76691, 59357, 1,594. **(D)** Example of an endothelial nucleus that protrudes intraluminally and causes local reduction in capillary diameter. Coordinates at: 71372, 45504, 1,467.

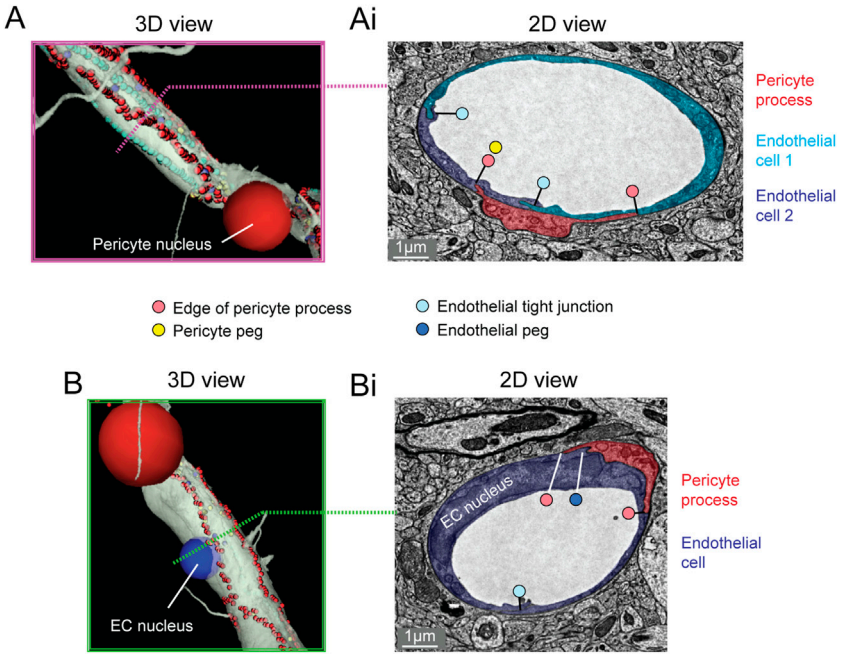

FIGURE 3 | Pericyte processes in relation to endothelial features. **(A)** The edge of a pericyte process annotated in Neuroglancer 3D view with red dots, alongside endothelial junctions in cyan dots. **(Ai)** The 2D cross section of one location (dotted magenta line) within the same capillary segment. **(B)** The pericyte process tends to exhibit greater endothelial coverage near endothelial somata. **(Bi)** The 2D cross section of one location (dotted green line) within the same capillary segment. EC, endothelial cell. Images adapted from (Ornelas et al., 2021). Link to annotations (See methods to register and agree to terms of service): https://neuromancer-seung-import.appspot.com/?json_url=https://globalv1.daf-apis.com/nglstate/api/v1/6082177280245760.

within the vascular segmentation due to their proximity to the vascular wall.

Pericyte-Endothelial Interaction

We noted that the capillary network contains 25 endothelial cell nuclei and five pericyte nuclei, consistent with individual pericytes covering multiple endothelial cells (**Figure 1A**). Pericytes were identified as cells on the abluminal side of endothelium with protruding cell somata and elongated, slender processes embedded in the vascular basement membrane. In the volume EM data, their abluminal processes could be traced back to the cell somata to verify its identity as a pericyte. Physical interlocking between pericytes and endothelial cells *via* peg-and-socket interactions is important for their communication and attachment. These structures could be discerned in the data (**Figure 1B**). By annotating the positions of peg-and-socket interactions in Neuroglancer, they were found to be concentrated near the somata of pericytes, implicating the pericyte somata as potential hot spots for direct communication with endothelial cells (**Figures 1B,C**). These interactions included both extension of pericytes pegs toward the adjacent endothelium, and less commonly, endothelial cells extending toward pericytes (**Figures 1B,D**).

Pericyte somata are often positioned at capillary bifurcations (**Figure 2A**) (Hartmann et al., 2015). This localization may play a role in how blood flow is partitioned down separate capillary branches during cerebral perfusion (Gonzales et al., 2020). Endothelial cell nuclei were located along capillary segments and also some capillary bifurcations (**Figure 2B**). The extra volume of the endothelial nuclei often manifested as abluminally-oriented protrusions, similar to pericyte somata (**Figure 2C**). However, we also noted many instances where the endothelial nuclei encroached upon the intraluminal space, reducing its diameter (**Figure 2D**). This suggests that the position of endothelial nuclei may influence blood cell flow in the capillary network by imparting blood flow resistance. This possibility has not been thoroughly examined in physiological studies, unlike blood flow in relation to the position of pericyte somata.

The majority of the capillary length in cortex (~90%) is contacted by the slender processes of pericytes (Grant et al., 2017;Berthiaume et al., 2018). To better understand the arrangement of pericyte processes in specific regions of interest, we manually labeled their edges with sequential annotations in Neuroglancer (red dots; **Figures 3A,Ai**). This allowed us to track the pericyte process alongside co-annotated endothelial features (somata, cell-cell junctions) (Ornelas et al., 2021). Pericyte processes were occasionally found to cover and track along with endothelial cell junctions, suggesting that they may provide structural support for this feature of the blood-brain barrier. When pericyte processes encountered the location of endothelial nuclei, they tended to increase their surface coverage and proximity to the nucleus (**Figures 3B,Bi**) (Ornelas et al., 2021). Heightened coverage of the endothelial nucleus may provide enhanced communication to influence nuclear functions, such as gene expression.

Endothelial Protrusions

"Microvilli" are small protrusions that extend from the endothelium into the intraluminal space (**Figure 4A**). They

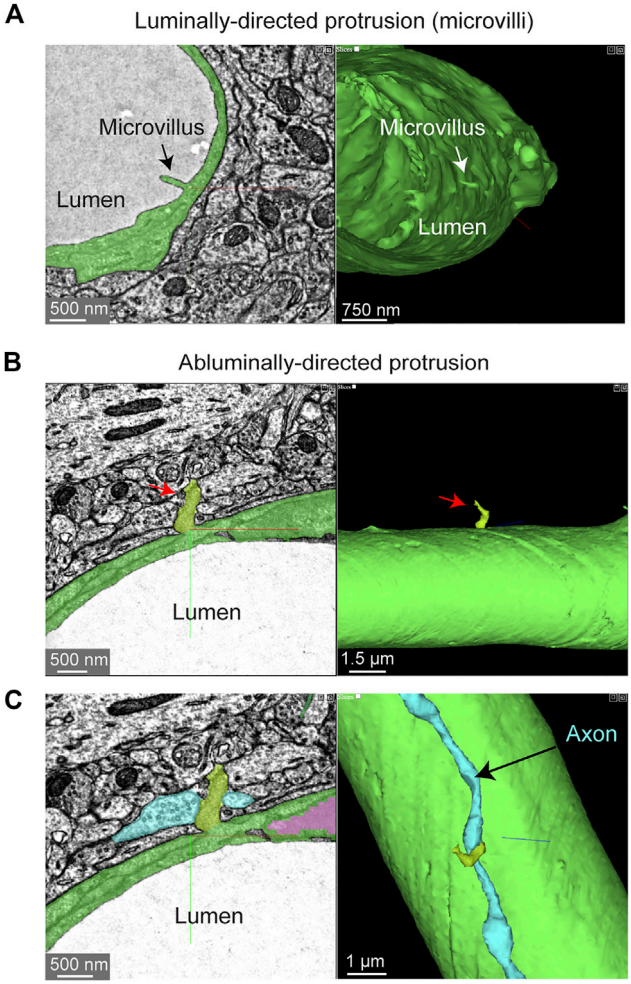

FIGURE 4 | Endothelial protrusions extend luminally and abluminally from the vessel wall. **(A)** Example of a luminally-directed endothelial protrusion (microvilli) within a capillary segment. Left panel shows the 2D cross section of the structure (black arrow). Right panel shows a 3D view of the same structure in segmented vasculature (white arrow). MICrONS Layer 2/3 x, y, z coordinates at: 62431, 48503, 1336. **(B)** Example of abluminally-directed endothelial protrusion. Left panel shows the 2D cross-section of the structure (black arrow). Right panel shows a 3D view of the same structure in segmented vasculature. MICrONS Layer 2/3 x, y, z coordinates at: 73675, 48870, 746. The structure is segmented separately from the vascular wall, but is in fact an extension of the endothelial cell. **(C)** The abluminally-directed endothelial protrusion is surrounded by neuronal axons and dendrites. One axon (cyan) exhibits a region of swelling (potential bouton) in direct contact with the endothelial structure.

have been widely observed across mammals and birds (Fujimoto et al., 1975; Makarov et al., 2015), though their physiological role has remained poorly understood. They could be important for sensing the passage of blood cells or impede the movement of blood cells by creating resistance. Indeed, prior studies have shown that microvilli incidence increases in cerebral ischemia, perhaps contributing to poor capillary blood flow and no reflow (Dietrich et al., 1984). 3D-EM data makes it possible to study the shape, prevalence and distribution of microvilli throughout the capillary network. Curiously, there were also some instances where the endothelium protruded abluminally toward the brain parenchyma (**Figure 4B**). Perhaps these are also specialized appendages for direct sensation of neural or astrocytic activity. In fact, the protrusion shown is surrounded by neurites and one axon swells into a bouton shape when in contact with the endothelium (**Figure 4C**).

Astrocyte Coverage

Astrocytes are extremely complex in structure and their multitude of fine processes interact with the vasculature in the form of "endfeet," which cover much of the abluminal surface (Mathiisen et al., 2010; Korogod et al., 2015). Astrocytic coverage of the vasculature contributes to blood-brain barrier integrity (Araya et al., 2008), release of vasoactive substances (Attwell et al., 2010), and water transport (Jin et al., 2013). The segmented astrocytes in the MICrONS data sets have classic astrocyte morphology (dense and highly ramified processes) with endfeet in subregions of the cell that covered the vascular wall. We observed that astrocytes covered the vasculature in discrete non-overlapping territories (**Figure 5A**). Along just one capillary segment, multiple astrocytes cooperated to establish coverage (Kubotera et al., 2019). However, it is difficult to know if individual astrocytes have been wholly segmented, given their morphological complexity. Thus, it is also possible that the image shows fragments of individual astrocytes. These data may also be useful to understand the extent and distribution of regions that lack astrocyte coverage, which may be relevant as sites of immune cell entry and interaction (Horng et al., 2017).

Microglial-Capillary Interaction

Microglia associate with the capillary wall and contribute to regulation of neurovascular structure and function (Joost et al., 2019;Bisht et al., 2021). Capillary-associated microglia could be detected in the data set and close inspection revealed that they abutted the vascular basement membrane without intervening contact with astrocytic endfeet (**Figure 5B**), consistent with prior studies (Mathiisen et al., 2010; Bisht et al., 2021). Individual microglia are segmented allowing for detailed structure and ultrastructural investigation of their interactions with other neurovascular cells.

Subcellular Features

Two subcellular features are often quantified in studies that assess blood-brain barrier integrity. First are electron dense tight junctions where individual endothelial cells are bound by a variety of adhesion proteins to form a barrier (claudins, occludin, junction adhesion molecules, cadherins) (Haseloff et al., 2015). Endothelial cell-cell junctions are not simply rigid physical barriers, but highly dynamic structures regulating the paracellular (between cell) passage of cells, water, ions and macromolecules. Second, small endothelial vesicles called caveolae facilitate transcellular (through cell) passage across the endothelium (Andreone et al., 2017). Both of these classic blood-brain barrier structures are clearly visualized in the Cortical Layer 2/3 data set (**Figure 6**).

We noticed that caveolae density varied among capillary segments, which may mean that transcellular permeability

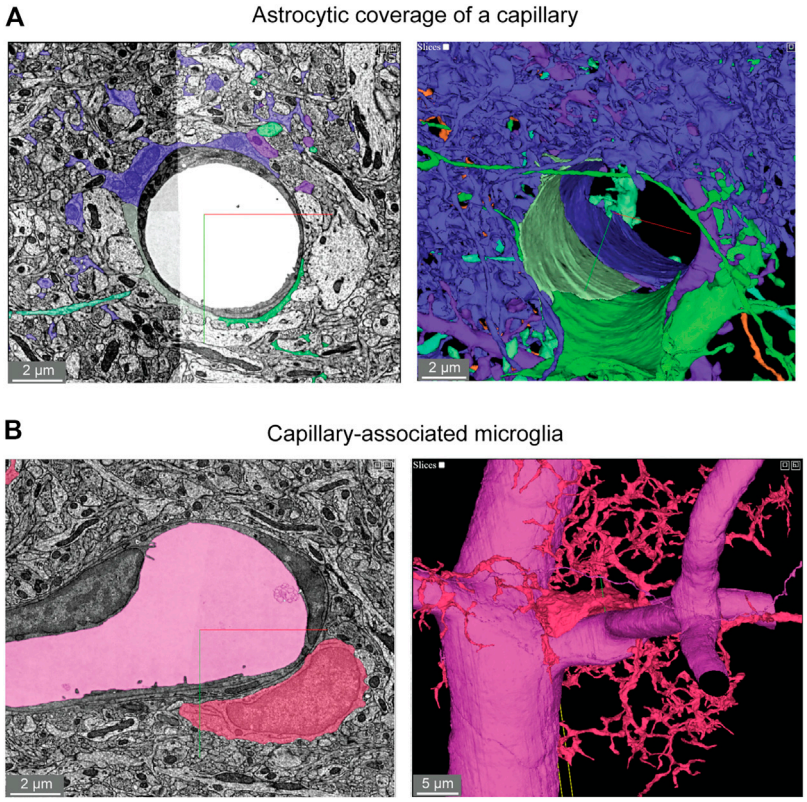

FIGURE 5 | Astroglial and microglial vascular interactions. **(A)** Three astrocytes (blue, green, light green) enwrap the capillary wall and their territories form a tiling pattern. Dendrites of a neuron (purple) course through the astrocytic territory. The vascular wall is not shown in the 3D view (right) to provide a clearer view of astrocyte contact with the vascular wall. MICrONS Layer 2/3 x, y, z coordinates at: 77091, 62413, 784. **(B)** A putative capillary-associated microglia. The 3D view shows the vascular lumen in fuchsia and a microglial soma (red) that drapes along the vessel surface at a bifurcation. Close inspection of this microglia will reveal that it directly contacts the vascular basement membrane without intervening astrocytic endfeet. MICrONS Layer 2/3 x, y, z coordinates at: 76302, 59416, 1641.

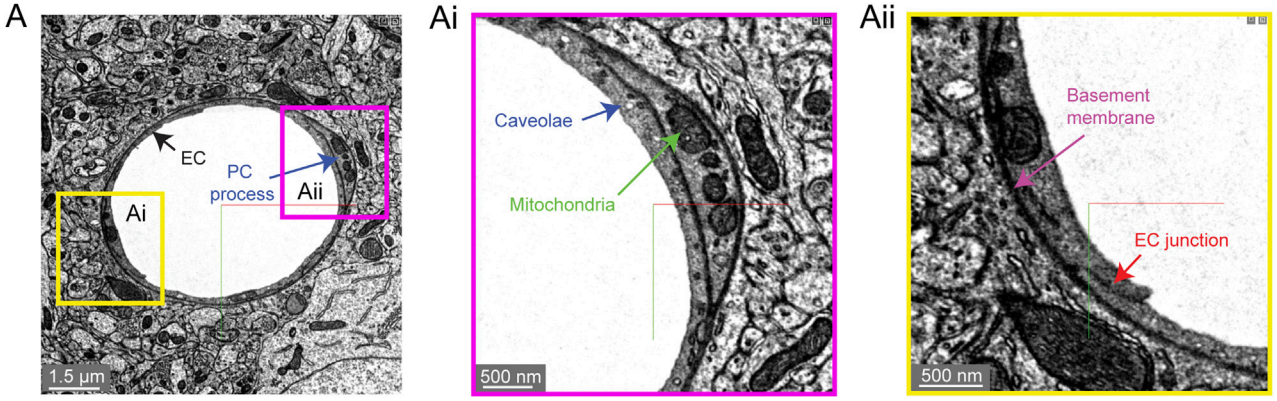

FIGURE 6 | Subcellular structures in the vasculature are visible with high contrast in the MICrONS Layer 2/3 data set. **(A)** A representative cross-section of a capillary with magnified insets showing commonly measured subcellular structures, including caveolae and mitochondria **(Ai)** and endothelial junctions and basement membrane **(Aii)**. MICrONS Layer 2/3 x, y, z coordinates at: 109802, 58170, 707.

occurs heterogeneously across the capillary network (not shown). 3D-EM data may potentially allow caveolae density and their characteristics to be charted across the microvascular network to better understand their distribution. Recent studies have already highlighted interesting zone-specific differences that involve caveolae. Venous endothelial cells and capillaries exhibit greater uptake of plasma proteins through transcytosis than arterioles (Yang et al., 2020). Similarly, post-capillary

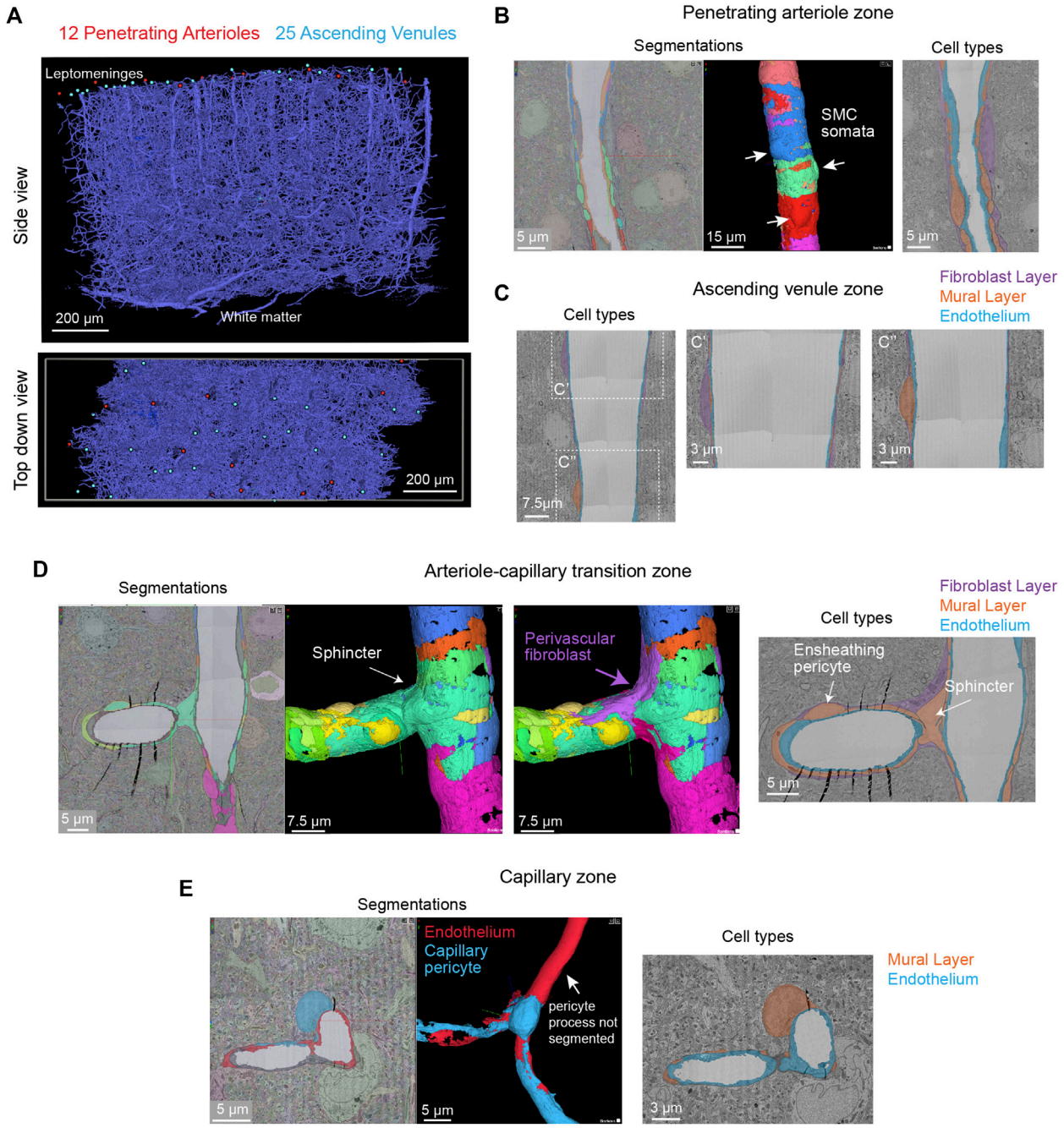

FIGURE 7 | All vascular zones are represented in the MICrONS Cortical MM^3 data set. **(A)** The vasculature captured includes 12 penetrating arterioles, 25 ascending venules, and extensive intervening capillary networks. The bottom panel shows a top-down view of the volume and reveals the originating position of penetrating vessels at the pial surface. Link to annotations: https://ngl.microns-explorer.org/#!gs://microns-static-links/mm3/vascular_annotation.json. **(B)** A penetrating arteriole with some smooth muscle cells selected for 3D viewing (arrows). On the right, the three distinct cell types that make up the vascular wall (endothelial cells, mural cells, and perivascular fibroblasts) are shown through manual labeling. MICrONS Cortical MM^3 x, y, z coordinates at: 225166, 107266, 18188. **(C)** An ascending venule exhibits a vascular wall that is thinner than the arteriole, but still contains endothelial cells, mural cells, and perivascular fibroblasts. These cell types were not well separated by segmentation and therefore only manual labeling of these cell layers is shown. Coordinates at: 262168, 104664, 24791. **(D)** The arteriole-capillary transition zone is a small segment of vasculature that intervenes between the penetrating arteriole and true capillary bed. The endothelium, mural cells (sphincter cell and ensheathing pericyte), and perivascular fibroblasts are generally segmented in this region of interest. Here, we show the mural cell layer (left and middle) which involved cobbling of many separately segmented structures to visualize the overall morphology of the sphincter cell and ensheathing pericyte. The sphincter cell was classified based on prior descriptions by Grubb et al. showing a cuff-like cell at the penetrating arteriole just before branching into the transitional zone, with local decrease in vessel diameter. On the right, we add a perivascular fibroblast, which may not have been captured in entirety but shows feasibility of its separate segmentation. On the right, the location of different cell layers is shown through manual labeling. Coordinates at: 168985, 165246, 19171. **(E)** The capillary wall consists

(*Continued*)

FIGURE 7 | of only endothelial cells and pericytes. These two cells are sometimes separately segmented, as in the case shown here. However, it is not consistent throughout the network. One process of the pericyte is segmented together with the endothelium. On the right, the location of these cells is shown through manual labeling. Note the fibroblast layer is absent in capillaries. Coordinates at: 231661, 104310, 24813.

venules show heightened receptor-mediated transport of nanoparticles useful for drug delivery (Kucharz et al., 2021). Interestingly, arteriole endothelial cells are not devoid of caveolae and in fact show an enrichment in caveolae essential to neurovascular signaling during functional hyperemia (Chow et al., 2020). Mitochondria are segmented throughout the data set, including in endothelial cells and mural cells (**Figures 6A,Ai**) (Turner et al., 2020). Prior studies have shown pericytes to be enriched with mitochondria (Mathiisen et al., 2010), which are likely needed to support the metabolic demands of solute transport at the blood-brain barrier.

Non-Cellular Features

An important component of the vascular wall is the basement membrane (BM) between cells that contribute to cellular adhesion and signaling. The basement membranes are thin and highly organized structures (50–100 nm in thickness) consisting mainly of collagen IV, fibronectin, laminins, nidogen and proteoglycan perlecan (Xu et al., 2019). There can be multiple BM layers depending on the microvascular zone. In capillaries, there is the endothelial BM that lies between the endothelium and the pericyte, and the parenchymal BM between the pericyte and the astrocyte. The basement membrane is very apparent in 3D-EM data because it is generally more electron dense than the neighboring cells (**Figures 6A,Aii**). At sites of pericyte-endothelial interaction, the basement membrane may become thin and harder to recognize. Increased basement membrane thickness is described in aging and conditions of poor vascular health such as in the tissues surrounding an ischemic stroke (Nahirney et al., 2015). This may indicate a loosening of the protein sheets or adverse production of BM proteins, both of which would reduce neurovascular communication.

MICrONS Cortical MMˆ3

A second study from the MICrONS consortium imaged a 1.4 × 0.87 × 0.84 mm volume from visual cortex, which is 400× larger than the prior Layer 2/3 sample. It spans all 6 cortical layers, including some white matter at its base. This significantly larger tissue volume provides the unique opportunity to study the neurovascular unit across different vascular zones, cortical layers, multiple cortical areas and between gray vs. white matter.

Microvascular Architecture

We first briefly discuss the vascular architecture of the cerebral cortex. Blood flow to the cortex enters through leptomeningeal arterioles on the brain surface. From the pial arteriolar network, penetrating arterioles branch and dive into the parenchyma to perfuse columns of tissue (Shih et al., 2015). Penetrating arterioles then send smaller offshoots called arteriole-capillary transitions (or pre-capillary arterioles) that successively ramify into dense and highly interconnected capillary networks. After passing the dense capillary network, blood then coalesces into ascending venules oriented in parallel with penetrating arterioles, that drain back to a network of leptomeningeal venules at the pial surface.

The vascular network of the MICrONS Cortical MMˆ3 data set can be visualized in entirety by selecting the segmentation of the intraluminal space. The data contains leptomeningeal vessels within the subarachnoid space of the meninges, which can be followed as they dive into penetrating vessels of the cortical parenchyma. In total, 12 penetrating arterioles and 25 ascending venules were captured within the volume (**Figure 7A**). The identity of the penetrating vessel was determined by examining the morphology of mural cells that lie abluminal to the endothelium. Arterioles are surrounded by concentric, ring-shaped smooth muscle cells (**Figure 7B**), whereas venules lack these cells (**Figure 7C**).

Endothelial and Mural Cells

Unlike the MICrONS Layer 2/3 data set, endothelial and mural cells have been segmented separately in Cortical MMˆ3. However, these segmentations are not consistent throughout the microvasculature. The segmented endothelium is not of individual cells, but of most of the endothelial layer. Further, mural cells are complex in structure and an individually segmented region may represent fragments of cells. Nevertheless, they demonstrate feasibility of segmenting vascular cells and provide biological insight. For example, smooth muscle cells of the penetrating arteriole viewed in 3D reveal the position of their somata, which bulge slightly from the vascular wall (**Figure 7B**, left, middle). The tiling of their individual territories and details of their circumferential processes can be examined. In an accompanying 2D image we verified the positions of different cell types along the same arteriole (**Figure 7B**, right). In contrast to the arteriole, the wall of ascending venules is much thinner, and as such, the segmentation of endothelial and mural cells along venules examined is less accurate than arterioles. We provide only labeling in 2D to show how vascular cells are positioned along the venular wall (**Figure 7C**).

The extensive microvascular network could be seen throughout the data set, including capillaries and the transitional zones bridging the capillaries to arterioles and venules. In one example, a small penetrating arteriole extends an offshoot toward the capillary network (**Figure 7D**). A pre-capillary sphincter cell (a presumed mural cell type) is seen as a cuff around the origin of this offshoot where the vessel diameter is locally decreased (Grubb et al., 2020). Sphincter cells are morphologically distinct from pericytes and exhibit high reactivity to vasoactive mediators during neurovascular

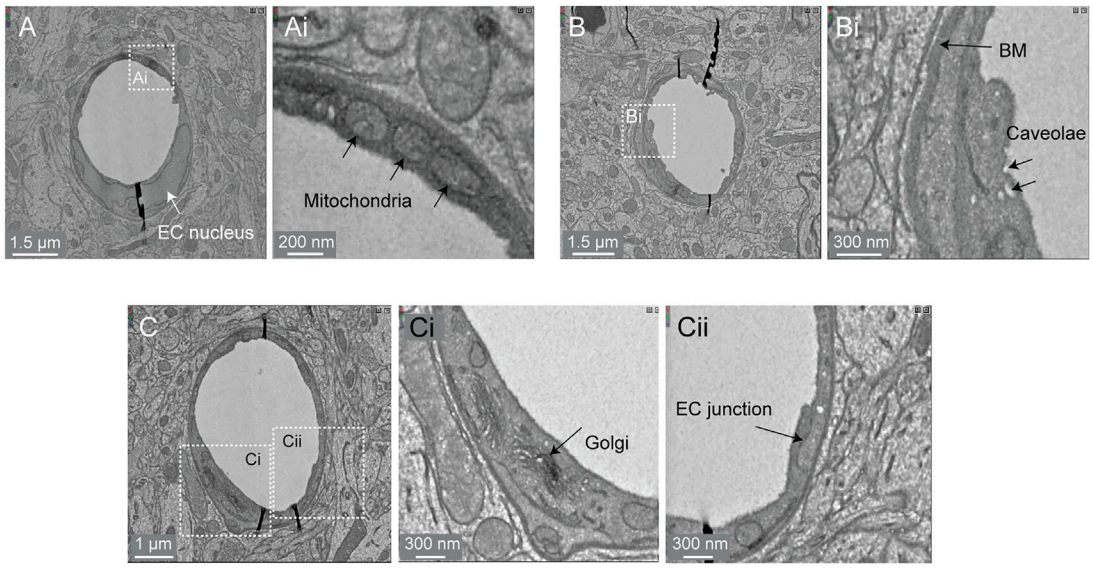

FIGURE 8 | Subcellular features of the endothelium in the MICrONS Cortical MM^3 data. **(A)** Capillary cross-section with inset **(Ai)** showing mitochondria. MICrONS Cortical MM^3 x, y, z coordinates at: 141179, 177334, 21310. **(B)** Capillary cross-section with inset **(Bi)** showing endothelial caveolae and basement membrane. Coordinates at: 167382, 134731, 20338. **(C)** Capillary cross-section with inset **(Ci)** showing Golgi cisternae and separate inset **(Cii)** showing endothelial junction. Coordinates at: 129596, 117071, 20179.

coupling (Zambach et al., 2021), as well as aberrant contraction during pathology (Khennouf et al., 2018).

The protruding soma of an ensheathing pericyte is visible just downstream of the sphincter (**Figure 7D**). Unlike the more prevalent capillary pericytes found deeper in the capillary network, and as described for the Layer 2/3 data, this pericyte subtype of the transitional zone exhibits longer processes than smooth muscle cells but shorter than those of capillary pericytes (Hartmann et al., 2021a;Hartmann et al., 2021b). However, the processes completely cover the vascular circumference with fine interdigitated projections (Grubb et al., 2020). Critically, in the image shown (**Figure 7D**, middle), the complexity of this cell is not captured by a single segmented volume. Rather, multiple segmented regions were cobbled together to obtain a general view of the cell coverage of the transitional segment. Ensheathing pericytes are reactive to vasoactive stimuli and the regions they cover dilate rapidly during functional hyperemia (Hall et al., 2014).

As described in the MICrONS Layer 2/3 data, capillary pericytes exhibit protruding somata and long processes that incompletely cover the circumference of endothelium (Grant et al., 2017). Pericytes of this morphology could be discerned throughout the extensive capillary beds of the sample. Pericyte and endothelial cells are occasionally segmented as individual cell types along the capillary wall (**Figure 7E**). However, the segmentation of individual pericytes may be incomplete, as evidenced by a missing process in the 3D view shown. Throughout the capillary network, the nuclei of pericytes and endothelial cells exhibited clear contrast, providing a unique opportunity to understand pericyte-endothelial positioning and arrangement in the microvasculature. This information may add an additional parameter to consider for *in silico* studies of capillary flow through cortical vascular networks.

Perivascular Fibroblasts

Perivascular fibroblasts lie just abluminal to the mural cells on larger parenchymal vessels in the brain (Bonney et al., 2021). However, they are absent in the capillary zone. The physiological role of perivascular fibroblasts remains largely unknown. Single cell transcriptomic analyses of brain vasculature have shed light on their gene expression profiles, which suggest potential roles in basement membrane protein production and contribution to cerebrovascular structure (Vanlandewijck et al., 2018). In some pathological scenarios, such as neurodegenerative disease, ischemia and injury, perivascular fibroblasts proliferate to form scar tissue (Soderblom et al., 2013). Consistent with prior work, we observed perivascular fibroblasts in arteriole, arteriole-capillary transition (**Figures 7B,D**), but not in capillaries (**Figure 7E**). They are also present on venules (**Figure 7C**), but more superficial of the brain surface and only on venules of larger diameter. Morphologically, perivascular fibroblasts exhibit flattened somata and thin lamellar processes that cover the vessel surface.

Perivascular Macrophages

Perivascular macrophages are resident immune cells of the brain with close association to the vasculature. They have been shown to communicate with other neurovascular cell types, are a source of reactive oxygen species, and contribute to a variety of disease processes (Faraco et al., 2016). They occupy the same perivascular space as fibroblasts and may also exhibit morphological similarities. Thus, detailed examination will be required to

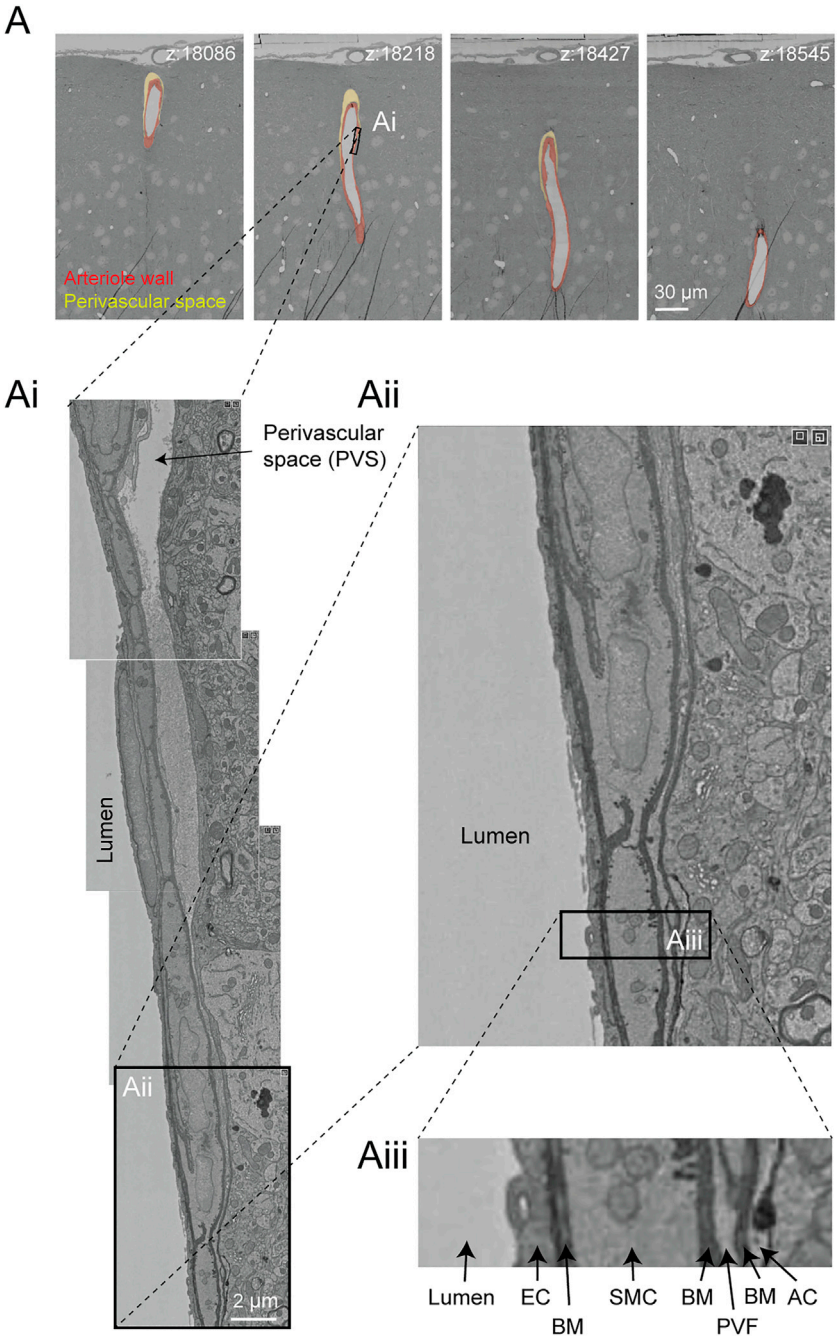

FIGURE 9 | Perivascular space and layers of the arteriole wall. **(A)** A large penetrating arteriole in the MICrONS Cortical MM^3 data set exhibits a clear perivascular space. **(Ai)** Magnified view of the arteriole wall showing the perivascular space diminishing in size with greater cortical depth. **(Aii, Aiii)** Magnified view showing layers of the arteriole wall, revealing that the perivascular space becomes continuous with the perivascular fibroblast layer as the perivascular space diminishes. EC—endothelial cell, BM—basement membrane, SMC—smooth muscle cell, PVF—perivascular fibroblast, AC—astrocyte. Coordinates of the penetrating arteriole: 175231, 117475, 19297.

understand how to separate these two cell types at the ultrastructural level. Perivascular macrophages are highly phagocytic and should presumably be distinguishable from fibroblasts by a higher density of electron dense lysosomes.

Subcellular Compartments

Image contrast in the Cortical MM^3 data was sufficient to resolve a variety of subcellular features (endothelial cell junctions, caveolae, Golgi cisternae, mitochondria) (**Figure 8A,Ai,B,Bi,C,Ci,Cii**). In

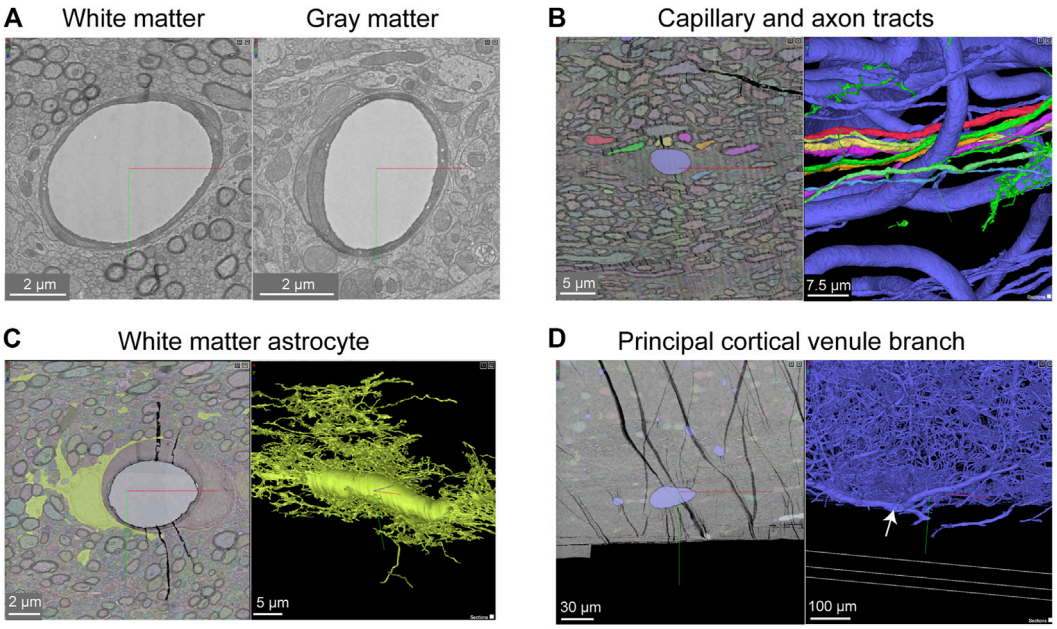

FIGURE 10 | White matter vessels in MICrONS Cortical MM^3 data. **(A)** Representative cross section of capillary-sized vessels in white matter (left) and gray matter (right). White matter capillary cross-section x, y, z coordinates at: 114029, 277354, 17647. Gray matter vessel cross-section x, y, z coordinates at: 109231, 208260, 17714. **(B)** A white matter capillary embedded within the axon tracts of the white matter (left). In 3D view, the vascular lumen segmentation is displayed, alongside select axons that have been segmented. Coordinates at: 155004, 269113, 21080. **(C)** A perivascular white matter astrocyte. In 3D view, the coverage of the capillary wall can be seen. Coordinates at: 150176, 279591, 18383. **(D)** A branch of a deep draining venule, principal cortical venule, is present within the data set. Coordinates at: 195156, 273647, 18192.

fact, instances of caveolar fusion with the endothelial plasma membrane were observed (**Figures 8B,Bi**).

Perivascular Space

The perivascular space is a fluid filled space surrounding larger brain vessels that is vital for influx and efflux of cerebrospinal fluid (CSF) in the clearance of metabolic waste from brain tissue (Iliff et al., 2012; Wardlaw et al., 2020). However, there remains a lack of clarity on the anatomy of the perivascular spaces, leading to controversy in pathways for CSF flow and where they reside in the vascular wall (Bakker et al., 2016). 3D-EM data may provide an opportunity to define the architecture of the perivascular space. Details including the vessel types that exhibit a perivascular space (arterioles vs. venules, small vs. large diameter vessels), the diameter/volume of these spaces, and the neurovascular cell types forming their boundaries could be examined in detail. However, caution is needed to ensure that these spaces are adequately preserved in fixed tissue specimens.

In the Cortical MM^3 data, perivascular spaces could be observed primarily around larger penetrating arterioles and ascending venules, and they were most apparent in the upper layers of cortex (**Figure 9A**). The perivascular space diminishes as the vessels become smaller in diameter (**Figure 9Ai**). The space eventually becomes continuous with the perivascular fibroblast layer, flanked by two layers of basement membrane (**Figures 9Aii,Aiii**). Smaller arterioles, arteriole-capillary transition zones, and capillaries did not exhibit overt perivascular spaces though they were encased in the basement membrane. This raises the question of whether CSF flows along the walls of the small vessels and capillaries, and if so whether it occurs within the vascular basement membrane. It also suggests that perivascular fibroblasts may be involved in adherence of the vascular basement membranes, and in doing so influence the extent of the perivascular space.

White Matter

The Cortical MM^3 data set contains white matter just below the cortex, where microvasculature is seen alongside densely packed myelinated axons (**Figures 10A,B**). There is sufficient contrast to discern the boundaries of endothelial cells and mural cells in white matter, as well as subcellular features, such as caveolae. The interaction of white matter astrocytes with the vascular wall may be accessible to study, as some of the white matter astrocytes have been segmented (**Figure 10C**). The vasculature in white matter also contains one branch of a principal cortical venule, which is a large ascending venule that serves as the primary drainage route for juxtacortical white matter (**Figure 10D**) (Duvernoy et al., 1981).

This gray-white matter sampling can help to clarify differences in composition and subcellular features of the neurovascular unit as blood vessels course into the white matter environment. For example, it should be possible to

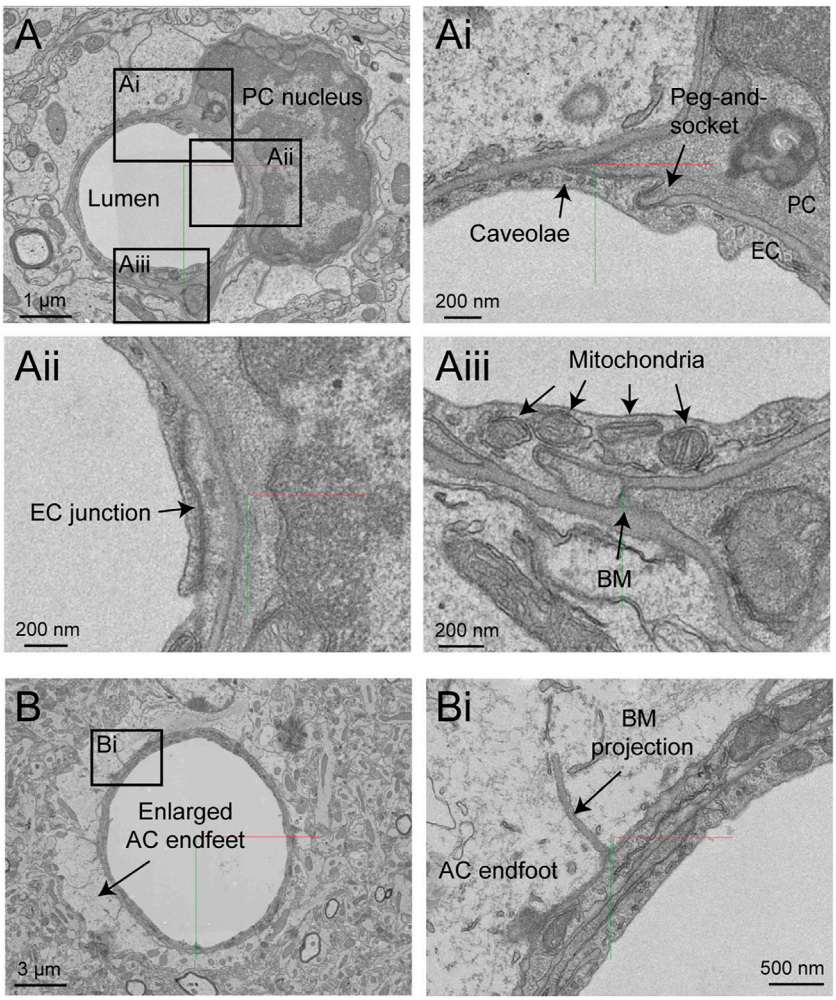

FIGURE 11 | Ultrastructural view of microvasculature in the mouse hippocampus. **(A)** Representative images from data of Bloss et al. taken from mouse hippocampus. The image shows a capillary cross-section where a pericyte soma is located. Insets from **(Ai–Aiii)** show a variety of subcellular structures that can be visualized. Coordinates at: 20865, 54458, 146. **(B)** A separate capillary cross-section taken from the same volume exhibits enlarged astrocytic endfeet against the vascular wall. An inset **(Bi)** shows a thin projection of the basement membrane extending abluminally. Coordinates at: 25774, 59225, 86.

understand structural differences in pericyte coverage and association with the endothelium, as well as the ratio of pericytes and endothelial cells per capillary length. Given the vulnerability of white matter to ischemia and in neurodegenerative diseases, understanding how the neurovascular unit differs between gray and white matter will be of great importance.

Accompanying Physiological Data

Remarkably, the 3D-EM data produced by the MICrONS consortium has accompanying multiphoton imaging data on neuronal activity from the same tissues, where the microvasculature served as a fiduciary to co-register *in vivo* and *post-mortem* data. This physiological data includes neuronal calcium dynamics during visual stimulation, and separately, vascular structure (intravenous fluorescent dye). This is proof-of-principle that ultrastructural features of the microvasculature may eventually be linked to neurovascular dynamics captured *antemortem.*

Additional Studies of Mouse Visual Cortex

A 2016 study by Lee et al. provided a sample from visual cortex layer 1 and layer 2/3 with a volume of 450 × 450 × 150 µm (Lee et al., 2016). Image contrast was high, allowing cellular and non-cellular (basement membrane) components of the vascular wall to be readily discerned. The volume contains a portion of a penetrating arteriole and surrounding capillary networks. However, the vascular-specific compartments (vascular lumen, wall, astrocytes) are not segmented.

Hippocampus

The hippocampus has a different vascular supply and microvascular architecture compared to the cerebral cortex, and these differences may underlie vulnerabilities to blood

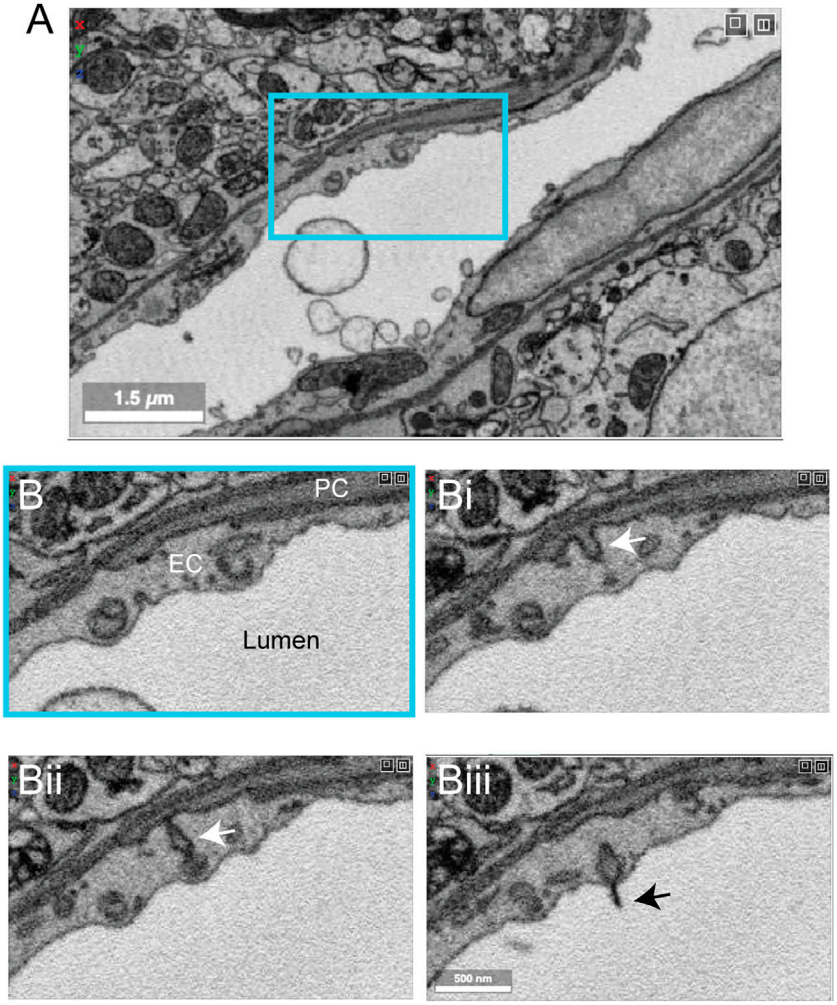

FIGURE 12 | Pericyte projection into vessel lumen in finch brain capillaries. **(A)** A capillary from finch basal ganglia (data set: j0251), located at x, y, z coordinates: 19129, 12810, 7,330. **(B–Biii)** Magnified view of inset in panel A showing a pericyte projecting into the luminal space and ending in a cilia-like structure. The four panels span 10 slices in the z dimension, corresponding to ~200 nm of distance.

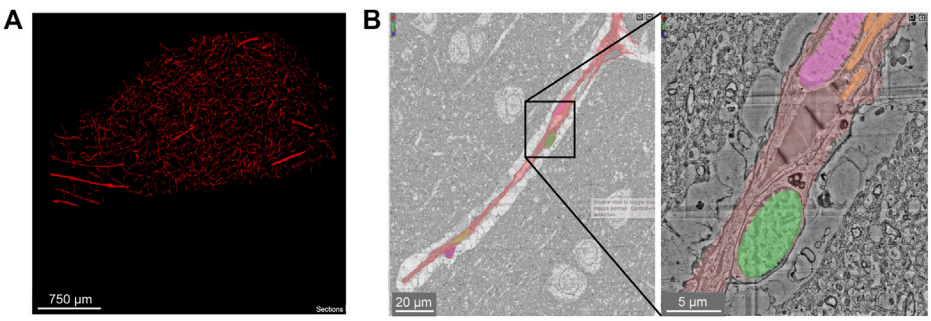

FIGURE 13 | Human cerebral cortex microvasculature. **(A)** Broad view of the microvasculature captured in the data set of Shapson-Coe et al. **(B)** A capillary-sized vessel showing general segmentation of the vasculature. The nuclei of vascular cells were separately segmented into pericytes or endothelial cells, based on their location relative to the blood vessel lumen and basement membrane layers, as well as their appearance in EM. In the example shown, the pericyte nucleus is green and the endothelial nucleus is pink. Left image x, y, z coordinates at: 297270, 74996, 5229. Right image x, y, z coordinates at: 299348, 73663, 5229.

flow insufficiency (Shaw et al., 2021). Thus, comparative 3D-EM studies across different brain regions will be valuable in future studies. A study by Bloss *et al.* imaged a volume of mouse hippocampal CA1 region spanning stratum radiatum and stratum lacunosum-moleculare (Bloss et al., 2018). The sample is 350 × 200 × 17 μm in size and contains portions of a venule network and some surrounding capillaries. The image contrast is excellent, allowing a clear separation of vascular cell types, subcellular structures, and the basement membrane layers (**Figure 11A**). Curiously, some vessels exhibit enlarged astrocytic endfeet not seen in the cortical data sets described above (**Figure 11B**). Thin projections of the vascular basement membrane also extended into the parenchyma. Whether these features are true distinctions of hippocampal vs. cortical vasculature or consequences of tissue preparation remain to be clarified.

Finch Basal Ganglia

Zebra finch is a widely used model system in behavioral research, particularly with respect to song development and auditory processing. Two zebra finch brain data sets (j0126 and j0251, basal ganglia, Area X) were imaged with high contrast 3D-EM and show many cellular and subcellular details of the avian vasculature (**Figure 12A**). The smaller j0126 data set (97.9 × 95.6 × 115 μm) contains a venule and surrounding capillaries. Close inspection of the capillaries revealed similar arrangement of endothelial cells and pericytes as seen in the mouse brain. Pericyte and endothelial interdigitations were widely observed, and in some cases pericyte pegs contacted the endothelial nucleus as reported previously in mouse (Ornelas et al., 2021). Interestingly, in the larger j0251 data set (256 × 256 × 384 μm), pericyte projections were seen to bypass the endothelial layer and protrude into the luminal space and end in small cilia-like structures (**Figures 12B–Biii**), opening the possibility that pericytes use these projections for direct sensation of blood flow. This is a feature that we have thus far not seen in the mouse brain.

Human Cortex

A recent study from Shapson-Coe et al. examined a small fragment of human cortex (temporal lobe), resected from a patient with drug-resistant epilepsy during surgery to remove an epileptic focus (Shapson-Coe et al., 2021). Immediately after excision, the sample was immersion-fixed overnight. The hippocampus was sclerotic and exhibited signs of pathology consistent with epilepsy, but the resected cortical sample appeared normal on traditional histopathology.

The sample spans ~3 mm at its longest width, ~2 mm at its longest height, and ~0.15 mm in thickness. It includes sections of parenchymal arterioles and venules and surrounding capillary networks (**Figure 13A**). Despite the vascular lumen being mostly collapsed, the nuclei of vascular cells could be categorized as mural cells or pericytes based on distance from the lumen and position relative to the endothelial and parenchymal basement membranes (**Figure 13B**). A total vascular length of 22.6 cm was segmented, in which the authors detected ~8k vascular cells (4604 endothelial cells, 3,549 pericytes, 574 smooth muscle cells and 79 fibroblast-like cells). The astrocyte endfeet surrounding the vasculature were swollen, which is unlike that seen in the samples prepared from mouse or finch and may be due to the limitations of *post-mortem* sample collection (**Figure 13B**).

A notable feature unique to this human tissue sample is the presence of many perivascular oligodendrocytes that lined the vascular wall, particularly the radially-oriented vessels of white matter. This may be why oligodendrocytes are a prevalent cell type isolated from vascular-enriched single cell transcriptomic studies (Yang et al., 2022). Another observation was the existence of string capillaries, which are basement membrane tubes with pericytes encased, but no endothelial cells. Their occurrence is not uncommon in the normal brain (Brown, 2010), but prevalence can increase in pathological context leading to reduced capillary connectivity and blood flow impairment (Challa et al., 2004).

DISCUSSION

We surveyed the vasculature in 7 recent large-scale 3D-EM studies (**Table 1**). These data spanned different species (mouse, finch, human) and brain regions (cortex, callosum, hippocampus, basal ganglia). The data sets captured images across different zones of the microvasculature (arterioles, capillaries, venules and transitional segments), and were of sufficient quality to visualize subcellular features relevant to blood-brain barrier function (endothelial junctions, caveolae, basement membrane, astrocytic coverage), blood flow (positioning of endothelial and pericyte nuclei, mural cell coverage, endothelial microvilli, microglial-vascular interaction), bioenergetics (mitochondria), cellular communication (caveolae, peg-and-socket interactions) and cerebrospinal fluid flow (perivascular space). The biological insight that can be garnered from these data is immense. Further work is needed to segment, annotate and quantify cerebrovascular features. These efforts will stimulate the development of new hypotheses, design of novel physiological studies, and improved *in silico* modeling approaches.

To fully leverage 3D-EM for vascular research, it will be necessary to accurately segment the cellular components of the vascular wall: endothelial cells, mural cells (pericytes and smooth muscle cells), perivascular fibroblasts, and perivascular macrophages. Together with already segmented parenchymal components (neurons, astrocytes, microglia, and oligodendrocytes), this would account for all cells that comprise the neurovascular unit, a framework used to understand how neurons and other cell types communicate with nearby vessels to serve metabolic needs of the brain (Schaeffer and Iadecola, 2021). Advances in the MICrONS Cortical MMˆ3 data set have shown feasibility of segmenting individual cell types of the vascular wall. However, further work is needed to improve accuracy and consistency of the current segmentations and to identify the specific challenges posed by vascular cells. In addition, existing data sets offer the possibility to identify and map innervating neurons of cerebral vessels, providing insights into flow regulation by direct release of neurotransmitter on the vascular wall (Hamel, 2006).

Mapping the prevalence and distribution of vascular ultrastructures is essential for our understanding of vascular functions across different zones. For example, the nuclei of endothelial cells and pericytes are easily distinguished in the MICrONS Cortical MMˆ3 data. How the nuclei localize in the network and impinge upon the luminal space, may hold insight into how blood flow is distributed through complex capillary networks (Østergaard et al., 2014;Schmid et al., 2017). Further, it is likely that endothelial microvilli contribute to blood flow resistance, and conceivably sense blood flow to convey signals to the endothelium and mural cells. Therefore, understanding their distribution at the level of individual capillary segments would be valuable.

Mapping endothelial junctions and caveolae on a large scale would generate an unprecedented 3D map of blood-brain barrier structure. Endothelial junctions and caveolae bear similarity to the post-synaptic density and pre-synaptic vesicles of neuronal synapses, respectively. Thus, existing machine learning algorithms are likely adaptable for detection of these vascular features. Identification of endothelial junctions will also reveal the boundaries of individual endothelial cells as they tile together to form the inner layer of the vascular tube. Additionally, mitochondria in vascular cells have a similar appearance to those already segmented in parenchymal cells (see MICrONS Layer 2/3). Mapping the density of mitochondria across the vasculature may reveal where energy-demanding processes, such as blood-brain barrier transport or maintenance of membrane potential, are most active.

The ability to manually annotate, and therefore count and quantify, the number of cellular/subcellular structures already provides significant insight on vascular structure. For example, we have annotated endothelial and pericyte nuclei, and traced pericyte processes and endothelial junctions. In prior work, basic distance measurements were performed in Neuroglancer allowing extraction of quantitative data on peg-and-socket contacts between endothelial cells and pericytes (Ornelas et al., 2021) These endeavors have only scratched the surface of information within these volumes, and there are no barriers to further exploration in this fashion, except time. Further, Neuroglancer is one of many browsers for exploration of volume imaging data, and others including webknossos, knossos, pyknossos, napari, bigdataviewer, may be more versatile for annotation. Thus, the availability of 3D-EM data through a variety of online tools will maximize their use by the scientific community.

A potential limitation and topic for further investigation is whether the parameters of tissue collection used in the current data sets (anesthetic, *post-mortem* interval, fixative, perfusion pressure, etc.) adequately preserved the native structure of the vascular lumen, vascular cell types, and perivascular space. The shape of the vessel wall can be easily distorted by contraction of mural cells or loss of intraluminal pressure, making quality of tissue preparation of utmost importance. It is already known that the choice of fixation approach greatly influences the size of the extracellular space (Cragg, 1980; Pallotto et al., 2015) and this may result in disparate outcomes for both neuronal and vascular structures alike. For example, brains prepared with aldehyde-based fixative for EM show nearly full coverage of blood vessels with astrocyte endfeet (Mathiisen et al., 2010) while only two-third coverage is seen with cryo-EM (Korogod et al., 2015). One way to optimize tissue preparation is to image the same regions both *in vivo* and *post-mortem*, as done in the MICrONS pipeline. The *in vivo* two-photon imaging data may then be compared to the 3D-EM data to understand how well vascular diameter and wall structure is preserved. Further, cautionary statements should be added to publications when there are signs of poor vascular preservation, include stacking of red blood cells in arterioles, wide-spread swelling of astrocytes, and ruffling of endothelial cells.

The work and costs involved in creating and analyzing large-scale 3D-EM on the scale of the MICrONS MMˆ3 data are extensive. It is not readily accessible to smaller, individual laboratories seeking to address specific questions in their studies. However, some labs may wish to generate more manageable 3D data sets for manual segmentation and annotation. The challenge is that vasculature is a relatively sparse in brain tissue compared to neurons, and one must know where to collect smaller data sets. A way to overcome this challenge is to first survey the broader vascular network with wider field imaging, and then perform high-resolution imaging in specific regions of interest (Guérin et al., 2019). The public resources described here can serve as valuable guides to decide where to collect vascular data for more targeted studies. Further, techniques such as X ray micro CT angiography (Ghanavati et al., 2014) could be used to survey vasculature across the whole brain prior to EM-level imaging within distinct brain regions.

DATA AVAILABILITY STATEMENT

The original contributions presented in the study are included in the figures and figure legends. Further inquiries can be directed to the corresponding authors.

ETHICS STATEMENT

This article surveys data from other groups that had ethics committee oversight.

AUTHOR CONTRIBUTIONS

AS and AK conceptualized the study. SB, VC-S, SFH, and AK surveyed the data to find notable vascular features. SB, VC-S, SFH, MT, AK, and AS contributed to preparation of figures. JK collected and provided access to finch data sets. AS wrote the manuscript with contributions and feedback from SB, VC-S, SFH, MT, JK and AK.

FUNDING

AS is supported by grants from the NIH/NINDS (NS106138, NS097775) and NIH/NIA (AG063031, AG062738). SB is

supported by an NIH NRSA fellowship (F32 NS117649). VC-S is supported by an American Heart Association post-doctoral fellowship (20POST35160001). AK is supported by grants from the Swiss National Science Foundation (310030_188952), the Synapsis Foundation (2019-PI02), Swiss Multiple Sclerosis Society.

ACKNOWLEDGMENTS

The authors thanks F. Collman and N. da Costa for helpful discussions. We also thank the Allen Institute for Brain Science founder, Paul G Allen, for his vision, encouragement, and support.

REFERENCES

Andreone, B. J., Chow, B. W., Tata, A., Lacoste, B., Ben-Zvi, A., Bullock, K., et al. (2017). Blood-Brain Barrier Permeability Is Regulated by Lipid Transport-dependent Suppression of Caveolae-Mediated Transcytosis. *Neuron* 94, 581–594. doi:10.1016/j.neuron.2017.03.043

Araya, R., Kudo, M., Kawano, M., Ishii, K., Hashikawa, T., Iwasato, T., et al. (2008). BMP Signaling through BMPRIA in Astrocytes Is Essential for Proper Cerebral Angiogenesis and Formation of the Blood-Brain-Barrier. *Mol. Cell Neurosci.* 38, 417–430. doi:10.1016/j.mcn.2008.04.003

Armulik, A., Genové, G., Mäe, M., Nisancioglu, M. H., Wallgard, E., Niaudet, C., et al. (2010). Pericytes Regulate the Blood-Brain Barrier. *Nature* 468, 557–561. doi:10.1038/nature09522

Attwell, D., Buchan, A. M., Charpak, S., Lauritzen, M., Macvicar, B. A., and Newman, E. A. (2010). Glial and Neuronal Control of Brain Blood Flow. *Nature* 468, 232–243. doi:10.1038/nature09613

Bakker, E. N. T. P., Bacskai, B. J., Arbel-Ornath, M., Aldea, R., Bedussi, B., Morris, A. W. J., et al. (2016). Lymphatic Clearance of the Brain: Perivascular, Paravascular and Significance for Neurodegenerative Diseases. *Cell Mol Neurobiol* 36, 181–194. doi:10.1007/s10571-015-0273-8

Berthiaume, A.-A., Grant, R. I., Mcdowell, K. P., Underly, R. G., Hartmann, D. A., Levy, M., et al. (2018). Dynamic Remodeling of Pericytes *In Vivo* Maintains Capillary Coverage in the Adult Mouse Brain. *Cel Rep.* 22, 8–16. doi:10.1016/j.celrep.2017.12.016

Bisht, K., Okojie, K. A., Sharma, K., Lentferink, D. H., Sun, Y.-Y., Chen, H.-R., et al. (2021). Capillary-associated Microglia Regulate Vascular Structure and Function through PANX1-P2ry12 Coupling in Mice. *Nat. Commun.* 12, 5289. doi:10.1038/s41467-021-25590-8

Bloss, E. B., Cembrowski, M. S., Karsh, B., Colonell, J., Fetter, R. D., and Spruston, N. (2018). Single Excitatory Axons Form Clustered Synapses onto CA1 Pyramidal Cell Dendrites. *Nat. Neurosci.* 21, 353–363. doi:10.1038/s41593-018-0084-6

Bonney, S. K., Sullivan, L. T., Cherry, T. J., Daneman, R., and Shih, A. Y. (2021). Distinct Features of Brain Perivascular Fibroblasts and Mural Cells Revealed by *In Vivo* Two-Photon Imaging. *J. Cereb. Blood Flow Metab.* (Online ahead of print). doi:10.1177/0271678x211068528

Brown, W. R. (2010). A Review of String Vessels or Collapsed, Empty Basement Membrane Tubes. *Jad* 21, 725–739. doi:10.3233/jad-2010-100219

Challa, V. R., Thore, C. R., Moody, D. M., Anstrom, J. A., and Brown, W. R. (2004). Increase of white Matter String Vessels in Alzheimer's Disease. *Jad* 6, 379–383. doi:10.3233/jad-2004-6404

Chow, B. W., Nuñez, V., Kaplan, L., Granger, A. J., Bistrong, K., Zucker, H. L., et al. (2020). Caveolae in CNS Arterioles Mediate Neurovascular Coupling. *Nature* 579, 106–110. doi:10.1038/s41586-020-2026-1

Consortium; MicronsBae, J. A., Baptiste, M., Bodor, A. L., Brittain, D., Buchanan, J., Bumbarger, D. J., et al. (2021). Functional Connectomics Spanning Multiple Areas of Mouse Visual Cortex. *bioRxiv* 2007, 2028. doi:10.1101/2021.07.28.454025

Cragg, B. (1980). Preservation of Extracellular Space during Fixation of the Brain for Electron Microscopy. *Tissue Cell* 12, 63–72. doi:10.1016/0040-8166(80)90052-x

Daneman, R., Zhou, L., Kebede, A. A., and Barres, B. A. (2010). Pericytes Are Required for Blood-Brain Barrier Integrity during Embryogenesis. *Nature* 468, 562–566. doi:10.1038/nature09513

Dietrich, W. D., Busto, R., and Ginsberg, M. D. (1984). Cerebral Endothelial Microvilli: Formation Following Global Forebrain Ischemia. *J. Neuropathol. Exp. Neurol.* 43, 72–83. doi:10.1097/00005072-198401000-00006

Dorkenwald, S., Schubert, P. J., Killinger, M. F., Urban, G., Mikula, S., Svara, F., et al. (2017). Automated Synaptic Connectivity Inference for Volume Electron Microscopy. *Nat. Methods* 14, 435–442. doi:10.1038/nmeth.4206

Dorkenwald, S., Turner, N. L., Macrina, T., Lee, K., Lu, R., Wu, J., et al. (2019). Binary and Analog Variation of Synapses between Cortical Pyramidal Neurons. *bioRxiv* 12, 890319. doi:10.1101/2019.12.29.890319

Duvernoy, H. M., Delon, S., and Vannson, JL (1981). Cortical Blood Vessels of the Human Brain. *Brain Res. Bull.* 7, 519–579. doi:10.1016/0361-9230(81)90007-1

Faraco, G., Sugiyama, Y., Lane, D., Garcia-Bonilla, L., Chang, H., Santisteban, M. M., et al. (2016). Perivascular Macrophages Mediate the Neurovascular and Cognitive Dysfunction Associated with Hypertension. *J. Clin. Invest.* 126, 4674–4689. doi:10.1172/jci86950

Fujimoto, S., Yamamoto, K., and Takeshige, Y. (1975). Electron Microscopy of Endothelial Microvilli of Large Arteries. *Anatomical Rec.* 183, 259–265. doi:10.1002/ar.1091830204

Ghanavati, S., Yu, L. X., Lerch, J. P., and Sled, J. G. (2014). A Perfusion Procedure for Imaging of the Mouse Cerebral Vasculature by X-ray Micro-CT. *J. Neurosci. Methods* 221, 70–77. doi:10.1016/j.jneumeth.2013.09.002

Gonzales, A. L., Klug, N. R., Moshkforoush, A., Lee, J. C., Lee, F. K., Shui, B., et al. (2020). Contractile Pericytes Determine the Direction of Blood Flow at Capillary Junctions. *Proc. Natl. Acad. Sci.* 117, 27022–27033. doi:10.1073/pnas.1922755117

Grant, R. I., Hartmann, D. A., Underly, R. G., Berthiaume, A.-A., Bhat, N. R., and Shih, A. Y. (2017). Organizational Hierarchy and Structural Diversity of Microvascular Pericytes in Adult Mouse Cortex. *J. Cereb. Blood Flow Metab.* 39, 411–425. doi:10.1177/0271678x17732229

Grubb, S., Cai, C., Hald, B. O., Khennouf, L., Murmu, R. P., Jensen, A. G. K., et al. (2020). Precapillary Sphincters Maintain Perfusion in the Cerebral Cortex. *Nat. Commun.* 11, 395. doi:10.1038/s41467-020-14330-z

Guérin, C. J., Kremer, A., Borghgraef, P., Shih, A. Y., and Lippens, S. (2019). *Combining Serial Block Face and Focused Ion Beam Scanning Electron Microscopy for 3D Studies of Rare Events*. United States: Academic Press.

Hall, C. N., Reynell, C., Gesslein, B., Hamilton, N. B., Mishra, A., Sutherland, B. A., et al. (2014). Capillary Pericytes Regulate Cerebral Blood Flow in Health and Disease. *Nature* 508, 55–60. doi:10.1038/nature13165

Hamel, E. (2006). Perivascular Nerves and the Regulation of Cerebrovascular Tone. *J. Appl. Physiol.* 100, 1059–1064. doi:10.1152/japplphysiol.00954.2005

Hartmann, D. A., Berthiaume, A. A., Grant, R. I., Harrill, S. A., Koski, T., Tieu, T., et al. (2021a). Brain Capillary Pericytes Exert a Substantial but Slow Influence on Blood Flow. *Nat. Neurosci.* 24, 633–645. doi:10.1038/s41593-020-00793-2

Hartmann, D. A., Coelho-Santos, V., and Shih, A. Y. (2021b). Pericyte Control of Blood Flow across Microvascular Zones in the Central Nervous System. *Annu. Rev. Physiol.* 84, 331. doi:10.1146/annurev-physiol-061121-040127

Hartmann, D. A., Underly, R. G., Grant, R. I., Watson, A. N., Lindner, V., and Shih, A. Y. (2015). Pericyte Structure and Distribution in the Cerebral Cortex Revealed by High-Resolution Imaging of Transgenic Mice. *Neurophotonics* 2, 041402. doi:10.1117/1.NPh.2.4.041402

Haseloff, R. F., Dithmer, S., Winkler, L., Wolburg, H., and Blasig, I. E. (2015). Transmembrane Proteins of the Tight Junctions at the Blood-Brain Barrier: Structural and Functional Aspects. *Semin. Cel Dev. Biol.* 38, 16–25. doi:10.1016/j.semcdb.2014.11.004

Horng, S., Therattil, A., Moyon, S., Gordon, A., Kim, K., Argaw, A. T., et al. (2017). Astrocytic Tight Junctions Control Inflammatory CNS Lesion Pathogenesis. *J. Clin. Invest.* 127, 3136–3151. doi:10.1172/jci91301

Iliff, J. J., Wang, M., Liao, Y., Plogg, B. A., Peng, W., Gundersen, G. A., et al. (2012). A Paravascular Pathway Facilitates CSF Flow through the Brain Parenchyma and the Clearance of Interstitial Solutes, Including Amyloid β. *Sci. Translational Med.* 4, 147ra111. doi:10.1126/scitranslmed.3003748

Jin, B. J., Zhang, H., Binder, D. K., and Verkman, A. S. (2013). quaporin-4-dependent K(+) and Water Transport Modeled in Brain Extracellular Space Following Neuroexcitation. *J. Gen. Physiol.* 141, 119–132. doi:10.1085/jgp.201210883

Joost, E., Jordão, M. J. C., Mages, B., Prinz, M., Bechmann, I., and Krueger, M. (2019). Microglia Contribute to the Glia Limitans Around Arteries, Capillaries and Veins under Physiological Conditions, in a Model of Neuroinflammation and in Human Brain Tissue. *Brain Struct. Funct.* 224, 1301–1314. doi:10.1007/s00429-019-01834-8

Khennouf, L., Gesslein, B., Brazhe, A., Octeau, J. C., Kutuzov, N., Khakh, B. S., et al. (2018). Active Role of Capillary Pericytes during Stimulation-Induced Activity and Spreading Depolarization. *Brain* 141, 2032–2046. doi:10.1093/brain/awy143

Kisler, K., Nelson, A. R., Rege, S. V., Ramanathan, A., Wang, Y., Ahuja, A., et al. (2017). Pericyte Degeneration Leads to Neurovascular Uncoupling and Limits Oxygen Supply to Brain. *Nat. Neurosci.* 20, 406–416. doi:10.1038/nn.4489

Kornfeld, J., and Denk, W. (2018). Progress and Remaining Challenges in High-Throughput Volume Electron Microscopy. *Curr. Opin. Neurobiol.* 50, 261–267. doi:10.1016/j.conb.2018.04.030

Korogod, N., Petersen, C. C., and Knott, G. W. (2015). Ultrastructural Analysis of Adult Mouse Neocortex Comparing Aldehyde Perfusion with Cryo Fixation. *Elife* 4, e05793. doi:10.7554/eLife.05793

Kubotera, H., Ikeshima-Kataoka, H., Hatashita, Y., Allegra Mascaro, A. L., Pavone, F. S., and Inoue, T. (2019). Astrocytic Endfeet Re-cover Blood Vessels after Removal by Laser Ablation. *Scientific Rep.* 9, 1263. doi:10.1038/s41598-018-37419-4

Kucharz, K., Kristensen, K., Johnsen, K. B., Lund, M. A., Lønstrup, M, Moos, T., et al. (2021). Post-capillary Venules Are the Key Locus for Transcytosis-Mediated Brain Delivery of Therapeutic Nanoparticles. *Nat. Commun.* 12, 4121. doi:10.1038/s41467-021-24323-1

Lee, W. C., Bonin, V., Reed, M., Graham, B. J., Hood, G., Glattfelder, K., et al. (2016). Anatomy and Function of an Excitatory Network in the Visual Cortex. *Nature* 532, 370–374. doi:10.1038/nature17192

Makarov, V., Zueva, L., Sanabria, P., Wessinger, W. D., Golubeva, T., Khmelinskii, I., et al. (2015). On the Role of the Blood Vessel Endothelial Microvilli in the Blood Flow in Small Capillaries. *J. Biophys.*, 529746. doi:10.1155/2015/529746

Mathiisen, T. M., Lehre, K. P., Danbolt, N. C., and Ottersen, O. P. (2010). The Perivascular Astroglial Sheath Provides a Complete Covering of the Brain Microvessels: An Electron Microscopic 3D Reconstruction. *Glia* 9, 1094–1103. doi:10.1002/glia.20990

Nahirney, P. C., Reeson, P., and Brown, C. E. (2015). Ultrastructural Analysis of Blood-Brain Barrier Breakdown in the Peri-Infarct Zone in Young and Aged Mice. *J. Cereb. Blood Flow Metab.* 36, 413–425. doi:10.1177/0271678x15608396

Nikolakopoulou, A. M., Montagne, A., Kisler, K., Dai, Z., Wang, Y., Huuskonen, M. T., et al. (2019). Pericyte Loss Leads to Circulatory Failure and Pleiotrophin Depletion Causing Neuron Loss. *Nat. Neurosci.* 22, 1089–1098. doi:10.1038/s41593-019-0434-z

Ornelas, S., Berthiaume, A. A., Bonney, S. K., Coelho-Santos, V., Underly, R. G., Kremer, A., et al. (2021). Three-dimensional Ultrastructure of the Brain Pericyte-Endothelial Interface. *J. Cereb. Blood Flow Metab.* 41, 2185. doi:10.1177/0271678x211012836

Østergaard, L., Engedal, T. S., Aamand, R., Mikkelsen, R., Iversen, N. K., Anzabi, M., et al. (2014). Capillary Transit Time Heterogeneity and Flow-Metabolism Coupling after Traumatic Brain Injury. *J. Cereb. Blood Flow Metab.* 34, 1585–1598. doi:10.1038/jcbfm.2014.131

Pallotto, M., Watkins, P. V., Fubara, B., Singer, J. H., and Briggman, K. L. (2015). Extracellular Space Preservation Aids the Connectomic Analysis of Neural Circuits. *Elife* 4, e08206. doi:10.7554/eLife.08206

Schaeffer, S., and Iadecola, C. (2021). Revisiting the Neurovascular Unit. *Nat. Neurosci.* 24, 1198–1209. doi:10.1038/s41593-021-00904-7

Schmid, F., Tsai, P. S., Kleinfeld, D., Jenny, P., and Weber, B. (2017). Depth-dependent Flow and Pressure Characteristics in Cortical Microvascular Networks. *PloS Comput. Biol.* 13, e1005392. doi:10.1371/journal.pcbi.1005392

Schneider-Mizell, C. M., Bodor, A. L., Collman, F., Brittain, D., Bleckert, A., Dorkenwald, S., et al. (2021). Structure and Function of Axo-Axonic Inhibition. *Elife* 10, e73783. doi:10.7554/eLife.73783

Shapson-Coe, A., Januszewski, M., Berger, D. R., Pope, A., Wu, Y., Blakely, T., et al. (2021). A Connectomic Study of a Petascale Fragment of Human Cerebral Cortex. *bioRxiv* 2005, 2029. doi:10.1101/2021.05.29.446289

Shaw, K., Bell, L., Boyd, K., Grijseels, D. M., Clarke, D., Bonnar, O., et al. (2021). Neurovascular Coupling and Oxygenation Are Decreased in hippocampus Compared to Neocortex Because of Microvascular Differences. *Nat. Commun.* 12, 3190. doi:10.1038/s41467-021-23508-y

Shih, A. Y., Ruhlmann, C., Blinder, P., Devor, A., Drew, P. J., Friedman, B., et al. (2015). Robust and Fragile Aspects of Cortical Blood Flow in Relation to the Underlying Angioarchitecture. *Microcirculation* 22, 204–218. doi:10.1111/micc.12195

Soderblom, C., Luo, X., Blumenthal, E., Bray, E., Lyapichev, K., Ramos, J., et al. (2013). Perivascular Fibroblasts Form the Fibrotic Scar after Contusive Spinal Cord Injury. *J. Neurosci.* 33, 13882–13887. doi:10.1523/jneurosci.2524-13.2013

Török, O., Schreiner, B., Schaffenrath, J., Tsai, H. C., Maheshwari, U., Stifter, S. A., et al. (2021). Pericytes Regulate Vascular Immune Homeostasis in the CNS. *Proc. Natl. Acad. Sci. U S A.* 118, e2016587. doi:10.1073/pnas.2016587118

Turner, N. L., Macrina, T., Bae, J. A., Yang, R., Wilson, A. M., Schneider-Mizell, C., et al. (2020). Multiscale and Multimodal Reconstruction of Cortical Structure and Function. *bioRxiv*. doi:10.1101/2020.10.14.338681

Vanlandewijck, M., He, L., Mäe, M. A., Andrae, J., Ando, K., Del Gaudio, F., et al. (2018). A Molecular Atlas of Cell Types and Zonation in the Brain Vasculature. *Nature* 554, 475–480. doi:10.1038/nature25739

Wardlaw, J. M., Benveniste, H., Nedergaard, M., Zlokovic, B. V., Mestre, H., Lee, H., et al. (2020). Perivascular Spaces in the Brain: Anatomy, Physiology and Pathology. *Nat. Rev. Neurol.* 16, 137–153. doi:10.1038/s41582-020-0312-z

White, J. G., Southgate, E., Thomson, J. N., and Brenner, S. (1986). The Structure of the Nervous System of the Nematode *Caenorhabditis elegans*. *Phil. Trans. R. Soc. Lond. Ser. B, Biol. Sci.* 314, 1–340. doi:10.1098/rstb.1986.0056

Xu, L., Nirwane, A., and Yao, Y. (2019). Basement Membrane and Blood-Brain Barrier. *Stroke Vasc. Neurol.* 4, 78–82. doi:10.1136/svn-2018-000198

Yang, A. C., Stevens, M. Y., Chen, M. B., Lee, D. P., Stähli, D., Gate, D., et al. (2020). Physiological Blood-Brain Transport Is Impaired with Age by a Shift in Transcytosis. *Nature* 583, 425–430. doi:10.1038/s41586-020-2453-z

Yang, A. C., Vest, R. T., Kern, F., Lee, D. P., Agam, M., Maat, C. A., et al. (2022). A Human Brain Vascular Atlas Reveals Diverse Mediators of Alzheimer's Risk. *Nature* (Online ahead of print). doi:10.1038/s41586-021-04369-3

Yin, W., Brittain, D., Borseth, J., Scott, M. E., Williams, D., Perkins, J., et al. (2020). A Petascale Automated Imaging Pipeline for Mapping Neuronal Circuits with High-Throughput Transmission Electron Microscopy. *Nat. Commun.* 11, 4949. doi:10.1038/s41467-020-18659-3

Zambach, S. A., Cai, C., Helms, H. C. C., Hald, B. O., Dong, Y., Fordsmann, J. C., et al. (2021). Precapillary Sphincters and Pericytes at First-Order Capillaries as Key Regulators for Brain Capillary Perfusion. *Proc. Natl. Acad. Sci. U S A.* 118, e2023749118. doi:10.1073/pnas.2023749118

Conflict of Interest: The authors declare that the research was conducted in the absence of any commercial or financial relationships that could be construed as a potential conflict of interest.

frontiers | Frontiers in Cell and Developmental Biology

ORIGINAL RESEARCH
published: 11 April 2022
doi: 10.3389/fcell.2022.829545

Correlative Organelle Microscopy: Fluorescence Guided Volume Electron Microscopy of Intracellular Processes

*Sergey V. Loginov[1], Job Fermie[1,2], Jantina Fokkema[1], Alexandra V. Agronskaia[1], Cilia De Heus[2], Gerhard A. Blab[1], Judith Klumperman[2], Hans C. Gerritsen[1] and Nalan Liv[2]**

[1]Molecular Biophysics, Debye Institute for Nanomaterials Science, Utrecht University, Utrecht, Netherlands, [2]Cell Biology, Center for Molecular Medicine, University Medical Center Utrecht, Utrecht University, Utrecht, Netherlands

Intracellular processes depend on a strict spatial and temporal organization of proteins and organelles. Therefore, directly linking molecular to nanoscale ultrastructural information is crucial in understanding cellular physiology. Volume or three-dimensional (3D) correlative light and electron microscopy (volume-CLEM) holds unique potential to explore cellular physiology at high-resolution ultrastructural detail across cell volumes. However, the application of volume-CLEM is hampered by limitations in throughput and 3D correlation efficiency. In order to address these limitations, we describe a novel pipeline for volume-CLEM that provides high-precision (<100 nm) registration between 3D fluorescence microscopy (FM) and 3D electron microscopy (EM) datasets with significantly increased throughput. Using multi-modal fiducial nanoparticles that remain fluorescent in epoxy resins and a 3D confocal fluorescence microscope integrated into a Focused Ion Beam Scanning Electron Microscope (FIB.SEM), our approach uses FM to target extremely small volumes of even single organelles for imaging in volume EM and obviates the need for post-correlation of big 3D datasets. We extend our targeted volume-CLEM approach to include live-cell imaging, adding information on the motility of intracellular membranes selected for volume-CLEM. We demonstrate the power of our approach by targeted imaging of rare and transient contact sites between the endoplasmic reticulum (ER) and lysosomes within hours rather than days. Our data suggest that extensive ER-lysosome and mitochondria-lysosome interactions restrict lysosome motility, highlighting the unique capabilities of our integrated CLEM pipeline for linking molecular dynamic data to high-resolution ultrastructural detail in 3D.

Keywords: correlative light and electron microscopy, volume electron microscopy, live-cell imaging, lysosome, organelle contact site

OPEN ACCESS

Edited by:
Christopher Guerin, Vlaams Instituut voor Biotechnologie, Belgium

Reviewed by:
Sebastian Ludwig V. Munck, VIB/KU Leuven Center for Brain & Disease Research, Belgium
Jemima Burden, University College London, United Kingdom

****Correspondence:***
Nalan Liv
n.liv@umcutrecht.nl

Specialty section:
This article was submitted to Cell Growth and Division, a section of the journal Frontiers in Cell and Developmental Biology

Received: *06 December 2021*
Accepted: *04 March 2022*
Published: *11 April 2022*

Citation:
Loginov SV, Fermie J, Fokkema J, Agronskaia AV, De Heus C, Blab GA, Klumperman J, Gerritsen HC and Liv N (2022) Correlative Organelle Microscopy: Fluorescence Guided Volume Electron Microscopy of Intracellular Processes. Front. Cell Dev. Biol. 10:829545. doi: 10.3389/fcell.2022.829545

1 INTRODUCTION

Eukaryotic cells are compartmentalized in organelles delimited by distinctive intracellular membranes, each with special biochemical functions yet functioning together to maintain cellular homeostasis. Complications in organelle performance are associated with many pathologies ranging from infection, neurodegeneration, and cancer (Wu et al., 2018; Ballabio and Bonifacino, 2019; Ferguson, 2019; Sironi et al., 2020). The next step in understanding cellular regulation is how interconnectivity between different types of organelles is important for function (Gatta and Levine, 2016). This calls for novel microscopy approaches to study spatial and temporal regulation of intracellular processes at the nanoscale level.

Electron microscopy (EM) has immensely contributed to the nanoscale understanding of complex intracellular structure that underlies diverse cellular functions. However, the biggest challenge for EM has been the characteristic lack of 3D information arising from the limited section thickness obtained by classical transmission electron microscopy (TEM). Building on the initial idea of collecting serial TEM or electron tomography (ET) images of consecutive sections to build a 3D volumetric reconstruction (Keene et al., 2008; Knott et al., 2008; Saalfeld et al., 2010), various volume EM approaches have now been developed: scanning EM (SEM) based volumetric approaches; array tomography, in which serial sections from the sample are collected on a substrate (Micheva and Smith, 2007), serial block-face SEM (SBF.SEM), in which the block face is imaged repeatedly after sectioning by an *in situ* ultramicrotome (Denk and Horstmann, 2004), and focused ion beam SEM (FIB.SEM), where an ion beam removes slices from the block face (Heymann et al., 2006). Particularly FIB.SEM, which offers isotropic sub-5 nm resolution in *x*, *y*, and *z*, allows gathering 3D EM information at resolutions able to address many significant biological questions (Bushby et al., 2011; Knott et al., 2011; Lucas et al., 2012; Kizilyaprak et al., 2014; Narayan et al., 2014; Peddie and Collinson, 2014). Volume EM data also open up the possibility of quantitative EM studies without the dimension restriction of 2D EM, by automizing collection of 3D ultrastructural data. Thus, the stage is ready for volume EM to deliver its promise in cell biology (Hoffman et al., 2020), just like confocal fluorescence microscopy (FM) did in the last decades by enhancing our understanding of 3D organization of molecules and organelles within cells.

The unique potential of volume EM is currently limited in throughput as, for each experiment, a relatively large cellular volume is imaged at high resolution. This is incompatible with most life science studies, which often require the analysis of small volumes of several independent samples. If the high-resolution acquisition could be limited to a pre-defined region of interest (ROI), the throughput of volume EM would be considerably enhanced (Burel et al., 2018; Ronchi et al., 2021). With the introduction of correlative light electron microscopy (CLEM), an ROI can be highlighted/selected with FM (a common driver for CLEM). Volume correlative light and electron microscopy (volume-CLEM) approaches offer a unique potential to explore molecular characteristics together with high-resolution ultrastructural details across the cell volume. Recent studies, especially on connectomics, provide very promising examples of volume-CLEM for tissue analysis (Oberti et al., 2011; Collman et al., 2015), for example, by visualizing glia in 3D reconstructions of mouse hippocampal tissue at nanometer resolution (Fang et al., 2018). Moreover, at the cellular level, state-of-the-art volume-CLEM studies visualize protein-ultrastructure relationships in three dimensions across whole cells by identification of morphologically complex structures within the crowded intracellular environment (Hoffman et al., 2020). However, an accurate and reliable correlation between separate 3D-FM and 3D-EM platforms datasets is far from trivial because of the resolution mismatch and the sample transfer in between the two modalities (Ronchi et al., 2021). Current efforts in volume-CLEM development focus on improving its accuracy, throughput, and accessibility. An integrated CLEM platform (i.e., combining FM and EM in one instrument) inherently resolves this correlation problem as the coordinate planes of the FM-EM are shared. Recently introduced integrated confocal FM and volume EM systems, which can record both confocal fluorescence and reflection images (Brama et al., 2016; Ando et al., 2018), can be used to achieve a robust and streamlined image acquisition. 3D-FM can identify 3D coordinates of ROIs within cells, which can be traced and imaged in volume EM in a targeted way, directly increasing the throughput of the method. Correlation precise enough to target a sub-cellular level ROI (e.g., an organelle) in 3D is specifically challenging and has thus far not been demonstrated.

Understanding intracellular processes (e.g., organelle interconnectivity) ultimately requires linking molecular and dynamic information from live cells to a high-resolution ultrastructure. Therefore, a next major step forward in volume EM will be to correlate EM data to functional information from (live-cell) FM (Blazques-Llorca et al., 2015; Hoffman et al., 2020). We and others have shown that linking functional or dynamic information obtained with live-cell imaging to the underlying fine structure of the cell opens up powerful possibilities to study mechanistic processes with respect to their ultrastructure (Russell et al., 2016; Collinson et al., 2017; Fermie et al., 2018). Correlation with live-cell FM also aids the identification and capture of rare cellular structures or events, which is very challenging, time demanding, and at times basically impossible without smart tracking for EM imaging (Burel et al., 2018; Delpiano et al., 2018). An integrated CLEM platform fulfills these requirements by enabling a direct translation between live-cell FM and volume EM and the targeting identified live-cell events for follow-up ultrastructural imaging. Therefore, an FM-guided imaging pipeline for volume EM data collection is essential to improve the efficiency, throughput, and quantitative capabilities of the technique.

We present an optimized imaging pipeline to identify and target single organelles for volume-CLEM within the complex cellular environment. Following live-cell FM and fixation, we prepare cells for volume EM imaging. We then use confocal laser scanning microscopy integrated into a FIB.SEM to quickly and accurately retrace single endo-lysosomes in the complete sample and generate the corresponding 3D volume EM dataset. With this pipeline, we correlate motile characteristics of targeted organelles to their morphology, yielding essential information on their identity and cellular surroundings, such as the number and types of contact sites with the endoplasmic reticulum (ER).

2 MATERIALS AND METHODS

2.1 Cell Culture

HeLa cells were cultured in a 37°C, 5% CO_2 incubator, in T75 culture bottles (Corning). Cells were maintained in Dulbecco's Modified Eagle's Medium (DMEM; Gibco) supplemented with 10% fetal bovine serum, 2 mM L-glutamine, 100 U/ml penicillin, and 100 µg/ml streptomycin (referred to as complete DMEM). Cells were passaged when confluency reached 85%–90%.

For CLEM, HeLa cells were grown on gridded glass coverslips, prepared as described earlier (Fermie et al., 2018). On the next day following seeding, the cells were transiently transfected with a construct encoding mEmerald-Sec61b-C1 (Nixon-Abell et al., 2016), which was a gift from Jennifer Lippincott-Schwartz (Addgene plasmid # 90992), for 16 h. Transfections were performed using Effectene transfection reagent (Qiagen) according to the manufacturer's instructions. Prior to FM, cells were incubated with fiducial markers (Fokkema et al., 2018) at a concentration of 1 µg/ml and cell-permeable lysosome stain SiR-Lysosome (SpiroChrome) at a concentration of 0.5 µM in complete DMEM and incubated for 3 h.

2.2 Fluorescence Microscopy

Live imaging was performed on a Deltavision RT widefield microscope (GE Healthcare) equipped with a conditioned imaging chamber set to 37°C and 5% CO_2. Time-lapse imaging was performed using a ×100/1.4 numerical aperture (NA) oil immersion objective, and images were recorded on a Cascade II EM-CCD camera (Photometrics). Live-cell imaging was performed for 3–5 min, after which the cells were fixed *in situ* by adding 1 ml of fixative containing 4% paraformaldehyde (Sigma) and 0.05% glutaraldehyde (25% solution in dH_2O, Merck) in 1 × PHEM buffer (60 mM PIPES, 25 mM HEPES, 10 mM EGTA, 2 mM $MgCl_2$, pH = 6.9) to the imaging holder with the camera still active, to obtain images until the cells are fixed. After fixation, a Z-stack was recorded for all fluorophores using a Zeiss LSM700 CLSM equipped with ×63/1.4 NA oil immersion objective. Z-stacks were collected with a 200 nm step size. The position of cells relative to the grid of the coverslips was recorded using polarized light.

2.3 Sample Preparation for Volume EM

Cells were prepared for electron microscopy according to a protocol described earlier, with minor modifications (van Donselaar et al., 2018). Briefly, samples were postfixed using 1% osmium tetroxide (w/v) with 1.5% potassium ferrocyanide (w/v) for 1 h on ice, incubated with 1% thiocarbohydrazide in dH_2O (w/v) for 15 min, followed by 1% osmium tetroxide in dH_2O for 30 min. Samples were EM stained with 2% uranyl acetate in dH_2O for 30 min and stained with Walton's lead aspartate for 30 min at 60°C. Dehydration was performed using a graded ethanol series. Samples were embedded in Spurr resin and polymerized for 48–60 h at 65°C following the extremely thin layer plastification method (van Donselaar et al., 2018). Resin embedded samples on the glass coverslips were subsequently coated with 8 nm carbon and carbon-tape mounted on aluminum stubs.

2.4 Electron Microscopy

A Scios FIB.SEM (ThermoFisher) was used. It included an Everhart–Thornley Detector (ETD), an in-lens detector of backscattered electrons (BSE), and an in-the-column detector of secondary electrons (SE). The ETD was used for imaging of sample surfaces. The BSE detector was used for imaging cellular ultrastructure in 3D. The in-the-column SE detector was used to enhance fiducial marker contrast. The FIB was equipped with a Ga-ion source; for the 3D acquisition, a current of 0.4 nA and an acceleration voltage of 30 kV were used. The 3D acquisition in the FIB.SEM was controlled by the Slice&View software version 3 (Thermo Fischer).

2.5 Integrated Confocal Laser Scanning Microscope

The integrated CLSM was equipped with a Nikon industrial inspection objective lens (ELWD series, Plan Apo 100x NA0.9). A lens of focal length 120 mm (25 mm diameter, OptoSigma anti-reflection coated doublet lens DLB-25–120 p.m.) was used as a tube lens. For lateral optical scanning, a Yanus scan head (FEI Munich) equipped with a 50 mm focal length scan lens was used. As an excitation source, a 532 nm laser (Omicron, integrated with an Acoustic Optical Modulator in LightHUB housing) coupled *via* a single-mode optical fiber was used. The excitation and detection light paths were combined inside the scanning head *via* a dichroic mirror (T560lpxr-UF2, Chroma). The detected light was coupled into a multi-mode fiber (FG010LDA, Thorlabs) with a core diameter of 10 µm (about 1 Airy disk). The light from the sample was split by a second dichroic mirror (T565LP, Chroma) into fluorescence and reflection parts. Backreflected light was detected by a PMT operating in current mode (PMMA01, Thorlabs). After bandpass filtering (ET585pxr-65, Chroma), the fluorescence signal was detected by a photon-counting PMT (H7422P-40, Hamamatsu). For sub-micrometer axial scanning, a single axis piezo-stage (E-601.1SL, Physik Instrumente) was mounted on top of the FIB.SEM stage. iCLSM was controlled *via* a National Instruments NI-6251 DAQ card using LabView software. The LabView codes can be found at https://github.com/UUtrechtTT/integrated_CLSM_control_software_LabView. See also **Supplementary Figure S1** for the iCLSM/FIB.SEM setup.

2.6 Integrated Confocal Laser Scanning Microscope and FIB.SEM Pipeline

Initially, a low magnification, low-exposure SEM image was acquired to find the main grid markings (numbers and letters). Using those markings, the square where the live-cell imaging was performed was found. Another low-exposure SEM image ("snapshot" at the current of 10 pA, dwell time 0.5 us, and pixel size of ~250 × 250 nm^2) was taken of the suspected square to verify that the correct cells were found. Performing these steps using SEM has an advantage because of the much wider field of view of SEM compared to that of the integrated CLSM (up to 350 µm) and the large depth-of-focus of the SEM. However, the topographical contrast of the SEM is much lower than of the reflection light channel of the integrated CLSM. The SEM exposure of the sample should be minimized as much as possible because the fluorescence quenches strongly under electron radiation. In the next step, the sample was transferred under the integrated CLSM. Herein, we made overview images with pixel size larger than 0.5 µm and a dwell time of 3 µs. In the reflected light channel, we can find the cells and refine the Z position of the sample. The shape of the cell is

then used to find ROI from the live-cell/fixed cell images. Next, we take a fine-resolution image (34×34 nm^2 pixels, Z step of 100 nm and dwell time of 24 μs) of cell area of 35×35 μm^2 or smaller. In the fluorescence channel in the acquired image, some of the nano-fiducial particles were visible. Their configuration allowed refining the position of the ROI relative to the surface features detected with the reflection light channel. All ROIs selected in the live-cell data were recorded in the same manner with the integrated CLSM. Next, the sample was transferred back under the FIB.SEM. At this step, the surface features of the cells were accurately studied in SEM with a pixel size of 17×17 nm and dwell time of 1 us and beam current of 50 pA because fluorescence quenching had become of no issue after the integrated CLSM imaging was performed. The surface features of the cell recorded at this step were used to refine the ROI in the SEM field of view and determine the acquisition volumes of the FIB/SEM itself.

2.7 Alignment of FIB.SEM Data

The raw SEM images of 3D FIB.SEM data were aligned using MATLAB (see https://github.com/UUtrechtTT/Slice_and_View_postprocessing_code_MatLab). The vertical alignment (*y*-axis in SEM images, *z*-axis in the original orientation) was performed *via* the detection of the glass substrate in the SEM images. The alignment in the *X* direction was performed using the correlation of consecutive images. The height of XY slices is calculated relative to the substrate level.

2.8 Correlation/Targeted Imaging Routine

In the live-cell data, the ER and the lysosomes are used to define the region of interest. After fixation, a CLSM image is collected of the same lysosomes and the ER and, additionally, the fiducial particles emitting in another channel. The shape of the cell visible in SEM and the ER configuration can be used for correlation. The fluorescence of the nanoparticles is visible in the integrated CLSM and allows for registration with the non-integrated CLSM. The fluorescence channel of integrated CLSM is directly linked with the reflection channel of the integrated CLSM. In the reflected light channel, the cell shape and cell topography are visible in fine detail. The same fine details (i.e., slopes, protrusions, and bumps) are visible in the reflection light channel of the integrated CLSM and the SEM image. These fine details can be used for the fine registration between these two (vacuum) modalities. Thus, the accurate finding of the ROI in the FIB.SEM relies on the following ladder of registration steps: from the fiducials in the non-integrated CLSM to the fiducials visible in the integrated CLSM. Next, the fiducials in the CLSM can be related exactly to the surface features of the cell, with are also visible in the SEM, albeit with different contrast.

2.9 Image Correlation, Analysis, and Segmentation

Registration of 3D CLSM and 3D FIB.SEM data was achieved by the following steps: first, 2D maximum intensity projection of CLSM data and 2D maximum intensity projection of integrated CLSM data were registered manually to find relative rotation angle. The registration was based on the clusters of fluorescent nanoparticles. Next, the whole 3D CLSM data were rotated around the *z*-axis by the angle found at the first step. Then, the sub-volume of 3D CLSM enclosing the ROI was copied with a several-pixel margin. Afterward, the sub-volume was interpolated to a smaller voxel size using the bilinear algorithm. The 3D FIB.SEM data were reordered to match those of CLSM data (the native orientation in Slice&View software is XZY), and voxel dimensions were equalized: binned along *X* and *Z* directions (SEM scanning directions) and interpolated along *Y* direction (FIB slicing direction). The voxel sizes matched those of the 3D CLSM data sub-volume at the previous step. Finally, the correct sub-volume of 3D CLSM data was selected manually, and the 3D FIB.SEM data were added to it as a fourth color channel.

We employed a semi-automated approach of the custom-written MATLAB code (see https://github.com/UUtrechtTT/Slice_and_View_postprocessing_code_MatLab) for segmentation of the 3D FIB/SEM datasets. The segmentation was performed consequently for each type of cell compartments. At first, the lysosomes were segmented. Then, the voxels of the lysosome were zeroed in the volume, and the segmentation was performed for the mitochondria (if any were present in the volume). As the last step, the ER segmentation was performed with all the previously segmented organelles zeroed in the volume.

The semi-automated segmentation "in bunches" was performed in the following manner. For every 10 2D slices, the average image (i.e., "bunched slices") was shown to the user. Then, the user drew a contour around the suspected organelle, which defined the area where the automated segmentation would be performed. All automated steps were performed on a 2D basis using the standard MATLAB Image Processing Toolbox functions. Otsu thresholding was performed (two levels in the case of lysosome and three levels in other cases) in the user-selected area of the averaged image. The highest level obtained from the Otsu algorithm was used for thresholding the suspect area of each of the substitute original slices of the stack. The images were then subjected to Canny edge detection, and the edges were morphologically filled. The automated steps were parallelized for the slices of the bunch. After the automated steps were performed, the new averaged image was shown to the user with zeroed detected areas. At this step, the user could define another area where the organelle was visible or accept the results of the automated steps and proceed to process the next bunch of the slices.

For each organelle, the segmentation procedure was performed three times along three main axes of the stack (for XY, XZ, and ZY slices). A pixel was considered belonging to the organelle if detected in any of the two steps.

3 RESULTS

3.1 Correlative Organelle Microscopy Workflow: Deep Sub-Cellular Precision Volume-CLEM Using Integrated 3D CSLM and FIB.SEM

Correlating single organelle-sized, intracellular regions-of-interest (ROIs) from fluorescence (FM) to electron microscopy (EM) is challenging due to the limited resolution of FM, the

inherently different contrast mechanisms of the two modalities, and the highly crowded content of the cell (Ando et al., 2018). These challenges are amplified when correlating 3D FM to 3D EM images and even further when using live-cell imaging as an FM method. Integrated CLEM instruments (with the LM built in the EM) greatly facilitate retracing the ROI from FM to EM (Liv et al., 2013; Koning et al., 2019) as the coordinate systems of the FM-EM are shared. Recently, multiple integrated (confocal) FM and volume EM systems were reported (Brama et al., 2016; Ando et al., 2018; Delpiano et al., 2018; Gorelick et al., 2019; Lane et al., 2019). We add to this a home-built system integrating a Confocal Laser Scanning Microscope (CLSM) into a Focused Ion Beam Scanning Electron Microscope (FIB.SEM), similar in geometry to a previously reported (Timmermans et al., 2016) integrated system, as outlined in **Supplementary Figure S1**. In short, the CLSM unit is mounted on one of the side ports of the FIB.SEM chamber. The FIB.SEM and CLSM image the sample from the same direction, while switching between the two modalities is simply accomplished by shuttling the specimen on the accurate motorized stage. The integrated CLSM (iCLSM) is equipped with a Nikon industrial inspection objective lens (ELWD series, Plan Apo 100x NA0.9).

3.1.1 Endocytic Fiducials for Improved 3D Correlation

Even in such an integrated CLEM platform, the accuracy of FM-EM registration/correlation is limited by FM resolution, especially in the z-dimension. Several organelles can be located within the same fluorescent spot, causing the risk of misidentification. We tackled this problem by adding gold core silica shell fiducials to cells prior to imaging. These fiducials, recently developed in our labs (Fokkema et al., 2018; Mohammadian et al., 2019), are visible and highly compatible with live-cell imaging. They are taken up by endocytosis, which generates a natural 3D distribution within the cell throughout the endo-lysosomal system (Fokkema et al., 2018; Prabhakar et al., 2020). The resulting array of well-distributed puncta provides an accurate 3D translation map between FM and EM and enables the identification and registration of even single organelles. Moreover, their fluorescence is retained after osmium fixation and serves as suitable anchors for the translation of coordinate systems between stand-alone CLSM, iCLSM, and volume EM.

We then set up the following high accuracy, live-cell volume-CLEM pipeline consisting of the steps: 1—image live cells in a stand-alone FM, 2—fix cells and make a confocal Z-stack, 3—prepare cells for FIB.SEM, 4—place and image the sample in the integrated platform-map confocal Z-stack to 3D iCLSM image, 5—target and image the pre-identified region in FIB.SEM. An outline of this high accuracy live-cell volume-CLEM workflow is shown in **Figure 1**, and detailed in **Supplementary Figure S2**.

3.1.2 Fluorescent Microscopy: From Live-Cells to 3D Confocal Z-Stacks

To demonstrate our approach, we labeled live HeLa cells for two distinct organelles; endoplasmic reticulum (ER) and lysosomes. Cells were cultured on gridded glass coverslips with etched marks (Polishchuk et al., 2000) and transiently transfected (16 h) with mEmerald-Sec61β, localizing to ER membranes. Then, the transfection medium was replaced with a medium containing SiR-lysosome (SiRLyso) (Lukinavičius et al., 2016), marking functionally active lysosomes and containing the above introduced endocytic fiducial nanoparticles, both for 3 h at 37°C. To view the dynamics of ER and lysosomes and their interactions, we performed live-cell imaging of individual fluorescent organelles. We recorded the mEmerald (ex/em 487/509 nm) and the SiRLyso (ex/em 652/674 nm) channels with 1s/frame over 2–3 min (**Figure 1A**). Then, cells were fixed *in situ* on the microscope stage by adding fixative directly in the imaging chamber. This assures no imaging gap between the last live-cell frame and the corresponding image after fixation. Following fixation, fluorescent confocal Z-stacks were recorded of the same cell capturing the 3D distribution of mEmerald-Sec61β, SiRLyso, and the fiducial particles (ex/em 543/576 nm). **Figure 1B** shows a maximum intensity projection of the Z-stack; fiducial particles (green), ER (blue), and lysosomes (red) are visible. With the confocal Z-stack, the exact *x-y-z* coordinates of ER and lysosomes are visualized with respect to the fiducial markers (**Figure 1C**).

3.1.3 Relocating the Region of Interest in FIB.SEM Using iCLSM

Samples were removed from the microscope stage, postfixed, with osmium-thiocarbohydrazide-osmium (R-OTO), and further stained with uranyl acetate and Walton's lead aspartate. Cells were embedded in resin following the "extremely thin layer plastification" (ETLP) method (van Donselaar et al., 2018). For a more in-depth description of these protocols, we refer to **Section 2**. After resin embedding, the cells were coated with carbon, mounted on a stub, and transferred to the integrated CLSM/FIB.SEM setup operating under high-vacuum (see **Supplementary Figure S1**). A quick re-localization of the cells imaged previously in the stand-alone CLSM was achieved using the SEM to show the markings on the coverslips (**Figures 1D–F**). Interference reflection contrast mode of iCLSM (Weber, 2003) can resolve some features of the cell (e.g., cellular contours) and allows easy correlation between the CSLM to find back the cells (**Figure 1E**). The interference contrast images expose various surface topology features of the cells. As many of these features are also visible in the SEM images, this registration generates a first 2D correlation map around the ROI (red rectangle in **Figures 1B,E**). Then, the confocal fluorescence image from iCLSM localizes fiducial nanoparticles (which notably retain their fluorescence in the epoxy resin) in *x*, *y*, and *z* (**Figure 1F**). iCLSM image of the fiducial particles directly matches the fiducial channel in the CLSM image collected before EM sample preparation (note the correspondence in **Figures 1C,F**) and provides a 3D translation anchor. After this, we could reliably start the 3D FIB.SEM acquisition of this targeted ROI.

3.1.4 Volume EM Imaging and 3D Correlation

In FIB.SEM, samples are imaged by scanning the surface of an ROI using the electron beam, after which a thin layer is ablated from the surface using the FIB (**Figure 1G**). This cycle is repeated until the ROI has been imaged, allowing a 3D reconstruction of the sample. We performed the slice-by-slice acquisition both with

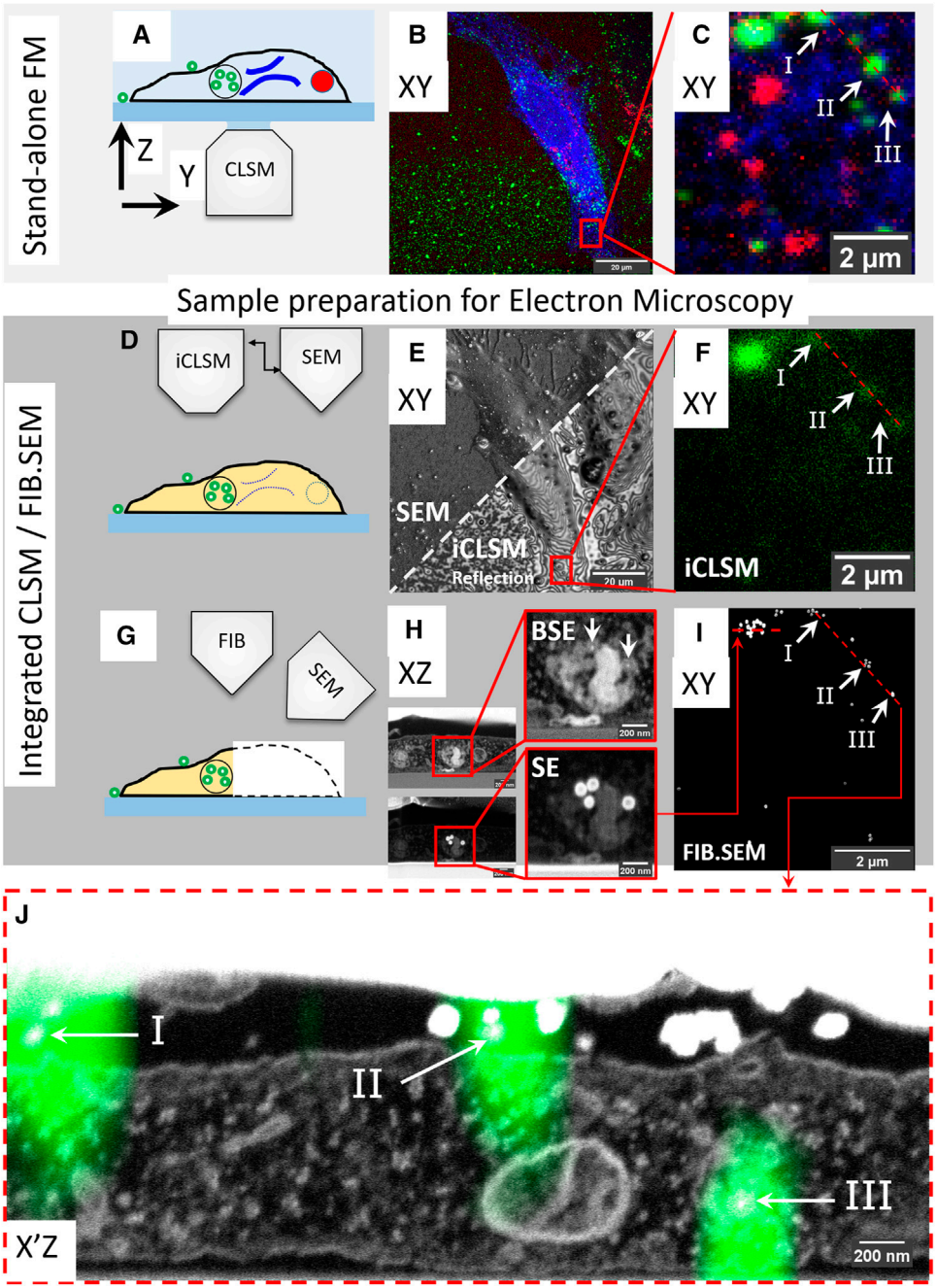

FIGURE 1 | High accuracy 3D correlation workflow from live-cell-to-volume EM with iCLSM. **(A–C)** Live-cell imaging and CLSM. **(A)** Live-cell imaging of cells on gridded coverslips in stand-alone CLSM followed by z-stack recording of fixed cells. **(B)** Maximum intensity projection of the CLSM Z-stack. ER (blue), active lysosomes (red), and endocytic fiducial particles (green). **(C)** The selected ROI, red square, within the cell in **(B)**. **(D–F)** Correlation with iCLSM. **(D)** Locating the ROI in the FIB.SEM chamber by iCLSM after EM preparation. **(E)** Reflection mode imaging in iCLSM to navigate through the gridded glass coverslip and fast-tracking of ROI by cell shape. iCLSM reflection image (lower half) relates easily with SEM (upper half). **(F)** The ROI can be localized by the fluorescence mode of iCLSM. The (remaining) fluorescence signal of the fiducial nanoparticles is used for correlation back to the CLSM image in **(C)**. **(G–I)** 3D FIB.SEM acquisition of the re-established ROI. **(H)** Slice-by-slice acquisition is performed with backscattered electrons (BSE, top) and secondary electrons (SE, bottom). Fiducial nanoparticles have a clear signature of a bright backscattering core (top) and shell in secondary electrons (bottom). **(I)** They can be thus filtered from the acquired data stack to aid precise correlation of ROI between CLSM and FIB.SEM. Note the one-to-one correspondence between panels **(C,F,I)**. **(J)** Overlay of 3D CLSM data from the fixed cell and the 3D FIB/SEM data. EM image corresponds to the plane of red dashed line in **(C,F,I)**.

backscattered electrons (BSE) (**Figure 1H**, top) and secondary electrons (SE) (**Figure 1H**, bottom). Fiducial nanoparticles have a clear signature, with a bright backscattering by both the gold core and a bright secondary electron emission by the silica shell, which improves their visibility and makes them well-suited for FIB.SEM image acquisition. The fiducial nanoparticles are found in endo-lysosomal compartments and can be detected at an individual particle level (**Figure 1H**). With the high resolution provided by FIB.SEM in *x*, *y*, and *z* dimensions, single particles can be identified and fitted to the fluorescence Z-stack data (**Figure 1J**). Using the fiducials, we correlated and registered the 3D CLSM data from the fixed cell with the 3D FIB.SEM dataset (**Figures 1I,J**, also see 3D-overlay **Supplementary Video S1**). **Figure 1J** shows the reconstructed EM image corresponding to the dashed line in the FM images in **Figures 1C,F**. The fluorescent spots I and II shown with arrows point to fiducials outside the cell and III to intracellular fiducials in an endosome. We show a correlation accuracy at the level of single, 90 nm sized nanoparticles, which is far below the *x*, *y*, *z* resolution limits of the FM and allows studying sub-organelle structures.

3.2 Correlation of Organelle Motility and Function to Morphology by Targeted Volume-CLEM

Next, we utilized our high-precision, live-cell-to-volume-CLEM pipeline to link the dynamic behavior of single, active endo-lysosomes to their morphology and neighboring environment at nanometer resolution. Besides motility, live-cell imaging was used to analyze functional characteristics of organelles, exploiting fluorescent reporter probes. As an example, we used the SiRLyso probe to report the activity state of lysosomal hydrolase cathepsin D in single lysosomes (Butkevich et al., 2017). In a previous 3D CLEM study (Fermie et al., 2018), we used a constellation pattern of at least three fluorescent spots found by live-cell imaging to retrace a similar pattern of endosomal organelles in the volume EM data. Although this proved a powerful approach, the correlation of 3D FM and 3D EM data by matching the organelle constellations was relatively time-consuming and limited in accuracy. With our current approach, the correlation of the fiducial signal between the pre-embedding CLSM z-stack and post-embedding iCLSM assures that we know the exact z-plane of each organelle imaged in live-cell FM. Moreover, our correlation is not limited to organelles bearing fiducial particles but extends to all fluorescent signals, even when lost after EM embedding, using the fluorescence signal from fiducial particles as an anchor in translating data to volume EM. Hence, we can correlate each live-cell imaged organelle to the volume EM data (see **Supplementary Figure S2**). This significantly eliminates the time and computational need for correlation of matching organelle constellations between datasets and hence notably increases the throughput (e.g., organelles analyzed per cell) of the live-cell CLEM workflow.

Live-cell imaging allows studying key temporal, functional (e.g., pH and hydrolase activity as we show here), and structural parameters of single organelles over an extended period of time, and by 3D CLEM, we correlate these directly to nanometer architecture, cellular context, and inter-organelle connections. As a proof of principle, **Figure 2** shows the correlation sequence from a live-cell movie of hydrolase active lysosomes and ER to volume EM. For live-cell imaging (**Figure 2A**), we recorded SiRLyso (lysosomes) and Sec61β (ER) channels in a single focal plane to reach the temporal resolution required to visualize transient events on a sub-second scale (<1 s between frames, see live-cell **Supplementary Video S2**). We analyzed 14 lysosomes (SiRLyso positive organelles) for their dynamic behaviors, such as speed, displacement, fusion, or interaction with other lysosomes and ER (**Figure 2B**). We then fixed cells *in situ* by adding fixative directly to the medium in the live-cell holder, while the camera was still acquiring images (**Figure 2C**). In the fixed material, Z-stacks of the ROI were recorded to visualize SiRLyso, Sec61β, and fiducial particles (**Figure 2C**). The samples were prepared for EM and imaged following the routine explained in the previous section and **Figure 1**. With the ultrastructural resolution of EM, we analyzed compartment identity, fusion profiles with other compartments, interactions with surrounding structures, and inter-organelle interactions. Finally, we integrated the multi-modal data collected per organelle, from live-cell imaging to 3D-EM (see 3D-overlay **Supplementary Video S1**).

The movies defined lysosome#1 as the most stable organelle of the whole set. It shows no displacement within 3 min, and its velocity is fixed at 0.07 μm/s, resembling the Brownian motion in a confined area. Lysosomes are heterologous in shape and, by EM, can be classified by morphological characteristics such as size and shape, as well as electron density and contours of their content (Meel and Klumperman, 2008; Fermie et al., 2018). The EM data identified lysosome#1 as an (auto)lysosome, showing a heterogeneous content with an electron-dense region and irregularly organized internal membranes. Its size is 0.71 × 0.69 × 0.74 μm. Intriguingly, this stable lysosome has extensive contact sites, covering two-thirds of its surface area, both with mitochondria and ER. Especially its interaction with the mitochondria wrapping it from three sides over a 2 μm^2 contact area creates a very confined space (**Figures 2D,E**).

In contrast to lysosome#1, lysosome#4 was very motile with an average velocity of 0.2 μm/s, traveling over a distance of 2.8 μm in 3 min before it reached the final position also visualized in EM. The organelle first exhibits directional movement toward (~100°) the nucleus and then meets lysosome#3 (which is quite stable until the meeting point) at 150s, after which they together move directionally toward (~270°) the plasma membrane (see live-cell **Supplementary Video S2**). The directional and stable trafficking characteristics indicate that lysosome#3 and lysosome#4 are transported *via* microtubules and associated motors. The size of lysosome#3 is 0.43 × 0.61 × 0.51 μm and, by EM, it shows a heterogeneous dense lumen. On the contrary, lysosome #4, with a size of 0.39 × 0.77 × 0.54 μm, has a relatively electron-lucent lumen compared to lysosomes#1 and #3, with irregularly organized internal membranes and numerous intraluminal vesicles (ILVs) (**Figures 2D–F**). In contrast to lysosome#1, lysosome#3 and lysosome#4 do not display contact sites with mitochondria and are not wrapped by ER cisternae. Rather, they

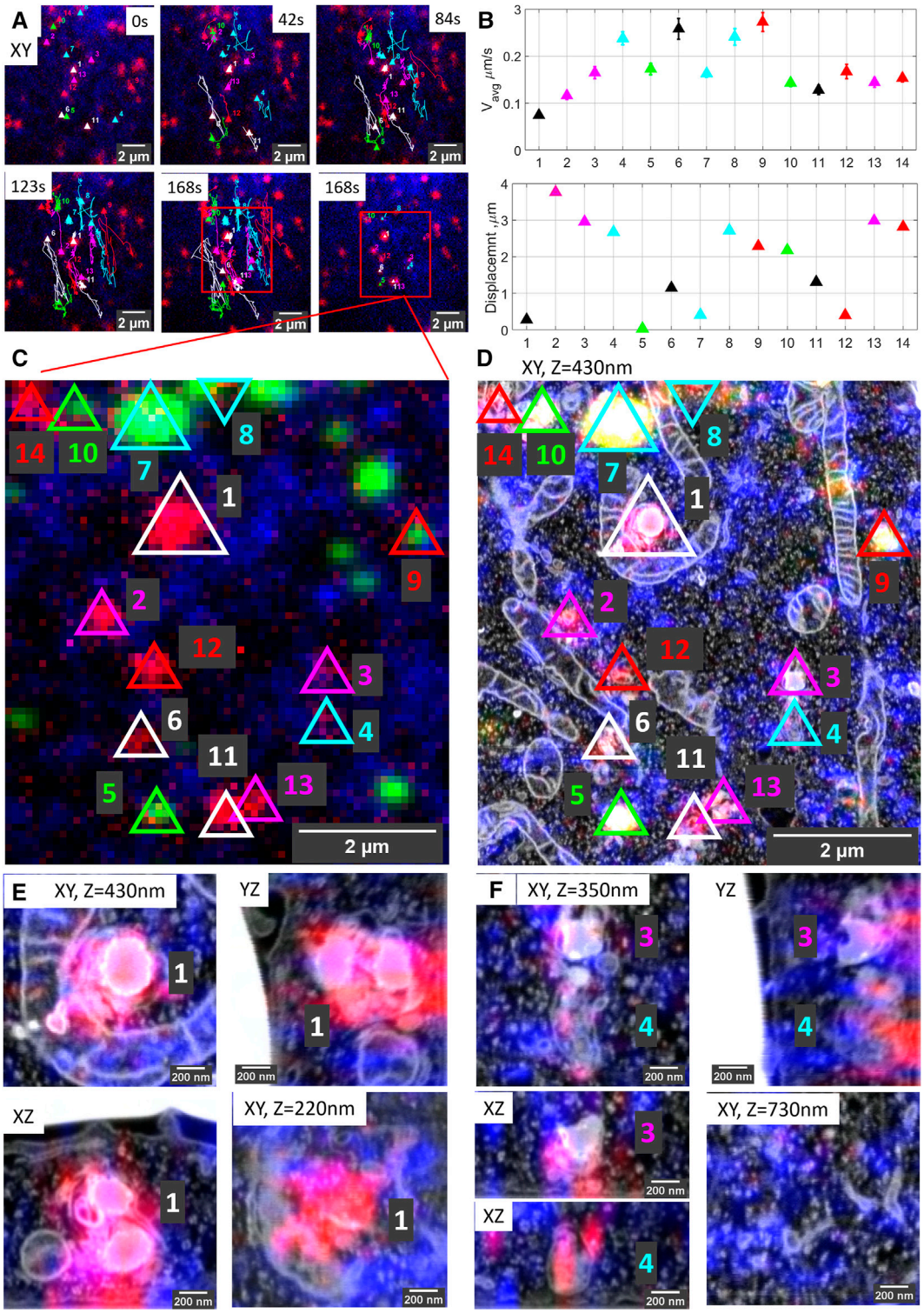

FIGURE 2 | Organelle dynamics directly correlated to morphology. **(A)** Time-lapse images from live-cell imaging. Lysosomes are stained with SiRLyso (red) and ER with mEmerald-Sec61β (blue), and the cells have endocytosed fiducial particles (green). We selected 14 SiRLyso positive, enzymatically active lysosomes and traced their dynamic behavior over 3 min. **(B)** Plot of the average velocity (µm/s) and total displacement of each selected organelle, numbered from lysosome#1 to lysosome#14 in the *x*-axis. For example, lysosome#1 is very static, whereas lysosome#4 moves fast over extended distances. **(C)** Max intensity projection of CLSM stack recorded on the same cell after fixation. Fiducial markers are visible in green. Each identified and analyzed organelle is numbered as in **(B)**. **(D)** Following live-cell imaging and CLSM, cells are prepared for EM, imaged, and high-precision correlation is achieved using iCLSM-FIB.SEM. **(E)** Higher magnification images of lysosome#1, lysosome#3, and lysosome#4 display their distinct morphologies from different planes and interaction with surrounding cellular organelles. See supplementary data for the rest of the lysosomes.

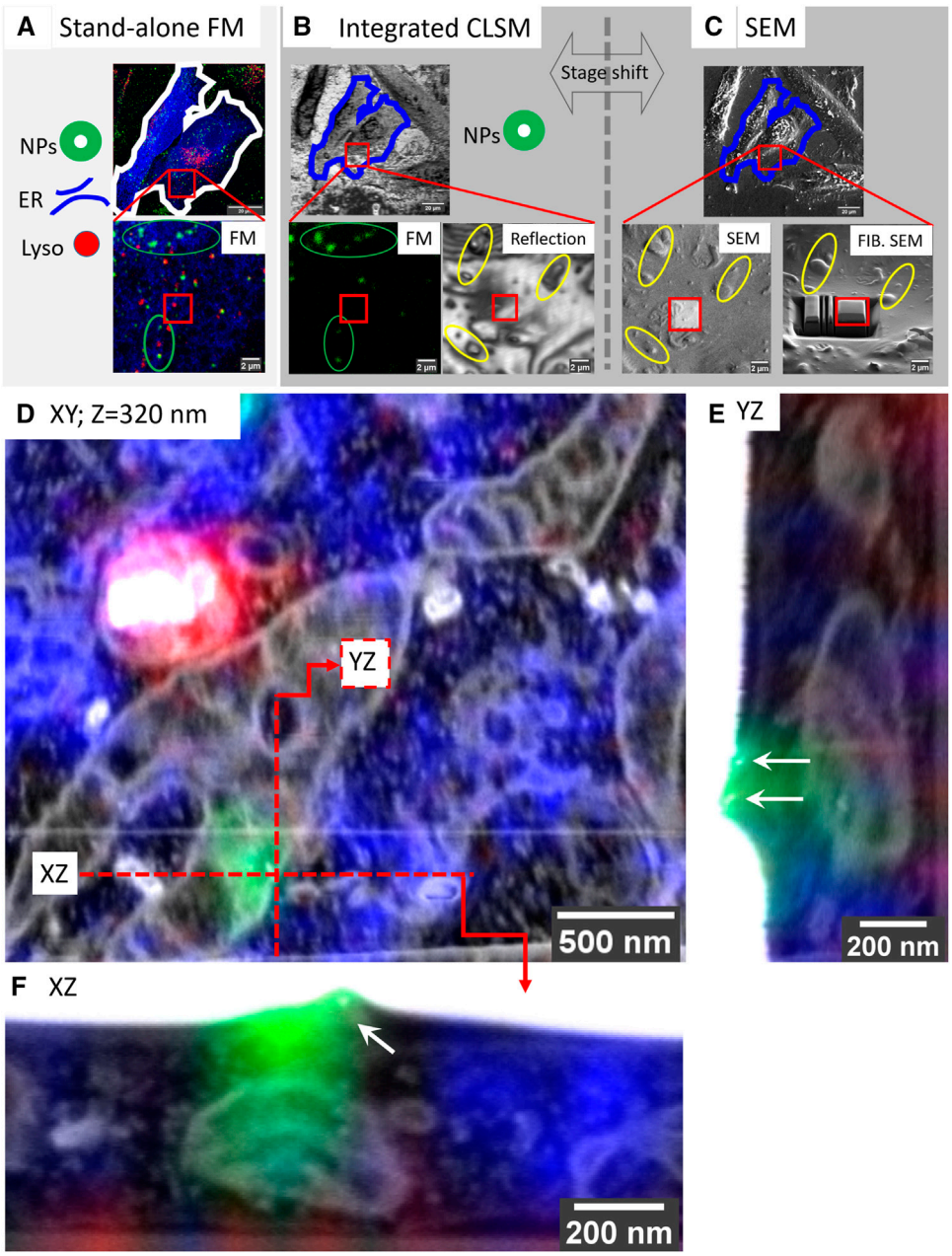

FIGURE 3 | Targeted imaging of minimized volumes in FIB.SEM using iCLSM. **(A–C)** High-accuracy correlation routine for targeted imaging in FIB.SEM. **(A)** Maximum intensity projection of a confocal z-stack collected at CLSM from fixed cells, following optional live-cell imaging. 3D CLSM data show ER (mEmerald-Sec61β, blue), lysosomes (SiRLyso, red), and endocytic fiducials (green). Red square indicates the ROI bearing a single lysosome selected for targeted volume EM. **(B)** The cells and the ROI are traced back after EM sample preparation. Fluorescence of endocytic fiducials is visualized by iCLSM and correlated to the CLSM data (green ellipses), providing the coordinates of the ROI, even when the ROI itself has no fiducial particles. Reflection image collected by iCLSM provides topographic information correlated with SEM for fine alignment (yellow ellipses). **(C)** Once precisely located, the Pt layer is deposited to protect the ROI from FIB, and trenches are prepared for imaging only the small ROI area. **(D)** The small ROI, bearing a single lysosome not reached by endocytic fiducial particles, is targeted and imaged in FIB.SEM. 3D CLSM data, ER, lysosomes, and endocytic fiducials, are overlaid with the 3D FIB.SEM data. **(E,F)** Two fiducial particles located on the plasma membrane are used as a blind target to assess correlation/targeting efficiency. Green fluorescence signal of the particles is correlated to their gold core with an accuracy of 60 nm in X **(E)**, 90 nm in Y **(F),** and 330 nm in Z.

only touch the ER at 2 and 3 points, respectively. As also reported by others (Cabukusta and Neefjes, 2018; Wong et al., 2019), these data indicate that interactions of lysosomes with other organelles have a defining role in their motile characteristics. Our high accuracy live-cell volume-CLEM workflow provides a unique means to mechanistically study these interactions. For further

analysis of the organelles in this ROI, see **Supplementary Figure S3**. Note that 10 out of the 14 organelles correlated and analyzed in the ROI have no fiducial particles.

3.3 Rapid Volume-CLEM of Targeted Subcellular Region of Interest With <100 nm Accuracy

The possibility of matching all coordinate planes between 3D-FM and 3D-EM modalities allows us to address a major bottleneck in volume EM approaches: the throughput. In most volume EM imaging techniques, especially in FIB.SEM, hitting the ROI within the imaging volume is ensured by maximizing the image area. This imposes a compromise between long imaging durations (days to weeks) and resolution (low to high). Herein, we tackle this problem using iCLSM to reliably identify and select a very confined ROI (e.g., a single lysosome) for volume EM data collection. Using this targeted approach, we lower the imaging time for a selected ROI from several days to 1-2 h.

To demonstrate the power of the targeted imaging approach in **Figure 3**, we selected a very small ROI of a single SiRLyso positive lysosome devoid of fiducial particles (**Figures 3A,B**, red square) for volume EM. The CLSM—iCLSM correlation provides an accurate 3D map between FM and EM and delivers the 3D coordinates of all organelles within the complete block using the endocytic fiducials in the surrounding organelles as an anchor, including the selected organelle without fiducial particles (e.g., the red labeled lysosomes in **Figure 3A** are not visible in **Figure 3B**). Because the *x*, *y*, and *z* coordinates of the identified organelles are exactly known a priori, only a very small volume needs to be imaged in FIB.SEM. This greatly minimizes the time spent on pre-imaging procedures (i.e., trench milling and Pt layer deposition, **Figure 3C**), as well as the actual image acquisition. Hence, the targeted lysosome was visualized in 3D within only ~2.5 h in FIB.SEM (with voxels of 1.2 × 1.2 × 10 nm and dwell time of 3 µs), by direct correlation with the corresponding FM data (**Figure 3D**; **Supplementary Video S3**). The CLEM data show, by FM, that the selected organelle is positive for active cathepsin D (SiRLyso signal) and not reached by endocytosed fiducial particles. By EM, we confirm the absence of fiducial particles and show that the lysosome has an electron-dense lumen with clearly degraded content, a spherical shape with an approximate diameter of 560 nm, and extensive contact sites with ER and mitochondria.

To measure our correlation precision with high accuracy, we next used a single fluorescent spot of the fiducial particles as a blind target. The faint green fluorescence signal visible in **Figure 3D**, originating from another z-plane (orthogonal planes depicted with the red lines), belongs to fiducial particles attached to the cell membrane (orthogonal views shown in **Figures 3E,F**). Blind correlation of the signal recorded from this single spot in CSLM, before EM preparation, with the volume EM data, placed the peak of the fluorescence signal 60 nm in X, 90 nm in Y, and 330 nm in *Z* direction from the center of mass of the two fiducial particles. This indicates that we can reach a correlation accuracy of sub-100 nm in the XY dimension and sub-350 nm in the *Z* direction.

Together these data show that our high-precision volume-CLEM approach allows targeting single organelles identified by CLSM, which within 1–2 h can be correlated, targeted, and imaged in volume EM with 100 nm confidence. This reliable targeted imaging approach greatly improves the throughput of the volume EM technique.

3.4 Targeted Volume-CLEM Efficiently Reveals Inter-Organelle Contact Sites

The possibility of rapid, targeted volume-CLEM with <100 nm precision opens new avenues for imaging at sub-organelle scale (e.g., organelle subdomains), as well as the correlation of rare or transient structures in cells. As an illustration for this application, we examined membrane contact sites (MSCs) between lysosomes and ER. Organelles can communicate with each other by vesicular traffic and MCSs, by which membranes are closely positioned and tethered, but there is no fusion. This special case of intracellular communication facilitates metabolic channeling between distinct (not homotypic) organelles. MSCs between ER and lysosomes mediate the exchange of signaling molecules, ions, metabolites, and lipids, which is important for endo-lysosome maturation and positioning (Friedman et al., 2013; Hönscher et al., 2014; Jongsma et al., 2016; Wijdeven et al., 2016). Only recently, the importance of MSCs in cell physiology was fully recognized, which has made them a focus of attention in contemporary cell biology studies (Phillips and Voeltz, 2015; Wu et al., 2018). However, studying MSCs with high spatial and temporal resolution remains a challenge because of their small size and transient and confined nature. ER-lysosome MSCs are identified as closely apposed (<20 nm) membranes over a distance of 20 nm (Scorrano et al., 2019; Huang et al., 2020). Hence, (3D) EM is essential to provide sufficient resolution to examine the presence and structure of these inter-organelle contacts. However, finding MSCs by EM is akin to seeking a needle in the haystack. We employ our targeted imaging pipeline to efficiently identify MSCs between ER and lysosomes in live cells and visualize their corresponding ultrastructure in 3D (**Figure 4**).

We started this experiment in live cells in which we imaged a single lysosome (SiRLyso) over 3 min for contact moments with ER (mEmerald-Sec61β) (**Figure 4**). In (live-cell) FM, even though the images are diffraction-limited and it is not possible to make a direct conclusion, all lysosomes appear to have contact with ER. As shown in **Figure 4A**, the targeted lysosome exhibits a diffusive movement. First, it moves toward the left following the ER tubules (**Figure 4A**, 21–98 s); then, it turns right but stops at a blockade formed by ER (**Figure 4A**, 98–103 s). After that, it turns left again and repeats this pattern (live-cell **Supplementary Video S4**). **Figures 4B,C** show the maximum intensity projection of the Z-stack. This analysis suggests that the dense ER visible on the right side of the lysosome defines a confined region for limited movement.

We then prepared the live-cell imaged cell for EM and imaged the particular lysosome-ER interaction site following our targeted imaging pipeline. This high-accuracy targeting is achieved without fiducial particles present in the targeted lysosome (**Figure 4C**). With the high confidence provided by our

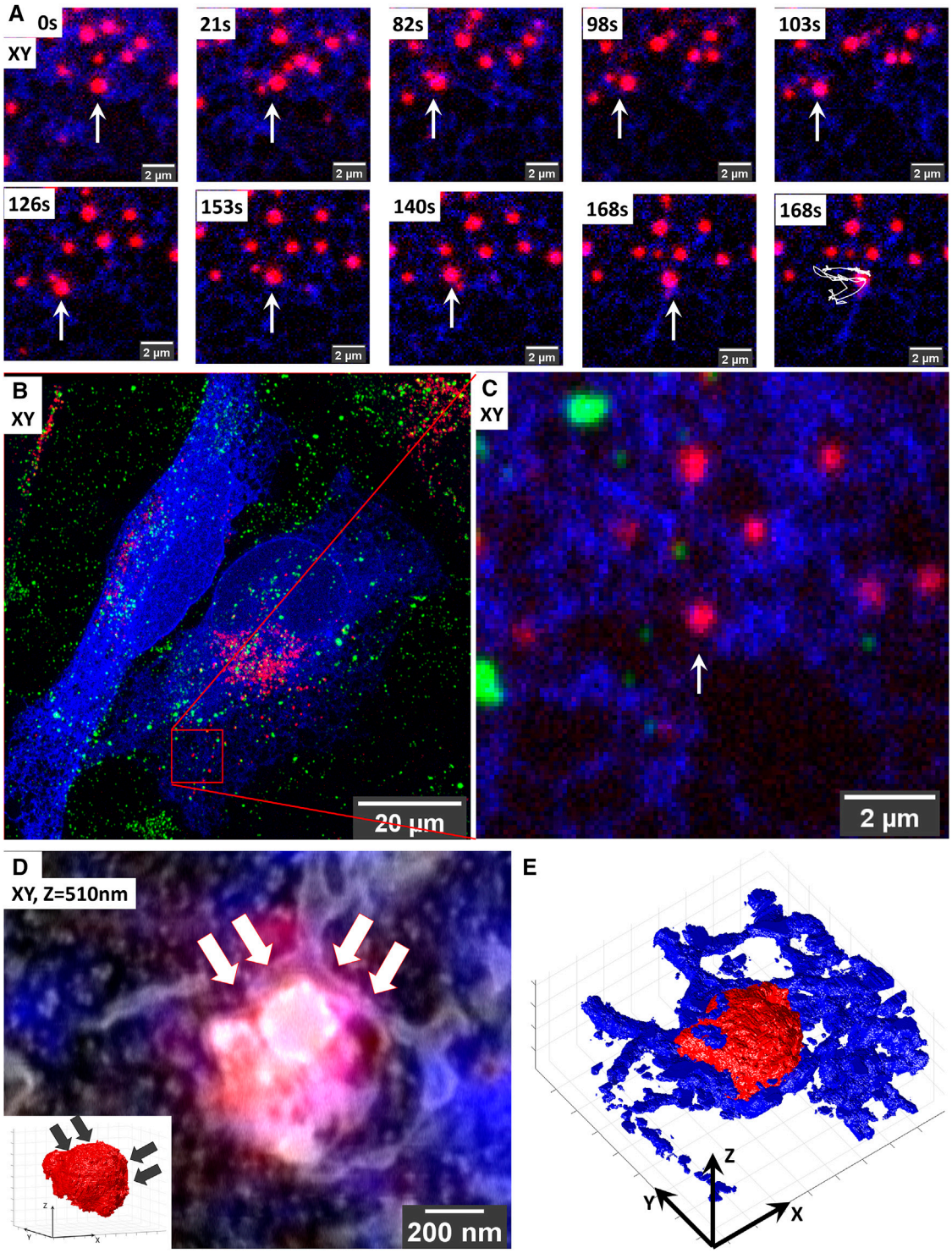

FIGURE 4 | Targeted volume-CLEM of ER-lysosome contact sites implicates ER in lysosomal motility. **(A)** Live-cell imaging of lysosome dynamics in relation to ER contacts. Lysosomes are stained with SiRLyso (red) and ER with mEmerald-Sec61β (blue). Arrow points to the lysosome targeted for imaging. At 168 s, the last image of the time-lapse panel, the dragon tail shows that the lysosome mainly follows the ER tubules and that ER contact on its right side confines its movement. **(B)** Maximum intensity projection of the CLSM stack recorded after *in situ* fixation; note the endocytic fiducial markers visible as green. **(B)** Image of entire cell indicating the imaged ROI. **(C)** Zoom-in to the ROI. **(D)** Overlay of 3D CLSM data from the fixed cell and the 3D FIB.SEM data showing the single targeted lysosome traced back after resin embedding using iCLSM/FIB.SEM. The small ROI includes the lysosome-ER contacts. Inset shows that the curvature of the lysosome surface is altered on the site of dense ER interaction indicated with arrows. **(E)** Segmentation of the lysosomes (red) and ER (blue) in the stack highlights the dense presence of ER on the right side of the lysosome.

method, we could target an ROI of only 1.7 μm wide (**Figure 4D**) and collected 3D ultrastructural data in as little as 190 min between iCSLM and FIB.SEM (with voxels of 1.7 × 1.7 × 10 nm and a dwell time of 10 μs). Note the extremely small size of the imaged ROI compared to the CLSM field of view (132.45 μm wide) (**Figures 4B,C**).

As presented in **Figure 4D**, the 3D-EM identified the targeted organelle as a lysosome with heterogeneous content, including electron-dense material and irregularly organized internal membranes (3D-overlay, **Supplementary Video S5**). Its size is 0.66 × 0.69 × 0.50 μm. Importantly, the 3D-EM data showed that, at its right side, the targeted lysosome is fully covered with the ER cisternae, which follow the limiting membrane of the lysosome, conforming to its shape (**Figure 4E**; 3D-segmentation, **Supplementary Videos S6, S7**). On its left side, we only found tips of ER cisterna touching the lysosome in a poking fashion. The ER on the left side showed a thin tubular lumen, whereas the right-sided ER, which had a blocking effect on lysosome movement, exhibits a sheet-like thicker lumen (**Figure 4D**). Interestingly, the curvature of the lysosome on the right side has a low convexity compared to its highly convex left site (inset, **Figure 4D**), indicating the role of ER contacts also on the shape and possibly composition of lysosome membrane domains. These data show that ER forms multiple types of contact sites with lysosomes, possibly with different functions, which, in addition to the exchange of biomaterials, also defines lysosomal shape and movements. With this example, we prove that our targeted CLEM approach provides a powerful tool to study MSCs from live cells to 3D EM, with high temporal and spatial resolution and a short processing time thanks to optimal ROI selection.

3.5 Volume-CLEM of Multiple Interacting Organelles Followed Over Time

Lysosomes receive input from the endocytic, autophagic, phagocytic, and trans-Golgi network pathways while they traffic throughout the cell (Saftig and Klumperman, 2009). They interact with other lysosomes and endosomes *via* kiss-and-run events or membrane fusion, resulting in the exchange of membranes and content (Huotari and Helenius, 2011; Pols et al., 2013; Jongsma et al., 2020). Although the essential features of lysosomal fusion events have been biochemically established, we do not yet comprehend the spatial and temporal regulation of these processes (Spang, 2016; Ferguson, 2018; van der Beek et al., 2019) simply because there is currently no means to analyze the ultrastructural background of multiple interacting lysosomes in an efficient way and 3D. The targeted volume-CLEM pipeline tackles this challenge by allowing analysis of interactions between multiple, dynamic organelles over time, both in live cells and by EM.

To demonstrate proof-of-principle for this application, we traced three interacting lysosomes over a period of 162 s (**Figure 5**), using the same experimental setup as in the previous experiments (lysosomes stained with SiRLyso, ER with mEmerald-Sec61β). The larger size lysosome#1 and relatively smaller lysosome#2 meet at 12 s and traffic a short range together until 65 s. At 72 s, lysosome#3 becomes visible, and all three organelles move through separate tracks between 94 and 162 s (**Figure 5A**). They all stop moving between 162 and 180 s (**Figure 5B**; see also live-cell **Supplementary Video S8**). The movement of lysosome#1 is short-ranged and diffusive, whereas the movements of lysosomes #2 and #3 are long-ranged and directional, indicating microtubule-based transport. Whether these lysosomes just interact or partially fuse during the course of live imaging is not possible to distinguish by FM. Lysosome#1 and lysosome#2 lack endocytic fiducials, whereas lysosome#3 displays a fluorescent signal from the fiducial particles (**Figure 5B**). After EM preparation, we used the position information of the fiducials to trace an extremely small volume across the cell (**Figures 5C–E**), in which we targeted three ROIs, each containing 1 identified lysosome, one by one. Each ROI is approximately 2 × 2 μm (*x*, *y*) in size (1.55 × 1.86 × 0.98 μm, 1.73 × 1.68 × 2.98 μm, and 2.16 × 2.24 × 1.24 μm exactly), and it required a little over 1 h (64, 68, and 96 min) to collect the complete FIB.SEM datasets. Therefore, within approximately 4 h, we collected three distinct FIB.SEM datasets around three targeted lysosomes that, by live-cell imaging, were seen to interact.

Upon ultrastructural examination and segmentation of the FIB.SEM data, lysosome#1 (red) was found to have a size of 0.56 × 0.56 × 0.51 μm *x*, *y*, *z*, with an asymmetrical shape, positioned at the cell rim between the ER (blue) and the plasma membrane. It had little interactions with ER (blue) (**Figure 5C**, see also 3D-overlay **Supplementary Video S9** and 3D-segmentation **Supplementary Videos S10, S11**). Lysosome#2 (red) had a diameter of 0.55 × 0.58 × 0.62 μm, with a rather spherical shape, positioned in the perinuclear region, touching the nuclear envelope and making contact with a mitochondrion (yellow) and occasional ER tubules (blue). Its luminal content with degraded membranes was comparable to lysosome#1 (**Figure 5D**, see also 3D-overlay **Supplementary Video S12**; 3D-segmentation **Supplementary Video S13**). Lastly, lysosome#3 (red) had a diameter of 0.49 × 0.53 × 0.46 μm *x*, *y*, *z*, with an almost spherical shape, positioned in mitochondria and ER-rich region so dense that the 3D representation became difficult (**Figure 5E**, see also 3D-overlay **Supplementary Video S14**; 3D-segmentation **Supplementary Video S15**). Lysosome#3 was completely surrounded by mitochondria, which may explain its block in movement between 162 and 180 s. In contrast to lysosomes #1 and #2, lysosome #3 contains less electron-dense material, multiple ILVs (arrowheads), and a single endocytic fiducial particle (arrow, bright spot), defining it as late endosome rather than lysosome.

These data show that targeted volume-CLEM provides a fast and feasible method to study time-resolved interactions between multiple organelles and with high resolution. When combined with overexpression or depletion of specific cargo or transport machinery proteins, this approach will provide a unique way to link molecular regulation to transport dynamics and organelle positioning.

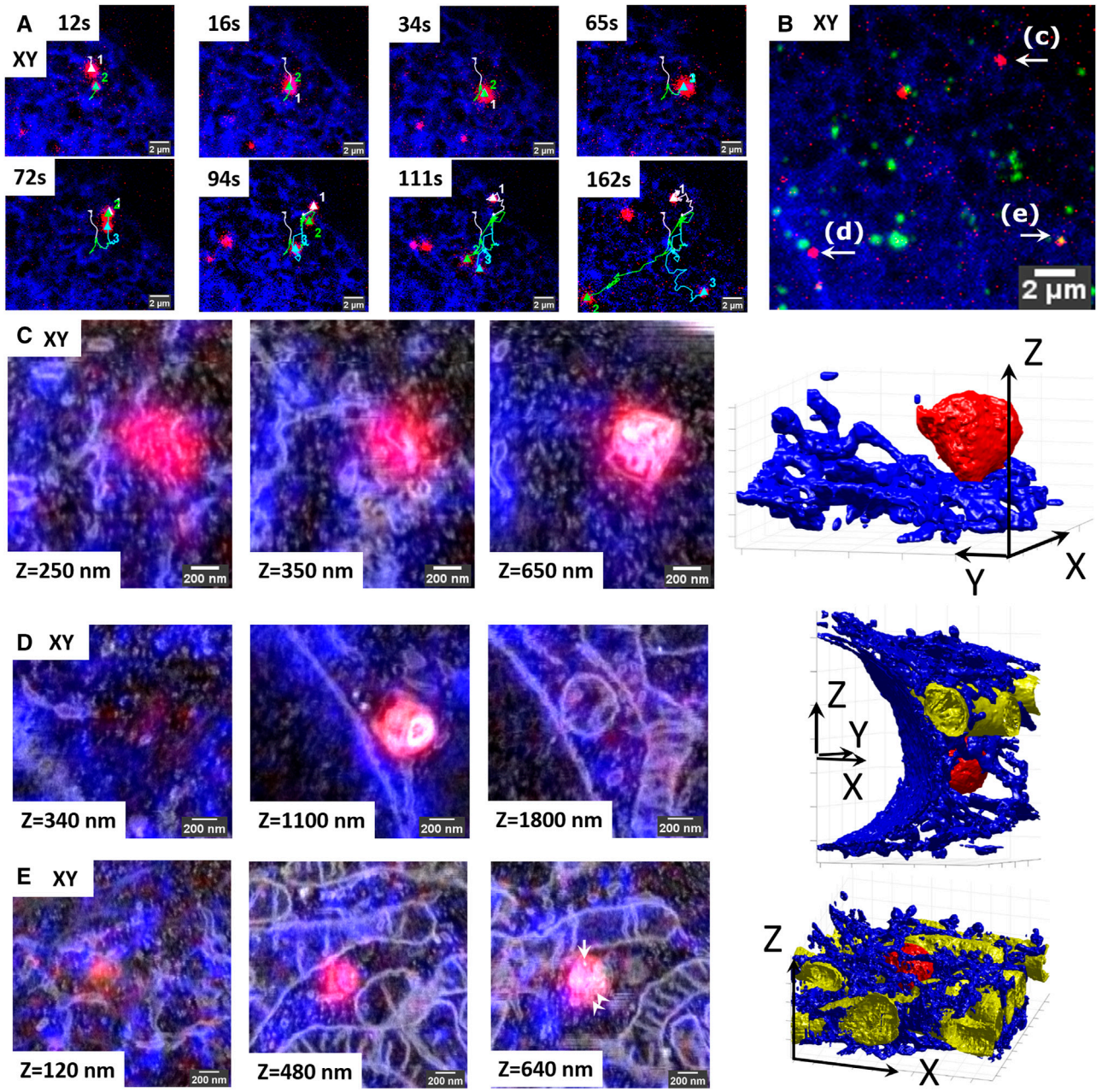

FIGURE 5 | Retracement of interacting organelles by targeted volume-CLEM. **(A)** Stills from the live-cell movie of three interacting lysosomes showing live lysosomes (SIRrLyso, red) and ER (mEmerald-Sec61β, blue). The lysosomes are initially visible as separate spots (65 s) and then split into two (72 s) and then three (94 s) spots that travel in different directions. **(B)** Maximum intensity projection of the Z-stack made after *in situ* fixation at 180 s. The Z-stack includes endocytosed fiducial particles (green). The three interacting lysosomes tracked in live-cell imaging are indicated as **(C–E)**. **(C–E)** Each lysosome is traced back for volume EM, following the targeted imaging routine. Volume-CLEM images of lysosome#1 **(C)**, lysosome#2 **(D)**, and lysosome #3 **(E)**, respectively, in 2 xy planes, showing the segmentation of the lysosomes (red), ER (blue), and mitochondria (yellow). Arrow points to the single endocytic fiducial particle, and arrowheads depict the ILVs.

4 DISCUSSION

Herein, we have established a volume-CLEM pipeline to correlate every organelle imaged in live cells to volume EM with high-throughput and high-precision. We reached this by bringing together recent developments in integrated CLEM instrumentation using an integrated CLSM-FIB.SEM, novel endocytic fiducial markers that remain fluorescent in resin embedded samples (Fokkema et al., 2018), and advances in sample preparation that minimize resin embedding (Schieber et al., 2017; van Donselaar et al., 2018). Using 3D z-stacks of endocytic fiducial particles as a 3D coordinate anchor between stand-alone CLSM and integrated CLSM platforms, we match the coordinate planes between 3D-FM and 3D-EM modalities and

identify exact coordinates for each organelle imaged in live-cell FM back in volume EM by FIB.SEM. In **Figure 2**, we show the direct correlation of live-cell imaging data of hydrolase active lysosomes and ER to volume EM data with a correlation precision far below the *x*, *y*, *z* resolution limits of the FM.

We succeeded in achieving the <100 nm sub-organelle level correlation accuracy between 3D-FM and 3D-EM datasets using only a few endocytosed fiducial particles, which function as anchor points between 3D FM and 3D EM. Importantly, correlation is not limited to organelles bearing fiducial particles. Furthermore, other fluorescence signals lost after EM embedding can be correlated to the volume EM data with high precision, using the fiducials as landmarks. Hence, we are not hindered in our EM analysis by the presence of abundant quantities of the fiducial marker. To realize this, we used Au core-silica shell particles recently developed in our labs, which preserve their fluorescence in epoxy resin (Fokkema et al., 2018). Other fiducial particles with the same properties (Kukulski et al., 2012; Takizawa et al., 2015; Han et al., 2019) are equally suited for our approach. Moreover, other fluorescent probes (Morrison et al., 2015; Paez-Segala et al., 2015; Hemelaar et al., 2017; Fu et al., 2020; Tanida et al., 2020), sample preparation routines (Peddie et al., 2014; Brama et al., 2015; Hohn et al., 2015; Andrian et al., 2020), and resins (Zhou et al., 2017) developed to retain the available fluorescence signal after EM sample preparation can be adapted and used within the here described pipeline, using fiducials as correlation anchor.

Precise correlation with *a priori* information from live-cell and confocal FM provides exact 3D coordinates of structures within the complete block and enables targeting for volume EM. In **Figure 3**, we show targeted volume-CLEM (i.e., using the FM identified coordinates to target the ROI in EM) of a single lysosome within the whole cell volume. Blind assessment of the 3D correlation accuracy showed that we could target a single point with sub-100 nm accuracy in the *x*, *y* direction and ~300 nm accuracy in the *Z* direction. Hence, an ROI identified in CLSM can be correlated, targeted, and imaged in volume EM with at least 100 nm confidence. This enables 3D EM visualization of a single organelle (e.g., the lysosome tracked in **Figure 3**) in a notably short time (~2.5 h) and directly correlating to the corresponding FM data. Also addressing homotypic organelle interactions, we investigated prolonged interactions of three lysosomes in live cells in **Figure 5**. Subsequent FIB.SEM of each three lysosomes one by one was completed in less than 4 h, highlighting the novel means that targeted volume-CLEM pipeline offers to analyze the ultrastructure of previously interacted organelles in a high throughput manner.

High-throughput volume-CLEM, including time-resolved functional imaging in live cells, opens up novel possibilities to study the regulation of rare, transient cellular processes with ultrastructural resolution. An extensive understanding of MCSs has been uncovered in the last years presented as one of our examples. In **Figure 4**, we provide the first direct evidence that ER-lysosome contacts regulate lysosome movement and shape in 3D with high temporal and spatial resolution. We analyzed the motility of a single lysosome with respect to its interactions with ER in live cells and visualized that the lysosome movements mainly follow the surrounding ER tubules. Interaction with dense (bright) ER on one (right) side seemed to obstruct its movement. Once tracked and imaged in volume EM, we showed that the non-obstructive ER at the left-side ER showed a thin tubular lumen, which only touches the lysosome. In contrast, dense ER on the obstacle-side exhibits a sheet-like thicker lumen and wraps the lysosome surface. Interestingly, the curvature of the lysosome on the ER wrapped site was much flatter than its left site (**Figure 4D**), indicating a role of ER contacts in shape and possibly composition of lysosome membrane domains. The data also confirmed the presence of multiple types of contact sites between ER and lysosomes, possibly with different functions (Garrity et al., 2016; Bonifacino and Neefjes, 2017; Fermie et al., 2018; Lim et al., 2019). Numerous proteins involved in MCSs are currently being identified, and many studies focus on addressing the role of these proteins in the spatial and temporal regulation of MCSs at the molecular level (Lim et al., 2019; Cabukusta et al., 2020; Huang et al., 2020). We believe our method, uniquely linking live-cell imaging of single organelles to ultrastructural detail, is promising to greatly accelerate understanding in temporal and structural regulation of MCSs at the system and molecular level.

Besides organelle biology, other fields of cell and developmental biology, model organism studies, and clinical studies can also benefit from our novel, targeted volume-CLEM pipeline. A specific development stage in a model organism, a specific cell within an organoid, and a certain cell cycle stage can be selected by live-cell imaging to address the ultrastructural changes in, for example, cellular differentiation, mechanisms of cellular polarization, and cytokinesis at the nanometer scale. High-precision correlation of 3D-FM and 3D-EM data will allow the use of 3D culture models (e.g., spheroids, organoids) in high-throughput volume-CLEM, which is currently far from trivial (Ando et al., 2018; Rios and Clevers, 2018).

Any fluorescence/light microscopy technique can be incorporated prior to EM sample preparation in the presented volume-CLEM pipeline. We have presented live-cell imaging and confocal FM, forming the foundation for other FM techniques. Specialized fluorescence methods to study organelle dynamics and membrane trafficking (FRAP), transient molecular interactions (FRET), and local exponential fluorescence decay rates in a sample (FLIM) can be directly incorporated within the workflow (De Los Santos et al., 2015) and also super-resolution techniques to study subcellular structures with greater temporal and/or spatial resolution (Hell et al., 2015; Schermelleh et al., 2019). The registration accuracy is currently limited by the FM resolution, and the volume-CLEM pipeline would clearly benefit from the improved lateral and axial resolution, that a super-resolution FM technique could provide (Shtengel et al., 2014; Fu et al., 2020). Similarly, the fluorescence labeling strategies can be adapted to include any types of fluorescent probes, functional reporters (as shown by SiRLyso), fluorescent proteins (as shown by mEmerald), and inorganic dyes (as shown by Rhodamine in fiducial particles). The targeted volume-CLEM pipeline is, therefore, fully flexible in terms of light microscopy approaches.

The targeted imaging strategy reported here would also be very beneficial in uniting with another exciting EM technique, cryo-electron tomography (cryo-ET) to aid cryo-CLEM workflows. These workflows include freezing the cells or tissues, first imaging them in cryo-FM to identify ROI, then transferring them to cryo-FIB.SEM to prepare lamella from the selected ROI (selected Z-plane), and then finally transferring them to the cryo-TEM to acquire the series of 2D images creating the 3D model. Even though being enormously powerful for studying cellular and molecular interactions *in situ* with unmatchable resolution, this method is very laborious, low throughput, and available to a limited number of groups in the world. The targeted imaging approach would also solve the main bottleneck also present in these approaches by increasing accuracy and throughput. Implementing a similar iCLSM in a cryo-FIB.SEM setup would assure the lamella preparation of the correct plane, bearing the ROI, for follow-up cryo-TEM imaging. This would unlock the true potential of cryo-CLEM to identify and study rare cellular processes *in situ*, with molecular resolution. Such integrated platforms are currently being commercialized (e.g., METEOR, Delmic).

Structure-function studies of (sub)cellular events require quantitative analyses, which necessitate repetitive imaging of smaller volumes from several independent samples. The targeted volume EM imaging presented herein is a powerful way to find back a small ROI within a large sample. This is especially relevant in a disruptive technique, such as FIB.SEM, and very important to unveil the true quantitative potential of volume EM, which we are just starting to fully utilize (Lucas et al., 2012; Peddie and Collinson, 2014; Hoffman et al., 2020). Another related asset of the targeted imaging approach presented here is the time and resource savings it provides. Usually, imaging a full mammalian cell with 5 nm isotropic resolution in FIB.SEM takes 5–7 days, whereas most of the cell volume does not contain relevant information on the dedicated research question. In contrast, our targeted volume-CLEM pipeline can identify, target, and image an ROI guaranteed to address the research question within 1-2 h, with high confidence. The reduced EM imaging duration saves both personnel and machine time, which is crucial for instruments such as FIB.SEMs often shared by multiple users in imaging facilities. It also considerably cuts back on the post-collection computational requirements of alignment, reconstruction, and segmentation of large 3D-EM datasets (e.g., of whole cells) and the possible correlation with the FM data, which can take as long as the experiment itself. The time for targeting, imaging, and correlation could be further shortened by integrating iCLSM and EM operating software [e.g., SBEM image (Titze et al., 2018), MAPS/Thermo Fischer, Atlas/Zeiss, ODEMIS/Delmic]. In addition, precise 3D-FM to 3D-EM correlation can facilitate automated image processing and provide ground truth for ongoing efforts on automatized segmentation of 3D-EM datasets (Xiao et al., 2018). Together, these will enable fast and user-independent quantification (e.g., volume and membrane interactions) of structures of interest in significant sample sizes.

DATA AVAILABILITY STATEMENT

The original contributions presented in the study are included in the article/**Supplementary Material**, further inquiries can be directed to the corresponding author.

AUTHOR CONTRIBUTIONS

NL, SL, JFe, HG and JK designed the study. JFe performed the cell culture, labeling, live-cell imaging, and confocal microscopy and analyzed the data with NL. JFo synthesized, characterized, and provided the endocytic fiducials. JFe and CdeH optimized and performed EM sample preparation. SL, AA, GB and HG designed and built the integrated CLSM. SL performed integrated CLSM and FIB.SEM imaging and analyzed the data with NL. SL did the 3D image correlation and segmentation and prepared the figures with NL. NL and SL wrote the paper with input from all authors. HG and JK reviewed the manuscript.

FUNDING

This work was supported by funding from Stichting voor de Technische Wetenschappen (STW), grant number 12715, granted to HG and JK. NL also acknowledges the Netherlands Organization for Scientific Research (NWO) for an ZonMW-TOP grant (91216006) awarded to JK. The authors also acknowledge NWO roadmap grant, The Netherlands Electron Microscopy Infrastructure (NEMI) chaired by JK.

SUPPLEMENTARY MATERIAL

The Supplementary Material for this article can be found online at: https://www.frontiersin.org/articles/10.3389/fcell.2022.829545/full#supplementary-material

REFERENCES

Ando, T., Bhamidimarri, S. P., Brending, N., Colin-York, H., Collinson, L., De Jonge, N., et al. (2018). The 2018 Correlative Microscopy Techniques Roadmap. *J. Phys. D: Appl. Phys.* 51, 443001. doi:10.1088/1361-6463/aad055

Andrian, T., Bakkum, T., van Elsland, D. M., Bos, E., Koster, A. J., Albertazzi, L., et al. (2020). Super-resolution Correlative Light-Electron Microscopy Using a Click-Chemistry Approach for Studying Intracellular Trafficking. *Methods Cel Biol.* 162, 303–331. doi:10.1016/bs.mcb.2020.09.001

Ballabio, A., and Bonifacino, J. S. (2019). Lysosomes as Dynamic Regulators of Cell and Organismal Homeostasis. *Nat. Rev. Mol. Cel Biol.* 21, 101–118. doi:10.1038/s41580-019-0185-4

Blazques-Llorca, L., Hummel, E., Zou, C., Burgold, S., Rietdorf, J., and Herms, J. (2015). Correlation of Two-Photon *In Vivo* Imaging and FIB/SEM Microscopy. *J. Microsc.* 259, 129–136. doi:10.1111/jmi.12231

Bonifacino, J. S., and Neefjes, J. (2017). Moving and Positioning the Endolysosomal System. *Curr. Opin. Cel Biol.* 47, 1–8. doi:10.1016/j.ceb.2017.01.008

Brama, E., Peddie, C. J., Jones, M. L., Domart, M. C., Snetkov, X., Way, M., et al. (2015). Standard Fluorescent Proteins as Dual-Modality Probes for Correlative Experiments in an Integrated Light and Electron Microscope. *J. Chem. Biol.* 8, 179–188. doi:10.1007/s12154-015-0143-3

Brama, E., Peddie, C. J., Wilkes, G., Gu, Y., Collinson, L. M., and Jones, M. L. (2016). miniLM: ultraLM and miniLM: Locator Tools for Smart Tracking of Fluorescent Cells in Correlative Light and Electron Microscopy. *Wellcome Open Res.* 1, 26. doi:10.12688/wellcomeopenres.10299.1

Burel, A., Lavault, M. T., Chevalier, C., Gnaegi, H., Prigent, S., Mucciolo, A., et al. (2018). A Targeted 3D EM and Correlative Microscopy Method Using SEM Array Tomography. *Development* 145, dev160879. doi:10.1242/dev.160879

Bushby, A. J., P'ng, K. M. Y., Young, R. D., Pinali, C., Knupp, C., and Quantock, A. J. (2011). Imaging Three-Dimensional Tissue Architectures by Focused Ion Beam Scanning Electron Microscopy. *Nat. Protoc.* 6, 845–858. doi:10.1038/nprot.2011.332

Butkevich, A. N., Lukinavičius, G., D'Este, E., and Hell, S. W. (2017). Cell-Permeant Large Stokes Shift Dyes for Transfection-free Multicolor Nanoscopy. *J. Am. Chem. Soc.* 139, 12378–12381. doi:10.1021/jacs.7b06412

Cabukusta, B., Berlin, I., van Elsland, D. M., Forkink, I., Spits, M., de Jong, A. W. M., et al. (2020). Human VAPome Analysis Reveals MOSPD1 and MOSPD3 as Membrane Contact Site Proteins Interacting with FFAT-Related FFNT Motifs. *Cell Rep* 33, 108475. doi:10.1016/j.celrep.2020.108475

Cabukusta, B., and Neefjes, J. (2018). Mechanisms of Lysosomal Positioning and Movement. *Traffic* 19, 761–769. doi:10.1111/tra.12587

Collinson, L. M., Carroll, E. C., and Hoogenboom, J. P. (2017). Correlating 3D Light to 3D Electron Microscopy for Systems Biology. *Curr. Opin. Biomed. Eng.* 3, 49–55. doi:10.1016/j.cobme.2017.10.006

Collman, F., Buchanan, J., Phend, K. D., Micheva, K. D., Weinberg, R. J., and Smith, S. J. (2015). Mapping Synapses by Conjugate Light-Electron Array Tomography. *J. Neurosci.* 35, 5792–5807. doi:10.1523/jneurosci.4274-14.2015

De Los Santos, C., Chang, C.-W., Mycek, M.-A., and Cardullo, R. A. (2015). FRAP, FLIM and FRET: Detection and Analysis of Cellular Dynamics on a Molecular Scale Using Fluorescence Microscopy. *Mol. Reprod. Dev.* 82, 587–604. doi:10.1002/mrd.22501

Delpiano, J., Pizarro, L., Peddie, C. J., Jones, M. L., Griffin, L. D., and Collinson, L. M. (2018). Automated Detection of Fluorescent Cells in In-Resin Fluorescence Sections for Integrated Light and Electron Microscopy. *J. Microsc.* 271, 109–119. doi:10.1111/jmi.12700

Denk, W., and Horstmann, H. (2004). Serial Block-Face Scanning Electron Microscopy to Reconstruct Three-Dimensional Tissue Nanostructure. *Plos Biol.* 2, e329. doi:10.1371/journal.pbio.0020329

Fang, T., Lu, X., Berger, D., Gmeiner, C., Cho, J., Schalek, R., et al. (2018). Nanobody Immunostaining for Correlated Light and Electron Microscopy with Preservation of Ultrastructure. *Nat. Methods* 15, 1029–1032. doi:10.1038/s41592-018-0177-x

Ferguson, S. M. (2018). Axonal Transport and Maturation of Lysosomes. *Curr. Opin. Neurobiol.* 51, 45–51. doi:10.1016/j.conb.2018.02.020

Ferguson, S. M. (2019). Neuronal Lysosomes. *Neurosci. Lett.* 697, 1–9. doi:10.1016/j.neulet.2018.04.005

Fermie, J., Liv, N., ten Brink, C., van Donselaar, E. G., Müller, W. H., Schieber, N. L., et al. (2018). Single Organelle Dynamics Linked to 3D Structure by Correlative Live-Cell - 3D Electron Microscopy. *Traffic* 19, 354–369. doi:10.1111/tra.12557

Fokkema, J., Fermie, J., Liv, N., van den Heuvel, D. J., Konings, T. O. M., Blab, G. A., et al. (2018). Fluorescently Labelled Silica Coated Gold Nanoparticles as Fiducial Markers for Correlative Light and Electron Microscopy. *Sci. Rep.* 8, 13625. doi:10.1038/s41598-018-31836-1

Friedman, J. R., Dibenedetto, J. R., West, M., Rowland, A. A., and Voeltz, G. K. (2013). Endoplasmic Reticulum-Endosome Contact Increases as Endosomes Traffic and Mature. *MBoC* 24, 1030–1040. doi:10.1091/mbc.e12-10-0733

Fu, Z., Peng, D., Zhang, M., Xue, F., Zhang, R., He, W., et al. (2020). mEosEM Withstands Osmium Staining and Epon Embedding for Super-resolution CLEM. *Nat. Methods* 17, 55–58. doi:10.1038/s41592-019-0613-6

Garrity, A. G., Wang, W., Collier, C. M. D., Levey, S. A., Gao, Q., and Xu, H. (2016). The Endoplasmic Reticulum, Not the pH Gradient, Drives Calcium Refilling of Lysosomes. *Elife* 5, e15887. doi:10.7554/eLife.15887

Gatta, A. T., and Levine, T. P. (2016). Piecing Together the Patchwork of Contact Sites. *Trends Cel Biol* 20, 359–366. doi:10.1016/j.tcb.2016.08.010

Gorelick, S., Buckley, G., Gervinskas, G., Johnson, T. K., Handley, A., Caggiano, M. P., et al. (2019). PIE-scope, Integrated Cryo-Correlative Light and FIB/SEM Microscopy. *Elife* 8, e45919. doi:10.7554/eLife.45919

Han, S., Raabe, M., Hodgson, L., Mantell, J., Verkade, P., Lasser, T., et al. (2019). High-Contrast Imaging of Nanodiamonds in Cells by Energy Filtered and Correlative Light-Electron Microscopy: Toward a Quantitative Nanoparticle-Cell Analysis. *Nano Lett.* 19, 2178–2185. doi:10.1021/acs.nanolett.9b00752

Hell, S. W., Sahl, S. J., Bates, M., Zhuang, X., Heintzmann, R., Booth, M. J., et al. (2015). The 2015 Super-resolution Microscopy Roadmap. *J. Phys. D. Appl. Phys.* 48, 443001. doi:10.1088/0022-3727/48/44/443001

Hemelaar, S. R., de Boer, P., Chipaux, M., Zuidema, W., Hamoh, T., Martinez, F. P., et al. (2017). Nanodiamonds as Multi-Purpose Labels for Microscopy. *Sci. Rep.* 7, 720. doi:10.1038/s41598-017-00797-2

Heymann, J. A. W., Hayles, M., Gestmann, I., Giannuzzi, L. A., Lich, B., and Subramaniam, S. (2006). Site-specific 3D Imaging of Cells and Tissues with a Dual Beam Microscope. *J. Struct. Biol.* 155, 63–73. doi:10.1016/j.jsb.2006.03.006

Hoffman, D. P., Shtengel, G., Xu, C. S., Campbell, K. R., Freeman, M., Wang, L., et al. (2020). Correlative Three-Dimensional Super-resolution and Block-Face Electron Microscopy of Whole Vitreously Frozen Cells. *Science* 367, eaaz5357. doi:10.1126/science.aaz5357

Hohn, K., Fuchs, J., Frober, A., Kirmse, R., Anders-Össwein, M., Walter, P., et al. (2015). Preservation of Protein Fluorescence in Embedded Human Dendritic Cells for Targeted 3D Light and Electron Microscopy. *J. Microsc.* 259, 121–128. doi:10.1111/jmi.12230

Hönscher, C., Mari, M., Auffarth, K., Bohnert, M., Griffith, J., Geerts, W., et al. (2014). Cellular Metabolism Regulates Contact Sites between Vacuoles and Mitochondria. *Dev. Cel* 30, 86–94. doi:10.1016/j.devcel.2014.06.006

Huang, X., Jiang, C., Yu, L., and Yang, A. (2020). Current and Emerging Approaches for Studying Inter-organelle Membrane Contact Sites. *Front. Cel Dev. Biol.* 8, 195. doi:10.3389/fcell.2020.00195

Huotari, J., and Helenius, A. (2011). Endosome Maturation. *EMBO J.* 30, 3481–3500. doi:10.1038/emboj.2011.286

Jongsma, M. L., Bakker, J., Cabukusta, B., Liv, N., van Elsland, D., Fermie, J., et al. (2020). SKIP-HOPS Recruits TBC1D15 for a Rab7-To-Arl8b Identity Switch to Control Late Endosome Transport. *EMBO J.* 39, e102301. doi:10.15252/embj.2019102301

Jongsma, M. L. M., Berlin, I., Wijdeven, R. H. M., Janssen, L., Janssen, G. M. C., Garstka, M. A., et al. (2016). An ER-Associated Pathway Defines Endosomal Architecture for Controlled Cargo Transport. *Cell* 166, 152–166. doi:10.1016/j.cell.2016.05.078

Keene, D. R., Tufa, S. F., Lunstrum, G. P., Holden, P., and Horton, W. A. (2008). Confocal/TEM Overlay Microscopy: a Simple Method for Correlating Confocal and Electron Microscopy of Cells Expressing GFP/YFP Fusion Proteins. *Microsc. Microanal.* 14, 342–348. doi:10.1017/s1431927608080306

Kizilyaprak, C., Bittermann, A. G., Daraspe, J., and Humbel, B. M. (2014). FIB-SEM Tomography in Biology. *Methods Mol. Biol.* 1117, 541–558. doi:10.1007/978-1-62703-776-1_24

Knott, G., Marchman, H., Wall, D., and Lich, B. (2008). Serial Section Scanning Electron Microscopy of Adult Brain Tissue Using Focused Ion Beam Milling. *J. Neurosci.* 28, 2959–2964. doi:10.1523/jneurosci.3189-07.2008

Knott, G., Rosset, S., and Cantoni, M. (2011). Focussed Ion Beam Milling and Scanning Electron Microscopy of Brain Tissue. *JoVE* 1, 2588. doi:10.3791/2588

Koning, R. I., Raja, A. S., Lane, R. I., Koster, A. J., and Hoogenboom, J. P. (2019). "Integrated Light and Electron Microscopy," in *Correlative Imaging* (Wiley), 119–135. doi:10.1002/9781119086420.ch7

Kukulski, W., Schorb, M., Welsch, S., Picco, A., Kaksonen, M., and Briggs, J. a. G. (2012). Precise, Correlated Fluorescence Microscopy and Electron Tomography of Lowicryl Sections Using Fluorescent Fiducial Markers. *Methods Cel. Biol.* 111, 235–257. doi:10.1016/b978-0-12-416026-2.00013-3

Lane, R., de Boer, P., Giepmans, B. N. G., and Hoogenboom, J. P. (2019). Integrated Array Tomography for High Throughput Electron Microscopy. *Microsc. Microanal.* 25, 1038–1039. doi:10.1017/s1431927619005920

Lim, C. Y., Davis, O. B., Shin, H. R., Zhang, J., Berdan, C. A., Jiang, X., et al. (2019). ER–lysosome Contacts Enable Cholesterol Sensing by mTORC1 and Drive Aberrant Growth Signalling in Niemann–Pick Type C. *Nat. Cel Biol.* 21, 1206–1218. doi:10.1038/s41556-019-0391-5

Liv, N., Zonnevylle, A. C., Narvaez, A. C., Effting, A. P. J., Voorneveld, P. W., Lucas, M. S., et al. (2013). Simultaneous Correlative Scanning Electron and High-NA Fluorescence Microscopy. *PLoS One* 8, e55707. doi:10.1371/journal.pone.0055707

Lucas, M. S., Günthert, M., Gasser, P., Lucas, F., and Wepf, R. (2012). Bridging Microscopes. *Methods Cel Biol* 111, 325–356. doi:10.1016/b978-0-12-416026-2.00017-0

Lukinavičius, G., Reymond, L., Umezawa, K., Sallin, O., D'Este, E., Göttfert, F., et al. (2016). Fluorogenic Probes for Multicolor Imaging in Living Cells. *J. Am. Chem. Soc.* 138, 9365–9368. doi:10.1021/jacs.6b04782

Meel, E., and Klumperman, J. (2008). Imaging and Imagination: Understanding the Endo-Lysosomal System. *Histochem. Cel Biol.* 129, 253–266. doi:10.1007/s00418-008-0384-0

Micheva, K. D., and Smith, S. J. (2007). Array Tomography: A New Tool for Imaging the Molecular Architecture and Ultrastructure of Neural Circuits. *Neuron* 55, 25–36. doi:10.1016/j.neuron.2007.06.014

Mohammadian, S., Fokkema, J., Agronskaia, A. V., Liv, N., de Heus, C., van Donselaar, E., et al. (2019). High Accuracy, Fiducial Marker-Based Image Registration of Correlative Microscopy Images. *Sci. Rep.* 9, 3211. doi:10.1038/s41598-019-40098-4

Morrison, I. E. G., Samilian, A., Coppo, P., Ireland, T. G., Fern, G. R., Silver, J., et al. (2015). Multicolour Correlative Imaging Using Phosphor Probes. *J. Chem. Biol.* 8, 169–177. doi:10.1007/s12154-015-0141-5

Narayan, K., Danielson, C. M., Lagarec, K., Lowekamp, B. C., Coffman, P., Laquerre, A., et al. (2014). Multi-resolution Correlative Focused Ion Beam Scanning Electron Microscopy: Applications to Cell Biology. *J. Struct. Biol.* 185, 278–284. doi:10.1016/j.jsb.2013.11.008

Nixon-Abell, J., Obara, C. J., Weigel, A. V., Li, D., Legant, W. R., Xu, C. S., et al. (2016). Increased Spatiotemporal Resolution Reveals Highly Dynamic Dense Tubular Matrices in the Peripheral ER. *Science* 354, aaf3928. doi:10.1126/science.aaf3928

Oberti, D., Kirschmann, M. A., and Hahnloser, R. H. (2011). Projection Neuron Circuits Resolved Using Correlative Array Tomography. *Front. Neurosci.* 5, 50–58. doi:10.3389/fnins.2011.00050

Paez-Segala, M. G., Sun, M. G., Shtengel, G., Viswanathan, S., Baird, M. A., Macklin, J. J., et al. (2015). Fixation-resistant Photoactivatable Fluorescent Proteins for CLEM. *Nat. Methods* 12, 215–218. doi:10.1038/nmeth.3225

Peddie, C. J., and Collinson, L. M. (2014). Exploring the Third Dimension: Volume Electron Microscopy Comes of Age. *Micron* 61, 9–19. doi:10.1016/j.micron.2014.01.009

Peddie, C. J., Liv, N., Hoogenboom, J. P., and Collinson, L. M. (2014). Integrated Light and Scanning Electron Microscopy of GFP-Expressing Cells. *Methods Cel Biol.* 124, 363–389. doi:10.1016/B978-0-12-801075-4.00017-3

Phillips, M. J., and Voeltz, G. K. (2015). Structure and Function of ER Membrane Contact Sites with Other Organelles. *Nat. Rev. Mol. Cel Biol.* 17, 69–82. doi:10.1038/nrm.2015.8

Pols, M. S., Ten Brink, C., Gosavi, P., Oorschot, V., and Klumperman, J. (2013). The HOPS Proteins hVps41 and hVps39 Are Required for Homotypic and Heterotypic Late Endosome Fusion. *Traffic* 14, 219–232. doi:10.1111/tra.12027

Prabhakar, N., Belevich, I., Peurla, M., Heiligenstein, X., Chang, H.-C., Sahlgren, C., et al. (2020). Cell Volume (3D) Correlative Microscopy Facilitated by Intracellular Fluorescent Nanodiamonds as Multi-Modal Probes. *Nanomaterials* 11, 14. doi:10.3390/nano11010014

Rios, A. C., and Clevers, H. (2018). Imaging Organoids: A Bright Future Ahead. *Nat. Methods* 15, 24–26. doi:10.1038/nmeth.4537

Ronchi, P., Machado, P., D'Imprima, E., Mizzon, G., Best, B. T., Cassella, L., et al. (2021). Fluorescence-based 3D Targeting of FIB-SEM Acquisition of Small Volumes in Large Samples. *bioRxiv* 1, 427072. doi:10.1101/2021.01.18.427072

Russell, M. R. G., Lerner, T. R., Burden, J. J., Nkwe, D. O., Pelchen-Matthews, A., Domart, M.-C., et al. (2016). 3D Correlative Light and Electron Microscopy of Cultured Cells Using Serial Blockface Scanning Electron Microscopy. *J. Cel Sci. jcs.* 130, 188433. doi:10.1242/jcs.188433

Saalfeld, S., Cardona, A., Hartenstein, V., and Tomančák, P. (2010). As-rigid-as-possible Mosaicking and Serial Section Registration of Large ssTEM Datasets. *Bioinformatics* 26, i57–63. doi:10.1093/bioinformatics/btq219

Saftig, P., and Klumperman, J. (2009). Lysosome Biogenesis and Lysosomal Membrane Proteins: Trafficking Meets Function. *Nat. Rev. Mol. Cel Biol.* 10, 623–635. doi:10.1038/nrm2745

Schermelleh, L., Ferrand, A., Huser, T., Eggeling, C., Sauer, M., Biehlmaier, O., et al. (2019). Super-resolution Microscopy Demystified. *Nat. Cel Biol.* 21, 72–84. doi:10.1038/s41556-018-0251-8

Schieber, N. L., Machado, P., Markert, S. M., Stigloher, C., Schwab, Y., and Steyer, A. M. (2017). Minimal Resin Embedding of Multicellular Specimens for Targeted FIB-SEM Imaging. *Methods Cel Biol.* 140, 69–83. doi:10.1016/bs.mcb.2017.03.005

Scorrano, L., De Matteis, M. A., Emr, S., Giordano, F., Hajnóczky, G., Kornmann, B., et al. (2019). Coming Together to Define Membrane Contact Sites. *Nat. Commun.* 10, 1–11. doi:10.1038/s41467-019-09253-3

Shtengel, G., Wang, Y., Zhang, Z., Goh, W. I., Hess, H. F., and Kanchanawong, P. (2014). Imaging Cellular Ultrastructure by PALM, iPALM, and Correlative iPALM-EM. *Methods Cel Biol.* 123, 273–294. doi:10.1016/b978-0-12-420138-5.00015-x

Sironi, L., Restelli, L. M., Tolnay, M., Neutzner, A., and Frank, S. (2020). Dysregulated Interorganellar Crosstalk of Mitochondria in the Pathogenesis of Parkinson's Disease. *Cells* 9, 233. doi:10.3390/cells9010233

Spang, A. (2016). Membrane Tethering Complexes in the Endosomal System. *Front. Cel Dev. Biol.* 4, 35. doi:10.3389/fcell.2016.00035

Takizawa, T., Powell, R. D., Hainfeld, J. F., and Robinson, J. M. (2015). FluoroNanogold: an Important Probe for Correlative Microscopy. *J. Chem. Biol.* 8, 129–142. doi:10.1007/s12154-015-0145-1

Tanida, I., Kakuta, S., Oliva Trejo, J. A., and Uchiyama, Y. (2020). Visualization of Cytoplasmic Organelles via In-Resin CLEM Using an Osmium-Resistant Far-Red Protein. *Sci. Rep.* 10, 11314. doi:10.1038/s41598-020-68191-z

Timmermans, F. J., Liszka, B., Lenferink, A. T. M., van Wolferen, H. A. G. M., and Otto, C. (2016). Integration of Correlative Raman Microscopy in a Dualbeam FIB SEM. *J. Raman Spectrosc.* 47, 956–962. doi:10.1002/jrs.4931

Titze, B., Genoud, C., and Friedrich, R. W. (2018). SBEMimage: Versatile Acquisition Control Software for Serial Block-Face Electron Microscopy. *Front. Neural Circuits* 12, 54. doi:10.3389/fncir.2018.00054

van der Beek, J., Jonker, C., van der Welle, R., Liv, N., and Klumperman, J. (2019). CORVET, CHEVI and HOPS - Multisubunit Tethers of the Endo-Lysosomal System in Health and Disease. *J. Cel Sci.* 132, jcs189134. doi:10.1242/jcs.189134

van Donselaar, E. G., Dorresteijn, B., Popov-čeleketić, D., Van De Wetering, W. J., Verrips, T. C., Boekhout, T., et al. (2018). Extremely Thin Layer Plastification for Focused-Ion Beam Scanning Electron Microscopy: an Improved Method to Study Cell Surfaces and Organelles of Cultured Cells. *J. Microsc.* 270, 359–373. doi:10.1111/jmi.12694

Weber, I. (2003). [2] Reflection Interference Contrast Microscopy. *Methods Enzymol.* 361, 34–47. doi:10.1016/S0076-6879(03)61004-9

Wijdeven, R. H., Janssen, H., Nahidiazar, L., Janssen, L., Jalink, K., Berlin, I., et al. (2016). Cholesterol and ORP1L-Mediated ER Contact Sites Control Autophagosome Transport and Fusion with the Endocytic Pathway. *Nat. Commun.* 7, 11808. doi:10.1038/ncomms11808

Wong, Y. C., Kim, S., Peng, W., and Krainc, D. (2019). Regulation and Function of Mitochondria-Lysosome Membrane Contact Sites in Cellular Homeostasis. *Trends Cel Biol.* 29, 500–513. doi:10.1016/j.tcb.2019.02.004

Wu, H., Carvalho, P., and Voeltz, G. K. (2018). Here, There, and Everywhere: The Importance of ER Membrane Contact Sites. *Science* 361, eaan5835. doi:10.1126/science.aan5835

Xiao, C., Chen, X., Li, W., Li, L., Wang, L., Xie, Q., et al. (2018). Automatic Mitochondria Segmentation for EM Data Using a 3D Supervised Convolutional Network. *Front. Neuroanat.* 12, 92. doi:10.3389/fnana.2018.00092

Zhou, H., Gang, Y., Chen, S., Wang, Y., and Xiong, Y. (2017). Development of a Neutral Embedding Resin for Optical Imaging of Fluorescently Labeled Biological Tissue. *J. Biomed. Opt.* 22, 1. doi:10.1117/1.jbo.22.10.106015

Conflict of Interest: The authors declare that the research was conducted in the absence of any commercial or financial relationships that could be construed as a potential conflict of interest.

frontiers | Frontiers in Cell and Developmental Biology

ORIGINAL RESEARCH
published: 17 May 2022
doi: 10.3389/fcell.2022.819571

Investigating the Role of Spermidine in a Model System of Alzheimer's Disease Using Correlative Microscopy and Super-resolution Techniques

D. Lumkwana[1], C. Peddie[2], J. Kriel[3], L. L. Michie[4], N. Heathcote[4], L. Collinson[2], C. Kinnear[5] and B. Loos[4]*

[1]Microscopy and Imaging Translational Technology Platform, Cancer Research UK, University College London, London, United Kingdom, [2]Science Technology Platform, Electron Microscopy, Francis Crick Institute, London, United Kingdom, [3]Central Analytical Facilities, Electron Microscopy Unit, Stellenbosch University, Stellenbosch, South Africa, [4]Department of Physiological Sciences, Stellenbosch University, Stellenbosch, South Africa, [5]DST/NRF Centre of Excellence in Biomedical Tuberculosis Research, SAMRC Centre for Tuberculosis Research, Division of Molecular Biology and Human Genetics, Faculty of Medicine and Health Sciences, Stellenbosch University, Cape Town, South Africa

OPEN ACCESS

Edited by:
Saskia Lippens, Vlaams Instituut voor Biotechnologie, Belgium

Reviewed by:
Charlotte Melia, University of Oxford, United Kingdom
Anna Steyer, European Molecular Biology Laboratory Heidelberg, Germany
Olivier Urwyler, University of Zurich, Switzerland

***Correspondence:**
D. Lumkwana
d.lumkwana@ucl.ac.uk

Specialty section:
This article was submitted to Cell Death and Survival, a section of the journal Frontiers in Cell and Developmental Biology

Received: *21 November 2021*
Accepted: *07 April 2022*
Published: *17 May 2022*

Citation:
Lumkwana D, Peddie C, Kriel J, Michie LL, Heathcote N, Collinson L, Kinnear C and Loos B (2022) Investigating the Role of Spermidine in a Model System of Alzheimer's Disease Using Correlative Microscopy and Super-resolution Techniques. Front. Cell Dev. Biol. 10:819571. doi: 10.3389/fcell.2022.819571

Background: Spermidine has recently received major attention for its potential therapeutic benefits in the context of neurodegeneration, cancer, and aging. However, it is unclear whether concentration dependencies of spermidine exist, to differentially enhance autophagic flux. Moreover, the relationship between low or high autophagy activity relative to basal neuronal autophagy flux and subsequent protein clearance as well as cellular toxicity has remained largely unclear.

Methods: Here, we used high-resolution imaging and biochemical techniques to investigate the effects of a low and of a high concentration of spermidine on autophagic flux, neuronal toxicity, and protein clearance in *in vitro* models of paraquat (PQ) induced neuronal toxicity and amyloid precursor protein (APP) overexpression, as well as in an *in vivo* model of PQ-induced rodent brain injury.

Results: Our results reveal that spermidine induces autophagic flux in a concentration-dependent manner, however the detectable change in the autophagy response critically depends on the specificity and sensitivity of the method employed. By using correlative imaging techniques through Super-Resolution Structured Illumination Microscopy (SR-SIM) and Focused Ion Beam Scanning Electron Microscopy (FIB-SEM), we demonstrate that spermidine at a low concentration induces autophagosome formation capable of large volume clearance. In addition, we provide evidence of distinct, context-dependent protective roles of spermidine in models of Alzheimer's disease. In an *in vitro* environment, a low concentration of spermidine protected against PQ-induced toxicity, while both low and high concentrations provided protection against cytotoxicity induced by APP overexpression. In the *in vivo* scenario, we demonstrate brain region-specific susceptibility to PQ-induced neuronal toxicity, with the hippocampus being highly susceptible compared to the cortex. Regardless of this, spermidine administered at both low and high dosages protected against paraquat-induced toxicity.

Conclusions: Taken together, our results demonstrate that firstly, administration of spermidine may present a favourable therapeutic strategy for the treatment of Alzheimer's disease and secondly, that concentration and dosage-dependent precision autophagy flux screening may be more critical for optimal autophagy and cell death control than previously thought.

Keywords: spermidine, autophagy, Alzheimer's disease, correlative light and electron microscopy, super-resolution structured illumination, direct stochastic optical reconstruction microscopy, focused ion beam scanning electron microscopy

1 INTRODUCTION

Alzheimer's disease (AD), the leading cause of dementia in the elderly (Andrieu et al., 2015), is characterised by a progressive loss of synapses and neurons in specific brain regions, such as the hippocampus and the cerebral cortex, leading to impaired cognitive function (Zare-Shahabadi et al., 2015). AD neuropathology is underpinned by two molecular hallmarks; intracellular neurofibrillary tangles (NFTs) composed of hyper-phosphorylated Tau and extracellular amyloid beta (Aβ) plaques, composed of Aβ peptides derived from the amyloid precursor protein (APP) (Nixon and Yang, 2011; Cai et al., 2012). Accumulation of toxic Aβ peptide due to increased APP cleavage or decreased Aβ degradation has been shown to be an early event in AD progression (Selkoe and Hardy, 2016). Thus, in addition to current therapeutic approaches which include the targeting of acetylcholine breakdown and glutamate production (Folch et al., 2016), enhancing the clearance of aggregate prone proteins such as Aβ and tau has received increasing attention (Galluzzi et al., 2017; Panda et al., 2019). One of the key pathways engaged in the clearance of long-lived and aggregate-prone proteins as well as damaged cytoplasmic organelles within eukaryotic cells is autophagy (Cui et al., 2016). Cargo to be degraded is initially recruited to a phagophore, which elongates to form an autophagosome, that matures, closes, and subsequently fuses with a lysosome to form an autolysosome where hydrolytic degradation takes place (Levine and Kroemer, 2008; Cai et al., 2012; Amaravadi et al., 2019). Importantly, autophagy dysfunction is highly implicated in the onset of neurodegenerative diseases (Hara et al., 2006; Komatsu et al., 2006; Lumkwana et al., 2017). The rate of protein degradation through the entire autophagy pathway, i.e., autophagic flux (Loos et al., 2014; Klionsky et al., 2016), and its precision control has received major attention as its decline is associated with cellular toxicity, degeneration, and aging (du Toit et al., 2018a). As a result, a major focus has been spent on identifying safe and effective pharmacological agents that can induce autophagy to effectively target key aspects of the molecular pathology in AD and other neurodegenerative diseases (Rubinsztein et al., 2012; Rubinsztein et al., 2015; Galluzzi et al., 2017; Menzies et al., 2017; Panda et al., 2019).

Spermidine is a naturally occurring polyamine that is produced from putrescine or a breakdown from spermine (Madeo et al., 2018). It is present in mammalian cells where its intracellular levels decline with aging (Eisenberg et al., 2009; Pucciarelli et al., 2012; Gupta et al., 2013). Studies revealed that dietary supplementation of spermidine in mice and humans increases blood polyamine concentrations (Soda et al., 2009; Soda et al., 2013). Importantly, several studies *in vitro* and *in vivo* have demonstrated that spermidine extends lifespan in an autophagy-dependent manner (Morselli et al., 2011; Minois et al., 2012; Minois et al., 2014; Pietrocola et al., 2015; Eisenberg et al., 2016; García-Prat et al., 2016) reducing aggregate prone proteins associated with neurodegeneration (Büttner et al., 2014; Wang et al., 2012). Moreover, the ability of spermidine to reduce oxidative stress and inflammation, to improve memory (Wirth et al., 2018; Wirth et al., 2019), mitochondrial function and health (Eisenberg et al., 2016; Qi et al., 2016; Fan et al., 2017), while preventing age-induced memory impairment (Gupta et al., 2013), highlights its potential use in the treatment of neurodegenerative diseases.

Although spermidine enhances autophagy and clears aggregate-prone proteins associated with neurodegeneration, the exact relationship between its concentration and the resulting effect on autophagy activity as well as protein clearance remains unclear. Moreover, whether a concentration-dependent effect on autophagy activity exists, that would result in a defined, yet distinguishable heightened autophagy flux that impacts neuronal toxicity favourably remains poorly understood. This contributes to the challenge of modulating autophagy with high precision and translational benefit (Loos et al., 2020). Hence, in this study, we examined the effect of a low and of a high concentration of spermidine on autophagic flux, by carefully dissecting autophagosome and autolysosome pool size, autophagosome flux, transition time, autophagosome volume and size. In addition, we assessed the impact of a low and of a high concentration of spermidine on AD-related neuropathology, autophagic activity, APP cluster clearance and microtubule acetylation, employing single molecule and correlative microscopy techniques in an *in vitro* and *in vivo* model of paraquat-induced neurotoxicity and a model of APP overexpression.

2 MATERIALS AND METHODS

2.1 *In Vitro* Model

Murine hypothalamus-derived GT1-7 neuronal cells and stably transfected mouse neuroblastoma cell lines (N2a) expressing Swedish mutant form (Swe) of the APP695 were used in this study. GT1-7 neuronal cells were received as a gift from Professor Pamela Mellon (University of California, San Diego,

United States) (Mellon et al., 1990). Cells were cultured in Dulbecco's Modified Eagle Medium (DMEM) (#41,965-062, Gibco®, Life Technologies, Johannesburg, South Africa) supplemented with 10% fetal bovine serum (FBS) (#S-0615, Biochrom, Berlin, Germany), and 1% penicillin/streptomycin (PenStrep, #15240-062, Life Technologies); 100 µg/ml streptomycin and 100 U/mL penicillin, and maintained in a humidified atmosphere in the presence of 5% CO2 at 37°C. N2aSwe cells were obtained from Professor Sangram Sisodia (Sisodia et al., 1990; Lo et al., 1994) (Department of Neurobiology, University of Chicago, United States). Cells were cultured in a 1:1 mixture of DMEM and Opti-MEM Reduced Serum Media (#31, 985,047, Gibco®, ThermoFisher Scientific) supplemented with 5% FBS and 1% PenStrep, and maintained at 5% CO2 at 37°C. Both GT1-7 cells and N2aSwe cells were sub-cultured using trypsin (#25,200,072, Life Technologies) to dissociate adherent cells from flasks (#707,003, WhiteSci). After trypsinisation, cells were collected in 15 ml falcon tubes (#50,015, Biocom Biotech, Centurion, South Africa) and supplemented with growth media added in a 2:1 ratio. Cells were centrifuged (5804R Centrifuge, Eppendorf, Johannesburg, South Africa) at 1,500 rpm for 3 min at room temperature (RT). The supernatant was discarded, and cells were re-suspended in growth media and seeded in either T25 (#500030, Porvair, Brackenfell, South Africa), T75 (#500029, Porvair) or T175 (#500028, Porvair) culturing flasks, or 6 well (#30,006, Bio-Smart Scientific, Edgemead, Cape Town), 48-well dishes (#30,048, Bio-Smart Scientific, Edgemead, Cape Town) or 35 mm glass-bottom dishes (#P35G-1.5-14-CGRD, MatTek Corporation, United States) for experimental purposes.

2.1.1 Treatment Conditions

To establish a suitable concentration of spermidine (Spd) (#S0266, Sigma-Aldrich, MO, United States), GT1-7 cells were treated with three different concentrations (0.1, 1 and 10 µM) for 8 h. For autophagic flux assessment, cells were treated with the vacuolar H^+ ATPase inhibitor bafilomycin A1 (BafA1) (#B0026, LKT labs), that prevents autophagosome-lysosome fusion (Yoshimori et al., 1991). Here, cells were treated with 400 nM BafA1 (du Toit et al., 2018b) for 4 h following treatment with spermidine. To assess the protective effects of a low and of a high concentration of spermidine against paraquat-induced neuronal toxicity, GT1-7 cells were treated with 1 and 10 µM Spd for 8 h followed by exposure to 3 mM of paraquat (PQ) for 6 h. To induce APP overexpression and assess the protective effects of a low and of a high concentration of spermidine, N2aSwe cells were treated with 5 mM butyric acid (BA) (#B103500, Sigma Aldrich, MO, United States) for 24 and 48 h. 8 h prior to the end of the treatment period, cells were incubated for further 8 h with a mixture of either 5 mM BA and 1 µM Spd or 5 mM BA and 10 µM Spd. After the completion of the treatment interventions, cells were harvested for western blot analysis or prepared for microscopy analysis or cellular viability assays.

2.1.2 Cellular Viability Assay

The effect of spermidine concentrations, PQ-induced cellular toxicity and APP-induced cellular toxicity on cellular viability was measured using a WST-1 assay. Briefly, GT1-7 cells and N2aSwe cells were seeded onto 48-well plates and incubated overnight in 200 ml of complete growth media. After overnight incubation, media was aspirated, and cells were treated as desired. Following treatment, WST-1 reagent was added to cell culture media at 10 µL/200 µl and incubated for 2 h at 37°C protected from light. Then, culture plates were placed in a shaking incubator (37°C, 200 RPM) and gently shaken for 2 min to dissolve the formazan crystals. Subsequently, colorimetric readings were measured at 595 nm using an EL800 universal microplate reader (BioTek Instruments Inc., VT, United States).

2.1.3 Protein Extraction and Western Blot Analysis

After treatments were completed, growth media was aspirated, and cells were rinsed three times with cold 1x PBS. Protein lysates were harvested with 200 µl RIPA lysis buffer (50 mM Tris-HCl, 1% NP-40, 0.25% Na-deoxycholate, 150 mM NaCl, 1 mM EDTA) containing 1:100 dilution of protease inhibitor cocktail (#11,873,580,001, Sigma Aldrich) and phosphatase inhibitors (1 mM PMSF, 1 mM NaF, 1 mM Na3VO4, 1 µg/ml leupeptin, 1 µg/ml aprotonin, 1 µg/ml benzamidine, and 10 µg/ml pepstatin). Cells were detached using a scraping method and cell lysates were collected, sonicated on ice using the Misonix sonicator (Fisher Scientific, Loughborough, United Kingdom, S-4000). Subsequently, cells were centrifuged at 8000 RPM (Labnet International, Edison, NJ, United States, Spectrafuge 16 M) for 10 min at 4°C. Protein content of the lysates was determined using a Direct Detect R infrared spectrometer (DDHW00010-WW, Merck). 50 mg/ml protein was mixed in 2:1 ratio in Laemli's sample buffer (6.5 mM Tris-HCl, 2% sodium dodecyl sulphate, 5% mercaptoethanol, 10% glycerol, 0.01% Bromophenol blue, pH 6.8). Samples were boiled at 95°C for 5 min, the protein was separated on 4%–20% polyacrylamide precast gels (#5671094, CriterionTM TGX TM Midi protein gel, Biorad). Proteins were separated at 100 V for approximately 2 h in Tris/Glycine/SDS running buffer (Bio- Rad, CA, United States). Proteins were subsequently transferred onto PVDF membranes (#170-84156, Bio-Rad) with the Midi Trans-Blot® Turbo Transfer kit (Bio- Rad, CA, United States) and the Trans-Blot® Turbo Transfer System (#170-4155, Bio-Rad Bio-rad), using the following conditions: 120 V and 400 A for 7 min. All membranes were blocked for 1 h in 5% fat-free milk prepared in TBS-T (137 mM NaCl, 20 mM Tris, 0.1% Tween-20, pH 7.6) followed by incubation in primary antibodies [anti-LC3B (#2775, Cell Signalling, 1:1000), anti-acetylated-α-tubulin 6-11B (#23950, Santa Cruz, 1:5000), anti-APP (#2452, Cell Signalling, 1:5000), Anti-LAMP2A (#ab18528, Abcam, 1:5000)] for overnight at 4°C. Subsequently, membranes were washed with TBS-T three times for 5 min and incubated in Horse Radish Peroxidase linked antibodies [anti-Rabbit IgG (#CST7074S, Cell Signalling, 1:5000) and anti-Mouse IgG (#CST7076S, Cell Signalling, 1:5000)] for 1 h at RT. Chemiluminescent detection was carried out with Clarity ECL Substrate (Bio-Rad, CA, United States) on the ChemiDoc MP imaging system (Bio-rad, CA, United States). The Stain-Free™ properties of the gels were used to determine

the total protein intensities of each membrane, which was used for normalization of protein-specific results (Davis et al., 2018). Bio-Rad Image Lab software was used to measure the intensity of the bands.

2.1.4 Plasmids and Transfections

GT1-7 cells were transfected at a confluency of 80%–85% using a Neon® 10 µl Transfection Kit (#MPK1025, Thermo Fischer Scientific) according to the manufacturer's instructions. Briefly, following trypsinization, 1,000,000 cells for a T25 vessel or 200,000 cells for 6 well plates were aliquoted out, washed in 1x PBS and spun down. The supernatant was discarded, and the pellet of cells was resuspended in a mixture of DNA plasmid [GFP-LC3-RFP-LC3ΔG or mRFP-GFP-LC3 (AddGene)] and Neon resuspension buffer in a ratio of 1:5, a total concentration of 10 µg for a T25 ml flask or 2.0 µg for a 6 well plate. Subsequently, the suspension was pipetted into a gold-plated Neon® Tip using a Neon® Pipette, with the tip inserted into Neon® Electrolytic buffer inside the Neon® Pipette Station. Following this process, cells were electroporated at 1350 V for 1 pulse lasting a duration of 30 ms and plated into T25 flasks or 6 well dishes containing fresh media (1:1 DMEM/OptiMEM with 10% FBS) and incubated for 48 h to allow transfection to take place.

2.1.5 Immunocytochemistry

GT1-7 or N2aSwe cells were seeded at a density of 150,000 cells on sterile coverslips in 6 well plates or 35 mm glass-bottom culture dishes and incubated overnight. Following incubation, cells were treated and fixed with 1:1 ratio of 4% v/v formaldehyde (FA) and growth media for 30 min. Subsequently, cells were rinsed 3 times with 1x PBS-A (in 1 L: 8 g NaCl, 0.20 g KCl, 2.20 g Na2HPO4.7H2O, 0.20 g KH2PO4 dissolved in dH2O, pH 7.4) and permeabilised with 0.2% Triton X-100 for 2 min. Cells were rinsed three times with 1x PBS-A, blocked with 5% v/v donkey serum for 30 min, at RT, before antibody staining. Cells were incubated overnight at 4°C in either anti-alpha (α)/beta (β)-tubulin rabbit, or anti-acetylated-α tubulin mouse, or anti- APP rabbit, diluted in 3% BSA (1:200). Thereafter, cells were rinsed three times with 1x PBS-A and then incubated for 50 min at RT in secondary antibodies; Alexa Fluor 568 donkey anti-rabbit, Alexa Fluor 488 donkey anti-mouse and Alexa Fluor 568 donkey anti-rabbit, respectively, diluted in 3% BSA (1:200). Cells were counterstained with 10 µg/ml Hoechst 33342 (Sigma-Aldrich, MO, United States) for 15 min before being mounted onto microscope slides with fluorescent mounting medium (Dako, Agilent Technologies, CA, United States). Images were acquired on Carl Zeiss laser scanning confocal microscope (LSM) 780 equipped with the ELYRA PS1 super-resolution and PALM/STORM platform (Carl Zeiss, Germany) using Zen Black imaging software (2012).

For dSTORM imaging, cells were fixed for a second time in 4% v/v FA for 10 min after secondary antibody incubation to stabilise fluorophore labelling and thereafter incubated in 100 mM PBS-G (0.75 g glycine in 100 ml PBS-A) for 2 min to terminate fixation. Subsequently, cells were washed three times with 1x PBS-A and stored in PBS-A until image acquisition.

2.1.6 Fluorescence Microscopy Imaging

2.1.6.1 Confocal Laser Scanning Microscopy

Following treatments, cells transfected with mRFP-GFP-LC3 were counterstained with Hoechst and imaged using Plan-Apochromat 63x/1.4 oil immersion objective. 8–10 z-slices were acquired at intervals of 0.60 µm. Hoechst, GFP and mRFP were excited using lasers 405, 488 and 561 nm, respectively, with the emission light detected between 410–468 nm for Hoechst, 490–535 nm for GFP and 591–660 nm for mRFP. For quantification of punctate structures, z-stacks were projected as maximum intensity using the Zeiss Zen Black Software (2012). Images were exported and analysed for the number of autophagosomes (nA, yellow puncta) and autolysosomes (nAL, red puncta) in Fiji analysis software (Schindelin et al., 2012) using a "click count" function.

2.1.6.2 Super Resolution-Structured Illumination Microscopy

Cells labelled for acetylated-α tubulin, α/(β)- tubulin and Hoechst were imaged using SR-SIM on the Elyra PS1 platform (Carl Zeiss, Germany). Images were acquired using 100x/1.46 Alpha Plan-Apochromatic oil immersion objective at 5 phase shifts and 3 rotations of the illumination grid per z-stack (0.50 µm interval). Image acquisition settings were set as follows; Hoechst: 405 nm excitation laser and BP 420–480 + LP 750 emission filter, acetylated-α tubulin: 488 nm excitation laser and BP 495–550 + LP 750 emission filter and α/(β)-tubulin: 561 nm excitation laser and BP 570–620 + LP 750 emission filter. For channel alignment, a slide containing multi-coloured 40 nm fluorescent beads was imaged under the same acquisition settings and used for an affine alignment of channels using the ZEN Black Elyra edition software (Carl Zeiss Microscopy).

2.1.6.3 Direct Stochastic Optical Reconstruction Microscopy

Single molecule microscopy of cells labelled for APP and acetylated-α tubulin was performed. Molecules were activated using super-resolution Abbelight buffer (a kind gift from Pierre Bauër, Abbelight) or 1 M MEA buffer (#M9768, Sigma Aldrich). Blinking events were acquired using 100x/1.46 Alpha Plan-Apochromatic oil immersion objective using a 561 nm laser and fluorescence was detected with the EM-CCD iXon DU 897 camera. Imaging was performed in TIRF-uHP mode, 100% laser power, camera integration of 33 ms and EM gain of 150 to bleach the sample and force fluorophores to enter the dark state. Laser power was reduced to 2% while recording the events. A total of 50,000 events were recorded per cell. Raw data images were processed using a ZEN Black software where images were corrected for drifting and outliers. For APP analysis, images were further processed using FIJI analysis software. APP clusters were segmented using the Li thresholding algorithm (Li and Tam, 1998), and sizes were measured using the "analyze particle" function (Schindelin et al., 2012).

2.1.7 Transmission Electron Microscopy

Following treatments cells were detached from the culture flask using Trypsin/EDTA. Thereafter, cells were washed with 1x PBS and fixed overnight at 4°C in 2.5% v/v glutaraldehyde (GA) in

0.1 M phosphate buffer (PB). Subsequently, cells were washed three times for 5 min with 0.1 M PB and embedded in 2% low melting agarose (Merck, SA) on ice. Small pieces (0.2 × 0.2 mm) of solidified agarose were post-fixed in 1% osmium tetroxide (SPI) in 0.1 M PB for 1 h and then washed for 5 min in 0.1 M PB followed by washing twice in dH2O. The samples were placed in sample baskets (3 wells) and underwent a process of dehydration and substitution using an automated tissue processor (Leica Biosystems), using the following conditions: 30 min in 2% uranyl acetate in 70% ethanol, 2 × 5 min in 70% ethanol, 5 min in 90% ethanol, 10 min in 2% uranyl nitrate in 96% ethanol, 3 × 10 min in 100% ethanol, 90 min in 1:1 Spurrs resin: 100% ethanol, and 2 × 1 h pure resin. After the cycle was complete, samples were embedded in Spurrs resin and capsules were polymerised at 60°C in the oven for 48 h. Ultra-thin sections, 150 nm thick were cut on a Leica EM UC7 ultramicrotome (Leica Microsystems, Germany), collected on 200 mesh copper grids (G200-Cu, Electron Microscopy Sciences) and stained with uranyl acetate and lead citrate. Grids were viewed in a JEOL JEM 1011 TEM (JEOL, Inc., Peabody, MA) operated at 120 kV and images were collected using a GATAN OneView camera.

Quantitative morphometric analysis was performed using Fiji software. Briefly, TEM images were exported as TIFF files and converted to 8-bit grayscale. After conversion, an outline was drawn using a drawing pen circulating autophagosomal and autolysosomal structures collectively known as autophagic vacuoles (AVs) (Eskelinen, 2008; Klionsky et al., 2016). Thereafter, images were thresholded using default settings; black and white (B & W) and dark background was used, and the grey values were set to 255 so that pixels with grey levels under a specified threshold were displayed as black, and those above as white pixels, thus demarcating the structures of interest against the background. The number and surface area (μm^2) of AVs were analysed using the "analyze particle" function.

2.1.8 3D Correlative Light and Electron Microscopy

2.1.8.1 Super-resolution Structured Illumination Microscopy

For correlative imaging, GT1-7 cells transfected with a GFP-LC3-RFP-LC3ΔG DNA plasmid were seeded at 150,000 cells overnight onto 35-mm gridded glass-bottom dishes (#P35G-1.5-14-CGRD, MatTek Corporation, United States). Cells were treated for 8 h with 1 and 10 μM Spd followed by treatment for 4 h in the presence and absence of 400 nM BAfA1. Thereafter, cells were fixed with 1:1 ratio of 8% v/v FA and culture medium for 15 min. Cells were rinsed 3x for 5 min and counterstained with 10 μg/ml Hoechst 33342 for 15 min. Thereafter, cells were rinsed 3x for 5 min and then imaged with SR-SIM. For each treatment group, cells were first imaged in the LSM mode with a low magnification (10x EC "Plan-Neofluar") using a tile scan (4 × 4) to acquire a wide field of view that is inclusive of the grid. Thereafter, cells of interest were imaged at higher magnification (100x/1.46 Alpha Plan-Apochromatic oil immersion) in the SIM mode at 5 phase shifts and 3 rotations per z-stack (0.50 μm interval) to obtain final images to correlate with the electron microscopy images. Acquisition settings were set as follows; Hoechst: 405 nm excitation laser and BP 420–480 nm emission filter, GFP: 488 nm excitation laser and BP 495–550 + LP 750 emission filter and RFP: 561 nm excitation laser and BP 570–620 + LP 750 emission filter. For channel alignment, a slide containing multi-coloured 40 nm fluorescent beads was imaged under the same acquisition settings and used for an affine alignment of channels using the ZEN Black Elyra edition software (Carl Zeiss Microscopy).

2.1.8.2 Focused Ion Beam Scanning Electron Microscopy

Following imaging with SR-SIM, as described above, cells were prepared for FIB-SEM imaging according to a published protocol (Russell et al., 2017). Briefly, cells were post-fixed in 2.5% (v/v) GA/4% (v/v) FA in 0.1 M PB for 30 min at RT. Subsequently, cells were washed in 0.1 M PB 5 × 3 min on ice, stained in 2% osmium tetroxide/1.5% potassium ferricyanide (v/v) for 60 min, on ice and washed in dH2O 5 × 3 min. Thereafter, cells were incubated in 1% thiocarbohydrazide in dH2O (w/v) for 20 min, washed in dH2O 5 × 3 min, before staining in 2% osmium tetroxide in dH2O (w/v) for 30 min. Following the staining procedure, cells were washed in dH2O for 5 × 3 min and incubated overnight in 1% aqueous uranyl acetate at 4°C. After overnight, cells were washed in dH2O, 5 × 3 min, stained with Walton's lead aspartate for 30 min, at 60°C, washed in dH2O, 5 × 3 min. Coverslips were detached using a razor blade, dehydrated on ice, using a pre-chilled alcohol series in the following order: 20%, 50%, 70%, 90%, 100% EtOH, 5 min each, on ice, anhydrous 100% EtOH, 5 min, on ice, followed by 10 min at RT. Next, cells were incubated in 1:1 propylene oxide and Durcupan ACM® (Sigma Aldrich, MO, United States) resin mixture for 60 min, followed by incubation in Durcupan ACM® for 90 min, twice and embedded in Durcupan ACM® for 48 h at 60°C.

Following polymerization of the resin, coverslips were removed by brief immersion in liquid nitrogen. Resin embed samples were trimmed to the region of interest with reference to grid coordinates and prior light microscopy images. After thinning to <1 mm, the ROIs were attached to a standard 12.7 mm SEM stub using silver paint, sputter coated with a 5 nm layer of platinum, and mounted in the FIB-SEM (Zeiss Crossbeam 540 running with Atlas 5). The specific cells of interest were relocated by imaging through the platinum coating at an accelerating voltage of 20 kV and correlating to previously acquired fluorescence microscopy images. After preparation for milling and tracking, images were acquired at a voxel size of 5 × 5 × 5 nm throughout each region of interest using a 6–10 μs dwell time, depending on imaging stability and the final size of the selected imaging ROI. During acquisition, the SEM was operated at an accelerating voltage of 1.5 kV with 1 nA current. The EsB detector was used with a grid voltage of 1200 V. Ion beam milling was performed at an accelerating voltage of 30 kV and a current of 700 pA.

2.1.8.3 Image Processing and Analysis

After initial registration (SIFT; Fiji, https://imagej.net/plugins/linear-stack-alignment-with-sift), the images were contrast normalised as required across the entire stack, and converted to 8-bit greyscale. The output images were batch processed to suppress noise, and to enhance sharpness and

contrast (i. small radius gaussian blur; ii. smart sharpening with highlights suppressed, iii. application of grey levels adjustment as needed; Adobe Photoshop CC 2015). The level of processing was tailored to each individual dataset. If required, each dataset was rotated sequentially in XY and YZ to accurately match the light microscopy data (equivalent to XZ).

To identify autophagosomes with high precision, a correlation of SR-SIM and FIB-SEM datasets was performed. For 2D overlays, image stacks from SR-SIM were projected to maximum intensity projection using Zeiss Zen Black Software (2012) and manually aligned to a representative region of the FIB-SEM stack using Ec-CLEM plugin on Icy (Paul-Gilloteaux et al., 2017), with FIB-SEM image set as "target" and SR-SIM image as "source". 20–30 matching landmarks were added within both datasets throughout the entire cell. The transformation was applied to the SR-SIM dataset to produce a 2D overlay and saved to be applied on another image in the FIB-SEM stack. Autophagosomes were identified from the 2D overlay, segmented manually from the FIB-SEM datasets and 3D reconstructions were made using 3dmod program of IMOD (Kremer et al., 1996). Briefly, the FIB-SEM stack was opened in IMOD and scaled to 5 nm pixel size. ROIs were located within the image stack based on the 2D overlay. Contours of each autophagosome were drawn manually on each slice through the entire volume. The "normal", "sculpting" and "warp" drawing tools were used and a z-bridge of 5 was maintained. The "interpolate" function was used to complete the remaining contours. A new object was added for each new autophagosome. A total of 15–25 autophagosomes were segmented for each cell, the number of contours varied according to the size of the autophagosomes. Once segmentation had been completed, the model was opened in "model view" to display z-buffered wireframe rendering of model contour data with adjustable perspective. Each object was "capped" and "meshed" to form a solid 3D object.

For morphometric analysis [volume (μm^3) and surface area (μm^2)] of each autophagosome, binary masks. mrc files were created from imod segmentation files (.mod) by using the "imodmop-mask" command in the Linux (Ubuntu 20.04) command line. Prior to importing files into Amira (2019), binary masks .mrc files were down sampled and converted to .tiff. Binary masks were then used to create volumetric renders in Amira, and manually overlayed with the FIB-SEM data sets. For quantification of each vacuole, the "label measurements" option was applied to each segmentation set and exported as .csv files.

For movie production, the SR-SIM image stack was aligned to the FIB-SEM stack using Bigwarp plugin of the Fiji framework (Bogovic et al., 2016), after which the SR-SIM dataset was exported at the native resolution of the FIB-SEM dataset. A merged SR-SIM/FIB-SEM dataset was also created. For subsequent processing, each dataset was reduced in resolution from 5 to 20 nm^3. Using Amira (2019.3, ThermoFisherSci), the warped SR-SIM, merged SR-SIM/FIB-SEM, and FIB-SEM datasets were visualised in combination with the model generated from segmentation in 3dmod and a movie was created and exported.

2.1.9 Flow Cytometry

Flow cytometry was used to measure the production of mitochondrial reactive oxygen species (ROS) as well as cell death onset using MitoSox and Propidium Iodide. After treatment with low and a high concentration (1 and 10 μM) of spermidine for 8 h and followed by exposure to 3 mM PQ for 6 h, cells were washed gently in warm 1x PBS. Thereafter, cells were incubated with 5 μM MitoSOX Red or 1 μg/ml PI solution for 10 min at 37°C, protected from light. Carbonyl cyanide m-chlorophenyl hydrazone (CCCP) at 5 μM was used as a positive control. The fluorescence intensity of MitoSOX Red and PI were measured on the BD FACSAria IIu flow cytometer (BD Biosciences, CA, United States). A minimum of 20,000 gated cells were collected using a 488 nm laser and 610/20 bandpass filter. The mean fluorescence intensity was assessed from three independent experiments. Results were expressed as a percentage of controls.

2.2 *In Vivo* Study

2.2.1 Animals

Eight-week-old male C57BL/6 mice expressing GFP-LC3 were used in this study. GFP-LC3 transgenic mice breeding pairs were purchased from Riken, Bio-Resource Centre in Japan (#BRC00806) and mice were bred at the breeding facility at Stellenbosch University according to the previously described protocol (Mizushima et al., 2004; Mizushima, 2009). 72 GFP-LC3 mice were randomly allocated into six treatment groups: control, PQ, 0.3 mM Spd, 0.3 mM + PQ, 3 mM Spd and 3 mM Spd + PQ, with a total of 12 mice (N = 12) per group. Mice were kept on a 12 h day/night cycle at a constant temperature of 22°C and 40% humidity. Mice were monitored and weighed for the duration of the study. All animals had free access to standard chow and drinking water *ad libitum*. All procedures for handling the mice in this study were reviewed and approved by the animal research ethics committee (SU-ACUD16-00175), at Stellenbosch University, South Africa.

2.2.2 Treatment Conditions

Mice in the control, PQ, and the combination groups (0.3 mM + PQ and 3 mM Spd + PQ) were subjected to a total of 6 injections of saline solution or PQ solution given at 10 mg/kg which was administered intraperitoneally every 3 days for 3 weeks (Chen L. et al., 2012). Animals in the spermidine group and the combination groups received previously reported doses of 0.3 and 3 mM Spd in drinking water (LaRocca et al., 2013; Eisenberg et al., 2016) every day for 21 days. Spermidine (Sigma-Aldrich, St Louis, MO, United States) was prepared fresh in tap water every 3 days from a 1 M aqueous stock solution (spermidine/HCl pH 7.4) stored at −20°C, while PQ (Sigma-Aldrich, St Louis, MO, United States) was prepared fresh in saline solution before injection.

2.2.3 Protein Extraction for Western Blot Analysis

Protein lysates were harvested from brain tissue (hippocampus and cerebral cortex) with RIPA buffer supplemented with

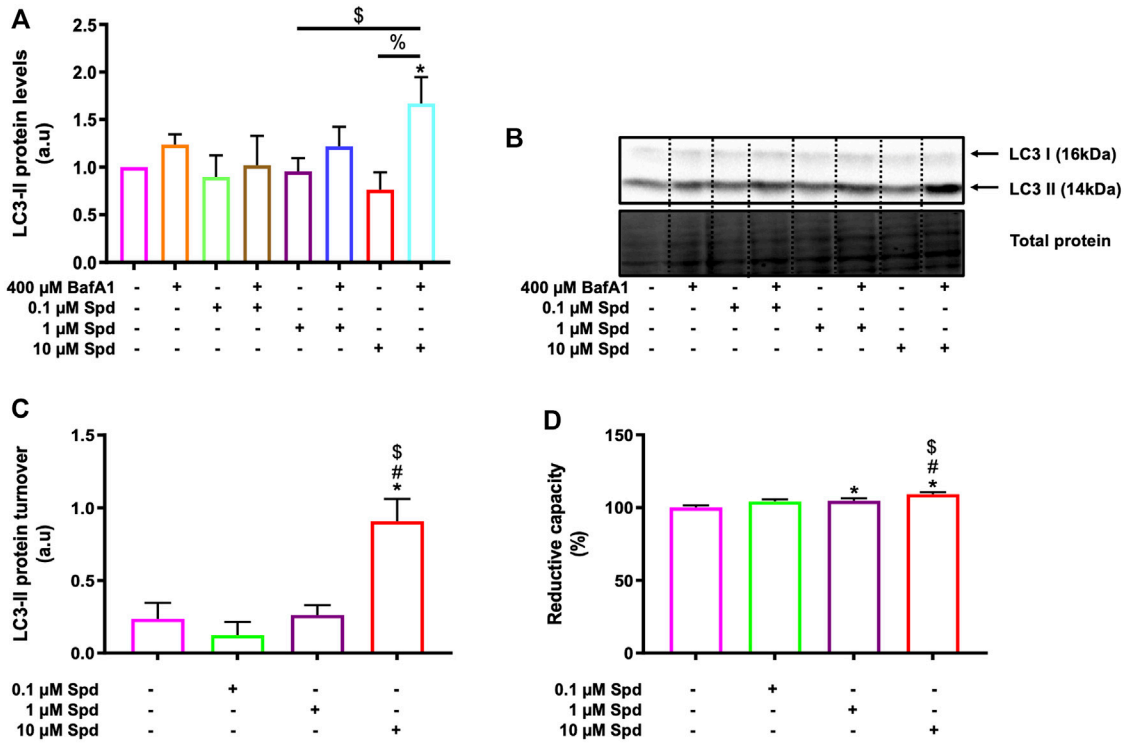

FIGURE 1 | Spermidine induces autophagic flux and improves cellular viability in a concentration-dependent manner. **(A)** densitometric quantification and **(B)** representative western blot for LC3-II protein levels upon autophagy induction using three different concentrations (0.1, 1 and 10 μM) of spermidine in the presence and absence saturating concentrations of bafilomycin. Data are presented as mean ± SEM, $n = 3$. * = $p < 0.05$ vs. control, $ = $p < 0.05$ vs. 0.1 μM Spd + BafA1 and % = $p < 0.05$ vs. 10 μM Spd, arbitrary units (a.u). **(C)** LC3-II turnover revealing a concentration-dependent flux by spermidine. * = $p < 0.05$ vs. control, # = $p < 0.05$ vs. 0.1 μM Spd and $ = $p < 0.05$ vs. 1 μM Spd. **(D)** Reductive capacity in GT1-7 cells following treatment with three different concentrations of spermidine. Data are presented as mean ± SEM, $n = 3$ with 6 replicates per group. * = $p < 0.05$ vs. control, # = $p < 0.05$ vs. 0.1 μM Spd and $ = $p < 0.05$ vs. 1 μM Spd.

protease and phosphatase inhibitors. In brief, brain tissue samples were minced in RIPA buffer using scissors while on ice, after which tissue samples were rapidly homogenised by sonication on ice, using 3 bursts of 5 s (Kine Matica Polytron PT2100 homogenizer, ThermoFischer Scientific). Protein content of the lysates was determined using the Direct Detect system and samples were prepared for western blotting as described above. Primary antibodies to anti-acetylated-α-tubulin 6-11B (#23950, Santa Cruz, 1:5000), anti-APP (#2452, Cell Signalling, 1:1000), anti-Sequestosome1/p62 (#ab56416, abcam, 1:5000), and 4-Hydroxy-2-nonenal (#ab46545, Abcam, 1:1000) as well as secondary Horse Radish Peroxidase linked antibodies anti-Rabbit IgG (#CST7074S, Cell Signalling, 1:5000) and anti-Mouse IgG (#CST7076S, Cell Signalling, 1:5000) were used.

2.3 Statistical Analysis

The results are expressed as mean values ±SEM and were analysed by one-way Analysis of Variance (ANOVA) with a Fischer LSD post hoc correction. Graph Pad Prism (v8) was employed to perform statistical tests. Data were considered statistically significant with a p-value < 0.05.

3 RESULTS

3.1 Spermidine Induces Autophagic Flux and Improves Cellular Viability in a Concentration-Dependent Manner

Three different concentrations of spermidine were tested in the presence and absence of BafA1 to determine a low and high concentration that induces autophagic flux without causing cellular death in GT1-7 cells. A WST-1 assay and western blotting were used to measure cellular viability and endogenous levels of LC3-II (microtubule-associated protein 1 light chain) respectively. LC3-II is a key component of mature autophagosomes (Kabeya et al., 2000) that is widely used to assess autophagosome abundance. LC3-II levels were significantly increased in the 10 μM Spd + BafA1 treated group compared to the control (untreated) group and 0.1 μM Spd + BafA1 treated group (**Figures 1A,B**). To reveal the effect of spermidine on LC3-II levels better, we assessed LC3-II turnover determined by subtracting mean values of BafA1 treated groups (BafA1, 0.1 μM Spd + BafA1, 1 μM Spd + Baf A1 and 10 μM Spd + BafA1) in **Figure 1A** from BafA1 untreated groups (control, 0.1 μM Spd, 1 μM Spd and 10 μM Spd), respectively. Spermidine

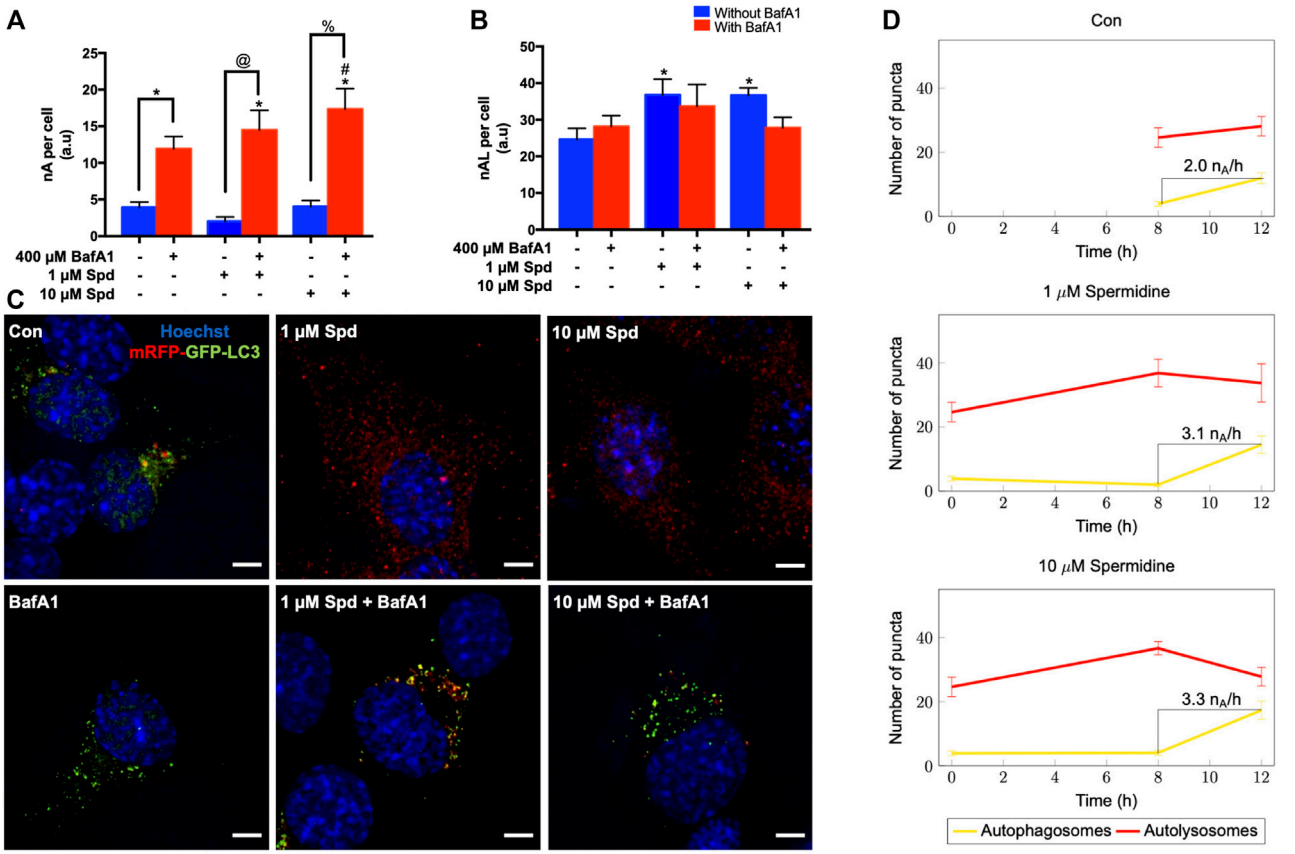

FIGURE 2 | Spermidine induces autophagic flux in a concentration-dependent manner. **(A,B)** quantitative analysis and **(C)** representative fluorescence micrographs of autophagosome pool size **(A,C)** and autolysosome pool size **(B,C)** in GT1-7 cells following treatment with 1 and 10 μM spermidine in the presence and absence of saturating concentrations bafilomycin. Data are presented as mean ± SEM, n = 3, with a total of 30 cells analysed per treatment group. * = $p < 0.05$ vs control, # = $p < 0.05$ vs BafA1, @ = $p < 0.05$ vs 1 μM Spd and % = $p < 0.05$ vs 10 μM Spd, arbitrary units (a.u). Scale bar: 5 μm. **(D)** Autophagosome flux under basal and induced conditions calculated from the initial slope of autophagosomes accumulation. Autophagosome flux increased in a concentration-depended manner, raising from 2.0 autophagosomes/h/cell under basal levels to 3.1 autophagosomes/h/cell and 3.3 autophagosomes/h/cell under induced conditions with 1 and 10 μM Spd respectively.

at 10 μM showed a significant increase in LC3-II levels compared to the control, 0.1 and 1 μM Spd treated groups (**Figure 1C**). The WST-1 assay revealed that spermidine at 1 and 10 μM improved cellular viability compared to the control group (**Figure 1D**). Based on these results spermidine at 1 and 10 μM were used for subsequent experiments.

3.2 Spermidine Induces Autophagic Flux in a Concentration-dependent Manner Which Is Most Sensitively Revealed Through Vesicle-Based Analysis

To further characterise the autophagic flux profile of 1 and 10 μM Spd, fluorescence and TEM-based analysis was performed in GT1-7 cells in the presence and absence of BafA1. For fluorescence-based analysis, GT1-7 cells expressing mRFP-GFP-LC3 were used to determine the number of autophagosomes (nA, yellow puncta) and autolysosomes (nAL, red puncta). In addition, autophagosome flux (J), which is the initial rate of increase in nA per cell after treatment with BafA1 and the transition time (τ) required for a cell to turnover its entire autophagosome pool were determined (Loos et al., 2014; du Toit et al., 2018a; du Toit et al., 2018b). mRFP-GFP-LC3 is a pH-sensitive tandem fluorescent probe that fluoresces red (mRFP) in the autolysosome due to the quenching of GFP signal because of the auto-lysosomal acidity, while fluorescing red (mRFP) and green (GFP) in the autophagosome resulting in a yellow signal (Yoshii and Mizushima, 2017). As such, when autophagic flux is increased, both yellow puncta (mRFP and GFP) and red puncta (mRFP only) are increased. Inhibition of autophagosome fusion with lysosomes results in an increase in the number of yellow puncta and a concurrent decrease in red puncta (Yoshii and Mizushima, 2017). Our results showed that 1 μM Spd + BafA1, 10 μM Spd + BafA1 and BafA1 treated groups significantly increased the number of autophagosomes compared to the control group (**Figures 2A,C**), while 1 and 10 μM Spd treatment significantly increased the number of autolysosomes (**Figures 2B,C**). Interestingly, only 10 μM Spd + BafA1 group enhanced the

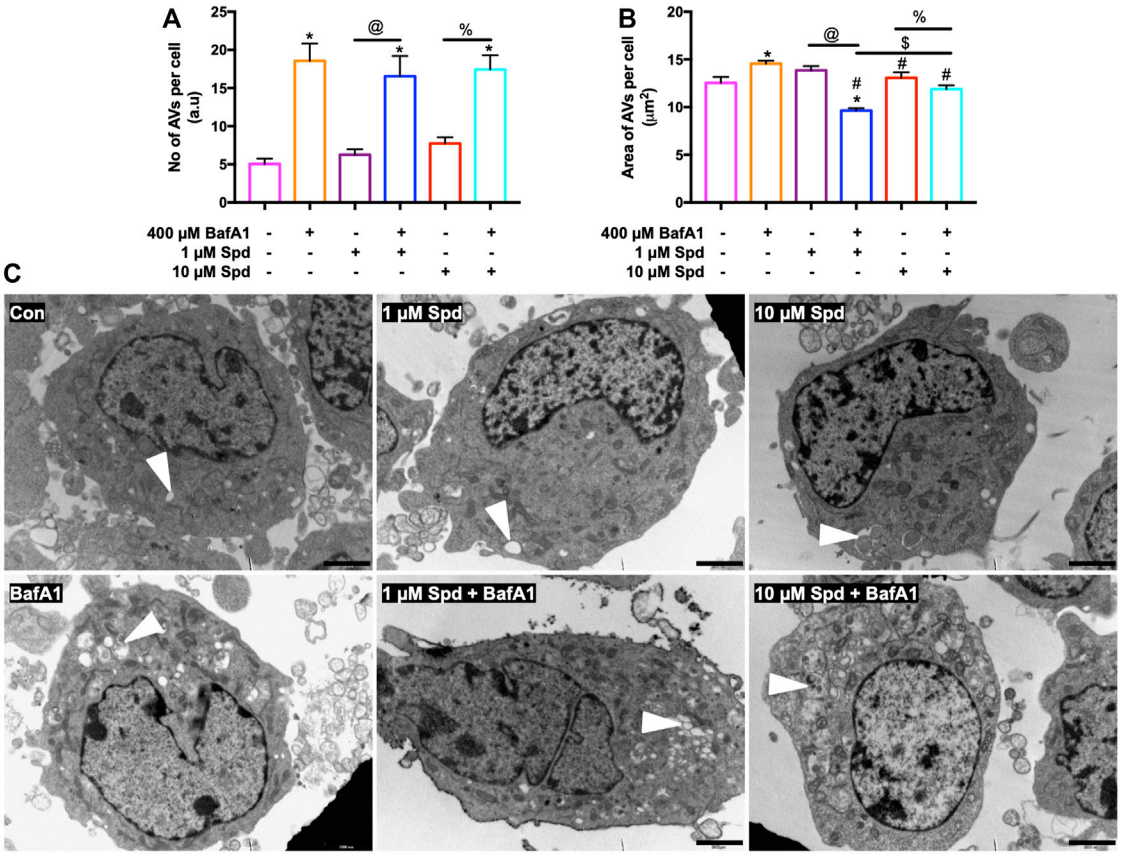

FIGURE 3 | Spermidine affects the size of AVs in a concentration-dependent manner but has no effect on the number of AVs. **(A,B)** morphometric analysis and **(C)** representative TEM micrographs of autophagic vacuoles (AVs) in GT1-7 cells following treatment with 1 and 10 µM spermidine in the presence and absence of saturating concentrations bafilomycin. Data are presented as mean ± SEM, $n = 2$ with a total of 30 images analysed per treatment group. * = $p < 0.05$ vs control, # = $p < 0.05$ vs. BafA1, $ = $p < 0.05$ vs. 1 µM Spd + BafA1, @ = $p < 0.05$ vs. 1 µM Spd and % = $p < 0.05$ vs. 10 µM Spd, arbitrary units (a.u). Arrowheads indicate AVs. Scale bar: 2000 nm.

accumulation of autophagosomes compared to BafA1 treated group, suggesting a concentration-dependent increase in autophagic flux. Furthermore, 1 µM Spd + BafA1 and 10 µM Spd + BafA1 significantly increased autophagosome accumulation compared to 1 µM Spd and 10 µM Spd, respectively. Autophagosome flux was enhanced in a concentration-dependent manner, raising from 2.01 nA/h/cell under basal levels to 3.1 nA/h/cell and 3.3 nA/h/cell under induced conditions using 1 and 10 µM Spd respectively (**Figure 2D**). Analysis of the transition time (τ) showed that 1 µM Spd treated cells required 0.64 h to turn over their autophagosome pool, while 10 µM Spd required 1.21 h compared to 2 h needed by the control cells to turn over its pool.

Morphometric analysis with TEM revealed that BafA1, 1 µM Spd + BafA1 and 10 µM Spd + BafA1 treated groups significantly increased the number of AVs compared to the control group (**Figures 3A,C**). No significant differences were observed in the 1 µM Spd + BafA1 and 10 µM Spd + BafA1 treated groups compared to BafA1 treated group (**Figures 3A,C**). Surface area was significantly reduced in 1 µM Spd + BafA1 compared to 1 µM Spd and in 10 µM Spd + BafA1 compared 10 µM Spd (**Figures 3B,C**). Importantly, 1 µM Spd + BafA1 reduced the size of AVs compared to 10 µM Spd + BafA1, suggesting a concentration-dependent effect.

3.3 Spermidine Induces Autophagosomal Recruitment of LC3-GFP, Supporting Autophagy Induction

To identify and localise GFP-LC3 positive structures i.e., autophagosomes, with high precision in the context of EM ultrastructure, and to monitor autophagic flux in the context of autophagosome formation, 3D-CLEM was performed using GT1-7 cells expressing GFP-LC3-RFP-LC3ΔG. This third-generation autophagy plasmid is a recently developed fluorescence probe that allows to measure and directly visualise autophagy flux (Kaizuka et al., 2016). When expressed in cells, it is cleaved by ATG4 into equimolar amounts of GFP-LC3 and RFP-LC3ΔG, where GFP-LC3 binds to the inner and outer membrane of the autophagosome and therefore is degraded during autophagy, while RFP-LC3ΔG

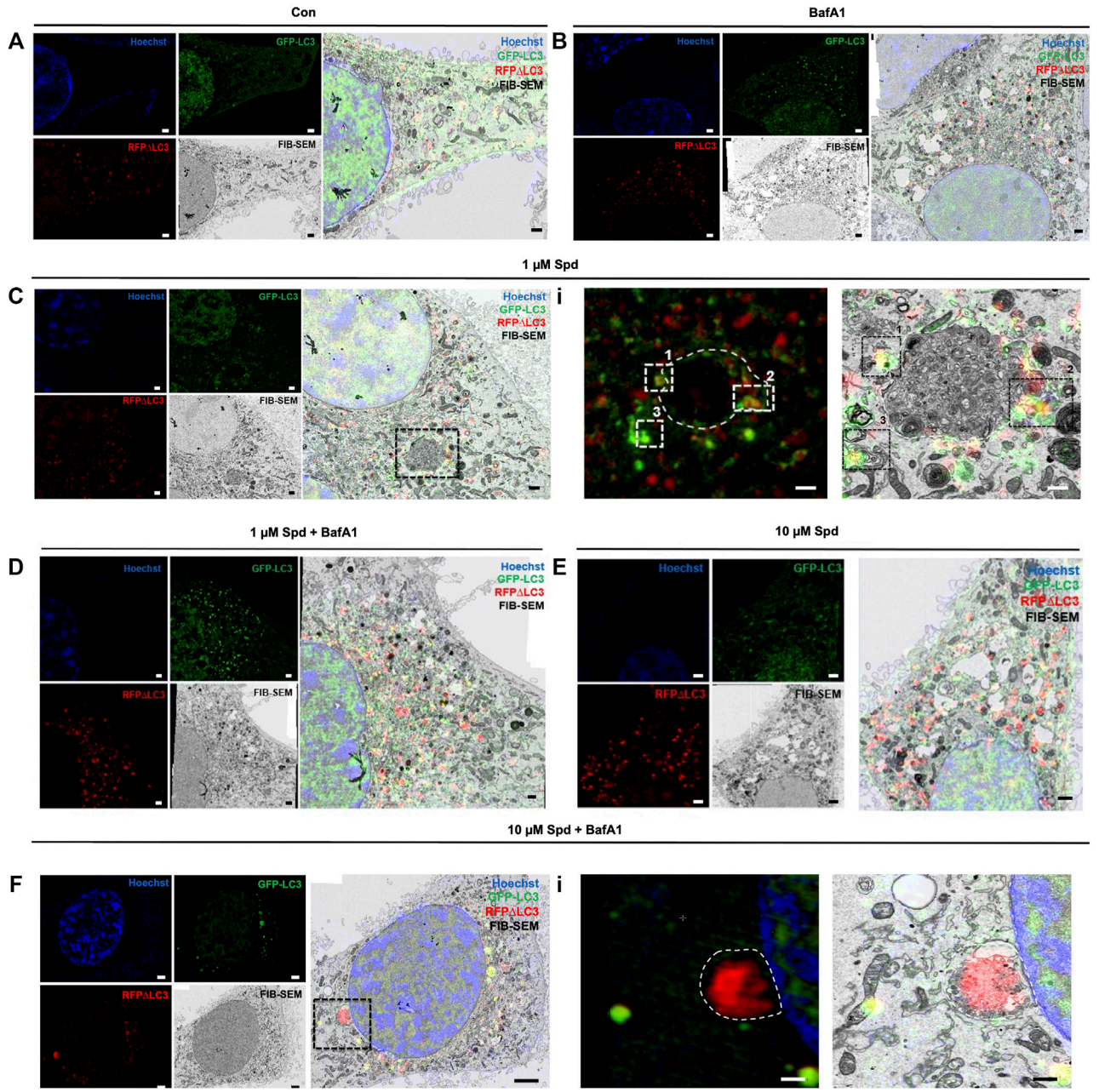

FIGURE 4 | Spermidine induces autophagy. **(A–F)** Three colour micrograph of SR-SIM, FIB-SEM and overlay of SR-SIM and FIB-SEM showing the accumulation of GFP-LC3 and RFP-LC3ΔG positive structures following treatments. **(C,F)** complex structures of high electron density. **(Ci)** region of interest showing GFP-LC3 and RFP-LC3ΔG positive structures decorating conglomerate structure. (**Fi**) region of interest showing the localisation of RFP-LC3ΔG positive structures inside the conglomerate structure as part of cytoplasmic cargo. Scale bar: 1 μm.

remains in the cytosol, thus serving as an internal control (Kaizuka et al., 2016). Autophagic flux can hence be estimated by monitoring a decrease in GFP fluorescence compared to RFP fluorescence. 3D CLEM analysis using SR-SIM and FIB-SEM (**Figure 4**) allowed high-resolution imaging where autophagosomes could be identified with high precision. Upon inspection of SR-SIM micrographs, an increase in RFP-LC3ΔG positive structures was observed in the 1 μM Spd (**Figure 4C**; **Supplementary Figure S1**), 10 μM Spd (**Figure 4E**; **Supplementary Figure S1**) treated group compared to the control (untreated) group (**Figure 4A**; **Supplementary Figure S1**), suggesting heightened autophagic flux. GFP-LC3 positive structures were increased in the BafA1 (**Figure 4B**; **Supplementary Figure S1**), 1 μM Spd + BafA1 (**Figure 4D**; **Supplementary Figure S1**), 10 μM Spd + BafA1 (**Figure 4F**; **Supplementary Figure S1**) treated groups compared to control

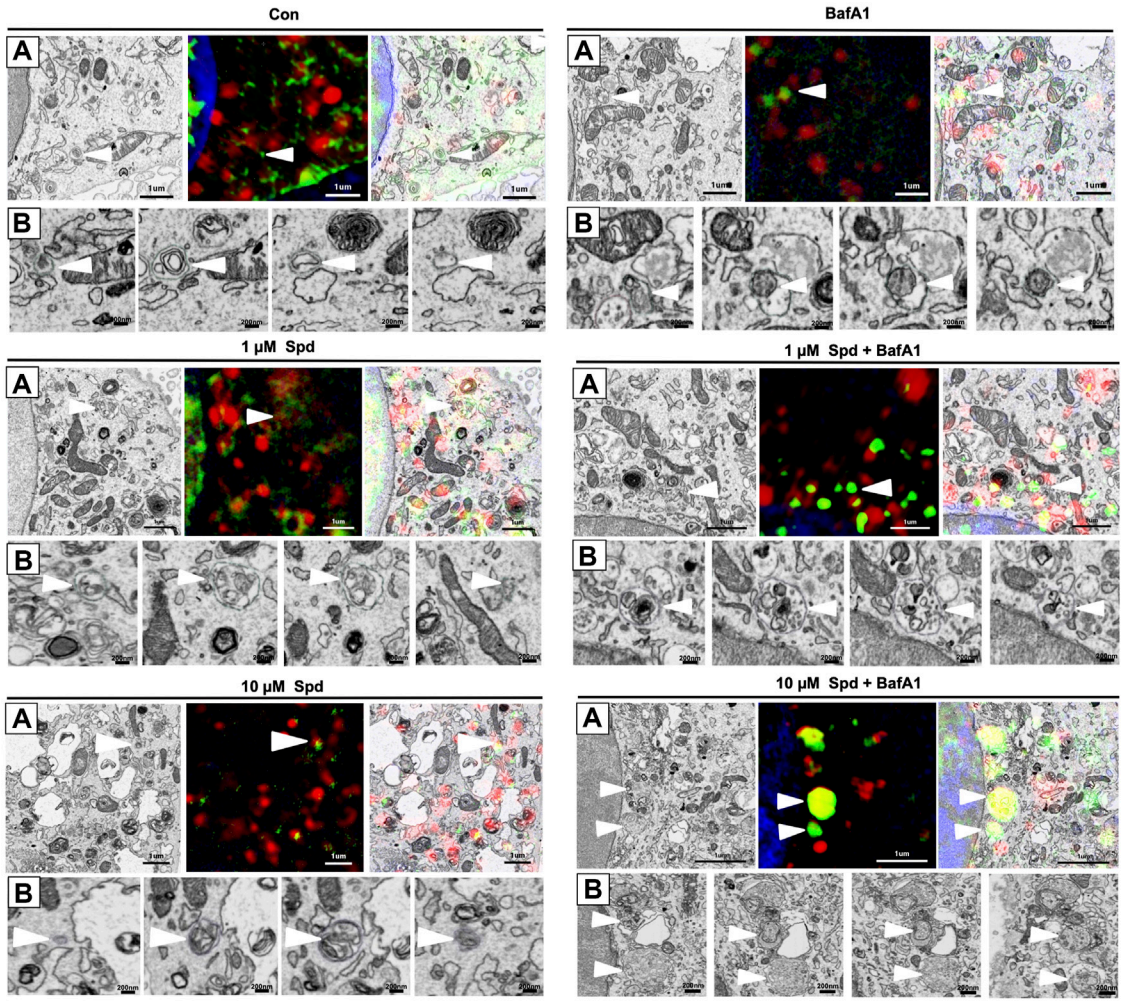

FIGURE 5 | Differential response in cargo selection upon treatment. **(A)** Selective region of interest indicating autophagosome (white arrow heads) in FIB-SEM (Left), SR-SIM (middle) and CLEM (right) for the control (untreated) group, 1 μM Spd, 1 μM Spd + BafA1, 10 μM Spd and 10 μM Spd + BafA1. **(B)** FIB-SEM micrograph showing distinct cargo contained within the autophagosome (white arrow heads) following treatments. 10 μM Spd + BafA1 treated group recruits cargo characterised by the abundance of small intra-autophagosomal vesicle-like structures of homogeneous electron density. Scale bar: 1 μm and 200 nm.

(untreated), 1 μM Spd and 10 μM Spd treated groups, respectively. Importantly, GFP-LC3 positive structures increased in abundance in the 1 μM Spd + BafA1 and 10 μM Spd + BafA1 treated group compared to the BafA1 treated group, suggesting an induced flux. Ultra-structural analysis with CLEM revealed the presence of complex structures in the 1 μM Spd and 10 μM Spd + BafA1 treated group that were GFP-LC3 and RFP-LC3ΔG positive (**Figures 4Ci**; **Supplementary Video S1** and **Figures 4Fi**), or only RFP-LC3ΔG positive (**Figures 4Fi**), localizing in vacuolar structures of high electron density, either decorating the conglomerate structure (**Figures 4Ci**; **Supplementary Video S1**) or forming part of the cytoplasmic cargo (**Figures 4Ci**; **Supplementary Video S1**; **Figures 4Fi**). GFP-LC3 positive structures appeared to be localised in vacuolar structures of relatively low electron density (**Figure 5**). However, the cargo material inside the vacuolar structures was distinct in each treatment, with 10 μM Spd + BafA1 treated cell presenting cargo characterised by the abundance of small intra-autophagosomal vesicle-like structures of homogeneous electron density.

3.4 The Effect of Spermidine on Cargo Clearance and Size Regulation

Taking advantage of the 3-dimensional data of both SR-SIM and FIB-SEM, we assessed whether 1 and 10 μM of spermidine influenced the surface area and volume of autophagosomes, providing a possible indication of size regulation but also the capacity of proteinaceous cargo clearance. Hence, autophagosomes were manually segmented through the entire volume of the cell to generate a three-dimensional model, which showcases their localization within the entire volume of the cell (**Figure 6A**; **Supplementary Figure S3**). Morphometric analysis revealed that treatment with 1 μM Spd significantly increased the volume of autophagosomes compared to the control

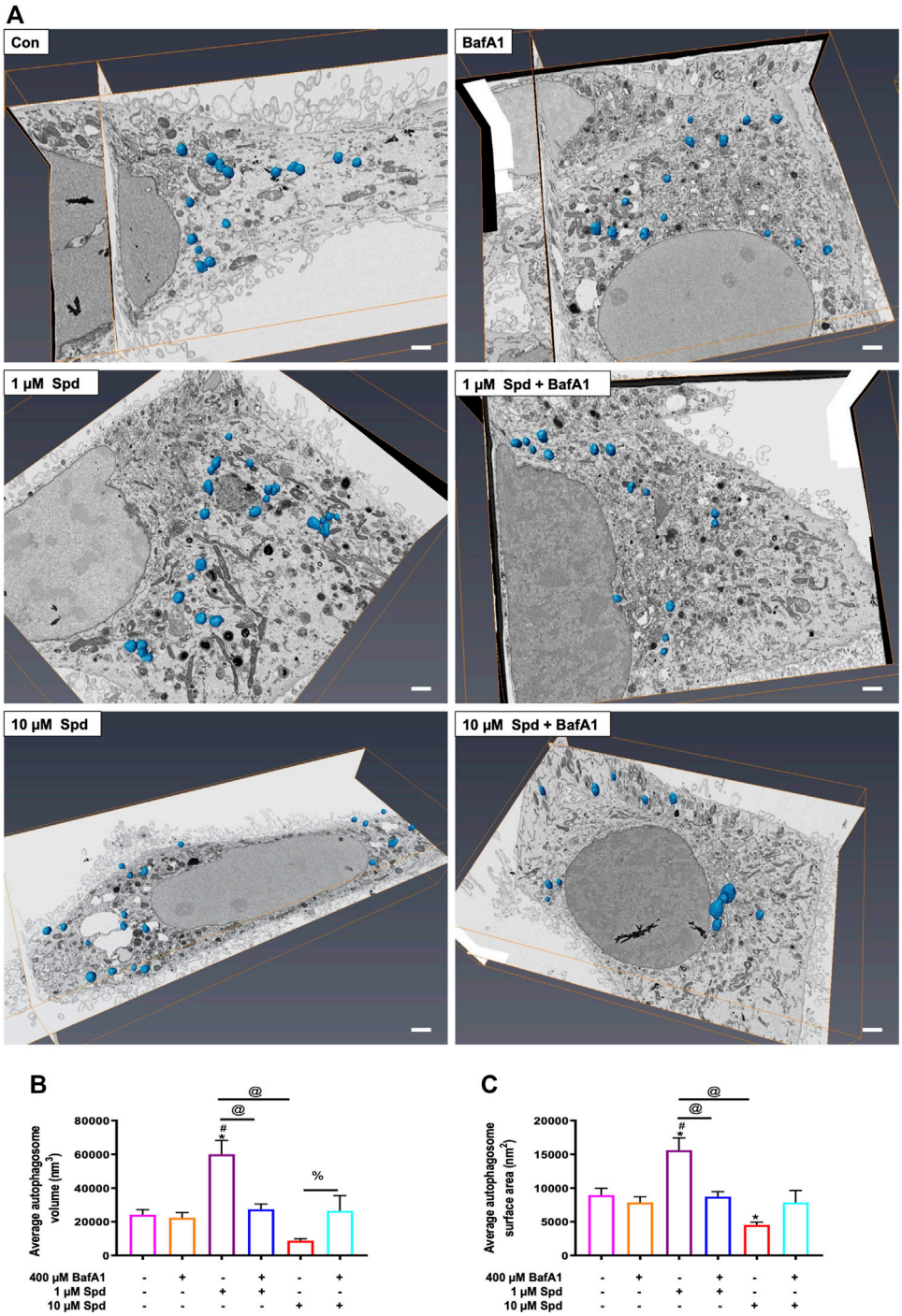

FIGURE 6 | Effect of spermidine on cargo clearance and size regulation. **(A)** Orthogonal views of FIB-SEM stack showing segmented autophagosomes (scale bar: 1 μm). **(B)** Morphometric analysis of autophagosome volume and **(C)** surface area following treatments. Data are presented as mean ± SEM. A total of 15–25 autophagosomes analysed per treatment group. Spermidine at low concentration induces autophagosomes capable of large volume clearance. * = $p < 0.05$ vs. control, # = $p < 0.05$ vs. BafA1, @ = $p < 0.05$ vs. 1 μM Spd and % = $p < 0.05$ vs. 10 μM Spd.

(untreated), BafA1, 1 μM Spd + BafA1 and 10 μM Spd treatment group (**Figure 6A,B**; **Supplementary Video S2**, **Supplementary Figure S3**). Similarly, autophagosome surface area was significantly increased in the 1 μM Spd group compared to the control (untreated), BafA1, 1 μM Spd + BafA1 and 10 μM Spd treatment group (**Figure 6A,C**; **Supplementary Figure S3**), while the surface area was significantly reduced in the 10 μM Spd treated group compared to the control (untreated) group.

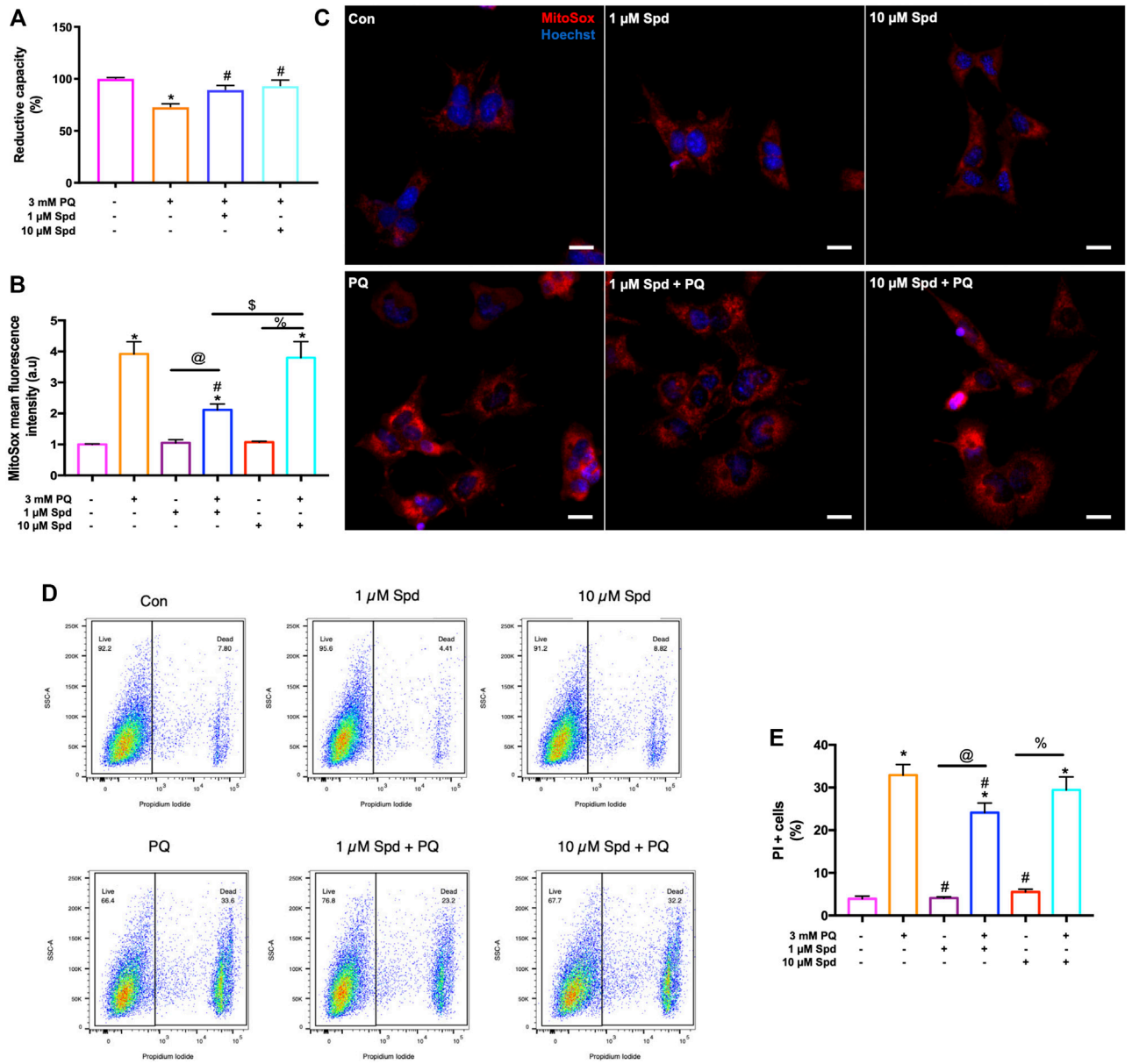

FIGURE 7 | Low concentration of spermidine reduces ROS production and delay cell death onset following paraquat-induced neurotoxicity. **(A)** Reductive capacity indicating an improvement in cellular viability in cells pre-treated with spermidine compared to PQ alone. Data are presented as mean ± SEM, $n = 3$ with 6 replicates per group. * = $p < 0.05$ vs control, # = $p < 0.05$ vs PQ. **(B)** quantitative analysis of mitochondrial ROS production and **(C)** representative fluorescence micrographs following treatments. MitoSox fluorescence intensity was increased in PQ treated group, while decreased with 1 μM Spd + PQ. Scale bar: 20 μm. **(D,E)** quantitative analysis of cell death onset following treatments. PI positive cells were reduced in 1 μM Spd + PQ compared to PQ treated group. Data are presented as mean ± SEM, $n = 3$ with 2 replicates per group. * = $p < 0.05$ vs control group, # = $p < 0.05$ vs. PQ, @ = $p < 0.05$ vs. 1 μM Spd, % = $p < 0.05$ vs. 10 μM Spd, and $ = $p < 0.05$ vs 1 μM Spd + PQ.

3.5 Low Concentration of Spermidine Improves Cellular Viability, Reduces ROS Production, and Protects Against Cell Death Onset in Paraquat Treated Cells

To assess concentration-dependent effects of spermidine, GT1-7 cells treated with 1 & 10 μM Spd followed by exposure to 3 mM PQ were assessed for cellular viability, ROS production and loss of membrane integrity [propidium iodide (PI) uptake] using a WST-1 assay and flow cytometry. Analysis showed that PQ treated groups displayed a significantly reduced cellular viability, while both 1 μM Spd + PQ and 10 μM Spd + PQ significantly improved cellular viability (**Figure 7A**). Flow cytometry and immunofluorescence analysis of ROS production revealed a significant increase in the PQ treated group (**Figures 7B,C**), whereas 1 μM Spd + PQ significantly decreased ROS production. PI positive cells were significantly increased in the PQ treated group while decreased in the 1 μM Spd + PQ treated group (**Figures 7D,E**).

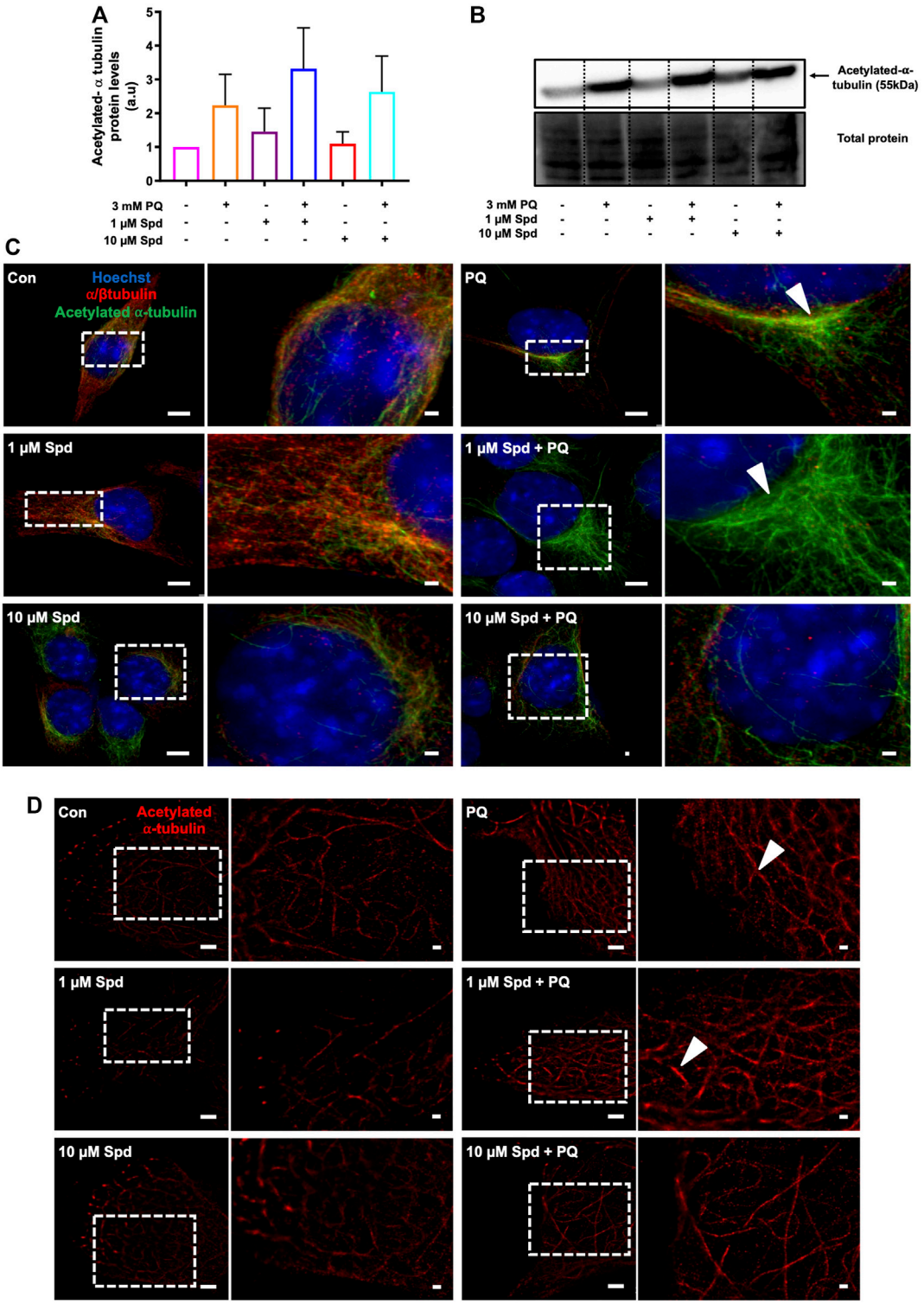

FIGURE 8 | Spermidine increases the acetylation signal of tubulin in paraquat treated cells. **(A)** densitometric quantification and **(B)** representative western blot for acetylated α-tubulin protein levels in GT1-7 cells following treatment with a low and high concentration of spermidine followed by exposure to paraquat. Data are presented as mean ± SEM, $n = 3$. **(C,D)** representative micrographs for acetylated α-tubulin with SR-SIM (scale bar: 5 and 1 μm) and dSTORM (scale bar: 2 and 0.5 μm) showing highest intensity signal with 1 μM Spd + PQ compared to PQ. Arrowheads indicate regions of strong acetylated α-tubulin signal.

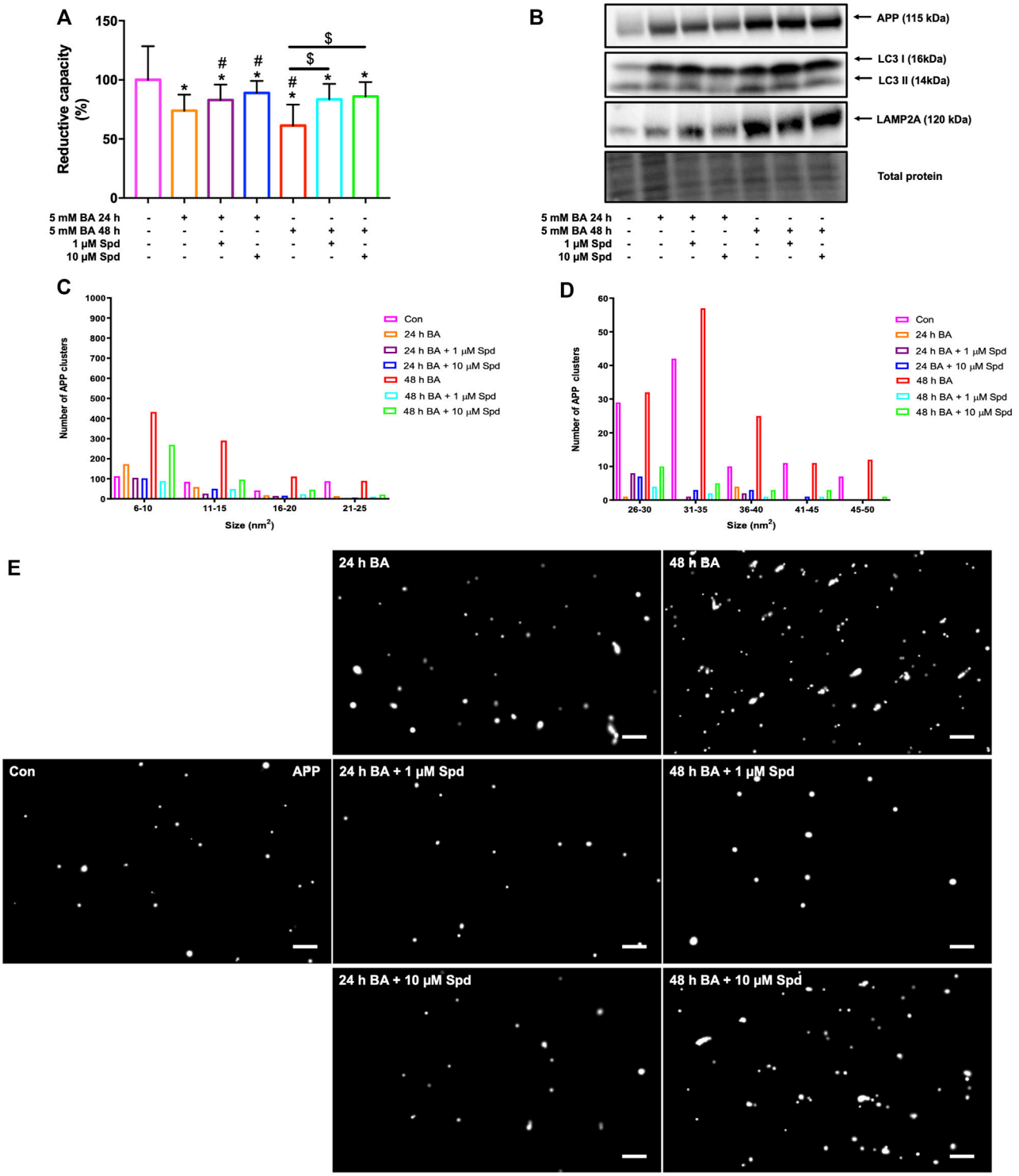

FIGURE 9 | Spermidine protects against APP-induced cytotoxicity and reduces the size and number of APP clusters. **(A)** Reductive capacity and **(B)** western blot analysis of APP, LC3-I/II and LAMP2A protein levels following treatment with a low and high concentration of spermidine in N2aSwe cells treated with BA overtime to overexpress APP ($n = 3$). * = $p < 0.05$ vs. control, # = $p < 0.05$ vs. 24 h BA and $ = $p < 0.05$ vs. 48 h BA. **(C–E)** Size distribution of APP clusters and representative dSTORM micrographs in Gauss mode showing the localisation of APP clusters. Spermidine reduces the size and number of APP clusters. Scale bar: 0.5 μm.

3.6 Low Concentration of Spermidine Increases the Acetylation of α-tubulins in Paraquat Treated Cells

Autophagosome transport relies on a functional tubulin network (Xie et al., 2010; Jahreiss et al., 2008) with the autophagy machinery closely engaging with the cell's acetylation processes (Pietrocola et al., 2015). Here we assessed the effect of a low and of a high concentration of spermidine on tubulin acetylation following PQ treatment. Western blot analysis revealed no significant differences in the levels of acetylated α-tubulin between treatment groups (**Figures 8A,B**), although a trend towards an increase was observed in the 1 μM Spd + PQ treated group compared to PQ alone. Upon visual inspection of the fluorescence micrographs from SR-SIM and single-molecule microscopy, acetylated α-tubulin signal and density was indeed enhanced in cells of the 1 μM Spd + PQ treated group compared to PQ alone (**Figures 8C,D**).

3.7 Spermidine Improves Cellular Viability and Reduces the Number of APP Clusters By Enhancing Autophagy in N2aSwe Cells

We next evaluated the protective effects of a low and of a high concentration of spermidine in N2aSwe cells overexpressing APP. A time-dependent decrease in cellular viability was observed following APP overexpression for 24 and 48 h, while spermidine treatment significantly improved cellular viability at both time points (**Figure 9A**). In addition, N2aSwe cells exhibited a time-dependent increase in APP, LC3-II and LAMP2A protein levels (**Figure 9B**). dSTORM analysis revealed a size distribution profile of APP clusters ranging from 6 to 50 nm^2 (**Figure 9C–E**; **Supplementary Figure S2**). Treatment with BA for 48 h resulted in an increase in the number of APP clusters of all sizes compared to the control, while BA for 24 h displayed a higher number of APP clusters at sizes 6–10 nm^2. In addition, spermidine treatment after 24 h BA resulted in the clearance of APP clusters as evident by the reduction in the number of APP clusters at sizes 6–25 nm^2, while treatment after 48 h BA cleared APP clusters, leading to a decrease in the number of APP clusters of all sizes (**Figures 9C–E**; **Supplementary Figure S2**).

3.8 Spermidine Reduces Lipid Peroxidation, and APP Protein Levels in the Hippocampus and Cortex in a Mouse Model of Paraquat-Induced Neuronal Injury

To confirm the protective effects of spermidine against neuronal toxicity associated with neurodegeneration, a mouse model of paraquat-induced neuronal injury was used. We focussed on the hippocampus and cerebral cortex, the two regions impacted in the early and late stages of AD, respectively. Paraquat exposure resulted in a significant increase in lipid peroxidation end-product 4-hydroxy-2-nonenal (4HNE), a marker for oxidative stress, in the hippocampus (**Figures 10A,B**), but not in the cortex (**Figures 10C,D**). Similarly, a significant increase in APP protein levels was observed in the hippocampus, while no significant changes were detected in the cortex, suggesting injury susceptibility. Combination treatment of spermidine with PQ caused a significant reduction in 4HNE and APP protein levels in both regions, suggesting protective effects of spermidine in this context.

3.9 Differential Impact of Spermidine on Tubulin Acetylation and Autophagic Activity in the Hippocampus and Cortex in a Mouse Model of Paraquat-Induced Neuronal Injury

Given the role of spermidine in autophagy and protein acetylation, we assessed the effects of spermidine on tubulin acetylation and p62 expression levels. Paraquat exposure resulted in a significant decrease in acetylated tubulin protein levels in the hippocampus (**Figures 11A,B**), while no significant changes were observed in the cortex (**Figures 11C,D**). Combination treatments of spermidine with paraquat in the hippocampus significantly increased acetylated α-tubulin protein levels compared to PQ treatment alone, while increasing the levels of p62 in a concentration-dependent manner. In the cortex region, combination treatment of the low concentration spermidine significantly increased p62 protein levels compared to PQ treatment alone, whereas co-treatment with the high concentration of spermidine significantly decreased acetylated α-tubulin while having no significant effect on p62 (**Figures 11C,D**).

4 DISCUSSION

In this study, we revealed three critical aspects with regards to autophagy and cell death control. Firstly, a concentration-dependent effect of autophagy-inducing drugs on autophagic flux exists and its detection is highly dependent on the sensitivity of the method employed. Secondly, higher autophagic flux does not necessarily confer a higher degree of neuronal protection; and thirdly, susceptibility to PQ exposure and associated protection in the brain shows region specificity.

4.1 A Concentration-Dependent Autophagic Flux Exists Upon Spermidine Exposure

Although autophagy modulation using pharmacological agents has received considerable attention over the past years and although many autophagy modulating drugs are now known, it remains unclear to what extent different concentrations would change autophagic activity or autophagic flux, especially given the dynamic and cell-specific nature of protein degradation and proteolysis. One of the challenges in this context is to accurately assess and dissect the pathway intermediates i.e., autophagosomal and autolysosomal pool sizes and their turnover in a highly sensitive manner, to better understand the underlying mechanisms that govern a particular autophagic activity. Here, we report that a concentration-

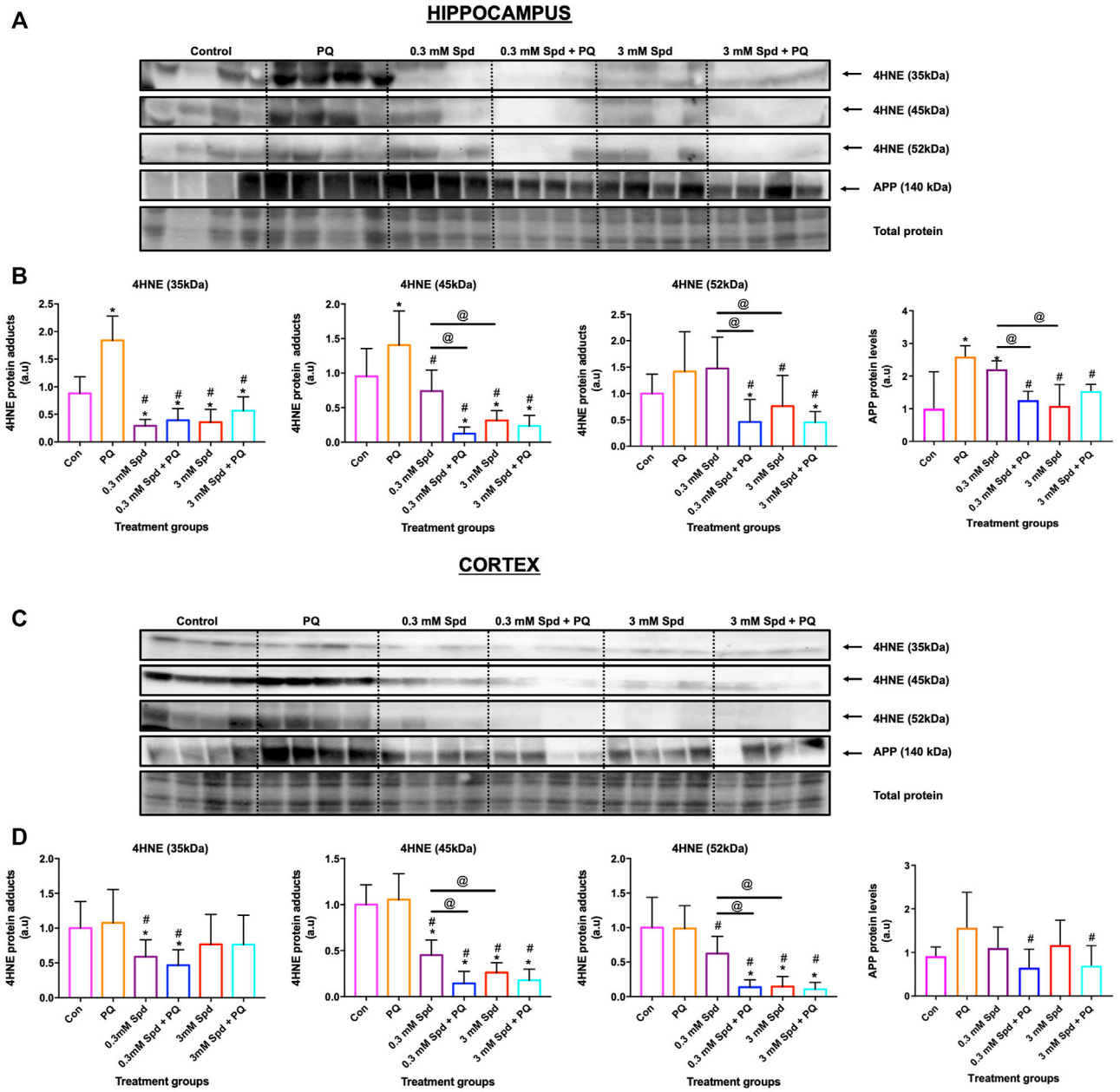

FIGURE 10 | Spermidine reduces lipid peroxidation and amyloidogenic processing in the hippocampus and cortex region. Representative western blot and densitometric analysis of 4HNE adducts (35, 45 and 52 kDa) and APP protein levels in the hippocampus **(A and B)** and **(C and D)** cortex. The data are expressed as mean ± SEM. A total of 6–10 animals were used per group ($n = 6–10$). Spermidine in combination with PQ reduced 4HNE and APP protein levels compared to PQ treated group. * = $p < 0.05$ vs. control, # = $p < 0.05$ vs. PQ and @ = $p < 0.05$ vs. 0.3 mM Spd, arbitrary units (a.u).

dependent effect on autophagy flux exists and that the detected change in flux is highly dependent on the sensitivity of the method used. Using western blotting, we found that only the high concentration of spermidine (10 μM) robustly induces autophagy activity (**Figures 1A–C**), while fluorescence-based analysis revealed that both low and high concentrations of spermidine (1 and 10 μM) enhance autophagy activity (**Figure 2**), whereas TEM analysis (i.e., number of AVs) showed that both the low and high concentration of spermidine do not enhance autophagic activity above basal levels (**Figures 3A,C**). These findings suggest that pool size assessment with FM is likely more sensitive. Indeed, FM allows for a relatively clear distinction between autophagosomes and autolysosomes using fluorescent labels which is not possible with western blotting or TEM, hence these structures in TEM are collectively called AVs. In addition, FM allows for imaging the whole cell using z-stacks, therefore providing data from the entire cell rather than one

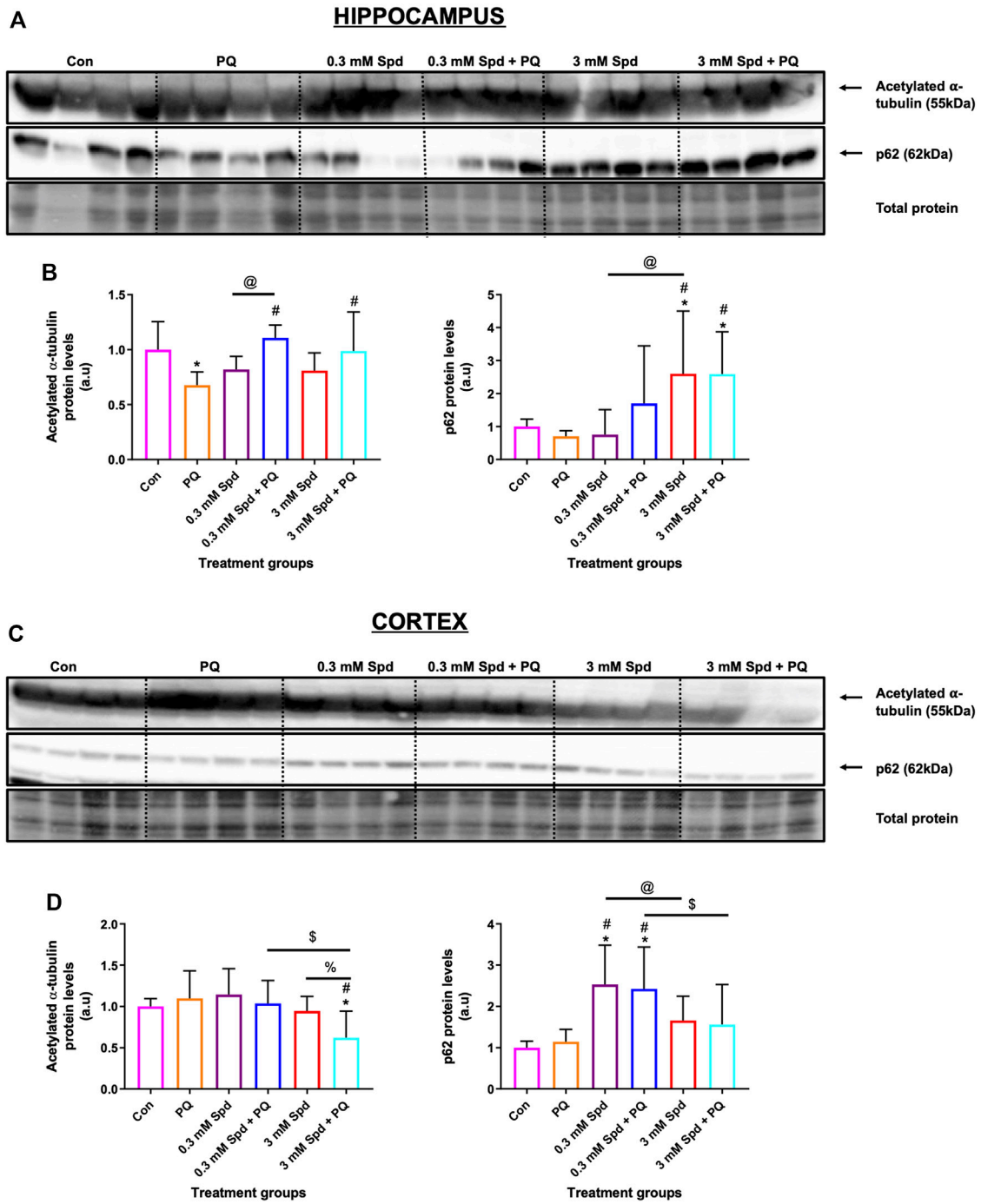

FIGURE 11 | Differential effect of spermidine on tubulin acetylation and autophagic activity in the hippocampus and cortex. **(A,B)** Representative western blot and densitometric analysis of acetylated α-tubulin and p62 protein levels in the hippocampus and **(C,D)** cortex. The data are expressed as mean ± SEM. A total of 6–10 animals were used per group (n = 6–10). Spermidine in combination with PQ increased acetylated α-tubulin and p62 compared to PQ treated group in the hippocampus. In the cortex region, combination treatment of the low concentration spermidine increased p62 protein levels, while co-treatment with the high concentration of spermidine decreased acetylated α-tubulin with no effect on p62 levels. * = $p < 0.05$ vs. control, # = $p < 0.05$ vs. PQ, @ = $p < 0.05$ vs. 0.3 mM Spd, $ = $p < 0.05$ vs. 0.3 mM Spd + PQ and % = $p < 0.05$ vs. 3 mM Spd, arbitrary units (a.u).

z-section from conventional TEM which was used here for EM-based quantification. This may indeed be a contributing factor why we observed no significant changes with TEM analysis (**Figures 3A,C**). Consistent with the FM results, our CLEM analysis supports the notion that 1 μM spermidine also induces autophagy activity as indicated by the increase in

RFP-LC3ΔG positive structures in the 1 and 10 μM spermidine treated cells (**Figure 4**; **Supplementary Figure S1**) and further suggests that a heightened flux has led subsequently to engulfment of cytoplasmic cargo. Such observations have not yet been reported and enrich the autophagy field, indicating the temporal effects of autophagy activity on the clearance of cytoplasmic content. Although commonly used techniques such as western blotting and TEM provide invaluable information about autophagic activity i.e., autophagy protein, autophagosome abundance and cargo type contained in autophagosome, their use in isolation could result in the misinterpretation of data as they are not able to distinguish between autophagosomes and autolysosome pool size.

Moreover, we report that the size in vacuolar structures in response to the autophagy induction plays a major role in autophagic flux. EM allows observing different sizes in structures and autolysosomes, all of which allows to gain insights into cargo clearance and pool size dynamics. Although we did not see any differences in the sizes of AVs in the cells treated with only spermidine compared to the control cells, the combination of spermidine with BafA1 decreased the size of AVs compared to BafA1 alone, with 1 μM Spd + BafA1 reducing the size more compared to 10 μM Spd + BafA1 (**Figures 3B,C**). To our knowledge, this is the first study to report a reduction in the size of AVs upon spermidine treatment in the presence of BafA1 and is in contrast with our 3D-CLEM results (**Figure 6**). Morphometric analysis of reconstructed autophagosomes (**Figure 6**; **Supplementary Figure S3**) showed that spermidine treatment at a low concentration increases the volume and surface area of autophagosomes (**Figure 6**; **Supplementary Video S2**, **Supplementary Figure S3**), suggesting size regulation and effective cargo clearance. To our surprise, spermidine at a high concentration resulted in a decrease in the volume and surface area of autophagosomes, with a significant decrease seen in the surface area. These results suggest a concentration-dependent effect of spermidine on the volume and surface area and may highlight the importance of cargo-specific turnover in the context of a given autophagosome flux. Indeed, several studies have shown that Atg8 plays an important role in the size regulation of autophagosomes (Xie et al., 2008; Jin and Klionsky, 2014). In these studies, it was demonstrated that autophagy induction using rapamycin or nitrogen starvation elevates both ATG8 mRNA and its protein product, increasing the size of autophagosomes. Here, we suspect that spermidine might elicit similar mechanisms leading to an increase in autophagosome volume. Taken together, our data indicate how the mammalian system may respond to an autophagy modulator through both flux control as well as autophagosome size/volume control, thereby impacting cargo clearance. This deserves further study.

4.2 Higher Autophagic Flux Does Not Necessarily Lead to a Higher Degree of Protection

Neurons depend vastly on a high degree of efficient autophagic flux to maintain proteostasis. Modulation of autophagy using pharmacological agents is widely accepted as one of the major therapeutic interventions for age-related pathologies. Spermidine has been shown to induce autophagy in neurons, thus enabling effective clearance of aggregate prone proteins associated with neurodegeneration (Büttner et al., 2014; Sigrist et al., 2014; Bhukel et al., 2017; Yang et al., 2017). Despite the autophagy enhancing effects of spermidine, the impact of different concentrations in autophagy modulation and on subsequent protein clearance and neuronal toxicity is unclear. Here, we report that exposure to PQ leads to cellular toxicity, increased ROS production and loss of membrane integrity, while pre-treatment with spermidine at a low concentration (1 μM Spd) protected against the cytotoxic effects induced by PQ (**Figure 7**). PQ is a neurotoxicant associated with Alzheimer's disease (Chen L. et al., 2012; Chen Y. W. et al., 2012; Jaroonwitchawan et al., 2017). It accumulates in the mitochondria, leading to ROS production (Jones and Vale, 2000; Yumino et al., 2002; Cochemé and Murphy, 2008) and cell death onset (Chun et al., 2001; González-Polo et al., 2004; Niso-Santano et al., 2006). Previous studies have shown that spermidine mediates protection against oxidative stress and cell death induced by H_2O_2 (Rider et al., 2007; Guo et al., 2011). Since spermidine is a known antioxidant, we speculate that it protects against ROS damage by increasing the generation of antioxidants enzymes such as superoxide dismutase (SOD) and glutathione peroxidase (GPX). In line with these findings, others have reported a decrease in PQ-induced ROS generation in SH-SY-5Y cells following pre-treatment with an antioxidant such as N-acetylcysteine (NAC) (Zhou et al., 2017) and curcumin (Jaroonwitchawan et al., 2017). Moreover, spermidine has been shown to serve dual roles, as it can also act as a substrate for enzymes responsible for ROS production (Murray Stewart et al., 2018). Thus, this might explain why pre-treatment with a high concentration of spermidine (10 μM Spd) failed to protect against ROS damage.

We also show that PQ exposure enhances the acetylation of α-tubulin compared to the control levels and that pre-treatment with low concentration of spermidine resulted in higher levels of acetylated α-tubulin compared to the PQ alone (**Figure 8**). These results suggest that PQ did not result in destabilization of microtubules but rather increased their stability, which appeared enhanced further in the presence of spermidine. We speculate that the increase in the stability of microtubules observed following PQ exposure might be the result of a stress response, likely in part due to autophagy activation. In support of this notion, various studies have reported that low concentrations of PQ stimulate characteristics of autophagy in *in vitro* models, with neurons ultimately succumbing to cell death (Niso-Santano et al., 2006; González-Polo et al., 2007a; González-Polo et al., 2007b; González-Polo et al., 2009). Due to the increased ROS generation, we observed following PQ treatment, this may suggest that PQ acts as a stressor that induces autophagy, probably in the initial stages, prior to mitochondrial dysfunction. Indeed, it has been shown that PQ induces an early ER stress response which was concurrent with activation of autophagy (González-Polo et al., 2007a; González-Polo et al., 2007b; Niso-Santano et al., 2011). Acetylation of microtubules is directly involved in autophagy as microtubules facilitate the transport of

autophagosomes to lysosomes for degradation (Xie et al., 2010; Phadwal et al., 2018). Thus, spermidine increases the acetylation of tubulin and may facilitate autophagy degradation. In line with these findings, Phadwal et al. (2018) reported that spermine, a precursor of spermidine, increased tubulin acetylation resulting in the degradation of aggregated proteins in an *in vitro* model of Prion disease.

Next, we report in N2aSwe cells that APP overexpression induces cytotoxicity in a time-dependent manner, while spermidine at both concentrations protects against cytotoxicity induced by APP overexpression (**Figure 9A**). To our knowledge, this study is the first to demonstrate the protective effects of spermidine in an APP overexpression model. Administration of autophagy modulators has been shown to protect against APP-induced cytotoxicity effects in N2aSwe cells (Lee et al., 2015). Overproduction of APP results in increased levels of Aβ and APP C-terminal fragments (CTFβ), both of which contribute to the pathology of AD (Walsh and Selkoe, 2007). Here, we show that APP overexpression for 24 and 48 h led to an increase in APP protein levels (**Figure 9B**) and APP clusters in a time-dependent manner (**Figures 9C–E**). Interestingly, we noted that autophagy activity remained functional at both time points, with LC3-II and LAMP2A levels increasing in a time-dependent manner. Although spermidine did not reduce the levels of APP after 48 h of overexpression, both concentrations enhanced the clearance of APP clusters, thus reducing their number, however, the low concentration of spermidine was more effective. To our knowledge, this study is the first to assess APP clusters and their clearance by spermidine using dSTORM in models of AD and supports the findings obtained through WST-1 analysis. We speculate that spermidine protects against APP-induced toxicity by inducing autophagy (indicated by the increase in LC3-I levels), thereby shifting the equilibrium of soluble and aggregated APP. Overall, this study contributes to the current body of literature, demonstrating that it must be considered which drug concentration to use, to better align flux control with the most favourable autophagy activity in the context of autophagy dysfunction.

4.3 Susceptibility to PQ in the Brain Is Region Specific

Although the mechanisms of action of PQ in AD are not fully elucidated, it is well known that PQ exerts its toxicity by inducing oxidative stress and mitochondrial damage (Lin and Beal, 2006; Drechsel and Patel, 2008; Baltazar et al., 2014), both of which have been implicated in the pathogenesis of AD (Lin and Beal, 2006; Chen L. et al., 2012). Multiple studies have reported high levels of lipid peroxidation, a marker for oxidative stress in the brains of patients with AD (Zhao and Zhao, 2013; Wang et al., 2014). Here, we report that PQ-induced toxicity impacts the brain regions differentially, with the hippocampus being highly susceptible to PQ-induced injury (**Figure 10**). Exposure to PQ enhanced lipid peroxidation and APP protein levels in the hippocampus, but not in the cortex, suggesting injury susceptibility. In addition, we show that PQ treatment resulted in the destabilization of microtubules i.e., a decrease in acetylated tubulin, in the hippocampus, but not in the cortex (**Figure 11**). These results may point towards region-specificity and are in line with the findings that the pathological changes of protein aggregation and neuronal loss are manifesting first in the hippocampus and later in the cortex, as the disease pathology progresses (Braak and Braak, 1991; Braak et al., 2004; Braak and Del Tredici, 2012). Both regions were favourably impacted by spermidine treatment in drinking water (0.3 mM Spd + PQ and 3 mM Spd + PQ) as evident by a decrease in 4HNE and APP protein levels, supporting the notion of a supplement-based adjuvant therapy. In addition, spermidine treatment rescued PQ-induced destabilization of the microtubules in the hippocampus but not in the cortex. Spermidine is known to increase the acetylation of tubulin by suppressing EP300, and in turn stimulate autophagic flux in this manner (Pietrocola et al., 2015; Madeo et al., 2018). Increased acetylation of microtubules facilitates the retrograde mobilization of autophagosomes from the periphery to the lysosomes localised in the cytoplasm for degradation (Xie et al., 2010; Phadwal et al., 2018). Therefore, we hypothesise that spermidine increases the acetylation of tubulin by suppressing EP300, leading to an increased autophagic flux, where toxic protein and damaged organelles induced by PQ treatment are engulfed in the autophagosomes and transported to the lysosomes for subsequent degradation. In support of this notion, here we report that spermidine at both dosages upregulated autophagy activity i.e., increase p62 levels in a concentration-dependent manner in the hippocampus, while only the low dose increased p62 in the cortex. Taken together, our findings shed light on the mechanisms of spermidine induced neuronal protection in this model system. Due to the importance of the hippocampus in neurodegeneration and memory formation, these results are of significance and point towards spermidine as a potential therapeutic agent for Alzheimer's disease.

5 CONCLUSION

Taken together, it becomes clear that autophagy assessment requires the use of multiple tools as not all techniques are sufficiently sensitive to detect differences in flux, with effects manifesting differently under control and pathological conditions, depending on the injury model, cell type, and model system employed. We provide evidence of the distinct, context dependent protective role of spermidine in an *in vitro* model of APP overexpression as well as *in vitro* and *in vivo* models of PQ-induced neuronal toxicity, suggesting that the cell type, nature of the injury, brain region and the drug concentration utilised should be critically considered when performing drug screening so that a given concentration can be most favourably aligned to offset autophagy dysfunction. It is widely known that neurons depend vastly on a high degree of efficient autophagic flux to survive due to their post-mitotic nature, high protein synthesis rate and energy demands. However, protein degradation and proteolysis are regional and cell-specific, requiring sensitive characterization of autophagic flux, autophagosomal and lysosomal pool sizes and transition

time to better understand the underlying mechanisms that govern a particular autophagic activity. While extensive data from preclinical studies provide strong evidence that autophagy upregulation provides therapeutic benefits for the treatment of AD, numerous unanswered questions remain regarding the efficiency of autophagy induction using such interventions. Therefore, a better understanding is required regarding the context of neuronal protection, including a quantitative approach to assess autophagy. This is critical in the context of brain-specific spatio-temporal autophagic activity in physiology and neuronal pathology, to better regulate autophagy and thereby control neuronal fate. In addition, autophagy modulation requires careful alignment with aggregate-prone protein cargo levels as well as markers of disease, to precision-target the autophagic machinery according to defect localization. Here, we have utilised dSTORM to assess APP clusters and 3D CLEM to assess autophagosome volume as a point of departure in this regard. Future work may, therefore, focus on improved methodologies, including high throughput-based, multi-scale approaches to advance translation. Our results suggest that the administration of spermidine may represent a favourable therapeutic strategy for the treatment of AD. Further studies using transgenic mouse models of APPSwe, PS1 and 3xTg AD are warranted to further verify the protective effects of spermidine. In such models, behavioural studies assessing cognitive function will provide invaluable information about the role of spermidine in learning and memory. Applications with this approach within the *in vitro* and *in vivo* environment will undoubtedly allow improved and progressive translation of autophagy control in preclinical and clinical settings and may advance autophagy modulation as a prime candidate for the treatment of neurodegeneration.

DATA AVAILABILITY STATEMENT

The original contributions presented in the study are included in the article/**Supplementary Material**, further inquiries can be directed to the corresponding author.

ETHICS STATEMENT

The animal study was reviewed and approved by Animal research ethics committee (SU-ACUD16-00175), Stellenbosch University, South Africa.

AUTHOR CONTRIBUTIONS

DL: Methodology, experimental conduct, data analysis and writing of the manuscript. BL and CK: Conceptualization, supervision, reviewing and editing. CP and LC: Performed FIB-SEM acquisition, alignment of FIB-SEM data and 3D registration of SR-SIM to FIB SEM. JK, LM, and NH: Performed CLEM analysis.

FUNDING

This research was funded by the National Research Foundation South Africa (NRF), the South African Medical Research Council (SAMRC), and the Cancer Association South Africa (CANSA). Furthermore, this work was supported by the Francis Crick Institute, which receives its core funding from Cancer Research UK (FC001999), the UK Medical Research Council (FC001999), and the Wellcome Trust (FC001999).

ACKNOWLEDGMENTS

We wish to thank Lize Engelbrecht and Rozanne Adams at the Central Analytical Facility, Stellenbosch University for technical assistance. We would like to acknowledge the National Research Foundation South Africa (NRF) for financial support for Dumisile Lumkwana.

SUPPLEMENTARY MATERIAL

The Supplementary Material for this article can be found online at: https://www.frontiersin.org/articles/10.3389/fcell.2022.819571/full#supplementary-material

Supplementary Figure S1 | Spermidine induces autophagy. SR-SIM micrographs showing the overview of GT1-7 cells expressing GFP-LC3-RFP-LC3ΔG after treatments. (Top panel) spermidine (1 and 10 μM) induces the accumulation of RFP-LC3ΔG positive structures compared to the control (untreated) cells, suggesting heightened autophagic flux. (Bottom panel), spermidine in combination with BafA1 induces the accumulation of GFP-LC3 positive structures compared to BafA1 treated group, suggesting an induced flux. Scale bar: 3 μm.

Supplementary Figure S2 | Spermidine reduces the size and number of APP clusters upon APP overexpression. Representative dSTORM micrographs in Gauss mode showing the localisation of APP clusters in the whole cell and their clearance by spermidine. Scale bar: 1 μm.

Supplementary Figure S3 | 3D model of autophagosomes. Overview of reconstructed autophagosomes from FIB-SEM stack showing different sizes of autophagosomes in the control (untreated) and BafA1 group (Left), 1 μM Spd and 1 μM Spd + BafA1 (middle) and 10 μM Spd & 10 μM Spd + BafA1 (right). Scale bar: 50 nm.

Supplementary Video S1 | 3D Correlative SR-SIM and FIB-SEM of 1 μM Spd treated cell showing the localisation of GFP-LC3 and RFP-LC3ΔG positive structures in vacuolar structures of high electron density. Both GFP-LC3 and RFP-LC3ΔG decorate the conglomerate structure. RFP-LC3ΔG localises inside the conglomerate structure as part of the cargo.

Supplementary Video S2 | 3D Correlative SR-SIM and FIB-SEM of 1 μM Spd treated cell. GT 1-7 neuronal cell expressing GFP-LC3-RFP-LC3ΔG is shown in relation to its rendered autophagosomes using FIB-SEM data. Segmentation of autophagosomes highlight large volume vesicles.

REFERENCES

Amaravadi, R. K., Kimmelman, A. C., and Debnath, J. (2019). Targeting Autophagy in Cancer: Recent Advances and Future Directions. *Cancer Discov.* 9, 1167–1181. doi:10.1158/2159-8290.CD-19-0292

Andrieu, S., Coley, N., Lovestone, S., Aisen, P. S., and Vellas, B. (2015). Prevention of Sporadic Alzheimer's Disease: Lessons Learned from Clinical Trials and Future Directions. *Lancet Neurol.* 14, 926–944. doi:10.1016/S1474-4422(15)00153-2

Baltazar, M. T., Dinis-Oliveira, R. J., de Lourdes Bastos, M., Tsatsakis, A. M., Duarte, J. A., and Carvalho, F. (2014). Pesticides Exposure as Etiological Factors of Parkinson's Disease and Other Neurodegenerative Diseases-A Mechanistic Approach. *Toxicol. Lett.* 230, 85–103. doi:10.1016/j.toxlet.2014.01.039

Bhukel, A., Madeo, F., and Sigrist, S. J. (2017). Spermidine Boosts Autophagy to Protect from Synapse Aging. *Autophagy* 13, 444–445. doi:10.1080/15548627.2016.1265193

Bogovic, J. A., Hanslovsky, P., Wong, A., and Saalfeld, S. (2016). "Robust Registration of Calcium Images by Learned Contrast Synthesis," in 2016 IEEE 13th International Symposium on Biomedical Imaging (ISBI 2016), Prague, Czech Republic, 13–16 April, 2016. doi:10.1109/ISBI.2016.7493463

Braak, H., and Braak, E. (1991). Neuropathological Stageing of Alzheimer-Related Changes. *Acta Neuropathol.* 82, 239–259. doi:10.1007/BF00308809

Braak, H., and Del Tredici, K. (2012). Alzheimer's Disease: Pathogenesis and Prevention. *Alzheimers Demen.* 8, 227–233. doi:10.1016/j.jalz.2012.01.011

Braak, H., Ghebremedhin, E., Rüb, U., Bratzke, H., and Del Tredici, K. (2004). Stages in the Development of Parkinson's Disease-Related Pathology. *Cell Tissue Res.* 318, 121–134. doi:10.1007/s00441-004-0956-9

Büttner, S., Broeskamp, F., Sommer, C., Markaki, M., Habernig, L., Alavian-Ghavanini, A., et al. (2014). Spermidine Protects against α-synuclein Neurotoxicity. *Cell Cycle* 13, 3903–3908. doi:10.4161/15384101.2014.973309

Cai, Z., Zhao, B., Li, K., Zhang, L., Li, C., Quazi, S. H., et al. (2012). Mammalian Target of Rapamycin: A Valid Therapeutic Target through the Autophagy Pathway for Alzheimer's Disease? *J. Neurosci. Res.* 90, 1105–1118. doi:10.1002/jnr.23011

Chen, L., Yoo, S.-E., Na, R., Liu, Y., and Ran, Q. (2012a). Cognitive Impairment and Increased Aβ Levels Induced by Paraquat Exposure Are Attenuated by Enhanced Removal of Mitochondrial H2O2. *Neurobiol. Aging* 33, e15–432. doi:10.1016/j.neurobiolaging.2011.01.008

Chen, Y. W., Yang, Y.-T., Hung, D.-Z., Su, C.-C., and Chen, K.-L. (2012b). Paraquat Induces Lung Alveolar Epithelial Cell Apoptosis via Nrf-2-Regulated Mitochondrial Dysfunction and ER Stress. *Arch. Toxicol.* 86, 1547–1558. doi:10.1007/s00204-012-0873-8

Chun, H. S., Gibson, G. E., DeGiorgio, L. A., Zhang, H., Kidd, V. J., and Son, J. H. (2001). Dopaminergic Cell Death Induced by MPP+, Oxidant and Specific Neurotoxicants Shares the Common Molecular Mechanism. *J. Neurochem.* 76, 1010–1021. doi:10.1046/j.1471-4159.2001.00096.x

Cochemé, H. M., and Murphy, M. P. (2008). Complex I Is the Major Site of Mitochondrial Superoxide Production by Paraquat. *J. Biol. Chem.* 283, 1786–1798. doi:10.1074/jbc.M708597200

Cui, D., Xiong, X., and Zhao, Y. (2016). Cullin-RING Ligases in Regulation of Autophagy. *Cell Div.* 11, 1. doi:10.1186/s13008-016-0022-5

Davis, T., van Niekerk, G., Peres, J., Prince, S., Loos, B., and Engelbrecht, A.-M. (2018). Doxorubicin Resistance in Breast Cancer: A Novel Role for the Human Protein AHNAK. *Biochem. Pharmacol.* 148, 174–183. doi:10.1016/j.bcp.2018.01.012

Drechsel, D. A., and Patel, M. (2008). Role of Reactive Oxygen Species in the Neurotoxicity of Environmental Agents Implicated in Parkinson's Disease. *Free Radic. Biol. Med.* 44, 1873–1886. doi:10.1016/j.freeradbiomed.2008.02.008

du Toit, A., De Wet, S., Hofmeyr, J.-H., Müller-Nedebock, K., and Loos, B. (2018a). The Precision Control of Autophagic Flux and Vesicle Dynamics-A Micropattern Approach. *Cells* 7, 94. doi:10.3390/cells7080094

du Toit, A., Hofmeyr, J.-H. S., Gniadek, T. J., and Loos, B. (2018b). Measuring Autophagosome Flux. *Autophagy* 14, 1–12. doi:10.1080/15548627.2018.1469590

Eisenberg, T., Knauer, H., Schauer, A., Büttner, S., Ruckenstuhl, C., Carmona-Gutierrez, D., et al. (2009). Induction of Autophagy by Spermidine Promotes Longevity. *Nat. Cel Biol.* 11, 1305–1314. doi:10.1038/ncb1975

Eisenberg, T., Abdellatif, M., Schroeder, S., Primessnig, U., Stekovic, S., Pendl, T., et al. (2016). Cardioprotection and Lifespan Extension by the Natural Polyamine Spermidine. *Nat. Med.* 22, 1428–1438. doi:10.1038/nm.4222

Eskelinen, E.-L. (2008). To Be or Not to Be? Examples of Incorrect Identification of Autophagic Compartments in Conventional Transmission Electron Microscopy of Mammalian Cells. *Autophagy* 4, 257–260. doi:10.4161/auto.5179

Fan, J., Yang, X., Li, J., Shu, Z., Dai, J., Liu, X., et al. (2017). Spermidine Coupled with Exercise Rescues Skeletal Muscle Atrophy from D-Gal-Induced Aging Rats through Enhanced Autophagy and Reduced Apoptosis via AMPK-FOXO3a Signal Pathway. *Oncotarget* 8, 17475–17490. doi:10.18632/oncotarget.15728

Folch, J., Petrov, D., Ettcheto, M., Abad, S., Sánchez-López, E., García, M. L., et al. (2016). Current Research Therapeutic Strategies for Alzheimer's Disease Treatment. *Neural Plasticity* 2016, 1–15. doi:10.1155/2016/8501693

Galluzzi, L., Bravo-San Pedro, J. M., Levine, B., Green, D. R., and Kroemer, G. (2017). Pharmacological Modulation of Autophagy: Therapeutic Potential and Persisting Obstacles. *Nat. Rev. Drug Discov.* 16, 487–511. doi:10.1038/nrd.2017.22

García-Prat, L., Martínez-Vicente, M., Perdiguero, E., Ortet, L., Rodríguez-Ubreva, J., Rebollo, E., et al. (2016). Autophagy Maintains Stemness by Preventing Senescence. *Nature* 529, 37–42. doi:10.1038/nature16187

González-Polo, R. A., Rodrı´guez-Martı´n, A., Morán, J. M., Niso, M., Soler, G., and Fuentes, J. M. (2004). Paraquat-induced Apoptotic Cell Death in Cerebellar Granule Cells. *Brain Res.* 1011, 170–176. doi:10.1016/j.brainres.2004.02.078

González-Polo, R. A., Niso-Santano, M., Ortiz-Ortiz, M. A., Gomez-Martin, A., Moran, J. M., Garcia-Rubio, L., et al. (2007a). Inhibition of Paraquat-Induced Autophagy Accelerates the Apoptotic Cell Death in Neuroblastoma SH-SY5Y Cells. *Toxicol. Sci.* 97, 448–458. doi:10.1093/toxsci/kfm040

González-Polo, R. A., Niso-Santano, M., Ortíz-Ortíz, M. A., Gómez-Martín, A., Morán, J. M., García-Rubio, L., et al. (2007b). Relationship between Autophagy and Apoptotic Cell Death in Human Neuroblastoma Cells Treated with Paraquat: Could Autophagy Be a "Brake" in Paraquat-Induced Apoptotic Death? *Autophagy* 3, 366–367. doi:10.4161/auto.4194

González-Polo, R. A., Niso-Santano, M., Morán, J. M., Ortiz-Ortiz, M. A., Bravo-San Pedro, J. M., Soler, G., et al. (2009). Silencing DJ-1 Reveals its Contribution in Paraquat-Induced Autophagy. *J. Neurochem.* 109, 889–898. doi:10.1111/j.1471-4159.2009.06020.x

Guo, X., Harada, C., Namekata, K., Kimura, A., Mitamura, Y., Yoshida, H., et al. (2011). Spermidine Alleviates Severity of Murine Experimental Autoimmune Encephalomyelitis. *Invest. Ophthalmol. Vis. Sci.* 52, 2696. doi:10.1167/iovs.10-6015

Gupta, V. K., Scheunemann, L., Eisenberg, T., Mertel, S., Bhukel, A., Koemans, T. S., et al. (2013). Restoring Polyamines Protects from Age-Induced Memory Impairment in an Autophagy-dependent Manner. *Nat. Neurosci.* 16, 1453–1460. doi:10.1038/nn.3512

Hara, T., Nakamura, K., Matsui, M., Yamamoto, A., Nakahara, Y., Suzuki-Migishima, R., et al. (2006). Suppression of Basal Autophagy in Neural Cells Causes Neurodegenerative Disease in Mice. *Nature* 441, 885–889. doi:10.1038/nature04724

Jahreiss, L., Menzies, F. M., and Rubinsztein, D. C. (2008). The Itinerary of Autophagosomes: From Peripheral Formation to Kiss-And-Run Fusion with Lysosomes. *Traffic* 9, 574–587. doi:10.1111/j.1600-0854.2008.00701.x

Jaroonwitchawan, T., Chaicharoenaudomrung, N., Namkaew, J., and Noisa, P. (2017). Curcumin Attenuates Paraquat-Induced Cell Death in Human Neuroblastoma Cells through Modulating Oxidative Stress and Autophagy. *Neurosci. Lett.* 636, 40–47. doi:10.1016/j.neulet.2016.10.050

Jin, M., and Klionsky, D. J. (2014). Regulation of Autophagy: Modulation of the Size and Number of Autophagosomes. *FEBS Lett.* 588, 2457–2463. doi:10.1016/j.febslet.2014.06.015

Jones, G. M., and Vale, J. A. (2000). Mechanisms of Toxicity, Clinical Features, and Management of Diquat Poisoning: A Review. *J. Toxicol. Clin. Toxicol.* 38, 123–128. doi:10.1081/CLT-100100926

Kabeya, Y., Mizushima, N., Ueno, T., Yamamoto, A., Kirisako, T., Noda, T., et al. (2000). LC3, A Mammalian Homologue of Yeast Apg8p, Is Localized in Autophagosome Membranes after Processing. *EMBO J.* 19, 5720–5728. doi:10.1093/emboj/19.21.5720

Kaizuka, T., Morishita, H., Hama, Y., Tsukamoto, S., Matsui, T., Toyota, Y., et al. (2016). An Autophagic Flux Probe that Releases an Internal Control. *Mol. Cel* 64, 835–849. doi:10.1016/j.molcel.2016.09.037

Klionsky, D. J., Abdelmohsen, K., Abe, A., Abedin, M. J., Abeliovich, H., Acevedo Arozena, A., et al. (2016). Guidelines for the Use and Interpretation of Assays for Monitoring Autophagy (3rd Edition). *Autophagy* 12, 1. doi:10.1080/15548627.2015.1100356

Komatsu, M., Waguri, S., Chiba, T., Murata, S., Iwata, J.-i., Tanida, I., et al. (2006). Loss of Autophagy in the central Nervous System Causes Neurodegeneration in Mice. *Nature* 441, 880–884. doi:10.1038/nature04723

Kremer, J. R., Mastronarde, D. N., and McIntosh, J. R. (1996). Computer Visualization of Three-Dimensional Image Data Using IMOD. *J. Struct. Biol.* 116, 71–76. doi:10.1006/jsbi.1996.0013

LaRocca, T. J., Gioscia-Ryan, R. A., Hearon, C. M., and Seals, D. R. (2013). The Autophagy Enhancer Spermidine Reverses Arterial Aging. *Mech. Ageing Develop.* 134, 314–320. doi:10.1016/j.mad.2013.04.004

Lee, H. R., Shin, H. K., Park, S. Y., Kim, H. Y., Bae, S. S., Lee, W. S., et al. (2015). Cilostazol Upregulates Autophagy via SIRT1 Activation: Reducing Amyloid-β Peptide and APP-CTFβ Levels in Neuronal Cells. *PLoS One* 10, e0134486. doi:10.1371/journal.pone.0134486

Levine, B., and Kroemer, G. (2008). Autophagy in the Pathogenesis of Disease. *Cell* 132, 27–42. doi:10.1016/j.cell.2007.12.018

Li, C. H., and Tam, P. K. S. (1998). An Iterative Algorithm for Minimum Cross Entropy Thresholding. *Pattern Recognit. Lett.* 19, 8. doi:10.1016/S0167-8655(98)00057-9

Lin, M. T., and Beal, M. F. (2006). Mitochondrial Dysfunction and Oxidative Stress in Neurodegenerative Diseases. *Nature* 443, 787–795. doi:10.1038/nature05292

Lo, A. C., Haass, C., Wagner, S. L., Teplow, D. B., and Sisodia, S. S. (1994). Metabolism of the "Swedish" Amyloid Precursor Protein Variant in Madin-Darby Canine Kidney Cells. *J. Biol. Chem.* 269, 30966–30973. doi:10.1016/s0021-9258(18)47376-0

Loos, B., Toit, A. d., and Hofmeyr, J.-H. S. (2014). Defining and Measuring Autophagosome Flux-Concept and Reality. *Autophagy* 10, 2087–2096. doi:10.4161/15548627.2014.973338

Loos, B., Klionsky, D. J., Du Toit, A., and Hofmeyr, J.-H. S. (2020). On the Relevance of Precision Autophagy Flux Control *In Vivo* - Points of Departure for Clinical Translation. *Autophagy* 16, 750–762. doi:10.1080/15548627.2019.1687211

Lumkwana, D., du Toit, A., Kinnear, C., and Loos, B. (2017). Autophagic Flux Control in Neurodegeneration: Progress and Precision Targeting-Where Do We Stand? *Prog. Neurobiol.* 153, 64–85. doi:10.1016/j.pneurobio.2017.03.006

Madeo, F., Eisenberg, T., Pietrocola, F., and Kroemer, G. (2018). Spermidine in Health and Disease. *Science* 359, 6374. doi:10.1126/science.aan2788

Mellon, P. L., Windle, J. J., Goldsmith, P. C., Padula, C. A., Roberts, J. L., and Weiner, R. I. (1990). Immortalization of Hypothalamic GnRH by Genetically Targeted Tumorigenesis. *Neuron* 5, 1–10. doi:10.1016/0896-6273(90)90028-e

Menzies, F. M., Fleming, A., Caricasole, A., Bento, C. F., Andrews, S. P., Ashkenazi, A., et al. (2017). Autophagy and Neurodegeneration: Pathogenic Mechanisms and Therapeutic Opportunities. *Neuron* 93, 1015–1034. doi:10.1016/j.neuron.2017.01.022

Minois, N., Carmona-Gutierrez, D., Bauer, M. A., Rockenfeller, P., Eisenberg, T., Brandhorst, S., et al. (2012). Spermidine Promotes Stress Resistance in *Drosophila melanogaster* through Autophagy-dependent and -independent Pathways. *Cell Death Dis.* 3, e401. doi:10.1038/cddis.2012.139

Minois, N., Rockenfeller, P., Smith, T. K., and Carmona-Gutierrez, D. (2014). Spermidine Feeding Decreases Age-Related Locomotor Activity Loss and Induces Changes in Lipid Composition. *PLoS One* 9, e102435. doi:10.1371/journal.pone.0102435

Mizushima, N., Yamamoto, A., Matsui, M., Yoshimori, T., and Ohsumi, Y. (2004). *In Vivo* analysis of Autophagy in Response to Nutrient Starvation Using Transgenic Mice Expressing a Fluorescent Autophagosome Marker. *MBoC* 15, 1101–1111. doi:10.1091/mbc.E03-09-0704

Mizushima, N. (2009). Methods for Monitoring Autophagy Using GFP-LC3 Transgenic Mice. *Methods Enzymol.* 452, 13. doi:10.1016/S0076-6879(08)03602-1

Morselli, E., Mariño, G., Bennetzen, M. V., Eisenberg, T., Megalou, E., Schroeder, S., et al. (2011). Spermidine and Resveratrol Induce Autophagy by Distinct Pathways Converging on the Acetylproteome. *J. Cel Biol.* 192, 615–629. doi:10.1083/jcb.201008167

Murray Stewart, T., Dunston, T. T., Woster, P. M., and Casero, R. A. (2018). Polyamine Catabolism and Oxidative Damage. *J. Biol. Chem.* 293, 18736–18745. doi:10.1074/jbc.TM118.003337

Niso-Santano, M., Mora´n, J. M., Garci´a-Rubio, L., Go´mez-Marti´n, A., Gonza´lez-Polo, R. A., Soler, G., et al. (2006). Low Concentrations of Paraquat Induces Early Activation of Extracellular Signal-Regulated Kinase 1/2, Protein Kinase B, and C-Jun N-Terminal Kinase 1/2 Pathways: Role of C-Jun N-Terminal Kinase in Paraquat-Induced Cell Death. *Toxicol. Sci.* 92, 507–515. doi:10.1093/toxsci/kfl013

Niso-Santano, M., Bravo-San Pedro, J. M., Gómez-Sánchez, R., Climent, V., Soler, G., Fuentes, J. M., et al. (2011). ASK1 Overexpression Accelerates Paraquat-Induced Autophagy via Endoplasmic Reticulum Stress. *Toxicol. Sci.* 119, 156–168. doi:10.1093/toxsci/kfq313

Nixon, R. A., and Yang, D.-S. (2011). Autophagy Failure in Alzheimer's Disease-Locating the Primary Defect. *Neurobiol. Dis.* 43, 38–45. doi:10.1016/j.nbd.2011.01.021

Panda, P. K., Fahrner, A., Vats, S., Seranova, E., Sharma, V., Chipara, M., et al. (2019). Chemical Screening Approaches Enabling Drug Discovery of Autophagy Modulators for Biomedical Applications in Human Diseases. *Front. Cel Dev. Biol.* 7, 38. doi:10.3389/fcell.2019.00038

Paul-Gilloteaux, P., Heiligenstein, X., Belle, M., Domart, M.-C., Larijani, B., Collinson, L., et al. (2017). eC-CLEM: Flexible Multidimensional Registration Software for Correlative Microscopies. *Nat. Methods* 14, 102–103. doi:10.1038/nmeth.4170

Phadwal, K., Kurian, D., Salamat, M. K. F., MacRae, V. E., Diack, A. B., and Manson, J. C. (2018). Spermine Increases Acetylation of Tubulins and Facilitates Autophagic Degradation of Prion Aggregates. *Sci. Rep.* 8, 1. doi:10.1038/s41598-018-28296-y

Pietrocola, F., Lachkar, S., Enot, D. P., Niso-Santano, M., Bravo-San Pedro, J. M., Sica, V., et al. (2015). Spermidine Induces Autophagy by Inhibiting the Acetyltransferase EP300. *Cell Death Differ.* 22, 509–516. doi:10.1038/cdd.2014.215

Pucciarelli, S., Moreschini, B., Micozzi, D., De Fronzo, G. S., Carpi, F. M., Polzonetti, V., et al. (2012). Spermidine and Spermine Are Enriched in Whole Blood of Nona/centenarians. *Rejuvenation Res.* 15, 590–595. doi:10.1089/rej.2012.1349

Qi, Y., Qiu, Q., Gu, X., Tian, Y., and Zhang, Y. (2016). ATM Mediates Spermidine-Induced Mitophagy via PINK1 and Parkin Regulation in Human Fibroblasts. *Sci. Rep.* 6, 1. doi:10.1038/srep24700

Rider, J. E., Hacker, A., Mackintosh, C. A., Pegg, A. E., Woster, P. M., and Casero, R. A. (2007). Spermine and Spermidine Mediate protection against Oxidative Damage Caused by Hydrogen Peroxide. *Amino Acids* 33, 231–240. doi:10.1007/s00726-007-0513-4

Rubinsztein, D. C., Codogno, P., and Levine, B. (2012). Autophagy Modulation as a Potential Therapeutic Target for Diverse Diseases. *Nat. Rev. Drug Discov.* 11, 709–730. doi:10.1038/nrd3802

Rubinsztein, D. C., Bento, C. F., and Deretic, V. (2015). Therapeutic Targeting of Autophagy in Neurodegenerative and Infectious Diseases. *J. Exp. Med.* 212, 979–990. doi:10.1084/jem.20150956

Russell, M. R. G., Lerner, T. R., Burden, J. J., Nkwe, D. O., Pelchen-Matthews, A., Domart, M.-C., et al. (2017). 3D Correlative Light and Electron Microscopy of Cultured Cells Using Serial Blockface Scanning Electron Microscopy. *J. Cel Sci.* 130, 1. doi:10.1242/jcs.188433

Schindelin, J., Arganda-Carreras, I., Frise, E., Kaynig, V., Longair, M., Pietzsch, T., et al. (2012). Fiji: an Open-Source Platform for Biological-Image Analysis. *Nat. Methods* 9, 676–682. doi:10.1038/nmeth.2019

Selkoe, D. J., and Hardy, J. (2016). The Amyloid Hypothesis of Alzheimer's Disease at 25 Years. *EMBO Mol. Med.* 8, 595–608. doi:10.15252/emmm.201606210

Sigrist, S. J., Carmona-Gutierrez, D., Gupta, V. K., Bhukel, A., Mertel, S., Eisenberg, T., et al. (2014). Spermidine-triggered Autophagy Ameliorates Memory during Aging. *Autophagy* 10, 178–179. doi:10.4161/auto.26918

Sisodia, S. S., Koo, E. H., Beyreuther, K., Unterbeck, A., and Price, D. L. (1990). Evidence that β-Amyloid Protein in Alzheimer's Disease Is Not Derived by Normal Processing. *Science* 248, 492–495. doi:10.1126/science.1691865

Soda, K., Dobashi, Y., Kano, Y., Tsujinaka, S., and Konishi, F. (2009). Polyamine-rich Food Decreases Age-Associated Pathology and Mortality in Aged Mice. *Exp. Gerontol.* 44, 727–732. doi:10.1016/j.exger.2009.08.013

Soda, K., Kano, Y., Chiba, F., Koizumi, K., and Miyaki, Y. (2013). Increased Polyamine Intake Inhibits Age-Associated Alteration in Global DNA Methylation and 1,2-Dimethylhydrazine-Induced Tumorigenesis. *PLoS One* 8, e64357. doi:10.1371/journal.pone.0064357

Walsh, D. M., and Selkoe, D. J. (2007). A Beta Oligomers-A Decade of Discovery. *J. Neurochem.* 101, 1172–1184. doi:10.1111/j.1471-4159.2006.04426.x

Wang, I.-F., Guo, B.-S., Liu, Y.-C., Wu, C.-C., Yang, C.-H., Tsai, K.-J., et al. (2012). Autophagy Activators rescue and Alleviate Pathogenesis of a Mouse Model with Proteinopathies of the TAR DNA-Binding Protein 43. *Proc. Natl. Acad. Sci. U.S.A.* 109, 15024–15029. doi:10.1073/pnas.1206362109

Wang, W., Zhang, H., Xue, G., Zhang, L., Zhang, W., Wang, L., et al. (2014). Exercise Training Preserves Ischemic Preconditioning in Aged Rat Hearts by Restoring the Myocardial Polyamine Pool. *Oxid. Med. Cell Longev.* 2014, 1–14. doi:10.1155/2014/457429

Wirth, M., Benson, G., Schwarz, C., Köbe, T., Grittner, U., Schmitz, D., et al. (2018). The Effect of Spermidine on Memory Performance in Older Adults at Risk for Dementia: A Randomized Controlled Trial. *Cortex* 109, 181–188. doi:10.1016/j.cortex.2018.09.014

Wirth, M., Schwarz, C., Benson, G., Horn, N., Buchert, R., Lange, C., et al. (2019). Effects of Spermidine Supplementation on Cognition and Biomarkers in Older Adults with Subjective Cognitive Decline (SmartAge)-Study Protocol for a Randomized Controlled Trial. *Alz Res. Ther.* 11, 1. doi:10.1186/s13195-019-0484-1

Xie, Z., Nair, U., and Klionsky, D. J. (2008). Atg8 Controls Phagophore Expansion during Autophagosome Formation. *MBoC* 19, 3290–3298. doi:10.1091/mbc.E07-12-1292

Xie, R., Nguyen, S., McKeehan, W. L., and Liu, L. (2010). Acetylated Microtubules Are Required for Fusion of Autophagosomes with Lysosomes. *BMC Cel Biol.* 11, 1. doi:10.1186/1471-2121-11-89

Yang, Y., Chen, S., Zhang, Y., Lin, X., Song, Y., Xue, Z., et al. (2017). Induction of Autophagy by Spermidine Is Neuroprotective via Inhibition of Caspase 3-mediated Beclin 1 Cleavage. *Cel Death Dis.* 8, e2738. doi:10.1038/cddis.2017.161

Yoshii, S. R., and Mizushima, N. (2017). Monitoring and Measuring Autophagy. *Int. J. Mol. Sci.* 18, 1865. doi:10.3390/ijms18091865

Yoshimori, T., Yamamoto, A., Moriyama, Y., Futai, M., and Tashiro, Y. (1991). Bafilomycin A1, A Specific Inhibitor of Vacuolar-type H(+)-ATPase, Inhibits Acidification and Protein Degradation in Lysosomes of Cultured Cells. *J. Biol. Chem.* 266, 17707–17712. doi:10.1016/S0021-9258(19)47429-2

Yumino, K., Kawakami, I., Tamura, M., Hayashi, T., and Nakamura, M. (2002). Paraquat- and Diquat-Induced Oxygen Radical Generation and Lipid Peroxidation in Rat Brain Microsomes. *J. Biochem.* 131, 565–570. doi:10.1093/oxfordjournals.jbchem.a003135

Zare-Shahabadi, A., Masliah, E., Johnson, G. V. W., and Rezaei, N. (2015). Autophagy in Alzheimer's Disease. *Rev. Neurosci.* 26, 4. doi:10.1515/revneuro-2014-0076

Zhao, Y., and Zhao, B. (2013). Oxidative Stress and the Pathogenesis of Alzheimer's Disease. *Oxid. Med. Cell Longev.* 2013, 1–10. doi:10.1155/2013/316523

Zhou, Q., Zhang, H., Wu, Q., Shi, J., and Zhou, S. (2017). Pharmacological Manipulations of Autophagy Modulate Paraquat-Induced Cytotoxicity in PC12 Cells. *Int. J. Biochem. Mol. Biol.* 8, 13–22.

Conflict of Interest: The authors declare that the research was conducted in the absence of any commercial or financial relationships that could be construed as a potential conflict of interest.

Publisher's Note: All claims expressed in this article are solely those of the authors and do not necessarily represent those of their affiliated organizations, or those of the publisher, the editors and the reviewers. Any product that may be evaluated in this article, or claim that may be made by its manufacturer, is not guaranteed or endorsed by the publisher.

frontiers | Frontiers in Cell and Developmental Biology

ORIGINAL RESEARCH
published: 08 June 2022
doi: 10.3389/fcell.2022.880696

Sample Preparation and Warping Accuracy for Correlative Multimodal Imaging in the Mouse Olfactory Bulb Using 2-Photon, Synchrotron X-Ray and Volume Electron Microscopy

Yuxin Zhang[1,2], *Tobias Ackels*[1,2], *Alexandra Pacureanu*[1,2,3], *Marie-Christine Zdora*[4,5,6,7], *Anne Bonnin*[7], *Andreas T. Schaefer*[1,2]* *and Carles Bosch*[1]*

[1]*Sensory Circuits and Neurotechnology Lab, The Francis Crick Institute, London, United Kingdom,* [2]*Department of Neuroscience, Physiology and Pharmacology, University College London, London, United Kingdom,* [3]*ESRF, The European Synchrotron, Grenoble, France,* [4]*Department of Physics and Astronomy, University College London, London, United Kingdom,* [5]*Diamond Light Source, Harwell Science and Innovation Campus, Didcot, United Kingdom,* [6]*School of Physics and Astronomy, University of Southampton, Highfield Campus, Southampton, United Kingdom,* [7]*Paul Scherrer Institut, Villigen, Switzerland*

OPEN ACCESS

Edited by:
Christopher Guerin, Vlaams Instituut voor Biotechnologie, Belgium

Reviewed by:
Yunfeng Hua, Shanghai Jiao Tong University, China
Kara Fulton, Harvard Medical School, United States

***Correspondence:**
Andreas T. Schaefer
andreas.schaefer@crick.ac.uk
Carles Bosch
carles.bosch@crick.ac.uk

Specialty section:
This article was submitted to Morphogenesis and Patterning, a section of the journal Frontiers in Cell and Developmental Biology

Received: *21 February 2022*
Accepted: *22 April 2022*
Published: *08 June 2022*

Citation:
Zhang Y, Ackels T, Pacureanu A, Zdora M-C, Bonnin A, Schaefer AT and Bosch C (2022) Sample Preparation and Warping Accuracy for Correlative Multimodal Imaging in the Mouse Olfactory Bulb Using 2-Photon, Synchrotron X-Ray and Volume Electron Microscopy. Front. Cell Dev. Biol. 10:880696. doi: 10.3389/fcell.2022.880696

Integrating physiology with structural insights of the same neuronal circuit provides a unique approach to understanding how the mammalian brain computes information. However, combining the techniques that provide both streams of data represents an experimental challenge. When studying glomerular column circuits in the mouse olfactory bulb, this approach involves e.g., recording the neuronal activity with *in vivo* 2-photon (2P) calcium imaging, retrieving the circuit structure with synchrotron X-ray computed tomography with propagation-based phase contrast (SXRT) and/or serial block-face scanning electron microscopy (SBEM) and correlating these datasets. Sample preparation and dataset correlation are two key bottlenecks in this correlative workflow. Here, we first quantify the occurrence of different artefacts when staining tissue slices with heavy metals to generate X-ray or electron contrast. We report improvements in the staining procedure, ultimately achieving perfect staining in ~67% of the 0.6 mm thick olfactory bulb slices that were previously imaged *in vivo* with 2P. Secondly, we characterise the accuracy of the spatial correlation between functional and structural datasets. We demonstrate that direct, single-cell precise correlation between *in vivo* 2P and SXRT tissue volumes is possible and as reliable as correlating between 2P and SBEM. Altogether, these results pave the way for experiments that require retrieving physiology, circuit structure and synaptic signatures in targeted regions. These correlative function-structure studies will bring a more complete understanding of mammalian olfactory processing across spatial scales and time.

Keywords: staining, warping, olfactory bulb, 2-photon calcium imaging, synchrotron X-ray, volume EM, correlative multimodal imaging

INTRODUCTION

Maps are essential tools to accelerate discovery. By providing information in an intuitive structure, they help design strategies that maximise gain while minimising risk. As it has occurred in a myriad of disciplines before, maps play a crucial role in supporting discovery in the life sciences and in neuroscience in particular (Niedworok et al., 2016; Winnubst et al., 2019; Claudi et al., 2020; Ueda et al., 2020; BRAIN Initiative Cell Census Network (BICCN), 2021). Mapping the brain at multiple scales can help gain mechanistic insights into its function from already existing data, and guide the exploration of the uncharted territories that hold the keys for further unsolved functions. Creating those maps requires recording the spatial distribution of relevant brain properties across a volume that encodes functional units at a resolution sufficient to discriminate between individual features. In the mammalian brain, neuronal circuits usually span >1 mm^3, while the dimensions of relevant features (nuclei, dendrites, axons, synapses) range between 10 µm and 10 nm (Helmstaedter, 2013; Klinger et al., 2021). Targeted maps carrying more detail (only) where it is needed offer a valuable solution to this vast challenge, and can be generated by means of correlative multimodal imaging (CMI) pipelines (Bock et al., 2011; Briggman et al., 2011; Karreman et al., 2016; Lee et al., 2016; Dyer et al., 2017; Bosch et al., 2022). The reliability of those brain maps will be directly influenced by two main factors: the quality of the images of each individual modality and the quality of their registration into a multimodal map.

The quality of an image is limited by multiple factors including optics, detector sensitivity, exposure time or the structure of the specimen leading to signal contrast. The latter is engineered and optimised by preparing the specimen for a particular imaging technique in a process often referred to as the sample preparation protocol (SPP). An SPP incorporates all transformations necessary to make a specimen compatible with an imaging technique and may involve mechanical procedures (such as slicing), chemical transformations (such as fixing) and signal transformations (such as staining). SPPs can be studied as a sequence of smaller-scale operations sharing a single goal, which we will refer to as "steps". In that way, a single step may involve slicing a fresh piece of brain tissue to a specific thickness under controlled constraints of temperature, osmolarity and time, while another might involve chemically staining a tissue slice with a buffered solution of osmium tetroxide while controlling for temperature, duration and agitation. Optimising an SPP presents therefore a multivariate challenge that can be approached by making informed decisions to optimise each step individually while monitoring global yields.

The maps guiding our understanding of how neuronal circuits operate in the mammalian brain should convey spatial and functional information across the critical dimensions specified above, recording tissue volumes in the order of 1 mm^3. While not a single technique is capable of providing structural and physiological insights at the required scales, two techniques are capable of providing both streams of data separately: serial block-face scanning electron microscopy (SBEM) is the volume electron microscopy technique capable of retrieving the largest continuous tissue volume with minimal specimen distortion (Denk and Horstmann, 2004; Kubota, 2015), whereas multiphoton microscopy offers a window to explore the physiological events taking place up to 1 mm deep inside tissue (Denk et al., 1994; Oheim et al., 2001; Yildirim et al., 2019). Finally, X-ray microscopy is an outstanding resource to reveal subcellular anatomy across large specimens (Kuan et al., 2020; Bosch et al., 2022). Altogether, the previously defined challenge can be addressed by a CMI pipeline that combines *in vivo* 2-photon (2P) microscopy of intracellular [Ca^{2+}], synchrotron X-ray computed tomography with propagation-based phase contrast (SXRT) and SBEM (Bosch et al., 2022). The SPP for this approach will therefore need to be compatible with all techniques involved and its optimal implementation will be the one that accomplishes two main requisites: 1) being able to deliver an optimal final map, therefore balancing inter-modality trade-offs towards the benefit of the initial research question; and 2) being able to provide the highest yield, making it compatible with more challenging research questions in the future.

The datasets carrying the best spatial resolution in this CMI pipeline will be provided by SBEM (Bosch et al., 2022). In these, the signal is generated by recording the back-scattered electrons arising from a 1–2 keV electron beam scanning the surface of a polished tissue block at an electron dose of typically <20 e^-/nm^2 (Kubota, 2015). For soft tissue to generate contrast under this regime, tissue is stained with heavy metals (Hayat, 2000). Heavy metals bind non-specifically to lipids and proteins, ultimately providing a sample with a topology that faithfully reproduces its ultrastructure (Buckley and Porter, 1967). SBEM adds one challenge to otherwise more conventional transmission electron microscopy imaging: here, part of the electron beam will be absorbed by the sample, locally increasing its charge and potentially influencing the trajectories of neighbouring back-scattered electrons. In order to prevent such charging artefacts, SBEM-specific SPP optimisations have incorporated elements that increase the conductivity of the sample — such as increasing the total metal load employed in staining, in terms of both the number of metallic compounds and their concentrations (Tapia et al., 2012). The diffusion mechanism used to deliver those metals through the tissue remains passive, and therefore incubation time is subject to a quadratic relationship with the distance each compound should travel (Ströh et al., 2021), imposing severe temporal burdens for staining specimens of dimensions beyond 1 mm (Mikula and Denk, 2015). Moreover, abnormalities arising from individual staining steps can interact with each other (Hua et al., 2015; Mikula and Denk, 2015), creating an additional challenge to ensure all compounds optimally stain the tissue across all dimensions. Nevertheless, some SPPs have reported acceptable SBEM results in mouse brain tissue samples of thicknesses ranging from 0.1 mm to a complete mouse brain (~10 mm) (Briggman et al., 2011; Tapia et al., 2012; Wilke et al., 2013; Hua et al., 2015; Mikula and Denk, 2015; Pallotto et al., 2015; Wanner et al., 2016; Genoud et al., 2018), providing a promising starting point for further optimisations aiming to obtain a multimodal brain map. Interestingly, such SBEM staining also provides good contrast in SXRT (Bushong et al., 2015) because

X-ray absorption is proportional to the atomic number. Hence heavy metal-stained samples of thicknesses <1 mm can be imaged efficiently with this technique.

Finally, the registration quality of the individual map layers needs to be accurate enough to correlate any feature of interest across all modalities. For maps aimed at pinpointing the structure of a neural circuit, registration should be accurate at single-cell precision. Since the largest feature to unequivocally identify a single cell within a circuit is its nucleus, the requirement becomes registering at a precision better than the inter-nucleus distance, which is approximately 20 μm in the mitral cell layer of the olfactory bulb (OB) (Panhuber et al., 1985; Frazier and Brunjes, 1988; Parrish-Aungst et al., 2007).

Here we show an optimization of a CMI pipeline aiming to map a mammalian brain circuit with 2P microscopy, SXRT and SBEM employing an automated tissue processor capable of staining up to 30 identified samples simultaneously. Using the mouse OB, we assessed and made improvements on the SPPs and quantified the registration accuracy across imaging modalities. We demonstrate that this pipeline is effective and that single-cell registration accuracy can be readily achieved between 2P and SXRT.

MATERIALS AND METHODS

All SPPs used in this study are described in detail in **Supplementary Table S2** and are available for further analysis (see Data availability statement). The experimental details of samples shown in the figures are listed in **Supplementary Table S3**. The acronyms used are listed in **Supplementary Table S8**.

Animals

All animals used were 8–24 week-old mice of C57/Bl background and mixed gender. Details of the transgenic mouse lines are listed in **Supplementary Table S4**. All animal protocols were approved by the Ethics Committee of the board of the Francis Crick Institute and the United Kingdom Home Office under the Animals (Scientific Procedures) Act 1986.

Craniotomy and Durectomy Surgery

In experiments involving *in vivo* 2-photon (2P) imaging, anaesthesia was induced and maintained with intraperitoneal injection of sleep mix (0.05 mg/kg fentanyl, 5 mg/kg midazolam, 0.5 mg/kg medetomidine) and its depth monitored by toe-pinch reflex tests. Body temperature of mice was measured with a rectal temperature probe and maintained at 36–38°C with a thermoregulator (DC Temperature Controller, FHC, ME United States) heat pad.

Following shaving, skin disinfection with 1% chlorhexidine and skin incision over the skull, a custom head-fix implant with a central hole was fixed to the skull with medical super glue (Vetbond, 3 M, Maplewood MN, United States) and dental cement (Paladur, Heraeus Kulzer GmbH, Hanau, Germany; Simplex Rapid Liquid, 437 Associated Dental Products Ltd., Swindon, United Kingdom) so that the nasal bone above olfactory bulbs were exposed through the headplate hole. A ~2 mm-diameter craniotomy over the left olfactory bulb was made with a dental drill (Success 40, Osada, Tokyo, Japan). ACSF (10 mM HEPES, 10 mM glucose, 125 mM NaCl, 5 mM KCl, 2 mM $MgSO_4.7H_2O$, 2 mM $CaCl_2.2H_2O$, pH = 7.4) was used to moisten the brain throughout the surgery. Exposed dura was removed with forceps and needles. Then a drop of warm 2% low-melt agarose diluted in ACSF was applied, quickly followed by the placement of a glass window cut from a coverslip [borosilicate glass #1 thickness (150 μm)]. The edge of the window was glued to the nasal bones with medical super glue (Vetbond, 3 M, Maplewood MN, United States).

Some SPPs also include measures to prevent the formation of edema, including the use of ice-cold ACSF during surgery to cool down the skull from drilling and the use of dexamethasone (20 μl/mouse intraperitoneal injection) 2–4 h prior to surgery or dissection (**Supplementary Table S2**).

In vivo 2-Photon Imaging

Following surgery, animals were transferred to a 2P microscope (Scientifica Multiphoton VivoScope coupled with a MaiTai DeepSee Laser tuned to 910–940 nm, <30 mW underneath objective) and held by a custom head-fix implant holder. Respiration was measured at the right nostril with a flow sensor (A3100, Honeywell, NC, United States) and the signal was digitised with a Power 1401 ADC board (CED, Cambridge, United Kingdom). Odours were delivered at inhalation onset through custom-made olfactometers (Ackels et al., 2021; Bosch et al., 2022) whose output port was <1 cm away from the left nostril. Images (512 × 512 pixels, field of view 550 × 550 μm) were taken with a resonant-galvo scanner at 30 Hz frame rate. Six or twelve planes covering ~300 μm in z, including the mitral cell layer, were acquired with a 16 × 0.8 NA water-immersion objective (Nikon) coupled to a piezo motor (PI Instruments, United Kingdom). The fluorescently labelled glomerulus was used to position the field-of-view.

Following functional imaging, blood vessels were fluorescently labelled by injecting the tracer sulforhodamine 101 intraperitoneally (50 μl of a 0.1 M solution) (Sigma Aldrich). A dataset with voxels sized 0.358 μm in x, y and 5 μm in z containing the entire functionally-recorded volume was then acquired. Red and green channels were used to capture the vasculature and the resting GCaMP signals, respectively.

Dissection, Slicing and Fixation

For immersion fixation, animals were culled by cervical dislocation or decapitation after intraperitoneal injection of an overdose of pentobarbital (600 mg/kg pentobarbitone with mepivacaine) or sleep mix (0.05 mg/kg fentanyl, 5 mg/kg midazolam, 0.5 mg/kg medetomidine). Ice-cold dissection solution (4.6% sucrose, 0.563 mM $CaCl_2$, 65.2 mM $NaH_2PO_4.H_2O$, with 0.02% sodium azide, bubbled with 95% O_2/5% CO_2, osmolarity 280–320 mOsm/l) was used both to keep the tissue cold during dissection and as the bathing solution during vibratome slicing (Leica VT1200S). Dorsal OB slices with nominal thicknesses of 0.4–1 mm were taken by near-horizontal slicing, setting the vibratome blade tangent to the OB

surface. Half and whole OB samples were cut with a scalpel. Specimens were then transferred to cold fixative (see below) and post-fixed overnight at 4°C. The time between sacrifice and fixation was kept to a minimum (achieving 10 min on average for the first samples dissected and sliced from an animal).

For perfusion, animals were anaesthetized with an overdose of pentobarbital (600 mg/kg pentobarbitone with mepivacaine) administered intraperitoneally. The skin over the chest was removed and incisions made medially-laterally across the abdomen muscle and across the diaphragm. Before cardiac arrest took place, room temperature fixative (see below) was delivered by a cannula inserted into the left atrium of the heart driven by a peristaltic pump (4.5–7.2 ml/min, 80–100 ml). The brain was dissected out and post-fixed overnight at 4°C and OBs vibratome-sliced on the following day in 0.15 M NCB [sodium cacodylate (aq.), pH = 7.4, 280–320 mOsm/l].

The fixatives used were:

a) 1% or 2% glutaraldehyde (GA) with 2 mM $CaCl_2$ and 0.02% sodium azide in 0.15 M sodium cacodylate buffer (NCB), based on Pallotto et al. (2015).
b) 1.25% GA and 2.5% paraformaldehyde (PFA) or 2% GA and 2.5% PFA with 2 mM $CaCl_2$ in 0.08 M NCB, based on Hua et al. (2015).
c) 0.5% GA or 1.25% GA or 2% GA or 1% PFA or 2.5% PFA or 4% PFA with 2 mM $CaCl_2$ in 0.08 M NCB.

Epifluorescence and *ex vivo* 2P Imaging

For samples containing a fluorescently-labelled glomerulus, after a brief contact with fixative, epifluorescence images tiling the entire specimen were recorded with a widefield fluorescence microscope (Olympus Axioplan2 with LEJ "ebq 100 isolated-z" lamp) before overnight postfixation.

After postfixation, two volumes covering the fluorescently-labelled glomerulus (located using the epifluorescence images as guides) and its surrounding regions were acquired and stitched together (voxels sized 1.074 µm in x, y and 5 µm in z) with the aforementioned 2P system (laser wavelength 800 nm). This dataset featured glomeruli and surface blood vessels from the autofluorescence signal and was used to aid the relocation of functionally imaged volume in later acquired SXRT/EM datasets as described in Bosch et al. (2022).

Staining, Dehydration and Embedding

Fixed OB slices were washed in 0.15 M NCB [sodium cacodylate (aq.) with or without 0.02% sodium azide, pH = 7.4, 280–320 mOsm/l, 3 × 1 h], then stained using an automated tissue processor (Leica EMTP). The full descriptions can be found in **Supplementary Table S2**. In brief, specimens were processed with one of the following staining protocols:

a) 2% OsO_4, 3% potassium ferrocyanide, 2 mM $CaCl_2$ in 0.15 M NCB (1 h, 4°C); 1% thiocarbohydrazide (TCH, aq., 1 h, 50°C); 2% OsO_4 (aq., 1 h, 20°C); 2% uranyl acetate (UA, aq., overnight, 4°C); lead aspartate (aq., pH = 5.5, 2 h, 60°C) with water washes between each step, protocol referred to as "1sRO half time".
b) same as a) but doubled incubation times of all steps except UA, protocol referred to as "1sRO".
c) 2% OsO_4 in 0.15 M NCB (1.5 h, 20°C) followed by 2.5% potassium ferrocyanide in 0.15 M NCB (1.5 h, 20°C) without water wash; 1% TCH (aq., 45 min, 40°C); 2% OsO_4 (aq., 1.5 h, 20°C); 1% UA (aq.) warmed to 50°C for 2 h after overnight at 4°C; lead aspartate (aq., pH = 5.0, 2 h, 50°C) with water washes between each step, protocol referred to as "2sRO".
d) same as c) but TCH (aq.) incubated for 1 h at 50°C and lead aspartate (pH = 5.5) at 60°C, used in exp. A and exp. B in **Figure 3B1**.
e) same as c) but all warm incubations happening at 60°C and all steps performed manually. There were 6 groups of samples in this SPP, corresponding to terminating the staining at each of the 6 reagents (**Figure 3D1**). Early finishing samples were pooled in water at room temperature while others finished their course of staining.

Samples were then dehydrated with 75%, 90%, 100%, 100% ethanol series, transferred to propylene oxide and infiltrated with 25%, 50%, 75%, 100%, 100% hard epon diluted in propylene oxide, and finally polymerized for 72 h at 60–70°C. For experiments in **Figures 3D1,2**, samples were dehydrated with 100% ethanol at 4°C overnight before being transferred to propylene oxide.

The use of an automated tissue processor enabled processing a large amount of identified samples simultaneously (theoretically up to 48, in this study the maximum processed in parallel was 30). This implementation allowed us to systematically compare different sources of staining variability at scale with samples processed in parallel. In turn, the optimised protocols obtained with this implementation will have a predictable success rate for reasonably large sample sizes and will provide a valuable starting point for estimating success rates of scaled-up approaches.

We considered a "sample" one piece of tissue, whether it comes from the same or different animals. We consider one "batch" the group of samples processed simultaneously in the same run of the automated tissue processor (**Supplementary Figure S2**). "Experiments" may contain samples arising from the same batch or from different batches. The relationship between samples, batches and experiments is described in detail in **Supplementary Table S7**.

LXRT Imaging

After staining and embedding, the samples were imaged with a laboratory-source X-ray microscope (LXRT; Zeiss Xradia 510 Versa, 40 kV, 3 W, LE2-4 filter, 1601 projections over 180° of sample rotation, 3–20 s exposure time per frame, one tile, 3–6 µm pixel size). The reconstructed tomogram was used to screen for artefacts.

SXRT Imaging

The SXRT dataset analysed in this work is C525, described previously in (Bosch et al., 2022). In brief, samples were

imaged with synchrotron X-ray computed tomography exploiting propagation-based phase contrast at the I13-2 beamline of the Diamond Lightsource (Didcot, United Kingdom; 22 keV, 3001 projections over 180° of sample rotation, 0.4 s exposure time per frame, 2–24 tiles, 325 nm isotropic voxel size). The reconstructed tomogram is referred to as the SXRT dataset.

Trimming and SBEM Imaging

To meet the sample size and conductance requirements of our electron microscopes, the resin embedded samples were further processed prior to electron microscopy. Firstly, trims were planned from rendered LXRT or SXRT datasets in Amira (Thermo Fischer Scientific) or Imaris (Bitplane). 2P datasets were warped into LXRT or SXRT space and overlaid on top to help target and preserve the functionally imaged volume in the trimmed block, as described in Bosch et al. (2022). With the help of this trimming plan, embedded samples were trimmed to a suitable shape and size with a razor blade and a glass and/or diamond knife (Diatome) at an ultramicrotome (Leica UC7). Subsequently, the sides of the sample were painted with silver colloidal suspension (SPI supplies) and sputter-coated with a layer of 10 nm-thick platinum (Quorum Q150R S).

2D images used for ultrastructure checks (**Supplementary Figure S4A**) were obtained in a 3View2—Zeiss Merlin SBEM under high vacuum (1.5 kV, 0.2 nA, 2 µs/pixel, 10 nm or 50 nm pixel size) using an OnPoint (Gatan) back-scattered electron detector.

The volume SBEM dataset analysed in this study comes from sample C525a, described previously in Bosch et al. (2022). This volume SBEM dataset was obtained with a 3View2—variable pressure Zeiss Sigma SBEM using focal charge compensation (2.5 kV, 30 µm aperture, $(80\ nm)^3$ voxel size).

Artefact Categorisation

After looking through all LXRT datasets, 12 types of artefacts were defined according to their appearance in the LXRT datasets (**Supplementary Table S1**). For each sample, a score of 0 (absent) or 1 (present) was given to each artefact type and the following variables compiled: "experiment ID," "experiment start date," "fixation method," "fixative formula," "staining method," "anaesthetics," "culling method," "use of dexamethasone," "use of cold buffer," "mouse line," "tissue type," "slice index," "thickness" and "2P history". For overall occurrence rate quantification, all samples from all experiments were included. Other analyses were done using samples from relevant experiments (**Supplementary Table S5**). Analyses were performed with Python3 (Van Rossum and Drake, 2009) in a Jupyter notebook (Kluyver et al., 2016). The artefact scoring tables and analysis scripts are available (see Data availability statement).

Sample Volume Estimation

In total, the final volume of 80 samples was measured from LXRT datasets of the resin-embedded samples (**Supplementary Table S6**). Sample volume was measured as the number of voxels containing tissue times the voxel size. The voxels containing tissue data were masked in Fiji (Schindelin et al., 2012) by thresholding the signal and discarding low-signal background voxels. For samples with "crack" artefact, the volume occupied by "crack" was excluded from the tissue voxel count.

To estimate the volume of the fresh tissue samples, we utilised landmark pairs from the set of "warping landmarks" used to calculate the warp field (see results and below). Paired landmarks mark the same features of a sample in both datasets. Changes in tissue volume after sample preparation will therefore be reflected in changes in distances between landmarks. For one sample, 20 landmarks from the 2P dataset were randomly selected and their distances to every other landmark calculated. The top 400 distances were taken (Df1_400). Distances between these landmarks were also calculated for the structural dataset of the same sample (Ds1_400). The amount of sample volume change (r) was taken to be the averaged ratio between Ds1_400 and Df1_400 cubed. The fresh sample volume is therefore the CT volume divided by r (**Supplementary Figure S5**).

Tracing, Warping and Warping Accuracy Estimation

Dataset annotations, including somata seeds and blood vessel tracings, were generated with the data storage, display and annotation tool webKnossos (Boergens et al., 2017).

Warping landmarks were seeded manually using the Fiji plugin BigWarp (Bogovic et al., 2016) and then exported. Landmarks were any distinguishable features shared by the datasets involved, such as blood vessel branching points. The warping function was then calculated using the exported landmark file and a function from the webKnossos skeleton analysis toolbox built in the Matlab (Mathworks) environment. This toolbox (Bosch et al., 2022) is available online (see Data availability statement).

For the C525a dataset, the warping function between 2P and SBEM was calculated using 171 landmarks seeded throughout the dataset (**Figure 6A**). Similarly, 64 and 51 landmarks were used for 2P to SXRT warping and SXRT to SBEM warping, respectively. These sets of paired landmarks were referred to as "warping landmarks" in the results section.

For warping accuracy quantification, blood vessels in the upper EPL within a $(160\ \mu m^3)$ bounding box were traced in the 2P, SXRT and SBEM datasets of sample C525a. To trace the same sets of blood vessels in all three datasets, the bounding boxes used were centred on a functionally imaged soma in 2P and its warped location in SXRT and SBEM. Due to the resolution limit, thin blood vessels were not traceable in the SXRT dataset and the corresponding blood vessel tracings in the 2P and SBEM datasets were deleted for consistency. After this, all blood vessels branching points (junctions) were named and matched across the three datasets using blood vessel shape as a guide. Lastly, freely ending blood vessel tracings were trimmed up until a junction. Therefore, the same blood vessels were covered to the same extent in all three datasets and hence could be

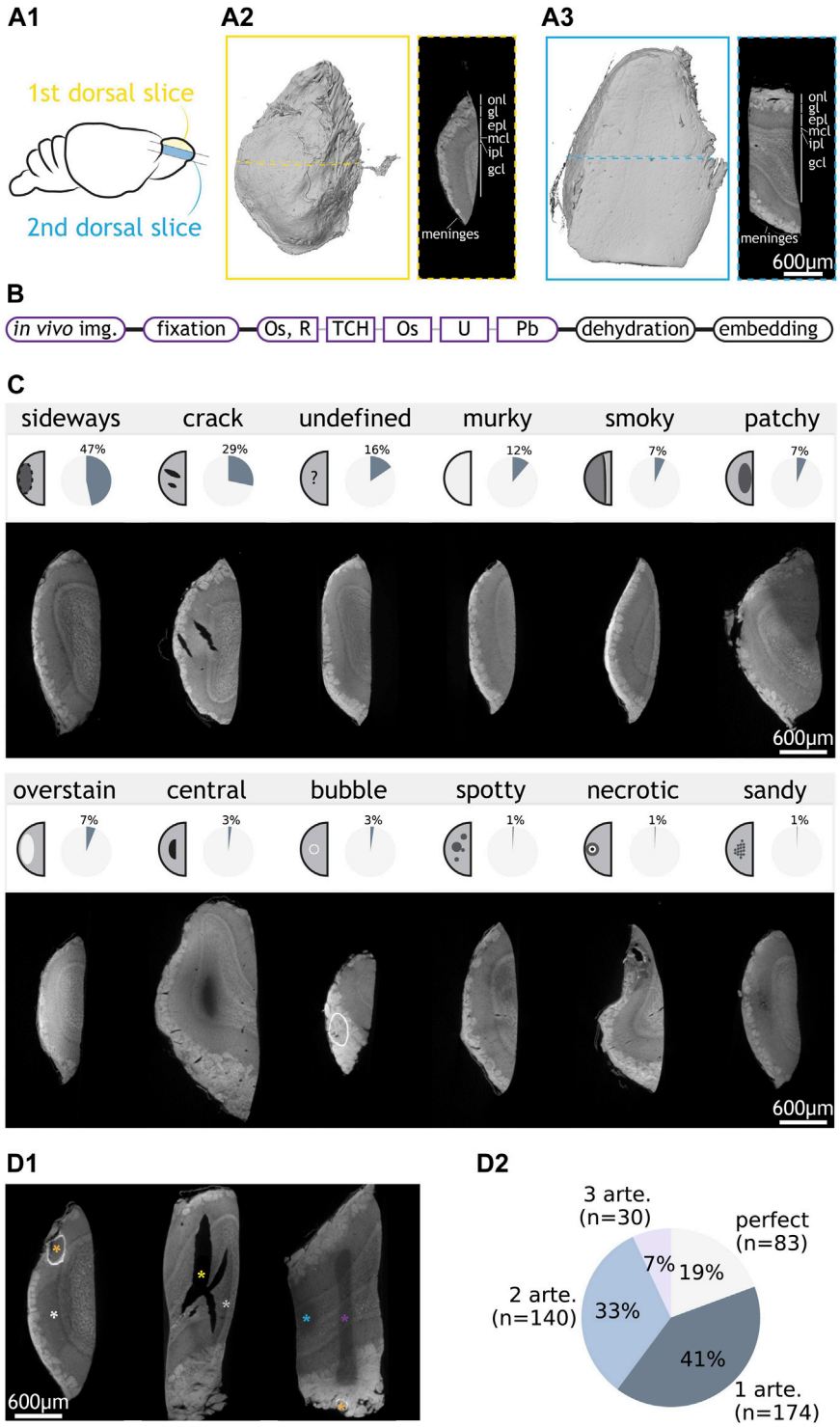

FIGURE 1 | Categorisation of staining artefacts from mouse olfactory bulb samples. **(A1)** Positions of the first and second dorsal slices taken from the mouse olfactory bulb. **(A2)** LXRT volume of a first dorsal slice and LXRT image of the dashed region in the volume. **(A3)** same as **(A2)** but for a second dorsal slice. **(B)** Structure of an SPP. Staining is split into key steps. Steps that vary between SPP tests are shown in coloured boxes. **(C)** 12 types of artefacts: name, schematic of appearance, overall occurrence rate in OB samples and LXRT image of a representative sample. **(D1)** Examples of samples with co-occurring artefacts. They respectively contain "sideways" (white asterisk) and "bubble" (orange); "crack" (yellow) and "smoky" (grey); and "undefined" (purple), "patchy" (blue) and "bubble" (orange). **(D2)** Number and percentage of OB samples with zero, one or multiple artefacts. Abbreviations: onl: olfactory nerve layer, gl: glomerular layer, epl: external plexiform layer, mcl: mitral cell layer, ipl: internal plexiform layer, gcl: granule cell layer, img: imaging. Os: osmium tetroxide, R: reducing agent e.g., potassium ferrocyanide, TCH: thiocarbohydrazide, U: uranyl acetate, Pb: lead aspartate, arte: artefact. Scale bars are shared across all images in the same panel.

compared later. Processed tracings containing those annotations in the different datasets are available online (see Data availability statement).

The blood vessel tracings were then warped into a common framework (e.g., SBEM space, **Figure 6C**). Each tracing was then split into segments at blood vessel junctions. For each segment, the average segment length (among 2P, SBEM and SXRT) was calculated. This length was then divided by an interpolation step size of 500 nm, giving the number of steps (n) to interpolate for this segment. Subsequently, each segment from each dataset was interpolated with n steps, giving n points on the blood vessel that are matched across all three datasets. The tracing accuracy at that location between any two datasets was then estimated to be the distance between the matched points (**Figure 6D**). The overall warping accuracy between any two datasets was taken to be the mean of all matched-point distances.

RESULTS

Variables Affecting Performance in Staining Soft Tissue

The olfactory bulb (OB) contains the first neuronal circuit in the olfactory sensory pathway, the glomerular column (Mori et al., 1999). Thick (>0.4 mm) dorsal slices of the bulb contain all the histological layers embedding that circuit (**Figure 1A**). We prepared 415 0.4-1 mm-thick vibratome-cut slices of mouse olfactory bulb for electron microscopy (**Figure 1A1**), of which 328 were first dorsal slices (**Figure 1A2**). However, first slices are asymmetrical, with one side containing biological features potentially capable of acting as a barrier for the diffusion of the staining solutions (e.g., meninges, tightly packed axon bundles), which could in turn translate into asymmetrical staining artefacts. To facilitate the identification of specific artefact patterns, we also prepared 87 second to fourth dorsal slices (**Figure 1A3**) which, while also containing all histological layers, present a symmetrical structure that allows free diffusion of staining solutions through their shortest dimension. Additionally, to account for possible effects only attributable to larger specimen sizes, we prepared 8 and 4 large samples consisting of complete and half olfactory bulbs, respectively, adding up to a total of 427 samples.

We processed the samples following a standard protocol structure (Briggman et al., 2011; Tapia et al., 2012; Wilke et al., 2013; Hua et al., 2015; Mikula and Denk, 2015; Pallotto et al., 2015; Wanner et al., 2016; Genoud et al., 2018) (**Figure 1B**). After all *in vivo* studies had finished on the animal, the brain tissue was fixed, stained with osmium tetroxide, reduced with potassium ferrocyanide, incubated with the bridging agent thiocarbohydrazide, and further stained with osmium tetroxide, uranyl acetate and lead aspartate. Finally, samples were dehydrated in a series of ethanol solutions, embedded in hard epon resin and cured in an oven for 72 h at 60°C. A number of variations were implemented to this protocol backbone with the aim to optimise the yield of samples holding optimal staining quality. Staining quality was routinely assessed with X-ray tomography using a laboratory-based micro-CT (LXRT), a technique well-suited to resolve the different histological layers (Bosch et al., 2022) as well as the dynamics of heavy metal diffusion when staining brain tissue (Ströh et al., 2021). Staining, dehydration and embedding steps were conducted on an automated tissue processor. Thereby staining variability would appear systematic, and large sample groups could be processed simultaneously to address specific staining variables.

Categories of Staining Artefacts

We observed a wide variety of SPP-derived artefacts (**Figure 1C**). Twelve artefact categories were defined: After examining all stained samples, we described all artefacts into eleven distinct types (**Supplementary Table S1**). An additional category "undefined" collected the samples (16%, 66/427) that showed poor staining but could not be categorised into any of the defined types. Each sample was assessed independently for the presence of any of the artefacts. Notably, more than one artefacts can co-occur in one sample (**Figure 1D**). Finally, around 20% of the samples do not contain any artefact and were referred to as "perfect" (**Figure 1D2**). In our samples, the most frequently observed artefacts were "sideways" and "crack", which collectively occurred in 60% of all samples. Other insights could be extracted from the prevalence (% of experiments affected) and penetrance (% of affected samples within an experiment) of the artefacts (**Supplementary Figures S1, S2**), yet we focussed our attention on understanding the aetiology of "sideways" and "crack", since even modest improvements in the occurrence of these two major artefacts would convey a meaningful improvement in the overall experimental yield.

Diffusion Kinetics and Reduction of Osmium Tetroxide Underly the Most Common "Sideways" Artefact

The "sideways" artefact consists of a poorly stained region which is fully enclosed within the sample and displaced closer towards the brain surface compared to the sliced surface in first slices (**Figure 2A**). The transition from well stained to poorly stained region may be abrupt, gradual, or both, giving "clear", "fuzzy", and "compound boundary sideways", respectively (**Figure 2B**). In second slices, where two sliced surfaces make up most of the surface area, the "sideways" artefact occurs at a different anatomical location yet the boundaries remain closer to the brain surface than to the sliced surfaces (**Figure 2A**). Moreover, in first slices where the brain surface was locally perturbed (because of e.g., some broken meninges exposing the underlying tissue), the distance from that point in the brain surface to the artefact border was similar to the distance between the artefact border and the sliced surface (**Figure 2A**). Finally, the overall pattern resembles that of a staining artefact previously described (Hua et al., 2015; Mikula and Denk, 2015) (**Supplementary Figure S3**).

Heavy metals passively diffuse through soft tissue following a quadratic kinetic (Mikula and Denk, 2015; Ströh et al., 2021), i.e., staining three times the depth takes nine times longer. From our observations, we hypothesised that the brain surface is less

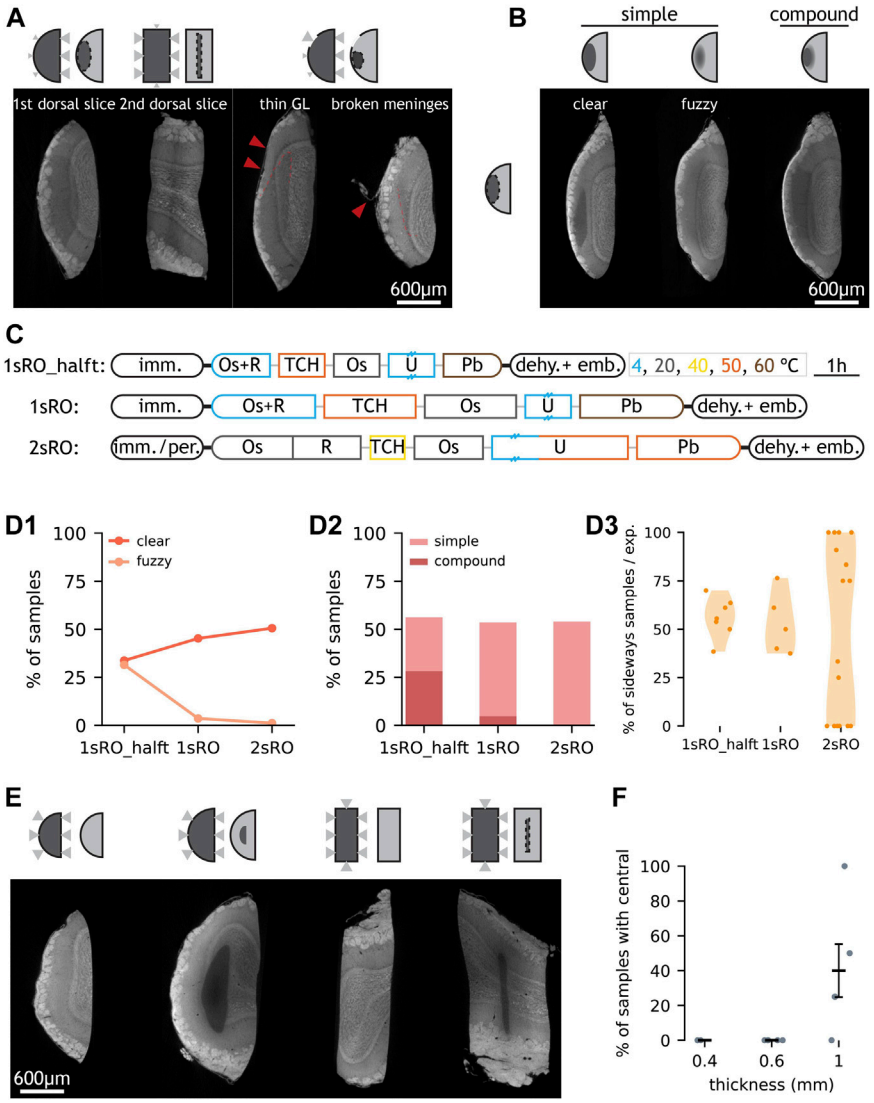

FIGURE 2 | Occurrence and proposed mechanism of "sideways" and "central" artefacts. **(A)** LXRT images of four samples with "sideways" and schematics of hypothesised causes. In the last two samples, the positions of thin GL and broken meninges are highlighted with arrowheads, and part of the "sideways" boundary is marked with a dashed line. In schematics, the size of triangles represent the diffusion rate. **(B)** Subdivision of "sideways" by boundary type and by complexity. **(C)** Summary of three SPPs. Staining is split into key steps. Length and colour of staining steps represent incubation time and temperature, respectively. Double dash on box represents overnight incubation. Thin lines connecting staining reagents represent water washes. **(D1)** Occurrence rate of "sideways" with "clear" and "fuzzy" boundaries in the three SPPs. **(D2)** Occurrence rate of "simple" or "compound" "sideways" in the three SPPs. **(D3)** Penetrance of "sideways" in experiments processed with the three SPPs. Each dot represents one experiment. **(E)** Samples with (2nd and 4th, 1 mm-thick) and without (1st and 3rd, 0.6 mm-thick) the "central" artefact. **(F)** Occurrence of "central" depends on slice nominal thickness. Each data point represents the % of samples with "central" artefact within an experimental batch (all samples stained with 2sRO protocols). Error bar shows mean ± standard error of mean. Abbreviations: GL: glomerular layer, imm: immersion, per: perfusion, dehy: dehydration, emb: embedding, Os: osmium tetroxide, R: potassium ferrocyanide, TCH: thiocarbohydrazide, U: uranyl acetate, Pb: lead aspartate. Scale bars are shared across all images in the same panel.

permeable than the sliced surface to the diffusion of heavy metals. If so, reagents would reach locations through the sliced (permeable) border more easily. This combined with insufficient incubation times could lead to the "sideways" artefacts we observed.

In order to assess whether diffusion time affected the presence of this artefact, we modified the protocol so the duration of all staining steps was doubled (**Figure 2C**). This led to a slight change in the pattern of the "sideways" artefact — with it now displaying only clear boundaries (**Figures 2D1,D2**).

A second mechanism that could contribute to the "sideways" artefact is the reduction of osmium VIII to osmium IV inside the tissue during staining (Hua et al., 2015). A prior study showed mm-thick mouse brain tissue samples could be evenly stained for SBEM

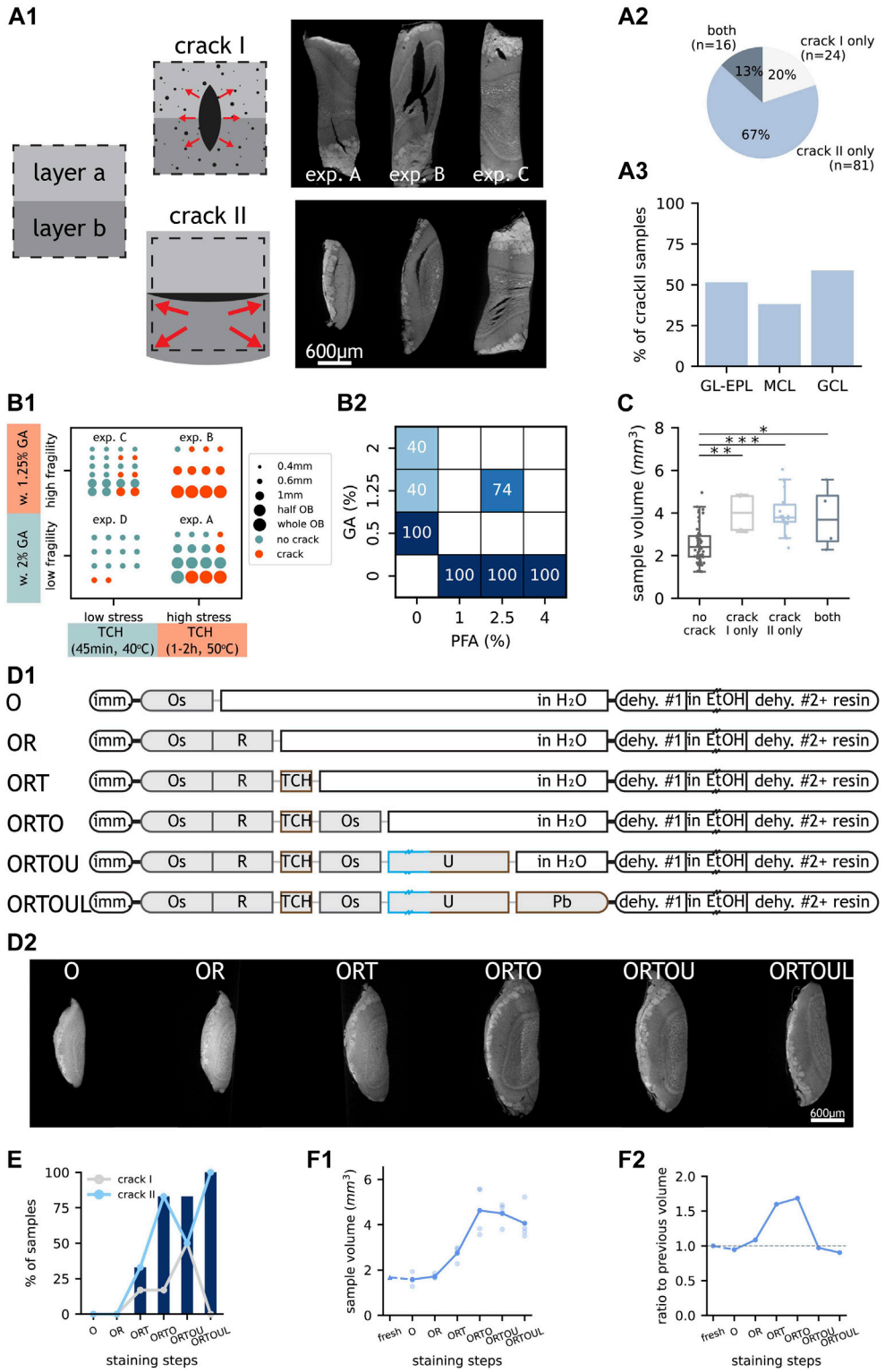

FIGURE 3 | Occurrence and proposed mechanisms of "crack" subtypes. **(A1)** LXRT images of samples with "crack" subtypes and schematics of their hypothesised causes. In schematics, "layer a" and "layer b" represent two tissue layers and the dashed box represents the starting tissue volume i.e., when fresh. Dots represent gas bubbles. Arrows represent expansive forces experienced by the tissue. Top, 0.6 mm-thick representative samples from experiments A, B and C referred to in **(B1)**. Bottom, samples showing "crack II" at GL-EPL boundary, MCL, and GCL, respectively. **(A2)** Number and percentage of "crack" samples with only

(*Continued*)

FIGURE 3 | "crack I" or "crack II" or with both "crack" subtypes. **(A3)** Percentage of "crack II" samples with the artefact occurring at GL-EPL boundary, MCL or GCL. **(B1)** "Crack" occurrence in samples from four experiments with different TCH incubation conditions and GA concentrations. **(B2)** "Crack" occurrence in 0.6 mm-thick samples fixed with different fixatives. Empty squares indicate non-evaluated cases. **(C)** Volume of samples that do and do not contain "crack". Each dot represents one sample. The boxes extend from the first to the third quartile, with the line representing the median. The whiskers extend to the most extreme, non-outlier data points. (*: $p < 0.5$, **: $p < 0.005$, ***: $p < 0.0005$, two-tailed paired *t*-test). **(D1)** Experimental design of a step-by-step investigation of artefact occurrence. Double dash on box represents overnight incubation. Length and colour of staining steps represent incubation time and temperature, respectively. **(D2)** LXRT images of representative samples from each experimental group described in **(D1)**. **(E)** Occurrence of "crack I" (grey line), "crack II" (blue line) and "crack" (blue bars) in each experimental group described in **(D1)**. **(F1)** Sample volumes of embedded samples of all experimental groups described in **(D1)**, measured in LXRT datasets. Each light dot represents one sample. Each dark dot represents the average of all samples from an experimental group. For the "fresh" group (triangle), the sample volume was estimated from warping data and the data point is connected to the next staining step with a dashed line. **(F2)** Ratio of the mean sample volume of each experimental group to that of the previous group. A dashed line marks ratio = 1 i.e., no volume change. Abbreviations: GL: glomerular layer, EPL: external plexiform layer, MCL: mitral cell layer, GCL: granule cell layer, w: with, GA: glutaraldehyde, TCH: thiocarbohydrazide, PFA: paraformaldehyde, imm: immersion, Os: osmium tetroxide, R: potassium ferrocyanide, TCH: thiocarbohydrazide, U: uranyl acetate, Pb: lead aspartate, dehy: dehydration, EtOH: ethanol. Scale bars are shared across all images in the same panel.

imaging if the reducing agent was presented after the tissue had been already stained with osmium tetroxide (instead of presenting the fresh tissue with reduced osmium tetroxide). We refer to this protocol as "2-step reduced osmium" (2sRO) (**Figure 2C**). 2sRO also differed in that the incubation of the bridging agent TCH was milder (in time and in temperature), the uranyl acetate incubation (typically overnight at 4°C) was extended with a short (2 h) hot (50°C) period and the incubation of lead aspartate was milder (in temperature). Finally, this protocol employed a distinct fixation method — perfusion — to the one used before — immersion. We implemented the complete 2sRO to replicate its reported performance and compared it across our benchmarked protocol (1sRO). Indeed, experiments stained with 2sRO displayed a distinct penetrance of the "sideways" artefact, now more variable and displaying extreme values – such as being entirely absent in all samples of 38% of the experiments (6/16) (**Figure 2D3**).

The diffusion of staining solutions through the specimen was also found associated with another artefact type: "central". "Central" displays a poorly stained region fully enclosed inside the sample, but in this case the unstained region presents virtually no metal staining — with no histological structure revealed by LXRT, and its location appears equally distant to all sample borders (**Figure 2E**). It is similar to previously reported artefacts associated with insufficient staining times (Hua et al., 2015; Mikula and Denk, 2015; Ströh et al., 2021), and it was completely absent in slices with thickness smaller or equal than 0.6 mm (**Figure 2F**).

Altogether, we identified two possible mechanisms behind the most prevalent artefact "sideways": diffusion kinetics of the staining solutions and reduction of osmium tetroxide during the first staining step, and the implemented changes removed this artefact from all samples in 38% of the batches.

"Cracks" can be Reduced With Glutaraldehyde Fixation and Gentle TCH Reactions

The second most prevalent artefact was "crack" (**Figure 1C**), whose presence precludes any further analysis on the affected sample: if this artefact occurs in the volume of interest, samples become unusable as cellular features cannot be annotated across even small cracks. In fact, even if "crack" artefacts were found outside of the volume of interest, the sample should also be treated as unusable because smaller cracks were likely to be found across the rest of the volume. We further classified the observed cracks into two non-mutually-exclusive subtypes, based on whether the crack did not follow any histological feature ("crack I") or whether it followed histological borders ("crack II") (**Figure 3A**).

"Crack" might be generated by expansive forces overwhelming the forces that keep the tissue together (**Figure 3A1**). Therefore, we expected chemical fixation to play a role in preventing the appearance of cracks — by making the tissue less fragile. Paraformaldehyde and glutaraldehyde are the two most commonly used fixatives for electron microscopy (EM), employed either alone or in combination (Morris, 1965). Glutaraldehyde provides a stronger fixation, derived from its two aldehyde groups that enable reactions cross-linking protein molecules (Kiernan, 2000). We compared sample batches fixed with commonly used fixative solutions employing distinct concentrations of glutaraldehyde. On the other hand, it has been reported that the bridging agent TCH generates gaseous nitrogen as a subproduct when binding to the fixed osmium (Guha and De, 1924; Seligman et al., 1966; Mikula and Denk, 2015). We assumed the stress generated would be related to the amount of gas created, which in turn should correlate with the amount of TCH-osmium reactions. We thereby devised two stress scenarios, differing in the duration and temperature of the TCH step. We observed that fewer samples carried "crack" artefact when processed with the milder TCH incubation, even when fixed with the milder fixative solution (**Figure 3B1**), and that crack severity decreased at the same time (**Figure 3A1**). Moreover, glutaraldehyde was required in the fixative solution in order to prevent the appearance of cracks (**Figure 3B2**). Finally, cracks of all types were more frequently present in larger samples (**Figure 3C**).

We then aimed to identify at which point in the staining protocol "crack" appeared by stopping the staining process at every single step (**Figure 3D**). As expected, "crack" started appearing during the TCH step, and their presence increased progressively throughout the consecutive staining steps

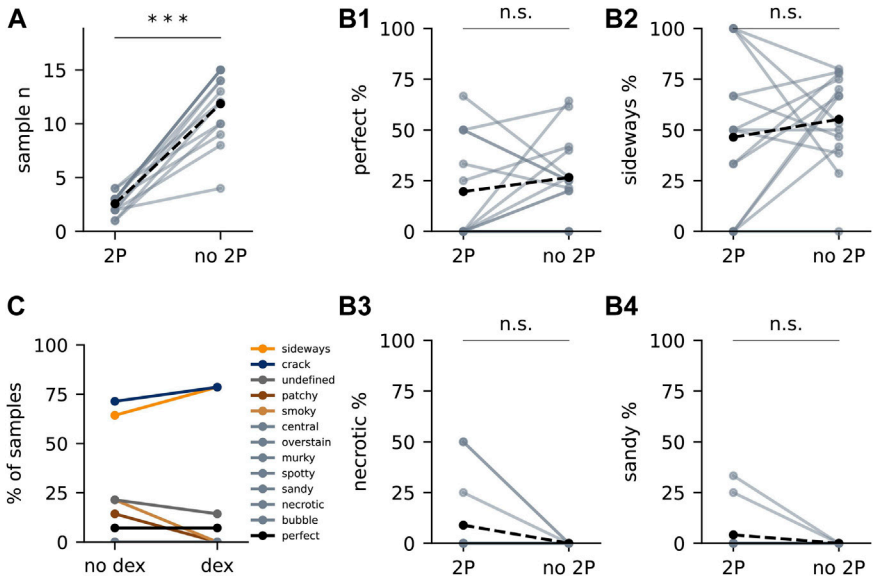

FIGURE 4 | The effect of 2P and dexamethasone on artefact occurrence. **(A)** Number of samples with ("2P") and without *in vivo* functional imaging ("no 2P") from each experiment. Each light dot represents "2P" samples or "no 2P" samples of one experiment. Solid lines connect "2P" samples to "no 2P"samples from the same experiment. Black dots represent the mean. Dashed lines connect the mean values. Asterisks represent statistical significance (***: $p < 0.0005$, two-tailed paired *t*-test). **(B1)** Percentage of perfect samples from each experiment. **(B2–B4)** Percentage of samples with "sideways" **(B2)**, "necrotic" **(B3)** and "sandy" **(B4)**. **(C)** Artefacts in samples administered with and without dexamethasone within the same experiment ($n = 13$ and 14, respectively).

(**Figure 3E**). Moreover, this experiment showed that samples expand during the staining protocol (**Figure 3D2**), that expansion starts during the TCH step and that samples continue to expand during the following osmium tetroxide step (**Figure 3F**).

Altogether, "crack" artefact can be prevented by including glutaraldehyde in the fixative and by minimising the TCH reaction.

The Effect of Prior *in vivo* 2P Imaging on Staining Success

Next, we evaluated the effect of prior *in vivo* 2P imaging on the experimental yield of the SPPs (**Figure 4**). The throughput (the number of samples processed per batch) was severely reduced by the addition of the *in vivo* imaging step (**Figure 4A**). Nevertheless, on average the success rate of the experiment remained unaltered by the incorporation of this imaging modality (**Figure 4B1**), despite introducing some 2P-specific artefacts (**Figures 4B3,B4**). Edema is considered a source of surgery-derived histology-scale damage (Betz and Coester, 1990; Judkewitz et al., 2009). To minimise this factor, we introduced a series of edema-preventing measures before and during surgery: mice were administered with the anti-inflammatory drug dexamethasone before the experiment, ice-cold buffer was frequently applied to cool down the drilling of the skull and laser exposure during imaging was minimised whenever possible. Nevertheless, we did not observe a significant effect of these additional measures (**Figure 4C**).

In sum, we optimised the SPP to obtain good quality images from all modalities with sufficient yield. At this point we turned our attention towards the second main factor affecting the throughput of the CMI workflow: the quality of the registration of the different modalities into a multimodal map.

Warping Accuracy Across Imaging Modalities

In order to reliably identify neurons functionally-recorded *in vivo* in the anatomical map acquired *ex vivo,* the datasets arising from each imaging modality need to be spatially correlated at cellular precision (Helmstaedter, 2013). By identifying conserved pairs of landmarks in two modalities reporting the same space, a warp field relating the two spaces can be computed (**Figure 5A1**) (Bogovic et al., 2016). This set of landmarks was termed "warping landmarks". This warp field can later be used to translate any spatial annotation across the two coordinate systems (**Figure 5A2**). Blood vessels can be used to set warping landmarks for correlating *in vivo* 2P and SBEM datasets, since their structures can be reliably retrieved by both modalities. They often describe chiral spatial patterns that occur at a density potentially sufficient to map tissue at single cell body precision (Bock et al., 2011; Briggman et al., 2011; Lee et al., 2016; Bosch et al., 2020; Miettinen et al., 2021; Bosch et al., 2022). As blood vessels are also resolved by SXRT, they can be used as a source for landmarks for warping across the three dataset modalities (**Figure 5B**).

We aimed to quantify the precision at which one could warp datasets obtained by those three modalities in a previously established correlative workflow (**Figures 6A,B**) (Bosch et al., 2022). For this purpose, we manually traced blood vessels in the same region spanning (160 μm^3) in each original dataset (**Figure 6A**). Then, these tracings were warped into a common

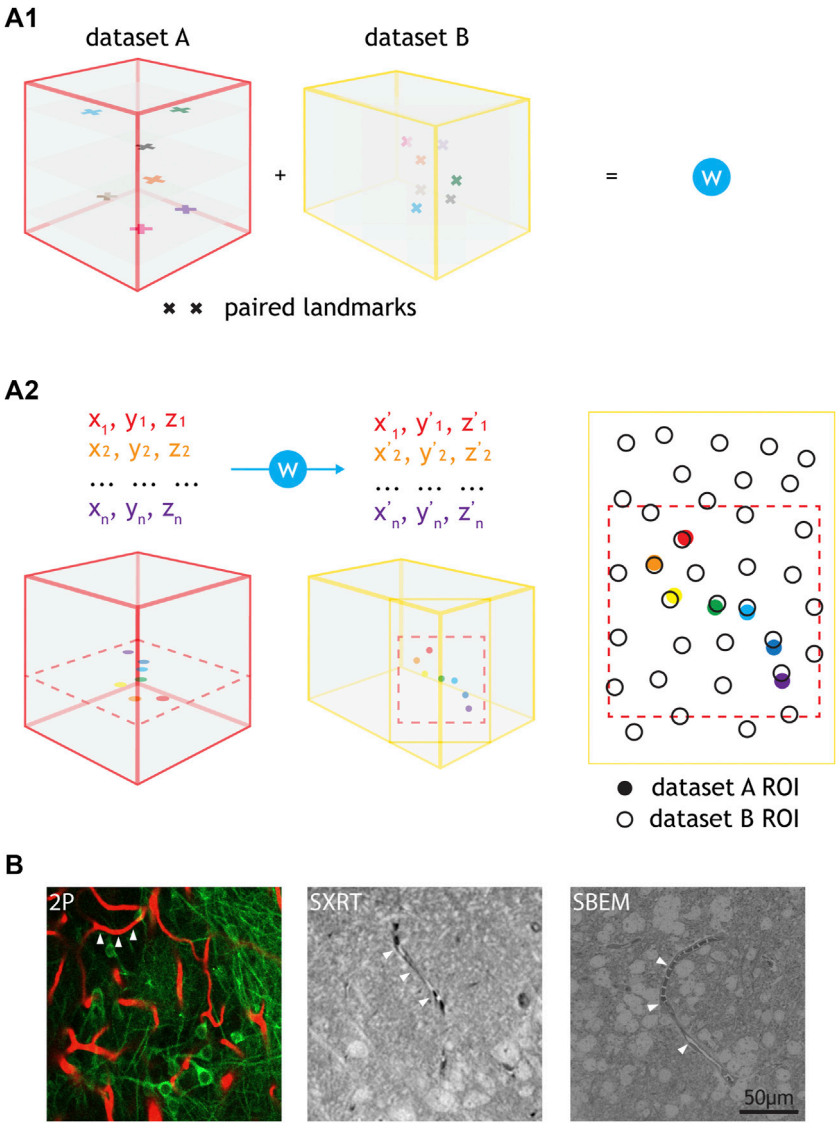

FIGURE 5 | Warping using common features e.g., blood vessels and cell correlation by annotation warping. **(A1)** Common features found throughout the volume of two datasets (i.e., paired landmarks) are used to calculate a warping function ("W"). **(A2)** The warping function can be used to warp any annotations from one dataset to another. The inputs needed are the x, y, z coordinates of the annotations in the native dataset space and the outputs are the x, y, z coordinates of those annotations in the target dataset space. Annotation warping is used to correlate ROIs from two datasets. ROIs can be correlated as long as the warped ROI falls to a position that is closer to the target ROI than any other ROI. For **(A1,A2)**, cubes represent datasets (e.g., 2P, LXRT, SXRT, SBEM), acquired from the same piece of tissue. The datasets may differ in the dimensions, voxel sizes and the exact region of the sample, differences here represented by cube dimensions, landmark sizes and landmark positions, respectively. Other differences may involve a reversed order in one of the spatial dimensions (such as an horizontal flip in all images), making it necessary to use chiral structures as a source for warping landmarks. **(B)** Example images showing different blood vessels (arrowheads) resolved by 2P, SXRT and EM datasets.

reference space using the warp field calculated with the previously described set of "warping landmarks" (**Figure 6C**). Blood vessel branching points are unique junctions and many of them ($n = 39$) could be identified across all imaging modalities, defining blood vessel segments ($n = 35$). We interpolated a defined number of points within each blood vessel segment in all modalities and paired the resulting nodes (**Figure 6D**). This allowed for calculating the distance across modalities between paired nodes of the blood vessel (**Figure 6E**). Warping accuracy depends on the accuracy at which landmarks are resolved across the dataset and therefore its value can vary throughout the dataset's topology. We observed that the range of warping accuracies recorded depended on the pair of imaging modalities being warped: it ranged between 0.6 and 27.3 µm when warping 2P to EM or to SXRT and between 0.2 and 9.9 µm when warping SBEM to SXRT (**Figures 6E,F**). On average, any point in the blood vessel could be mapped at ~14 µm accuracy between the 2P and the SBEM dataset and at ~9 µm accuracy between the 2P and the SXRT dataset, and regions between SXRT and SBEM could be mapped at an accuracy of ~2 µm (**Figures 6F,G**), implying that

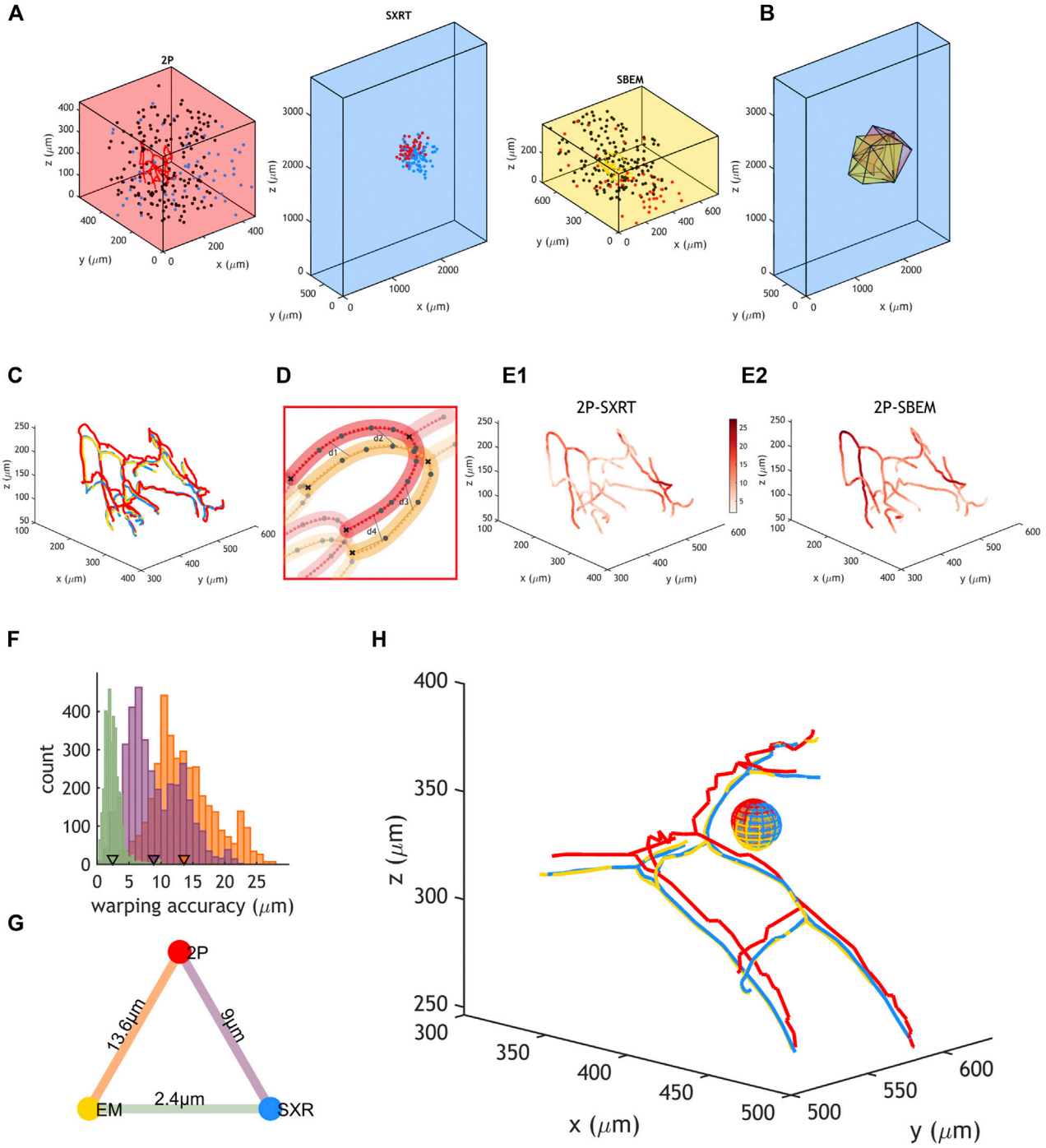

FIGURE 6 | Accurate warping allows for cell correlation among 2P, SXRT and SBEM. **(A)** Position of landmarks used to generate warping functions between two datasets and position of blood vessel tracings used to quantify warping accuracy in 2P, SXRT and SBEM datasets of a sample. Blue, black and red dots represent landmarks used between 2P and SXRT datasets, between 2P and SBEM datasets and between SXRT and SBEM datasets, respectively. **(B)** Fields of view of 2P (red, warped), SBEM (yellow, warped) and SXRT (blue, native space) datasets. **(C)** Same blood vessels traced in the 2P (red, warped), SXRT (blue, warped) and SBEM (yellow, native space) datasets. **(D)** Quantification of warping accuracy. The nodes in the blood vessel traced in one imaging modality (red) are paired to the equivalent nodes in the other modality (yellow). The distance between two paired nodes (e.g., "d1") reflects the warping accuracy at that location. Large dots represent nodes in the original tracing. Lines represent paths of the original tracing. Small dots represent nodes interpolated along the tracing path. **(E1,E2)** Native SBEM blood vessel tracing coloured by the mapped 2P-SXRT and 2P-SBEM warping accuracy, respectively. **(F)** Distribution of warping accuracies (i.e., distances between paired nodes). Purple, orange and green represent 2P-SXRT, 2P-SBEM and SXRT-SBEM accuracies, respectively. Mean warping accuracies are marked by triangles. **(G)** Mean warping accuracy between each pair of imaging modalities. **(H)** Example mitral cell and surrounding blood vessels warped from 2P (red) and SXRT (blue) datasets into SBEM (yellow) space. The diameter of the sphere is 20 μm, similar to the diameter of a mitral cell soma.

any region can be mapped across any of the three imaging modalities at single cell precision (**Figure 6H**).

DISCUSSION

We have identified and addressed two major bottlenecks in the performance of a correlative multimodal imaging pipeline capable of resolving the structure and function of a neural circuit in the mouse olfactory bulb: the yield of sample preparation and the accuracy of dataset correlation across 2P, SXRT and SBEM modalities.

Our study focuses on mouse olfactory bulb (OB) dorsal slices. The OB contains the first neuronal circuit in the olfactory sensory pathway (Mori et al., 1999), the glomerular column. The architecture of these columns is compact (<1 mm^3) and modular (>1000 columns in each OB hemisphere) (Schwarz et al., 2018) and their anatomical location makes them accessible for *in vivo* studies involving minimally invasive surgeries (e.g., imaging intracellular [Ca^{2+}] through a cranial window). Combined, these properties make the OB a good model for studying systems neuroscience in the mammalian brain (Schaefer and Margrie, 2007). For *in vivo* experiments aimed at recording the circuit's function, 2P datasets can map a dorsal field of view of ~mm^2, but depth resolution of 2P is poorer than the lateral one (Chaigneau et al., 2011). Moreover, its signal-to-noise ratio decreases with the depth of the region being imaged, making it increasingly challenging to retrieve a signal beyond a depth of 0.5 mm deep inside the brain (Wachowiak et al., 2013; Ackels et al., 2020).

Our horizontal slices provide a maximal overlap between the 2P-imaged region and the stained tissue that will later be imaged at higher structural resolution with SXRT and SBEM. However, these dorsal sections present anatomical asymmetries: one of their sides is a vibratome-cut surface, whereas the other side is the anatomically-preserved surface of the brain. We generated a set of samples that would present a more symmetrical disposition to diffusing solutions: second slices from the same brain region.

Two main artefacts dominated the sample preparation protocol (SPP). An asymmetrical unstained region here denoted "sideways" was the most frequent artefact type. Its pattern was reminiscent of an artefact defined previously (Hua et al., 2015; Mikula and Denk, 2015) although in our samples it displayed an asymmetrical morphology (**Supplementary Figure S3**). We found it to be related to two independent parameters: the diffusion of heavy metals through the tissue and the reduction of the first osmium tetroxide staining step. This is consistent with its symmetrical appearance in previous reports that analysed punch-dissected tissue cylinders presenting a symmetrical structure to freely diffusing solutions (Hua et al., 2015). Addressing those two factors allowed for removing its presence in all samples in a subset of experimental batches.

The next most common artefact was the presence of cracks in the stained tissue, possibly generated by an imbalance between expansive and cohesive forces in the tissue during sample preparation. It is known that osmium tetroxide can provoke both the expansion and the shrinkage of brain tissue samples during staining (Ströh et al., 2021) and that the bridging agent TCH generates gaseous nitrogen as a by-product of binding to fixed osmium (Guha and De, 1924; Seligman et al., 1966; Mikula and Denk, 2015). Consistent with that, we found that a milder TCH reaction can minimise the generation of cracks in samples extending multiple mm^3 in volume, while not compromising the overall staining quality. On the other hand, strong sample fixation with glutaraldehyde was necessary to prevent tissue from cracking during the staining process. Finally, larger samples displayed cracks more frequently. While dehydration can lead to severe shrinkage of fresh soft tissues (Buytaert et al., 2014) we observed tissue had overall expanded after dehydration. Altogether, these findings allowed extracting simple specific requirements for future protocols to minimise the appearance of cracks: 1) employing fixatives containing at least 1.25% glutaraldehyde, 2) reducing the strength of the TCH reaction, and 3) minimising the smallest dimension of the sample being processed whenever possible. Further, albeit more difficult to implement improvements are: 1) finding optimal formulations for fixative solutions for a specific sample, 2) replacing TCH for a reagent that does not create bubbles — such as pyrogallol (Mikula and Denk, 2015; Song et al., 2022), and 3) minimising the sample expansion processes by e.g., counteracting osmium-derived effects with suitable additives (Hua et al., 2015; Ströh et al., 2021).

A subset of the experiments reported were obtained by chemically fixing the tissue by immersion in fixative (**Supplementary Table S2**). All artefacts in immersion-fixed samples could be diagnosed by observing an LXRT dataset covering the entire sample. Such 3D datasets can be obtained at a rate of multiple samples per day with benchtop LXRTs (Metscher, 2009; Bushong et al., 2015; Gutiérrez et al., 2018) and of nearly one sample per minute at specialised hard X-ray microtomography beamlines at synchrotron X-ray facilities (Walker et al., 2014; Rau, 2017; Harkiolaki et al., 2018; Walsh et al., 2021; Bosch et al., 2022). A distinct approach could involve fixing the samples via intracardiac perfusion of the fixative (Gage et al., 2012) (**Supplementary Figure S4**). Doing so could prevent some artefacts that might be specific to immersion-fixation (**Supplementary Figure S4A**) and would remove the requirement of a fast dissection of the tissue of interest, making this approach compatible with processing some regions that might be out of reach or processing multiple different regions in the same animal. On the other hand, maintaining ultrastructural integrity is generally more challenging with perfusion (Palay et al., 1962; Crang et al., 1988; Maunsbach and Afzelius, 1999; Tao-Cheng et al., 2007; Glauert and Lewis, 2014) (**Supplementary Figure S4B**). It is worth noting that evaluating sample quality by its ultrastructure has a lower throughput than relying on LXRT for that purpose. Therefore, choosing perfusion as a fixation method could create a quality control bottleneck in the experimental pipeline (**Supplementary Figure S4C**).

The yield of perfectly stained samples in an experiment was not altered when extending the pipeline with prior *in vivo* 2P imaging. However, those experiments have a much lower throughput (**Figure 4A**). A low throughput combined with a moderate yield can make it challenging to predict future stock of samples with both optimal 2P imaging and optimal staining. Importantly, sample preparation does not end with staining: trimming the specimen will be necessary to accommodate its dimensions to some acquisition techniques (**Supplementary Figure S4C**) (Karreman et al., 2016; Ronchi et al., 2021; Bosch et al., 2022), hard X-ray tomography imaging may inflict damage from radiation dose and temperature changes (Henderson, 1995; Howells et al., 2009; Du and Jacobsen, 2018), volume electron microscopy techniques imply slicing or destruction of the sample and therefore add their own risk of a specific sample becoming irreversibly damaged, and optimal targeting of the features of interest to be imaged with the distinct modalities precludes extracting the information sought by the initial experimental question (Bosch et al., 2020; Walter et al., 2020). In light of these successive challenges, it is imperative for a successful CMI experiment to prepare a sufficient number of samples at the first stage. Given the low throughput nature of *in vivo* 2P experiments (in particular in e.g., awake or even behaving animals), this can currently partially be achieved by e.g., obtaining samples from multiple brain regions in a given experiment or by coordinated efforts of multiple researchers or even research labs. Notably, any improvement to the SPP will reduce this initial experimental burden and allow for increasingly complex physiological analysis to be combined with structural investigations. The approach described in this study highlights the major bottlenecks in a protocol, but it does not provide an exhaustive readout of all sources of variability, nor does it describe the spectrum of ultrastructural defects one can encounter in optimally-stained specimens as assessed by LXRT. Therefore, it may be useful in the future to both reassess the performance of novel protocols with higher throughputs and efficiencies — to find the causes for rarer staining deficits — and to conduct focussed analyses on the quality of ultrastructure. This iterative process can guide the development of more efficient and robust protocols, able to stain larger specimens reliably.

Finally, we demonstrated that tissue locations imaged *in vivo* can be recalled at single-cell precision in an SXRT dataset. Because SXRT datasets can be obtained on multi-mm^3 specimens, this strategic improvement provides an early readout of circuit structure and can inform on how to precisely trim precious specimens, preserving virtually all 2P-imaged cells in a trimmed specimen for follow-up higher resolution structural imaging techniques that impose limitations on sample dimensions and require extraordinary sample quality control standards. Notably, this approach may also be useful for experiments requiring a correlation accuracy better than 10 μm: in those cases, it would narrow the landscape containing the feature of interest from multiple mm^3 down to a volume of ~$(10\ \mu m)^3$. This would relax the requirements imposed to a further disambiguation algorithm, which would operate in the range between $(10\ \mu m)^3$ and the required accuracy. Direct 2P-SXRT correlation therefore generates experimental compatibility of *in vivo* 2P with not only the different implementations of volume EM but also with other synchrotron hard X-ray modalities such as nanoholotomography (Kuan et al., 2020), laminography (Helfen et al., 2013; Witte et al., 2020) or ptychography (Rodenburg et al., 2007; Holler et al., 2017; Shahmoradian et al., 2017). Adding non-destructive techniques to the workflow not only enables more diverse insights to be recalled from the same sample, but also makes it more resilient, ensuring insights are obtained from a larger yield of samples. Additionally, combining multimodal insights from a single sample may allow developing more robust image processing algorithms, by providing insights free from technique-specific artefacts (e.g., using blood vessels from the X-ray CT datasets, with isotropic resolution, to guide the fine alignment of volume EM images). Altogether, we are confident that improved staining and reliable warping will enable exhaustive studies retrieving physiology, circuit structure and synaptic signatures in targeted regions of slices covering multiple mm^3.

Our optimisation was aimed at obtaining a single sample preparation protocol that is compatible with both SXRT and SBEM, since staining for the latter did provide a sufficient signal-to-noise ratio in the former. However, it is possible that better SXRT datasets could be obtained if the samples were prepared following specially SXRT-optimised preparation protocols. Those could, for example, aim to maximise the phase contrast in the detected X-ray beam while minimising the absorption and thereby bring benefits in terms of both image contrast and specimen size. Doing so could be envisaged by using weaker metal stainings. This could modify, in turn, the landscape of compatible techniques for future multimodal imaging approaches in systems neuroscience and biological soft tissue research more generally, e.g., enable to extract insights on molecular composition and transcriptomic expression in the tissue alongside its function and structure (Ståhl Patrik et al., 2016; Domart et al., 2020; Close et al., 2021).

Altogether, we report improvements in two limiting steps of a correlative multimodal imaging pipeline for systems neuroscience in the mouse olfactory bulb in sample preparation and in dataset correlation accuracy. These insights will allow us to make informed decisions to troubleshoot and improve the yield of the existing protocols and to design novel pipelines relying solely on hard X-rays to retrieve the location of the cell bodies of interest. These frameworks will pave the way for the design of more resilient workflows to interrogate both structure and function of neural circuits in the mammalian brain.

DATA AVAILABILITY STATEMENT

The datasets presented in this study can be found in the online repositories: https://github.com/FrancisCrickInstitute/protocolBLAST, https://github.com/FrancisCrickInstitute/warpAnnotations.

ETHICS STATEMENT

The animal study was reviewed and approved by Ethics Committee of the board of the Francis Crick Institute and the United Kingdom Home Office under the Animals (Scientific Procedures) Act 1986.

AUTHOR CONTRIBUTIONS

YZ, ATS and CB conceptualised the research project and designed experiments; YZ, TA, AP, M-CZ, AB, and CB performed experiments and acquired data; YZ, ATS and CB analysed and interpreted the data; YZ, ATS and CB wrote the manuscript draft; YZ and CB generated the figures, and all authors reviewed and provided input to the manuscript.

FUNDING

This research was funded in whole, or in part, by the Wellcome Trust (FC001153). For the purpose of Open Access, the author has applied a CC BY public copyright licence to any Author Accepted Manuscript version arising from this submission. This work was carried out with the support of Diamond Light Source, beamline I13-2 (proposal 20274) and the TOMCAT beamline of the Swiss Light Source at the Paul Scherrer Institut (proposal 20190417). This work was supported by the Francis Crick Institute, which receives its core funding from Cancer Research UK (FC001153), the UK Medical Research Council (FC001153), and the Wellcome Trust (FC001153); by the UK Medical Research Council (grant reference MC_UP_1202/5) to ATS, by a Physics of Life grant to ATS and AP (grant reference EP/W024292/1) and a DFG postdoctoral fellowship to TA. ATS is a Wellcome Trust Investigator (110174/Z/15/Z). AP acknowledges funding from the European Research Council under the European Union's Horizon 2020 Research and Innovation Programme (grant No. 852455).

ACKNOWLEDGMENTS

We are grateful to the biological research and electron microscopy science technology platforms of the Francis Crick Institute. We thank Marta Pallotto, Kara Fulton and Kevin Briggman for support and critical discussions on the initial configuration of the staining protocol, to Manuel Berning for support in developing the warpAnnotations toolbox, to Norman Rzepka for support in the webknossos infrastructure, and to the members of the sample preparation working group of the volumeEM community for insightful discussions on the topic.

SUPPLEMENTARY MATERIAL

The Supplementary Material for this article can be found online at: https://www.frontiersin.org/articles/10.3389/fcell.2022.880696/full#supplementary-material

REFERENCES

Ackels, T., Erskine, A., Dasgupta, D., Marin, A. C., Warner, T. P. A., Tootoonian, S., et al. (2021). Fast Odour Dynamics Are Encoded in the Olfactory System and Guide Behaviour. *Nature* 593 (7860), 558–563. doi:10.1038/s41586-021-03514-2

Ackels, T., Jordan, R., Schaefer, A. T., and Fukunaga, I. (2020). Respiration-Locking of Olfactory Receptor and Projection Neurons in the Mouse Olfactory Bulb and its Modulation by Brain State. *Front. Cell. Neurosci.* 14, 220. doi:10.3389/fncel.2020.00220

Betz, A. L., and Coester, H. C. (1990). Effect of Steroids on Edema and Sodium Uptake of the Brain During Focal Ischemia in Rats. *Stroke* 21 (8), 1199–1204. doi:10.1161/01.STR.21.8.1199

Bock, D. D., Lee, W.-C. A., Kerlin, A. M., Andermann, M. L., Hood, G., Wetzel, A. W., et al. (2011). Network Anatomy and *In Vivo* Physiology of Visual Cortical Neurons. *Nature* 471 (7337), 177–182. doi:10.1038/nature09802

Boergens, K. M., Berning, M., Bocklisch, T., Bräunlein, D., Drawitsch, F., Frohnhofen, J., et al. (2017). webKnossos: Efficient Online 3D Data Annotation for Connectomics. *Nat. Methods* 14 (7), 691–694. doi:10.1038/nmeth.4331

Bogovic, J. A., Hanslovsky, P., Wong, A., and Saalfeld, S. (2016). "Robust Registration of Calcium Images by Learned Contrast Synthesis," in 2016 IEEE 13th International Symposium on Biomedical Imaging (ISBI) (IEEE), 1123–1126. doi:10.1109/isbi.2016.7493463

Bosch, C., Ackels, T., Pacureanu, A., Zhang, Y., Peddie, C. J., Berning, M., et al. (2022). Functional and Multiscale 3D Structural Investigation of Brain Tissue through Correlative *In Vivo* Physiology, Synchrotron Micro-Tomography and Volume Electron Microscopy. *Nat. Commun.* 13 (1), 2923. doi:10.1038/s41467-022-30199-6

Bosch, C., Schaefer, A. T., Pacureanu, A., Walter, A., Karreman, M. A., and Dykas, M. (2020). "Correlated Multimodal Imaging Across Scales," in *Imaging Modalities in Biological and Preclinical Research: A Compendium*. Editor A. Walter (Bristol, United Kingdom: IoP-IPEM), III.3-1–III.3-11.

BRAIN Initiative Cell Census Network (BICCN) (2021). A Multimodal Cell Census and Atlas of the Mammalian Primary Motor Cortex. *Nature* 598 (7879), 86–102. doi:10.1038/s41586-021-03950-0

Briggman, K. L., Helmstaedter, M., and Denk, W. (2011). Wiring Specificity in the Direction-Selectivity Circuit of the Retina. *Nature* 471 (7337), 183–188. doi:10.1038/nature09818

Buckley, I. K., and Porter, K. R. (1967). Cytoplasmic Fibrils in Living Cultured Cells. *Protoplasma* 64 (4), 349–380. doi:10.1007/BF01666538

Bushong, E. A., Johnson, D. D., Kim, K.-Y., Terada, M., Hatori, M., Peltier, S. T., et al. (2015). X-Ray Microscopy as an Approach to Increasing Accuracy and Efficiency of Serial Block-Face Imaging for Correlated Light and Electron Microscopy of Biological Specimens. *Microsc. Microanal.* 21 (1), 231–238. doi:10.1017/S1431927614013579

Buytaert, J., Goyens, J., De Greef, D., Aerts, P., and Dirckx, J. (2014). Volume Shrinkage of Bone, Brain and Muscle Tissue in Sample Preparation for Micro-CT and Light Sheet Fluorescence Microscopy (LSFM). *Microsc. Microanal.* 20 (4), 1208–1217. doi:10.1017/S1431927614001329

Chaigneau, E., Wright, A. J., Poland, S. P., Girkin, J. M., and Silver, R. A. (2011). Impact of Wavefront Distortion and Scattering on 2-photon Microscopy in Mammalian Brain Tissue. *Opt. Express* 19 (23), 22755–22774. doi:10.1364/OE.19.022755

Claudi, F., Petrucco, L., Tyson, A., Branco, T., Margrie, T., and Portugues, R. (2020). BrainGlobe Atlas API: A Common Interface for Neuroanatomical Atlases. *Joss* 5 (54), 2668. doi:10.21105/joss.02668

Close, J. L., Long, B. R., and Zeng, H. (2021). Spatially Resolved Transcriptomics in Neuroscience. *Nat. Methods* 18 (1), 23–25. doi:10.1038/s41592-020-01040-z

Crang, R. F. E., Crang, R. F. E., and Klomparens, K. L. (1988). *Artifacts in Biological Electron Microscopy*. Springer US.

Denk, W., Delaney, K. R., Gelperin, A., Kleinfeld, D., Strowbridge, B. W., Tank, D. W., et al. (1994). Anatomical and Functional Imaging of Neurons Using 2-Photon Laser Scanning Microscopy. *J. Neurosci. Methods* 54 (2), 151–162. doi:10.1016/0165-0270(94)90189-9

Denk, W., and Horstmann, H. (2004). Serial Block-Face Scanning Electron Microscopy to Reconstruct Three-Dimensional Tissue Nanostructure. *PLoS Biol.* 2 (11), e329. doi:10.1371/journal.pbio.0020329

Domart, F., Cloetens, P., Roudeau, S., Carmona, A., Verdier, E., Choquet, D., et al. (2020). Correlating STED and Synchrotron XRF Nano-Imaging Unveils Cosegregation of Metals and Cytoskeleton Proteins in Dendrites. *eLife* 9, e62334. doi:10.7554/eLife.62334

Du, M., and Jacobsen, C. (2018). Relative Merits and Limiting Factors for X-Ray and Electron Microscopy of Thick, Hydrated Organic Materials. *Ultramicroscopy* 184, 293–309. doi:10.1016/j.ultramic.2017.10.003

Dyer, E. L., Gray Roncal, W., Prasad, J. A., Fernandes, H. L., Gürsoy, D., De Andrade, V., et al. (2017). Quantifying Mesoscale Neuroanatomy Using X-Ray Microtomography. *Eneuro* 4 (5), 1–18. doi:10.1523/ENEURO.0195-17.2017

Frazier, L. L., and Brunjes, P. C. (1988). Unilateral Odor Deprivation: Early Postnatal Changes in Olfactory Bulb Cell Density and Number. *J. Comp. Neurol.* 269 (3), 355–370. doi:10.1002/cne.902690304

Gage, G. J., Kipke, D. R., and Shain, W. (2012). Whole Animal Perfusion Fixation for Rodents. *JoVE* (65), e3564. doi:10.3791/3564

Genoud, C., Titze, B., Graff-Meyer, A., and Friedrich, R. W. (2018). Fast Homogeneous *En Bloc* Staining of Large Tissue Samples for Volume Electron Microscopy. *Front. Neuroanat.* 12, 76. doi:10.3389/fnana.2018.00076

Glauert, A. M., and Lewis, P. R. (2014). *Biological Specimen Preparation for Transmission Electron Microscopy*. Princeton University Press.

Guha, P. C., and De, S. C. (1924). CXLVII.-A New Method for the Preparation of Thiocarbohydrazide: Mono- and Di-thio-p-urazine. *J. Chem. Soc. Trans.* 125 (0), 1215–1218. doi:10.1039/CT9242501215

Gutiérrez, Y., Ott, D., Töpperwien, M., Salditt, T., and Scherber, C. (2018). X-Ray Computed Tomography and its Potential in Ecological Research: A Review of Studies and Optimization of Specimen Preparation. *Ecol. Evol.* 8 (15), 7717–7732. doi:10.1002/ece3.4149

Harkiolaki, M., Darrow, M. C., Spink, M. C., Kosior, E., Dent, K., and Duke, E. (2018). Cryo-Soft X-Ray Tomography: Using Soft X-Rays to Explore the Ultrastructure of Whole Cells. *Emerg. Top. life Sci.* 2 (1), 81–92. doi:10.1042/etls20170086

Hayat, M. A. (2000). In *Principles and Techniques of Electron Microscopy : Biological Applications*. Editor M. A. Hayat (Cambridge: Cambridge University Press).

Helfen, L., Xu, F., Suhonen, H., Urbanelli, L., Cloetens, P., and Baumbach, T. (2013). Nano-Laminography for Three-Dimensional High-Resolution Imaging of Flat Specimens. *J. Inst.* 8 (05), C05006. doi:10.1088/1748-0221/8/05/c05006

Helmstaedter, M. (2013). Cellular-Resolution Connectomics: Challenges of Dense Neural Circuit Reconstruction. *Nat. Methods* 10 (6), 501–507. doi:10.1038/nmeth.2476

Henderson, R. (1995). The Potential and Limitations of Neutrons, Electrons and X-Rays for Atomic Resolution Microscopy of Unstained Biological Molecules. *Quart. Rev. Biophys.* 28 (2), 171–193. doi:10.1017/S003358350000305X

Holler, M., Guizar-Sicairos, M., Tsai, E. H. R., Dinapoli, R., Müller, E., Bunk, O., et al. (2017). High-Resolution Non-Destructive Three-Dimensional Imaging of Integrated Circuits. *Nature* 543 (7645), 402–406. doi:10.1038/nature21698

Howells, M. R., Beetz, T., Chapman, H. N., Cui, C., Holton, J. M., Jacobsen, C. J., et al. (2009). An Assessment of the Resolution Limitation Due to Radiation-Damage in X-Ray Diffraction Microscopy. *J. Electron. Spectrosc. Relat. Phenom.* 170 (1-3), 4–12. doi:10.1016/j.elspec.2008.10.008

Hua, Y., Laserstein, P., and Helmstaedter, M. (2015). Large-Volume *En-Bloc* Staining for Electron Microscopy-Based Connectomics. *Nat. Commun.* 6 (1), 7923–7927. doi:10.1038/ncomms8923

Judkewitz, B., Rizzi, M., Kitamura, K., and Häusser, M. (2009). Targeted Single-Cell Electroporation of Mammalian Neurons *In Vivo*. *Nat. Protoc.* 4 (6), 862–869. doi:10.1038/nprot.2009.56

Karreman, M. A., Mercier, L., Schieber, N. L., Solecki, G., Allio, G., Winkler, F., et al. (2016). Fast and Precise Targeting of Single Tumor Cells *In Vivo* by Multimodal Correlative Microscopy. *J. Cell Sci.* 129 (2), 444–456. doi:10.1242/jcs.181842

Kiernan, J. A. (2000). Formaldehyde, Formalin, Paraformaldehyde and Glutaraldehyde: What They Are and What They Do. *Micros. Today* 8 (1), 8–13. doi:10.1017/S1551929500057060

Klinger, E., Motta, A., Marr, C., Theis, F. J., and Helmstaedter, M. (2021). Cellular Connectomes as Arbiters of Local Circuit Models in the Cerebral Cortex. *Nat. Commun.* 12 (1), 2785. doi:10.1038/s41467-021-22856-z

Kluyver, T., Ragan-Kelley, B., Pérez, F., Granger, B. E., Bussonnier, M., Frederic, J., et al. (2016). *Jupyter Notebooks-A Publishing Format for Reproducible Computational Workflows*.

Kuan, A. T., Phelps, J. S., Thomas, L. A., Nguyen, T. M., Han, J., Chen, C.-L., et al. (2020). Dense Neuronal Reconstruction Through X-Ray Holographic Nano-Tomography. *Nat. Neurosci.* 23 (12), 1637–1643. doi:10.1038/s41593-020-0704-9

Kubota, Y. (2015). New Developments in Electron Microscopy for Serial Image Acquisition of Neuronal Profiles. *Microscopy* 64 (1), 27–36. doi:10.1093/jmicro/dfu111

Lee, W.-C. A., Bonin, V., Reed, M., Graham, B. J., Hood, G., Glattfelder, K., et al. (2016). Anatomy and Function of an Excitatory Network in the Visual Cortex. *Nature* 532 (7599), 370–374. doi:10.1038/nature17192

Maunsbach, A. B., and Afzelius, B. A. (1999). "Fixative Application," in *Biomedical Electron Microscopy*. Editors A. B. Maunsbach, and B. A. Afzelius (San Diego: Academic Press), 79–102. doi:10.1016/b978-012480610-8/50006-8

Metscher, B. D. (2009). MicroCT for Comparative Morphology: Simple Staining Methods Allow High-Contrast 3D Imaging of Diverse Non-Mineralized Animal Tissues. *BMC Physiol.* 9 (1), 11. doi:10.1186/1472-6793-9-11

Miettinen, A., Zippo, A. G., Patera, A., Bonnin, A., Shahmoradian, S. H., Biella, G. E. M., et al. (2021). Micrometer-Resolution Reconstruction and Analysis of Whole Mouse Brain Vasculature by Synchrotron-Based Phase-Contrast Tomographic Microscopy. bioRxiv, 2021.2003.2016.435616. doi:10.1101/2021.03.16.435616

Mikula, S., and Denk, W. (2015). High-Resolution Whole-Brain Staining for Electron Microscopic Circuit Reconstruction. *Nat. Methods* 12 (6), 541–546. doi:10.1038/nmeth.3361

Mori, K., Nagao, H., and Yoshihara, Y. (1999). The Olfactory Bulb: Coding and Processing of Odor Molecule Information. *Science* 286 (5440), 711–715. doi:10.1126/science.286.5440.711

Morris, J. K. (1965). A Formaldehyde Glutaraldehyde Fixative of High Osmolality for Use in Electron Microscopy. *J. Cell. Biol.* 27, 1A–149A.

Niedworok, C. J., Brown, A. P. Y., Jorge Cardoso, M., Osten, P., Ourselin, S., Modat, M., et al. (2016). aMAP Is a Validated Pipeline for Registration and Segmentation of High-Resolution Mouse Brain Data. *Nat. Commun.* 7 (1), 11879. doi:10.1038/ncomms11879

Oheim, M., Beaurepaire, E., Chaigneau, E., Mertz, J., and Charpak, S. (2001). Two-Photon Microscopy in Brain Tissue: Parameters Influencing the Imaging Depth. *J. Neurosci. Methods* 111 (1), 29–37. doi:10.1016/S0165-0270(01)00438-1

Palay, S. L., McGee-Russell, S. M., Gordon, S., Jr., and Grillo, M. A. (1962). Fixation of Neural Tissues for Electron Microscopy by Perfusion with Solutions of Osmium Tetroxide. *J. Cell Biol.* 12 (2), 385–410. doi:10.1083/jcb.12.2.385

Pallotto, M., Watkins, P. V., Fubara, B., Singer, J. H., and Briggman, K. L. (2015). Extracellular Space Preservation Aids the Connectomic Analysis of Neural Circuits. *Elife* 4, e08206. doi:10.7554/eLife.08206

Panhuber, H., Laing, D. G., Willcox, M. E., Eagleson, G. K., and Pittman, E. A. (1985). The Distribution of the Size and Number of Mitral Cells in the Olfactory Bulb of the Rat. *J. Anat.* 140 (Pt 2) (Pt 2Pt 2), 297–308.

Parrish-Aungst, S., Shipley, M. T., Erdelyi, F., Szabo, G., and Puche, A. C. (2007). Quantitative Analysis of Neuronal Diversity in the Mouse Olfactory Bulb. *J. Comp. Neurol.* 501 (6), 825–836. doi:10.1002/cne.21205

Rau, C. (2017). Imaging with Coherent Synchrotron Radiation: X-Ray Imaging and Coherence Beamline (I13) at Diamond Light Source. *Synchrotron Radiat. News* 30 (5), 19–25. doi:10.1080/08940886.2017.1364530

Rodenburg, J. M., Hurst, A. C., Cullis, A. G., Dobson, B. R., Pfeiffer, F., Bunk, O., et al. (2007). Hard-X-Ray Lensless Imaging of Extended Objects. *Phys. Rev. Lett.* 98 (3), 034801. doi:10.1103/PhysRevLett.98.034801

Ronchi, P., Mizzon, G., Machado, P., D'Imprima, E., Best, B. T., Cassella, L., et al. (2021). High-Precision Targeting Workflow for Volume Electron Microscopy. *J. Cell Biol.* 220 (9), e202104069. doi:10.1083/jcb.202104069

Schaefer, A. T., and Margrie, T. W. (2007). Spatiotemporal Representations in the Olfactory System. *Trends Neurosci.* 30 (3), 92–100. doi:10.1016/j.tins.2007.01.001

Schindelin, J., Arganda-Carreras, I., Frise, E., Kaynig, V., Longair, M., Pietzsch, T., et al. (2012). Fiji: An Open-Source Platform for Biological-Image Analysis. *Nat. Methods* 9 (7), 676–682. doi:10.1038/nmeth.2019

Schwarz, D., Kollo, M., Bosch, C., Feinauer, C., Whiteley, I., Margrie, T. W., et al. (2018). Architecture of a Mammalian Glomerular Domain Revealed by Novel Volume Electroporation Using Nanoengineered Microelectrodes. *Nat. Commun.* 9 (1), 183. doi:10.1038/s41467-017-02560-7

Seligman, A. M., Wasserkrug, H. L., and Hanker, J. S. (1966). A New Staining Method (Oto) for Enhancing Contrast of Lipid-Containing Membranes and Droplets in Osmium Tetroxide-Fixed Tissue with Osmiophilic Thiocarbohydrazide (Tch). *J. Cell. Biol.* 30 (2), 424–432. doi:10.1083/jcb.30.2.424

Shahmoradian, S. H., Tsai, E. H. R., Diaz, A., Guizar-Sicairos, M., Raabe, J., Spycher, L., et al. (2017). Three-Dimensional Imaging of Biological Tissue by Cryo X-Ray Ptychography. *Sci. Rep.* 7 (1), 6291. doi:10.1038/s41598-017-05587-4

Song, K., Feng, Z., and Helmstaedter, M. (2022). High-Contrast En-Bloc Staining of Mouse Whole-Brain Samples for EM-Based Connectomics. *bioRxiv* [Preprint]. doi:10.1101/2022.03.30.486341

Ståhl, P. L., Salmén, F., Vickovic, S., Lundmark, A., Navarro, J. F., Magnusson, J., et al. (2016). Visualization and Analysis of Gene Expression in Tissue Sections by Spatial Transcriptomics. *Science* 353 (6294), 78–82. doi:10.1126/science.aaf2403

Ströh, S., Hammerschmith, E. W., Tank, D. W., Seung, H. S., and Wanner, A. A. (2021). *In Situ* X-Ray Assisted Electron Microscopy Staining for Large Biological Samples. *bioRxiv*.

Tao-Cheng, J.-H., Gallant, P. E., Brightman, M. W., Dosemeci, A., and Reese, T. S. (2007). Structural Changes at Synapses after Delayed Perfusion Fixation in Different Regions of the Mouse Brain. *J. Comp. Neurol.* 501 (5), 731–740. doi:10.1002/cne.21276

Tapia, J. C., Kasthuri, N., Hayworth, K. J., Schalek, R., Lichtman, J. W., Smith, S. J., et al. (2012). High-Contrast *En Bloc* Staining of Neuronal Tissue for Field Emission Scanning Electron Microscopy. *Nat. Protoc.* 7 (2), 193–206. doi:10.1038/nprot.2011.439

Ueda, H. R., Dodt, H.-U., Osten, P., Economo, M. N., Chandrashekar, J., and Keller, P. J. (2020). Whole-Brain Profiling of Cells and Circuits in Mammals by Tissue Clearing and Light-Sheet Microscopy. *Neuron* 106 (3), 369–387. doi:10.1016/j.neuron.2020.03.004

Van Rossum, G., and Drake, F. (2009). 10. CA: Scotts Valley, 1593511. CreateSpace. Python 3 Reference Manual.

Wachowiak, M., Economo, M. N., Diaz-Quesada, M., Brunert, D., Wesson, D. W., White, J. A., et al. (2013). Optical Dissection of Odor Information Processing *In Vivo* Using GCaMPs Expressed in Specified Cell Types of the Olfactory Bulb. *J. Neurosci.* 33 (12), 5285–5300. doi:10.1523/JNEUROSCI.4824-12.2013

Walker, S. M., Schwyn, D. A., Mokso, R., Wicklein, M., Müller, T., Doube, M., et al. (2014). *In Vivo* Time-Resolved Microtomography Reveals the Mechanics of the Blowfly Flight Motor. *PLoS Biol.* 12 (3), e1001823. doi:10.1371/journal.pbio.1001823

Walsh, C. L., Tafforeau, P., Wagner, W. L., Jafree, D. J., Bellier, A., Werlein, C., et al. (2021). Imaging Intact Human Organs with Local Resolution of Cellular Structures Using Hierarchical Phase-Contrast Tomography. *Nat. Methods* 18 (12), 1532–1541. doi:10.1038/s41592-021-01317-x

Walter, A., Paul-Gilloteaux, P., Plochberger, B., Sefc, L., Verkade, P., Mannheim, J. G., et al. (2020). Correlated Multimodal Imaging in Life Sciences: Expanding the Biomedical Horizon. *Front. Phys.* 8. doi:10.3389/fphy.2020.00047

Wanner, A. A., Genoud, C., Masudi, T., Siksou, L., and Friedrich, R. W. (2016). Dense EM-Based Reconstruction of the Interglomerular Projectome in the Zebrafish Olfactory Bulb. *Nat. Neurosci.* 19 (6), 816–825. doi:10.1038/nn.4290

Wilke, S. A., Antonios, J. K., Bushong, E. A., Badkoobehi, A., Malek, E., Hwang, M., et al. (2013). Deconstructing Complexity: Serial Block-Face Electron Microscopic Analysis of the Hippocampal Mossy Fiber Synapse. *J. Neurosci.* 33 (2), 507–522. doi:10.1523/JNEUROSCI.1600-12.2013

Winnubst, J., Bas, E., Ferreira, T. A., Wu, Z., Economo, M. N., Edson, P., et al. (2019). Reconstruction of 1,000 Projection Neurons Reveals New Cell Types and Organization of Long-Range Connectivity in the Mouse Brain. *Cell* 179 (1), 268–281 e213. doi:10.1016/j.cell.2019.07.042

Witte, K., Späth, A., Finizio, S., Donnelly, C., Watts, B., Sarafimov, B., et al. (2020). From 2D STXM to 3D Imaging: Soft X-Ray Laminography of Thin Specimens. *Nano LettNano*, doi:10.1021/acs.nanolett.9b04782

Yildirim, M., Sugihara, H., So, P. T. C., and Sur, M. (2019). Functional Imaging of Visual Cortical Layers and Subplate in Awake Mice with Optimized Three-Photon Microscopy. *Nat. Commun.* 10 (1), 177. doi:10.1038/s41467-018-08179-6

Conflict of Interest: The authors declare that the research was conducted in the absence of any commercial or financial relationships that could be construed as a potential conflict of interest.

Publisher's Note: All claims expressed in this article are solely those of the authors and do not necessarily represent those of their affiliated organizations, or those of the publisher, the editors and the reviewers. Any product that may be evaluated in this article, or claim that may be made by its manufacturer, is not guaranteed or endorsed by the publisher.

frontiers | Frontiers in Cell and Developmental Biology

REVIEW
published: 30 June 2022
doi: 10.3389/fcell.2022.866472

One for All, All for One: A Close Look at In-Resin Fluorescence Protocols for CLEM

Xavier Heiligenstein[1†] *and Miriam S. Lucas*[2*†]

[1]CryoCapCell, Le Kremlin-Bicêtre, Paris, France, [2]Scientific Center for Light and Electron Microscopy (ScopeM), ETH Zurich, Zurich, Switzerland

Sample preparation is the novel bottleneck for high throughput correlative light and electron microscopy (CLEM). Protocols suitable for both imaging methods must therefore balance the requirements of each technique. For fluorescence light microscopy, a structure of interest can be targeted using: 1) staining, which is often structure or tissue specific rather than protein specific, 2) dye-coupled proteins or antibodies, or 3) genetically encoded fluorescent proteins. Each of these three methods has its own advantages. For ultrastructural investigation by electron microscopy (EM) resin embedding remains a significant sample preparation approach, as it stabilizes the sample such that it withstands the vacuum conditions of the EM, and enables long-term storage. Traditionally, samples are treated with heavy metal salts prior to resin embedding, in order to increase imaging contrast for EM. This is particularly important for volume EM (vEM) techniques. Yet, commonly used contrasting agents (e.g., osmium tetroxide, uranyl acetate) tend to impair fluorescence. The discovery that fluorescence can be preserved in resin-embedded specimens after mild heavy metal staining was a game changer for CLEM. These so-called in-resin fluorescence protocols present a significant leap forward for CLEM approaches towards high precision localization of a fluorescent signal in (volume) EM data. Integrated microscopy approaches, combining LM and EM detection into a single instrument certainly require such an “all in one” sample preparation. Preserving, or adding, dedicated fluorescence prior to resin embedding requires a compromise, which often comes at the expense of EM imaging contrast and membrane visibility. Especially vEM can be strongly hampered by a lack of heavy metal contrasting. This review critically reflects upon the fundamental aspects of resin embedding with regard to 1) specimen fixation and the physics and chemistry underlying the preservation of protein structure with respect to fluorescence and antigenicity, 2) optimization of EM contrast for transmission or scanning EM, and 3) the choice of embedding resin. On this basis, various existing workflows employing in-resin fluorescence are described, highlighting their common features, discussing advantages and disadvantages of the respective approach, and finally concluding with promising future developments for in-resin CLEM.

Keywords: correlative light and electron microscopy (CLEM), in-resin fluorescence, contrasting for electron microscopy, preserving fluorescence, resin embedding, vitrification, freeze-substitution

OPEN ACCESS

Edited by:
Christopher Guerin, Vlaams Instituut voor Biotechnologie, Belgium

Reviewed by:
Carles Bosch, Francis Crick Institute, United Kingdom
Erin M. Tranfield, Gulbenkian Institute of Science (IGC), Portugal

***Correspondence:**
Miriam S. Lucas
miriam.lucas@scopem.ethz.ch

[†]These authors have contributed equally to this work

Specialty section:
This article was submitted to Morphogenesis and Patterning, a section of the journal Frontiers in Cell and Developmental Biology

Received: *31 January 2022*
Accepted: *13 June 2022*
Published: *30 June 2022*

Citation:
Heiligenstein X and Lucas MS (2022) One for All, All for One: A Close Look at In-Resin Fluorescence Protocols for CLEM. Front. Cell Dev. Biol. 10:866472. doi: 10.3389/fcell.2022.866472

1 INTRODUCTION

The term "correlative microscopy" refers to the application of two or more imaging techniques to an identical sample, and at the exact same position, with the aim to combine the benefits of each respective technique. It has become state of the art technology in biomedical research (Su et al., 2010; Caplan et al., 2011; Jahn et al., 2012; Loussert Fonta and Humbel, 2015; Howes et al., 2018). Combining information from different methodologies to get a holistic understanding of the object of investigation is a fundamental concept in research, and was consequently adopted by microscopists soon after the advent of the transmission electron microscope (TEM). As early as 1944, Dubin and Sharp investigated the effect of sample preparation for TEM on the size of *B. megatherium* by means of correlating light microscopy (LM) images of air dried bacteria with TEM micrographs of the very same specimen (Dubin and Sharp, 1944). In doing so, they stumbled across the two major challenges of correlative microscopy: 1) how to prepare a sample such that it is suitable for all projected imaging techniques, and 2) how to relocate a region of interest (ROI) previously chosen with one microscopy method for correlation in the following, usually higher resolving microscope? And while science has since witnessed immense further developments of both, microscopes and sample preparation methods, these two challenges remain. Although the two topics are not fully unrelated, it would go beyond the scope of this review to discuss both, and we will focus on the former aspect of sample preparation.

Light and electron microscopy are routinely used in the field of life sciences. LM is an indispensable tool for biomedical research due to its time-resolving imaging capabilities and its ability to visualize individual proteins by means of immunofluorescence, or genetically encoded tagging (Giepmans et al., 2006). Electron microscopy (EM) perfectly complements LM, inasmuch as it visualizes a structure of interest at the nm-scale, and within its ultrastructural context. Consequently, the majority of correlative microscopy applications are variations of what has become known as "CLEM," i.e., correlative light and electron microscopy. Countless variations of the concept are possible, allowing researchers to tailor a solution for basically every question to be addressed by means of microscopy, be it on the cellular level (Brown et al., 2009; Buser, 2010), for smaller organisms (Kolotuev et al., 2012; Goetz et al., 2015), tissue specimens (Wilke et al., 2008; Höhn et al., 2015), plants (Jahn et al., 2012; Bell et al., 2013) and animals (Karreman et al., 2014), at room temperature or cryogenic temperatures (Verkade, 2008; Yahav et al., 2011), for two-dimensional (Polishchuk et al., 2000; Giepmans et al., 2005; Keene et al., 2008) or three-dimensional (3D) imaging (Lucas et al., 2012; Wacker et al., 2015; Fermie et al., 2018). Indeed, there are so many possibilities, reflected by an ever increasing number of publications in the past decade, that recently an entire book chapter was dedicated to proposing guidelines to help researchers choose a suitable approach to CLEM (Scher and Avinoam, 2021).

EM requires high vacuum conditions to allow the electrons to travel from the source to a target detector, en route interacting with the sample. This imaging environment triggers a couple of pre-requisites for imaging hydrated biological material, in order to avoid sublimation of water and thus damage the specimen. To observe the material in close to physiological conditions, water (free, and partially also bound) must either be solidified, i.e., vitrified and imaged under cryogenic conditions, or removed. Specimen integrity has to be preserved under controlled conditions, e.g., by critical point drying (Bray, 2000), or ultimately by replacing vitrified water with a vacuum resistant substitute, i.e., embedding in resin. For the latter case several aspects are to be considered:

- Water represents a major constituent of biological material (Levitt and Gaudino, 1950; Reinoso et al., 1997; Ling, 2004). Its removal must be carried out carefully to avoid deformations or collapse of hydrated structures (**Figure 1A**). To turn the biological material into a vacuum resistant object, water is commonly substituted by a solvent, which in turn is substituted by a liquid resin, which is finally polymerized to form a solid sample.
- To maintain the ultrastructure during water substitution, the specimen needs to be stabilized, either by chemical fixation to create bonds between proteins, carbohydrates and lipids, or by maintaining the specimen in a frozen state after physical fixation, i.e., vitrification, such that the biological material is stabilized until its solidification by the resin.
- Finally, biological structures are mainly composed of molecules containing light elements, such as carbon (C, 12 g/mol), hydrogen (H, 1 g/mol), oxygen (O, 16 g/mol), and nitrogen (N, 14 g/mol), which renders them largely electron transparent. What is more, embedding resins consist of hydrocarbons, i.e., the identical light elements (C, H, O), and it is therefore hard to differentiate between biological material and surrounding embedding resin. To compensate for this lack of contrast, decoration with heavier atoms is commonly applied, e.g., using uranyl acetate or osmium tetroxide, to locally stop or deviate electrons from their trajectory and thus improve the resulting EM image.

This review summarizes the main strategies deployed over EM history for imaging biological material at room temperature. Cryogenic EM represents an independent research area and as such is not topic of this review. Consequently, we will focus here on the basic principles of sample fixation, contrast enhancement and resin embedding, particularly with regard to multimodal imaging strategies such as CLEM.

2 SAMPLE IMMOBILIZATION, DEHYDRATION AND EMBEDDING: A PRE-REQUISITE FOR ELECTRON MICROSCOPY WITH CONSEQUENCES

The first step toward rendering a specimen suitable for EM is immobilization, either chemically, or physically. This is followed by dehydration. After chemical fixation, dehydration can be

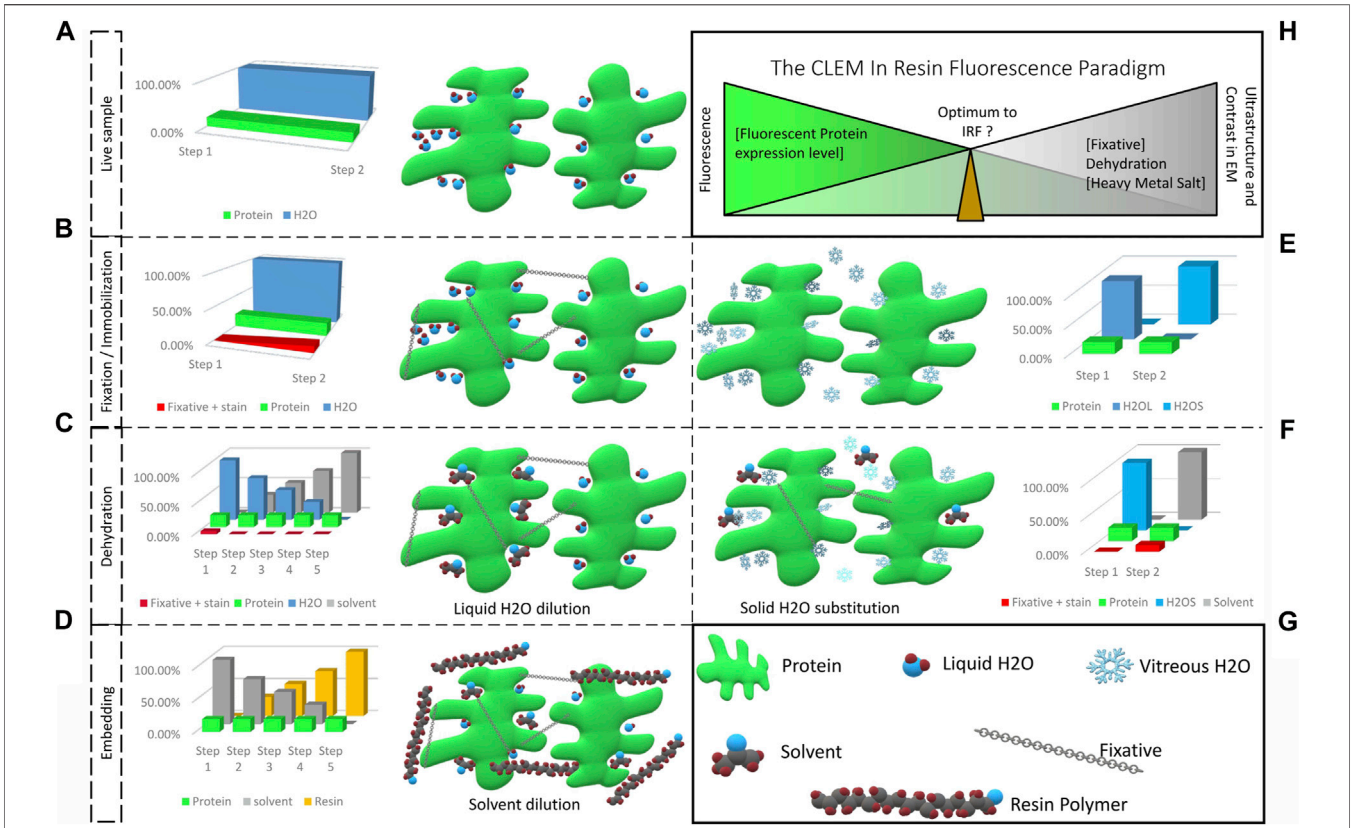

FIGURE 1 | From a living fluorescent biological sample to an embedded specimen for light and electron microscopy, pitfalls and trade-offs. **(A)** Living matter is essentially composed of water and proteins, lipids and carbohydrates. Protein functions are related to their structural shape, supported by several scaffolding proteins. **(B)** During chemical fixation the sample is immobilized by cross-linking. The fixative, mostly aldehyde compounds, creates bonds between proteins, lipids and carbohydrates. Diffusion and fixation efficiency is affected by the sample's density and the pH of local sub-compartments. **(C)** In the following dehydration in increasing concentrations of solvent, unbound fixative is progressively eluted together with the water bound in the sample. **(D)** The solvent is then progressively replaced by resin and polymerization is initiated (by heat or UV polymerization). Depending on the type of resin, chemical bonds can be formed between sample and resin, which provide complementary fixation. **(E)** Physical fixation, on the other hand, instantaneously and homogeneously immobilizes the entire sample, going from a hydrated living state (H_2OL) to a cryo-immobilized state (H_2OS) in a matter of milliseconds. Ice crystal growth resulting in damage of the ultrastructure is prevented and the water molecules remain in place. **(F)** The vitrified specimen is dehydrated in solvent at –90°C. The solvent substitutes the solid water, molecule by molecule. If chemical fixatives are added, these are simultaneously diffused into the specimen. These fixatives become active only above –60°C. **(G)** Graphical legend. **(H)** The CLEM in-resin fluorescence paradigm. Moving from the living, fluorescent sample to the ideal fixed electron microscopy material inevitably causes fluorescent protein quenching. The ideal IRF protocol is a compromise between acceptable fluorescence loss to identify the protein of interest after resin embedding, and adequate ultrastructure preservation and imaging contrast to achieve exploitable EM images.

performed either at room temperature, or while progressively lowering the temperature (Carlemalm et al., 1985; Robertson et al., 1992), depending on the embedding resin to be used. Physical fixation is followed by dehydration at temperatures below the melting point of water in order to prevent recrystallization of vitrified water, so-called freeze-substitution (FS). Contrast enhancement, as well as staining or labelling steps can be included at virtually every step of the process, as discussed later.

Infiltration with aldehyde compounds is the most commonly used standard for chemical fixation (Hayat, 1981). Aldehydes react with proteins, and to a certain extent, also with lipids, to create carbonyl bonds, which cross-link and thus preserve cellular ultrastructure (**Figure 1B**). Several factors influence the cross-linking reaction and with that the quality of the resulting fixation: temperature, pH, type and concentration of the applied aldehyde compound, optimal agitation and duration. The fixative locally affects the pH of the specimen (and is influenced by local pH, too), disturbing the ionic balance and affecting osmolality (Murk et al., 2003). Fixation at lower temperature generally reduces formation of artefacts, such as extraction of cellular components, granularity of the cytosol, or volume changes (Collins et al., 1977; Murk et al., 2003). However, infiltration speed and quality can be negatively affected at low temperature, e.g., for dense samples, while perfusion at room temperature is faster than in the cold (Hayat, 1981). Agitation additionally improves perfusion. Glutaraldehyde proved the most efficient and reliable, and most widely applicable aldehyde compound for fixation of biological specimens. It preserves ultrastructure best and causes the least conformational protein changes. Formaldehyde penetrates specimen faster than glutaraldehyde, but its reactions with proteins are reversible and it can be removed by washing

with water (Hayat, 1981; Newman and Hobot, 1993). Therefore, combinations of both aldehyde types are widely used to combine the positive effects of speed and cross-linking quality (Karnovsky, 1965). Glutaraldehyde is commonly used at a concentration of 0.5%–2%, and formaldehyde at 0.5%–4%. Higher concentrations may cause severe shrinkage (Hayat, 1981). These aspects have to be carefully balanced and adapted to the respective specimen type.

With regard to preservation of antigenicity or fluorescence, formaldehyde is to be preferred over glutaraldehyde. Formaldehyde fixation preserves antigenicity and fluorescence when applied in concentrations up to 5% (Betzig et al., 2006; van Rijnsoever et al., 2008; Brown and Verkade, 2010; Hodgson et al., 2014). Glutaraldehyde on the other hand causes auto-fluorescence (excitation 540 nm, emission 560 nm). However, this can be quenched by sodium borohydride without quenching the target fluorescence of a fluorescent protein (Tagliaferro et al., 1997; Clancy and Cauller, 1998). The auto-fluorescence of aldehyde-based fixatives can even be favourably employed, as sole source of fluorescence in biopsies to navigate and choose a ROI at the LM level prior to targeted EM (Prior et al., 1999).

Following fixation, the sample is dehydrated by progressively diluting the contained water into a solvent (most commonly used: ethanol or acetone) of increasing concentration (from 25% to 100%; **Figure 1C**). Primarily, free water in the sample is diluted, and the water serving as a scaffolding for proteins, is progressively replaced by solvent molecules. As solvent and water molecules differ in size and properties, the proteins suffer some conformational changes that alter in part their properties (Buser and Walther, 2008). However, the initial fixation with aldehydes compensates partly for this deformation. Following the dehydration step, the solvent is then gradually replaced by resin, which is finally polymerized (**Figure 1D**). A similar suboptimal maintenance of the protein shape and properties as during dehydration can be assumed at this step. This can again be compensated for by the fixatives.

For physical fixation, the temperature of the sample is rapidly (>2 K/ms) lowered below the crystallization point of water (−135˚C). This cryo-immobilizes the sample, and transfers the contained water into a glassy state, the so-called vitreous water (**Figure 1E**) (Moor, 1973; Riehle and Hoechli, 1973; Dubochet et al., 1987). In this state, water density and organization is most similar to its organization in liquid form, and therefore the sample is (to date) considered to be preserved closest to its native form. Maintaining the water in its solid form below the recrystallization point for water, prevents water sublimation and is the entry point to all cryo-EM workflows. For resin embedding, the vitrified sample is then subjected to FS. Comparable to room temperature dehydration, the sample is dehydrated in a solvent, but at temperatures below, or close to −90˚C. At this temperature, the water molecules undergo conformational changes: from amorphous below −135˚C, to crystalline cubic, until crystalline hexagonal form near −90˚C. Frozen water remains solid until it is substituted, locally, by the solvent (Hippe-Sanwald, 1993). The dehydration process therefore does not cause extreme movements of water, which could impact the ultrastructure. As proteins and nucleic acids are insoluble in organic solvents, replacing water by solvents will result in aggregation of biological macromolecules. This aggregation cannot be avoided, but it can be limited in size, accounting for the superior ultrastructural preservation of FS compared to chemical fixation. This enables reliable volumetric analyses or measurements. Removing the hydration shell of proteins does not cause shrinkage, but potentially causes conformational changes. However, this effect can be limited at lower temperatures (Kellenberger, 1987). Replacement of the solvent and resin infiltration can finally be done at temperatures suitable for the resin of choice (**Figure 1D**).

Especially with regard to preserving fluorescence of genetically encoded labels, protein collapse or denaturation has to be strictly avoided (as discussed in detail in chapter 5). Prolonged exposure to acetone during dehydration was identified as potential reason for fluorescence loss, which was addressed successfully with significantly shortened FS-protocols (McDonald and Webb, 2011; Peddie et al., 2014). Acetone is often preferred over ethanol as dehydration medium during FS. It is described to be less extracting on the cytoplasm and a mild fixative (Weibull and Christiansson, 1986). However, it can impede polymerization of acrylic resins. For optimal results, a transition from acetone to ethanol prior to resin infiltration during FS is recommended (Monaghan et al., 1998; Watanabe et al., 2011). To further optimize ultrastructure preservation, fixatives can be added to the solvents in low concentrations. As aldehydes are estimated to become active only above −60˚C (Wild et al., 2001; Buser and Walther, 2008), they can be considered inactive and insensitive to pH at the start of the substitution process (**Figure 1F**; **Figure 1G**). They are homogeneously distributed in the sample together with the solvent. Activation by slowly raising the temperature in the course of the FS enables the use of much lower concentrations of fixatives. Thus, artefacts associated with chemical fixatives, such as extensive aggregation of bio-macromolecules, or shrinkage can be minimized.

3 CHOICE OF THE RESIN TO PRESERVE FLUORESCENCE

In addition to the aforementioned impact of fixation and dehydration on the specimen, the nature of the resin is also of importance for preserving fluorescence. Embedding in epoxy resins, such as Epon, Durcupan or Spurrs, offers optimal structural preservation (Luft, 1961; McDonald, 2007). But these resins are cured at high temperatures, i.e., above 50˚C, which potentially causes protein denaturation (Lepock, 1997). Moreover, they form chemical bonds with nucleophiles present in proteins, which also results in denaturation of proteins. This reduces antigenicity or, in the case of fluorescent proteins, the ability to fluoresce (Causton, 1985; Matsko and Mueller, 2005). On the other hand, it improves the homogeneity of the sample by forming interpenetrating polymer networks, linking tissue and resin. This accounts for the excellent cutting property of these resins (Luft, 1961; Newman and Hobot, 1993). What is more, epoxy resins exhibit an auto-fluorescence, predominant in the "green" range of light (approx. 500–550 nm), which coincides

with the maximum emission wavelength of commonly used fluorophores, such as green fluorescent protein (GFP) (Zhou et al., 2017; Fu et al., 2020).

Acrylic resins, e.g., HM20, K4M, GMA, LR White, or R221, on the other hand, mostly react with themselves and form bonds with proteins at sulphydryl and thioether sites only (Carlemalm et al., 1985; Causton, 1985; Kellenberger et al., 1987). Biomolecules are not incorporated into the polymer, and therefore, acrylic resins form weaker links to the sample material (Keene et al., 2008). The strength of these links, as well as hardness and brittleness of the resin depend on the length of the composing monomer chains (short with HM20 and K4M, longer with R221), and the amount of applied crosslinker. As bonds are formed only at the ends of each monomer chain, longer monomer chains will result in a lower crosslink density (Carlemalm et al., 1982). What is more, these resins have a better tolerance of residual water in the embedded material. If a specimen is not fully dehydrated, the remaining water content maintains the scaffolding for proteins, and thus preserves their conformation (Walther and Ziegler, 2002; Buser and Walther, 2008). In order to further enhance the stability of the biological material during the embedding procedure, most acrylic resins are designed for application at low temperature, i.e., below approximately −20°C (Carlemalm et al., 1982). An important aspect to be considered with respect to the preservation of fluorescence or antigenicity is the pH of the resin. Several acrylic resins are too acidic when used in the standard formulation, and hence can cause substantial loss of fluorescence (Watanabe et al., 2011; Zhou et al., 2017). Nevertheless, proteins can be sustained in, or close to the natural, hydrated state, which prevents conformational changes. They are therefore more accessible for antigen detection (Berryman and Rodewald, 1990; Hayat, 2002). Additionally, the electron mobility in (fluorescent) proteins is maintained, so that excitation and fluorescence emission remain possible (Nixon et al., 2009). This makes acrylic resins the better choice for fluorescence preservation.

4 CONTRAST ENHANCEMENT: A NECESSARY EVIL?

The last important step for EM on resin-embedded materials is to enhance the contrast of the structures of interest. Organic materials consist mainly of low atomic number elements (such as carbon, hydrogen, oxygen), and consequently such specimens do not generate much electron scattering contrast in the EM. What is more, embedding resins are composed of similar elements with low electron density. And although it is desirable for the embedding resins to produce little or no background contrast, this underlines the necessity of contrast enhancement, to visualize the biological specimen and distinguish it from the resin. This is generally achieved by staining with heavy metal compounds, with more or less specific affinity for proteins or lipids. Contrast enhancement steps can be carried out during, or after, fixation and (or) during dehydration. It is interesting to observe that the literature was very rich between the 1950s and 1980s with efforts to highlight specific cellular compartments according to their chemistry. Various heavy metal compounds were investigated, with varying success. Hayat (1993) provides an excellent collection of these findings. Of these tested staining agents, only a few prevail and are used to date, the most common being uranyl acetate and osmium tetroxide. At that time, EM images were recorded on negative film and the target structures were identified on the fluorescent screen of the EM. Since the advent of more sensitive digital cameras, image recording has become fast and straightforward in operation. Corrections can be made live on the computer screen in order to optimize focus and contrast. This, among other things, allowed researchers to reduce the efforts put into optimizing staining procedures and consequently, the vast majority have returned to standard protocols based on uranyl acetate and osmium tetroxide. However, osmium tetroxide is well-known to impair fluorescence (Watanabe et al., 2011), this effect being predominant with fluorophores emitting in the "green" range of light (approx. 500–550 nm). Fluorophores emitting in the "red- to far-red" range (approx. 630–750 nm) are less susceptible, or even resistant to this impairment (Lucas et al., 2012; Lucas M. S. et al., 2017; Fu et al., 2020). Uranyl acetate was demonstrated to have a weak fluorescence, which can still be detected in resin-embedded samples (Biel et al., 2003; Tuijtel et al., 2017). And, although this effect can be neglected in the presence of strong fluorescent labels, it still impairs the signal-to-noise ratio and limits the detection of weak fluorescent signals.

In recent years, use of uranyl acetate is subject to tighter legislation, which triggered a new search for alternatives (Inaga et al., 2007; Yamaguchi et al., 2010; Nakakoshi et al., 2011; Hosogi et al., 2015; Kuipers and Giepmans, 2020). However, as most of these staining compounds are insoluble in organic solvents, their application is reduced to room temperature embedding procedures and poststaining of resin sections. An alternative for FS applications remains to be discovered, and uranyl acetate remains the gold standard.

A noteworthy aspect of any contrasting procedure is the fact that the employed heavy metal compounds simultaneously act as fixatives (Sabatini et al., 1963; Ginsburg and Wolosin, 1979; Erickson et al., 1987; Hayat, 1993). This reinforces the primary fixation, but concomitantly reduces a proteins' ability to fluoresce (Berryman and Rodewald, 1990; Nixon et al., 2009). Hence, consensus has grown around the need to minimize fixatives as well as contrasting agents in order to preserve fluorescence after resin embedding (Biel et al., 2003; Nixon et al., 2009; Kukulski et al., 2011; Lucas et al., 2012; Peddie et al., 2014; Delevoye et al., 2016; Baatsen et al., 2021). For TEM applications, sensitive detection systems (EMCCD, CMOS and direct electron detectors) enable minimal use of uranyl acetate, at concentrations below 1% in FS protocols, yielding impressive image quality (Hawes et al., 2007). Unfortunately, improved detection sensitivity is not the most critical parameter for volume EM (vEM) approaches, such as serial blockface SEM, focused ion beam-SEM (FIB-SEM), or array tomography. Upon scanning the surface of a sample, electron charging builds up rapidly, compromising iterative imaging approaches. To

compensate for the charging, the conductivity of *en bloc* samples can be increased by enhanced heavy metal staining (Deerinck et al., 2010). While this has the additional advantage of increasing the contrast in the EM, it entails the complete loss of fluorescence. The recent development of a focal charge compensation (Deerinck et al., 2018), significantly reduces the need for such highly (over- ?) stained samples. Reducing the heavy metal salt loading again offers the possibility to preserve the fluorescence.

5 ONE SAMPLE FOR ALL IMAGING MODES OR THE IDEAL CLEM SAMPLE: MYTH OR REALITY?

The basic concept of CLEM to investigate the exact same structure with LM and EM was addressed by countless approaches (**Table 1**). Many of them rely on staggered sample preparation protocols, i.e., performing LM and EM separately, one after the other, in order to maintain optimum conditions for both LM and EM (Mironov et al., 2000; Sims et al., 2006; van Rijnsoever et al., 2008; Knott et al., 2009; Lucas M. S. et al., 2017). However, the ideal sample for CLEM would be suitable for all imaging modes at once, i.e., the preparation should balance preservation of fluorescence labels and heavy metal staining, while avoiding structural changes to the specimen **Figure 1H**. The emergence of integrated light and electron microscopes (Timmermans and Otto, 2015) even made this a requirement.

So-called "in-resin fluorescence" (IRF) protocols, were developed to meet this requirement. However, as pointed out above, preserving fluorescence even after resin embedding is a complex endeavour. Virtually every single one of the four challenges, namely fixation, dehydration, contrasting and resin embedding may impair the capacity of fluorescent proteins or other labels to be excited and emit fluorescence. What the majority of IRF protocols have in common: they base 1) on cryo-fixation, e.g., HPF, 2) low-temperature, and in particular incomplete dehydration, in order to preserve the hydration shell of the proteins, and 3) a minimal use of contrasting agents for EM, with osmium tetroxide even completely omitted in most cases. This is followed by 4) embedding in acrylic resins which have a low interaction with the sample.

5.1 Non-Specific Labelling for a Morphological Ultrastructure Identification

One of the first approaches to allow LM and EM on an identical sample was designed by Biel et al. (2003). They employed the auto-fluorescence of uranyl acetate in resin-embedded tissue for *en bloc* imaging using confocal laser scanning microscopy (CLSM). A recent work further demonstrated the benefit of uranyl acetate auto-fluorescence, which was observed to increase significantly at low temperatures, i.e., below −100°C. This auto-fluorescence detected in resin sections could be matched precisely with the contrast obtained by TEM, facilitating a "on-section" image registration (Tuijtel et al., 2017). Biel at al. (2003) also included fluorescent dyes in the staining and dehydration cocktail during FS. In this way, high-pressure frozen samples could be fluorescently stained and contrasted with uranyl acetate prior to resin embedding. The resulting specimens were equally suitable for LM and EM, and combined the excellent structural preservation provided by high-pressure freezing (HPF) with staining for *en bloc* CLSM. Despite the labelling not being specific, this technique allowed a detailed overview of complex tissue samples using LM. The LM map was then used to select a ROI within the resin-embedded specimen to facilitate targeted ultramicrotomy for TEM. This approach paved the way for what is today referred to as "in-resin fluorescence protocols." Later, we advanced this protocol for FIB-SEM imaging (**Figure 2B**), using the fluorescent labelling as guidance to identify the ROI for targeted FIB-milling (Lucas et al., 2012). While Biel et al. (2003) had omitted any heavy metal salts except for uranyl acetate, we again included osmium tetroxide during FS, in order to enhance imaging quality and contrast in FIB-SEM. Despite its well-known interference with fluorescence, we found only minimal changes in fluorescence signal distribution and intensity of the tested dyes, when removing the osmium from the FS-cocktail at −50°C. Still, the osmium staining did improve the visibility of cellular membranes at the EM level as compared to using only uranyl acetate. Even though this approach identifies a ROI based on the morphology of fluorescent features rather than by specific labelling, it is easy to implement and can be applied to nearly any specimen.

Besides their simplicity, a main benefit of these approaches is the maintenance of specimen integrity. Potential damage to the ultrastructure, e.g., due to permeabilisation to introduce stains, are completely avoided, because all labels or stains are applied only after HPF. The observation of the entire sample allows the identification of a ROI prior to targeted ultramicrotomy, or FIB-SEM milling and imaging. Karreman et al. developed a similar strategy of global 3D mapping of the readily embedded sample, by using soft-X-ray imaging to relocate a ROI previously identified in a living animal. However, this approach did not allow the preservation of in-resin fluorescence (Karreman et al., 2016; Karreman et al., 2017).

5.2 Genetically Encoded Labels

Efficient identification of a structure of interest is essential for CLEM. Specific labelling and precise relocation of the labelled structure across different imaging modalities therefore becomes the pivot point. As discussed above, labelling may be altered during sample preparation for EM. In its early stages of discovery, GFP demonstrated a good tolerance to fixatives such as formaldehyde and glutaraldehyde (Chalfie et al., 1994; Ward, 2006), although the latter fixative can cause imaging difficulties due to its high auto-fluorescence. GFP was reported to denature when dehydrated in pure, dried organic solvents (Ward, 2006). As a result, its fluorescence is quenched, with the extent of the quenching depending on the grade of dehydration. Luby-Phelps et al. (2003) showed on aldehyde-fixed GFP-tagged photoreceptors in the retina of zebrafish embryo that retaining a specific fluorescence label is possible after incomplete dehydration in organic solvents, and resin embedding. They completely omitted heavy metal stains commonly used for EM, and embedded the samples in LR White. Using one-µm

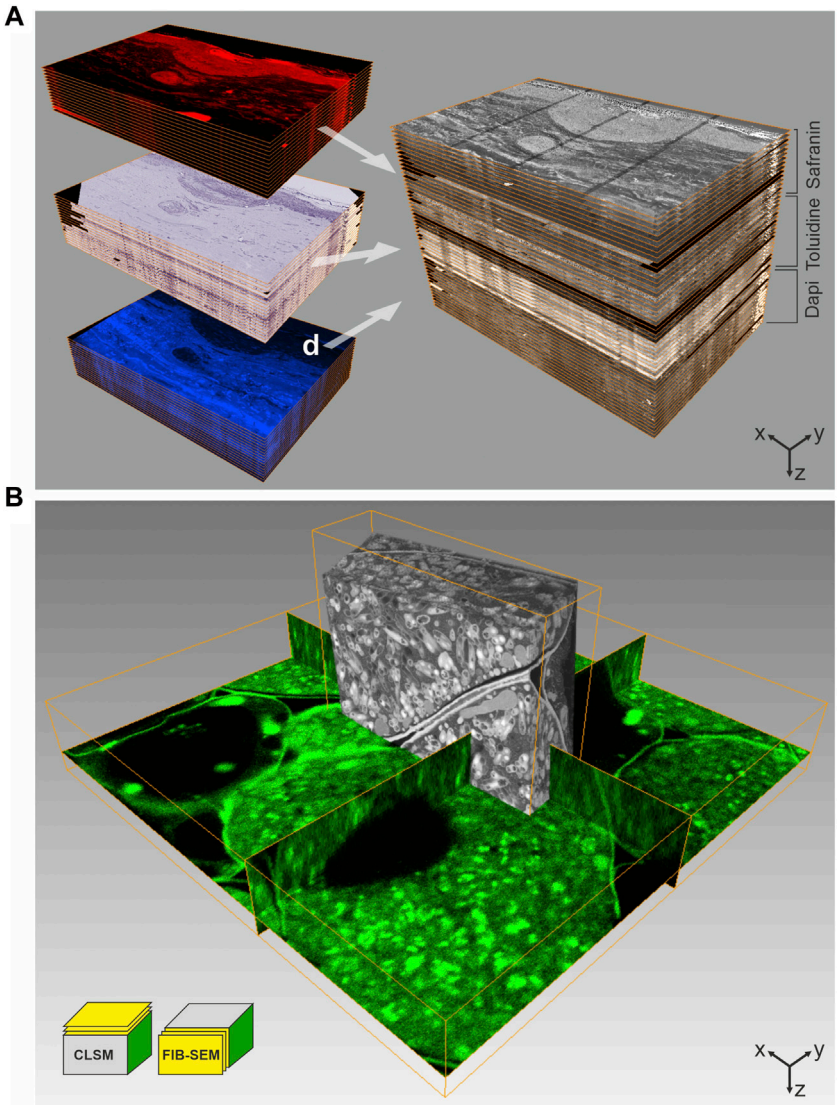

FIGURE 2 | CLEM using IRF samples. **(A)** Array tomography. 100 nm thick serial sections of a human skin biopsy, high-pressure frozen, freeze-substituted with uranyl acetate, osmium tetroxide and Safranin O, and embedded in HM20 were mounted on ITO-coated glass coverslips. This approach allows multiple on-section labeling to complement IRF. The top subset was imaged by fluorescence LM without further staining, using the Safranin O signal introduced during FS, the middle subset shows on-section staining with Toluidine, and the subset of sections was stained with Dapi. Following LM, all sections were imaged by SEM at 2 kV using in-lens SE detection. Combination of all images yields a volume that comprises multiple levels of information, ideal for in-depth characterization of complex biological structures. Volume size (x-y-z): LM stack: 321.0 × 221.5 × 5.1 µm³, SEM stack: 226.4 × 170.0 × 5.1 µm³. **(B)** 3D CLEM of root nodule from mung bean (*Vigna radiata*), colonized with nitrogen-fixing bacteria (*B. japonicum*). 200 µm thick sections were high-pressure frozen after degassing in 1-hexadecene, followed by FS and embedding in HM20. The FS-medium contained uranyl acetate, osmium tetroxide and Acridine orange for fluorescent labeling of the bacteria. En bloc CLSM was performed to identify a ROI, which was subsequently targeted by FIB-SEM. The CLSM and FIB-SEM volumes were merged using the Amira software package. The imaging plane of FIB-SEM is perpendicular to that of CLSM. Volume size (x-y-z): CLSM 57.2 × 57.2 × 9.0 µm³, FIB-SEM 21.8 × 6.2 × 15.9 µm³. Figure adapted from Lucas et al. (2012) with permission of Elsevier Ltd.

thick sections, they could for the first time demonstrate fluorescence detection from within the resin-embedded material. This first proof that GFP fluorescence can indeed survive EM sample preparation at room temperature was a major breakthrough and the protocol was later successfully adapted to maize tissue (Rizzo et al., 2016).

Independently, Walther and Ziegler demonstrated that FS of vitrified specimens in solvents containing up to 20% water resulted in improved ultrastructural preservation, and especially enhanced the visibility of biological membranes (Walther and Ziegler, 2002). FS in strictly dried solvents, on the other hand, resulted in significantly reduced contrast and definition of membranes. Putting two and two together, Nixon et al. (2009) made use of this incomplete dehydration to combine the excellent ultrastructural preservation of HPF/FS with preservation of GFP fluorescence in HM20 embedded zebrafish embryo samples. This major discovery of

the ability to preserve genetically encoded fluorescence after HPF and FS, including EM staining, opened a new era in correlative microscopy. IRF was used with high accuracy and relatively high throughput to localize endocytosis in yeast (Kukulski et al., 2011). Since then, the technique has been applied to a wide range of biological questions. IRF is a highly versatile tool, and can be combined with the follow-up EM method of choice. A staggered approach employed consecutive sections, starting with relatively thick sections (i.e., 300 nm) for LM in order to improve detection of IRF and target the structure of interest for TEM, which was then performed on 50–70 nm thin sections (Delevoye et al., 2016). Bypassing the consecutive sectioning approach and directly analysing the thicker sections by electron tomography, moved IRF applications into the third dimension (Kukulski et al., 2012; Bissig et al., 2017). The combination with live cell imaging prior to HPF makes IRF an even more versatile and powerful tool, enabling even the study of dynamic processes (Heiligenstein et al., 2014; Ripoll et al., 2018).

IRF was also employed in CLEM approaches based on vEM, to make use of the larger field of view and stable, automated acquisition methods for volume data (Peddie and Collinson, 2014; Titze and Genoud, 2016). The fluorescence signal can e.g., be used to screen serial sections, so-called arrays, and identify a ROI for high-resolution SEM, a technique dubbed "array tomography" (Micheva and Smith, 2007; Wacker and Schroeder, 2013). To reduce charging artefacts during SEM imaging, the arrays are mounted onto conductive supports such as silicone wafer, or indium tin oxide (ITO)-coated glass. The latter being transparent, makes it advantageous for LM (Lucas et al., 2012). These arrays can be stored and re-investigated, as well as further stained or contrasted, making array tomography highly suited to localize rare cellular structures or events in complex tissue samples (Micheva et al., 2010; Oberti et al., 2010; Burel et al., 2018; Lane et al., 2022). Analogous to approaches described in the previous subchapter, Höhn et al. (2015) detected mCherry-labeled virus particles by *en bloc* CLSM, prior to acquisition of volume data by FIB-SEM. The development of the "ultraLM" and "miniLM" allows fluorescence detection from within a resin block to be directly combined with ultramicrotomy applications (Brama et al., 2016). The "ultraLM" is directly mounted onto a standard ultramicrotome to locate and follow fluorescent target structures while trimming. The "miniLM," an add-on to a serial-blockface SEM, presents an integrated solution for consecutive detection of fluorescence signal and recording of blockface scans for vEM data in a single instrument. Another highly sensitive microtome-integrated microscope solution monitors the fluorescence in sections floating in the diamond knife boat directly after cutting. Here, hydration of the sections additionally promotes the fluorescence, which is used to identify sections of interest for further analysis (Lemercier et al., 2017).

5.3 Non-Genetically Encoded Specific Labels

For historical reasons, GFP, RFP and mCherry are the most commonly used fluorescent proteins, although they often show a low quantum yield and a low brightness (Wall et al., 2015; Prangsma et al., 2020). Fluorescent dyes, such as i.e., Alexa dyes on the other hand are very bright, and tolerate fixation, dehydration and resin embedding very well. Associating them to a specific and physiological label yields a reliable tool for CLEM. Delevoye et al. (2016) for instance, added a transferrin protein coupled to an Alexa-dye to the culture medium of HeLa cells prior to HPF and subsequent processing. The internalized transferrin labelled the endocytic pathway homogeneously and produced a very bright fluorescence signal in resin sections. This served as a guide to identify the most promising phenotype, and locate the fainter fluorescent signal obtained from a genetically encoded mutant. As another example, phalloidin coupled to Alexa dyes can be included in the FS cocktail for pre-embedding specific labelling of actin (Lucas et al., 2012).

It is noteworthy, that besides using genetically encoded tags, additional on-section staining with other specific labels can be performed to complement IRF and aid navigation between LM and EM (**Figure 2A**). Nucleic stains such as DAPI or Hoechst can be easily applied on sections, both on SEM and TEM sample supports. These specific, intercalating dyes can still interact with chromatin in resin-embedded samples, and yield a bright and stable fluorescent signal (Lucas et al., 2012; Delevoye et al., 2016; Lane et al., 2022).

5.4 Optical Super-Resolution Comes Into Play

With super-resolution LM becoming widely available, efforts were also made towards super-resolution CLEM to close the resolution gap between fluorescence LM and EM. Super-resolution LM can be well implemented on resin sections mounted on ITO coated glass slides as used for array tomography. However, this requires specialized labels, which remain photoactivatable even after resin embedding, and if possible also tolerate EM contrasting agents (Kopek et al., 2017). First approaches were made based on chemical fixation. Betzig et al. (2006) correlated photoactivated localization microscopy (PALM) and TEM using chemically fixed cryo-sections. Stimulated emission depletion (STED) microscopy and PALM on resin-embedded samples was then demonstrated by Watanabe et al. (2011), using the fluorescent proteins citrine and tdEos. Paez-Segala et al. (2015) reported the photoconvertible Eos fluorescent protein to fluoresce and photoconvert normally in samples treated with osmium tetroxide, and embedded in acrylic resin. Another variant of the "Eos protein family," mEosEM, even tolerates embedding in epoxy resin (Fu et al., 2020). In-resin super-resolution microscopy for standard fluorescent proteins such as mGFP, mVenus and mRuby2 after cryo-fixation and FS, was established by Johnson at al. (2015). They showed that single molecule photo-switching can be detected from HM20-embedded specimens containing fluorescent proteins when mounting TEM sections in a glycerol-based mounting medium. With this single molecule localization microscopy approach they achieved a structural resolution of approx. 50 nm in fluorescence microscopy. That some fluorescent

TABLE 1 | Fluorescent labels for IRF.

Label name	Demonstrated for	Highlighting	Application		References
			In the freeze-substitution	On-section labeling	
Non-specific labels					
1.8 ANS	Mammalian tissue	Collagen and/or elastic fibers	✓		Biel et al. (2003)
Acridine orange	Mammalian tissue	Nuclei, cytoplasm	✓		Biel et al. (2003)
	Cultured cells, bacteria	Cytoplasm, nuclei	✓		Lucas et al. (2012)
Bodipy 560	Mammalian tissue	Nuclei, cell membranes	✓		Biel et al. (2003)
DCVJ	Mammalian tissue	Nuclei, collagen and/or elastic fibers	✓		Biel et al. (2003)
DiD	Mammalian tissue	Lipophilic domains, cell membranes	✓		Biel et al. (2003)
	Cultured cells	Lipophilic domains, cell membranes	✓		Lucas et al. (2012)
$DiIC_{18}$	Mammalian tissue	Lipophilic domains, cell membranes	✓		Biel et al. (2003)
	Cultured cells	Cell membranes	✓		Lucas et al. (2012)
$DiOC_6$	Mammalian tissue	Cytoplasm (lipophilic domains)	✓		Biel et al. (2003)
Nile blue sulfate	Mammalian tissue	Nuclei, cytoplasm, collagen, elastic fibers	✓		Biel et al. (2003)
	Model organisms, e.g., *C. elegans*	Cytoplasm, cell membranes	✓		Lucas et al. (2012)
	Cultured cells	Nuclei, cytoplasm, cytoskeleton*	✓		Lucas et al. (2012)
Nile red	Cultured cells	Nuclei, cytoplasm	✓		Lucas et al. (2012)
Oregon Green	Mammalian tissue	Nuclei, collagen, elastic fibers	✓		Biel et al. (2003)
Safranin O	Mammalian tissue	Nuclei, cytoplasm, collagen, elastic fibres	✓		Biel et al. (2003)
	Cultured cells	Nuclei, cytoplasm	✓		Lucas et al. (2012)
	Model organisms, e.g., *C. elegans*	Nuclei, cytoplasm, cell membranes	✓		Lucas et al. (2012)
	Plant tissue	Entire tissue, unspecific	✓		Lucas et al. (2012)
Syto 24	Cultured cells	Entire cell, unspecific	✓		Lucas et al. (2012)
Syto 83	Cultured cells	Entire cell, unspecific	✓		Lucas et al. (2012)
Sytox Green	Cultured cells	Entire cell incl. membranes, unspecific	✓		Lucas et al. (2012)
Tannin	Mammalian tissue	Nuclei	✓		Biel et al. (2003)
Uranyl acetate	Any type of biological specimen	Entire tissue or cell	✓	✓ Note the temperature dependency!	(Biel et al., 2003; Tuijtel et al., 2017)
Specific labels					
Dapi	Any type of biological specimen	Nuclei		✓	
Hoechst	Any type of biological specimen	Nuclei		✓	Delevoye et al. (2016)
Phalloidin Alexa 488	Cultured cells and mammalian tissue	Cytoskeleton	✓		Lucas et al. (2012)

Genetically encoded tags	Standard IRF	Super-resolution LM	References
Citrine	✓		Watanabe et al. (2011)
GFP/mGFP	✓	✓	(van Rijnsoever et al., 2008; Nixon et al., 2009; Kukulski et al., 2011; Johnson et al., 2015; Delevoye et al., 2016; Bissig et al., 2017; Peddie et al., 2017; Burel et al., 2018; Ripoll et al., 2018)
mCherry	✓	✓	(Höhn et al., 2015; Ripoll et al., 2018)
mEos-derivatives		✓	(Watanabe et al., 2011; Paez-Segala et al., 2015; Kopek et al., 2017; Fu et al., 2020)
mRuby2		✓	Johnson et al. (2015)
mVenus		✓	Johnson et al. (2015)
YFP	✓		(Heiligenstein et al., 2014; Delevoye et al., 2016)

Table adapted from Lucas et al. (2012) with permission of Elsevier Ltd.

proteins show the blinking behaviour employed for single molecule localization microscopy also in dry mounted resin sections, and even under vacuum conditions was discovered by Peddie et al. (2017). *In vacuo* single molecule localization microscopy allowed them to take advantage of an integrated light and SEM setup to directly acquire both, super-resolution LM and

SEM images on the same resin section. As the sample is not moved between the two imaging modalities, it allows a direct and precise overlay of the LM and EM images, and thus overcomes the problem of relocating a ROI after imaging in separate microscopes.

6 FUTURE PERSPECTIVES

The major disadvantage of minimizing the heavy metal staining in order to preserve fluorescence in resin-embedded specimen is the compromise on EM imaging contrast, i.e., visibility of key features such as membranes. To overcome this, routine poststaining procedures, e.g., involving Reynold's lead citrate and aqueous uranyl acetate, can be applied on sections to improve imaging contrast for TEM, or (serial) section SEM. It seems reasonable to add this step after fluorescence imaging, to avoid artefacts, caused by the auto-fluorescence of uranyl acetate. However, the penetration depth of poststaining agents into resin is limited (Hayat, 1993). Especially the commonly used uranyl acetate produces a detectable concentration gradient in depth already in sections of 300 nm thickness, while lead citrate showed a homogenous distribution throughout the section (Tranfield et al., 2014). This can have adverse effects especially for electron tomography applications. The recent improvements in TEM detector sensitivity may even make poststaining obsolete (Faruqi and McMullan, 2011; Clough et al., 2014; Fermie et al., 2020; Levin, 2021). For integrated microscopy solutions (Agronskaia et al., 2008; Liv et al., 2013; Brama et al., 2016), as well as for *en bloc* vEM applications, however, poststaining is impossible. Especially for vEM, imaging contrast remains a critical factor, as it mostly relies on the detection of backscattered electrons, and therefore requires contrasting by heavy metal compounds. Efforts are ongoing to improve those detection systems, too. Retarding (or deceleration) fields applied between electron objective lens and sample have been shown to improve imaging contrast in SEM and FIB-SEM, and therefore allow the reduction of heavy metal staining (Lane et al., 2021). Lately, Vos et al. (2020) have successfully applied a retarding (or deceleration) field in an integrated fluorescence and SEM setup.

Besides technological improvements, new labelling approaches are being explored. Moving away from fluorescent proteins, or other classical fluorescent labels for LM, several attempts were made to utilize nano-diamonds and nano-crystals as probes for CLEM (Hemelaar et al., 2017; Keevend et al., 2020). These labels retain their fluorescence even after treatment with osmium tetroxide and resin embedding. Besides being fluorescent, and well detectable in the SEM *via* their back-scattered electron signal, they also exhibit cathodoluminescence, which enables a new form of integrated microscopy for simultaneous imaging. To date, these probes are quite large in size (40–70 nm), which limits their application due to artefacts associated with incorporation into cells. The strong fluorescent or cathodoluminescence signals of these probes, as well as those of quantum-dots (Giepmans et al., 2006), have the large advantage that they can be well detected also against the background-fluorescence of epoxy resins. This again opens up possibilities for room temperature embedding approaches.

Alternative EM stains, such as lanthanides, platinum blue or Oolong tea extract have been investigated as potential replacement for uranyl acetate (Sato et al., 2003; Inaga et al., 2007; Hosogi et al., 2015). And although so far none of these substances can fully replace uranyl acetate, some are routinely used for EM sample preparation (Kremer et al., 2015). Lately, a more promising candidate has been proposed: neodymium acetate (Kuipers and Giepmans, 2020). Even though neodymium is still a heavy metal compound and is insoluble in solvents, its full potential remains to be explored, also with respect to CLEM. In general, contrasting agents with low chemical activity are of interest, and uranyl acetate remains to date the best compromise, providing a gentle stabilization of proteins, and good imaging contrast, while exhibiting a low auto-fluorescence at room temperature.

With respect to the dehydration medium, acetone is commonly preferred over ethanol (Humbel and Schwarz, 1989; Monaghan et al., 1998; Wild et al., 2001; Walther and Ziegler, 2002; Biel et al., 2003; Giddings, 2003; Hawes et al., 2007). However, the lower melting point of ethanol (−117°C vs. −95°C for acetone), as well as the higher polarity of the solvent could be worth exploring with regard to the preservation of fluorescence (Walther and Ziegler, 2002; Buser and Walther, 2008).

Another addition to the IRF toolbox is the newly developed embedding resin R221 (Heiligenstein et al., 2021; Jansen et al., 2021). This acrylic based resin was developed to reduce electron charge accumulation at the surface of the resin block. Initial results demonstrate high EM imaging contrast, even with very low concentrations of uranyl acetate staining (0.05% UA, with the addition of 5% H_2O), allowing preservation of bio-fluorescence, while displaying fine contrast at high resolution in EM.

Altogether, the last decade witnessed the emergence of several innovative tools to reduce the gap between LM and EM using resin-embedded samples. Imaging the exact same sample with multiple microscopy techniques bears such great scientific potential that multiple solutions were developed independently. In the coming years, it can be expected that the increasing demand for CLEM will see a combination of all these tools into one single pipeline to achieve high throughput, at high speed, and high accuracy analysis of multiplexed samples.

AUTHOR CONTRIBUTIONS

XH and ML contributed equally to the preparation of the manuscript.

ACKNOWLEDGMENTS

We thank Stephan S.A. Gerstl, Falk Lucas, and Daniel Smith (all ScopeM ETH Zurich) for critical reading of the manuscript and helpful discussions.

REFERENCES

Agronskaia, A. V., Valentijn, J. A., van Driel, L. F., Schneijdenberg, C. T., Humbel, B. M., van Bergen En Henegouwen, P. M., et al. (2008). Integrated Fluorescence and Transmission Electron Microscopy. *J. Struct. Biol.* 164, 183–189. doi:10.1016/j.jsb.2008.07.003

Baatsen, P., Gabarre, S., Vints, K., Wouters, R., Vandael, D., Goodchild, R., et al. (2021). Preservation of Fluorescence Signal and Imaging Optimization for Integrated Light and Electron Microscopy. *Front. Cell Dev. Biol.* 9, 737621. doi:10.3389/fcell.2021.737621

Bell, K., Mitchell, S., Paultre, D., Posch, M., and Oparka, K. (2013). Correlative Imaging of Fluorescent Proteins in Resin-Embedded Plant Material. *Plant Physiol.* 161 (4), 1595–1603. doi:10.1104/pp.112.212365

Berryman, M. A., and Rodewald, R. D. (1990). An Enhanced Method for Post-Embedding Immunocytochemical Staining Which Preserves Cell Membranes. *J. Histochem Cytochem.* 38 (2), 159–170. doi:10.1177/38.2.1688894

Betzig, E., Patterson, G. H., Sougrat, R., Lindwasser, O. W., Olenych, S., Bonifacino, J. S., et al. (2006). Imaging Intracellular Fluorescent Proteins at Nanometer Resolution. *Science* 313 (5793), 1642–1645. doi:10.1126/science.1127344

Biel, S. S., Kawaschinski, K., Wittern, K.-P., Hintze, U., and Wepf, R. (2003). From Tissue to Cellular Ultrastructure: Closing the Gap between Micro- and Nanostructural Imaging. *J. Microsc.* 212 (1), 91–99. doi:10.1046/j.1365-2818.2003.01227.x

Bissig, C., Hurbain, I., Raposo, G., and van Niel, G. (2017). PIKfyve Activity Regulates Reformation of Terminal Storage Lysosomes from Endolysosomes. *Traffic* 18 (11), 747–757. doi:10.1111/tra.12525

Brama, E., Peddie, C. J., Wilkes, G., Gu, Y., Collinson, L. M., and Jones, M. L. (2016). ultraLM and miniLM: Locator Tools for Smart Tracking of Fluorescent Cells in Correlative Light and Electron Microscopy. *Wellcome Open Res.* 1, 26. doi:10.12688/wellcomeopenres.10299.1

Bray, D. (2000). Critical Point Drying of Biological Specimens for Scanning Electron Microscopy. *Methods Biotechnol. Supercrit. Fluid Methods Protoc.* 13, 1716. doi:10.1385/1-59259-030-6:235

Brown, E., Mantell, J., Carter, D., Tilly, G., and Verkade, P. (2009). Studying Intracellular Transport Using High-Pressure Freezing and Correlative Light Electron Microscopy. *Seminars Cell and Dev. Biol.* 20, 910–919. doi:10.1016/j.semcdb.2009.07.006

Brown, E., and Verkade, P. (2010). The Use of Markers for Correlative Light Electron Microscopy. *Protoplasma* 244 (1-4), 91–97. doi:10.1007/s00709-010-0165-1

Burel, A., Lavault, M.-T., Chevalier, C., Gnaegi, H., Prigent, S., Mucciolo, A., et al. (2018). A Targeted 3D EM and Correlative Microscopy Method Using SEM Array Tomography. *Development* 145 (12), dev160879. doi:10.1242/dev.160879

Buser, C. (2010). Toward Sub-second Correlative Light and Electron Microscopy of *Saccharomyces cerevisiae*. *Methods Cell Biol.* 96, 217–234. doi:10.1016/s0091-679x(10)96010-x

Buser, C., and Walther, P. (2008). Freeze-Substitution: The Addition of Water to Polar Solvents Enhances the Retention of Structure and Acts at Temperatures Around -60Å°C. *J. Microsc.* 230 (2), 268–277. doi:10.1111/j.1365-2818.2008.01984.x

Caplan, J., Niethammer, M., Taylor, R. M., Czymmek, K. J., and Czymmek, K. J. (2011). The Power of Correlative Microscopy: Multi-Modal, Multi-Scale, Multi-Dimensional. *Curr. Opin. Struct. Biol.* 21 (5), 686–693. doi:10.1016/j.sbi.2011.06.010

Carlemalm, E., Garavito, R. M., and Villiger, W. (1982). Resin Development for Electron Microscopy and an Analysis of Embedding at Low Temperature*. *J. Microsc.* 126 (2), 123–143. doi:10.1111/j.1365-2818.1982.tb00362.x

Carlemalm, E., Villiger, W., Hobot, J. A., Acetarin, J.-D., and Kellenberger, E. (1985). Low Temperature Embedding with Lowicryl Resins: Two New Formulations and Some Applications. *J. Microsc.* 140 (Pt 1), 55–63. doi:10.1111/j.1365-2818.1985.tb02660.x

Causton, B. E. (1985). Does the Embedding Chemistry Interact with Tissue. *Scanning Electron Microsc.* 4, 209–214. The science of biological specimen preparation for microscopy and microanalysis.

Chalfie, M., Tu, Y., Euskirchen, G., Ward, W. W., and Prasher, D. C. (1994). Green Fluorescent Protein as a Marker for Gene Expression. *Science* 263 (5148), 802–805. doi:10.1126/science.8303295

Clancy, B., and Cauller, L. J. (1998). Reduction of Background Autofluorescence in Brain Sections Following Immersion in Sodium Borohydride. *J. Neurosci. Methods* 83 (2), 97–102. doi:10.1016/s0165-0270(98)00066-1

Clough, R. N., Moldovan, G., and Kirkland, A. I. (2014). Direct Detectors for Electron Microscopy. *J. Phys. Conf. Ser.* 522, 012046. doi:10.1088/1742-6596/522/1/012046

Collins, V. P., Arborgh, B., and Brunk, U. (1977). A Comparison of the Effects of Three Widely Used Glutaraldehyde Fixatives on Cellular Volume and Structure. A TEM, SEM, Volumetric and Cytochemical Study. *Acta Pathol. Microbiol. Scand. A* 85A (2), 157–168. doi:10.1111/j.1699-0463.1977.tb00413.x

Deerinck, T., Bushong, E., Lev-Ram, V., Shu, X., Tsien, R., and Ellisman, M. (2010). Enhancing Serial Block-Face Scanning Electron Microscopy to Enable High Resolution 3-D Nanohistology of Cells and Tissues. *Microsc. Microanal.* 16 (Suppl. 2), 1138–1139. doi:10.1017/S1431927610055170

Deerinck, T. J., Shone, T. M., Bushong, E. A., Ramachandra, R., Peltier, S. T., and Ellisman, M. H. (2018). High-performance Serial Block-Face SEM of Nonconductive Biological Samples Enabled by Focal Gas Injection-Based Charge Compensation. *J. Microsc.* 270 (2), 142–149. doi:10.1111/jmi.12667

Delevoye, C., Heiligenstein, X., Ripoll, L., Gilles-Marsens, F., Dennis, M. K., Linares, R. A., et al. (2016). BLOC-1 Brings Together the Actin and Microtubule Cytoskeletons to Generate Recycling Endosomes. *Curr. Biol.* 26 (1), 1–13. doi:10.1016/j.cub.2015.11.020

Dubin, I. N., and Sharp, D. G. (1944). Comparison of the Morphology of Bacillus Megatherium with Light and Electron Microscopy. *J. Bacteriol.* 48 (3), 313–329. doi:10.1128/jb.48.3.313-329.1944

Dubochet, J., Adrian, M., Chang, J.-J., Lepault, J., and McDowall, A. W. (1987). Cryoelectron Microscopy of Vitrified Specimens. *Cryotechniques Biol. Electron Microsc.*, 114–131. doi:10.1007/978-3-642-72815-0_5

Erickson, P. A., Anderson, D. H., and Fisher, S. K. (1987). Use of uranyl acetate *en bloc* to improve tissue preservation and labeling for post-embedding immunoelectron microscopy. *J. Elec. Microsc. Tech.* 5 (4), 303–314. doi:10.1002/jemt.1060050403

Faruqi, A. R., and McMullan, G. (2011). Electronic Detectors for Electron Microscopy. *Quart. Rev. Biophys.* 44 (3), 357–390. doi:10.1017/S0033583511000035

Fermie, J., Liv, N., ten Brink, C., van Donselaar, E. G., Müller, W. H., Schieber, N. L., et al. (2018). Single Organelle Dynamics Linked to 3D Structure by Correlative Live-Cell Imaging and 3D Electron Microscopy. *Traffic* 19 (5), 354–369. doi:10.1111/tra.12557

Fermie, J., Zuidema, W., Wolters, A. H. G., Giepmans, B. N., and Hoogenboom, J. P. (2020). "Rapid and Seamless Imaging of Biological Specimens Using a Novel Optical Scanning Transmission Electron Detector," in *European Microscopy Congress 2020*.

Fu, Z., Peng, D., Zhang, M., Xue, F., Zhang, R., He, W., et al. (2020). mEosEM Withstands Osmium Staining and Epon Embedding for Super-resolution CLEM. *Nat. Methods* 17 (1), 55–58. doi:10.1038/s41592-019-0613-6

Giddings, T. H. (2003). Freeze-Substitution Protocols for Improved Visualization of Membranes in High-Pressure Frozen Samples. *J. Microsc.* 212 (1), 53–61. doi:10.1046/j.1365-2818.2003.01228.x

Giepmans, B. N. G., Adams, S. R., Ellisman, M. H., and Tsien, R. Y. (2006). The Fluorescent Toolbox for Assessing Protein Location and Function. *Science* 312 (5771), 217–224. doi:10.1126/science.1124618

Giepmans, B. N. G., Deerinck, T. J., Smarr, B. L., Jones, Y. Z., and Ellisman, M. H. (2005). Correlated Light and Electron Microscopic Imaging of Multiple Endogenous Proteins Using Quantum Dots. *Nat. Methods* 2 (10), 743–749. doi:10.1038/nmeth791

Ginsburg, H., and Wolosin, J. M. (1979). Effects of Uranyl Ions on Lipid Bilayer Membranes. *Chem. Phys. Lipids* 23 (2), 125–131. doi:10.1016/0009-3084(79)90040-9

Goetz, J. G., Monduc, F., Schwab, Y., and Vermot, J. (2015). Using Correlative Light and Electron Microscopy to Study Zebrafish Vascular Morphogenesis. *Tissue Morphog. Methods Protoc.* 1189, 31–46. doi:10.1007/978-1-4939-1164-6_3

Hawes, P., Netherton, C. L., Mueller, M., Wileman, T., and Monaghan, P. (2007). Rapid Freeze-Substitution Preserves Membranes in High-Pressure Frozen Tissue Culture Cells. *J. Microsc.* 226 (2), 182–189. doi:10.1111/j.1365-2818.2007.01767.x

Hayat, M. A. (1981). *Fixation for Electron Microscopy*. New York: Academic Press.

Hayat, M. A. (1993). *Stains and Cytochemical Methods*. New York, USA and London, UK: Plenum Press.

Hayat, M. A. (2002). *Microscopy, Immunohistochemistry, and Antigen Retrieval Methods for Light and Electron Microscopy*. New York, Boston, Dordrecht, London, Moscow: Kluwer Academic Publishers.

Heiligenstein, X., de Beer, M., Heiligenstein, J., Eyraud, F., Manet, L., Schmitt, F., et al. (2021). HPM Live µ for a Full CLEM Workflow. *Methods Cell Biol.* 162, 115–149. doi:10.1016/bs.mcb.2020.10.022

Heiligenstein, X., Heiligenstein, J., Delevoye, C., Hurbain, I., Bardin, S., Paul-Gilloteaux, P., et al. (2014). The CryoCapsule: Simplifying Correlative Light to Electron Microscopy. *Traffic* 15 (6), 700–716. doi:10.1111/tra.12164

Hemelaar, S. R., de Boer, P., Chipaux, M., Zuidema, W., Hamoh, T., Martinez, F. P., et al. (2017). Nanodiamonds as Multi-Purpose Labels for Microscopy. *Sci. Rep.* 7 (1), 720. doi:10.1038/s41598-017-00797-2

Hippe-Sanwald, S. (1993). Impact of Freeze Substitution on Biological Electron Microscopy. *Microsc. Res. Tech.* 24 (5), 400–422. doi:10.1002/jemt.1070240506

Hodgson, L., Nam, D., Mantell, J., Achim, A., and Verkade, P. (2014). Retracing in Correlative Light Electron Microscopy: Where is my Object of Interest?*Methods Cell Biol.* 124, 1–21. doi:10.1016/b978-0-12-801075-4.00001-x

Höhn, K., Fuchs, J., Fröber, A., Kirmse, R., Glass, B., Anders-österwein, M., et al. (2015). Preservation of Protein Fluorescence in Embedded Human Dendritic Cells for Targeted 3D Light and Electron Microscopy. *J. Microsc.* 259 (2), 121–128. doi:10.1111/jmi.12230

Hosogi, N., Nishioka, H., and Nakakoshi, M. (2015). Evaluation of Lanthanide Salts as Alternative Stains to Uranyl Acetate. *Microsc. (Tokyo)* 64 (6), 429–435. doi:10.1093/jmicro/dfv054

Howes, S. C., Koning, R. I., and Koster, A. J. (2018). Correlative Microscopy for Structural Microbiology. *Curr. Opin. Microbiol.* 43, 132–138. doi:10.1016/j.mib.2018.01.009

Humbel, B. M., and Schwarz, H. (1989). "Freeze-substitution for Immunochemistry," in *Immuno-Gold Labeling in Cell Biology*. Editors A. J. Verkleij and J. L. M. Leunissen (Boca Raton, FL: CRC Press), 115–134.

Inaga, S., Katsumoto, T., Tanaka, K., Kameie, T., Nakane, H., and Naguro, T. (2007). Platinum Blue as an Alternative to Uranyl Acetate for Staining in Transmission Electron Microscopy. *Archives Histology Cytol.* 70 (1), 43–49. doi:10.1679/aohc.70.43

Jahn, K. A., Barton, D. A., Kobayashi, K., Ratinac, K. R., Overall, R. L., and Braet, F. (2012). Correlative Microscopy: Providing New Understanding in the Biomedical and Plant Sciences. *Micron* 43 (5), 565–582. doi:10.1016/j.micron.2011.12.004

Jansen, J., Reimer, K. C., Nagai, J. S., Varghese, F. S., Overheul, G. J., de Beer, M., et al. (2021). SARS-CoV-2 Infects the Human Kidney and Drives Fibrosis in Kidney Organoids. *Cell Stem Cell* 29, 217–231. doi:10.1016/j.stem.2021.12.010

Johnson, E., Seiradake, E., Jones, E. Y., Davis, I., Grünewald, K., and Kaufmann, R. (2015). Correlative In-Resin Super-resolution and Electron Microscopy Using Standard Fluorescent Proteins. *Sci. Rep.* 5, 9583. doi:10.1038/srep09583

Karnovsky, M. J. (1965). A Formaldehyde-Glutaraldehyde Fixative of High Osmolality for Use in Electron Microscopy. *J. Cell Biol.* 27 (2), A137–A138.

Karreman, M. A., Hyenne, V., Schwab, Y., and Goetz, J. G. (2016). Intravital Correlative Microscopy: Imaging Life at the Nanoscale. *Trends Cell Biol.* 26 (11), 848–863. doi:10.1016/j.tcb.2016.07.003

Karreman, M. A., Mercier, L., Schieber, N. L., Shibue, T., Schwab, Y., and Goetz, J. G. (2014). Correlating Intravital Multi-Photon Microscopy to 3D Electron Microscopy of Invading Tumor Cells Using Anatomical Reference Points. *Plos One* 9 (12), e114448. doi:10.1371/journal.pone.0114448

Karreman, M. A., Ruthensteiner, B., Mercier, L., Schieber, N. L., Solecki, G., Winkler, F., et al. (2017). Find Your Way with X-Ray: Using MicroCT to Correlate *in Vivo* Imaging With 3D Electron Microscopy. *Methods Cell Biol.* 140, 277–301. doi:10.1016/bs.mcb.2017.03.006

Keene, D. R., Tufa, S. F., Lunstrum, G. P., Holden, P., and Horton, W. A. (2008). Confocal/TEM Overlay Microscopy: a Simple Method for Correlating Confocal and Electron Microscopy of Cells Expressing GFP/YFP Fusion Proteins. *Microsc. Microanal.* 14 (4), 342–348. doi:10.1017/s1431927608080306

Keevend, K., Krummenacher, R., Kungas, E., Gerken, L. R. H., Gogos, A., Stiefel, M., et al. (2020). Correlative Cathodoluminescence Electron Microscopy: Immunolabeling Using Rare-Earth Element Doped Nanoparticles. *Small* 16 (44), 2004615. doi:10.1002/smll.202004615

Kellenberger, E., Dürrenberger, M., Villiger, W., Carlemalm, E., and Wurtz, M. (1987). The Efficiency of Immunolabel on Lowicryl Sections Compared to Theoretical Predictions. *J. Histochem Cytochem.* 35 (9), 959–969. doi:10.1177/35.9.3302020

Kellenberger, E. (1987). "The Response of Biological Macromolecules and Supramolecular Structures to the Physics of Specimen Cryopreparation," in *Cryotechniques in Biological Electron Microscopy*. Editors R. A. Steinbrecht and K. Zierold (Berlin, Heidelberg: Springer Berlin Heidelberg), 35–63. doi:10.1007/978-3-642-72815-0_2

Knott, G. W., Holtmaat, A., Trachtenberg, J. T., Svoboda, K., and Welker, E. (2009). A Protocol for Preparing GFP-Labeled Neurons Previously Imaged *In Vivo* and in Slice Preparations for Light and Electron Microscopic Analysis. *Nat. Protoc.* 4 (8), 1145–1156. doi:10.1038/nprot.2009.114

Kolotuev, I., Bumbarger, D. J., Labouesse, M., and Schwab, Y. (2012). Targeted Ultramicrotomy: A Valuable Tool for Correlated Light and Electron Microscopy of Small Model Organisms. *Methods Cell Biol.* 111, 203–222. doi:10.1016/b978-0-12-416026-2.00011-x

Kopek, B. G., Paez-Segala, M. G., Shtengel, G., Sochacki, K. A., Sun, M. G., Wang, Y., et al. (2017). Diverse Protocols for Correlative Super-resolution Fluorescence Imaging and Electron Microscopy of Chemically Fixed Samples. *Nat. Protoc.* 12 (5), 916–946. doi:10.1038/nprot.2017.017

Kremer, A., Lippens, S., Bartunkova, S., Asselbergh, B., Blanpain, C., Fendrych, M., et al. (2015). Developing 3D SEM in a Broad Biological Context. *J. Microsc.* 259, 80–96. doi:10.1111/jmi.12211

Kuipers, J., and Giepmans, B. N. G. (2020). Neodymium as an Alternative Contrast for Uranium in Electron Microscopy. *Histochem Cell Biol.* 153 (4), 271–277. doi:10.1007/s00418-020-01846-0

Kukulski, W., Schorb, M., Kaksonen, M., and Briggs, J. A. G. (2012). Plasma Membrane Reshaping during Endocytosis Is Revealed by Time-Resolved Electron Tomography. *Cell* 150 (3), 508–520. doi:10.1016/j.cell.2012.05.046

Kukulski, W., Schorb, M., Welsch, S., Picco, A., Kaksonen, M., and Briggs, J. A. G. (2011). Correlated Fluorescence and 3D Electron Microscopy with High Sensitivity and Spatial Precision. *J. Cell Biol.* 192 (1), 111–119. doi:10.1083/jcb.201009037

Lane, R., Vos, Y., Wolters, A. H. G., Kessel, L. v., Chen, S. E., Liv, N., et al. (2021). Optimization of Negative Stage Bias Potential for Faster Imaging in Large-Scale Electron Microscopy. *J. Struct. Biol. X* 5, 100046. doi:10.1016/j.yjsbx.2021.100046

Lane, R., Wolters, A. H. G., Giepmans, B. N. G., and Hoogenboom, J. P. (2022). Integrated Array Tomography for 3D Correlative Light and Electron Microscopy. *Front. Mol. Biosci.* 8, 822232. doi:10.3389/fmolb.2021.822232

Lemercier, N., Middel, V., Hentsch, D., Taubert, S., Takamiya, M., Beil, T., et al. (2017). Microtome-Integrated Microscope System for High Sensitivity Tracking of In-Resin Fluorescence in Blocks and Ultrathin Sections for Correlative Microscopy. *Sci. Rep.* 7, 11. doi:10.1038/s41598-017-13348-6

Lepock, J. R. (1997). Protein Denaturation During Heat Shock. *Adv. Mol. Cell Biol.* 19, 223–259. doi:10.1016/s1569-2558(08)60079-x

Levin, B. D. A. (2021). Direct Detectors and Their Applications in Electron Microscopy for Materials Science. *J. Phys. Mat.* 4 (4), 042005. doi:10.1088/2515-7639/ac0ff9

Levitt, M. F., and Gaudino, M. (1950). Measurement of Body Water Compartments. *Am. J. Med.* 9 (2), 208–215. doi:10.1016/0002-9343(50)90024-6

Ling, R. (2004). Introduction. *Physiol. Chem. Phys. Med. NMR* 36 (1), 1–19. doi:10.1016/b978-155860936-5/50001-5

Liv, N., Zonnevylle, A. C., Narvaez, A. C., Effting, A. P. J., Voorneveld, P. W., Lucas, M. S., et al. (2013). Simultaneous Correlative Scanning Electron and High-NA Fluorescence Microscopy. *Plos One* 8 (2), e55707. doi:10.1371/journal.pone.0055707

Loussert Fonta, C., and Humbel, B. M. (2015). Correlative Microscopy. *Archives Biochem. Biophysics* 581, 98–110. doi:10.1016/j.abb.2015.05.017

Luby-Phelps, K., Ning, G., Fogerty, J., and Besharse, J. C. (2003). Visualization of Identified GFP-Expressing Cells by Light and Electron Microscopy. *J. Histochem Cytochem.* 51 (3), 271–274. doi:10.1177/002215540305100301

Lucas, F., Günthert, M., Wepf, R., and Lucas, M. S. (2017). *Towards Improved In-Resin Fluorescence Protocols for CLEM: A Method to Monitor Fluorescence Quenching during Sample Preparation*.

Lucas, M. S., Günthert, M., Bittermann, A. G., de Marco, A., and Wepf, R. (2017). Correlation of Live-Cell Imaging with Volume Scanning Electron Microscopy. *Methods Cell Biol.* 140, 123–148. doi:10.1016/bs.mcb.2017.03.001

Lucas, M. S., Günthert, M., Gasser, P., Lucas, F., and Wepf, R. (2012). Bridging Microscopes: 3D Correlative Light and Scanning Electron Microscopy of Complex Biological Structures. *Methods Cell Biol.* 111, 325–356. doi:10.1016/b978-0-12-416026-2.00017-0

Luft, J. H. (1961). Improvements in Epoxy Resin Embedding Methods. *J. Biophysical Biochem. Cytol.* 9 (2), 409–414. doi:10.1083/jcb.9.2.409

Matsko, N., and Mueller, M. (2005). Epoxy Resin as Fixative during Freeze-Substitution. *J. Struct. Biol.* 152 (2), 92–103. doi:10.1016/j.jsb.2005.07.005

McDonald, K. (2007). Cryopreparation Methods for Electron Microscopy of Selected Model Systems. *Methods Cell Biol.* 79, 23–56. doi:10.1016/s0091-679x(06)79002-1

McDonald, K. L., and Webb, R. I. (2011). Freeze Substitution in 3 hours or Less. *J. Microsc.* 243 (3), 227–233. doi:10.1111/j.1365-2818.2011.03526.x

Micheva, K. D., O'Rourke, N., Busse, B., and Smith, S. J. (2010). Array Tomography: Immunostaining and Antibody Elution. *Cold Spring Harb. Protoc.* 2010 (11), pdb. pdb prot5525. doi:10.1101/pdb.prot5525

Micheva, K. D., and Smith, S. J. (2007). Array Tomography: A New Tool for Imaging the Molecular Architecture and Ultrastructure of Neural Circuits. *Neuron* 55 (1), 25–36. doi:10.1016/j.neuron.2007.06.014

Mironov, A. A., Polishchuk, R. S., and Luini, A. (2000). Visualizing Membrane Traffic *In Vivo* by Combined Video Fluorescence and 3D Electron Microscopy. *Trends Cell Biol.* 10 (8), 349–353. doi:10.1016/s0962-8924(00)01787-6

Monaghan, P., Perusinghe, N., and Muller, M. (1998). High-pressure Freezing for Immunocytochemistry. *J. Microsc.* 192 (3), 248–258. doi:10.1046/j.1365-2818.1998.00387.x

Moor, H. (1973). "Cryotechnology for the Structural Analysis of Biological Material," in *Freeze-etching Techniques and Applications*. Editors E. L. Benedetti and P. Favard (Paris: Societe Franqaise de Microscopic Electronique).

Murk, J. L. A. N., Posthuma, G., Koster, A. J., Geuze, H. J., Verkleij, A. J., Kleijmeer, M. J., et al. (2003). Influence of Aldehyde Fixation on the Morphology of Endosomes and Lysosomes: Quantitative Analysis and Electron Tomography. *J. Microsc.* 212 (1), 81–90. doi:10.1046/j.1365-2818.2003.01238.x

Nakakoshi, M., Nishioka, H., and Katayama, E. (2011). New Versatile Staining Reagents for Biological Transmission Electron Microscopy that Substitute for Uranyl Acetate. *J. Electron Microsc.* 60 (6), 401–407. doi:10.1093/jmicro/dfr084

Newman, G. R., and Hobot, J. A. (1993). *Resin Microscopy and On-Section Immunocytochemistry*. Berlin, Heidelberg: Springer.

Nixon, S. J., Webb, R. I., Floetenmeyer, M., Schieber, N., Lo, H. P., and Parton, R. G. (2009). A Single Method for Cryofixation and Correlative Light, Electron Microscopy and Tomography of Zebrafish Embryos. *Traffic* 10 (2), 131–136. doi:10.1111/j.1600-0854.2008.00859.x

Oberti, D., Kirschmann, M. A., and Hahnloser, R. H. (2010). Correlative Microscopy of Densely Labeled Projection Neurons Using Neural Tracers. *Front. Neuroanat.* 4, 24. doi:10.3389/fnana.2010.00024

Paez-Segala, M. G., Sun, M. G., Shtengel, G., Viswanathan, S., Baird, M. A., Macklin, J. J., et al. (2015). Fixation-resistant Photoactivatable Fluorescent Proteins for CLEM. *Nat. Methods* 12 (3), 215–218. doi:10.1038/nmeth.3225

Peddie, C. J., Blight, K., Wilson, E., Melia, C., Marrison, J., Carzaniga, R., et al. (2014). Correlative and Integrated Light and Electron Microscopy of In-Resin GFP Fluorescence, Used to Localise Diacylglycerol in Mammalian Cells. *Ultramicroscopy* 143, 3–14. doi:10.1016/j.ultramic.2014.02.001

Peddie, C. J., and Collinson, L. M. (2014). Exploring the Third Dimension: Volume Electron Microscopy Comes of Age. *Micron* 61, 9–19. doi:10.1016/j.micron.2014.01.009

Peddie, C. J., Domart, M.-C., Snetkov, X., O'Toole, P., Larijani, B., Way, M., et al. (2017). Correlative Super-resolution Fluorescence and Electron Microscopy Using Conventional Fluorescent Proteins In Vacuo. *J. Struct. Biol.* 199 (2), 120–131. doi:10.1016/j.jsb.2017.05.013

Polishchuk, R. S., Polishchuk, E. V., Marra, P., Alberti, S., Buccione, R., Luini, A., et al. (2000). Correlative Light-Electron Microscopy Reveals the Tubular-Saccular Ultrastructure of Carriers Operating between Golgi Apparatus and Plasma Membrane. *J. Cell Biol.* 148 (1), 45–58. doi:10.1083/jcb.148.1.45

Prangsma, J. C., Molenaar, R., van Weeren, L., Bindels, D. S., Haarbosch, L., Stouthamer, J., et al. (2020). Quantitative Determination of Dark Chromophore Population Explains the Apparent Low Quantum Yield of Red Fluorescent Proteins. *J. Phys. Chem. B* 124 (8), 1383–1391. doi:10.1021/acs.jpcb.9b10396

Prior, D. A. M., Oparka, K. J., and Roberts, I. M. (1999). En Blocoptical Sectioning of Resin-Embedded Specimens Using a Confocal Laser Scanning Microscope. *J. Microsc.* 193 (1), 20–27. doi:10.1046/j.1365-2818.1999.00433.x

Reinoso, R. F., Telfer, B. A., and Rowland, M. (1997). Tissue Water Content in Rats Measured by Desiccation. *J. Pharmacol. Toxicol. Methods* 38 (2), 87–92. doi:10.1016/S1056-8719(97)00053-1

Riehle, U., and Hoechli, M. (1973). "The Theory and Technique of High Pressure Freezing," in *Freeze-etching Techniques and Applications*. Editors E. L. Benedetti and P. Favard (Paris: Societe Francaise de Microscopic Electronique), 11–19.

Ripoll, L., Heiligenstein, X., Hurbain, I., Domingues, L., Figon, F., Petersen, K. J., et al. (2018). Myosin VI and Branched Actin Filaments Mediate Membrane Constriction and Fission of Melanosomal Tubule Carriers. *J. Cell Biol.* 217 (8), 2709–2726. doi:10.1083/jcb.201709055

Rizzo, N. W., Duncan, K. E., Bourett, T. M., and Howard, R. J. (2016). Backscattered Electron SEM Imaging of Resin Sections from Plant Specimens: Observation of Histological to Subcellular Structure and CLEM. *J. Microsc.* 263 (2), 142–147. doi:10.1111/jmi.12373

Robertson, D., Monaghan, P., Clarke, C., and Atherton, A. J. (1992). An Appraisal of Low-Temperature Embedding by Progressive Lowering of Temperature into Lowicryl HM20 for Immunocytochemical Studies. *J. Microsc.* 168, 85–100. doi:10.1111/j.1365-2818.1992.tb03253.x

Sabatini, D. D., Bensch, K., and Barrnett, R. J. (1963). Cytochemistry and Electron Microscopy. The Preservation of Cellular Ultrastructure and Enzymatic Activity by Aldehyde Fixation. *J. Cell Biol.* 17 (1), 19–58. doi:10.1083/jcb.17.1.19

Sato, S., Sasaki, Y., Adachi, A., Dai, W., Liu, X.-L., and Namimatsu, S. (2003). Use of Oolong Tea Extract (OTE) for Elastin Staining and Enhancement in Ultrathin Sections. *Med. Electron Microsc.* 36 (3), 179–182. doi:10.1007/s00795-003-0216-1

Scher, N., and Avinoam, O. (2021). 50 Shades of CLEM: How to Choose the Right Approach for You. *Methods Cell Biol.* 162, 1–11. doi:10.1016/bs.mcb.2020.08.001

Sims, P., Albrecht, R., Pawley, J. B., Centonze, V., Deerinck, T., and Hardin, J. (2006). When Light Microscope Resolution Is Not Enough:Correlational Light Microscopy and Electron Microscopy. *Handb. Biol. Confocal Microsc.*, 846–860. doi:10.1007/978-0-387-45524-2_49

Su, Y., Nykanen, M., Jahn, K. A., Whan, R., Cantrill, L., Soon, L. L., et al. (2010). Multi-dimensional Correlative Imaging of Subcellular Events: Combining the Strengths of Light and Electron Microscopy. *Biophys. Rev.* 2 (3), 121–135. doi:10.1007/s12551-010-0035-2

Tagliaferro, P., Tandler, C. J., Ramos, A. J., Pecci Saavedra, J., and Brusco, A. (1997). Immunofluorescence and Glutaraldehyde Fixation. A New Procedure Based on the Schiff-Quenching Method. *J. Neurosci. Methods* 77 (2), 191–197. doi:10.1016/s0165-0270(97)00126-x

Timmermans, F. J., and Otto, C. (2015). Contributed Review: Review of Integrated Correlative Light and Electron Microscopy. *Rev. Sci. Instrum.* 86 (1), 011501. doi:10.1063/1.4905434

Titze, B., and Genoud, C. (2016). Volume Scanning Electron Microscopy for Imaging Biological Ultrastructure. *Biol. Cell* 108 (11), 307–323. doi:10.1111/boc.201600024

Tranfield, E. M., Heiligenstein, X., Peristere, I., and Antony, C. (2014). Correlative Light and Electron Microscopy for a Free-Floating Spindle in *Xenopus laevis* Egg Extracts. *Methods Cell Biol.* 124, 111–128. doi:10.1016/b978-0-12-801075-4.00006-9

Tuijtel, M. W., Mulder, A. A., Posthuma, C. C., van der Hoeven, B., Koster, A. J., Bárcena, M., et al. (2017). Inducing Fluorescence of Uranyl Acetate as a Dual-Purpose Contrast Agent for Correlative Light-Electron Microscopy with Nanometre Precision. *Sci. Rep.* 7 (1), 10442. doi:10.1038/s41598-017-10905-x

van Rijnsoever, C., Oorschot, V., and Klumperman, J. (2008). Correlative Light-Electron Microscopy (CLEM) Combining Live-Cell Imaging and Immunolabeling of Ultrathin Cryosections. *Nat. Methods* 5 (11), 973–980. doi:10.1038/nmeth.1263

Verkade, P. (2008). Moving EM: the Rapid Transfer System as a New Tool for Correlative Light and Electron Microscopy and High Throughput for High-

Pressure Freezing. *J. Microsc.* 230 (2), 317–328. doi:10.1111/j.1365-2818.2008.01989.x

Vos, Y., Lane, R. I., Peddie, C. J., Wolters, A. H. G., and Hoogenboom, J. P. (2020). Retarding Field Integrated Fluorescence and Electron Microscope. *Microsc. Microanal.* 27, 109–120. doi:10.1017/S1431927620024745

Wacker, I., Chockley, P., Bartels, C., Spomer, W., Hofmann, A., Gengenbach, U., et al. (2015). Array Tomography: Characterizing FAC-Sorted Populations of Zebrafish Immune Cells by Their 3D Ultrastructure. *J. Microsc.* 259 (2), 105–113. doi:10.1111/jmi.12223

Wacker, I., and Schroeder, R. R. (2013). Array Tomography. *J. Microsc.* 252 (2), 93–99. doi:10.1111/jmi.12087

Wall, K. P., Dillon, R., and Knowles, M. K. (2015). Fluorescence Quantum Yield Measurements of Fluorescent Proteins: A Laboratory Experiment for a Biochemistry or Molecular Biophysics Laboratory Course. *Biochem. Mol. Biol. Educ.* 43 (1), 52–59. doi:10.1002/bmb.20837

Walther, P., and Ziegler, A. (2002). Freeze Substitution of High-Pressure Frozen Samples: the Visibility of Biological Membranes Is Improved when the Substitution Medium Contains Water. *J. Microsc.* 208 (1), 3–10. doi:10.1046/j.1365-2818.2002.01064.x

Ward, W. W. (2006). Biochemical and Physical Properties of Green Fluorescent Protein. *Green Fluoresc. Protein Prop. Appl. Protoc.* 47, 39–65.

Watanabe, S., Punge, A., Hollopeter, G., Willig, K. I., Hobson, R. J., Davis, M. W., et al. (2011). Protein Localization in Electron Micrographs Using Fluorescence Nanoscopy. *Nat. Methods* 8 (1), 80–84. doi:10.1038/nmeth.1537

Weibull, C., and Christiansson, A. (1986). Extraction of Proteins and Membrane Lipids during Low Temperature Embedding of Biological Material for Electron Microscopy. *J. Microscopy-Oxford* 142, 79–86. doi:10.1111/j.1365-2818.1986.tb02739.x

Wild, P., Schraner, E. M., Adler, H., and Humbel, B. M. (2001). Enhanced Resolution of Membranes in Cultured Cells by Cryoimmobilization and Freeze-Substitution. *Microsc. Res. Tech.* 53 (4), 313–321. doi:10.1002/jemt.1098

Wilke, K., Wick, K., Keil, F. J., Wittern, K. P., Wepf, R., and Biel, S. S. (2008). A Strategy for Correlative Microscopy of Large Skin Samples: towards a Holistic View of Axillary Skin Complexity. *Exp. Dermatol* 17 (1), 73–81. doi:10.1111/j.1600-0625.2007.00635.x

Yahav, T., Maimon, T., Grossman, E., Dahan, I., and Medalia, O. (2011). Cryo-electron Tomography: Gaining Insight into Cellular Processes by Structural Approaches. *Curr. Opin. Struct. Biol.* 21, 670–677. doi:10.1016/j.sbi.2011.07.004

Yamaguchi, K., Suzuki, K. i., and Tanaka, K. (2010). Examination of Electron Stains as a Substitute for Uranyl Acetate for the Ultrathin Sections of Bacterial Cells. *J. Electron Microsc.* 59 (2), 113–118. doi:10.1093/jmicro/dfp045

Zhou, H., Gang, Y., Chen, S., Wang, Y., Xiong, Y., Li, L., et al. (2017). Development of a Neutral Embedding Resin for Optical Imaging of Fluorescently Labeled Biological Tissue. *J. Biomed. Opt.* 22 (10), 1–7. doi:10.1117/1.JBO.22.10.106015

Conflict of Interest: XH was employed by CryoCapCell, Le Kremlin-Bicêtre.

The remaining author declares that the research was conducted in the absence of any commercial or financial relationships that could be construed as a potential conflict of interest.

Publisher's Note: All claims expressed in this article are solely those of the authors and do not necessarily represent those of their affiliated organizations, or those of the publisher, the editors and the reviewers. Any product that may be evaluated in this article, or claim that may be made by its manufacturer, is not guaranteed or endorsed by the publisher.

frontiers | Frontiers in Cell and Developmental Biology

TYPE Methods
PUBLISHED 08 August 2022
DOI 10.3389/fcell.2022.933376

OPEN ACCESS

EDITED BY
Saskia Lippens,
Vlaams Instituut voor Biotechnologie, Belgium

REVIEWED BY
Wiebke Möbius,
Max Planck Institute for Multidisciplinary Sciences, Germany
Eija Jokitalo,
University of Helsinki, Finland

*CORRESPONDENCE
Kirk J. Czymmek,
kczymmek@danforthcenter.org

SPECIALTY SECTION
This article was submitted to Cell Growth and Division, a section of the journal Frontiers in Cell and Developmental Biology

RECEIVED 30 April 2022
ACCEPTED 08 July 2022
PUBLISHED 08 August 2022

CITATION
Bélanger S, Berensmann H, Baena V, Duncan K, Meyers BC, Narayan K and Czymmek KJ (2022), A versatile enhanced freeze-substitution protocol for volume electron microscopy. *Front. Cell Dev. Biol.* 10:933376. doi: 10.3389/fcell.2022.933376

A versatile enhanced freeze-substitution protocol for volume electron microscopy

Sébastien Bélanger[1], Heather Berensmann[2,3], Valentina Baena[2,3], Keith Duncan[1], Blake C. Meyers[1,4], Kedar Narayan[2,3] and Kirk J. Czymmek[1,5]*

[1]Donald Danforth Plant Science Center, Saint Louis, MO, United States, [2]Center for Molecular Microscopy, Center for Cancer Research, National Cancer Institute, National Institutes of Health, Bethesda, MD, United States, [3]Cancer Research Technology Program, Frederick National Laboratory for Cancer Research, Frederick, MD, United States, [4]Division of Plant Science and Technology, University of Missouri–Columbia, Columbia, MO, United States, [5]Advanced Bioimaging Laboratory, Donald Danforth Plant Science Center, Saint Louis, MO, United States

Volume electron microscopy, a powerful approach to generate large three-dimensional cell and tissue volumes at electron microscopy resolutions, is rapidly becoming a routine tool for understanding fundamental and applied biological questions. One of the enabling factors for its adoption has been the development of conventional fixation protocols with improved heavy metal staining. However, freeze-substitution with organic solvent-based fixation and staining has not realized the same level of benefit. Here, we report a straightforward approach including osmium tetroxide, acetone and up to 3% water substitution fluid (compatible with traditional or fast freeze-substitution protocols), warm-up and transition from organic solvent to aqueous 2% osmium tetroxide. Once fully hydrated, samples were processed in aqueous based potassium ferrocyanide, thiocarbohydrazide, osmium tetroxide, uranyl acetate and lead acetate before resin infiltration and polymerization. We observed a consistent and substantial increase in heavy metal staining across diverse and difficult-to-fix test organisms and tissue types, including plant tissues (*Hordeum vulgare*), nematode (*Caenorhabditis elegans*) and yeast (*Saccharomyces cerevisiae*). Our approach opens new possibilities to combine the benefits of cryo-preservation with enhanced contrast for volume electron microscopy in diverse organisms.

KEYWORDS

freeze-substitution fixation, volume electron microscopy (vEM), OTO, *C. elegans*, *Saccharomyces cerevisiae*, plant specimens, high-pressure freezing (HPF), quick freeze-substitution (QFS)

Introduction

A number of three-dimensional (3D) approaches have been developed that enable intermediate and high-resolution imaging of cells and tissues, each with their own merits and limitations (Watanabe et al., 2014; Collman et al., 2015; Mahamid et al., 2015; Sydor et al., 2015; Hoffman et al., 2020; Otegui, 2020; Wu et al., 2020). Volume electron microscopy (vEM), is particularly suitable when the collection of nanometer scale data from relatively large samples (100–1000 s of um^3) and 100–1000 s of serial sections of resin embedded specimen is required (Titze and Genoud, 2016). This can be achieved by generating consecutive sections arranged in arrays on a substrate, termed array tomography (AT) (Mendenhall, Kuwajima and Harris, 2017; Smith, 2018) or by the serial removal of a thin surface layer and imaging the exposed block-face (Narayan et al., 2014; Guérin et al., 2019; Lippens et al., 2019). With AT, sections cut into ribbons and attached to a surface, post-stained with heavy metals and rendered conductive, allows many traditional fixation/staining protocols as well as affinity probe labeling for correlative microscopy. For serial block-face imaging, an in-chamber ultramicrotome repeatedly shaves the resin surface using a diamond knife and is known as serial block-face scanning electron microscopy (SBF-SEM) (Denk and Horstmann, 2004). Alternatively, a focused ion beam "mills" the resin surface, termed focused ion beam scanning electron microscopy (FIB-SEM) (Narayan and Subramaniam, 2015). Both SBF-SEM or FIB-SEM rely on heavy metal-induced backscatter electrons to generate image contrast, and all metal staining steps of the bulk sample must be performed "*en bloc*," prior to resin infiltration and polymerization. Furthermore, image quality (signal-to-noise), structure, resolution and sample conductivity are highly dependent upon the levels of metal staining of the sample constituents. Arguably, one of the significant technical advances that helped propel the adoption of SBF-SEM for volume electron microscopy (vEM) studies was the amplification of metal staining via osmium-thiocarbohydrazide-osmium (OTO), often with potassium ferrocyanide, lead and uranium salts (Deerinck et al., 2018).

Conventional fixative protocols at ambient temperatures often result in subcellular changes due to fixation artifacts. Immobilizing cellular structures within milliseconds, using freezing, offers optimal morphological preservation of many cellular structures, preserving them in their near-native state (Gilkey and Staehelin, 1986). While freeze-substitution fixation with organic solvent-based staining protocols provides remarkable cellular renditions via post-stained resin sections and transmission electron microscopy (TEM), it often results in very low contrast in certain cell structures (i.e., membranes and cell walls) and overall intense metal staining of traditional freeze-substitution preparations comparable to aqueous OTO remains elusive. Poor membrane visibility often can be addressed by the addition of up to 5% water in the freeze-substitution solution (Buser and Walther, 2008), or other substitution fluid modifications (Guo et al., 2020). SBF-SEM in particular is more sensitive to reduced sample conductivity when samples have large non-cellular voids (i.e., vacuoles and/or air spaces). The use of organic solvent-based OTO and/or *en bloc* lead and uranium salts have indeed helped improved contrast and signal-to-noise for vEM (Tsang et al., 2018; Czymmek et al., 2020), including increased chamber pressure and local gas injection strategies (Deerinck et al., 2018) and the inclusion of conductive resins (Nguyen et al., 2016) to suppress charge. Despite these improvements, the level of metalization, compared with aqueous OTO protocol counterparts, still limits a number of SBF-SEM and FIB-SEM experiments where improved resolution (x-y, z), speed of acquisition and sample tolerance to beam dosage are required.

To address this, we developed an approach that builds on the work of others using rehydration strategies with HPF freeze-substituted samples (Ripper, Schwarz and Stierhof, 2008; Tsang et al., 2018). We transitioned from organic solvent to an aqueous osmium tetroxide (OsO_4) solution upon warm-up, and followed this with an aqueous solvent-based metal staining protocol designed to improve uniformity of OTO preparations in larger samples (Hua, Laserstein and Helmstaedter, 2015; Genoud et al., 2018; Duncan et al., 2022). Our strategy was based upon the notion that the reduced solubility and staining capacity of metal stain components in polar organic vs. aqueous solvents for cryo-preparations could be surmounted and further improved. We developed and evaluated our Freeze-Substitution and aqueous OTO protocol (FSaqOTO) using several diverse and challenging plant, animal, and yeast test samples. We included side-by-side aqueous vs. organic FS comparisons that demonstrated substantial signal improvement and distinctive staining patterns of certain cell structures with the FSaqOTO protocol. Additionally, our FSaqOTO protocol was versatile; it is compatible with manual, automated and quick-freeze substitution warm-up regimes. While not a panacea, our current FSaqOTO protocol is likely suitable for many organisms and studies for which cryo-preservation is the gold-standard approach, but aqueous enhanced metalization is required to substantially improve signal-to-noise, throughput, and enhanced staining of certain cell structures for intermediate resolution vEM structural studies.

Materials and methods

High-pressure freezing approach for tested specimen

All specimens were frozen in a Leica EM ICE High-Pressure Freezer (Leica Microsystems, Inc., Buffalo Grove, IL, United States) as follows:

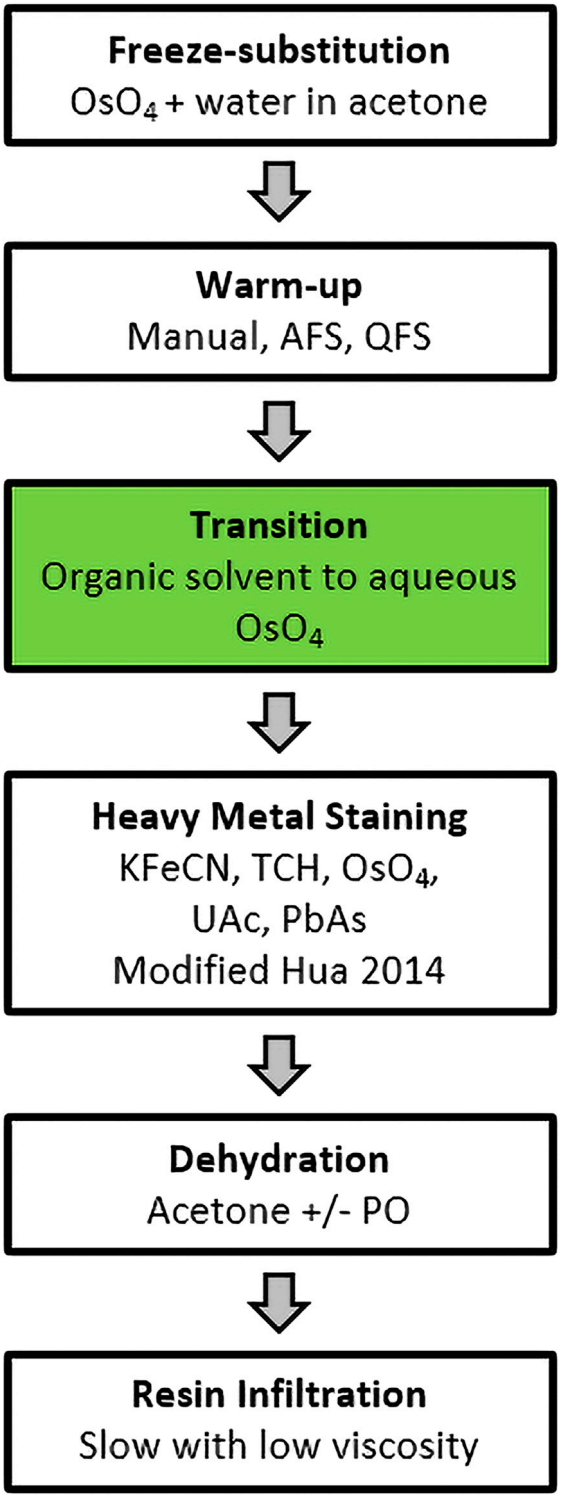

FIGURE 1
FSaqOTO general protocol overview. The major steps in the FSaqOTO protocol include freeze-substitution, warm-up to 0–4°C, the critical step (green filled) transition from organic solvent to aqueous buffer with osmium tetroxide (OsO_4), heavy metal staining with potassium ferrocyanide (KFeCN), thiocarbohydrazide (TCH), osmium tetroxide (OsO_4), uranyl acetate (UAc) and lead acetate (PbAs). Dehydration in acetone with/without propylene oxide and resin infiltration, slow (increased duration and/or steps) and low viscosity.

Plant: Root tips and anthers (0.8 and 1.5 mm) were excised via scalpel from barley (*Hordeum vulgare ssp. vulgare*) and placed in 3 mm gold-coated copper planchettes (one Type A, Cat # 16770152 and one Type B, Cat# 16770152, cavity space 400 um) with 50 mM sucrose in 75 mM PIPES buffer (pH 7.2) as a space filler and high-pressure frozen.

Nematode: *Caenorhabditis elegans* were maintained on MYOB agar plates seeded with *E. coli* OP50 bacteria and prepared for high pressure freezing as described previously (Rahman et al., 2021). Briefly, nematodes were collected in cellulose capillary tubes (Leica catalog number 16706869) and placed in 3 mm gold-coated copper planchettes (Type A and B, cavity space 300 um) with 20% dextran as a space filler and high-pressure frozen.

Yeast: *Saccharomyces cerevisiae* (strain BJ5494) was grown in YEPD medium to mid-log phase in a shaker flask at 60 RPM and 32°C, harvested by gentle centrifugation on a tabletop device to create a paste and placed in 3 mm gold-coated copper planchettes (Type A and B, cavity space 100 um) without additional space filler and high-pressure frozen.

Freeze-substitution and rehydration

High-pressure frozen samples were processed for freeze-substitution, heavy metal stained and resin infiltrated according to the general protocol overview shown in Figure 1. The overall approach was robust and allowed variations in substitution fluid, resin formulation and warm-up strategy.

HPF frozen plant materials were placed in mPrep/s capsules (Microscopy Innovations, Cat # 2250) without mPrep screens and held in mPrep CPD Holder (Microscopy Innovations, Cat # 2250) that was then placed in a 50 ml PTFE beaker (EMS Diasum, Cat# 60942) containing LN_2 frozen substitution fluid (2% OsO_4 in acetone with 3% water) and subsequently moved to −85°C for 3–4 days (Supplementary Data S1). Specifically, the mPrep capsule/CPD holder/PTFE assembly and pre-chilled substitution fluids were prepared by placing in adjacent Styrofoam containers with dry ice in a chemical fumehood. Next, the substitution fluid was added to the PTFE assembly until the fluid level was flush with the top of the mPrep CPD holder. The substitution fluid filled PTFE assembly was then carefully transferred (with forceps) and slowly lowered to the bottom of a shallow Styrofoam container with a few inches of LN_2 (be sure LN_2 level is maintained ~1 cm below top of PTFE container) until the solution was frozen. Aluminum planchettes and substitution containers should be avoided as the heavy metal

staining steps react with aluminum (i.e. TCH) turning the solution black and subsequent use of aluminum containers with this chemistry resulted in their failure (leakiness). Samples were then transferred step-wise and held at −55°C and −20°C for 3 h each and moved to 4°C for 1 h and room temperature for 1 h. At 4°C, a second mPrep/s capsule was inserted into each initial mPrep/s capsule to entrap and immerse the small specimen during subsequent aqueous-based processing steps. This prevented specimen loss and ensured the buoyant plant specimens were completely submerged in all reagents, thus minimizing uneven staining and/or inadequate reagent exchange. The critical organic solvent to aqueous transition step was performed at 4°C, where samples were rehydrated (20 min each step) in 1% OsO_4 using the following graded series of water:acetone 1:4, 1:1, 4:1 and finally moved to room temperature in 1% OsO_4 in 0.1 M sodium cacodylate buffer (pH 7.4) for 1 h.

For protocol comparison purposes, freeze-substitution was applied using a traditional Automated Freeze-substitution System (AFS, Leica Microsystems) (Rahman et al., 2021) without FSAqOTO, and Quick Freeze-Substitution (QFS) (Mcdonald and Webb, 2011) with our enhanced aqueous metalization approach to the model organisms *S. cerevisiae* and *C. elegans*. With AFS, the freeze-substitution cocktail was 1% OsO_4 and 1% glutaraldehyde in 1% water in acetone. 1 ml of freeze-substitution cocktail was placed in each cryovial and frozen under liquid nitrogen. The planchettes holding the frozen samples were transferred under liquid nitrogen vapors into the cryovials containing the frozen freeze-substitution cocktail. The cryovials were then capped and placed in the Leica AFS 2 chamber (set to −90°C) in aluminum containers with pre-cooled ethanol. The AFS program was run as follows: −90°C for 48 h, −90°C to −60°C for 6 h (5°C/h), −60°C for 2 h, −60°C to −20°C for 8 h (5°C/h), −20°C for 2 h, -20–0°C for 4 h (5°C/h). After freeze-substitution, the samples were rinsed with pre-cooled (to 0°C) acetone 3 times for 10 min each. After the third wash, samples were removed from the AFS chamber and allowed to reach room temperature. Samples were placed in 1% uranyl acetate in acetone for 1 h at room temperature followed by 3 acetone washes for 10 min each before proceeding to resin infiltration (see below).

In addition to AFS, we applied a Quick Freeze-Substitution aqueous OTO protocol for both the *S. cerevisiae* and *C. elegans* samples. Briefly, after high pressure freezing in an Leica EM ICE, the FSaqOTO protocol was performed largely following Rahman (Rahman et al., 2021) and McDonald (McDonald, 2014), but with slight changes to the actual freeze-substitution solvent and stain mixtures (referred to as SubMix). For *S. cerevisiae* samples, a SubMix of 1% w/v OsO_4 and 1% w/v UAc dissolved in 90% acetone +5% methanol +5% water was prepared. For *C. elegans*, a SubMix of 1% w/v OsO_4 dissolved in 97% acetone +3% water was prepared. Briefly, 1 ml of these SubMixes were aliquoted into cryovials and inserted into a metal block, which was laid on its side in an ice bucket. The bucket was filled with liquid nitrogen, and after the SubMixes were frozen, the high-pressure frozen planchettes with the samples were quickly transferred to the cryovials. The liquid nitrogen was poured out and dry ice packed in (for a detailed step-by-step protocol with images and catalog numbers, please see Rahman (Rahman et al., 2021)). The ice bucket was put on a rotary shaker set at 60 rpm, and rotated for 3 h with the lid on, 1 h with the dry ice poured out but the lid still on, and finally with the lid off until the temperature reached 0°C, typically 1 h. At this point, rather than continue with the freeze-substitution in the mostly anhydrous SubMix, the metal block was surrounded by ice packs to maintain temperatures around 0°C. Then, the SubMix was carefully replaced with previously made and cooled dilutions of the SubMix. Thus, the samples were incubated with 1 ml pre-chilled solutions of SubMix:water ratios of 3:1, 1:1, 1:3 each for 20 min, with the shaker still set at 60 rpm. Finally, the solution was replaced with 1% OsO_4 in 0.1 M sodium cacodylate buffer and allowed to equilibrate to room temperature for 1 h. After this step, the Hua heavy metal staining protocol (Hua et al., 2015) was largely followed, except we used PolyBed resin, hard formulation (resin infiltration details below).

Heavy metal staining

We subsequently performed a modified version of the OTO staining method developed by Hua et al. (2015) for sample metallization of large mouse brain specimens. We removed the OsO_4 solution and placed directly into 2.5% potassium ferrocyanide (#9387-100G; Sigma-Aldrich, St Louis, MO, United States) in 0.1 M sodium cacodylate at pH 7.4 for 90 min at room temperature. We then washed samples (2 × 30 min in water) and transferred samples into 1% TCH (#21900; EMS, Hatfield, PA, United States) in water for 45 min at 40°C. We washed samples (2 × 30 min in water) at room temperature again and transferred samples into 2% OsO_4 in water for 90 min at room temperature. We washed samples (2 × 30 min in water) and transferred samples in an unbuffered 1% aqueous uranyl acetate at 4°C, overnight. The samples in 1% aqueous uranyl acetate were then moved to 50°C for 2 h and washed (2 × 30 min in water) and transferred to lead aspartate in water for 2 h at 50°C. The lead aspartate was prepared with 0.04 g L-aspartic acid (#a9256; Sigma-Aldrich, St Louis, MO, United States) and 0.066 g lead nitrate (#203580-10G; Sigma-Aldrich, St Louis, MO, United States) in 10 ml water and the pH was adjusted to 5.5. Finally, samples were washed (2 × 30 min in water) at room temperature.

Sample dehydration, infiltration and embedding

For *H. vulgare,* prior to infiltration and sample embedment, we performed a graded dehydration series of 30, 50, 70, 80, 90, 100 and

100% acetone at 4°C for 30 min each. The dehydrated samples were exchanged 2X in 100% propylene oxide (#20401; EMS, Hatfield, PA, United States) for 30 min each. Samples were then resin infiltrated with a graded series of 25, 50, 75 and 100% Quetol resin (hard formulation) in propylene oxide without DMP-30 (#14640; EMS, Hatfield, PA, United States) at room temperature for 24 h each step on a rocking platform to enhance resin infiltration. Please note that with our tested plant samples, improved consistency in block quality and uniformity was achieved with use of propylene oxide. However, due to its toxicity, use of propylene oxide is sample dependent and can be omitted and replaced with acetone for resin infiltration steps for less challenging samples. All samples were removed from the mPrep/s capsules at the 50% acetone graded series step and then processed in glass vials for remaining steps. Subsequently, two overnight 100% resin exchanges were made with DMP-30. Finally, samples were embedded in freshly made 100% Quetol using flat embedding molds (#70900; EMS, Hatfield, PA, United States).

For *C. elegans* and *S. cerevisiae*, resin infiltration (using Polybed 812, DDSA, NMA, Polysciences, Inc. BDMA, Electron Microscopy Sciences) was done at room temperature as follows: *C. elegans* - 1:3 resin:acetone for 2 h, 1:1 resin:acetone for 2 h, 3:1 resin:acetone overnight, 100% resin for 5 h. *S. cerevisiae* - 1:3 resin:acetone for 2 h, 1:1 resin:acetone overnight, 3:1 resin:acetone for 3 h, 100% resin overnight. Samples were embedded in molds with fresh resin and polymerized in a 60°C oven for 2 days. The resin embedded samples were trimmed and sectioned to expose the sample on the section face, after which the resin block was cut, mounted on a stub, gold coated and introduced into a CrossBeam550 (ZEISS, Oberkochen, Germany) for high-resolution FIB milling and SEM imaging.

All major steps in sample preparation conditions from fixation to resin are detailed in Supplementary Data S2.

SBF-SEM, FIB-SEM, STEM and TEM image acquisition

Embedded tissues were mounted on a 1.4 mm standard Gatan flat pin using silver conductive epoxy (Chemtronics, CW2400, Kennesaw, GA, United States), trimmed and sectioned using the Leica Ultracut UCT (Leica Microsystems Inc., Buffalo Grove, IL, United States). Due to the extremely opaque nature of the metalized samples prepared in this way, sample quality was assessed with any of the following approaches: whole block imaging by X-ray microscopy or unstained semi thick sections (350 nm) via light microscopy. For TEM ultrathin sections (~70 nm) were imaged at 80 kV using a Hitachi H7650 equipped with an Advanced Microscopy Techniques model XR41 digital camera with 2048 × 2048 pixel resolution and 2 nm pixel size. For SBF-SEM, pins with resin blocks were sputter coated with an ~50 nm layer of gold/palladium. Then, over 1000 sequential images at a 10 k x 10 k pixel resolution and 5 nm x-y, 50 nm z-step size were collected on a ZEISS GeminiSEM 300 SEM at 5 kV (current of 1 pA, and 3 µs dwell time) using a Gatan 3-View® 2XP and local N_2 gas injection via a Focal Charge Compensation (FCC) needle set between 10 and 35%.

FIB-SEM imaging was performed on a Zeiss CrossBeam 550, using the ATLAS3D module, as previously described (Narayan et al., 2014). After the specimen were coated with a patterned platinum and carbon pad, images were acquired at either 3 or 5 nm pixel sampling and 4 µs total pixel dwell time, with electron beam parameters of 1.5 kV and 1 nA and the grid voltage at the in-column backscatter detector set at 900 V. The FIB-SEM was operated at 30 kV, 1.5 µA, with a step size of either 9 nm or 15 nm, respectively. The resulting image stacks were registered, contrast inverted and binned to yield isotropic image volumes. STEM images were acquired on a Zeiss GeminiSEM 450 equipped with a STEM detector and operated at 30 kV. Images were acquired at 3, 10, or 15 nm x-y pixel sampling.

All manuscript figures and corresponding imaging conditions are detailed in Supplementary Data S3.

Image processing, segmentation, reconstruction and visualization of specimen volumes

Three-dimensional volumes of selected specimens were generated using the Object Research Solutions (ORS, Montréal, Canada) Dragonfly Version 2020.2 Build 941. For segmentation and deep learning, an ~180 image 10 k x10 k subset of the full stack was processed using the ORS Segmentation Wizard. Three slices were fully trained representing eight target features. A three-level Sensor 3D deep learning model with a patch size of 64 (Supplementary Data S4) yielded good results for our aqueous OTO freeze-substitution protocol for plant cell walls, mitochondria, Golgi and vesicles in 3D surface renderings (Figure 1E).

Results

FSaqOTO protocol enhanced staining of whole-mount plant tissues

In plants, some of the primary challenges when applying vEM is related to the cell walls, large air voids and water filled vacuoles which impede not only fixation and staining, but also impair overall sample conductivity, resulting in sensitivity to beam damage and charging artifacts. These difficulties are further exacerbated when working with cryo-fixation and freeze-substitution protocols, as organic solvent-based metal staining can be relatively limited due to low solubility, reduced chemical reactivity and overall poor staining of certain cell membranes (i.e., endoplasmic reticulum, nuclear envelope, mitochondria and thylakoids). Recent work applying vEM to freeze-substituted

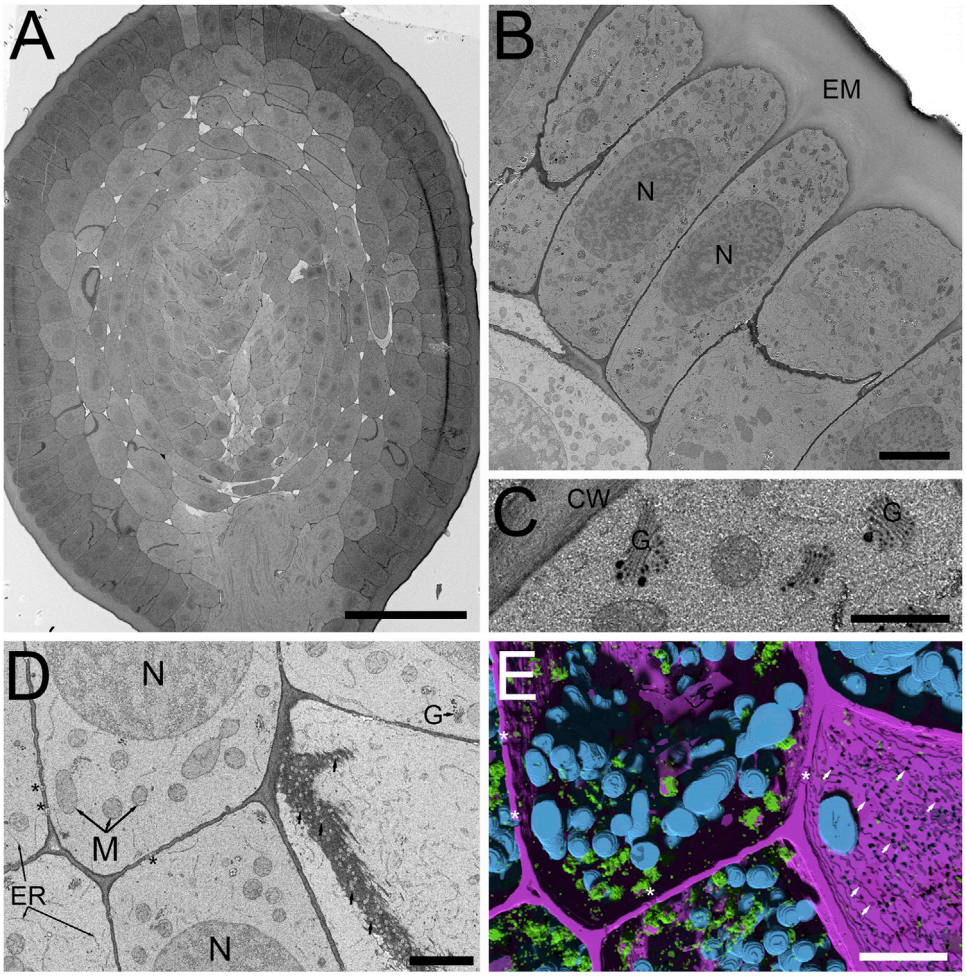

FIGURE 2
SBF-SEM of high-pressure frozen *H. vulgare* root prepared by FSaqOTO. **(A)**. SBF-SEM overview of root cross-section near the root apical meristem prepared by FSaqOTO. Scale = 100 µm. **(B)**. High-resolution SBF-SEM slice from **(A)** showing the outermost protoderm cells with nuclei (N), a normal array of other organelles and covered by a thin electron dense cell wall with a thick extracellular matrix (EM) on the root exterior. Scale = 5 µm. **(C)**. High magnification of a protoderm cell with well-stained Golgi membranes, cell wall and trans-Golgi vesicle contents. Scale = 0.5 µm. **(D)**. Rapidly dividing cells in the ground meristem exhibited well contrasted cell walls (CW) Golgi/vesicles (G) with clearly delineated nuclei (N), mitochondria (M) and electron transparent plasmodesmata (arrows). Scale = 1 µm. **(E)**. 3D rendering of **(D)** using Sensor 3D deep learning segmentation for mitochondria (cyan), Golgi and secretory vesicles (green) and cell wall (magenta) as well as intersecting plasmodesmata voids (asterisks). Scale = 1 µm.

anthers with organic solvent based OTO *en bloc* staining in combination with SBF-SEM and FCC, did improve accessibility for many biological questions in these important plant structures in our hands (Duncan et al., 2022). Despite considerable effort, we were unable to realize the full contrast benefits observed in traditional conventionally fixed specimens using aqueous-based OTO protocols while maintaining a strictly organic solvent-based processing routine after cryo-fixation. However, based on our recent success using conventional fixation with tobacco leaf tissues, the Hua protocol (Hua et al., 2015) was shown to be highly suitable for vEM and X-Ray microscopy. Thus, we reasoned that a modification of our freeze-substitution protocol with a graded transition from an organic solvent-based (in our case acetone) 1% OsO_4 solution (containing water), to full rehydration in 1% OsO_4 aqueous buffer, followed by the Hua heavy metal staining steps, would enhance staining of freeze-substituted plant samples. Indeed, this concept worked with good effect in barley roots (Figure 2) and anthers (Figure 3) with SBF-SEM and FCC. A low magnification cross-section of a HPF FSaqOTO prepared barely root near the meristem (Figure 2A) showed high-density ground cytoplasmic matrix of the epidermal and cortex cells and elevated staining and electron density of the plant cell walls and vacuolar compartments (Figures 2B–D), Golgi apparatus and trans Golgi secretory

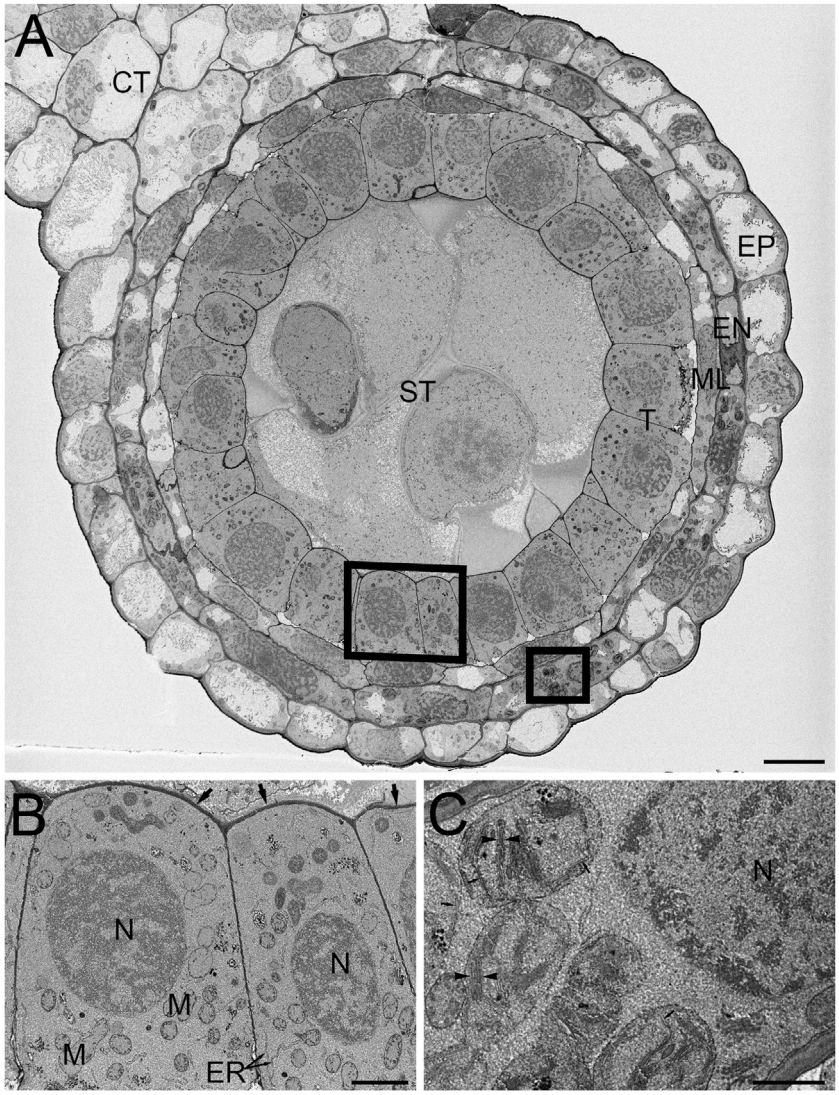

FIGURE 3
SBF-SEM of high-pressure frozen *H. vulgare* anther prepared by FSaqOTO. **(A)**. SBF-SEM overview of anther cross-section showing epidermal (EP), endothecium (EN), middle layer (ML), tapetum (T), sporogenous (ST) and connective tissue (CT). Scale = 10 µm. **(B)**. High magnification slice from region **(A)** (left box) showing the tapetum cells with nuclei (N), mitochondria (M) endoplasmic reticulum (ER) and covered by a thin electron dense cell wall (arrows). Scale = 1 µm. **(C)**. High magnification from region **(A)** (right box) well-stained well-stained chloroplastic membranes (arrows) and grana stacking readily visible (arrowheads). Scale = 0.5 µm.

vesicles (Figure 2C). Additionally, the plasma membrane, mitochondrial membranes and endoplasmic reticulum, while not heavily stained compared to conventional fixation OTO protocols, were readily discerned (Figure 2D). Indeed, this aided the success of deep learning segmentation (Sensor 3D, ORS Dragonfly) for 3D renderings (Figure 2E) of mitochondria (blue), Golgi and secretory vesicles (green) and cell wall (magenta) as well as intersecting plasmodesmata voids (arrows). Interestingly, plasmodesmata, which normally are more electron dense relative to the cell wall via electron microscopy, had inverted contrast (appeared electron transparent in a more electron dense cell wall) (Figure 2D, Supplementary Video S1).

We then evaluated the FSaqOTO protocol for SBF-SEM and FCC on barley anthers, the male reproductive structure responsible for pollen production in plants. A low magnification overview of a single barley anther lobe allowed a clear assessment of the epidermal (EP), endothecium (EN), middle layer (ML), tapetum (T), sporogenous (ST) and connective tissue (CT) (Figure 3A). Similar to root tissues (Figure 2), the FSaqOTO showed elevated electron density in cells with high cytoplasmic density (Figures 3A–C) and highly

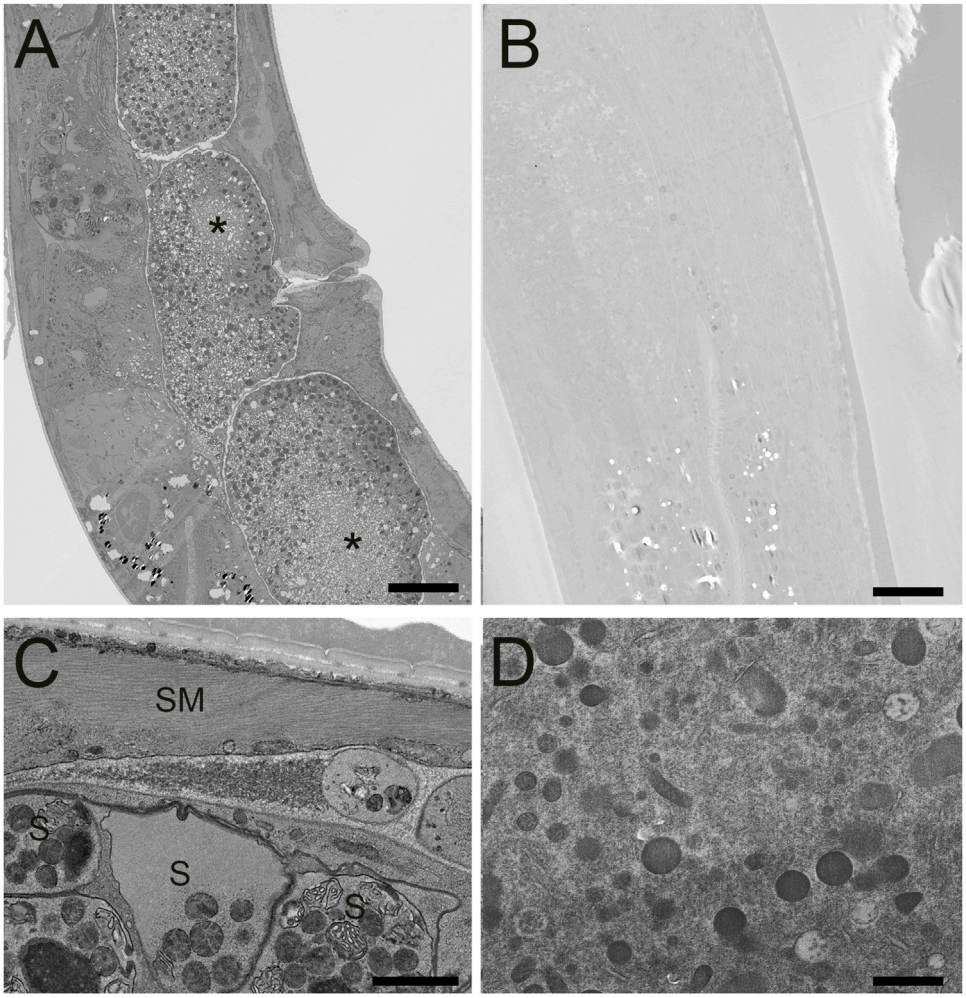

FIGURE 4
STEM of high-pressure frozen *C. elegans* prepared by FSaqOTO and traditional AFS. **(A)**. Low resolution overview longitudinal section of the nematode demonstrated very high contrast staining using FAaqOTO and using identical imaging conditions for **(B)** compared to a traditional AFS staining protocol. Local freeze-damage (asterisk). A and B, scale = 10 µm. **(C)**. FSaqOTO prepped sample at increased magnification with smooth muscle fibers (SM) clearly delineated, and well-stained membranes of spermathecal (S), including the plasma membrane, mitochondria, other membranous organelles. Scale = 1 µm. **(D)**. Corresponding high magnification (compare to **4C**) with identical acquisition conditions of an AFS processed *C. elegans* but with a rescaled histogram demonstrated the normal complement of organelles but with notably relatively much reduced contrast, especially most cell membranes. Scale = 1 µm.

contrasted cell walls. Closer inspection of the tapetum (Figure 3B) revealed good contrast and discrimination of mitochondrial membranes, Golgi apparatus, endoplasmic reticulum and cell wall. While the nuclear envelope was visible, the elevated staining of the heterochromatin and nucleoplasm relative to the nuclear envelope, made it less conspicuous, especially in oblique profiles (Figures 2D),3B,C. In the endothecium, chloroplast thylakoid and grana membranes were readily contrasted and resolved (Figure 3C). Interestingly, in both plant tissues, non-membranous components of the cytoplasm, chloroplast stroma and nucleoplasm appeared to have a granular or textured appearance. In both tissue types, over 1000 consecutive 10,000 × 10,000 pixel serial images were readily obtained at 5 nm x-y pixel resolution and 50 nm z-slice interval.

FSaqOTO protocol enhanced staining of whole-mount *C. elegans*

After verifying improved conductivity and overall elevated staining characteristics of our FSaqOTO protocol using SBF-SEM on challenging plant tissues, we tested if the method also provided similar improved staining with other

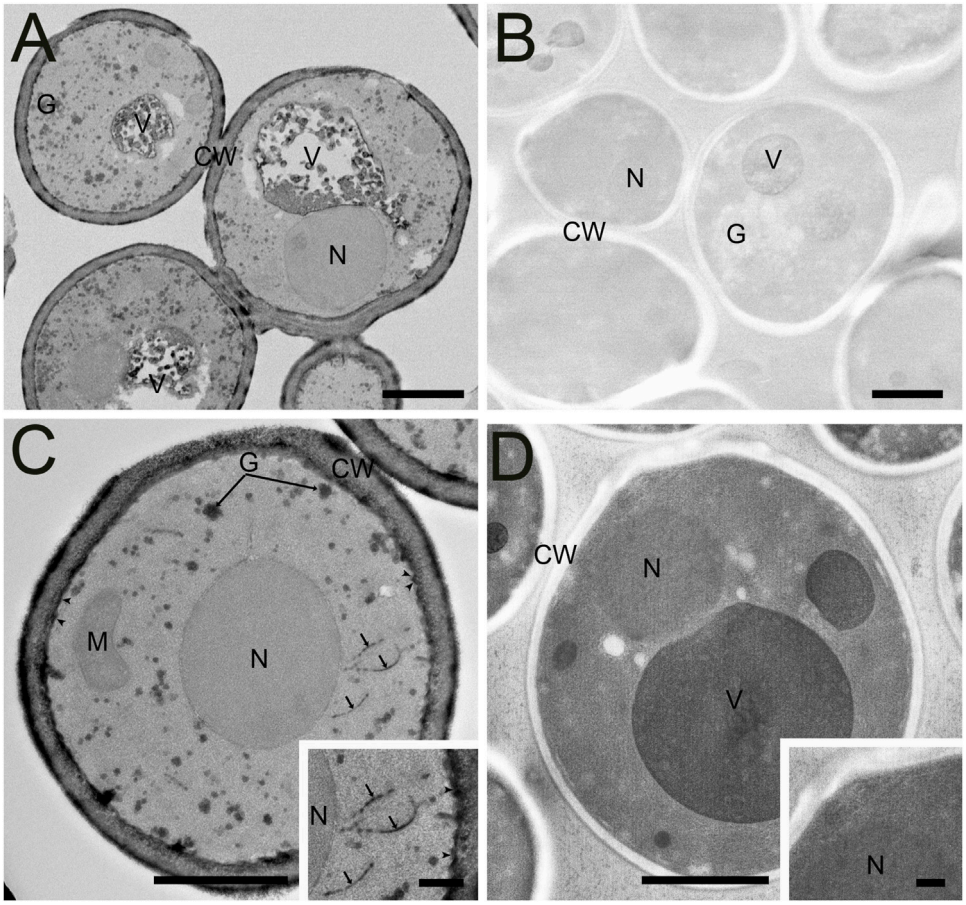

FIGURE 5
Comparison of high-pressure frozen yeast *S. cerevisiae* prepared by FSaqOTO and traditional AFS protocols and imaged via STEM and TEM. **(A)**. Overview STEM image of *S. cerevisiae* demonstrated very high contrast staining of the cell wall (CW), vacuolar contents (V) and their delimiting membrane and glycogen (G) using FAaqOTO and using identical imaging condition for **(B)** compared to a traditional AFS staining protocol. **(C)** and inset. FSaqOTO prepped yeast sample at increased magnification with well-labeled cell walls (CW), glycogen (G), plasmamembrane (arrowheads) cisternae (arrows), and elevated nuclear (N) and mitochondria (M) staining compared to AFS (5D) revealed. Scale = 1 µm. **(D)** and inset. Corresponding high magnification (compare to **5C**) with identical acquisition conditions of an AFS processed yeast but with a rescaled histogram demonstrated the normal complement of organelles but with much reduced contrast, especially cell membranes. **(A-D)** Scale = 1 µm, **(C)** and **(D)** insets = 100 nm.

phylogenetically distinct organisms. Furthermore, we wanted to compare the relative increase and differences in staining of cell structures when a quick freeze-substitution (QFS) protocol was used versus a traditional AFS freeze-substitution protocol. QFS is an excellent option for freeze-substitution in the absence of expensive instrumentation, with the added advantage of speed compared to AFS or freezer-based FS methods. For this work, we chose the model organisms *C. elegans* and *S. cerevisiae*; both represented challenging tests for EM staining protocols on account of their cuticle and cell wall, respectively, and were likely to show significant differences in staining with increased metallization, including vEM. For *C. elegans*, we noted a substantial contrast improvement across the organism when side-by-side AFS versus FSaqOTO comparisons of worm longitudinal sections were made under identical image acquisition conditions (Figures 4A,B). We observed some freezing artifacts of the embryos (Figure 4A asterisk), which is unsurprising given the large size of the intact worm and chitinaceous shell of the embryo. It is likely that freezing was slowest at these depths, significantly away from the freezing surfaces during the HPF step. Nevertheless, at increased magnification, FSaqOTO of *C. elegans* demonstrated high contrast of various tissue and cell features. The fibers of smooth muscle were clearly delineated, and membranes of spermatheca, including the plasma membrane, mitochondria, and membranous organelles were well stained (Figure 4C). Similar to plant tissues, these samples had a textured cytoplasm and nucleoplasm. Under matched

image acquisition conditions (e.g. Figures 4C,D), but rescaled display histogram (Figure 4D only), the traditional AFS protocol lacked strong cytoplasmic and membrane staining, especially for the mitochondria and endoplasmic reticulum.

Like *C. elegans*, a direct comparison of traditional AFS and FSaqOTO protocols with the yeast, *S. cerevisiae*, evaluated by TEM demonstrated a substantial improvement in staining and contrast for FSaqOTO (Figures 5A,B) under identical acquisition and image display conditions. Of note is the strong contrast of the yeast cell wall, glycogen, plasma membrane, cisternae (Golgi equivalent) and vacuolar membrane and its contents (Figures 5A,C) compared to its AFS counterpart (Figures 5B,D). As with plant roots, anthers, and nematode samples, the ground cytoplasmic and nucleoplasm matrices exhibited a textured or slightly granular appearance (Figure 5C). While mitochondria and nuclei staining were notably elevated and visible in FSaqOTO (Figure 5C and inset) versus traditional AFS prepared *S. cerevisiae*, its mitochondrial membranes, nuclear envelope, and endoplasmic reticulum were essentially lacking in the AFS protocol, even after histogram rescaling the identically acquired image (Figure 5D and inset). FIB-SEM serial-sections of the FSaqOTO sample blocks were consistent with TEM data in contrasted structures (Supplementary Video S2).

Discussion

Over the last decade, a number of studies have applied the benefits of improved structural preservation, realized by combining cryo-preservation and freeze-substitution with vEM techniques, including yeast (Wei et al., 2012), nematode (Hall, Hartwieg and Nguyen, 2013; Rahman et al., 2021), plants (Czymmek et al., 2020; Reagan and Burch-Smith, 2022), fruit fly and mouse brain (Tsang et al., 2018), to name just a few. Continued improvements, such as by Guo et al. (2020), applied an organic solvent-based freeze-substitution protocol with a cocktail of OsO_4, tannic acid, uranyl acetate and potassium permanganate (without water) for improved membrane contrast and conductivity with FIB-SEM in a broad array of specimens (mouse brain, plants, algae, yeast and nematodes). Notably, earlier investigations with freeze-substitution with TEM in yeast demonstrated the benefits of adding very small amounts of water to the substitution fluid (1–5%) to specifically enhance the visibility of some cell membranes that were otherwise poorly contrasted (Buser and Walther, 2008). Other studies also showed the benefits of water in the initial freeze-substitution fluid for preserving fluorescent protein signals (and other fluorophores) within acrylic resin blocks for both vEM, lending such samples to more efficient correlative microscopy workflows (Peddie et al., 2014). Furthermore, organic solvent freeze-substitution protocols (with water) followed by the transition to an aqueous buffer and Tokuyasu cryo-sectioning (Ripper, Schwarz and Stierhof, 2008) demonstrated notably improved antigenicity and morphology for several difficult plant, nematode, and fruit fly specimens using the Tokuyasu protocol. A related strategy to combine the benefits of freeze-substitution followed by rehydration with correlative workflows, termed "CryoChem" was recently developed (Tsang et al., 2018). This versatile approach used 0.2% glutaraldehyde plus 5% water in acetone before transitioning to buffer before further processing for fluorescence microscopy (fluorescent protein or DRAQ5), diaminobenzidine (DAB) reaction for APEX2 labeling (Lam et al., 2015; Martell et al., 2017) followed by OTO-based heavy metalization, resin infiltration before X-ray microscopy and/or FIB-SEM.

Our vEM FSaqOTO protocol was differentiated from the other freeze-substitution aqueous rehydration protocols, as we did not have a requirement for non-osmicated tissues to initially preserve fluorescence or other chemistries. As such, we were able to obtain the full benefits of a strong initial fixation with 2% OsO_4 (e.g., potentially reduced extraction) and a simplified protocol. Also of note, structures that are carbohydrate dense usually have very limited osmication and metal staining in standard EM protocols. However, in our work, we found that the addition of potassium ferrocyanide, followed by the direct exchange into OsO_4 (without rinsing) per Hua (Hua et al., 2015), consistently provided very strong contrast of certain carbohydrate dense plant cell walls, yeast cell walls, the lumen of Golgi and secretory vesicles and glycogen (Figures 2B–D; Figures 3A,B; Figures 5A,C). This observation is consistent with the well-known properties of some potassium salts (e.g., potassium permanganate and potassium ferrocyanide) to enhance glycogen contrast in conventional fixation preparations (Revel et al., 1960; Goldfischer et al., 1981). Not surprisingly, for plants, algae and yeast, when potassium permanganate was included in the freeze-substitution fluid of the FIBSEM protocol used by Guo (Guo et al., 2020), a similar increased labeling of cell walls in these organisms and glycogen in yeast was observed.

As mentioned previously, the addition of a small percentage of water to substitution fluid improves certain organelle membrane visibility in freeze-substitution (Buser and Walther, 2008). This is especially evident when we compare chloroplastic, thylakoid and grana membranes, which normally lack significant contrast in non-aqueous freeze-substitution preparations (Bourett et al., 1999; Bobik, Dunlap and Burch-Smith, 2014; Czymmek et al., 2020) but are very conspicuous in most conventional fixation (Kaneko and Walther, 1995; McDonald, 2014; Anderson et al., 2021). While the addition of water alone to the substitution will have some benefit, we observed that in combination with our FSaqOTO approach that chloroplast membranes were very prominent (Figure 3C) with easy visualization of individual stacks of grana membrane and lumen via vEM will open doors to improved resolution, 3D visualization and quantification of these cryo-preserved structures in bulk samples. Furthermore, while not nearly as prominent an improvement as membranes in conventional

fixation OTO methods, overall, our protocol did appear to enhance all cytoplasmic structures including cellular membranes of *C. elegans* and *S. cerevisiae* over our traditional AFS (compare Figures 4A,C with Figures 4B,D; Figures 5A,C with Figures 5B,D). Indeed, much groundwork has been laid in the field for vEM of both *S. cerevisiae* (Winey et al., 1995; Buser and Walther, 2008; Wei et al., 2012; Wu et al., 2020) and *C. elegans* (Hall et al., 2013; Rahman et al., 2020, 2021) with cryo-preservation and freeze-substitution. Specifically, our traditional AFS protocol used here was very similar to substitution chemistry with prior Narayan lab work in *C. elegans*. However, here, virtually all structures (membrane or not) had elevated staining beyond our other standard method (Compare Figures 4A,C with Figures 4B,D, Figures 5A,C with Figures 5B,D) which benefited overall sample signal, contrast, and conductivity for vEM. We wanted to directly compare our FSaqOTO and traditional freeze-substitution AFS protocols using identical image acquisition and display conditions (Compare 4A with 4B, 5A with 5B) via STEM and TEM. Our comparison was specifically optimized for our FSaqOTO samples and then we reproduced the same imaging conditions for the AFS processed samples. We note that for both our *C. elegans* and *S. cerevisiae* specimens, the beam conditions to acquire a high quality FSaqOTO image were inadequate for the AFS processed samples. While it is true that our acquisition conditions could be further optimized for our AFS prepared samples, our comparison sought to allow a side-by-side appreciation of the substantial sample staining improvement using the high-contrast FSaqOTO samples as the baseline. Furthermore, at higher magnification, the freeze-substitution staining of sensitive membrane structures (e.g., thylakoid, endoplasmic reticulum, nuclear envelope) could not be appreciably recovered in either AFS specimen (Compare Figure 4C with Figures 4D, Figure 5C with Figure 5D), even with optimized imaging conditions. The metallization staining gains allowed in our tested samples also enabled the samples to tolerate increased beam dosage without noticeable beam damage artifacts. Indeed, elevation of the sample stain allowed enhanced conductivity, increased and more signal from selected sample features, which resulted in improved overall signal-to-noise and resolution. To appreciate this, comparison with previous work using a polar solvent-based OTO freeze-substitution protocol on *Arabidopsis thaliana* anthers (Czymmek et al., 2020) and using the same SBF-SEM system with FCC, reflected the electron dosage this sample could tolerate (accelerating voltage 2.5 kV, beam current 1 pA, dwell-time 0.8 µs, z-slice 70 nm, pixel size 5 nm pixels). While for the *H. vulgare* anthers analyzed here, we used the same pixel size (5 nm) and probe current (1 pA), but were able to double the accelerating voltage to 5 kV with a 3.75-fold greater dwell-time (3 µs/pixel) as well as reliably cutting at a thinner z-slice of 50 nm (Figures 2, 3, Supplementary Video S1). Likewise, our FSaqOTO prepared yeast 3D FIB-SEM volumes (Supplementary Video S2) versus our previous work using traditional freeze-substitution via FIB-SEM (Wei et al., 2012) had nearly identical beam acquisition conditions for our FSaqOTO samples (accelerating voltage 1.5 keV, probe current ~1 nA). However, at 381 µsec/pixel average total dwell-time/image calculated from the earlier work versus FSaqOTO at 3 µsec/pixel average total dwell-time/image reflects over a 100-fold reduction in average pixel dwell-time/image. Thus, in both the anther and yeast instances, much improved throughput and/or signal-to-noise and could allow significant gains for many other types of similarly cryo-prepared vEM samples.

Not unlike the morphological differences in staining selectivity between conventional fixation OTO versus traditional non-OTO EM protocols, our FSaqOTO protocol had a different appearance and staining pattern when compared to traditional freeze-substitution. Notably, while the overall organelle/membrane enhancement appeared to be improved, the selectivity was less prominent compared to conventional fixation OTO protocols. Strictly aqueous-based conventional fixation OTO protocols have remarkably enhanced membrane contrast (Deerinck et al., 2018; Lippens et al., 2019). While FSaqOTO had a different appearance from other standard freeze-substitution protocols, it was characterized by consistently elevated tissue staining in all tested samples and fixation conditions. Furthermore, we noted that the cytoplasm and nucleoplasm of all cell types exhibited a granular/textured appearance that may reflect some level of nano-aggregation artifact of unknown origin. While this granular phenomenon may in part aid in the improved overall sample metallization and conductivity, it brings attention to the limits of the approach for certain questions that require high-fidelity, high-resolution ultrastructural studies.

Overall, our improved FSaqOTO method allowed more reliable vEM data acquisition and extended the experimental possibilities for cryo-preserved samples that are otherwise limited by low contrast and low conductivity organic solvent-based staining protocols. The addition of water in the substitution fluid and a straightforward solvent to water transition for heavy metal staining enabled noteworthy improvement in contrast with many structures. Furthermore, these samples realized a much-improved sample tolerance to electron beam dosage which enabled longer integration times and increased resolution resulting in better signal-to-noise for a given pixel size. Alternatively, the approach can allow increased throughput for freeze-substituted vEM studies enabling more samples or larger volumes imaged per unit time. Finally, there are numerous opportunities for the modification and/or improvement of our staining strategy via adjustments to the substitution fluid (Ripper et al., 2008; Guo et al., 2020), aqueous OTO and metalization steps (Deerinck et al., 2018; Genoud et al., 2018) and/or combination with correlative approaches (Caplan et al., 2011; Tsang et al., 2018; Duncan et al., 2022). Ultimately, we hope that our modified freeze-substitution vEM staining strategy will stimulate more labs to explore other recipes for improved selection and enhancement of target cell structures while

maintaining the full benefits of cryo-preservation and freeze-substitution.

Data availability statement

The raw data supporting the conclusions of this article will be made available by the authors, without undue reservation.

Author contributions

KC conceived of approach, SB, HB, VB, KC, KD, and KN performed sample preparation and/or imaging. KC and KN wrote and edited manuscript. SB, KD, and BM edited manuscript.

Acknowledgments

We thank Mohammad Rahman and Orna Cohen-Fix, NIDDK, for the *C. elegans* samples, and Lucyna Lubkowska and Mikhail Kashlev, NCI, for the yeast samples. We acknowledge the Advanced Bioimaging Laboratory (RRID: SCR_018951) at the Donald Danforth Plant Science Center for support with sample preparation including screening samples with LEO 912AB TEM acquired through an NSF Major Research Instrumentation grant (DBI-0116650). We acknowledge the DOE BER (DBI-0116650) to KJC and USDA NIFA Grant Nos.2019-67013-29010 to B. C. Meyers. We thank Steven Goodman and Microscopy Innovations, Inc. For guidance on handling mPrep/s capsules under cryo-genic temperatures. We also thank Joel Mancuso and Ruth Redman (Zeiss) for excellent support and Lisa Chan (Zeiss) collecting the high-resolution SBF-SEM datasets of *H. vulgare* anther and root samples. This project has been funded in whole or in part with Federal funds from the National Cancer Institute, National Institutes of Health, under Contract Nos. 75N91019D00024. The content of this publication does not necessarily reflect the views or policies of the Department of Health and Human Services, nor does mention of trade names, commercial products, or organizations imply endorsement by the U.S. Government.

Conflict of interest

The authors declare that the research was conducted in the absence of any commercial or financial relationships that could be construed as a potential conflict of interest.

Publisher's note

All claims expressed in this article are solely those of the authors and do not necessarily represent those of their affiliated organizations, or those of the publisher, the editors and the reviewers. Any product that may be evaluated in this article, or claim that may be made by its manufacturer, is not guaranteed or endorsed by the publisher.

Supplementary material

The Supplementary Material for this article can be found online at: https://www.frontiersin.org/articles/10.3389/fcell.2022.933376/full#supplementary-material

References

Anderson, C. M., Mattoon, E. M., Zhang, N., Becker, E., McHargue, W., Yang, J., et al. (2021). High light and temperature reduce photosynthetic efficiency through different mechanisms in the C4 model Setaria viridis. *Commun. Biol.* 4 (1), 1092. doi:10.1038/s42003-021-02576-2

Bobik, K., Dunlap, J. R., and Burch-Smith, T. M. (2014). Tandem high-pressure freezing and quick freeze substitution of plant tissues for transmission electron microscopy. *J. Vis. Exp.* (92), e51844. doi:10.3791/51844

Bourett, T. M., Czymmek, K. J., and Howard, R. J. (1999). Ultrastructure of chloroplast protuberances in rice leaves preserved by high-pressure freezing. *Planta* 208 (4), 472–479. doi:10.1007/s004250050584

Buser, C., and Walther, P. (2008). Freeze-substitution: The addition of water to polar solvents enhances the retention of structure and acts at temperatures around -60 degrees C. *J. Microsc.* 230 (2), 268–277. doi:10.1111/j.1365-2818.2008.01984.x

Caplan, J., Niethammer, M., Taylor, R. M., and Czymmek, K. J. (2011). The power of correlative microscopy: Multi-modal, multi-scale, multi-dimensional. *Curr. Opin. Struct. Biol.* 21 (5), 686–693. doi:10.1016/j.sbi.2011.06.010

Collman, F., Buchanan, J., Phend, K. D., Micheva, K. D., Weinberg, R. J., and Smith, S. J. (2015). Mapping synapses by conjugate light-electron array tomography. *J. Neurosci.* 35 (14), 5792–5807. doi:10.1523/JNEUROSCI.4274-14.2015

Czymmek, K., Sawant, A., Goodman, K., Pennington, J., Pedersen, P., Hoon, M., et al. (2020). "Imaging plant cells by high-pressure freezing and serial block-face scanning electron microscopy," in *Springer protocols, plant Endosomes*. Editor M. S. Ortegui (Springer US), 69–81. doi:10.1007/978-1-0716-0767-1_7

Deerinck, T. J., Shone, T. M., Bushong, E. A., RamachandRa, R., Peltier, S. T., and Ellisman, M. H. (2018). High-performance serial block-face SEM of nonconductive biological samples enabled by focal gas injection-based charge compensation. *J. Microsc.* 270 (2), 142–149. doi:10.1111/jmi.12667

Denk, W., and Horstmann, H. (2004). Serial block-face scanning electron microscopy to reconstruct three-dimensional tissue nanostructure. *PLoS Biol.* 2 (11), e329. doi:10.1371/journal.pbio.0020329

Duncan, K. E., Czymmek, K. J., Jiang, N., Thies, A. C., and Topp, C. N. (2022). X-ray microscopy enables multiscale high-resolution 3D imaging of plant cells, tissues, and organs. *Plant Physiol.* 188 (2), 831–845. doi:10.1093/plphys/kiab405

Genoud, C., Titze, B., Graff-Meyer, A., and Friedrich, R. W. (2018). Fast homogeneous *en bloc* staining of large tissue samples for volume electron microscopy. *Front. Neuroanat.* 12, 76. doi:10.3389/fnana.2018.00076

Gilkey, J. C., and Staehelin, L. A. (1986). Advances in ultrarapid freezing for the preservation of cellular ultrastructure. *J. Electron Microsc. Tech.* 3 (2), 177–210. doi:10.1002/jemt.1060030206

Goldfischer, S., Kress, Y., Coltoff-Schiller, B., and Berman, J. (1981). Primary fixation in osmium-potassium ferrocyanide: The staining of glycogen, glycoproteins, elastin, an intranuclear reticular structure, and intercisternal trabeculae. *J. Histochem. Cytochem.* 29 (9), 1105–1111. doi:10.1177/29.9.6169760

Guérin, C. J., Kremer, A., Borghgraef, P., and Lippens, S. (2019). Targeted studies using serial block face and focused ion beam scan electron microscopy. *J. Vis. Exp.* (150). doi:10.3791/59480

Guo, J., Wang, G., Tang, W., Song, D., Wang, X., Hong, J., et al. (2020). An optimized approach using cryofixation for high-resolution 3D analysis by FIB-SEM. *J. Struct. Biol.* 212 (1), 107600. doi:10.1016/j.jsb.2020.107600

Hall, D. H., Hartwieg, E., and Nguyen, K. (2013). *WormAtlas anatomical methods - OTO fixation for SEM blockface imaging*. WormAtlas: L. A. Herndon. doi:10.3908/wormatlas.9.8

Hoffman, D. P., Shtengel, G., Xu, C. S., Campbell, K. R., Freeman, M., Wang, L., et al. (2020). Correlative three-dimensional super-resolution and block-face electron microscopy of whole vitreously frozen cells. *Science*, 367 (6475), eaaz5357. doi:10.1126/science.aaz5357

Hua, Y., Laserstein, P., and Helmstaedter, M. (2015). Large-volume *en-bloc* staining for electron microscopy-based connectomics. *Nat. Commun.*, 6, 1–7. doi:10.1038/ncomms8923

Kaneko, Y., and Walther, P. (1995). Comparison of ultrastructure of germinating pea leaves prepared by high-pressure freezing-freeze substitution and conventional chemical fixation. *J. Electron Microsc.* 44 (2), 104–109. doi:10.1093/oxfordjournals.jmicro.a051149

Lam, S. S., Martell, J. D., Kamer, K. J., Deerinck, T. J., Ellisman, M. H., Mootha, V. K., et al. (2015). Directed evolution of APEX2 for electron microscopy and proximity labeling. *Nat. Methods* 12 (1), 51–54. doi:10.1038/nmeth.3179

Lippens, S., Kremer, A., Borghgraef, P., and Guérina, C. J. (2019). Serial block face-scanning electron microscopy for volume electron microscopy. *Methods Cell Biology,Three-Dimensional Electron Microsc.*, 69–85. doi:10.1016/bs.mcb.2019.04.002

Mahamid, J., et al. (2015). A focused ion beam milling and lift-out approach for site-specific preparation of frozen-hydrated lamellas from multicellular organisms. *J. Struct. Biol.*, 192. Elsevier, 262–269. doi:10.1016/j.jsb.2015.07.012

Martell, J. D., Deerinck, T. J., Lam, S. S., Ellisman, M. H., and Ting, A. Y. (2017). Electron microscopy using the genetically encoded APEX2 tag in cultured mammalian cells. *Nat. Protoc.* 12 (9), 1792–1816. doi:10.1038/nprot.2017.065

McDonald, K. L. (2014). Out with the old and in with the new: Rapid specimen preparation procedures for electron microscopy of sectioned biological material. *Protoplasma* 251 (2), 429–448. doi:10.1007/s00709-013-0575-y

Mcdonald, K. L., and Webb, R. I. (2011). Freeze substitution in 3 hours or less. *J. Microsc.* 243 (3), 227–233. doi:10.1111/j.1365-2818.2011.03526.x

Mendenhall, J. M., Kuwajima, M., and Harris, K. M. (2017). Automated serial section large-field transmission-mode scanning electron microscopy (tSEM) for volume Analysis of Hippocampus ultrastructure. *Microsc. Microanal.* 23 (S1), 562–563. doi:10.1017/S143192761700349X

Narayan, K., Danielson, C. M., Lagarec, K., Lowekamp, B. C., Coffman, P., Laquerre, A., et al. (2014). Multi-resolution correlative focused ion beam scanning electron microscopy: Applications to cell biology. *J. Struct. Biol.*, 185. Elsevier, 278–284. doi:10.1016/j.jsb.2013.11.008

Narayan, K., and Subramaniam, S. (2015). Focused ion beams in biology. *Nat. Methods*, 12, 1021–1031. doi:10.1038/nmeth.3623

Nguyen, H. B., Thai, T. Q., Saitoh, S., Wu, B., Saitoh, Y., Shimo, S., et al. (2016). Conductive resins improve charging and resolution of acquired images in electron microscopic volume imaging. *Sci. Rep.* 6, 1–10. doi:10.1038/srep23721

Otegui, M. S. (2020) 'Electron tomography and immunogold labeling of plant cells'. *Methods Cell Biology,Plant Cell Biol.* 21–36. doi:10.1016/bs.mcb.2020.06.005

Peddie, C. J., Blight, K., Wilson, E., Melia, C., Marrison, J., Carzaniga, R., et al. (2014). Correlative and integrated light and electron microscopy of in-resin GFP fluorescence, used to localise diacylglycerol in mammalian cells. *Ultramicroscopy* 143 (100), 3–14. doi:10.1016/j.ultramic.2014.02.001

Rahman, M., Chang, I. Y., Cohen-Fix, O., and Narayan, K. (2021). A workflow for high-pressure freezing and freeze substitution of the *Caenorhabditis elegans* embryo for ultrastructural analysis by conventional and volume electron microscopy. *Bio. Protoc.* 11 (7), e3981. doi:10.21769/BioProtoc.3981

Rahman, M., Chang, I. Y., Harned, A., Maheshwari, R., Amoateng, K., Narayan, K., et al. (2020). C. elegans pronuclei fuse after fertilization through a novel membrane structure. *J. Cell Biol.* 219 (2), e201909137. doi:10.1083/jcb.201909137

Reagan, B. B., and Burch-Smith, T. M. (2022). "Focused ion beam-scanning electron microscopy for investigating plasmodesmal densities," in *Plasmodesmata: Methods and protocols*. Editors M.Y. HeinleinBenitez-Alfonso. 978-1-0716-2131-8.

Revel, J. P., Napolitano, L., and Fawcett, D. W. (1960). Identification of glycogen in electron micrographs of thin tissue sections. *J. Biophys. Biochem. Cytol.* 8 (3), 575–589. doi:10.1083/jcb.8.3.575

Ripper, D., Schwarz, H., and Stierhof, Y.-D. (2008). Cryo-section immunolabelling of difficult to preserve specimens: Advantages of cryofixation, freeze-substitution and rehydration. *Biol. Cell* 100 (2), 109–123. doi:10.1042/bc20070106

Smith, S. J. (2018). Q& a: Array tomography', *BMC biology*. *BMC Biol.* 16 (1), 98. doi:10.1186/s12915-018-0560-1

Sydor, A. M., Czymmek, K. J., Puchner, E. M., and Mennella, V. (2015). Super-resolution microscopy: From single molecules to supramolecular assemblies. *Trends Cell Biol.* 25 (12), 730–748. doi:10.1016/j.tcb.2015.10.004

Titze, B., and Genoud, C. (2016). Volume scanning electron microscopy for imaging biological ultrastructure. *Biol. Cell* 108 (11), 307–323. doi:10.1111/boc.201600024

Tsang, T. K., Bushong, E. A., Boassa, D., Hu, J., Romoli, B., Phan, S., et al. (2018). High-quality ultrastructural preservation using cryofixation for 3d electron microscopy of genetically labeled tissues. *eLife* 7, e35524. doi:10.7554/eLife.35524

Watanabe, S., Lehmann, M., Hujber, E., Fetter, R. D., Richards, J., Sohl-Kielczynski, B., et al. (2014). Nanometer-resolution fluorescence electron microscopy (nano-EM) in cultured cells. *Methods Mol. Biol.* 1117, 503–526. doi:10.1007/978-1-62703-776-1_22

Wei, D., Jacobs, S., Modla, S., Zhang, S., Young, C. L., Cirino, R., et al. (2012). High-resolution three-dimensional reconstruction of a whole yeast cell using focused-ion beam scanning electron microscopy. *BioTechniques* 53 (1), 41–48. doi:10.2144/000113850

Winey, M., Mamay, C. L., O'Toole, E. T., Mastronarde, D. N., Giddings, T. H., McDonald, K. L., et al. (1995). Three-dimensional ultrastructural analysis of the *Saccharomyces cerevisiae* mitotic spindle. *J. Cell Biol.* 129 (6), 1601–1615. doi:10.1083/jcb.129.6.1601

Wu, G.-H., Mitchell, P. G., Galaz-Montoya, J. G., Hecksel, C. W., Sontag, E. M., Gangadharan, V., et al. (2020). Multi-scale 3D cryo-correlative microscopy for vitrified cells. *Structure* 28, 1231–1237. doi:10.1016/j.str.2020.07.017

Frontiers in
Cell and Developmental Biology

Explores the fundamental biological processes of life, covering intracellular and extracellular dynamics.

The world's most cited developmental biology journal, advancing our understanding of the fundamental processes of life. It explores a wide spectrum of cell and developmental biology, covering intracellular and extracellular dynamics.

Discover the latest Research Topics

See more →

Frontiers

Avenue du Tribunal-Fédéral 34
1005 Lausanne, Switzerland
frontiersin.org

Contact us

+41 (0)21 510 17 00
frontiersin.org/about/contact